Functional Inorganic Nanoparticle/Polymer Hybrid Materials: Synthesis, Characterization and Self-assembly Behavior

Submitted in partial fulfillment of the requirements for the degree of

Doctor of Philosophy in

Department of Chemistry

Zongyu Wang

Carnegie Mellon University

Pittsburgh, PA

December 2019

Abstract

This thesis describes the preparation of ZnO/polymer hybrid and polymer grafted silica particle brushes and explores their properties and applications.

The introductory chapter (Chapter 1) reviews the history and development of ZnO/polymer hybrid synthesis. The synthetic approaches include “grafting from”, “grafting onto” and “polymer templates” methods.

Chapters 2-6 cover the synthesis of polymer capped ZnO nanocrystals by the “ligand exchange” method and their applications. In Chapter 2, the preparation of PSAN capped ZnO nanocrystals from octylamine capped ZnO nanoparticles by the “ligand exchange” method is discussed. The morphologies of the product were tuned by the ratios of ZnO nanoparticle/polymer ligands in the reaction mixture. Chapter 3 shows a detailed characterization of the polymer ligands/surfactants capped ZnO nanocrystals by MALDI-TOF mass spectrum. ZnO-based materials exhibit excellent optical, thermal, photocatalytic and electrical properties. Chapters 4-6 discuss three important properties and applications of the obtained nano-ZnO/polymer composites, which include high refractive index glass fillers, photocatalyst, and high stability ZnO/carbon supercapacitors.

The second part of the thesis (Chapters 7-13) focuses on the study of polymer grafted silica particle brushes. By using surface-initiated atom transfer polymerization, polymer chains were grown from the surfaces of nanoparticles. With covalent bonding, comparing to ZnO/polymer hybrids synthesized by the “ligand exchange” method, the chemistry to synthesize polymer grafted silica particle brush system is more robust and well established. Chapters 7-8 illustrate the synthesis of SiO_2-*g*-PMMA/PS particle brushes by low ppm catalyst ATRP. The

effect of initiator and catalyst concentrations on the polymerization was investigated. Chapter 9 describes the synthesis of ultra-high molecular weight SiO_2-*g*-PMMA particle brushes and Chapter 10 presents the mechanical properties of SiO_2-*g*-PMMA/PS particle brushes with different grafting densities. The preparation and phase separation study of SiO_2-*g*-PMMA-*b*-PS block copolymer particle brushes is included in Chapter 11. Their unique self-assembly behavior is explored. At last, the study of gradient copolymer grafted silica particle brushes are covered in Chapter 12-13. Chapter 12 emphasizes the synthesis of SiO_2-*g*-PBA-*grad*-PMMA particle brushes by semi-batch copolymerization method, and Chapter 13 highlights their mechanical properties and compositionally sensitive self-healing features.

Two published works with minor relevance to this thesis (polymerization-induced self-assembly of acrylonitrile and organoSiO_2-*g*-PMMA particle brushes synthesis) are included as appendices.

Acknowledgments

I would like to express my sincerest appreciation to my advisors Prof. Krzysztof Matyjaszewski and Prof. Michael Bockstaller, for their support and guidance during my Master's and Ph.D. study at Carnegie Mellon University. I joined Bockstaller's Lab 7 years ago and transferred to Matyjaszewski's Lab 6 years ago. Prof. Matyjaszewski and Prof. Bockstaller's intelligence, integrity, and devotion to science have always been inspiring. With their advice, patience, and instruction, I learned so much from them and become a better researcher.

I would like to thank my family, my parents, and my twin brother, for their constant encouragement and support.

I would like to express my appreciation for my committee members: Prof. Robert Tilton, who has agreed to be one of my Ph.D. defense committee members and Prof. Rongchao Jin, the chair of my committee, who gave me many research advice during my graduate seminar, progress report exam, and original proposal.

At last, I would like to thank my collaborators and friends at CMU. Collaborations have always been a big part of my research. Both Matyjaszewski and Bockstaller's group members have provided a very warm and motivated atmosphere. I received tremendous help from our group members, the discussion and brainstorming in the office and lab. Specifically, I would like to thank Dr. Clare Mahoney and Dr. Chin Ming Hui, for their guidance and teaching at my initial stage of research; Dr. Jiajun Yan, for being the best officemate for four and half years; Sipei Li, for being such a good friend all the time; and our reliable collaborators from Bockstaller's group, Zhao Lu, Dr. Jaejun Lee, and Yuqi Zhao.

Table of Contents

List of Abbreviations

2BiB	α-bromoisobutyryl bromide
AA	acrylic acid
AFM	atomic force microscope
AGET	activator generated by electron transfer
AN	acrylonitrile
ARGET	activator regenerated by electron transfer
ATRP	atom transfer radical polymerization
BA	*n*-butyl acrylate
BiB	α-bromoisobutyrate
BiBADA	12-(α-bromoisobutyramido)dodecanoic acid
BPA	α-bromophenylacetate
BPADA	12-(α-bromophenylacetamido)dodecanoic acid
BPN	2-bromopropionitrile
bpy	2,2'-bipyridine

conv.	conversion
CPB	concentrated polymer brush
CRP	controlled radical polymerization
CTA	chain transfer agent
CuAAC	copper-catalyzed alkyne-azide cycloaddition
CV	cyclic voltammetry
d_{TEM}	mean diameter measured by transmission electron microscope
$Đ$	dispersity
DCM	methylene chloride
D_h	hydrodynamic diameter
DLS	dynamic light scattering
DMA	dimethylacetamide
DMAP	4-dimethylaminopyridine
DMF	dimethylformamide
DMSO	dimethylsulfoxide
dNbpy	4,4'-di(*n*-nonyl)-2,2'-bipyridine
DP	degree of polymerization

DPE	diphenyl ether
DP_t	target degree of polymerization
dRI	differential refractive index
DSC	differential scanning calorimetry
DVB	divinylbenzene
E	Young's modulus
*e*ATRP	electrochemically-mediated atom transfer radical polymerization
EBiB	ethyl α-bromoisobutyrate
EBPA	ethyl 2-bromo-2-phenylacetate
EDC	1-ethyl-3-(3-dimethylaminopropyl)carbodiimide
equiv	equivalence
f	weight fraction
FRP	free radical polymerization
GPC	gel permeation chromatography
H	hardness
I	initiator
ICAR	initiators for continuous activator regeneration

J	coupling constant
k	rate constant
K	equilibrium constant
L	ligand
LCST	lower critical solution temperature
MA	methyl acrylate
Me_6TREN	tris(2-(dimethylamino)ethyl)amine
mechanoATRP	mechanically mediated atom transfer radical polymerization
M	monomer
MI	macroinitiator
MMA	methyl methacrylate
M_n	number-average molecular weight
MW	molecular weight
M_w	weight-average molecular weight
MWD	molecular weight distribution
M_w/M_n	dispersity
n	refractive index

N	degree of polymerization
N_A	Avogadro's number
N_c	critical degree of polymerization
N_e	entanglement limit
NMR	nuclear magnetic resonance
NHS	*N*-hydroxysuccinimde
NP	nanoparticle
OA	octylamine
PAA	poly(acrylic acid)
PBA	poly(*n*-butyl acrylate)
PDMS	poly(dimethylsiloxane)
photoATRP	photochemically mediated atom transfer radical polymerization
PMDETA	*N*,*N*,*N*',*N*'',*N*''-pentamethyldiethylenetriamine
PMMA	poly(methyl methacrylate)
PS	polystyrene
PSAN	poly(styrene-*co*-methacrylate)
P*t*BA	poly(*tert*-butyl acrylate)

R_0	particle radius
r_1	longitudinal relaxivity
r_2	transverse relaxivity
RAFT	reversible addition-fragmentation chain-transfer
RDRP	reversible deactivation radical polymerization
r.t.	room temperature
R_p	rate of polymerization
S	styrene
SARA	supplemental activator and reducing agent
SDPB	semi-dilute polymer brush
SEC	size exclusion chromatography
SEM	scanning electron microscope
SI-ATRP	surface-initiated atom transfer radical polymerization
SI-CRP	surface-initiated controlled radical polymerization
SI-RAFT	surface-(initiated) reversible addition-fragmentation chain-transfer
$Sn(EH)_2$	tin(II) 2-ethylhexanoate
t	time

*t*BA	*tert*-butyl acrylate
TEA	triethylamine
TEM	transmission electron microscope
temp.	temperature
TFA	trifluoroacetic acid
T_g	glass transition temperature
TGA	thermogravimetric analysis
THF	tetrahydrofuran
TPMA	tris(2-pyridinylmethyl)amine
TSI	thermal self-initiation
UV	ultraviolent
UV-vis	ultraviolent-visible spectrometer
V	volume
V_e	elution volume
vol	volume
wt	weight
XRD	x-ray diffraction

ZnO	zinc oxide
$Zn(EH)_2$	zinc 2-ethylhexanoate
$Zn(OAc)_2$	zinc acetate
ρ	density
σ	grafting density
ϕ	volume fraction

List of Figures

List of Tables_Toc24812584_Toc24812585

List of Schemes

Chapter 1 ZnO/Polymer Hybrid Materials

1.1. Zinc oxide as multifunctional materials

ZnO nanoparticles are still a hot area for research even though the ample work has been done by researchers across the world. It is a versatile material for doping of different transition metals for other metal oxides. Having a larger family of morphological structures, high electron mobility, and n-type carrier defects, it is suitable for many applications such as memory devices, spintronics, optoelectronic devices, solar cells, and sensors.[1]

Zinc oxide is an inorganic compound found in powder form which is white in color and insoluble in water. In powder form, it is mainly used in lubricants, paints, rubber, ointments, batteries, glass, cosmetics, and paper. Zinc oxide is an II-VI binary semiconducting material having pyroelectric and piezoelectric properties. In the nano range, it has a bandgap of 3.37,eV,[2] large exciton binding energy 60 meV,[3] and Hall mobility of the order of 200 cm^2 V^{-1} S^{-1},[4-5] at room temperature. It is useful for making optoelectronic devices, laser diodes,[6-8] LEDs (light-emitting diodes),[9-10] ultraviolet photodetectors,[11-12] and electronic devices such as varistors,[13-15] diodes, and transistors.[16] Its piezoelectric properties[17], large electromechanical coupling, and lack of center of symmetry make it a promising material for piezoelectric transducers,[18-19] sensors, and mechanical actuators.[20] The unique nanostructures indicate that ZnO probably has the riches family of nanostructures among all materials, both in structures and in properties.[21-28] In comparison to other metal oxide semiconductors, ZnO has a high redox potential, superior physical and chemical stability, and nontoxicity. Photocatalytic activity[28-31] of ZnO depends on various factors such as phase purity, surface areas, crystalline size, nature of dopants, and method of preparation. The sensing ability is mainly dependent upon the variation of carrier

defects without the presence of sensing gases. These carrier defects are mainly oxygen vacancies. The oxygen vacancies can be significantly increased by doping and thus the performance of devices can be further enhanced. Performance of optoelectronic devices, which mainly depends upon the electron or hole mobility,[32] in different types of semiconductors can be improved by increasing mobility.[33]

Nanotechnology can be applied to ZnO in many areas.[34-36] Nanotechnology deals with particles in the range of 1-100 nm. As the size of particle decreases, the number of atoms or molecules available at the surface in comparison to the atoms or molecules inside the bulk increases. In such conditions, we have to consider the contribution of surface particles in different physical properties. At such a small scale quantum size, effect,[37-39] comes into effect, which alters catalytic activity, chemical reactivity, optical properties, electrical and conductivity, heat capacity,[40], etc.

The inorganic-polymer hybrid nanomaterials present the properties of both the inorganic nanoparticles and the polymer by combining thermal stability, mechanical strength, electrical and optical properties with flexibility and the capacity.[41] Therefore, these nanocomposite particles offer many potential applications in such diverse areas as photocatalysis,[42] lithography,[43] optics,[44] biotechnology[45], and electronic devices.[46] However, inorganic nanoparticles are very easy to agglomerate in media and show poor dispersion in polymers, hence the applications of many nanosized particles are largely limited. From the practical point of view, these nanoparticles have to be dispersed in the polymer matrix to form nanocomposites for the purpose of gaining stability and processability.[47] To prevent the formation of agglomerated nanoparticle in polymers, the combination of inorganic particles with polymers is usually accomplished by surface modification. The grafting of polymers onto inorganic

nanoparticles is one of the most effective and versatile methods for this modification purpose. It can significantly enhance the stability of nanoparticles dispersing in polymer solvents by increasing the affinity of the surface for organic substances.[48]

There are two methods of surface grafting: one is that the end-functionalized polymers are grafted onto the surface of inorganic particles, the other is that the polymer is grafted from (i.e. grown) the surface of inorganic particles.[49-50] As regards with the first method, metal oxide nanoparticles having reactive hydroxyl groups on the surfaces, surface grafting is carried out by the reaction of end-reactive polymers with isocyanate, alkoxysilane, etc. with hydroxyl groups.[51-52] Concerning the second method, the polymerization of vinyl monomers can be initiated by introducing the reactive groups such as azo groups[53] peroxy ester group[54] onto the surface of inorganic particles and then converted to initiating sites. In addition, the double bonds introduced onto the surface of inorganic particles can also copolymerize with other vinyl monomers,[55-56] The introduction of the initiating groups onto the surface of the inorganic particles usually need multi-step synthesis, while the introduction of the double bonds can be achieved by one-step synthesis using silane coupling agent containing double bonds to modify the surface of the inorganic particles.

1.2. Synthesis of ZnO/polymer hybrid materials

One approach to modify the surfaces of inorganic materials is based on grafting synthetic polymers to the substrate surface, which enhances the chemical functionality and alters the surface topology of the native inorganic materials. Such polymer grafted inorganic nanoparticles are considered to be organic-inorganic nanocomposite particles.[57-60] A higher percentage of successful grafts can be obtained in polymer grafted inorganic particles by initiating the graft polymerization from initiating groups placed on the particles' surfaces. The method of producing

controlled radical polymerization from the surfaces of silica nanoparticles using atom transfer radical polymerization systems was proposed by von Werne and Patten.[61]

Grafting from

The surface modification of nanoparticles by chemical treatments is a useful method to improve the dispersion stability of nanoparticles in various liquid media. (**Figure 1.1**) The concept of silane coupling agents to improve the compatibility between the particle and polymer surfaces and the properties of composite materials have been reported.[62-63] The modified nanoparticles behave differently within organic solvents or polymer matrices compared to unmodified nanoparticles, e.g. the modified nanoparticles show comparatively better dispersion in both media. The surface of nanoparticles may also be modified through reactions with metal alkoxides, epoxides, such as propylene oxide, and alkyl or aryl isocyanates.[64]

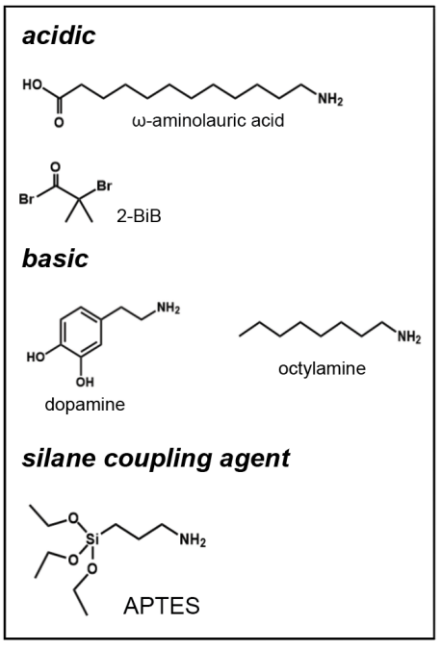

Figure 1.1. Surface modifications of ZnO nanoparticles by chemical treatments.

The selection of a suitable coupling agent is important for a successful "grafting-from" method. In **Scheme 1.1**, 2-BiB was chosen as a surface modifier for pristine ZnO nanoparticles to introduce active -Br onto the surface of nanoparticles which were used as ATRP initiators. Sato and coworkers reported the synthesis of carbazole polymer (PCEM)/ZnO nanocomposites, with high molecular weight PCEM with narrow molecular weight distributions, and ZnO nanoparticles were successfully prepared by atom transfer polymerization initiated by 2-Bromo-2-methylpropionyl group introduced directly onto the ZnO nanoparticle surfaces (**Figure 1.2**a).[65] Hu and coworkers reported the synthesis of poly(poly(ethylene glycol) methyl ether monomethacrylate) (PPEGMA) grafted zinc oxide (ZnO) nanoparticles via the surface-initiated atom transfer radical polymerizations (ATRP) from the surfaces functionalized ZnO nanoparticles. The 2-bromoisobutyrate (BIB) was immobilized onto the surface of the ZnO nanoparticles through the reaction between 2-bromoisobutyrate bromide (BIBB) and the hydroxyl groups on nanoparticles, serving as the initiator to induce the ATRP of poly(ethylene glycol) monomethacrylate (PEGMA) (**Figure 1.2**b).[66]

Scheme 1.1. Functionalization of ZnO nanoparticle by ATRP initiator and synthesis of ZnO/polymer hybrid by SI-ATRP

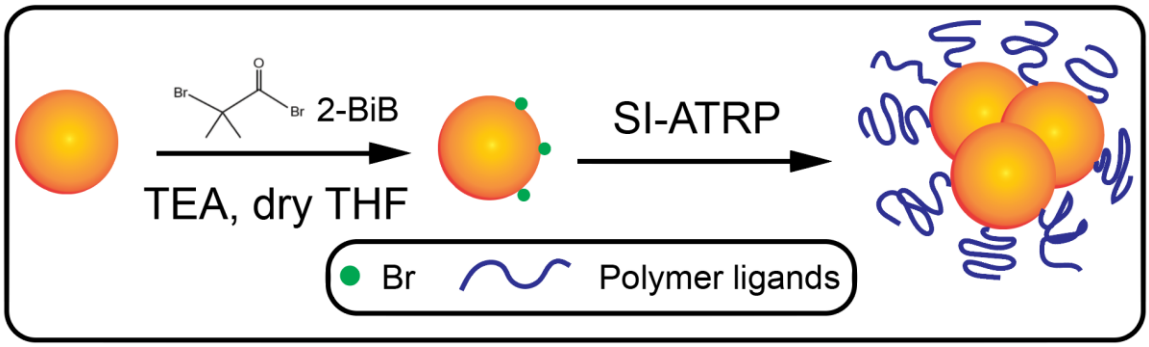

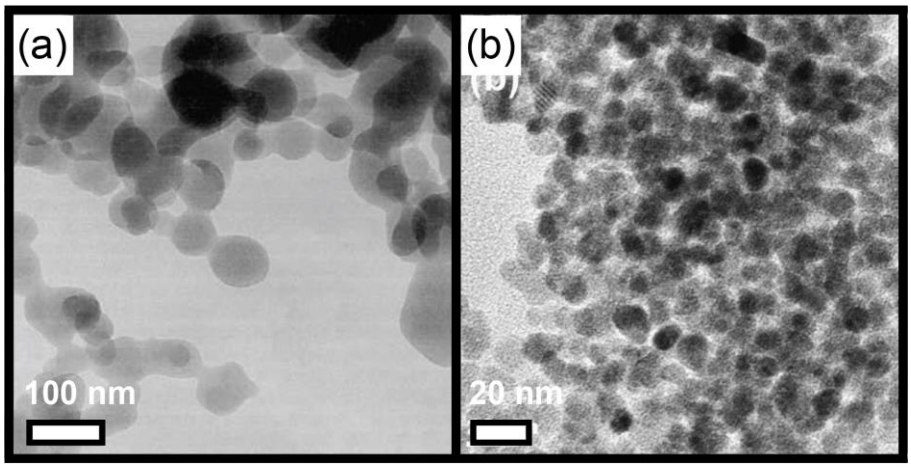

Figure 1.2. TEM images of (a) carbazole polymer (PCEM)/ZnO nanocomposites,[65] (b) ZnO@PPEGMA poly(poly(ethylene glycol) methyl ether monomethacrylate) nanoparticles after polymerization for 10 h.[66]

The surface modification of ZnO particles was reported using different silane coupling agents, such as 3-aminopropyltriethoxysilane, n-propyltriethoxysilane and 3-methacryloxypropyltrimethoxysilane, KH570 silane coupling agent.[67-69] The silane coupling agent is adsorbed on the surface of the nanoparticles at its hydrophilic end and interacts with hydroxyl groups that are pre-existing on the nanoparticle's surface (**Scheme 1.2**).

Scheme 1.2. Functionalization of ZnO nanoparticle by silane coupling agents and synthesis of ZnO/polymer hybrid by SI-ATRP

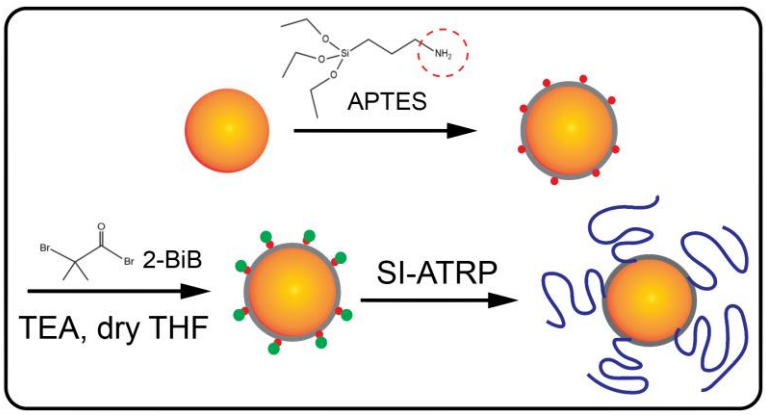

As shown in **Figure 1.3**a, a smart thermal responsive ZnO@PNIPAM (poly(N-isopropyl acrylamide) hybrid was prepared by Wei and coworkers via surface-initiated atom transfer

radical polymerization. The amino-functionalized ZnO was prepared by treatment with APTES of the surface of ZnO nanoparticles, then the ZnO-NH_2 nanoparticles were treated with 2-bromoisobutyrate to introduce ATRP initiators before polymerization. These ZnO@PNIPAM hybrids could work as a thermal responsive drug delivery system and pH-sensitive drug release.[70] Abbasian and coworkers reported a method to prepare ZnO nanoparticles with a covalently bonded poly(methyl methacrylate) (PMMA) shell by surface-initiated atom transfer radical polymerization. The surface of ZnO nanoparticle was treated with 3-aminopropyl triethoxysilane, and then this functionalized nanoparticle was reacted with chlorophenyl acetyl chloride to prepare ATRP macroinitiator. After polymerization of MMA, the hybrid nanoparticles had an exceptionally good dispersibility in organic solvents (**Figure 1.3**b).[71]

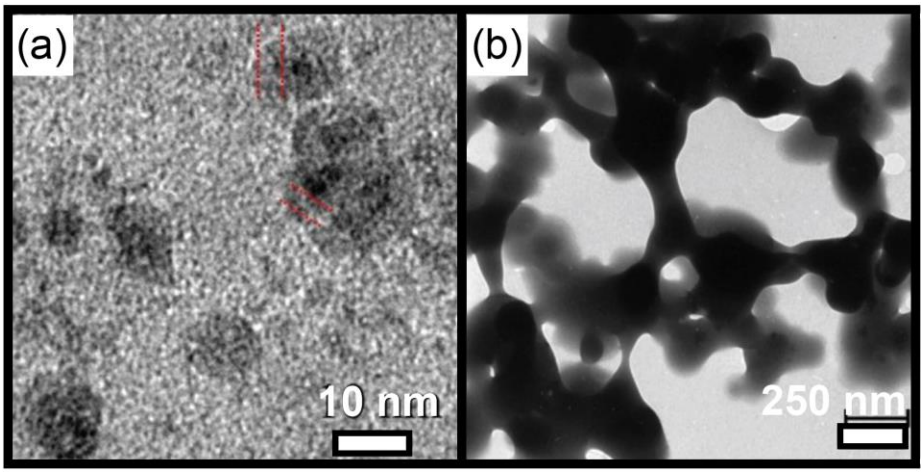

Figure 1.3. TEM images of (a) ZnO@PNIPAM,[70] (b) PMMA grafted ZnO.[71]

A universal tetherable initiator, derived from the structure of fatty acids, for surface-initiated atom transfer radical polymerization (SI-ATRP) from metal oxide surfaces, were prepared by Yan and coworkers.[72] A simple amidation between 2-bromoisobutyrate bromide and ω-amino lauric acid allowed preparation of 12-(2-bromoisobutyramido)dodecanoic acid

(BiBADA). After facile purification, BiBADA was used as a tetherable initiator for a broad range of metal oxide nanoparticles. The modified nanoparticles were grafted with methyl methacrylate or n-butyl acrylate via SI-ATRP with a high grafting density. As the amino group in ω-amino lauric acid is highly accessible to multiple types of functionalization, this method can potentially serve as a proof-of-concept for a versatile platform for surface modification of a large range of metal oxide nanoparticles. **Scheme 1.3** and **Figure 1.4** show the example of PMMA grafted ZnO prepared through BiBADA functionalized ZnO nanoparticles.

Scheme 1.3. Functionalization of ZnO nanoparticle by BiBADA initiator and synthesis of ZnO/polymer hybrid by SI-ATRP

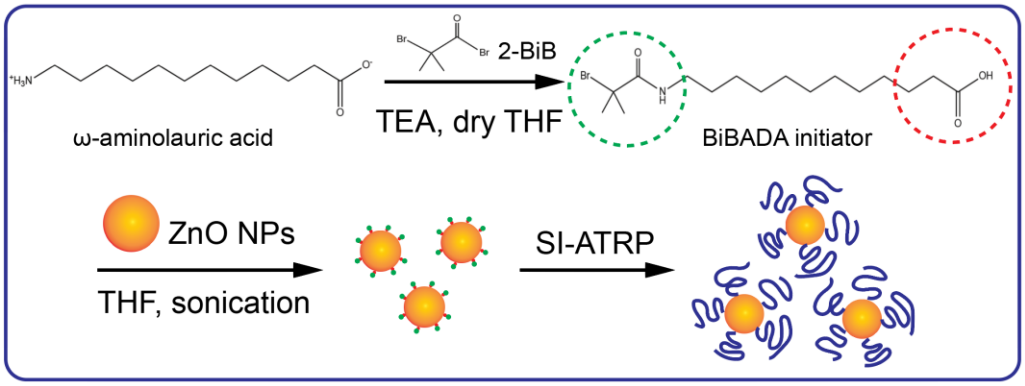

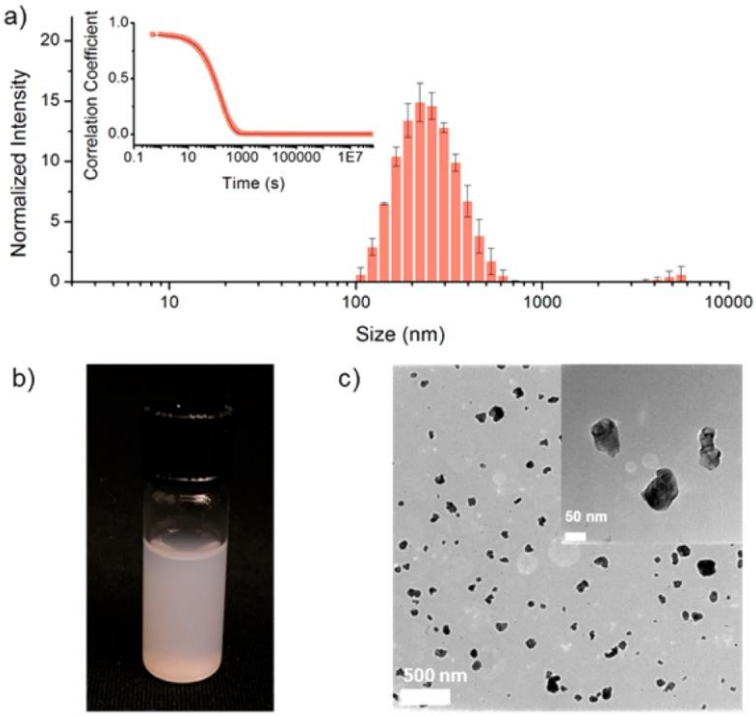

Figure 1.4. Characterization of PMMA-grafted ZrO_2 nanoparticles: (a) intensity-weighted hydrodynamic size distributions of ZrO_2-*g*-PMMA as an example; inset: correlation function (red square) and its single exponential fitting (black line) indicating a nearly monodisperse population; (b) photo of a uniform 2.0 mg/mL dispersion of ZrO_2-*g*-PMMA in THF with slight opalescence; (c) the TEM images of ZrO_2-*g*-PMMA; (d) characteristic load-displacement curves for ZrO_2-*g*-PMMA.[72]

Grafting onto

The "grafting-onto" process involves the coupling of pre-synthesized polymers to functional groups that are exposed at the surface. The principal advantage of "grafting-onto" modification is the simplicity and scalability of the process; however, the low density of tethered chains limits the overall control of material properties.

Scheme 1.4 shows an example of the grafting of PMMA or PSAN brushes onto ZnO nanoparticles accomplished via exploitation of the strong affinity of carboxylates to the ZnO surfaces

Scheme 1.4. Synthesis of ZnO/polymer hybrid through "grafting-onto" method with pre-synthesized diblock copolymers

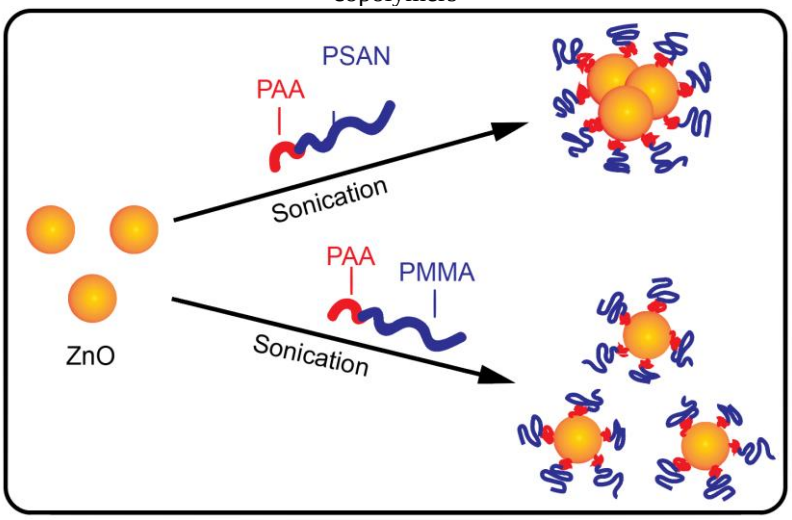

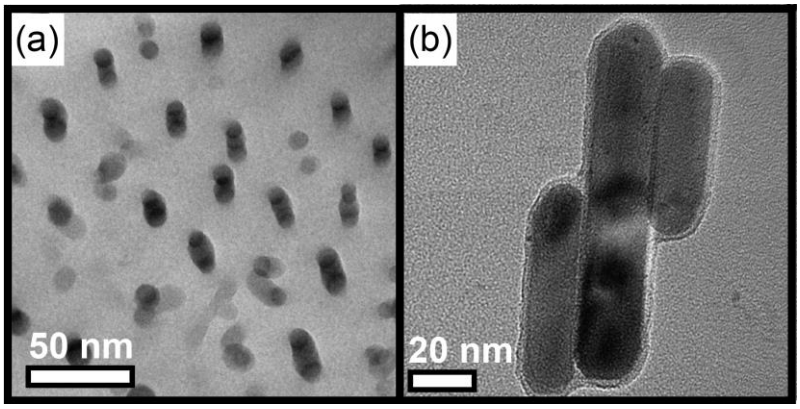

Figure 1.5. TEM images of (a) water-soluble ZnO nanoparticles,[73] (b) ZnO@P3HT nanorods.[74]

Sammynaiken and coworkers reported water-soluble ZnO nanoparticle coated with poly(ethylene glycol) biscarboxylate ($PEG(COOH)_2$) prepared in ethanol/water solutions. The ZnO nanoparticles have a hexagonal structure with an average size of 10 nm (**Figure 1.5**a).[73] The addition of the stabilizer ($PEG(COOH)_2$) separated the particles limiting the particle size. Awada and coworkers demonstrated the efficient grafting procedure of triethoxysilane terminated P3HT onto zinc oxide nanorods. The raw ZnO nanorods were grafted with triethoxysilane terminated P3HT by a one-step procedure of condensation. TEM images for the

three hybrids materials show a continuous and homogeneous polymer shell 4 ± 1 nm,[74] not only linked to the polymer molar mass but also to the grafting density.

The ligand exchange method to prepare ZnO/polymer hybrid is discussed in **Chapter 2**.

polymer template

An alternative approach to fabricate inorganic/polymer hybrid materials is by templating of grafted-copolymer "nanoreactors".[75-78] A grafted copolymer contains multiple linear polymer arms connected to a backbone (one-dimensional, also called molecular bottlebrush) or at a central core (zero-dimensional, also called star polymer). Star polymers with block copolymer arms are useful nanoreactors for the synthesis of inorganic materials because they form thermodynamically stable unimolecular micelles that enable high uniformity of particle products. Previous studies demonstrated the successful fabrication of star polymer nanoreactors via ATRP of block copolymers from a multifunctional core ("core-first").[79] A large variety of uniform nanoscale polymer/inorganic hybrid materials were successfully synthesized within the star polymer nanoreactors. These well-defined hybrid materials were applied in a broad range of fields.[80-87] One convenient method to form star polymers is to crosslink a functional chain end on pre-existing polymeric chains to form the core of the star ("arm-first").[88] The "arm-first" approach enabled higher graft density in star polymers, and consequently in the hybrid nanoparticles. In addition to spherical star polymer, molecular bottlebrushes were also used as single-molecule templates for fabricating one-dimensional nanostructures such as nanowires and nanotubes due to their worm-like morphologies.[75, 89-96] Nanoparticles were prepared by *in situ* conversion of the inorganic precursors immobilized within the functional block via a specific bonding.[96] Advantages of the "grafted-copolymer nanoreactor" approach include high achievable particle size uniformity, the variability of the resulting ligand

composition, and good stability of the particle-polymer bonding. The methodology is particularly interesting for ZnO and other ceramic material systems for which covalent and/or dense tethering of ligands is limited by the particle surface chemistry.

Pang and coworkers reported a general strategy for crafting ZnO nanocrystals with precisely controlled dimensions, compositions, and architectures by using star-like block copolymers as nanoreactors (**Figure 1.6a**).[78] This approach enables the facile synthesis of organic solvent- and water-soluble nearly monodisperse nanocrystals with desired composition and architecture. As shown in **Figure 1.6**b,[97] in Ding's work, polymer tethered ZnO nanoparticles are synthesized in a one-step procedure using PSAN-*b*-PAA-PDVB star polymers and PAA-*b*-PS copolymer brushes as a template. $Zn(NO_3)_2$, $Zn(EH)_2$, and $Zn(OAc)_2$ were studied as precursors of ZnO formed within the PAA-core of the star copolymers, among which $Zn(EH)_2$ turned out to be the best choice taking cost, yield, and quality into account. Excellent particle size uniformity was obtained using the star template method and dispersions were stable without indication of aggregation.

Scheme 1.5 Synthesis of ZnO/polymer hybrids from star polymer templates

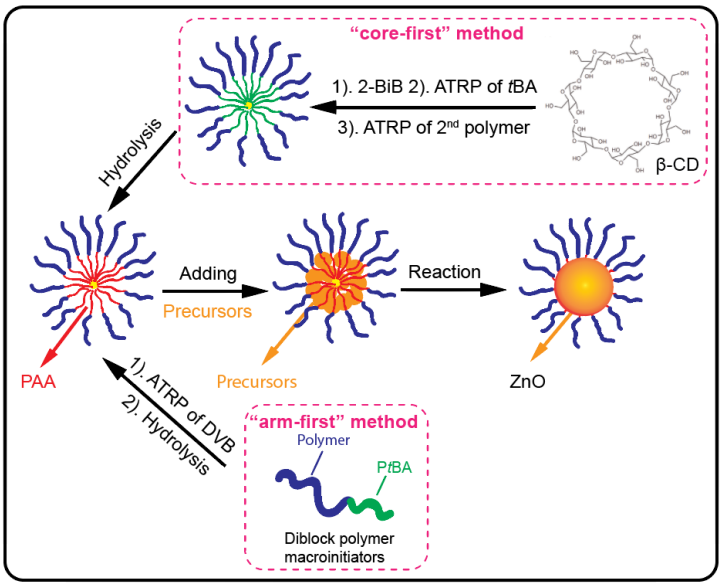

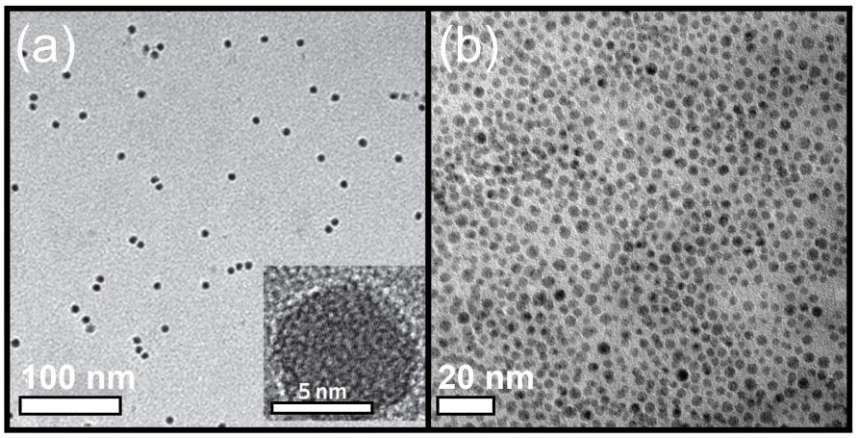

Figure 1.6. TEM images of (a) ZnO nanoparticles synthesized using star-like PAA-*b*-PS templates-type ZnO, D_{ZnO} = 6.3+0.3 nm,[78] (b) TEM images of PSAN capped ZnO synthesized by $PSAN_{70}$-*b*-PAA_{40}–PDVB star copolymer template and ZnO precursors: $Zn(NO_3)_2$ and KOH.[97]

Scheme 1.6. Synthesis of ZnO/polymer hybrids using bottlebrush polymer templates

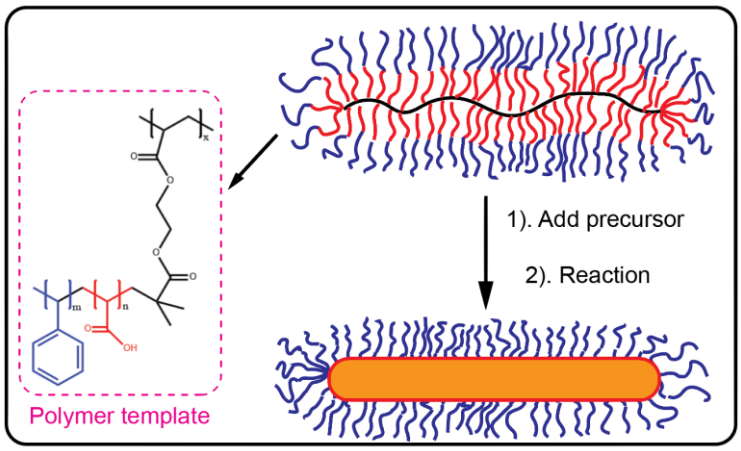

ZnO nanoparticles were also prepared using brush-like templates (PBiBEM$_{372}$-*g*-(PAA$_{47}$-*b*-PS$_{92}$)) with PAA-*b*-PS side chains, as previously reported. Anisotropic nanoparticles with a worm-like structure were observed in the TEM images (**Scheme 1.6** and **Figure 1.7**).[89] The statistical analysis of TEM images indicates the number-average lengths of the worm-like nano-objects 75 nm with dispersity (L_w/L_n) = 1.08. The length of each repeat unit in the backbone is calculated to be 0.16 nm, indicating the backbone of the brush-like template does not adapt fully extended conformation.[97]

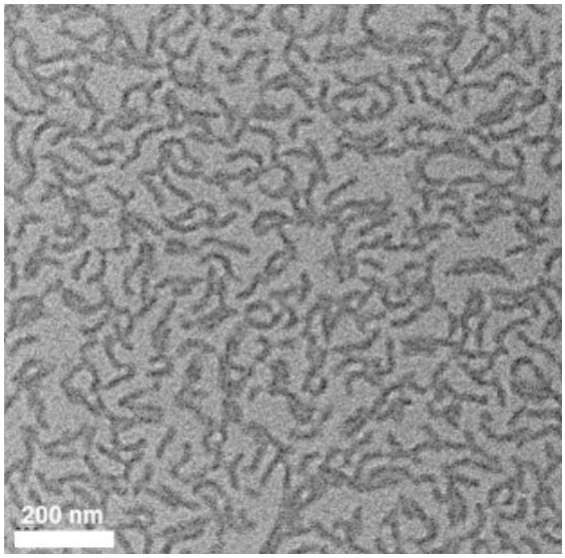

Figure 1.7. TEM images of ZnO nanoparticles prepared from brush-like templates.[97]

1.3. Application of ZnO/polymer nanocomposites

Semiconductors and magnetic materials are the basis of most of today's electronic devices.[98-99] The pure ZnO sample is diamagnetic in nature. ZnO/polymer nanocomposites have excellent magnetic, photocatalytic, optical, and electrical properties. These materials have wide usages in the field of sensors, photodiodes, LED, solar cells, paper industry and medical applications.[1] The detailed examples of the ZnO/hybrid materials applications will be discussed in **Chapter 4** to **Chapter 6**.

1.4. References

(1) Singh, P.; Kumar, R.; Singh, R. K., Progress on Transition Metal-Doped ZnO Nanoparticles and Its Application. *Industrial & Engineering Chemistry Research* **2019,** *58* (37), 17130-17163.

(2) Zhang, T.; Dong, W.; Keeter-Brewer, M.; Konar, S.; Njabon, R. N.; Tian, Z. R., Site-Specific Nucleation and Growth Kinetics in Hierarchical Nanosyntheses of Branched ZnO Crystallites. *J. Am. Chem. Soc.* **2006,** *128* (33), 10960-10968.

(3) Wang, Z.; Gong, J.; Su, Y.; Jiang, Y.; Yang, S., Six-Fold-Symmetrical Hierarchical ZnO Nanostructure Arrays: Synthesis, Characterization, and Field Emission Properties. *Crystal Growth & Design* **2010,** *10* (6), 2455-2459.

(4) Tsubota, T.; Ohtaki, M.; Eguchi, K.; Arai, H., Thermoelectric properties of Al-doped ZnO as a promising oxide material for high-temperature thermoelectric conversion. *J. Mater. Chem.* **1997,** *7* (1), 85-90.

(5) Hartlieb, K. J.; Raston, C. L.; Saunders, M., Controlled Scalable Synthesis of ZnO Nanoparticles. *Chem. Mater.* **2007,** *19* (23), 5453-5459.

(6) Bagnall, D. M.; Chen, Y. F.; Zhu, Z.; Yao, T.; Koyama, S.; Shen, M. Y.; Goto, T., Optically pumped lasing of ZnO at room temperature. *Appl. Phys. Lett.* **1997,** *70* (17), 2230-2232.

(7) Chu, S.; Olmedo, M.; Yang, Z.; Kong, J.; Liu, J., Electrically pumped ultraviolet ZnO diode lasers on Si. *Appl. Phys. Lett.* **2008,** *93* (18), 181106.

(8) Huang, J.; Chu, S.; Kong, J.; Zhang, L.; Schwarz, C. M.; Wang, G.; Chernyak, L.; Chen, Z.; Liu, J., ZnO p–n Homojunction Random Laser Diode Based on Nitrogen-Doped p-type Nanowires. *Advanced Optical Materials* **2013,** *1* (2), 179-185.

(9) Liu, L.; Tan, X.; Teng, D.; Wu, M.; Wang, G., Simultaneously Enhancing the Angular-Color Uniformity, Luminous Efficiency, and Reliability of White Light-Emitting Diodes by ZnO@SiO2 Modified Silicones. *IEEE Transactions on Components, Packaging and Manufacturing Technology* **2015,** *5* (5), 599-605.

(10) Choi, M.-J.; Kim, M.-H.; Choi, D.-K., A transparent diode with high rectifying ratio using amorphous indium-gallium-zinc oxide/SiNx coupled junction. *Appl. Phys. Lett.* **2015,** *107* (5), 053501.

(11) Suehiro, J.; Nakagawa, N.; Hidaka, S.-i.; Ueda, M.; Imasaka, K.; Higashihata, M.; Okada, T.; Hara, M., Dielectrophoretic fabrication and characterization of a ZnO nanowire-based UV photosensor. *Nanotechnology* **2006,** *17* (10), 2567-2573.
(12) Gimenez, A. J.; Yáñez-Limón, J. M.; Seminario, J. M., ZnO−Paper Based Photoconductive UV Sensor. *J. Phys. Chem. C* **2011,** *115* (1), 282-287.
(13) Mukae, K.; Tsuda, K.; Nagasawa, I., Capacitance ‐ vs ‐ voltage characteristics of ZnO varistors. *J. Appl. Phys.* **1979,** *50* (6), 4475-4476.
(14) Mahan, G. D.; Levinson, L. M.; Philipp, H. R., Theory of conduction in ZnO varistors. *J. Appl. Phys.* **1979,** *50* (4), 2799-2812.
(15) Gupta, T. K., Application of Zinc Oxide Varistors. *J. Am. Ceram. Soc.* **1990,** *73* (7), 1817-1840.
(16) Goldberger, J.; Sirbuly, D. J.; Law, M.; Yang, P., ZnO Nanowire Transistors. *J. Phys. Chem. B* **2005,** *109* (1), 9-14.
(17) Park, S.-E.; Shrout, T. R., Ultrahigh strain and piezoelectric behavior in relaxor based ferroelectric single crystals. *J. Appl. Phys.* **1997,** *82* (4), 1804-1811.
(18) Roundy, S.; Wright, P. K., A piezoelectric vibration based generator for wireless electronics. *Smart Mater. Struct.* **2004,** *13* (5), 1131-1142.
(19) Zhou, Q. F.; Sharp, C.; Cannata, J. M.; Shung, K. K.; Feng, G. H.; Kim, E. S., Self-focused high frequency ultrasonic transducers based on ZnO piezoelectric films. *Appl. Phys. Lett.* **2007,** *90* (11), 113502.
(20) Kim, H. C.; Song, S.; Kim, J., Fabrication of a Miniaturized ZnO Nanowire Accelerometer and Its Performance Tests. *Sensors* **2016,** *16* (9), 1499.
(21) Tomizaki, K.-y.; Kubo, S.; Ahn, S.-A.; Satake, M.; Imai, T., Biomimetic Alignment of Zinc Oxide Nanoparticles along a Peptide Nanofiber. *Langmuir* **2012,** *28* (37), 13459-13466.
(22) Raula, M.; Rashid, M. H.; Paira, T. K.; Dinda, E.; Mandal, T. K., Ascorbate-Assisted Growth of Hierarchical ZnO Nanostructures: Sphere, Spindle, and Flower and Their Catalytic Properties. *Langmuir* **2010,** *26* (11), 8769-8782.
(23) Kozhummal, R.; Yang, Y.; Güder, F.; Hartel, A.; Lu, X.; Küçükbayrak, U. M.; Mateo-Alonso, A.; Elwenspoek, M.; Zacharias, M., Homoepitaxial Branching: An Unusual Polymorph of Zinc Oxide Derived from Seeded Solution Growth. *ACS Nano* **2012,** *6* (8), 7133-7141.
(24) Waltz, F.; Wißmann, G.; Lippke, J.; Schneider, A. M.; Schwarz, H.-C.; Feldhoff, A.; Eiden, S.; Behrens, P., Evolution of the Morphologies of Zinc Oxide Mesocrystals Under the Influence of Natural Polysaccharides. *Crystal Growth & Design* **2012,** *12* (6), 3066-3075.
(25) Qiu, Y.; Chen, W.; Yang, S.; Zhang, B.; Zhang, X. X.; Zhong, Y. C.; Wong, K. S., Hierarchical Hollow Spheres of ZnO and Zn1−xCoxO: Directed Assembly and Room-Temperature Ferromagnetism. *Crystal Growth & Design* **2010,** *10* (1), 177-183.
(26) Venkataiah, G.; Huang, M. R. S.; Su, H. L.; Liu, C. P.; Huang, J. C. A., Microstructure and Magnetic Properties of Ni:ZnO Nanorod/Zn:NiO Nanowall Composite Structures. *J. Phys. Chem. C* **2010,** *114* (39), 16191-16196.
(27) Tahir, N.; Karim, A.; Persson, K. A.; Hussain, S. T.; Cruz, A. G.; Usman, M.; Naeem, M.; Qiao, R.; Yang, W.; Chuang, Y.-D.; Hussain, Z., Surface Defects: Possible Source of Room Temperature Ferromagnetism in Co-Doped ZnO Nanorods. *J. Phys. Chem. C* **2013,** *117* (17), 8968-8973.
(28) Lupan, O.; Chow, L.; Ono, L. K.; Cuenya, B. R.; Chai, G.; Khallaf, H.; Park, S.; Schulte, A., Synthesis and Characterization of Ag- or Sb-Doped ZnO Nanorods by a Facile Hydrothermal Route. *J. Phys. Chem. C* **2010,** *114* (29), 12401-12408.

(29) Vaishampayan, M. V.; Mulla, I. S.; Joshi, S. S., Optical and Photocatalytic Properties of Single Crystalline ZnO at the Air–Liquid Interface by an Aminolytic Reaction. *Langmuir* **2011,** *27* (20), 12751-12759.
(30) Olaru, N.; Calin, G.; Olaru, L., Zinc Oxide Nanocrystals Grown on Cellulose Acetate Butyrate Nanofiber Mats and Their Potential Photocatalytic Activity for Dye Degradation. *Industrial & Engineering Chemistry Research* **2014,** *53* (46), 17968-17975.
(31) Huang, M.; Weng, S.; Wang, B.; Hu, J.; Fu, X.; Liu, P., Various Facet Tunable ZnO Crystals by a Scalable Solvothermal Synthesis and Their Facet-Dependent Photocatalytic Activities. *J. Phys. Chem. C* **2014,** *118* (44), 25434-25440.
(32) Norris, B. J.; Anderson, J.; Wager, J. F.; Keszler, D. A., Spin-coated zinc oxide transparent transistors. *J. Phys. D: Appl. Phys.* **2003,** *36* (20), L105-L107.
(33) Montazer, M.; Maali Amiri, M., ZnO Nano Reactor on Textiles and Polymers: Ex Situ and In Situ Synthesis, Application, and Characterization. *J. Phys. Chem. B* **2014,** *118* (6), 1453-1470.
(34) Lu, X.-H.; Wang, D.; Li, G.-R.; Su, C.-Y.; Kuang, D.-B.; Tong, Y.-X., Controllable Electrochemical Synthesis of Hierarchical ZnO Nanostructures on FTO Glass. *J. Phys. Chem. C* **2009,** *113* (31), 13574-13582.
(35) Tak, Y.; Yong, K., Controlled Growth of Well-Aligned ZnO Nanorod Array Using a Novel Solution Method. *J. Phys. Chem. B* **2005,** *109* (41), 19263-19269.
(36) Zhou, X.; Zhang, D.; Zhu, Y.; Shen, Y.; Guo, X.; Ding, W.; Chen, Y., Mechanistic Investigations of PEG-Directed Assembly of One-Dimensional ZnO Nanostructures. *J. Phys. Chem. B* **2006,** *110* (51), 25734-25739.
(37) Fu, Y.-S.; Ji, S.-H.; Chen, X.; Ma, X.-C.; Wu, R.; Wang, C.-C.; Duan, W.-H.; Qiu, X.-H.; Sun, B.; Zhang, P.; Jia, J.-F.; Xue, Q.-K., Manipulating the Kondo Resonance through Quantum Size Effects. *Phys. Rev. Lett.* **2007,** *99* (25), 256601.
(38) Satoh, N.; Nakashima, T.; Kamikura, K.; Yamamoto, K., Quantum size effect in TiO2 nanoparticles prepared by finely controlled metal assembly on dendrimer templates. *Nature Nanotechnology* **2008,** *3* (2), 106-111.
(39) Daniel, M.-C.; Astruc, D., Gold Nanoparticles: Assembly, Supramolecular Chemistry, Quantum-Size-Related Properties, and Applications toward Biology, Catalysis, and Nanotechnology. *Chem. Rev.* **2004,** *104* (1), 293-346.
(40) Wang, B.-X.; Zhou, L.-P.; Peng, X.-F., Surface and Size Effects on the Specific Heat Capacity of Nanoparticles. *Int. J. Thermophys.* **2006,** *27* (1), 139-151.
(41) Zhang, M.; Gao, G.; Li, C. Q.; Liu, F. Q., Titania-Coated Polystyrene Hybrid Microballs Prepared with Miniemulsion Polymerization. *Langmuir* **2004,** *20* (4), 1420-1424.
(42) Ringwald, S. C.; Pemberton, J. E., Adsorption interactions of aromatics and heteroaromatics with hydrated and dehydrated silica surfaces by raman and FTIR spectroscopies. *Environ. Sci. Technol.* **2000,** *34* (2), 259-265.
(43) Chen, L. X.; Rajh, T.; Wang, Z.; Thurnauer, M. C., XAFS studies of surface structures of TiO2 nanoparticles and photocatalytic reduction of metal ions. *J. Phys. Chem. B* **1997,** *101* (50), 10688-10697.
(44) Rajh, T.; Tiede, D. M.; Thurnauer, M. C., Surface modification of TiO2 nanoparticles with bidentate ligands studied by EPR spectroscopy. *J. Non-Cryst. Solids* **1996,** *205-207* (2), 815-820.

(45) Yokoyama, R.; Suzuki, S.; Shirai, K.; Yamauchi, T.; Tsubokawa, N.; Tsuchimochi, M., Preparation and properties of biocompatible polymer-grafted silica nanoparticle. *Eur. Polym. J.* **2006,** *42* (12), 3221-3229.
(46) Dang, Z.; Fan, L.; Zhao, S.; Nan, C., Dielectric properties and morphologies of composites filled with whisker and nanosized zinc oxide. *Mater. Res. Bull.* **2003,** *38* (3), 499-507.
(47) Rong, M. Z.; Zhang, M. Q.; Wang, H. B.; Zeng, H. M., Surface modification of magnetic metal nanoparticles through irradiation graft polymerization. *Appl. Surf. Sci.* **2002,** *200* (1-4), 76-93.
(48) Kim, S.; Kim, E.; Kim, S.; Kim, W., Surface modification of silica nanoparticles by UV-induced graft polymerization of methyl methacrylate. *J. Colloid Interface Sci.* **2005,** *292* (1), 93-98.
(49) Tsubokawa, N.; Kogure, A., Surface grafting of polymers onto inorganic ultrafine particles: Reaction of functional polymers with acid anhydride groups introduced onto inorganic ultrafine particles. *J. Polym. Sci., Part A: Polym. Chem.* **1991,** *29* (5), 697-702.
(50) Prucker, O.; Rühe, J., Mechanism of Radical Chain Polymerizations Initiated by Azo Compounds Covalently Bound to the Surface of Spherical Particles. *Macromolecules* **1998,** *31* (3), 602-613.
(51) Shirai, Y.; Kawatsura, K.; Tsubokawa, N., Graft polymerization of vinyl monomers from initiating groups introduced onto polymethylsiloxane-coated titanium dioxide modified with alcoholic hydroxyl groups. *Prog. Org. Coat.* **1999,** *36* (4), 217-224.
(52) Chujo, Y.; Ihara, E.; Ihara, H.; Saegusa, T., A novel silane coupling agent. 1. Synthesis of trimethoxysilyl-terminated poly(N-acetylethylenimine). *Macromolecules* **1989,** *22* (5), 2040-2043.
(53) Tsubokawa, N.; Shirai, Y.; Tsuchida, H.; Handa, S., Photografting of vinyl polymers onto ultrafine inorganic particles: Photopolymerization of vinyl monomers initiated by AZO groups introduced onto these surfaces. *J. Polym. Sci., Part A: Polym. Chem.* **1994,** *32* (12), 2327-2332.
(54) Hayashi, S.; Fujiki, K.; Tsubokawa, N., Grafting of hyperbranched polymers onto ultrafine silica: Postgraft polymerization of vinyl monomers initiated by pendant initiating groups of polymer chains grafted onto the surface. *React. Funct. Polym.* **2000,** *46* (2), 193-201.
(55) Espiard, P.; Guyot, A., Poly(ethyl acrylate) latexes encapsulating nanoparticles of silica: 2. Grafting process onto silica. *Polymer* **1995,** *36* (23), 4391-4395.
(56) Li, H.; Zhao, H.; Zhang, X.; Lu, Y.; Hu, Y., A novel route to the synthesis of PP-g-PMMA copolymer via ATRP reaction initiated by Si-Cl bond. *Eur. Polym. J.* **2007,** *43* (1), 109-118.
(57) Kango, S.; Kalia, S.; Celli, A.; Njuguna, J.; Habibi, Y.; Kumar, R., Surface modification of inorganic nanoparticles for development of organic–inorganic nanocomposites—A review. *Prog. Polym. Sci.* **2013,** *38* (8), 1232-1261.
(58) Tran, Y.; Auroy, P., Synthesis of poly(styrene sulfonate) brushes. *J. Am. Chem. Soc.* **2001,** *123* (16), 3644-3654.
(59) Mansky, P.; Liu, Y.; Huang, E.; Russell, T. P.; Hawker, C., Controlling polymer-surface interactions with random copolymer brushes. *Science* **1997,** *275* (5305), 1458-1460.
(60) Prucker, O.; Rühe, J., Synthesis of poly(styrene) monolayers attached to high surface area silica gels through self-assembled monolayers of azo initiators. *Macromolecules* **1998,** *31* (3), 592-601.

(61) von Werne, T.; Patten, T. E., Atom transfer radical polymerization from nanoparticles: A tool for the preparation of well-defined hybrid nanostructures and for understanding the chemistry of controlled/"living" radical polymerizations from surfaces. *J. Am. Chem. Soc.* **2001,** *123* (31), 7497-7505.
(62) Owen, M. J., Coupling agents: Chemical bonding at interfaces. *Adhesion Science and Engineering* **2002,** *2*, 403-431.
(63) P lueddemann, E. P., Adhesion Through Silane Coupling Agents. *The Journal of Adhesion* **1970,** *2* (3), 184-201.
(64) Lin, F., Preparation and Characterization of Polymer TiO₂ Nanocomposites via In-situ Polymerization. UWSpace: **2006**.
(65) Sato, M.; Kawata, A.; Morito, S.; Sato, Y.; Yamaguchi, I., Preparation and properties of polymer/zinc oxide nanocomposites using functionalized zinc oxide quantum dots. *Eur. Polym. J.* **2008,** *44* (11), 3430-3438.
(66) Peng, X.; Chen, Y.; Li, F.; Zhou, W.; Hu, Y., Preparation and optical properties of ZnO@PPEGMA nanoparticles. *Appl. Surf. Sci.* **2009,** *255* (16), 7158-7163.
(67) Tang, E.; Liu, H.; Sun, L.; Zheng, E.; Cheng, G., Fabrication of zinc oxide/poly(styrene) grafted nanocomposite latex and its dispersion. *Eur. Polym. J.* **2007,** *43* (10), 4210-4218.
(68) Sabzi, M.; Mirabedini, S. M.; Zohuriaan-Mehr, J.; Atai, M., Surface modification of TiO2 nano-particles with silane coupling agent and investigation of its effect on the properties of polyurethane composite coating. *Prog. Org. Coat.* **2009,** *65* (2), 222-228.
(69) Ma, J.; Yang, X.; Nurulla, I., Study on synthesis and swelling behavior of salt tolerating water absorbent gels. *Shiyou Huagong/Petrochemical Technology* **2005,** *34* (3), 278-281.
(70) Tan, L.; Liu, J.; Zhou, W.; Wei, J.; Peng, Z., A novel thermal and pH responsive drug delivery system based on ZnO@PNIPAM hybrid nanoparticles. *Materials Science and Engineering: C* **2014,** *45*, 524-529.
(71) Abbasian, M.; Aali, N. K.; Shoja, S. E., Synthesis of Poly (methyl methacrylate)/Zinc Oxide Nanocomposite with Core-Shell Morphology by Atom Transfer Radical Polymerization. *Journal of Macromolecular Science, Part A* **2013,** *50* (9), 966-975.
(72) Yan, J.; Pan, X.; Wang, Z.; Lu, Z.; Wang, Y.; Liu, L.; Zhang, J.; Ho, C.; Bockstaller, M. R.; Matyjaszewski, K., A Fatty Acid-Inspired Tetherable Initiator for Surface-Initiated Atom Transfer Radical Polymerization. *Chem. Mater.* **2017,** *29* (11), 4963-4969.
(73) Woo, B. K.; Chen, W.; Joly, A. G.; Sammynaiken, R., The Effects of Aging on the Luminescence of PEG-Coated Water-Soluble ZnO Nanoparticle Solutions. *J. Phys. Chem. C* **2008,** *112* (37), 14292-14296.
(74) Awada, H.; Medlej, H.; Blanc, S.; Delville, M.-H.; Hiorns, R. C.; Bousquet, A.; Dagron-Lartigau, C.; Billon, L., Versatile functional poly(3-hexylthiophene) for hybrid particles synthesis by the grafting onto technique: Core@shell ZnO nanorods. *J. Polym. Sci., Part A: Polym. Chem.* **2014,** *52* (1), 30-38.
(75) Yuan, J.; Xu, Y.; Walther, A.; Bolisetty, S.; Schumacher, M.; Schmalz, H.; Ballauff, M.; Müller, A. H. E., Water-soluble organo-silica hybrid nanowires. *Nat. Mater.* **2008,** *7* (9), 718-722.
(76) Müllner, M.; Yuan, J.; Weiss, S.; Walther, A.; Förtsch, M.; Drechsler, M.; Müller, A. H. E., Water-Soluble Organo−Silica Hybrid Nanotubes Templated by Cylindrical Polymer Brushes. *J. Am. Chem. Soc.* **2010,** *132* (46), 16587-16592.

(77) Zheng, Z.; Daniel, A.; Yu, W.; Weber, B.; Ling, J.; Müller, A. H. E., Rare-Earth Metal Cations Incorporated Silica Hybrid Nanoparticles Templated by Cylindrical Polymer Brushes. *Chem. Mater.* **2013,** *25* (22), 4585-4594.
(78) Pang, X.; Zhao, L.; Han, W.; Xin, X.; Lin, Z., A general and robust strategy for the synthesis of nearly monodisperse colloidal nanocrystals. *Nature Nanotechnology* **2013,** *8*, 426.
(79) Pang, X.; Zhao, L.; Han, W.; Xin, X.; Lin, Z., A general and robust strategy for the synthesis of nearly monodisperse colloidal nanocrystals. *Nature Nanotechnology* **2013,** *8* (6), 426-431.
(80) He, M.; Pang, X.; Liu, X.; Jiang, B.; He, Y.; Snaith, H.; Lin, Z., Monodisperse Dual-Functional Upconversion Nanoparticles Enabled Near-Infrared Organolead Halide Perovskite Solar Cells. *Angewandte Chemie - International Edition* **2016,** *55* (13), 4280-4284.
(81) Wang, M.; Pang, X.; Zheng, D.; He, Y.; Sun, L.; Lin, C.; Lin, Z., Nonepitaxial growth of uniform and precisely size-tunable core/shell nanoparticles and their enhanced plasmon-driven photocatalysis. *Journal of Materials Chemistry A* **2016,** *4* (19), 7190-7199.
(82) Jiang, B.; Pang, X.; Li, B.; Lin, Z., Organic-Inorganic Nanocomposites via Placing Monodisperse Ferroelectric Nanocrystals in Direct and Permanent Contact with Ferroelectric Polymers. *J. Am. Chem. Soc.* **2015,** *137* (36), 11760-11767.
(83) Xu, H.; Xu, Y.; Pang, X.; He, Y.; Jung, J.; Xia, H.; Lin, Z., A general route to nanocrystal kebabs periodically assembled on stretched flexible polymer shish. *Science Advances* **2015,** *1* (2), e1500025.
(84) Yang, D.; Pang, X.; He, Y.; Wang, Y.; Chen, G.; Wang, W.; Lin, Z., Precisely size-tunable magnetic/plasmonic core/shell nanoparticles with controlled optical properties. *Angew. Chem.* **2015,** *127* (41), 12259-12264.
(85) Xu, H.; Pang, X.; He, Y.; He, M.; Jung, J.; Xia, H.; Lin, Z., An Unconventional Route to Monodisperse and Intimately Contacted Semiconducting Organic-Inorganic Nanocomposites. *Angew. Chem.* **2015,** *127* (15), 4719-4723.
(86) Zheng, D.; Pang, X.; Wang, M.; He, Y.; Lin, C.; Lin, Z., Unconventional Route to Hairy Plasmonic/Semiconductor Core/Shell Nanoparticles with Precisely Controlled Dimensions and Their Use in Solar Energy Conversion. *Chem. Mater.* **2015,** *27* (15), 5271-5278.
(87) Feng, C.; Pang, X.; He, Y.; Chen, Y.; Zhang, G.; Lin, Z., A versatile strategy for uniform hybrid nanoparticles and nanocapsules. *Polym. Chem.* **2015,** *6* (29), 5190-5197.
(88) Gao, H.; Matyjaszewski, K., Arm-first method as a simple and general method for synthesis of miktoarm star copolymers. *J. Am. Chem. Soc.* **2007,** *129* (38), 11828-11834.
(89) Xie, G.; Ding, H.; Daniel, W. F. M.; Wang, Z.; Pietrasik, J.; Sheiko, S. S.; Matyjaszewski, K., Preparation of titania nanoparticles with tunable anisotropy and branched structures from core–shell molecular bottlebrushes. *Polymer* **2016,** *98*, 481-486.
(90) Djalali, R.; Li, S. Y.; Schmidt, M., Amphipolar core-shell cylindrical brushes as templates for the formation of gold clusters and nanowires. *Macromolecules* **2002,** *35* (11), 4282-4288.
(91) Huang, K.; Rzayev, J., Well-defined organic nanotubes from multicomponent bottlebrush copolymers. *J. Am. Chem. Soc.* **2009,** *131* (19), 6880-6885.
(92) Müllner, M.; Lunkenbein, T.; Breu, J.; Caruso, F.; Müller, A. H. E., Template-directed synthesis of silica nanowires and nanotubes from cylindrical core-shell polymer brushes. *Chem. Mater.* **2012,** *24* (10), 1802-1810.
(93) Müllner, M.; Lunkenbein, T.; Schieder, M.; Gröschel, A. H.; Miyajima, N.; Förtsch, M.; Breu, J.; Caruso, F.; Müller, A. H. E., Template-directed mild synthesis of anatase hybrid

nanotubes within cylindrical core-shell-corona polymer brushes. *Macromolecules* **2012,** *45* (17), 6981-6988.
(94) Yuan, J.; Lu, Y.; Schacher, F.; Lunkenbein, T.; Weiss, S.; Schmalz, H.; Müller, A. H. E., Template-directed synthesis of hybrid titania nanowires within core-shell bishydrophilic cylindrical polymer brushes. *Chem. Mater.* **2009,** *21* (18), 4146-4154.
(95) Yuan, J.; Schacher, F.; Drechsler, M.; Hanisch, A.; Lu, Y.; Ballauff, M.; Müller, A. H. E., Stimuli-responsive organosilica hybrid nanowires decorated with metal nanoparticles. *Chem. Mater.* **2010,** *22* (8), 2626-2634.
(96) Yuan, J.; Drechsler, M.; Xu, Y.; Zhang, M.; Müller, A. H. E., Cadmium selenide nanowires within core-shell cylindrical polymer brushes: Synthesis, characterization and the double-loading process. *Polymer* **2008,** *49* (6), 1547-1554.
(97) Ding, H.; Yan, J.; Wang, Z.; Xie, G.; Mahoney, C.; Ferebee, R.; Zhong, M.; Daniel, W. F. M.; Pietrasik, J.; Sheiko, S. S.; Bettinger, C. J.; Bockstaller, M. R.; Matyjaszewski, K., Preparation of ZnO hybrid nanoparticles by ATRP. *Polymer* **2016,** *107*, 492-502.
(98) Jeong, D.; Keem, K.; Park, B.; Cho, K.; Kim, S., Electrical Characteristics of Hybrid Nanoparticle–Nanowire Devices. *IEEE Transactions on Nanotechnology* **2009,** *8* (5), 650-653.
(99) Waser, R.; Dittmann, R.; Staikov, G.; Szot, K., Redox-Based Resistive Switching Memories – Nanoionic Mechanisms, Prospects, and Challenges. *Adv. Mater.* **2009,** *21* (25 – 26), 2632-2663.

Chapter 2 Well-defined Hybrid Materials by Polymer Ligand Exchange of ZnO Nanoparticles

2.1. Preface

Polymer hybrid materials PSAN capped ZnO nanoparticles (NPs) were synthesized by "ligand exchange" methods. The octylamine (OA) capped ZnO NPs were prepared using OA and zinc 2-ethylhexanoate ($Zn(EH)_2$). The PSAN-NH_2 polymer ligands were synthesized by ARGET ATRP. By utilization the low boiling point of OA, the PSAN-NH_2 chains were efficiently exchanged with OA ligands on the ZnO particle surface. By altering the ratio between OA and polymer ligands, the morphology of nanocomposite was controlled. The resulted ZnO/polymer nanocomposites were stable in THF with narrow size distribution and varying grafting density from 0.9 to 2.5 nm^{-2}. A clear bulk film with high transparency was fabricated from the blend of linear PMMA (M_w=120,000) and PSAN capped ZnO NPs.

In this chapter, the synthesis of PSAN capped ZnO nanocrystal is discussed. I designed the entire project and performed all synthetic work and part of the characterization in the project. I would like to thank especially my collaborators, Jiajun Yan for extensive discussion on the initial stage of the project design. Clare Mahoney, Zhao Lu, Rachel Ferebee and Danli Luo from Bockstaller's group assisted in the characterization work. Professor Matyjaszewski and Professor Bockstaller conceived and organized the project and together with me wrote the manuscript.

This paper was published in *Langmuir*, (**Zongyu Wang**, Clare Mahoney, Jiajun Yan, Zhao Lu, Rachel Ferebee, Danli Luo, Michael R Bockstaller, Krzysztof Matyjaszewski, "Preparation of well-defined poly (styrene-co-acrylonitrile)/ZnO hybrid nanoparticles by an efficient ligand exchange strategy", *Langmuir*, **2016**, 32 (49), 13207-13213).

This work was supported by NSF (DMR 1501324), the Department of Energy (DE-EE0006702) and the National Science Center (grant UMO-2014/14/A/ST5/00204).

2.2. Introduction

The remarkable growth of nanotechnology has led to wide-scale use of functional nanocomposites in many applications.[1-3] The utility of nanomaterials can be attributed to their small size rendering large surface area to volume ratios and high reactivity. Polymer nanocomposites, including polymer-inorganic hybrids, have attracted increasing levels of interest due to the enhanced optical, biological, mechanical, thermal, electronic, and magnetic properties, relative to conventional organic materials. However, it is challenging to homogeneously disperse nanofillers in a targeted matrix. Consequently, the concentration gradients of filler incorporated into polymer matrices result in defects in the material, resulting in inferior mechanical and optical properties as well as premature failure of these materials.

ZnO nanoparticles (NPs) have widespread use in cosmetic products, electronic sensors, and manufacturing industries.[4] Due to their antifungal property, they are also employed in food products, plastics and as pigments.[5] ZnO NPs have unique UV absorption and photocatalytic properties.[6, 7] Besides, they are being examined in cancer diagnosis and therapy.[8]

In previous work, two well-established approaches are used to synthesize polymeric hybrid nanocomposites, which are "grafting from" and "polymer templates" methods. The most established method to form nanoparticles with polymer brushes tethered on the surfaces is the "grafting from" method. Typically, in a "grafting from" procedure, polymer brushes are grown from the initiator sites which are covalently attached to the nanoparticle's surface. In this approach, the most essential step is the modification of the NPs surfaces with initiator compounds, which is extremely hard for ZnO due to its inert nature and weak bonding of the surface. The block copolymer template method is another way to prepare inorganic particle/polymer hybrids.[9-12] Nanoparticles can be prepared by reducing the precursors immobilized within the functional block via a specific binding.[13] For example, it has recently been demonstrated that star polymer templates are useful nanoreactors for the synthesis of inorganic materials because they are essentially thermodynamically stable unimolecular micelles.[9] The drawback of this method is a complicated purification process and low inorganic contents due to the high contents of polymer template residuals in the hybrid products.

Another alternative way to stabilize NPs with polymer brushes is the "ligand exchange" method. In this approach, pristine nanocrystals are first stabilized by low molar mass organic surfactant/ligands, for example, alkyl phosphine, amine or carboxylic acids.[14] Under certain circumstances, those short ligands can be efficiently exchanged by presynthesized polymer brushes with functional end-groups. Comparing to other approaches, by applying the "ligand

exchange" method, it is possible to achieve high grafting density (>1 chain/nm^2), and inorganic contents.

In recent years, the controlled radical polymerization (CRP) has been proven to be a powerful method to synthesize precisely designed polymers with well-defined architecture and morphology. Polymer ligands that are synthesized by CRP have a well-controlled molecular weight (MW), narrow molecular weight distribution (MWD) and high site-specific functionality, which are all crucial for "ligand exchange" process.

Herein, we report an efficient way to synthesize PSAN capped ZnO NPs by ligand exchange method.

2.3. Results and Discussion

The three steps of the synthesis of PSAN capped ZnO NPs are the synthesis of OA capped ZnO, the synthesis of amino-functionalized PSAN-NH_2 and the ligand exchange between OA and PSAN-NH_2 on the surface of ZnO.

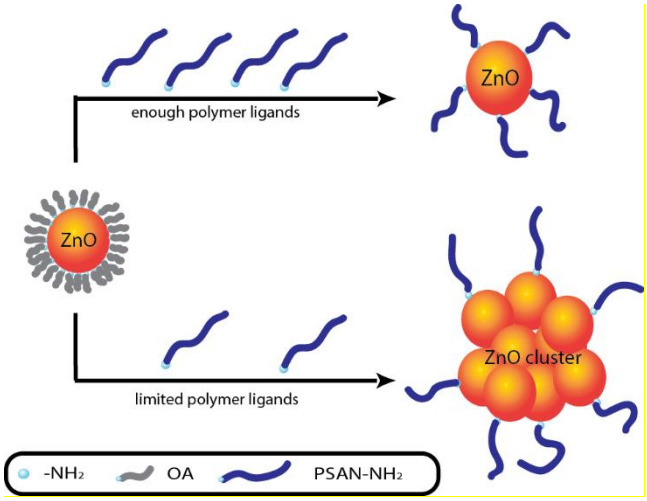

Scheme 2.1. Synthesis of PSAN capped ZnO NPs by "ligand exchange" method

The OA capped ZnO nanoparticles were synthesized via thermal decomposition of $Zn(EH)_2$ in the presence of surfactant OA according to the reference.[15] The obtained OA capped ZnO NPs can dissolve in THF/solvent form stable solutions for months. Dispersions were characterized by TEM and DLS (**Figure 2.1**), respectively, which showed an average size of around 5 nm with narrow size distribution. The crystallinity of ZnO nanoparticles was identified by X-ray diffraction (XRD) (**Figure S2.1),** which shows good crystallinity and agreement with the wurtzite ZnO pattern. Also, the nanoparticles were analyzed by TGA measurement, which gave a ZnO content of 83 %. With the mean diameter (5 nm) and bulk density of ZnO nanoparticles (5.6 g/cm^3), the molecular weight of OA and the weight fraction of amine ligands from the TGA measurement, a ligand density of 4.4 chains/nm^2 was calculated for the OA capped ZnO NPs shown in **Figure 2.1**.

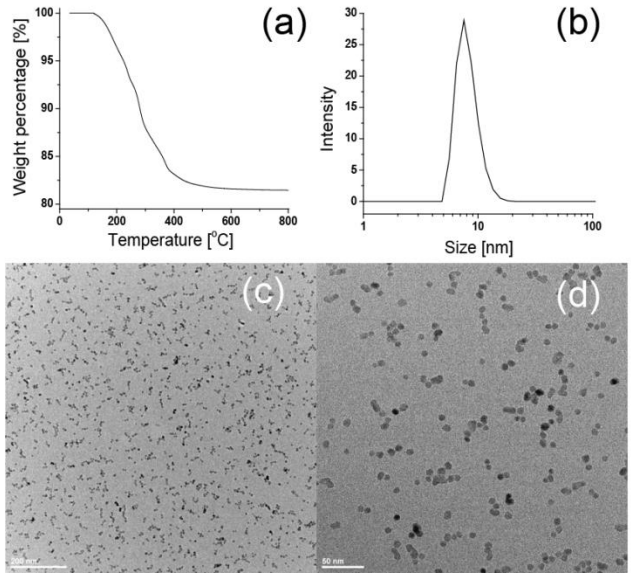

Figure 2.1. (a) TGA curve for OA capped ZnO NPs; (b) The size distribution of OA capped ZnO NPs measured by DLS measurements in THF; (c) and (d) TEM images of the OA capped ZnO NPs.

PSAN-NH_2 polymer ligands were synthesized through three steps: synthesis of ATRP initiator, polymer ligand synthesis via ARGET ATRP and deprotection of NH_2 chain end.

(**Scheme 2.2**) α-bromoisobutyrate bromide was reacted with N-(2-hydroxyethyl)phthalimide and triethylamine in dry THF to get ATRP initiator. PSAN polymer ligands were synthesized via ARGET ATRP, by altering the target degree of polymerization and reaction time, the resulted PSAN polymers have M_n from 1300 to 8000 with M_w/M_n from 1.20 to 1.32. (**Figure S2.3**) The protection group was removed by hydrazine in THF solutions to obtain PSAN-NH_2 polymer ligands.

Ligand exchange between OA and PSAN-NH_2 ligands was driven by the lower boiling point (180 ℃) of OA. The OA capped ZnO NPs were stable in THF or hexane for weeks, however, the obtained PSAN capped ZnO was completely precipitated by addition to hexane after the ligand exchange reaction. By applying "selective precipitation, centrifugation, dissolving" method for several cycles, free polymer ligands can be removed from the system.[16, 17] The resulting product can be easily redispersed in THF and formed a stable solution used for further studies. The effect of concentration and DP of used PSAN-NH_2 and on the target PSAN capped ZnO were systematically investigated (

).

Table 2.1. Summary of ligand exchange reactions between OA capped ZnO with PSAN-NH2 polymer ligands

Entry	The molar ratio between OA: PSAN-NH_2	M_n [b]	Size (nm)[c]	Inorganic fraction	Grafting density (nm^{-2})[f]
1	2:1	1300	10	47%	2.5
2	2:1	2000	12	36%	2.4
3	6:1	3800	24	45%	0.9
4	2:1	3800	14	28%	1.9
5	2:1	8000	21	19%	1.5
6[g]	2:0	129	5	83%	4.4

[a] 1 g OA capped ZnO nanoparticles were used in all ligand exchange reactions. [b] Determined by SEC; [c] determined by DLS; [d] determined by TGA; [e] theoretical inorganic contents were calculated from the molar ratio of OA/PSAN-NH_2 and M_n of PSAN-

NH_2. [f] calculated from inorganic fraction and polymer molar mass assuming the spherical shape of nanoparticles; [g] OA capped ZnO.

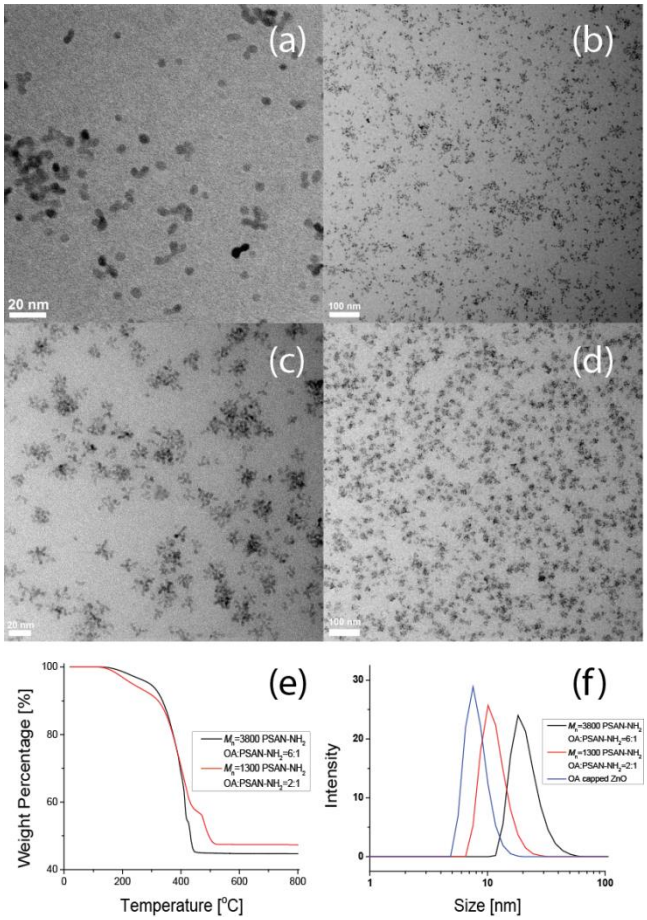

Figure 2.2. TEM images of PSAN capped ZnO NPs prepared from OA capped ZnO NPs, M_n=1300 PSAN-NH_2, OA: PSAN-NH_2=2:1, (a) and (b); M_n=3800 PSAN-NH_2, OA: PSAN-NH_2=6:1, (c) and (d); TGA curves of PSAN capped ZnO NPs (e), and DLS results of OA capped ZnO and PSAN capped ZnO NPs in THF solutions (f).

After the reaction, the product could be precipitated in hexane, which is a good solvent for OA capped ZnO NPs, but a non-solvent for PSAN capped ZnO NPs. In this case, PSAN capped ZnO NPs product was purified by removing DPE solvent and byproduct in hexane. The resulting yellow powders were characterized by TEM, DLS, and TGA. To study the effect of polymer ligands on the morphology of nanocomposite, we applied different PSAN-NH_2 polymer ligands and manipulate the molar ratio between them and OA. For example, in Table 2.1 entry a and c, two different polymer ligands M_n=1300 and M_n=3800 were used, while the molar ratio

between PSAN-NH_2 and OA were controlled to 1:2 and 1:6. In **Figure 2.2** a,b,c,d and h, TEM and DLS data confirmed good dispersibility and increase of the size of ZnO NPs after modification with PSAN. Upon decreasing the molar ratio of polymer ligands to OA ligands, ZnO NPs formed some clusters (**Figure 2.2**c, d). This could result from the limited amount of PSAN-NH_2 added to the system producing ZnO NPs with bare surfaces, which formed clusters and shared ligands after removal of OA (**Scheme**). In **Figure 2.2**h, DLS indicates that the ZnO clusters have the largest size (24 nm) in THF dispersion, while single ZnO NPs are smaller (10 nm). Graft densities (0.9 and 2.5 chain/nm^2) are lower than for OA capped ZnO NPs, as listed in Table 2.1. The lowest grafting density, 0.9 nm^{-2}, was sufficient to well stabilize the dispersions.

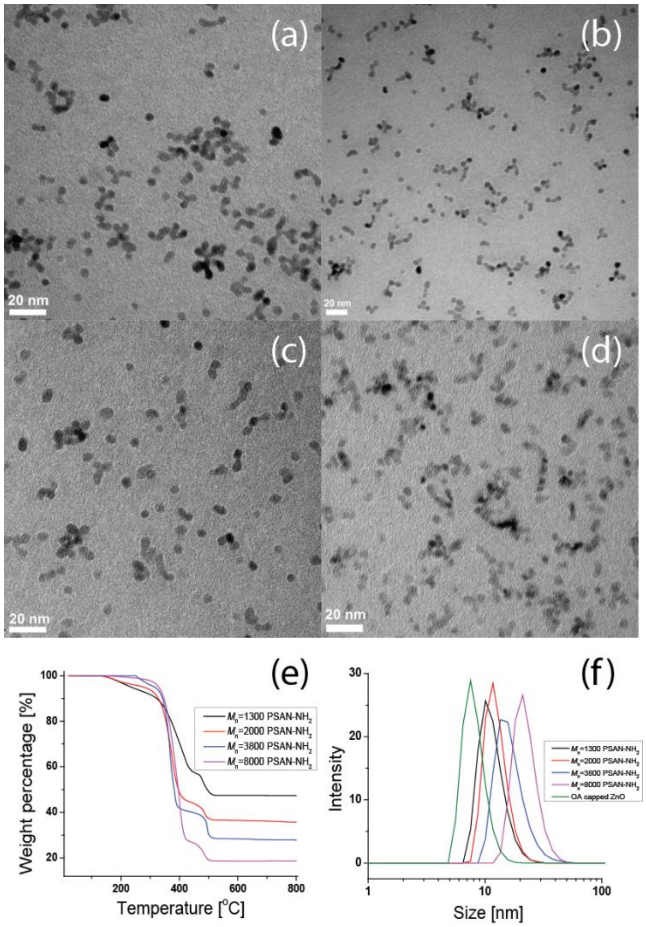

Figure 2.3. TEM images of PSAN capped ZnO synthesized using OA capped ZnO NPs and PSAN-NH_2 polymer ligand OA: PSAN-NH_2=2:1, (M_n=1300), (a); M_n=2000, (b); M_n=3800, (c); M_n=8000, (d); TGA data for PSAN capped ZnO NPs, (e); DLS results for OA capped ZnO and PSAN capped ZnO NPs in THF solutions, (f).

Figure 2.3 shows examples of ZnO nanoparticles coated by PSAN-NH_2 ligands with different molecular weights. To achieve comparable results, the molar ratio between OA ligand and polymer ligands were fixed at 2:1. By adjusting the PSAN molecular weight, the PSAN capped ZnO particle size increased with the polymer chain length (from 10 nm to 21 nm), and the ZnO contents decreased (from 47 wt% to 19 wt%). As shown in Table 2.1, after ligand exchange, PSAN capped ZnO NPs had lower grafting density comparing to OA capped ZnO NPs. As the molecular weight of polymer ligand increased (from 1300 to 8000), the grafting density decreased (from 2.5 nm^{-2} to 1.5 nm^{-2}).

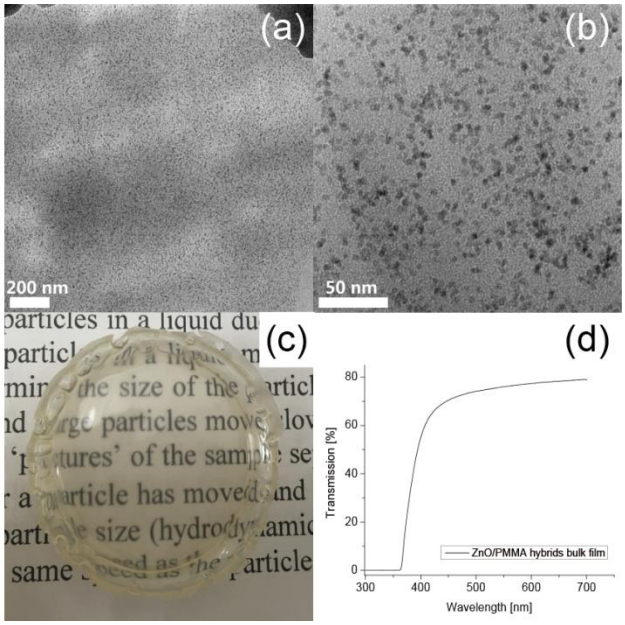

Figure 2.4. (a) and (b) TEM images of ZnO/PMMA hybrids bulk film, PSAN capped ZnO NPs have 34.5 wt% ZnO content, PSAN polymer has M_n=2000; (c) photograph of ZnO/PMMA hybrids bulk film (0.65 mm, 6.6 wt%); (d) plot of transmission vs. wavelength of ZnO/PMMA bull film under UV and visible light regime.

Due to the favorable interaction between PSAN and PMMA, PSAN capped ZnO NPs can be used as nanofillers to blend with the PMMA matrix. By applying the solvent casting method,

ZnO/PMMA hybrid materials bulk film can be fabricated from a mixture of PSAN capped ZnO NPs and linear PMMA polymer (M_w=120,000) in THF solvent. **Figure 2.4** (a) and (b) show the PSAN capped ZnO NPs can be well dispersed in the PMMA matrix with 6.6 wt% (**Figure S2.2**) inorganic contents without any aggregation. The bulk film has good transparency as shown in **Figure 2.4** (c). On the other hand, in different wavelengths, this bulk film has different responses, **Figure 2.*4*** (d), it has 80% transmission in the visible regime, while, it can also totally block UV when the wavelength is below 350 nm.

2.4. Supporting Information

Materials

Monomers: styrene (S, 99%, Aldrich), acrylonitrile (AN, 99%, Alrich) were purified by passing through a column filled with basic alumina to remove the inhibitor. Tris[(2-pyridyl)methyl]amine (TPMA) was synthesized according to the previously published procedure.[1] Tis(2-dimethylaminoethyl)amine (Me_6TREN, 99%, Alfa), and zinc 2-ethylhexanoate ($Zn(EH)_2$, 80% in mineral spirits, Alfa), N-(2-hydroxyethyl)phthalimide (NHP, 99%, Acros), hydrochloric acid (HCl, 36.5-38.0%, Sigma), anisole (99%, Aldrich), methylene chloride (DCM, 99.5%, Fisher) tetrahydrofuran (THF, 99%, VWR), methanol (99%, VWR), hexane (99%, VWR), acetone (99%, VWR), N,N-dimethylformamide (DMF, 99%, VWR), α-bromoisobutyryl bromide (2-BiBB, Aldrich), ethyl 2-bromoisobutyrate (EBiB, 98%, Aldrich), copper(II) bromide ($CuBr_2$, 99%, Aldrich), triethylamine (TEA, 98%, Aldrich), diphenyl ether (DPE, 99%, Aldrich) , tin(II) 2-ethylhexanoate ($Sn(EH)_2$, 95%, Aldrich), poly(methyl methacrylate (PMMA, M_w=120,000 by GPC, Aldrich) and octylamine (OA, 99%, Aldrich) were used as received without further purification.

Synthesis of octylamine capped ZnO nanocrystals

ZnO nanoparticles were synthesized as reported by Epifaniand and Weber.[2] In a 250-mL three-neck flask equipped with a condenser and a thermometer, $Zn(EH)_2$ (80% in mineral spirits) (45 g, 100.8 mmol) was mixed with 80 mL of DPE and OA (90 mL, 503.97 mmol). The reaction mixture was stirred and heated to 175 ºC under an N_2 atmosphere. The temperature is maintained for 45 minutes before heating the mixture to 230 ºC for another 60 minutes. After cooling to room temperature, the nanoparticles were isolated by precipitation in cold methanol. The resulted products were dispersed in THF. A stock solution of 40 mg mL^{-1} was used for further experiments.

Synthesis of PSAN polymer ligands

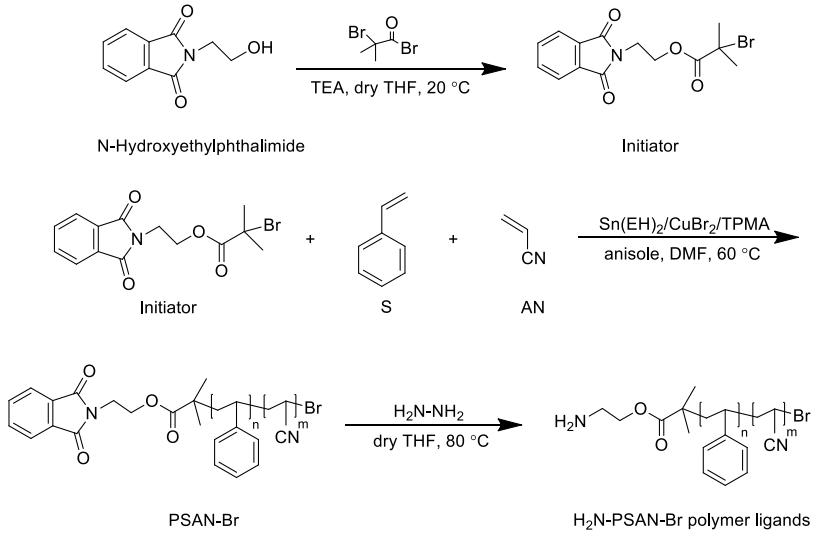

Scheme S2.1. Synthesis of PSAN-NH_2 polymer ligands

Synthesis of PSAN polymer ligands consists of three steps: the synthesis of the initiator, ATRP of PSAN, deprotection of amine end group.

The initiator was synthesized as follows: NHP(16.3 g, 81.96 mmol) and TEA (14.28 mL, 102.45 mmol) was dissolved in 200 mL dry THF in a 500 mL round bottom flask fitted with a

stirring bar and the contents were stirred in an ice bath, 2-BiB (12.67 mL, 102.45 mmol) was then added drop by drop into the mixture. The flask was stirred for another 24 h under r.t. The mixture was then concentrated and the residue dissolved in 100 mL ethyl acetate. Then it was washed with saturated $NaHCO_3$ aqueous solution (200 mL) twice and brine solution once to remove salt and byproducts. The ethyl acetate was then removed by rotary evaporation.

PSAN was synthesized via ARGET ATRP. A general procedure follows: a clean and dry 50 mL Schlenk flask was charged with St (16 mL, 139.85 mmol), AN (5.5 mL, 83.91 mmol), Me_6TREN (0.075 mL, 0.28 mmol), anisole (7.2 mL), and 0.03 mol/L solution of $CuBr_2$ in DMF (0.5 mL, 0.015 mmol). The flask was sealed, and the resulting solution was bubbled with N_2 for 30 minutes. Next, 300 mM solution of $Sn(EH)_2$ in anisole (1 mL, 0.30 mmol) was added into the flask to reduce the $CuBr_2$. Then the flask was immersed into a 60 ºC oil bath, and the reaction mixture was kept under these conditions for the desired time. The reaction mixture was exposed to air to stop the polymerization. The product was precipitated by addition to cold hexane and dried in air. The synthesis and post-purification procedures in each ATRP reaction were similar to the procedures above but with different target degrees of polymerization.

In the deprotection of the amino end group step, PSAN ligands (8.3 g, 7 mmol, M_n=1,200 g/mol) was mixed with dry THF (150 mL) and hydrazine (1.08 mL, 34.5 mmol) in a 250 mL three-neck flask equipped with a condenser and a thermometer. The reaction mixture was stirred and heated to 80 ºC under an N_2 atmosphere for 8 h. After cooling to room temperature, the non-soluble byproduct was removed by centrifugation. The resulting clear solution was concentrated by rotary evaporation. The product was isolated by precipitation in cold hexane and dried in air. The synthesis and post-purification procedures in other PSAN ligands were similar to the procedures above with the same molar ratio of PSAN/hydrazine.

Synthesis of PSAN capped ZnO by ligand exchange

A general procedure for ligand exchange between PSAN-NH_2 ligand and OA ligand is as follows: in a 100 mL two-neck flask equipped with a bubbler, OA capped ZnO stock solution in THF (40 mg mL^{-1}, 25 mL) was mixed with DPE (30 mL) and PSAN-NH_2 ligands (M_n = 1,300 g/mol, 300 mg, 0.25 mmol). The contents of the flask were bubbled with N_2 gas before and during the reaction. The reaction mixture was stirred and heated to 150 ºC in N_2 atmosphere. The temperature is maintained for 20 minutes to remove THF solvents. Next, the mixture was heated to 230 ºC for another 2 h. After cooling to r.t., the nanoparticles were isolated by precipitation in cold hexane.

Fabrication of ZnO/PMMA hybrid materials bulk film

PSAN capped ZnO NPs solution (THF solvent) and linear PMMA powders were prepared. Air dry 5mL solution and weight the residual to calculate the concentration of the solution. 1g linear PMMA powders and 10mL PSAN capped ZnO NPs solution were mixed and formed homogenous solution after 24 hours stirring. 5mL resulted solution was injected into a 1.2-inch diameter cylindrical Teflon mold. After slowly evaporating solvent, the clear bulk film will form after 48 hours. Later the bulk film was transferred into a vacuum oven, by preciously and slowly increasing the temperature at the rate of 10 ºC per 24 hours up to 150 ºC, the residual solvent was removed.

Characterization

Number average molecular weight (M_n) and molecular weight distribution (M_w/M_n) were determined by SEC, conducted with a Waters 515 pump and Waters 2414 different refractometer using PSS columns (Styrogel 105,103, 102 A) in THF as eluent (35 ºC, flow rate of 1 mL min-1). Linear polystyrene (PS) and PMMA standards were used for calibration. The conversion was calculated by detecting the decrease of the monomer peak area relative to the peak area of the internal standards. ^{1}H NMR spectroscopy used for polymerization monitoring was performed using a Bruker Advance 300 MHz NMR spectroscopy with $CDCl_3$ as a solvent.

Transmission electron microscopy (TEM) was performed using a JEOL 2000 EX electron microscope operated at 200kV. The size of the particles was determined from the statistical analysis of the TEM micrographs using ImageJ software. To confirm results obtained from TEM, dynamic light scattering (DLS) using a Malvern Zetasizer Nano ZS was also employed to determine volume-weighted average hydrodynamic radius and distribution. The particles were suspended in filtered THF or DMF (220 nm PTFE filter) at micro concentrations. To characterize the structure and crystallinity, a Philips X'Pert (Philips Analytical, Netherlands) X-ray diffractometer (XRD) (Cu Kα radiation) was operated at 45 kV and 40 mA in grazing incidence mode. The fraction of ZnO content was measured by thermogravimetric analysis (TGA), TA Instrument 2950, and the data were analyzed with TA Universal Analysis. The heating procedure involved 4 steps: 1) samples were placed on a Platinum pan and the temperature jumped to 120 ºC in air atmosphere; 2) hold at 120 ºC for 10 mins; 3) ramp up at a rate of 20 ºC/min to 800 ºC; 4) hold for 5 mins. The TGA plots were normalized to the total weight after holding at 120 ºC. The grafting densities of hybrid particles were calculated by the following equation:

$$\sigma_{\mathrm{TGA}} = \frac{(1 - f_{\mathrm{ZnO}}) N_A \, \rho_{\mathrm{ZnO}} d}{6 \, f_{\mathrm{ZnO}} \, M_{\mathrm{n}}} \tag{1}$$

where is the ZnO fraction measured by TGA after exclusion of any residual solvent; N_A is the Avogadro number; is the density of zinc oxide NPs; d is the average diameter of ZnO NPs; M_n is the overall number average MW of polymer brushes.

The UV-vis transmission vs. wavelength plot was measured by Varian 50 Bio UV-Visible Spectrophotometer.

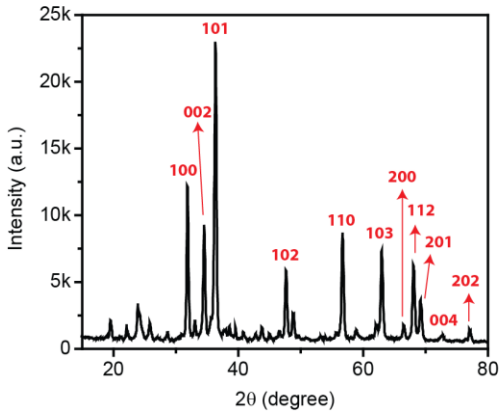

Figure S2.1 XRD pattern of OA capped ZnO

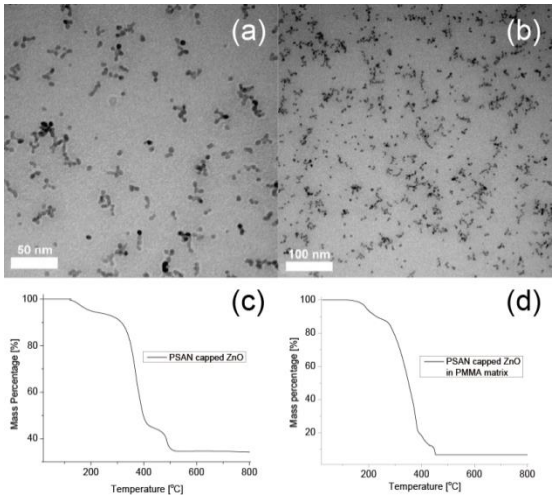

Figure S2.2. (a) and (b) TEM images of PSAN capped ZnO nanoparticles, M_n=2000; (c) TGA data of PSAN capped ZnO nanoparticles, inorganic content is 34.5 wt%; (d) TGA data of ZnO/PMMA hybrids bulk film, inorganic content is 6.6 wt%.

Table S2.1. Results of PSAN-NH_2 polymer ligands

Entry	Monomer	$DP_{target,}$[b]	$M_{n,}$[a]	DP	M_w/M_n[a]
1	S & AN	40	1300	15	1.32
2	S & AN	40	2000	23	1.20

3	S & AN	80	3800	45	1.29
4	S & AN	240	8000	94	1.21

a)Molecular weights and molecular weights distribution were measured by THF SEC using linear PS standards; b)Reaction conditions: Initiator/S/AN/$CuBr_2$/Me_6TREN/$Sn(EH)_2$ = 1/0.63DP_{target}/0.37DP_{target}/0.005/0.1/0.1, T = 60 ^oC, in anisole (25 vol-%), DMF (2.5 vol-%).

1. Xia, J.; Matyjaszewski, K., Controlled/"Living" Radical Polymerization. Atom Transfer Radical Polymerization Catalyzed by Copper(I) and Picolylamine Complexes. *Macromolecules* **1999,** 32, (8), 2434-2437.

2. a)Epifani, M.; Arbiol, J.; Díaz, R.; Perálvarez, M. J.; Siciliano, P.; Morante, J. R., Synthesis of SnO2 and ZnO Colloidal Nanocrystals from the Decomposition of Tin(II) 2-Ethylhexanoate and Zinc(II) 2-Ethylhexanoate. *Chemistry of Materials* **2005,** 17, (25), 6468-6472; b)Weber, D.; Botnaras, S.; Pham, D. V.; Steiger, J.; De Cola, L., Functionalized ZnO nanoparticles for thin-film transistors: support of ligand removal by non-thermal methods. *Journal of Materials Chemistry C* **2013,** 1, (18), 3098-3103.

2.5. Conclusions

We reported here, ZnO/polymer hybrid materials were synthesized by the "ligand exchange" method, OA capped ZnO nanoparticles and PSAN-NH_2 polymer ligands with different chain lengths were synthesized first. By utilizing the lower boiling point of OA, PSAN-NH_2 polymer ligand can be efficiently attached to the ZnO NPs' surfaces under high-temperature conditions. The morphology of PSAN capped ZnO nanocomposites can be controlled by altering the molar ratio between OA and polymer ligands. The resulted ZnO hybrid materials can be easily dissolved in the nonpolar solvent and form stable solutions. As nanofillers, PSAN capped ZnO NPs were blended with PMMA matrix, the resulted ZnO/PMMA hybrids can be fabricated to bulk films with high transparency. This working board the method to synthesize ZnO/polymer

nanocomposites, and the application of ZnO based materials on optical sensors, electronics devices, and plastics additive fields.

2.6. References

1. Dickerson, R. R.; Kondragunta, S.; Stenchikov, G.; Civerolo, K. L.; Doddridge, B. G.; Holben, B. N., The Impact of Aerosols on Solar Ultraviolet Radiation and Photochemical Smog. *Science* **1997,** 278, (5339), 827-830.
2. Masui, T.; Yamamoto, M.; Sakata, T.; Mori, H.; Adachi, G.-y., Synthesis of BN-coated CeO2 fine powder as a new UV blocking material. *Journal of Materials Chemistry* **2000,** 10, (2), 353-357.
3. Mora-Seró, I.; Bisquert, J.; Fabregat-Santiago, F.; Garcia-Belmonte, G.; Zoppi, G.; Durose, K.; Proskuryakov, Y.; Oja, I.; Belaidi, A.; Dittrich, T.; Tena-Zaera, R.; Katty, A.; Lévy-Clément, C.; Barrioz, V.; Irvine, S. J. C., Implications of the Negative Capacitance Observed at Forward Bias in Nanocomposite and Polycrystalline Solar Cells. *Nano Letters* **2006,** 6, (4), 640-650.
4. Teow, Y.; Asharani, P. V.; Hande, M. P.; Valiyaveettil, S., Health impact and safety of engineered nanomaterials. *Chemical Communications* **2011,** 47, (25), 7025-7038.
5. Li, X. H.; Xing, Y. G.; Li, W. L.; Jiang, Y. H.; Ding, Y. L., Antibacterial and Physical Properties of Poly(vinyl chloride)-based Film Coated with ZnO Nanoparticles. *Food Science and Technology International* **2010,** 16, (3), 225-232.
6. Li, S.; Toprak, M. S.; Jo, Y. S.; Dobson, J.; Kim, D. K.; Muhammed, M., Bulk Synthesis of Transparent and Homogeneous Polymeric Hybrid Materials with ZnO Quantum Dots and PMMA. *Advanced Materials* **2007,** 19, (24), 4347-4352.
7. Faria, J. C. D.; Campbell, A. J.; McLachlan, M. A., ZnO Nanorod Arrays as Electron Injection Layers for Efficient Organic Light-Emitting Diodes. *Advanced Functional Materials* **2015,** 25, (29), 4657-4663.
8. Rasmussen, J. W.; Martinez, E.; Louka, P.; Wingett, D. G., Zinc oxide nanoparticles for selective destruction of tumor cells and potential for drug delivery applications. *Expert Opinion on Drug Delivery* **2010,** 7, (9), 1063-1077.
9. Pang, X.; Zhao, L.; Han, W.; Xin, X.; Lin, Z., A general and robust strategy for the synthesis of nearly monodisperse colloidal nanocrystals. *Nat Nano* **2013,** 8, (6), 426-431.
10. Yuan, J.; Xu, Y.; Walther, A.; Bolisetty, S.; Schumacher, M.; Schmalz, H.; Ballauff, M.; Muller, A. H. E., Water-soluble organo-silica hybrid nanowires. *Nat Mater* **2008,** 7, (9), 718-722.
11. Müllner, M.; Yuan, J.; Weiss, S.; Walther, A.; Förtsch, M.; Drechsler, M.; Müller, A. H. E., Water-Soluble Organo−Silica Hybrid Nanotubes Templated by Cylindrical Polymer Brushes. *Journal of the American Chemical Society* **2010,** 132, (46), 16587-16592.
12. Zheng, Z.; Daniel, A.; Yu, W.; Weber, B.; Ling, J.; Müller, A. H. E., Rare-Earth Metal Cations Incorporated Silica Hybrid Nanoparticles Templated by Cylindrical Polymer Brushes. *Chemistry of Materials* **2013,** 25, (22), 4585-4594.
13. Leong, W. L.; Lee, P. S.; Lohani, A.; Lam, Y. M.; Chen, T.; Zhang, S.; Dodabalapur, A.; G. Mhaisalkar, S., Non-Volatile Organic Memory Applications Enabled by In Situ Synthesis of Gold Nanoparticles in a Self-Assembled Block Copolymer. *Advanced Materials* **2008,** 20, (12), 2325-2331.

14. Park, J.; Joo, J.; Kwon, S. G.; Jang, Y.; Hyeon, T., Synthesis of Monodisperse Spherical Nanocrystals. *Angewandte Chemie International Edition* **2007,** 46, (25), 4630-4660.
15. Epifani, M.; Arbiol, J.; Díaz, R.; Perálvarez, M. J.; Siciliano, P.; Morante, J. R., Synthesis of SnO2 and ZnO Colloidal Nanocrystals from the Decomposition of Tin(II) 2-Ethylhexanoate and Zinc(II) 2-Ethylhexanoate. *Chemistry of Materials* **2005,** 17, (25), 6468-6472.
16. Ehlert, S.; Taheri, S. M.; Pirner, D.; Drechsler, M.; Schmidt, H.-W.; Förster, S., Polymer Ligand Exchange to Control Stabilization and Compatibilization of Nanocrystals. *ACS Nano* **2014,** 8, (6), 6114-6122.
17. Ehlert, S.; Stegelmeier, C.; Pirner, D.; Förster, S., A General Route to Optically Transparent Highly Filled Polymer Nanocomposites. *Macromolecules* **2015,** 48, (15), 5323-5327.

Chapter 3 Characterization of ZnO Nanoparticles using Superconducting Tunnel Junction Cryodetection Mass Spectrometry

3.1. Preface

Zinc oxide (ZnO) nanoparticles coated with either *n*-octylamine (OA) or *α*-amino poly(styrene-*co*-acrylonitrile) (PSAN) ligands (L) were analyzed using laser desorption/ionization and matrix-assisted laser desorption/ionization (MALDI) time-of-flight (TOF) superconducting tunnel junction (STJ) cryodetection mass spectrometry. STJ cryodetection has the advantage of high *m*/*z* detection and allows for the determination of average molecular weights and dispersity for 500–600 kDa ZnO-L nanoparticles. The ability to detect the relative energies deposited into the STJs has allowed for the investigation of ZnO-L metastable fragmentation. ZnO-L precursor ions gain enough internal energy during the MALDI process to undergo metastable fragmentation in the flight tube. These fragments produced a lower energy peak, which was assigned to ligand-stripped ZnO cores whereas the individual ligands were at too low energy to be observed. From these STJ energy-resolved peaks, the

average weight percentage of inorganic material making up the nanoparticle was determined, where ZnO-OA and ZnO-PSAN nanoparticles are comprised of ~62% and ~68% wt ZnO, respectively. In one example, grafting densities were calculated based on the metastable fragmentation of ligands from the core to be 16 and 1.1 nm^{-2} for ZnO-OA and ZnO-PSAN, respectively, and compared with values determined by thermogravimetric analysis (TGA) and transmission electron microscopy (TEM).

In this chapter, the characterization of OA capped ZnO and PSAN capped ZnO nanoparticles by mass spectrum is discussed. I performed all synthetic work and part of the characterization with Logan Plath in this project, Logan did all of the mass spectra in Professor Bier's lab. I would like to thank especially my collaborators, Logan Plath and Professor Mark E. Bier for their help and extensive discussion during this project. Jiajun Yan assisted in the synthesis work.

This paper was published in *Journal of The American Society for Mass Spectrometry*, (Logan D Plath, Zongyu Wang, Jiajun Yan, Krzysztof Matyjaszewski, Mark E Bier, "Characterization of ZnO Nanoparticles using Superconducting Tunnel Junction Cryodetection Mass Spectrometry", Journal of The American Society for Mass Spectrometry, 2017, 6 (28), 1160-1165.).

This work was supported by the National Science Foundation for funding under grant DBI 454980, funding under CHE 1611146 and DMR 1501324.

3.2. Introduction

Zinc oxide (ZnO) nanoparticles have received significant attention in the field of nanotechnology due to the unique optical and electronic properties associated with these

structures.[1-2] For example, ZnO nanoparticles have been incorporated into textile construction for UV protection properties and also in inorganic-polymer photovoltaic cells as ultra-fast charge carriers.[3-4] For these inorganic-polymer nanocomposite hybrids, researchers are often concerned about the structure, size distribution, stability, and degree of surface modification of particles. Characterization of these heterogeneous nanoparticles, where the above measurements can be made accurately and efficiently, would greatly help to advance the field. The use of specialized mass spectrometry (MS) method using cryodetection is shown here as a new tool to improve such nanoparticle characterization.

Cryodetection MS was first introduced by Twerenbold and coworkers in 1996 by coupling a superconducting tunnel junction (STJ) to a matrix-assisted laser desorption ionization (MALDI) time-of-flight (TOF) mass spectrometer.[5] They demonstrated high *m*/*z* analysis sensitivity, where ion velocity dependence of conventional detectors show reduced signal response.[6-7] Since then, results have been obtained using STJ cryodetection for ultra-high mass macromolecules such as 13 MDa bacteriophage capsids, 2 MDa polystyrene, von Willebrand factor (1.5 MDa), IgM (1 MDa), and heterogeneous systems such as ferritin (~850 kDa).[8-11]

In this report, ZnO nanoparticles (~5 nm in diameter) attached with protecting ligands (L): *n*-octylamine (OA, MW=129 Da) and a synthetic copolymer, *α*-amino poly(styrene-*co*-acrylonitrile) (PSAN, M_n=1500 Da), were analyzed at low charge states by laser desorption ionization (LDI) and MALDI-TOF cryodetection MS. As demonstrated herein, there is analytical utility when studying these large heterogeneous nanoparticles at low-charge states with STJ cryodetectors. Determining the molecular weight of these large, heterogeneous particles at a high charge may also be possible, but would require resolving individual charge states at high resolution. Since these ZnO nanoparticles are dispersed, this may not be readily obtainable. In

this work, in addition to determining the mass and dispersity of theses ZnO-L nanoparticles, the energies deposited into the STJ cryodetector are used to measure metastable fragment masses. The capability of making these energy measurements, unique to STJ MS, is investigated for the quantification of ligand loading on the ZnO nanoparticle surface.

3.3. Experimental Section

Materials and Synthesis

Zinc(II) 2-ethylhexanoate and tris(2-dimethylaminoethyl)amine (Me_6TREN) were obtained from Alfa Aesar (Haverhill, MA, USA). Styrene (St), acrylonitrile (AN), diphenyl ether, *n*-octylamine (OA), triethylamine TEA), *α*-bromoisobutyryl bromide (BiBB), sodium bicarbonate ($NaHCO_3$), copper(II) bromide ($CuBr_2$), tin(II) 2-ethylhexanoate ($Sn(EH)_2$, hydrazine, sinapinic acid (SA), and monoclonal immunoglobulin G1 (IgG1) were obtained from Sigma-Aldrich (St. Louis, MO, USA). N-(2-hydroxyethyl)phthalimide (NHP) was obtained from Acros (Fair Lawn, NJ, USA). Tetrahydrofuran (THF) was obtained from VWR (Radnor, PA, USA) and Fisher Scientific (Fair Lawn, NJ, USA). Additional solvents: acetonitrile, ethyl acetate, anisole, dimethylformamide (DMF), dichloromethane, methanol, hexane, acetone, and water were of 99% purity or greater and obtained from VWR (Radnor, PA, USA), Fisher Scientific (Fair Lawn, NJ, USA), or Sigma-Aldrich (St. Louis, MO, USA). ZnO-OA nanoparticles were synthesized as reported by Epifani et al. and Weber *et al.*[12,13] ZnO-PSAN nanoparticles were synthesized from ZnO-OA using a ligand exchange protocol described previously.[14] Details regarding the synthesis of PSAN ligands can be found in the Supplementary Materials.

LDI/MALDI-TOF-STJ MS Experimental Details

All MS data were acquired on a modified Macromizer[10] (Comet AG, Flamatt, Switzerland) incorporating a 3.75 m flight tube. LDI and MALDI experiments were performed in positive

ion/linear mode using 20 kV accelerating voltages except where noted. In all experiments, the extraction grid lens was pulsed to 17 kV and the middle element of the Einzel lens was held at 10.25 kV. The extraction delay time was set to 5 μs. The 16-channel STJ array was held at 0.34 K and detectors were biased at 350 μV. For LDI experiments, ZnO-OA (12 mg/mL in THF) and ZnO-PSAN (40 mg/mL in THF) were spotted directly onto the plate and allowed to dry in the air before introduction into the instrument ion source. For MALDI experiments, ZnO-OA (12 mg/mL in THF) and ZnO-PSAN (40 mg/mL in THF) samples were spotted on top of dried SA depositions to produce the highest ion flux. When ZnO-L and matrix solutions were mixed in the liquid phase, depositions had a noticeable color change and did not produce intact ions. Sample concentrations were estimated based on preparations from the dry mass. Samples ionized best at the previously mentioned concentrations. Depositions were ablated with 337 nm radiation using a pulsed nitrogen laser (Spectra-Physics 337201-01, Santa Clara, CA, USA) with a maximum pulse energy of 260 μJ. For most mass spectra, 2000 shots were collected. Laser intensities were attenuated to levels just above ion production threshold levels to minimize fragmentation.

Data Processing

STJ cryodetection MS data was processed in a Mathematica program developed in-house.[15] The *m*/*z* response of the instrument was calibrated using monoclonal IgG multimers. The non-linear energy response of the STJs was calibrated using ZnO-OA nanoparticles analyzed at different acceleration voltages. Through this approach, a seven-point curve of measured STJ energy response versus ion kinetic energy was fit to a second-order polynomial with an r 2 value > 0.99.

3.4. Result and Discussion

Synthesized ZnO-OA and ZnO-PSAN nanoparticles were previously characterized by traditional non-MS techniques: X-ray diffraction (XRD), transmission electron microscopy (TEM), dynamic light scattering (DLS), and thermogravimetric analysis (TGA) similar to the previous report by Wang *et al*.[14] Results from these traditional characterization techniques can be found in the supporting information. ZnO-OA nanoparticles were found to have an average core diameters of 5.2 ± 0.8 nm, based on TEM analysis on 93 individual particles. ZnO-PSAN nanoparticles were found to have an average core diameter of 5.4 ± 0.9 nm, based on the TEM analysis of 97 particles. TGA results suggested that ZnO-OA and ZnO-PSAN nanoparticles were comprised of 81% and 70% wt inorganic material, respectively. Thorough knowledge of the size, density, molecular weight, and relative mass contribution of core/ligand materials, grafting densities (σ),[16] that is, the ligand-loadings on the surface of the nanoparticles, were calculated. Using these results, σ_{trad} values were determined to be 5.3 and 0.9 nm^{-2} for ZnO-OA and ZnO-PSAN nanoparticles, respectively.[14]

Cryodetection MS was next used to study the composition of synthesized ZnO nanoparticles. By measuring intact molecular weights, MS may be able to provide more exact determinations of nanoparticle size and composition. MS analysis is also rapid since the analyses are done in the gas phase and it provides quality statistics since thousands of ions make up the data. A 3D MALDI-TOF-STJ mass spectrum of ZnO-OA nanoparticles is shown in **Figure 3.1**a. The data have shown highlight the additional detection capabilities of STJ MS, where the energies deposited by impacting particles are measured in addition to *m*/z. In **Figure 3.1**a, intact ZnO-OA particles were detected as singly charged species with the apex of the

mass distribution (M_p) at 600 kDa. The full width at half maximum (FWHM) of this singly charged distribution was 780 kDa, which describes a broad mass dispersity of these nanoparticles arising from varying numbers of Zn and O atoms in the core and also the variability of the number of ligands attached to the surface. A significant broad peak of near equal ion abundance was detected at an energy level below that of the singly charged species as shown in **Figure 3.1**b. This broad peak with M_p at 630 kDa was assigned to products from metastable fragmentation of the ZnO-L precursor ions. Since fragmentation occurs post-acceleration, these ions are not mass analyzed directly by TOF. Instead, metastable fragments are detected at *m*/*z* values corresponding to the parent ion, but at lower energy levels reflecting the partitioning of energy with mass [$m_{product} = m^*_{parent} (E_{product}/E_{parent})$].

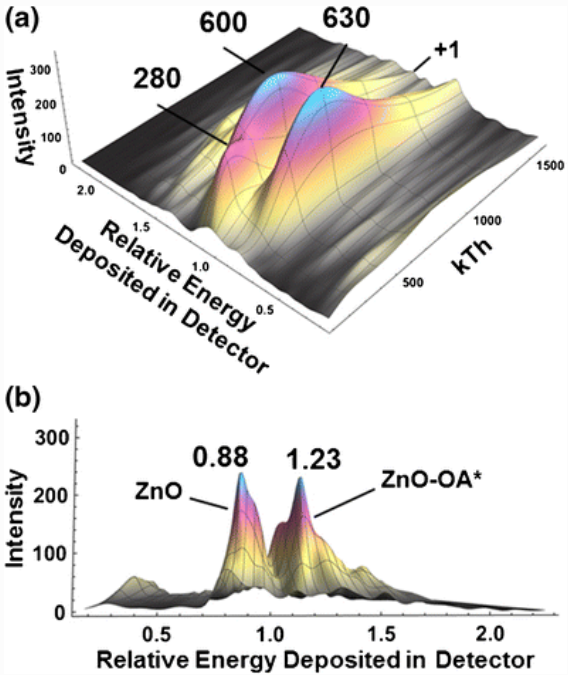

Figure 3.1. (a) 3D MALDI-TOF-STJ MS mass and energy spectrum generated by the analysis of ZnO-OA using sinapinic acid as matrix. The broad peak at 600 kTh represents ZnO-OA at the singly charged energy level. The broad peak at 630 kTh has been assigned to ZnO core fragments resulting from ligand dissociation by metastable fragmentation in the flight tube. (b) STJ energy spectrum of ZnO-OA as viewed from the energy axis in (a). Two distinct peaks at different energy levels are observed. The peak at the higher arbitrary energy (1.23) has been assigned as ZnO-OA. The peak at lower arbitrary energy levels (0.88) has been assigned to ZnO cores that lost OA ligands. The asterisk (*) denotes ions, which may undergo metastable fragmentation

Even when protected by ligands that are expected to have weak ionization efficiencies, these ZnO-L nanoparticles produced intense signals by both LDI and MALDI. It is important to note that nanoparticles are typically coated with protecting ligands to ensure stability and prevent aggregation in solution. The strong absorption of ZnO below 400 nm may provide the energy requirements for extensive desorption, ionization, and fragmentation. LDI-TOF-STJ MS results from the analysis of ZnO-OA nanoparticles are shown in **Figure 3.2**. LDI experiments showed reduced *m*/*z* values for intact ZnO nanoparticles and an absence of a lower energy metastable fragment signal. These results are consistent with the conclusion that LDI imparts more energy into the nanoparticles causing extensive in-source fragmentation resulting in ligand removal and partial ZnO core dissociation before ion acceleration. The M_p of the ZnO-OA signal from the LDI analysis was detected at 160 kTh, as shown in **Figure 3.2**a. Assuming that all ligands have dissociated via in-source fragmentation during the LDI process, this *m*/*z* determination should correspond to an average ZnO core size of ~4.5 nm in diameter, much smaller than the 5.2 ± 0.8 nm sizes measured by TEM. These results serve as evidence that some additional core material is fragmenting from the nanoparticles during LDI.

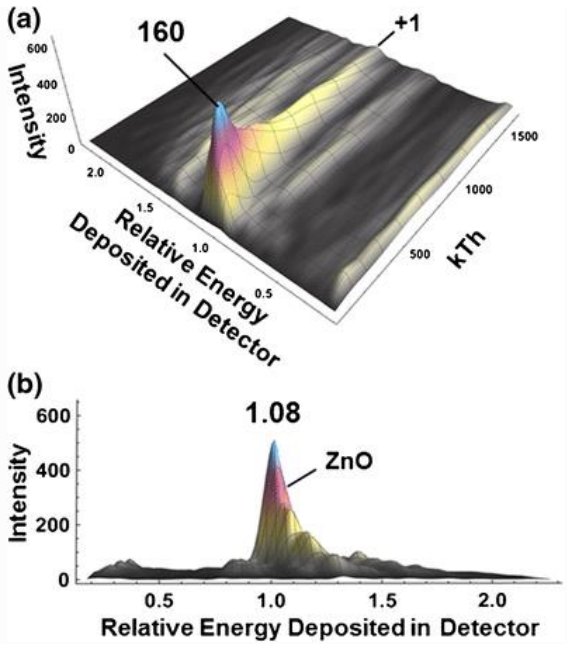

Figure 3.2. (a) 3D LDI-TOF-STJ MS mass and energy spectrum generated by the analysis of ZnO-OA nanoparticles. A sole singly charged peak was observed at 160 kTh, a shift towards lower *m/z* from 600 kTh in Figure 1 (MALDI), which has been assigned to predominately ZnO cores after the loss of ligands and some core material by in-source fragmentation during the LDI process. (b) STJ energy spectrum of ZnO-OA as viewed from the energy axis in (a). For LDI-TOF-STJ MS analyses, no low energy metastable fragment peaks were observed, indicating that most dissociation occurs in the ion source rather than through metastable fragmentation post ion acceleration

Observation of a distinct, well-resolved lower energy peak in **Figure 3.1** suggested that ZnO-OA nanoparticles were fragmenting to a stable product. After correcting for nonlinear responses of the STJ detectors, a metastable fragment mass was assigned. Through this STJ energy measurement, it was determined that the low energy signal was ~62% of the mass of the parent ion mass distribution. We hypothesized that this mass difference was a result of primarily OA ligand dissociation from intact ZnO-OA as a result of metastable fragmentation in the flight tube. The energy resolution was not high enough to conclusively state whether all ligands were dissociated from the core or whether small pieces of ZnO were also removed. In any regard, the resolved energy peak suggests that fragmentation is occurring to a stable product during the remaining mass analysis timescale (<2.7 ms).

In a similar approach, MALDI-TOF-STJ MS was used to characterize ZnO-PSAN nanoparticles. The result of this analysis is shown in **Figure 3.3**. **Figure 3.3**a shows the 3D-mass and energy spectrum from the analysis of ZnO-PSAN. Intact singly charged nanoparticles were detected with the M_p of the mass distribution of 520 kDa and a broad FWHM of 750 kDa. Again, a lower energy peak was observed, which has been assigned as predominately ZnO cores as a result of ligand stripping of PSAN. For these ZnO-PSAN nanoparticles, the low energy peak was determined to be ~68% of the mass of the intact ZnO-PSAN parent ions. PSAN ligands appear to be bound more strongly to the ZnO core compared with the OA binding to ZnO as shown by the lower relative abundance of ~50% of the metastable fragment peak in **Figure 3.3**. This binding strength is also supported by TGA analysis. It should be noted that the ligands arising from the metastable fragmentation of ZnO-L nanoparticles are not observed at low energies in the STJ mass spectra. Since the mass contribution of a single ligand is less than 0.3% of the intact nanoparticle mass and is well below the energy detection limit of this STJ mass spectrometer, the signal was not observed. Intriguingly, the relative energy deposited into the STJ detector was 1.23 and 1.14 for ZnO–OA and ZnO–PSAN analyzed by MALDI and 1.08 for ZnO-OA and ZnO-PSAN nanoparticles analyzed by LDI. These differences are currently being investigated and will be discussed in a future paper about ion energy deposition into STJs.

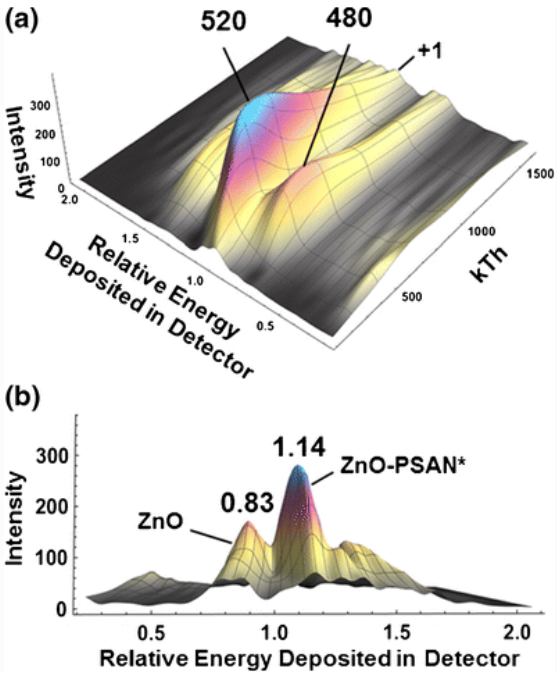

Figure 3.3 (a) MALDI-TOF-STJ MS 3D-mass and energy spectrum generated by the analysis of ZnO-PSAN using sinapinic acid. The peak at 520 kTh represents ZnO-PSAN at the higher singly charged energy level. The peak at half the relative abundance at 480 kTh has been assigned to ZnO core fragments resulting from ligand dissociation during metastable fragmentation. (b) STJ energy spectrum of ZnO-PSAN as viewed from the energy axis in (a). Two distinct features at different energy levels are observed. The feature at the higher arbitrary energy (1.14) has been assigned as ZnO-PSAN. The feature at lower arbitrary energy levels (0.83) has been assigned to ZnO cores that lost PSAN ligands. The asterisk (*) denotes ions that may undergo metastable fragmentation

LDI-TOF-STJ MS analyses were also performed on ZnO-PSAN nanoparticles and results are shown in **Figure 3.4**. LDI experiments showed reduced *m*/*z* values for ZnO nanoparticles and an absence of a lower energy metastable fragment signal, similar to LDI experiments performed on ZnO-OA nanoparticles as shown in **Figure 3.2**. The M_p of the ZnO-PSAN signal from the LDI analysis was detected at 230 kTh, which was assigned to ligand-free ZnO cores with an average size of 5.0 nm. Again, these are smaller than sizes measured by TEM (i.e., 5.4 ± 0.9 nm), as expected, although much closer than those calculated from the LDI analysis of ZnO-OA, providing additional support that the ZnO-PSAN is more robust compared with ZnO-OA nanoparticles. Higher energy signals were also observed in LDI-TOF-STJ MS experiments on ZnO-PSAN nanoparticles. These signals had peak *m*/*z* values of 380

and 410 kTh and have been tentatively assigned to simultaneous multiple particle impacts arising from high ion fluxes to the detector.

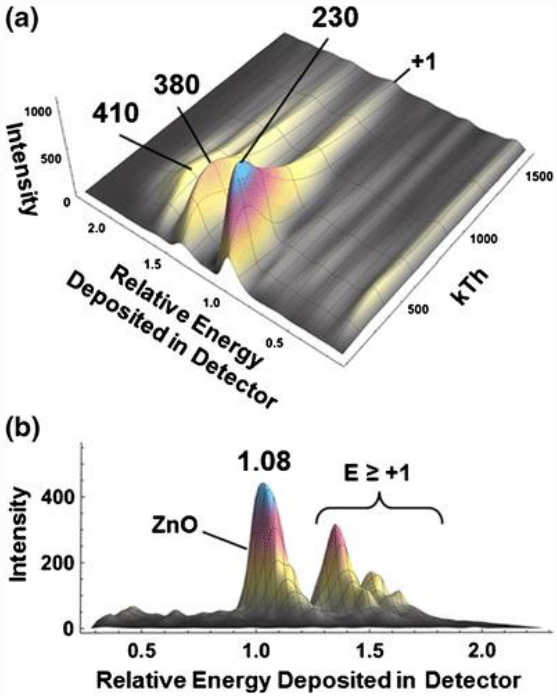

Figure 3.4 (a) 3D LDI-TOF-STJ MS mass and energy spectrum generated by the analysis of ZnO-PSAN nanoparticles. A single singly charged peak was observed at 230 kTh, which is a shift towards lower *m*/*z* from 520 kTh in Figure 3 (MALDI). This peak was assigned to predominately ZnO cores after the loss of ligands and some core material by in-source fragmentation during the LDI process. (b) STJ energy spectrum of ZnO-OA as viewed from the energy axis in (a). For LDI-TOF-STJ MS analyses, no low energy metastable fragment peaks were observed; however, higher energy signals at 380 and 410 kTh were detected. These signals have been tentatively assigned to simultaneous multiple particle impacts due to high ion flux.

While metastable fragments at lower energies are detected at *m*/*z* values identical to that of the parent ions, differences in the most abundant species were observed. **Figure 3.1**a shows that for ZnO-OA, metastable fragments at lower energy show increased abundance for larger molecular weight parent ions. In contrast, **Figure 3.3**a shows that for ZnO-PSAN, metastable fragments show an increased abundance for lower molecular weight parent ions. Due to the limited *m*/*z* resolution, individual ZnO and/or ligand species cannot be resolved. Previous studies in our lab have shown the adduction of ligands and nanoparticle core species and that these adducts can disassociate metastably before detection on an STJ.[17] We suspect that some

minor contributions to the *m*/*z* assignment of intact and metastable distributions in **Figures 3.1** and **3.3** could be affected by differences in the adduction of core/ligand fragments. The asymmetric peak shape of intact ZnO-L nanoparticles with tailing towards higher *m*/*z* also suggested that some adduction was occurring.

Table 3.1 provides a comparison of analytical characterizations made on ZnO-OA and ZnO-PSAN nanoparticles using MALDI-TOF-STJ MS to more traditional techniques of TEM, TGA, and XRD. MALDI-TOF-STJ MS provided intact mass measurements for ZnO-L nanoparticles, where the most abundant ZnO-OA and ZnO-PSAN species were observed at 600 and 520 kDa, respectively. Assuming that low energy signals observed in STJ MS experiments resulted from only ligand dissociation via metastable fragmentation, we determined that ZnO core average molecular weights were 370 and 350 kDa for ZnO-OA and ZnO-PSAN, respectively. XRD analysis confirmed that the ZnO nanoparticles synthesized were of wurtzite structure and using the estimated core molecular weights, MALDI-TOF-STJ MS calculated ZnO core sizes were found to be 5.9 and 5.8 nm for ZnO-OA and ZnO-PSAN, respectively. These measurements, based on MALDI-TOF-STJ MS results, are consistent with ZnO core size determinations made by TEM (5.2 ± 0.8 nm and 5.4 ± 0.9 nm for ZnO-OA and ZnO-PSAN, respectively). While 5.2 and 5.4 nm ZnO cores have calculated molecular weights of ~250 and ~280 kDa, respectively, the STJ MS determined core sizes are within one standard deviation. Assuming that no ligand material remained after metastable fragmentation, the STJ MS-based core sizing should be statistically more accurate as the analysis is based on thousands of ions.

Table 3.1. Comparison of ZnO Nanoparticle Characterization by MALDI-TOF-STJ Cryodetection MS and Traditional Analytical Techniques (i.e., XRD, TGA, and TEM)

	Particle MW_{avg}(kDa)	% wt Inorganic	Calc. core MW_{avg}(kDa)	Core diameter (nm)	Calc. number ligands	σ (nm^{-2})	Core fragmentation adjusted* $\sigma_{STJ\text{-}MS}$ (nm^{-2})
ZnO-OA (STJ-MS)	600	62%	370	5.9	1800	16	8.6
ZnO-PSAN (STJ-MS)	520	68%	350	5.8	110	1.1	1.0
ZnO-OA (traditional methods)	310	81%	250	5.2	460	5.3	-
ZnO-PSAN (traditional methods)	400	70%	280	5.4	80	0.9	-

*Calculation includes loss of one ZnO per ligand.

In addition to characterizing the size of ZnO-L nanoparticles, we attempted to provide grafting densities based on STJ MS results ($\sigma_{STJ\text{-}MS}$). Assuming that all ligands were removed through metastable fragmentation during the MALDI-TOF-STJ MS analyses, $\sigma_{STJ\text{-}MS}$ for the ZnO cores detected at low energies were calculated to be 16 and 1.1 nm^{-2} for ZnO-OA and ZnO-PSAN, respectively. The $\sigma_{STJ\text{-}MS}$ results for ZnO-OA and ZnO-PSAN were ~3× and ~1.2× higher, respectively than those calculated by TGA (σ_{trad}). The MS results suggested that the metastable fragmentation of L from ZnO may include some ZnO material from the surface of the core. Assuming that one ZnO moiety leaves the core with each ligand removal, the calculated number of molecules tethered to the core becomes 1100 and l10, respectively (77% and 70% wt inorganic), and this gives an adjusted $\sigma_{STJ\text{-}MS}$ values of 8.6 and 1.0 nm^{-2} for ZnO-OA and ZnO-PSAN, respectively (See **Table 3.1**). These values are in much better agreement with the TGA results. Low *m*/*z* LDI and MALDI experiments performed in reflector mode on a higher resolution conventional MALDI-TOF mass spectrometer (Applied Biosystems Foster City, CA, USA, Voyager DE MALDI-TOF-sSTR) showed the presence of free Zn and OA

ions, particularly for LDI analyses, indicating that some inorganic species were dissociating from the core during the ionization processes. In the low *m*/*z* MALDI experiments, a multitude of low mass peaks was observed but the assignment was not possible. It is, however, likely that some of these peaks mixed with matrix ions corresponded to Zn containing species.

3.5. Supporting Information

Synthesis of PSAN Ligands

Synthesis of *α*-amino poly(styrene-*co*-acrylonitrile) (PSAN) ligands consisted of three steps: the synthesis of the initiator, atom transfer radical polymerization (ATRP) of PSAN, and deprotection of the amine end group. The initiator was synthesized as follows: NHP (16.3 g, 81.96 mmol) and TEA (14.28 mL, 102.45 mmol) was dissolved in 200 mL dry THF in a 500 mL round bottom flask fitted with a stirring bar and the contents were stirred in an ice bath. 2-BiBB (12.67 mL, 102.45 mmol) was then added drop by drop into the mixture. The flask was stirred for another 24 h under room temperature. The mixture was then concentrated and the residue dissolved in 100 mL ethyl acetate. Then it was washed with saturated $NaHCO_3$ aqueous solution (200 mL) twice and brine solution once to remove salt and byproducts. The ethyl acetate was then removed by rotary evaporation.

PSAN was synthesized via activators regenerated by electron transfer (ARGET) ATRP. A general procedure follows: a clean and dry 50 mL Schlenk flask was charged with St (16 mL, 139.85 mmol), AN (5.5 mL, 83.91 mmol), Me_6TREN (0.075 mL, 0.28 mmol), anisole (7.2 mL), and 0.03 mol/L solution of $CuBr_2$ in DMF (0.5 mL, 0.015 mmol). The flask was sealed, and the resulting solution was bubbled with N_2 for 30 minutes. Next, 300 mM solution of $Sn(EH)_2$ in anisole (1 mL, 0.30 mmol) was added into the flask to reduce the $CuBr_2$. Then the flask was

immersed into a 60 ºC oil bath, and the reaction mixture was kept under these conditions for the desired time. The reaction mixture was exposed to air to stop the polymerization. The product was precipitated by addition to cold hexane and dried in air. The synthesis and post-purification procedures in each ATRP reaction were similar to the procedures above but with different target degrees of polymerization.

In the deprotection of the amino end group step, PSAN ligands (11.75 g, 7 mmol) were mixed with dry THF (150 mL) and hydrazine (1.08 mL, 34.5 mmol) in a 250 mL three-neck flask equipped with a condenser and a thermometer. The reaction mixture was stirred and heated to 80 ºC under an N_2 atmosphere for 8 h. After cooling to room temperature, the non-soluble byproduct was removed by centrifugation. The resulting clear solution was concentrated by rotary evaporation. The product was isolated by precipitation in cold hexane and dried in air. The synthesis and post-purification procedures in other PSAN ligands were similar to the procedures above with the same molar ratio of PSAN/hydrazine. This synthetic route has been previously reported.

Characterization Techniques by Traditional Methods

Number average molecular weight (M_n) and molecular weight distribution (M_w/M_n) were determined by GPC, conducted with a Waters 515 pump and Waters 2414 refractometer using PSS columns (Styrogel 105,103, 102 A) in THF as eluent (35 ºC, flow rate of 1 mL min^{-1}). Linear polystyrene (PS) and PMMA standards were used for calibration. The conversion was calculated by detecting the decrease of the monomer peak area relative to the peak area of the internal standards. ^1H NMR spectroscopy used for polymerization monitoring was performed using a Bruker Advance 300 MHz NMR spectroscopy with $CDCl_3$ as a solvent.

Transmission electron microscopy (TEM) was performed using a JEOL 2000 EX electron microscope operated at 200 kV. The size of the particles was determined from the statistical analysis of the TEM micrographs using ImageJ software. To confirm results obtained from TEM, dynamic light scattering (DLS) using a Malvern Zetasizer Nano ZS was also employed to determine volume-weighted average hydrodynamic radius and distribution. The particles were suspended in filtered THF (220 nm PTFE filter) at micro concentrations. To characterize the structure and crystallinity, a Philips X'Pert (Philips Analytical, Netherlands) X-ray diffractometer (Cu Ka radiation) was operated at 45 kV and 40 mA in grazing incidence mode. The fraction of ZnO content was measured by thermogravimetric analysis (TGA), TA Instrument 2950, and the data were analyzed with TA Universal Analysis. The heating procedure involved 4 steps: 1) samples were placed on a platinum pan and the temperature jumped to 120 ºC in air atmosphere; 2) hold at 120 ºC for 10 mins; 3) ramp up at a rate of 20 ºC/min to 800 ºC; 4) hold for 5 mins. The TGA plots were normalized to the total weight after holding at 120 ºC.

Low Mass LDI-TOF Mass Spectrometry on a Commercial Instrument

LDI- and MALDI-TOF MS experiments on ZnO-OA nanoparticles were performed on a Voyager DE-STR mass spectrometer (Applied Biosystems, Foster City, CA) in positive ion/reflector mode. The acceleration voltage was set to 20 kV and the grid voltage was set to 67.3% (13,460 V). The extraction delay time was set to 50 ns and the low mass gate was enabled and set to 50 Da. The 337 nm nitrogen laser was pulsed at 20 Hz. The spectra produced were an average of 500 laser shots. Spectra were calibrated using intact molecular ions and fragment ions of a sinapinic acid matrix.

For LDI experiments, ZnO-OA (12 mg/mL in THF) and ZnO-PSAN (40 mg/mL in THF) were spotted directly onto the plate and allowed to dry in the air before introduction into the instrument ion source. For MALDI experiments, ZnO-OA (12 mg/mL in THF) and ZnO-PSAN (40 mg/mL in THF) samples were spotted on top of dried SA depositions.

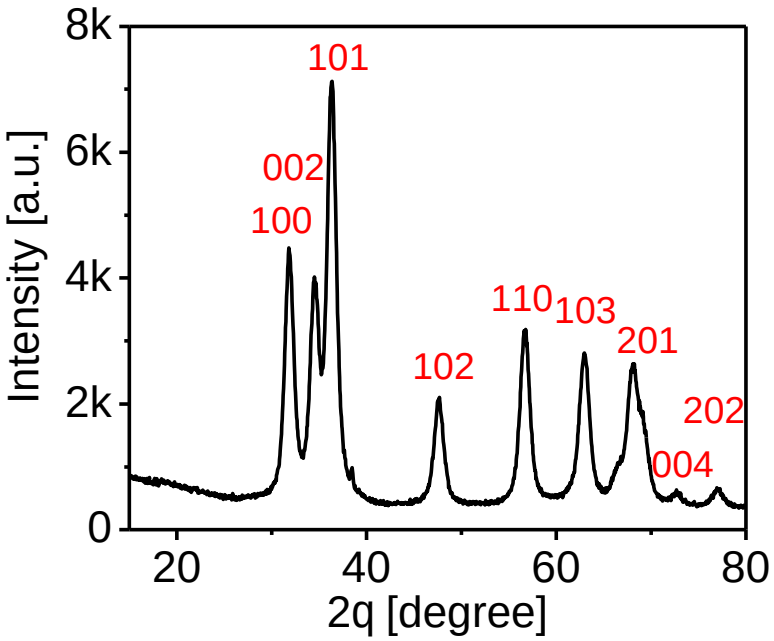

Figure S3.1. XRD characterization of ZnO-OA nanoparticles. The XRD analysis demonstrated that the ZnO core material was of the wurtzite structure.

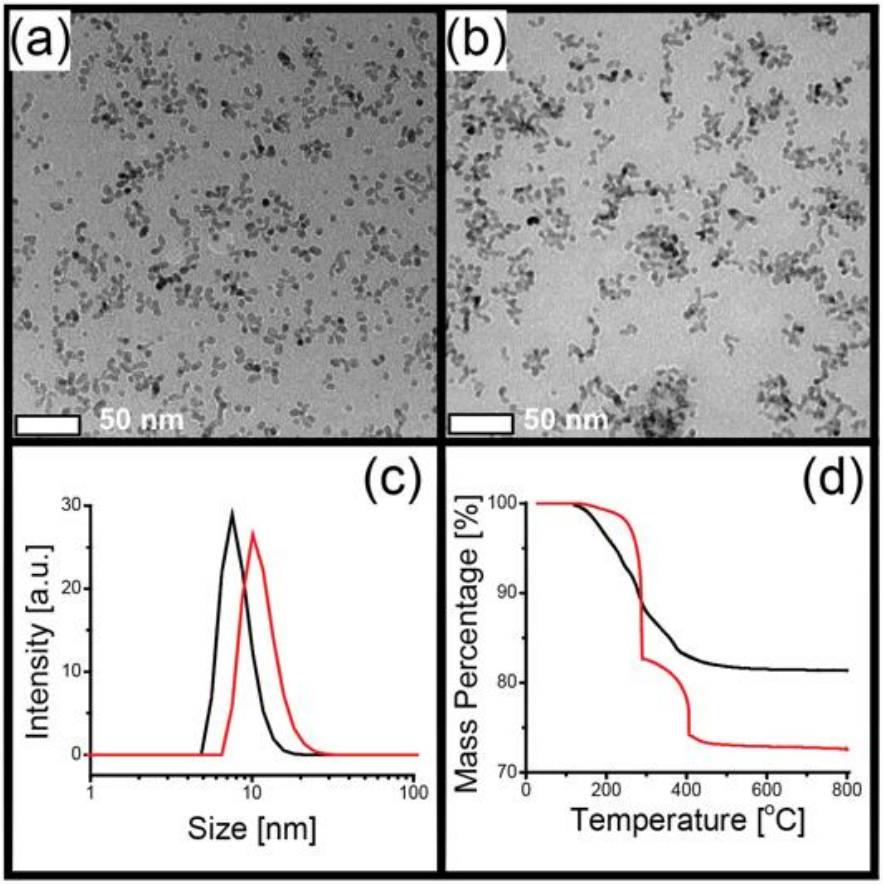

Figure S3.2. The TEM analysis of (a) ZnO-OA and (b) ZnO-PSAN nanoparticles. TEM analysis showed that average ZnO core diameters were 5.2 ± 0.8 nm and 5.4 ± 0.9 nm for ZnO-OA and ZnO-PSAN, respectively. Scale bars shown in TEM images in (a-b) represent 50 nm. (c) DLS characterization showed diameters of 8.1 nm and 11.4 nm of ZnO-OA (black trace) and ZnO-PSAN (red trace), respectively. Note that DLS measures the hydrodynamic diameter of nanoparticles in solution rather than only core sizes as in vacuum TEM. (d) TGA analysis of ZnO-OA (black trace) and ZnO-PSAN (red trace). From the TGA analyses, ZnO-OA was estimated to be composed of ~81% wt inorganic material and ZnO-PSAN was estimated to be composed of ~70% wt inorganic material. The stepwise TGA trace for ZnO-PSAN nanoparticles is suspected to be a result of ligand dissociation for temperatures up to ~275˚C followed by pyrolysis of remaining PSAN ligands on the surface of the nanoparticle. From ~275˚C to ~400˚C it is believed that CO_2 attached to the nanoparticle surface from PSAN pyrolysis is gradually expelled, and above ~400˚C only inorganic core material remains.

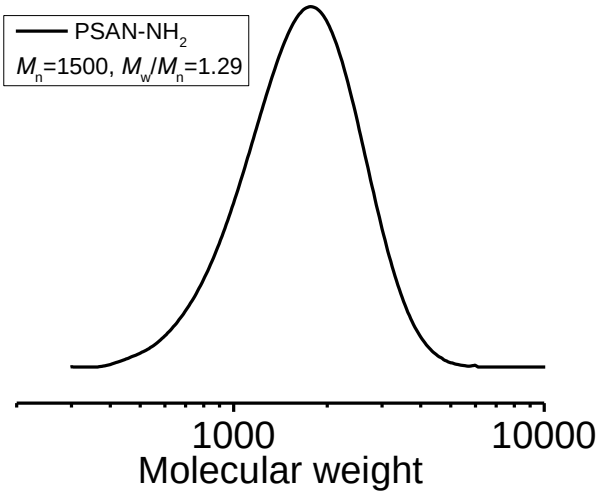

Figure S3.3. SEC analysis of PSAN-NH_2 monomers. By carefully controlling the ARGET-ATRP reactions, controlled polymerization could be achieved producing polymeric monomers of low dispersity. For the ZnO-PSAN nanoparticles studied in this report, PSAN with M_n ~1500 Da were used.

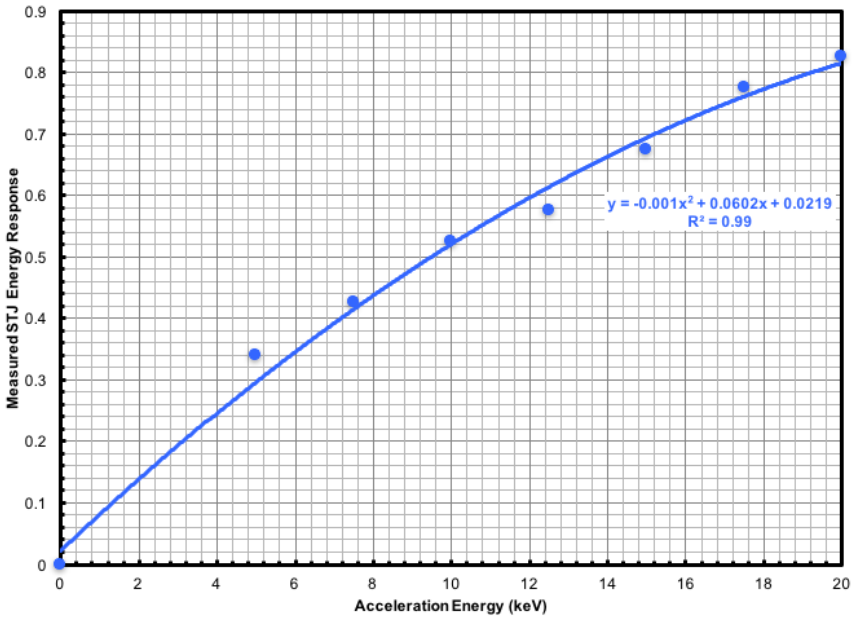

Figure S3.4. The plot of STJ energy responses versus acceleration energy for the ZnO-OA MALDI-TOF-STJ MS analysis. A clear nonlinear energy response was observed and was fitted with a second-order polynomial to provide an energy correction necessary for assigning masses to fragments detected at lower energies as a result of metastable fragmentation.

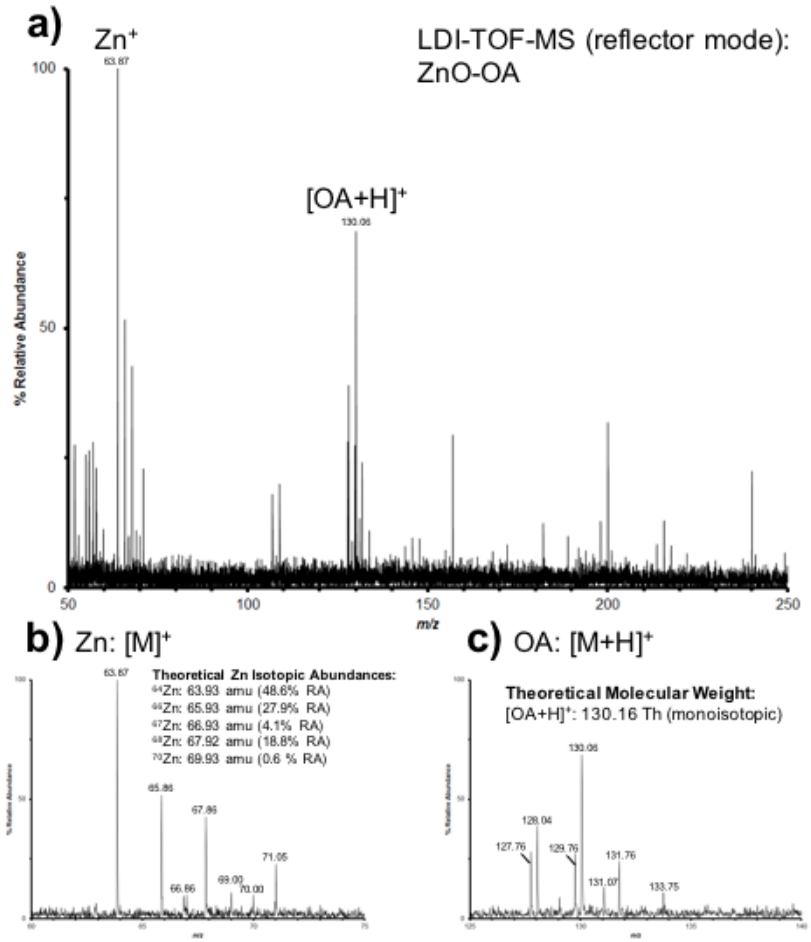

Figure S3.5. (a) LDI-TOF MS mass spectrum of ZnO-OA collected in positive ion/reflector modes on a Voyager DE-STR mass spectrometer (Applied Biosystems). (b) Zoomed spectrum showing the isotope pattern corresponding to free Zn^+ cations detected. (c) Zoomed spectrum showing the region of detection for free $[OA+H]^+$. Other ions observed were not identified and may represent additional fragment ions.

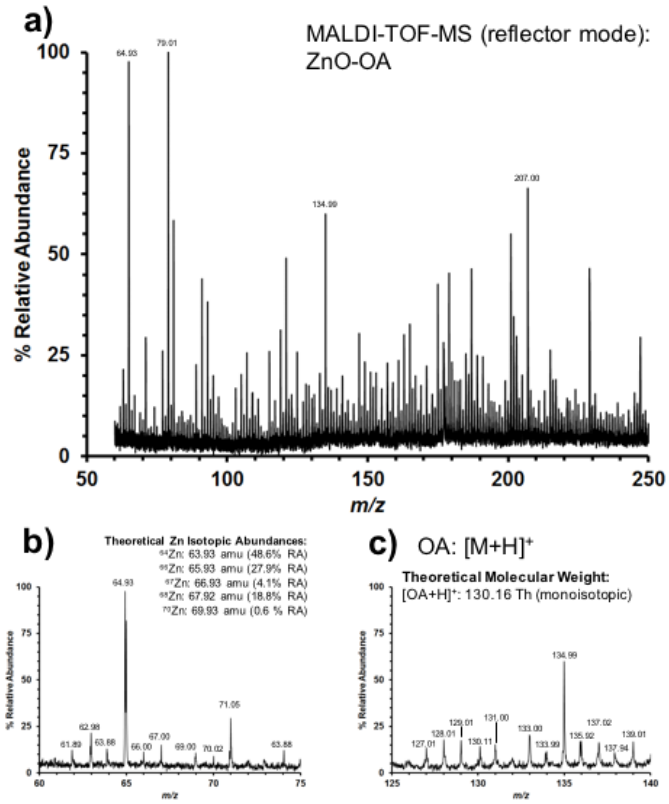

Figure S3.6. (a) MALDI-TOF MS mass spectrum of ZnO-OA collected in positive ion/reflector modes on a Voyager DE-STR mass spectrometer (Applied Biosystems). (b) Zoomed spectrum showing the region of the spectrum where free Zn^+ would be detected. (c) Zoomed spectrum showing the region of detection for free $[OA+H]^+$. Other ions observed were not identified and may represent additional fragment ions. Free Zn^+ and $[OA+H]^+$ may be present but are difficult to uniquely identify due to the complex spectra and potential overlap of unassigned ions.

3.6. Conclusion

Results from this study demonstrate the advantages of using MALDI-TOF-STJ cryodetection MS for the characterization of large heterogeneous ZnO-L nanoparticles. Using this approach, ZnO-L nanoparticle molecular weights and dispersity were measured intact at high *m*/*z* values (>500 kTh) and with low charge states. Besides, based on metastable fragmentation, a method for determining ligand-loading (grafting densities, $\sigma_{\text{STJ-MS}}$) was presented and ZnO core sizes were explored.

MALDI TOF STJ cryodetection should afford advantages for studying other large, heterogeneous systems while maintaining high sensitivity at high *m*/*z* and provide additional information about particle compositions and stability through energy analysis of metastable fragments.

3.7. References

1. Wang, Z.L.: Zinc oxide nanostructures: growth, properties, and applications. *J. Phys. Condens. Matter*. 16, R829–R858 (**2004**)
2. Rajalakshmi, M., Arora, A.K., Bendre, B.S., Mahamuni, S.: Optical phonon confinement in zinc oxide nanoparticles. *J. Appl. Phys*. 87, 2445–2448 (**2000**)
3. Becheri, A., Durr, M., Lo Nostro, P., Baglioni, P.: Synthesis and characterization of zinc oxide nanoparticles: application to textiles as UV-absorbers. *J. Nanoparticle Res*. 10, 679–689 (**2008**)
4. Beek, W.J.E., Wienk, M.M., Janssen, R.A.J.: Efficient hybrid solar cells from zinc oxide nanoparticles and a conjugated polymer. *Adv. Mater*. 16, 1009–1013 (**2004**)
5. Twerenbold, D., Vuilleumier, J., Gerber, D., Tadsen, A., van den Brandt, B., Gillevet, P.M.: Detection of single macromolecules using a cryogenic particle detector coupled to a biopolymer mass spectrometer. *Appl. Phys. Lett.* 68, 3503–3505 (**1996**)
6. Twerenbold, D., Gerber, D., Gritti, D., Gonin, Y., Netuschill, A., Rossel, F., Schenker, D., Vuilleumier, J.L. Single-molecule detector for mass spectrometry with mass-independent detection efficiency. *Proteomics 1*, 66–69 (**2001**)
7. Westmacott, G., Frank, M., Labov, S., Benner, W.: Using a superconducting tunnel junction detector to measure the secondary electron emission efficiency for a microchannel plate detector bombarded by large molecular ions. *Rapid Commun. Mass Spectrom*. 14, 1854–1861 (**2000**)
8. Ozdemir, A., Aksenov, A.A., Firek, B.A., Hendrix, R.W., Bier, M.E.: The analysis of biomacromolecules using a MALDI TOF mass spectrometer incorporating a superconducting tunnel junction (STJ) cryodetector. *Proceeding of the 55th ASMS Conference on Mass Spectrometry and Allied Topics*, June 2007; Indianapolis, IN, USA (**2007**)
9. Aksenov, A.A., Bier, M.E.: The analysis of polystyrene and polystyrene aggregates into the mega dalton mass range by cryodetection MALDI TOF MS. *J. Am. Soc. Mass Spectrom*. 19, 219–230 (**2008**)
10. Wenzel, R.J., Matter, U., Schultheis, L., Zenobi, R.: Analysis of megadalton ions using cryodetection MALDI time-of-flight mass spectrometry. *Anal. Chem*. 77, 4329–4337 (**2005**)
11. Plath, L.D., Ozdemir, A., Aksenov, A.A., Bier, M.E.: Determination of iron content and dispersity of intact ferritin by superconducting tunnel junction cryodetection mass spectrometry. *Anal. Chem*. 87, 8985–8993 (**2015**)
12. Epifani, M., Arbiol, J., Diaz, R., Peralvarez, M.J., Siciliano, P., Morante, J.R.: Synthesis of SnO2 and ZnO colloidal nanocrystals from the decomposition of Tin(II) 2-ethylhexanoate and zinc(II) 2-ethylhexanoate. *Chem. Mater*. 17, 6468–6472 (**2005**)

13. Weber, D., Botnaras, S., Pham, D.V., Steiger, J., De Cola, L.: Functionalized ZnO nanoparticles for thin-film transistors: support of ligand removal by non-thermal methods. *J. Mater. Chem. C* 1, 3098–3103 (**2013**)
14. Wang, Z., Mahoney, C., Yan, J., Lu, Z., Ferebee, R., Luo, D., Bockstaller, M.R., Matyjaszewski, K.: Preparation of well-defined poly(styrene-co-acrylonitrile)/ZnO hybrid nanoparticles by an efficient ligand exchange strategy. *Langmuir* 32, 13207–13213 (**2016**)
15. Sipe, D.M., Wang, F., Duda, R.L., Hendrix, R.W., Bier, M.E.: 3D-histograms improve visualization and charge state determination from macromolecular STJ cryodetection MS Data. *Proceeding of the 61st ASMS Conference on Mass Spectrometry and Allied Topics*, June 2013; Minneapolis, MN, USA (**2013**)
16. Benoit, D.N., Zhu, H., Lilierose, M.H., Verm, R.A., Ali, N., Morrison, A.N., Fortner, J.D., Avendano, C., Colvin, V.L.: Measuring the grafting density of nanoparticles in solution by analytical ultracentrifugation and total organic carbon analysis. *Anal. Chem*. 84, 9238–9245 (**2012**)
17. Plath, L.D., Zeng, C., Chen, Y., Jin, R., Bier, M.E.: Tandem MS of synthetic nanoparticles through analysis of metastable fragments using MALDI-TOF MS with superconducting tunnel junction cryodetection. *Proceedings of the 64th ASMS Conference on Mass Spectrometry and Allied Topics*, June 2016; San Antonio, TX, USA (**2016**)

Chapter 4 Transparent and High Refractive Index Thermoplastic Polymer Glasses Using Evaporative Ligand Exchange of Hybrid Particle Fillers

4.1. Preface

Continued developments in advanced photonic devices require procedures for the preparation of optically transparent polymer materials with a high refractive index (*n*). Evaporative ligand exchange is shown to present a promising route to synthesize polymer-tethered zinc oxide (ZnO) particle fillers that exhibit excellent miscibility in poly(methyl methacrylate) (PMMA) matrix. Favorable filler-matrix interactions were shown to enable the synthesis of hybrid materials with an inorganic content exceeding 25% by weight that displayed high levels of optical transparency (>0.8/mm) and increased elastic modulus as compared to pristine PMMA. A refractive index n >1.6 in the visible wavelength range was determined for

high loading levels of ZnO. Given the optical transparency of the resulting hybrid materials, this increase of refractive index could render thermoplastic commodity polymer glasses viable alternatives to expensive specialty polymers in applications ranging from sensing to optical components.

In this chapter, the fabrication of PSAN capped ZnO/PMMA hybrid bulk films and their optical property characterization is discussed. I designed the entire project and performed all synthetic work and part of the characterization in the project. I would like to thank especially my collaborator, Zhao Lu, for his careful and dedicated characterization work and extensive discussion during the collaboration. Clare Mahoney, Rachel Ferebee and Danli Luo from Bockstaller's group assisted in the characterization work. Jiajun Yan assisted in the synthesis work. Professor Matyjaszewski and Professor Bockstaller conceived and organized the project and together with Zhao and I wrote the manuscript.

This project was published in *ACS applied materials & interfaces*, (**Zongyu Wang**, Zhao Lu, Clare Mahoney, Jiajun Yan, Rachel Ferebee, Danli Luo, Krzysztof Matyjaszewski, Michael R Bockstaller, "Transparent and High Refractive Index Thermoplastic Polymer Glasses Using Evaporative Ligand Exchange of Hybrid Particle Fillers", *ACS applied materials & interfaces*, **2017**, 9 (8), 7515-7522.).

This work was supported by the NSF (Grants DMR 1501324 and DMR 1410845), the Department of Energy (Grant DEEE0006702), the National Science Center (Grant UMO-2014/14/A/ST5/00204), and the Scott Institute for Energy Technologies at Carnegie Mellon University.

4.2. Introduction

Optically transparent polymers with high refractive index offer opportunities for advanced and innovative designs in applications ranging from sensing,[1] solid-state lighting[2-3] and optics.[4] The development of chemical routes to realize transparent high refractive polymer materials has thus become an important objective in materials engineering. Two important routes to realize high refractive polymers are the strategic design of highly polarizable repeat units and the addition of high refractive fillers to polymer materials.[5-6] The inclusion of sulfur-, phosphorous- or halogen-containing polyaromatic groups into repeat and backbone structures are a particularly effective means to realize high refractive properties.[7-10] Examples include polyimides or polycarbazole as well as organometallic polymers that have demonstrated to enable a refractive index $n > 1.7$.[11] However, the chemical attributes of highly polarizable repeat units also give rise to features that are undesirable or limited in many applications. Examples include the reduction of photothermal stability due to the presence of aromatic groups, potential birefringence due to the increased persistence length of polymer backbones as well as environmental concerns (for example, associated with halogens).

An alternative route to enable high refractive index (n) is the addition of high refractive index inorganic particle fillers.[12] This 'nanocomposite' approach is fundamentally motivated by 'effective medium models' that predicts the average refractive index of the composite to be a weighted average of the properties of the constituents – ideally without compromising any of the other desirable physicochemical properties of the polymer matrix.[13] The advantages of the 'nanocomposite approach' encompass the economic viability of constituent materials and the possibility of augmenting the properties of thermoplastics for which effective processing methods are readily available. The prospect of broadening the range of applications for

commodity and engineering plastics provides thus a major impetus for research in high refractive index composite materials.

Many high refractive index semiconducting inorganic nanofillers, such as ZnS,[14] ZnO[15] and TiO_2,[5] have been studied as additives to increase the *n* of polymer matrices. ZnO is a wide bandgap semiconductor that exhibits a high refractive index (n ~ 2.0 at 630 nm),[16] high chemical stability, low absorption in the visible range,[17] high catalytic activity, and effective antibacterial and bactericide properties.[18-20] ZnO also has shown to be an effective scavenger for several compounds (such as H_2S) that are detrimental to the stability and performance of optoelectronic devices. ZnO nanofillers have thus attracted particular interest in applications ranging from solar cells,[21-22] organic light-emitting diode (OLED),[23-24] UV-shielding materials,[25-26] to field-emission displays, and optical sensors.[27-28] However, while high refractive index ZnO-polymer composite materials have been demonstrated, the synthesis of optically transparent ZnO hybrids with sufficient inorganic content to significantly raise the materials' refractive index remains an elusive goal.

The challenge of realizing transparent hybrid materials may be understood by consideration of the governing parameters that determine scattering losses in composite materials. In particular, the scattering cross-section of particle fillers depends approximately on the square of the particle volume and dielectric contrast ($C^{sca} \sim V_p^2(\varepsilon_m - \varepsilon_p)^2$, with ε_m and ε_p denoting the dielectric constant of embedding medium and particle filler, respectively). This translates into the need for uniform dispersion of filler particles in the matrix polymer.[29-30]

The tethering of polymers that form miscible blends with the respective matrix polymer has shown to be particularly effective in stabilizing particle-in-polymer dispersions even at high

inorganic volume fractions.[31-34] The tethering of polymers through exchange reactions with (typically low MW) ligands (i.e. 'grafting-to') is a particularly viable means to accomplish polymer modification. Unfortunately, the absence of functional groups with strong binding affinity to ZnO renders ligand exchange reactions difficult.

Here we present a novel approach for the efficient ligand exchange of ZnO nanoparticles and their subsequent stable dispersion in poly(methyl methacrylate) (PMMA) – an amorphous polymer that is widely used in optical components. In this approach, a volatile ligand (octylamine, OA) is used to enable the synthesis of nano-sized ZnO particles. The ligand is exchanged under evaporative conditions with low molecular polymeric tethers that are chosen to form a miscible blend with the target matrix polymer. This second step enables the formation of a uniform dispersion of particle fillers with high inorganic loadings. For the particular example of poly(styrene-co-acrylonitrile) (PSAN) tethered ZnO, the approach is demonstrated to enable the synthesis of transparent poly(methyl methacrylate) (PMMA)/ZnO films with inorganic content exceeding 25 wt% and refractive index $n \sim 1.65$.

4.3. Experimental Section

Materials.

Monomers: styrene (S, 99%, Aldrich), acrylonitrile (AN, 99%, Aldrich) were purified by passing through a column filled with basic alumina to remove the inhibitor. Tris(2-dimethylaminoethyl)amine (Me_6TREN, 99%, Alfa), zinc 2-ethylhexanoate ($Zn(EH)_2$, 80% in mineral spirits, Alfa), N-(2-hydroxyethyl)phthalimide (NHP, 99%, Acros), hydrochloric acid (HCl, 36.5-38.0%, Sigma), anisole (99%, Aldrich), methylene chloride (DCM, 99.5%, Fisher), tetrahydrofuran (THF, 99%, VWR), methanol (99%, VWR), hexane (99%, VWR), acetone (99%,

VWR), N,N-dimethylformamide (DMF, 99%, VWR), α-bromoisobutyryl bromide (2-BiBB, Aldrich), ethyl 2-bromoisobutyrate (EBiB, 98%, Aldrich), copper(II) bromide ($CuBr_2$, 99%, Aldrich), triethylamine (TEA, 98%, Aldrich), diphenyl ether (DPE, 99%, Aldrich)， tin(II) 2-ethylhexanoate ($Sn(EH)_2$, 95%, Aldrich), poly(methyl methacrylate (PMMA, M_w = 120,000 by GPC, Aldrich) and octylamine (OA, 99%, Aldrich) were used as received without further purification.

Synthesis of PSAN capped ZnO nanoparticles.

The three steps for the synthesis of PSAN capped ZnO NPs consist of a) the synthesis of OA-capped ZnO, b) the synthesis of PSAN-NH_2 ligands, and c) ligand exchange reaction between OA and polymer ligands. OA-capped ZnO NPs were synthesized as reported by Epifani and Weber.[35-36] The resulting product was dispersed in THF. A stock solution was prepared for use in further experiments. As shown in **Scheme 4.1**, NHP and TEA were reacted with 2-BiB in dry THF solution to form ATRP initiator. Low MW PSAN (M_n = 2300 with M_w/M_n = 1.13) with a protected NH_2 end group was synthesized via ARGET ATRP using 2-(phthalimido)ethyl 2-bromoisobutyrate with a protected amine functional group as an initiator, $CuBr_2/Me_6TREN$ as catalytic complex and $Sn(EH)_2$ as reducing agent. The PSAN-NH_2 was obtained by the deprotection of the NH_2 group with hydrazine. The ligand exchange reactions were conducted under an N_2 atmosphere. OA-capped ZnO stock solution and polymer ligands were mixed in DPE to obtain a clear mixture at 220 ºC for 2 h. The products were washed with cold hexanes. Three "selective precipitation, centrifugation, and dissolving" cycles were applied to completely remove the unattached polymer ligands.[37]

Scheme 4.1. Synthesis of PSAN-NH_2 polymer ligands and PSAN capped ZnO nanoparticles.

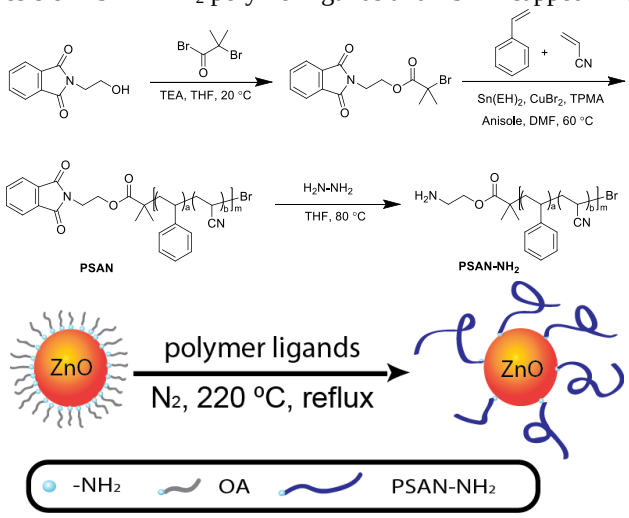

Fabrication of thin and bulk films of ZnO/PMMA hybrid materials.

The PSAN capped ZnO NPs were dispersed in THF via sonication. The concentration was measured gravimetrically by air-drying 5 mL of the dispersion. Specific amounts of linear poly(methyl methacrylate) (PMMA, M_n = 120,000) powder and PSAN/OA-capped ZnO NPs dispersion were mixed to cast films with a series of different weight fraction of ZnO. After stirring for 24 h, 500 μL of the homogeneous dispersions were diluted with 10 mL THF. Thin films (<100 nm) were prepared by spin-casting the diluted solution on silica wafer at the rate of 3000 rpm. The remaining bulk dispersions were transferred into 1.2-inch-diameter cylindrical Teflon molds. After slowly evaporating the solvent over 48 h at room temperature, transparent nanocomposite films of thickness ~ 0.5 mm formed. The residual solvent was removed from the bulk films by transferring it to a vacuum oven and slowly increasing the temperature at the rate of 10 ºC per 24 h to 150 ºC. Four specific bulk film compositions were investigated to systematically elucidate the effect of surface modification and the inorganic fraction on the

thermo-mechanical and optical properties of nanocomposite films. The respective sample compositions and sample-IDs are summarized in **Table 4.1**.

Table 4.1. Compositions of pure PMMA and PMMA/PSAN capped ZnO bulk films

Sample ID	f_{ZnO}[a]	$f_{PSAN/OA}$[b]	f_{PMMA}[b]
Pure PMMA	0	0	100
OA-ZnO/PMMA	10	1.8	88.2
PSAN-ZnO/PMMA-1	10	6.7	83.3
PSAN-ZnO/PMMA-2	18	12	70.0
PSAN-ZnO/PMMA-3	27	18	55.0

a Determined by TGA; b calculated according to TGA data.

Characterization.

Transmission electron microscopy (TEM) was carried out using a JEOL 2000 EX electron microscope operated at 200 kV. The average sizes of the ZnO NPs were determined from statistical analysis of the TEM micrographs using ImageJ software. Dynamic light scattering (DLS) using a Malvern Zetasizer Nano ZS was performed to confirm the results obtained from TEM. It was also employed to determine volume-weighted average hydrodynamic diameters and distribution. A Philips X'Pert (Philips Analytical, Netherlands) X-ray diffractometer (XRD) (Cu Kα radiation) was operated at 45 kV and 40 mA in grazing incidence mode to characterize the structure and crystallinity.

Thermogravimetric analysis (TGA) with TA Instruments 2950 was used to measure the fraction of ZnO in the hybrids. The data were analyzed with TA Universal Analysis. The TGA plots were normalized to the total weight after holding at 120 ºC.

$$\sigma_{\mathrm{TGA}} = \frac{(1-f_{\mathrm{ZnO}})N_{\mathrm{Av}}\,\rho_{\mathrm{ZnO}}\,d}{6\,f_{\mathrm{ZnO}}\,M} \qquad (1)$$

where f_{ZnO} is the ZnO fraction measured by TGA, N_{Av} is the Avogadro number, ρ_{ZnO} is the density of ZnO NPs (5.6 g/cm^3), d is the average diameter of ZnO NPs (5 nm), M is the molar mass of the capping agent.

The glass transition temperature (T_g) of PSAN capped ZnO in the PMMA matrix with different inorganic content was measured by differential scanning calorimetry (DSC) with TA Instrument QA-2000. The same procedure was run three times, each involving the following steps: 1) hold at 25 ºC for 5 min; 2) heat to 150 ºC at a rate of 10 ºC/min; 3) hold for 5 min; 4) cool down to 25 ºC. The DSC data were analyzed with TA Universal Analysis and the T_g was directly acquired.

UV-Vis Spectrophotometry. The light transmission of the bulk films was determined using a Varian 50 Bio UV-Vis Spectrophotometer over the wavelength range from 300 nm to 800 nm. To quantitatively compare the transparency of films with different thickness, the measured data were normalized to equal thickness using the described logarithmic relationship. In this study, the transmittance was normalized to 300 μm.

Ellipsometry. The refractive index of the thin films was measured using AutoEL-II Automatic Ellipsometer equipped with a helium-neon laser (λ = 632.8 nm). The angle of incidence was fixed at 70° and a two homogeneous layer film model (silica + nanocomposite) was utilized for the analysis. At least 5 different spots were measured for each film.

Nanoindentation. The mechanical properties (elastic modulus and hardness) of the bulk films were measured using MTS Nanoindenter XP with a nanoscopic diamond-based Berkovich tip. The indentations were performed at a displacement rate of 0.05 nm per second up to a maximum load at 2 μm depth. The maximum load indentation was held for 10 s followed by the elastic recovery of the material. 100 indentations were performed in each film.

Polymer ligands were characterized by GPC and NMR, the detailed information was included in Supporting Information.

4.4. Results and Discussion

Octylamine (OA) was chosen as ligand because of its appropriate boiling point of 175 ºC that prevents rapid evaporation during the thermolysis of $Zn(EH)_2$. **Figure 4.1**a and **4.1**b depict representative electron micrographs (TEM) of OA-capped ZnO, revealing a uniform particle size with average diameter <*d*> = 5.23 ± 0.61 nm.

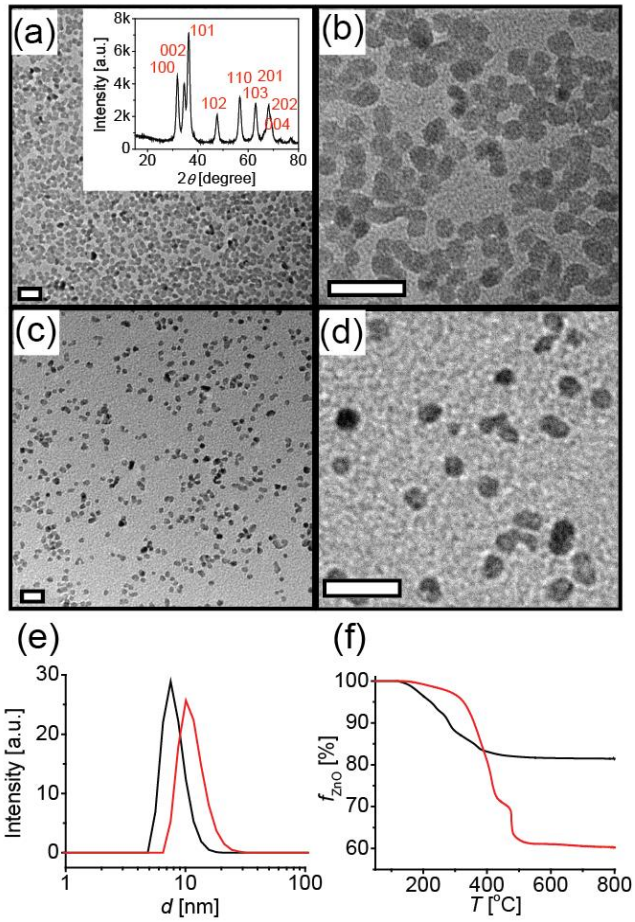

Figure 4.1. (a) and (b) TEM images of OA-capped 5 nm ZnO NPs, inset: XRD pattern of OA-capped ZnO; (c) and (d) TEM images of PSAN capped 5 nm ZnO NPs, M_n = 2300, M_w/M_n = 1.13; (e) Size distribution of OA/PSAN capped ZnO NPs measured by DLS in THF solution, intensity average particle size: OA-capped ZnO NPs, 7.5 nm, PSAN capped ZnO NP, 10.1 nm; (f) TGA traces of OA/PSAN capped ZnO NPs. The black line: OA-capped ZnO, red line: PSAN capped ZnO. Scale bars = 20 nm. Inset in Figure 1a depicts a representative XRD pattern of OA-capped ZnO. Reflections correspond to the (100), (002), (101), (102) and (110) planes (PDF card nos: JCPDS-36-1451).

The typical particle yield was 23%. X-ray diffraction analysis (see inset of **Figure 4.1**a) confirmed the Wurtzite structure of ZnO. Dispersions of OA-capped ZnO NPs were stable in tetrahydrofuran (THF) or hexane for weeks, with negligible aggregation. Dynamic light scattering (DLS, **Figure 4.1**e) confirmed an intensity-average hydrodynamic size of about 7 nm in excellent agreement with TEM results. Thermogravimetric analysis revealed 83 wt% inorganic content (**Figure 4.1**f). From the inorganic content f_{ZnO} the ligand grafting density was determined to be 4.4 chains/nm^2. PSAN was selected as polymer tether for ligand exchange because PMMA/PSAN constitutes a miscible polymer blend with LCST behavior that shows reversible transition between miscible and phase-separated states provided that the molar ratio χ = n(AN):n(S) is within the miscibility window $0.09 < \chi < 0.38$.[38] The interaction parameter of the PSAN/PMMA system depends on both the constitution of PSAN as well as the composition of the blend. In the present study, the molar composition of the random copolymer is S: AN = 3:1 – the corresponding interaction parameter is $\chi_{MMA/SAN} \approx -0.15$ (at $T \approx 25$ ºC).

Ligand exchange of OA with PSAN-NH_2 was performed in DPE at T = 180 ºC to concurrently drive the replacement reaction and extract unbound OA from the reaction mixture. The replacement reaction gave rise to a distinctive change in solubility characteristics. Whereas OA-capped ZnO NPs were stable in THF or hexane, PSAN-capped ZnO NPs after ligand exchange precipitated in hexane. Thus, free PSAN-NH_2 was removed by applying "selective precipitation, centrifugation, and dissolution" cycles.[37] As shown in **Figure 4.1**e, the DLS

confirmed the ligand replacement by revealing an increase of the hydrodynamic diameter from 7.5 to 10.1 nm. Electron micrographs of the final ZnO-PSAN product (**Figure 4.1**c and **4.1**d) further revealed the negligible aggregation of particles after ligand exchange. The purified PSAN capped ZnO NPs contain 60 wt% of ZnO (**Figure 4.1**f). Due to the large difference in steric hindrance, the grafting density of PSAN capped ZnO (0.7 chain/nm^2) was lower than OA-capped ZnO (4.4 chains/nm^2).

To understand the role of PSAN modification on particle/matrix interactions, we evaluated the thermomechanical properties of films as well as their microstructure. **Figure 4.2** depicts heat flow curves of pristine and ZnO-PSAN filled PMMA revealing an increase of the glass transition temperature with particle filling content from T_g = 104 ºC (for pristine PMMA) to T_g ~ 115 ºC (for f_{ZnO} = 0.18). The increase of T_g supports previous reports on PMMA composites with PSAN-modified silica particle fillers and can be interpreted as a consequence of the attractive interactions between PSAN tethers and PMMA matrix.[31] Interestingly, the T_g of ZnO-PSAN/PMMA composites levels off at a ZnO filling fraction of f_{ZnO} ~ 0.18 (in fact a small reduction in T_g is observed for f_{ZnO} ~ 0.27). We rationalize this trend as a consequence of the large specific surface area of 5 nm ZnO fillers that implies the saturation of surface segment interactions at rather low particle filling fractions. However, it should be noted that the effect of particle additives on T_g is a rather complex subject and alternative mechanisms could apply.[39-40]

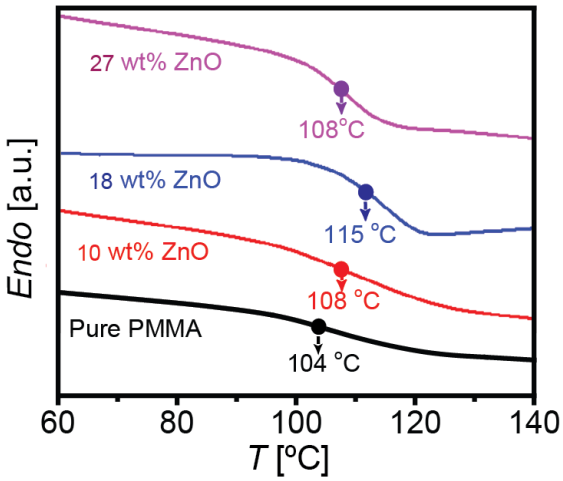

Figure 4.2. Heat flow curves of PSAN capped the ZnO NPs system and corresponding PMMA reference polymer. The glass transition temperature(T_g) increased for PSAN capped ZnO materials.

The favorable interactions between ZnO-PSAN particle fillers and the PMMA matrix were confirmed by evaluation of the elastic modulus of composite films that were measured using nanoindentation of ~500 μm thick films. **Figure 4.3** summarizes the elastic moduli and hardness values that were determined for the distinct ZnO-PSAN/PMMA systems.

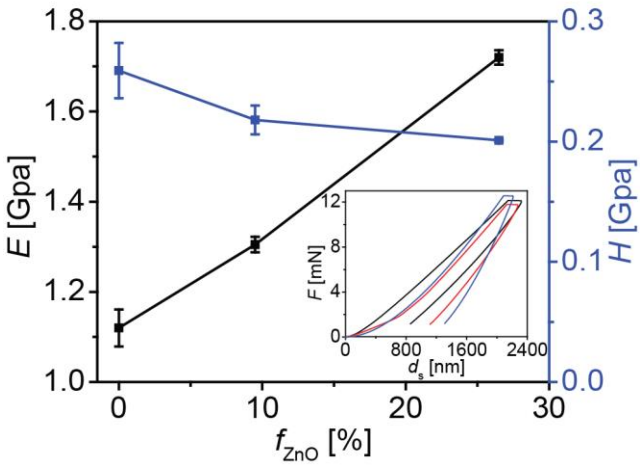

Figure 4.3. Nanoindentation measurement of PSAN capped ZnO in PMMA with different ZnO content indicate an increase of elastic modulus (E) and a small decrease of hardness (H) with increasing ZnO content; inset: Characteristic load (F)−displacement (d_s) curves for PSAN capped ZnO in PMMA with different ZnO content showing similar response: pure PMMA (black), 10 wt% ZnO (red), 27 wt% ZnO (blue).

The figure reveals an increase of the elastic modulus (*E*) from 1.12 Gpa for pure PMMA to 1.31 Gpa for 10 wt% PSAN capped ZnO and 1.72 Gpa when the inorganic content was 27 wt%. Since the resistance to elastic deformation directly depends on the bonding strength in materials, the 55% increase as compared to pristine PMMA provides clear support for increased dispersion interactions in the miscible PSAN/PMMA system. Here, a comment should be made regarding the application of nanoindentation to measure the elastic properties of polymer films. Nanoindentation was chosen primarily because of the ability to evaluate the mechanical properties of small material volumes. Because the mechanical characteristics are deduced from the interpretation of indent geometries rather than direct stress-strain measurements, the absolute values often differ from bulk values (sometimes by up to 20%).[41-42] However, trends are correctly reproduced.

Characterization of the microstructure of PMMA/ZnO-PSAN composites by transmission electron microscopy (TEM) confirmed the randomly dispersed morphology, expected for miscible blends. **Figure 4.4** depicts representative TEM images taken on micro-sections of bulk films of PMMA filled with PSAN and OA tethered ZnO particles at $f_{ZnO} \sim 0.1$.

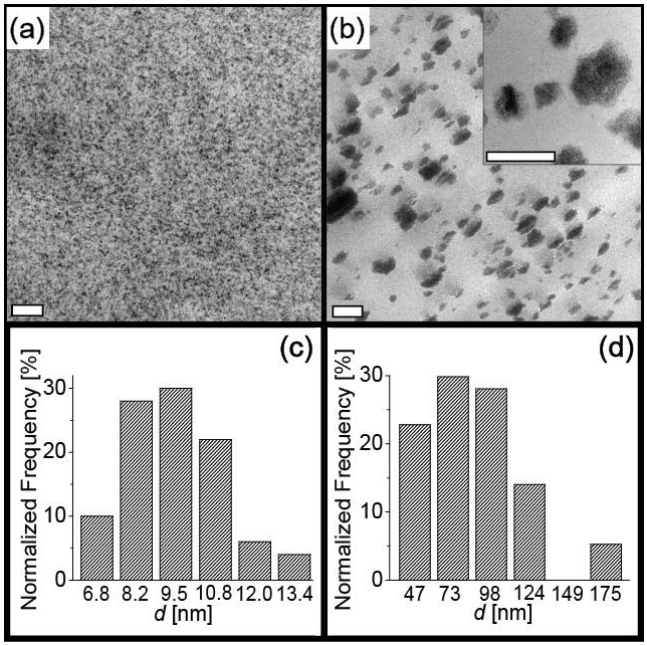

Figure 4.4. TEM images of ZnO/PMMA bulk films with 10 wt% ZnO contents (a) PSAN capped ZnO, (b) OA-capped ZnO, (c) and (d) size distributions of ZnO nanocomposite in the matrix, (c) PSAN capped ZnO, (d) OA-capped ZnO. Inset: higher magnification TEM images of OA-capped ZnO NPs in the PMMA matrix. Scale bars are 200 nm.

Image analysis of micrographs such as **Figure 4.4**a reveals an average particle distance in the PMMA/ZnO-PSAN system (**Figure 4.4**a) is $<d_{p\text{-}p}>$ = 1.06 nm, approximately equal to the expected particle distance of randomly dispersed structures $d_{th} = (V/N_p)^{1/3}$ =0.96 nm (with N_p/V denoting the volume density of particles). A further indicator of a thermodynamically stable particle dispersion is the particle size distribution (**Figure 4.4**c) and the average particle diameter $<d>$ = 10.1 nm (determined by image analysis) closely matches the value of the pristine ZnO-PSAN particles. This is in contrast to the microstructure observed in PMMA/ZnO-OA systems (**Figure 4.4**b) that reveals the formation of aggregates with an average size of $<d_{aggr}>$ = 99.3 nm. The formation of aggregates is indicative of a phase separating system in which the balance of dynamics and thermodynamic driving forces determine the respective aggregate dimension. The different dispersion characteristics of ZnO-PSAN and ZnO-OA particle fillers have a profound impact on the optical properties of PMMA composite films. **Figure 4.5** depicts photographs of

films with a systematic variation of ZnO content with and without PSAN modification. The figure reveals that optical transparency in ZnO-PSAN based composites (**Figure 4.5**b, **4.5**c) is comparable to pristine PMMA (**Figure 4.5**a) while a significant loss of transparency is incurred upon dispersion of ZnO-OA particles in PMMA (**Figure 4.5**d) despite the significantly lower inorganic content. The opacity of ZnO-OA based composite films can be rationalized as a direct consequence of the aggregation behavior that is discerned from the micrograph shown in **Figure 4.4**b. In particular, the scattering cross-section of particle fillers depends on the square of the particle volume and hence on the sixth power of the particle size ($C_{sca} \sim V_p^2 \sim r_p^6$).[29-30] The clustering of ZnO particles observed in the immiscible PMMA/ZnO-OA system thus dramatically raises the scattering losses in phase-separating polymer/particle blend systems. ZnO containing particle films in **Figure 4.5** exhibits a weak yellowish coloration. The latter is attributed to partial oxidation of excess amine ligands as well as to the preferential scattering of short wavelengths of small particle fillers (see below).

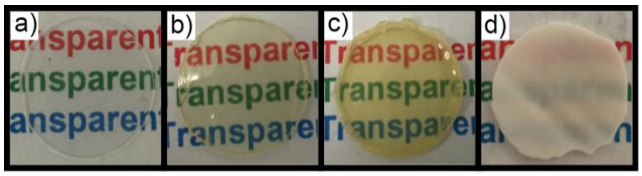

Figure 4.5. Photographs of pure PMMA, PSAN-capped ZnO/PMMA and OA-capped ZnO/PMMA hybrid bulk films: a) Pure PMMA (thickness: 666 μm); b) PSAN capped ZnO/PMMA-1 (10 wt% ZnO, 570 μm); c) PSAN capped ZnO/PMMA-2 (18 wt% ZnO, 646 μm); d) OA-capped ZnO/PMMA (10 wt% ZnO, 590 μm). The image area is 9 cm^2.

The transparency of the bulk films was quantitatively measured using UV-vis spectroscopy. Since each film had a different thickness, the measured data were normalized to equal film thickness as described in the experimental section. **Figure 4.6** depicts the transmission curves (normalized to equal film thickness) for pristine PMMA and ZnO-PSAN/PMMA blend

materials The figure reveals that optical transparency over 0.8/mm^{-1} has retained for wavelengths $\lambda > 500$ nm up to particle loadings of $f_{ZnO} = 0.18$.

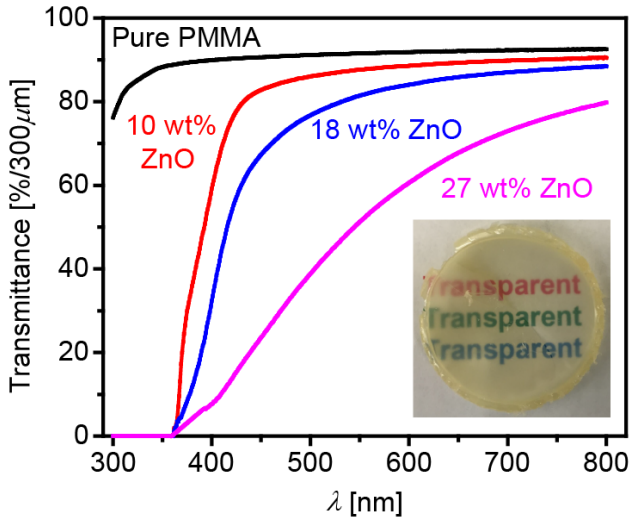

Figure 4.6. Normalized UV–vis transmittance spectra of the pure PMMA and the PSAN capped ZnO in the PMMA matrix. The normalized transmittance corresponds to films with a thickness of 300 μm. Inset: photograph of PSAN capped ZnO/PMMA bulk films with 27 wt% ZnO (370 μm).

Optical transmission of 0.8 is commonly considered to be the threshold for a material to be recognized as transparent 'to the eye'.[43] All transmission curves shown in **Figure 4.6** reveal a λ^{-x} dependence that is characteristic for scattering losses (in the limit of Rayleigh scattering x = 4). As expected, scattering losses increase with particle loadings, however, even at $f_{ZnO} = 0.27$ a transparency T ~ 0.6 (length)$^{-1}$ (at $\lambda = 500$ nm) is retained. For all systems, the transmittance vanished in the 300-365 nm range, due to UV absorption. This UV-blocking coincides with the absorption edge of 5 nm ZnO NPs that is estimated to be at 3.37 eV (or 369 nm).[26, 44] The high transparency in the visible range combined with a complete UV-cutoff could render PMMA/ZnO-PSAN composites interesting candidate materials for applications as transparent UV filters.

An intriguing application of low-scattering ZnO-particle fillers is in the fabrication of high refractive index polymer glasses that play an important role as optical materials. This is because ZnO exhibits a refractive index of n_{ZnO} = 1.973-2.105 in the visible range. Tethering of polymer chains alters the refractive index of particle fillers. The effective refractive index of ZnO-PSAN core-shell particles can be estimated using homogenization models such as Maxwell-Garnett (MG) theory as:

$$n_{\mathrm{eff,p}}{}^2 = n_{\mathrm{shell}}{}^2[1 + \frac{3\phi x}{1-\phi x}] \qquad (2)$$

where $x = (n_{core}^2 - n_{shell}^2)/(n_{core}^2 + 2\, n_{shell}^2)$; n_{shell} and n_{core} represent the refractive index of the shell and core, respectively; and ¢ = $v_{\mathrm{core}}/(v_{\mathrm{core}} + v_{\mathrm{shell}})$ is the relative core volume. In this study, the n_{ZnO} and n_{PSAN} were assumed to be 1.989 and 1.558, corresponding to λ = 632 nm).[45] Using the compositional values as determined from TGA measurements, the effective refractive index of PSAN capped ZnO was calculated to be $n_{\mathrm{eff,p}}$ = 1.650. Note that the use of low MW polymer tethers is a critical prerequisite to enable high $n_{\mathrm{eff,p}}$ of particle fillers since it facilitates a high inorganic content of the core-shell particles.

The effective refractive index of PMMA/ZnO-PSAN of composites formed with different concentrations of PSAN capped ZnO in a PMMA matrix measured using ellipsometry at λ = 632 nm on thin-film samples that were fabricated by spin coating of particle/polymer solutions (corresponding thick films could not be prepared due to the limited availability of particle systems). **Table 4.2** summarizes the results, revealing that the effective index of PMMA/ZnO-PSAN composites increases to ~ 1.53 at f_{ZnO} = 0.27. Further increase of the particle concentration allowed us to realize n_{eff} ~ 1.64 at the maximum achievable inorganic loading in thin films.

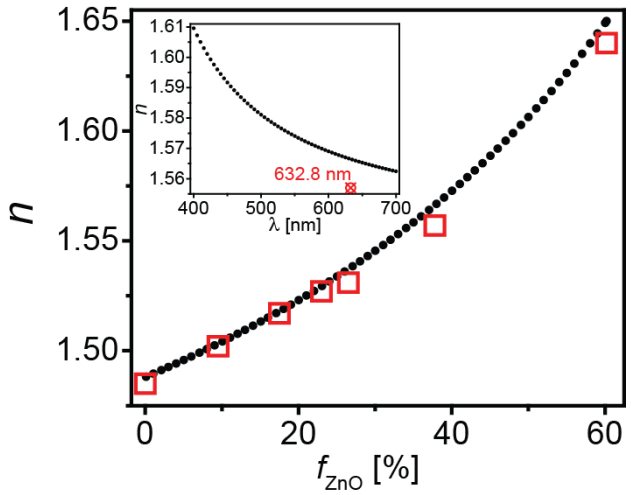

Figure 4.7. Dependence of refractive index on ZnO content in hybrid thin films dashed line: theoretical trend line calculated using Maxwell Garnett theory; red squares: measured refractive index at 632.8 nm. Inset: refractive index of ZnO/PMMA hybrid bulk film (38 wt% ZnO contents) at a different wavelength.

Table 4.2. Compositions, *n* and calculated *n* of pure PMMA and PMMA/PSAN capped ZnO thin films.

Sample ID	f_{ZnO}[a]	f_{PSAN}[b]	f_{PMMA}[b]	n_{exp}[c]	n_{cal}[c]
Pure PMMA	0	0	100	1.485	1.488
ZnO/PMMA-1	10	6.7	83.3	1.502	1.504
ZnO/PMMA-2	18	12	70.0	1.517	1.518
ZnO/PMMA-3	27	18	55.0	1.531	1.537
ZnO/PMMA-4	38	25.3	37.7	1.557	1.566
Pure PSAN capped ZnO	60	40	0	1.640	1.650

a Determined by TGA; b calculated according to TGA data; c determined by ellipsometry

The excellent agreement between experimental and theoretical values further supports the uniform distribution of particle fillers that is an assumption of the effective medium model. Note that due to the optical dispersion characteristics of ZnO a higher refractive index is expected at a shorter wavelength (see inset of **Figure 4.7**).

4.5. Supporting Information

Number average MW (M_n) and dispersity (M_w/M_n) were determined by GPC, conducted with a Waters 515 pump and Waters 2414 different refractometer using PSS columns (Styrogel 10^5,10^3, 10^2 A) in THF as an eluent (35 ºC, flow rate of 1 mL min^{-1}), using linear polystyrene (PS) and PMMA standards for calibration. ^{1}H NMR spectroscopy used for polymerization monitoring was performed using a Bruker Advance 300 MHz NMR spectrometer with $CDCl_3$ as a solvent. The conversion was calculated by measuring the decrease of the monomer peak area relative to the peak area of the internal standards.

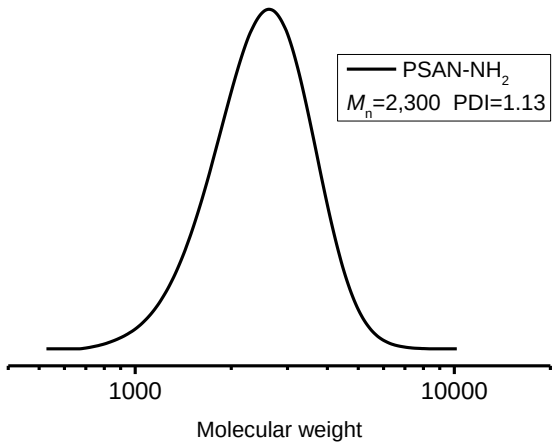

Figure S4.1. GPC trace of PSAN-NH_2 polymer ligands

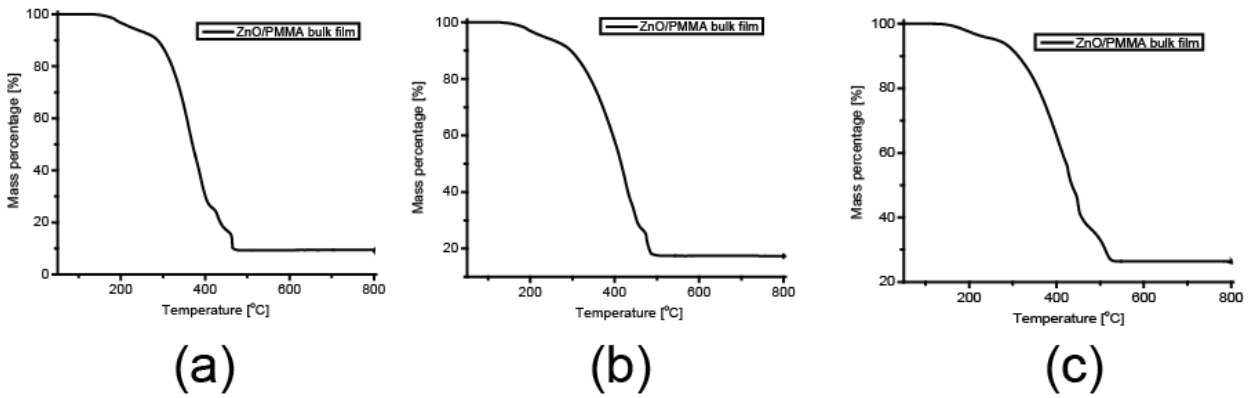

Figure S4.2. TGA curves of ZnO/PMMA bulk films with different ZnO contents:
(a) 10 wt% ZnO contents; (b) 18 wt%; (c) 27 wt%.

4.6. Conclusion

We have demonstrated a new method for the synthesis of optically transparent PMMA/ZnO hybrids with a refractive index exceeding 1.6 in the visible range. The method rests on the application of PSAN tethers that enable the stable dispersion of particles in the polymer host up to high inorganic loadings. PSAN capped 5 nm ZnO NPs were synthesized in high yield through evaporative ligand exchange. Particles were shown to be readily dispersible in PMMA up to weight fractions over 35% resulting in films with high optical transparency (>0.8/mm) and refractive index exceeding 1.6 in the short wavelength visible range. Favorable filler/matrix interactions gave rise to concurrent enhancement of the mechanical properties (stiffness) of films. The observed increase of $n > 1.6$ presents a substantial increase in the refractive index of pristine PMMA that could promote its application in a range of optical applications. We note that this reported increase does not represent a fundamental limit in the achievable gain in the refractive index. Rather, a reduction in the degree of polymerization (or reduction of grafting density) of PSAN is expected to allow a further increase in the refractive index. The optimization of these parameters is the subject of our current research.

4.7. References

(1) Maffli, L.; Rosset, S.; Ghilardi, M.; Carpi, F.; Shea, H., Ultrafast all-polymer Electrically Tunable Silicone Lenses. *Advanced Functional Materials* **2015,** *25* (11), 1656-1665.

(2) Shen, T.-Z.; Hong, S.-H.; Song, J.-K., Electro-optical switching of graphene oxide liquid crystals with an extremely large Kerr coefficient. *Nat Mater* **2014,** *13* (4), 394-399.

(3) Schulz, H.; Mädler, L.; Pratsinis, S. E.; Burtscher, P.; Moszner, N., Transparent Nanocomposites of Radiopaque, Flame-Made Ta_2O_5/SiO_2 Particles in an Acrylic Matrix. *Adv. Funct. Mater.* **2005,** *15* (5), 830-837.

(4) Ucar, A. B.; Velev, O. D., Microfluidic elastomer composites with switchable vis-IR transmittance. *Soft Matter* **2012,** *8* (44), 11232-11235.

(5) Lee, L.-H.; Chen, W.-C., High-Refractive-Index Thin Films Prepared from Trialkoxysilane-Capped Poly(methyl methacrylate)−Titania Materials. *Chemistry of Materials* **2001,** *13* (3), 1137-1142.

(6) Griebel, J. J.; Namnabat, S.; Kim, E. T.; Himmelhuber, R.; Moronta, D. H.; Chung, W. J.; Simmonds, A. G.; Kim, K.-J.; van der Laan, J.; Nguyen, N. A.; Dereniak, E. L.; Mackay, M. E.; Char, K.; Glass, R. S.; Norwood, R. A.; Pyun, J., New Infrared Transmitting Material via Inverse Vulcanization of Elemental Sulfur to Prepare High Refractive Index Polymers. *Advanced Materials* **2014,** *26* (19), 3014-3018.

(7) Fan, Z.; Serrano, M. K.; Schaper, A.; Agarwal, S.; Greiner, A., Polymer/Nanoparticle Hybrid Materials of Precise Dimensions by Size-Exclusive Fishing of Metal Nanoparticles. *Advanced Materials* **2015,** *27* (26), 3888-3893.

(8) Beecroft, L. L.; Ober, C. K., Nanocomposite Materials for Optical Applications. *Chemistry of Materials* **1997,** *9* (6), 1302-1317.

(9) Janáky, C.; Rajeshwar, K., The role of (photo)electrochemistry in the rational design of hybrid conducting polymer/semiconductor assemblies: From fundamental concepts to practical applications. *Progress in Polymer Science* **2015,** *43*, 96-135.

(10) Barbey, R.; Lavanant, L.; Paripovic, D.; Schüwer, N.; Sugnaux, C.; Tugulu, S.; Klok, H.-A., Polymer Brushes via Surface-Initiated Controlled Radical Polymerization: Synthesis, Characterization, Properties, and Applications. *Chemical Reviews* **2009,** *109* (11), 5437-5527.

(11) Wei, Q.; Pötzsch, R.; Liu, X.; Komber, H.; Kiriy, A.; Voit, B.; Will, P.-A.; Lenk, S.; Reineke, S., Hyperbranched Polymers with High Transparency and Inherent High Refractive Index for Application in Organic Light-Emitting Diodes. *Advanced Functional Materials* **2016,** *26* (15), 2545-2553.

(12) Liu, J.-g.; Ueda, M., High refractive index polymers: fundamental research and practical applications. *Journal of Materials Chemistry* **2009,** *19* (47), 8907-8919.

(13) Maldovan, M.; Bockstaller, M. R.; Thomas , E. L.; Carter, W. C., Validation of the effective-medium approximation for the dielectric permittivity of oriented nanoparticle-filled materials: effective permittivity for dielectric nanoparticles in multilayer photonic composites. *Applied Physics B* **2003,** *76* (8), 877-884.

(14) Zhang, G.; Zhang, J.; Yang, B., Fabrication of polymerizable ZnS nanoparticles in N, N[prime or minute]-dimethylacrylamide and the resulting high refractive index optical materials. *Polymer Chemistry* **2013,** *4* (14), 3963-3967.

(15) Demir, M. M.; Koynov, K.; Akbey, Ü.; Bubeck, C.; Park, I.; Lieberwirth, I.; Wegner, G., Optical Properties of Composites of PMMA and Surface-Modified Zincite Nanoparticles. *Macromolecules* **2007,** *40* (4), 1089-1100.

(16) Bond, W. L., Measurement of the Refractive Indices of Several Crystals. *Journal of Applied Physics* **1965,** *36* (5), 1674-1677.
(17) Khan, Z.; Khan, M.; Zulfequar, M.; M. Shahid Khan, Optical and Structural Properties of ZnO Thin Films Fabricated by Sol-Gel Method. *Materials Sciences and Applications* **2011,** *2* (5), 340-345.
(18) Zhang, Z.-Y.; Xu, Y.-D.; Ma, Y.-Y.; Qiu, L.-L.; Wang, Y.; Kong, J.-L.; Xiong, H.-M., Biodegradable ZnO@polymer Core-Shell Nanocarriers: pH-Triggered Release of Doxorubicin In Vitro. *Angewandte Chemie International Edition* **2013,** *52* (15), 4127-4131.
(19) Xiong, H.-M., ZnO Nanoparticles Applied to Bioimaging and Drug Delivery. *Advanced Materials* **2013,** *25* (37), 5329-5335.
(20) Noimark, S.; Weiner, J.; Noor, N.; Allan, E.; Williams, C. K.; Shaffer, M. S. P.; Parkin, I. P., Dual-Mechanism Antimicrobial Polymer–ZnO Nanoparticle and Crystal Violet-Encapsulated Silicone. *Advanced Functional Materials* **2015,** *25* (9), 1367-1373.
(21) Small, C. E.; Chen, S.; Subbiah, J.; Amb, C. M.; Tsang, S.-W.; Lai, T.-H.; Reynolds, J. R.; So, F., High-efficiency inverted dithienogermole-thienopyrrolodione-based polymer solar cells. *Nature Photonics* **2012,** *6* (2), 115-120.
(22) You, J.; Dou, L.; Yoshimura, K.; Kato, T.; Ohya, K.; Moriarty, T.; Emery, K.; Chen, C.-C.; Gao, J.; Li, G.; Yang, Y., A polymer tandem solar cell with 10.6% power conversion efficiency. *Nature Communications* **2013,** *4*, 1446.
(23) Yang, Q.; Liu, Y.; Pan, C.; Chen, J.; Wen, X.; Wang, Z. L., Largely Enhanced Efficiency in ZnO Nanowire/p-Polymer Hybridized Inorganic/Organic Ultraviolet Light-Emitting Diode by Piezo-Phototronic Effect. *Nano Letters* **2013,** *13* (2), 607-613.
(24) Faria, J. C. D.; Campbell, A. J.; McLachlan, M. A., ZnO Nanorod Arrays as Electron Injection Layers for Efficient Organic Light-Emitting Diodes. *Advanced Functional Materials* **2015,** *25* (29), 4657-4663.
(25) Huang, X.; Wang, X.; Wang, S.; Yang, J.; Zhong, L.; Pan, J., UV and dark-triggered repetitive release and encapsulation of benzophenone-3 from biocompatible ZnO nanoparticles potential for skin protection. *Nanoscale* **2013,** *5* (12), 5596-5601.
(26) Zhang, Y.; Zhuang, S.; Xu, X.; Hu, J., Transparent and UV-shielding ZnO@PMMA nanocomposite films. *Optical Materials* **2013,** *36* (2), 169-172.
(27) Xiong, M.; Gu, G.; You, B.; Wu, L., Preparation and characterization of poly(styrene butyl acrylate) latex/nano-ZnO nanocomposites. *Journal of Applied Polymer Science* **2003,** *90* (7), 1923-1931.
(28) Lova, P.; Manfredi, G.; Boarino, L.; Comite, A.; Laus, M.; Patrini, M.; Marabelli, F.; Soci, C.; Comoretto, D., Polymer Distributed Bragg Reflectors for Vapor Sensing. *ACS Photonics* **2015,** *2* (4), 537-543.
(29) Bombalski, L.; Dong, H.; Listak, J.; Matyjaszewsk, K.; Bockstaller, M. R., Null-Scattering Hybrid Particles Using Controlled Radical Polymerization. *Advanced Materials* **2007,** *19* (24), 4486-4490.
(30) Dang, A.; Ojha, S.; Hui, C. M.; Mahoney, C.; Matyjaszewski, K.; Bockstaller, M. R., High-Transparency Polymer Nanocomposites Enabled by Polymer-Graft Modification of Particle Fillers. *Langmuir* **2014,** *30* (48), 14434-14442.
(31) Ojha, S.; Dang, A.; Hui, C. M.; Mahoney, C.; Matyjaszewski, K.; Bockstaller, M. R., Strategies for the Synthesis of Thermoplastic Polymer Nanocomposite Materials with High Inorganic Filling Fraction. *Langmuir* **2013,** *29* (28), 8989-8996.

(32) Braunecker, W. A.; Matyjaszewski, K., Controlled/living radical polymerization: Features, developments, and perspectives. *Progress in Polymer Science* **2007,** *32* (1), 93-146.
(33) Pyun, J.; Matyjaszewski, K., Synthesis of Nanocomposite Organic/Inorganic Hybrid Materials Using Controlled/"Living" Radical Polymerization. *Chemistry of Materials* **2001,** *13* (10), 3436-3448.
(34) Matyjaszewski, K.; Tsarevsky, N. V., Nanostructured functional materials prepared by atom transfer radical polymerization. *Nat Chem* **2009,** *1* (4), 276-288.
(35) Epifani, M.; Arbiol, J.; Díaz, R.; Perálvarez, M. J.; Siciliano, P.; Morante, J. R., Synthesis of SnO2 and ZnO Colloidal Nanocrystals from the Decomposition of Tin(II) 2-Ethylhexanoate and Zinc(II) 2-Ethylhexanoate. *Chemistry of Materials* **2005,** *17* (25), 6468-6472.
(36) Weber, D.; Botnaras, S.; Pham, D. V.; Steiger, J.; De Cola, L., Functionalized ZnO nanoparticles for thin-film transistors: support of ligand removal by non-thermal methods. *Journal of Materials Chemistry C* **2013,** *1* (18), 3098-3103.
(37) Ehlert, S.; Taheri, S. M.; Pirner, D.; Drechsler, M.; Schmidt, H.-W.; Förster, S., Polymer Ligand Exchange to Control Stabilization and Compatibilization of Nanocrystals. *ACS Nano* **2014,** *8* (6), 6114-6122.
(38) Paul, D. R.; Barlow, J. W., A binary interaction model for miscibility of copolymers in blends. *Polymer* **1984,** *25* (4), 487-494.
(39) Moll, J.; Kumar, S. K., Glass Transitions in Highly Attractive Highly Filled Polymer Nanocomposites. *Macromolecules* **2012,** *45* (2), 1131-1135.
(40) Evans, C. M.; Sandoval, R. W.; Torkelson, J. M., Glass Transition Temperature of a Component near Infinite Dilution in Binary Polymer Blends: Determination via Fluorescence Spectroscopy. *Macromolecules* **2011,** *44* (17), 6645-6648.
(41) Choi, J.; Hui, C. M.; Pietrasik, J.; Dong, H.; Matyjaszewski, K.; Bockstaller, M. R., Toughening fragile matter: mechanical properties of particle solids assembled from polymer-grafted hybrid particles synthesized by ATRP. *Soft Matter* **2012,** *8* (15), 4072-4082.
(42) Oliver, W. C.; Pharr, G. M., Measurement of hardness and elastic modulus by instrumented indentation: Advances in understanding and refinements to methodology. *Journal of Materials Research* **2004,** *19* (01), 3-20.
(43) Narayanan, S.; Hajzus, J. R.; Treacy, C. E.; Bockstaller, M. R.; Porter, L. M., Polymer Embedded Silver-Nanowire Network Structures – A Platform for the Facile Fabrication of Flexible Transparent Conductors. *ECS Journal of Solid State Science and Technology* **2014,** *3* (11), P363-P369.
(44) Tang, E.; Cheng, G.; Pang, X.; Ma, X.; Xing, F., Synthesis of nano-ZnO/poly(methyl methacrylate) composite microsphere through emulsion polymerization and its UV-shielding property. *Colloid and Polymer Science* **2005,** *284* (4), 422-428.
(45) Lee, Y.-J.; Ruby, D. S.; Peters, D. W.; McKenzie, B. B.; Hsu, J. W. P., ZnO Nanostructures as Efficient Antireflection Layers in Solar Cells. *Nano Letters* **2008,** *8* (5), 1501-1505.

Chapter 5 Photocatalytic Active Mesoporous Carbon/ZnO Hybrid Materials from Block Copolymer Tethered ZnO Nanocrystals

5.1. Preface

Severe water pollution issues present an important contemporary challenge that drives the development and advancement of efficient and environmentally benign photocatalysts that enable the degradation of pollutants upon visible light irradiation. One example is zinc oxide/carbon (ZnO/C) hybrid materials that are effective photocatalysts. To maximize the effectiveness of ZnO/C hybrids, materials with a high accessible surface area of ZnO are required. Here, a novel strategy is presented to enable the synthesis of fine dispersions of ZnO nanoparticles within a porous carbon matrix. The synthesis entails the grafting of ZnO nanoparticles with polystyrene-*b*-poly(styrene-*co*-acrylonitrile) (PS-*b*-PSAN) block copolymer and subsequent pyrolysis of the material under inert gas (N_2) atmosphere. During the pyrolysis process, the PS block effectively prevents agglomeration of ZnO particles, thus resulting in a fine dispersion of ZnO nanocrystals within a porous C matrix. Materials exhibited a dye adsorption capacity of 125 mg g^{-1} (from a methylene blue aqueous solution with a concentration of 305 mg L^{-1}) and a dye degradation rate constant of 0.012 min^{-1}. The significant increase of effective surface area and degradation efficacy (as compared to ZnO/C synthesized by the pyrolysis of binary PSAN/ZnO blends) is rationalized as a consequence of the increased porosity that promoted dye adsorption and transport within the hybrid material.

In this chapter, the synthesis of carbon/ZnO hybrids and their photocatalytic property characterization is discussed. I designed the entire project and performed all synthetic work and part of the characterization in the project. I would like to thank especially my collaborators,

Siyuan Liu for his big effort on the photocatalyst characterization. Jianan Zhang and Jiajun Yan assisted in the synthesis work. Clare Mahoney, Rachel Ferebee and Danli Luo from Bockstaller's group assisted in the characterization work. Professor Matyjaszewski and Professor Bockstaller conceived and organized the project and together with Siyuan and I wrote the manuscript.

This project was published in *Langmuir*, (**Zongyu Wang**, Siyuan Liu, Jianan Zhang, Jiajun Yan, Yepin Zhao, Clare Mahoney, Rachel Ferebee, Danli Luo, Joanna Pietrasik, Michael R Bockstaller, Krzysztof Matyjaszewski, "Photocatalytic Active Mesoporous Carbon/ZnO Hybrid Materials from Block Copolymer Tethered ZnO Nanocrystals", *Langmuir*, **2017**, 33 (43), 12276-12284.).

This work was supported by the National Science Foundation (via grants DMR 1501324 and CMMI 1663305) as well as the Scott Institute for Energy Technologies at Carnegie Mellon University.

5.2. Introduction

Dyes and pigments such as tartrazine (C.I. Acid Yellow 23), erythrosine B and methylene blue, are present in myriads of foods and drugs.[1] Various segments of industrial manufacturing, such as the dye manufacturing and textile finishing, release dyes and pigments, which are not readily biodegradable, into wastewater. They have been reported as a possible cause of many diseases, including asthma, urticarial and angioedema.[2-3] Photocatalysis is a promising technique for solving water treatment issues due to its ability for the destruction of pollutants and broad compound applicability.[4] A suitable photocatalyst should be non-toxic, low cost, and with high optical quantum yield.[5-6] Semiconductor photocatalysis is an efficient oxidation process, which can conveniently degrade dye pollutants.[7] Semiconductors such as ZnO and TiO_2 have been

increasingly utilized in the area of photocatalysis, primarily because of their high photocatalytic activity, low cost, and commercial availability.[8] However, although the bandgap of both materials is very similar (at about 3.1-3.3 eV) their photo-catalytic behavior has been shown to differ significantly.[9] In general, TiO_2 has been found to have a significantly higher photocatalytic activity and hence has been pursued much more extensively as a platform for photocatalysts. However, ZnO presents many features such as complementary biocidal characteristics as well as a more rapid environmental degradation (and hence reduced environmental accumulation) that render it an attractive alternative to TiO_2 based photocatalysts. Moreover, some studies have highlighted the fact that ZnO exhibits a higher efficiency than TiO_2 in the photocatalytic degradation of some dyes in water and in photoelectric conversion.[10]

The reduced efficiency of ZnO has been attributed to the predominant absorption of ZnO in the UV region, which makes only for 3-5% spectral contribution of ambient sunlight, hence limiting its effective spectral range.[11] Furthermore, the well-known photo-corrosion, which leads to a severe decrease in the photostability of ZnO in the recycle process under light irradiation, also limits the application of ZnO based photocatalysts.[12] To address these issues, extensive efforts have been devoted to altering the electronic band structures of ZnO for visible light harvesting by doping with cations, anions, metals, and nonmetals.[13-14] In recent years, composites of ZnO supported by nanoscale carbonaceous materials have drawn much attention and hybridization of ZnO with carbon materials was proven to be a promising and effective way to improve the photocatalytic activity and stability of ZnO.[15]

Porous carbon materials are generally used as catalyst support due to their high surface area and unique chemical properties.[16-18] In addition to its abundance and low cost, carbon materials have excellent electrical conductivity. The electron affinity of carbon-based materials

can contribute to an improvement in the separation of charge carriers.[19] Furthermore, carbon materials exhibit high chemical stability and corrosion resistance along with high adsorption efficacy towards a wide range of organic (and inorganic) materials that render carbon materials interesting as components of photocatalysts.[4, 20-22] For example, in previous reports, C_{60}, carbon nanotubes, carbon quantum dots, graphene oxide, as well as graphene and its derivatives were used as fillers to modify ZnO-based composites and to enhance their photocatalytic efficiencies.[12, 23-31] However, while these C/ZnO hybrids have shown great promise for the design of efficient photocatalysts, the high costs associated with the C nanomaterials and the control of the microstructure remain outstanding challenges.

A viable route for the synthesis of nanocarbon is based on the so-called hard template-assisted pyrolysis of polyacrylonitrile (PAN).[32-36] For example, commercial colloidal silica has been widely used as hard template for the fabrication of nanocarbon because of the economic viability and amenability to surface modification.[37] Recent advances have been enabled by the application of surface-grafting techniques to facilitate polymer-tethered particles that can be assembled into 'one-component' hybrid materials with well-controlled microstructure that can subsequently be pyrolyzed to form inorganic/nanocarbon hybrid materials presents intriguing opportunities for the design of novel ZnO-based photocatalysts with high efficacy.[38-40] This is because the major elements of the process are based on techniques already used in industry (such as particle surface modification and pyrolysis) that should promote the potential scale-up of the process.

In this contribution, we present a convenient synthetic route for the preparation of carbon-coated ZnO nanohybrids with high photocatalytic activity based on block copolymer-capped ZnO nanocrystal precursors. ZnO nanocrystals were coated with pre-synthesized

poly(styrene-*co*-acrylonitrile-*b*-styrene) (PSAN-*b*-PS) copolymers using a recently developed 'evaporative ligand exchange' method.[41] The block copolymer coating is shown to accomplish two goals: First, the PSAN 'inner block' is shown to provide a template for the subsequent pyrolysis into nanoporous carbon with similar characteristics as PAN. This presents an important advancement since PSAN has more versatile solubility characteristics as compared to PAN and is thus amenable to a wider range of process conditions. Second, the PS 'outer block' is shown to stabilize particles during pyrolysis and to prevent their crosslinking and agglomeration of the product. The resulting nanocarbon-coated ZnO particles are shown to exhibit high photocatalytic activity towards the degradation of methylene blue with efficiency similar to TiO_2. The increase in efficiency is rationalized as a consequence of the carbon coating to narrow the bandgap of ZnO thus increasing the range of wavelengths that support the formation of reactive oxygen species.

5.3. Experimental Section

Materials.

Monomers: styrene (S, 99%, Aldrich), acrylonitrile (AN, 99%, Aldrich) were purified by passing through a column filled with basic alumina to remove the inhibitor. Tris(2-dimethylaminoethyl)amine (Me_6TREN, 99%, Alfa), zinc 2-ethylhexanoate ($Zn(EH)_2$, 80% in mineral spirits, Alfa), N-(2-hydroxyethyl)phthalimide (NHP, 99%, Acros), hydrochloric acid (HCl, 36.5-38.0%, Sigma), anisole (99%, Aldrich), methylene chloride (DCM, 99.5%, Fisher), tetrahydrofuran (THF, 99%, VWR), methanol (99%, VWR), hexane (99%, VWR), acetone (99%, VWR), N,N-dimethylformamide (DMF, 99%, VWR), α-bromoisobutyryl bromide (2-BiBB, Aldrich), ethyl 2-bromoisobutyrate (EBiB, 98%, Aldrich), copper(II) bromide ($CuBr_2$, 99%, Aldrich), triethylamine (TEA, 98%, Aldrich), hydrazine (98%, Aldrich), diphenyl ether (DPE,

99%, Aldrich)， tin(II) 2-ethylhexanoate ($Sn(EH)_2$, 95%, Aldrich), methylene blue (MB, 82% in water, Sigma Aldrich), ZnO powders (99.95%, 18 nm, US Nano), and octylamine (OA, 99%, Aldrich) were used as received without further purification.

Synthesis of PSAN capped ZnO precursors

The synthesis of PSAN capped ZnO NPs precursors included three steps: First, the synthesis of OA-capped ZnO NPs, synthesis of PSAN polymer ligands, second the exchange of OA and polymer ligands using evaporative ligand exchange following a previously published procedure.[42] OA-capped ZnO NPs were synthesized using the procedure reported by Epifani and Weber.[43-44]

Synthesis of Carbon Coated ZnO NPs

The procedures for synthesizing carbon-coated ZnO NPs are illustrated in **Scheme 5.1**. The final products were prepared by pyrolyzing PSAN/OA capped ZnO mixture, PSAN capped ZnO and PS-*b*-PSAN capped ZnO, the products are named ZnO-C_{LSAN}, ZnO-C_{SAN}, and ZnO-$C_{SAN\text{-}S}$, respectively. The polymer-capped ZnO NPs were pyrolyzed in a tube furnace at 800 ºC over 3 hours under N_2 flow and a 10 ºC/min heating rate. A pure ZnO sample was prepared by pyrolyzing PSAN/OA capped ZnO mixture in a tube furnace at 800 ºC for 3 hours in the air for comparison.

Characterization

Number average molecular weight (M_n) and dispersity ($Đ$) were determined by size exclusion chromatography (SEC), conducted with a Waters 515 pump and Waters 2414 different

refractometer using PSS columns (Styrogel 10^5,10^3, 10^2 Å) in THF as an eluent (35 ºC, flow rate of 1 mL min^{-1}), using linear polystyrene (PS) standards for calibration.

Transmission electron microscopy (TEM) was carried out using a JEOL 2000 EX electron microscope operated at 200 kV. High-resolution transmission electron microscopy (HRTEM) images were taken by FEI Titan G2 80-300. A scanning electron microscope (SEM) was carried out using a quanta 600 environmental scanning electron microscope. A Philips X'Pert (Philips Analytical, Netherlands) X-ray diffractometer (XRD) (Cu Kα radiation) was operated at 45 kV and 40 mA in grazing incidence mode to characterize the structure and crystallinity. Thermogravimetric analysis (TGA), TA Instrument 2950, was used to measure the fraction of ZnO. The data were analyzed with TA Universal Analysis. The heating procedure involved 4 steps: 1) samples were placed on a platinum pan and the temperature increased to 120 ºC in an air atmosphere; 2) hold at 120 ºC for 10 min; 3) ramp up at a rate of 20 ºC/min to 800 ºC; 4) hold for 5 min. The TGA plots were normalized to the total weight after holding at 120 ºC. Surface areas of pure ZnO, ZnO/carbon nanocomposite were measured by a Brunauer-Emmett-Teller (BET) Gemini VII 2390 Surface Area Analyzer.

Adsorption Measurements Time-dependent methylene blue (MB) adsorption experiments were performed in glass vials by using 15 mg sample and 10 ml 0.2 mM MB solution. The vials were sealed and placed in the darkroom. The mixture of sample and MB solution was continuously stirred using a magnetic stir bar. Adsorption isotherms measurement were performed by adding 0.15 g of ZnO-C_{SAN-S} into 200 mL solutions of MB, with the different initial concentration of MB, 20~400 mg L^{-1}. The mixtures of MB solution and ZnO-C_{SAN-S} were placed in 250 mL flasks. The flasks were kept in an isothermal shaker (25±1 ºC) for 48 h to reach equilibrium. The whole system was kept in the dark during the experiment.

Photocatalytic efficiency

The photocatalytic activity of samples was measured via photodegradation of MB solution using a 300W Hg lamp. A UV cut-off filter was used to block the UV light (λ < 420 nm) from the lamp. And an IR cut-off filter was used to cut off the light with wavelength λ > 1200 nm. The light intensity was adjusted to 100 mW/cm^2. 15 mg of the test sample was added to 10 mL of MB solution and the mixture was kept stirring in dark to reach the equilibrium before irradiation. Due to the difference in adsorbability of MB, the initial concentration of MB solution for each sample was adjusted to make sure the MB concentration after dark equilibrium was equal to 0.03 mM, which was considered as C_0. The sampled solution was centrifuged at 21,000 × g for 30 min before the absorbance of the solution was measured using a Varian Cary 5000 UV-vis-NIR spectrometer.

5.4. Results and Discussion

ZnO/C hybrid materials were synthesized by pyrolysis of ZnO/PSAN precursor materials in the N_2 atmosphere. To evaluate the role of precursor morphology on the structure and properties of ZnO/C hybrids, four distinct material systems that differ in the connectivity of ZnO and PSAN components are compared: First, binary blends of ZnO nanocrystals and PSAN matrix polymer (system I and II); second, ZnO-PSAN brush particles in which the PSAN matrix polymer is covalently tethered to the ZnO particle (system III); and third, ZnO-PSAN-*b*-PS block copolymer brush particles (system IV). Systems I and II differ in the pyrolysis condition (air and N_2 atmosphere, respectively) and are chosen as reference materials for 'conventional' PSAN/ZnO composite precursor materials. Because particle-in-polymer dispersions are generally unstable (except in the presence of favorable surface-polymer interactions) particle aggregation occurs during pyrolysis that reduces the accessible surface area in ZnO/C hybrids.[45]

To prevent particle aggregation, system III presents the case of a 'one-component hybrid material' in which the tethering of polymer chains prevents the aggregation or phase separation of inorganic and organic components. As a consequence, system III is expected to result in well-dispersed ZnO/C morphologies. However, the crosslinking of PSAN tethers during pyrolysis is also expected to result in a contiguous carbon matrix that will inhibit the transport of reactants and hence limit the photocatalytic performance of materials. The formation of a contiguous carbon matrix is prevented in system IV by 'encapsulating' ZnO-PSAN hybrid particles with a protective shell of PS. This is accomplished by the use of PSAN-*b*-PS copolymer tethers. Because the outer PS block degrades during pyrolysis a more porous structure of ZnO/C is expected. The different ligand systems and the resulting particle morphologies during the carbonization reaction are illustrated in **Scheme 5.1**.

Scheme 5.1. Comparison of the synthetic routes I-IV towards ZnO/C hybrid materials and resulting morphology of ZnO/C hybrid materials.

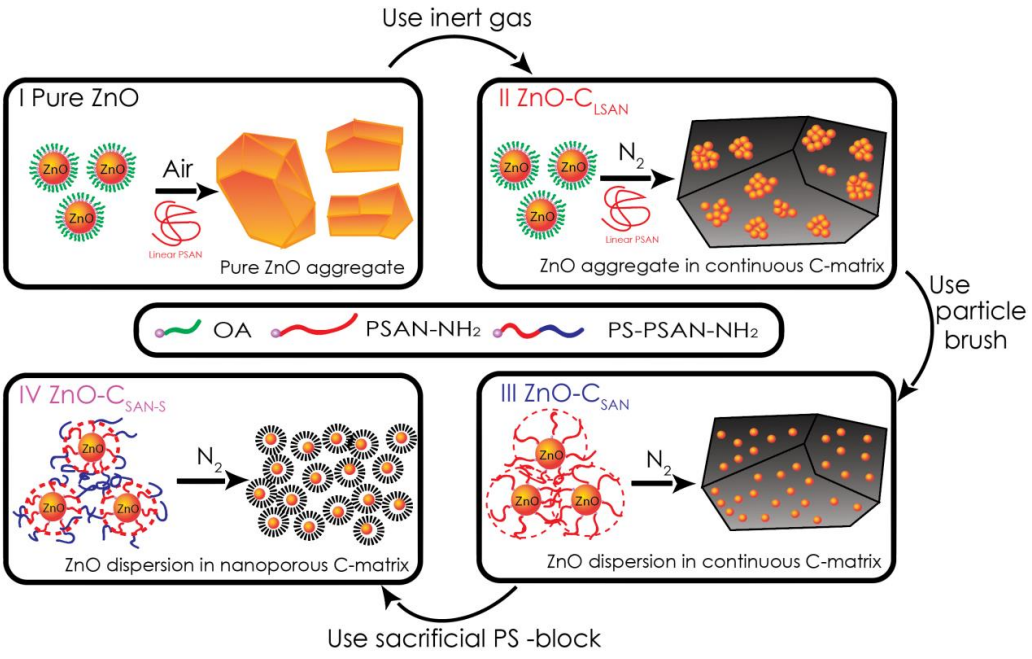

The synthesis of polymer and block copolymer-tethered ZnO nanoparticles followed a three-step procedure, whereby in a first step OA-capped ZnO NPs were synthesized using a thermal decomposition method by controlled decomposition of zinc(II) 2-ethylhexanoate in the presence of octylamine. Subsequently, OA ligands were replaced with acrylonitrile (AN) containing polymer ligands to facilitate subsequent carbonization. Two types of polymer ligands were pursued: poly(styrene-*r*-acrylonitrile) (PSAN) as well as poly(styrene-*r*-acrylonitrile-*b*-styrene) random and block copolymer systems. This choice of ligands was pursued to overcome two separate challenges: First, to enable the dissolution of OA-functionalized ZnO and polymer ligands in a common solvent to facilitate ligand replacement. We note that pristine polyacrylonitrile (PAN) that is commonly pursued carbonization reactions cannot be used here due to the poor solubility characteristics of PAN. To enable solubility in common solvents, and nonpolar co-monomer – styrene (S) – was introduced into the chain. A molar ratio of S: AN = 3:1 was found to provide adequate solubility of polymer ligands in nonpolar solvents and to provide for sufficient AN content to enable the formation of carbon nanoparticles during carbonization. A second challenge that needed to be resolved is concerning interparticle crosslink reactions during carbonization reactions. The latter was found to result in the agglomeration of carbon-coated particles and thus the reduction of effective surface area and photocatalytic activity. To stabilize particles against agglomeration and promote *intra*particle carbonization, a PS 'outer block' was introduced as a 'sacrificial separation layer'. This approach was found to be highly effective in promoting the formation of a dispersed morphology of ZnO particles within a mesoporous carbon matrix.

Solutions of OA-capped ZnO particles in THF (a good solvent for PSAN-Br, PSAN-NH_2, and PS-*b*-PSAN-NH_2) were clear and stable. Polymer ligands with different chain lengths were

synthesized using ARGET ATRP and characterized by NMR and SEC (**Table S5.1**).[39, 46-50] Finally, ligand exchange of the octylamine ligand on the ZnO surfaces with PSAN-NH_2 or PS-*b*-PSAN-NH_2 polymer ligands was performed using a recently developed evaporative ligand exchange process. The low boiling point octylamine ligands promotes its replacement with polymer ligands at ~220 ºC in a high boiling point solvent, DPE. After the removal of solvent and excess free polymers, PSAN- and PS-*b*-PSAN-capped ZnO nanoparticles were isolated and dissolved in THF to form clear solutions, which were subsequently characterized by TEM (**Figure S5.3**). Four precursors were synthesized to prepare carbon-coated ZnO nanocomposites, their properties are listed in **Table 5.1**.

Table 5.1. Information of polymer/ZnO precursors and polymer ligands

Precursor	Polymer	$[M]_0/[I]_0$[b]	M_n[a]	DP	M_w/M_n[a]	ϕ_{ZnO}[c]
ZnO/PSAN-Br (I)	PSAN-Br	40	2000	15	1.20	36.5%
ZnO/PSAN-Br (II)	PSAN-Br	40	1800	13	1.18	40.0%
ZnO-PSAN (III)	PSAN-NH_2	40	1300	23	1.20	47.0%
ZnO-PSAN-*b*-PS (IV)	PS-*b*-PSAN-NH_2	40/40	1750/4000	20/(20+22)	1.18/1.13	32.0 %

a) Molecular weight (M_n) and molecular weight distribution (M_w/M_n) of the polymer ligands were measured by SEC; b) reaction conditions: I-III: Initiator/S/AN/$CuBr_2$/Me_6TREN/Sn$(EH)_2$ = 1/0.63DP_{target}/0.37DP_{target}/0.005/0.1/0.1, T = 60 ºC, in anisole (25 vol%), DMF (2.5 vol%); IV: Initiator/S/$CuBr_2$/Me_6TREN/Sn$(EH)_2$ = 1/DP_{target}/0.005/0.1/0.1, T = 60 ºC, in anisole (25 vol%), DMF (2.5 vol%); c) inorganic content was determined by TGA, ϕ_{ZnO} denotes the inorganic volume fraction.

ZnO/polymer precursor was pyrolyzed in the N_2 or air atmosphere except for system I that was pyrolyzed in the air (as a reference state). Note that in the absence of an inert atmosphere (the system I), oxidation results in only ZnO products. In contrast, in the presence of N_2 during pyrolysis, acrylonitrile units in the PSAN block would initially crosslink and on further heating carbonize to form the carbon matrix. The XRD diffraction patterns for all four samples are shown in **Figure 5.1**. XRD analysis confirmed the presence of hexagonal ZnO (ICSD-01-079-0206) in all samples. Note that the FWHM of the pyrolyzed product of block

copolymer-tethered ZnO hybrid significantly exceeds the respective value for pristine PSAN-tethered particles. This supports the hypothesis that the outer PS block provides a barrier that prevents particle aggregation during the carbonization stage thus resulting in smaller crystalline regions.

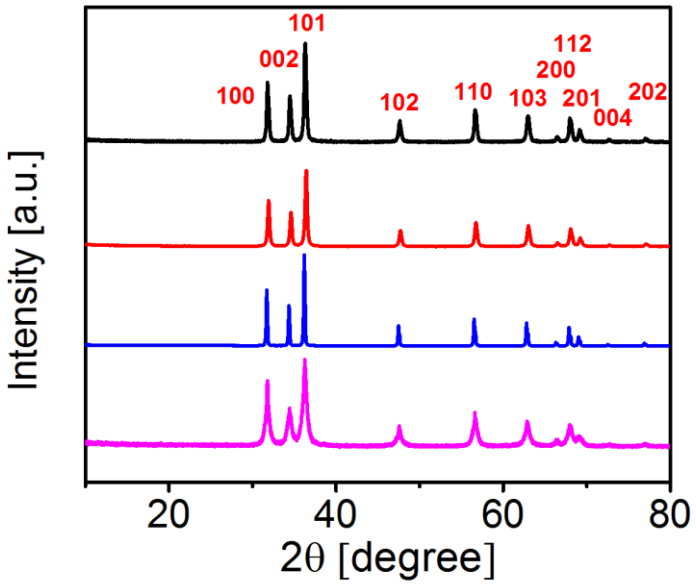

Figure 5.1. XRD pattern of ZnO-C_{SAN-S} (magenta) composite, ZnO-C_{SAN} (blue), ZnO-C_{LSASN} (red) and pure ZnO (black), the XRD analysis confirmed the presence of ZnO in all four samples, the magenta curve(ZnO-C_{SAN-S}) has larger FWHM, which indicates a more nanocrystalline structure.

Figure 5.2 depicts scanning electron micrographs of the respective pyrolysis products. The micrographs reveal that in all cases contiguous materials were obtained (ZnO in case of system 1, ZnO/C hybrids in case of systems II-IV). Films were brittle and fractured during SEM sample preparation thus giving rise to the particulate morphology that is seen in **Figure 5.2**.

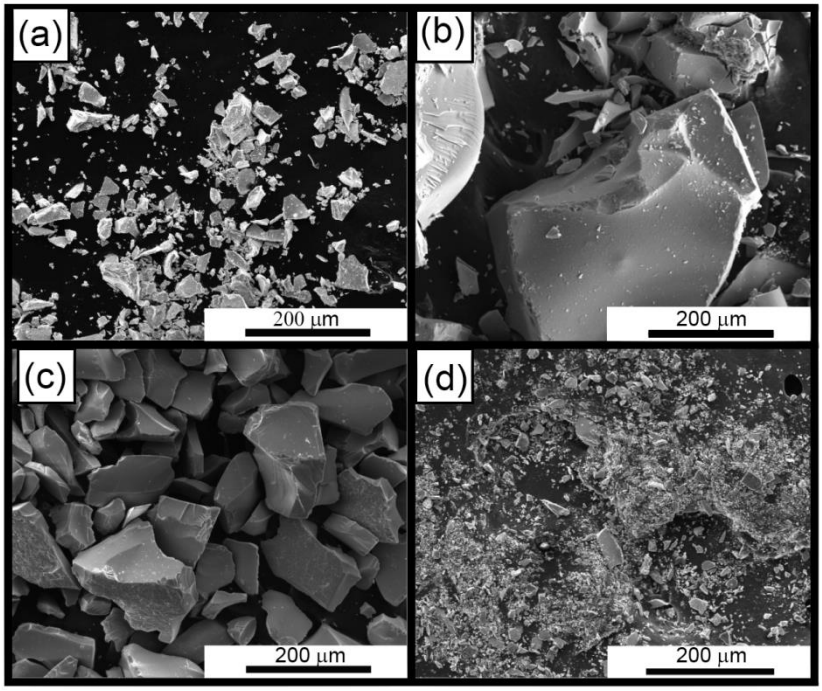

Figure 5.2. SEM images of pure ZnO and ZnO-carbon composites: (a) pure ZnO; (b) ZnO-C_{LSAN}; (c) ZnO-C_{SAN}; (d) ZnO-$C_{SAN\text{-}S}$.

To better understand the effect of precursor morphology on the structure and properties of pyrolysis products, transmission electron microscopy was performed. In the reference system I, the air was the carrier gas during the pyrolysis. Pyrolysis at temperatures above 450 ºC resulted in the removal of all organic phase and ZnO crystals aggregated to form a white powder that was impenetrable to electrons (not shown). In contrast, the application of N_2 as carrier gas (system II), resulting in aggregates of ZnO particles within a contiguous carbon matrix (**Figure 5.3**a and **5.3**b). A similar microstructure was observed when PSAN was tethered to the particle surface (system III, **Figure 5.3**c and **Figure 5.3**d). However, the dispersion state of ZnO particles was significantly improved when brush particles were used as precursors rather than binary PSAN/ZnO blends. Single ZnO nanoparticles of 10-15 nm diameter were observed in the thick layer edge of the ZnO/C hybrid in **Figure 5.3**d. In both systems II and III, the pyrolysis product is impenetrable to the electron beam (see **Figure 5.3**a and **Figure 5.3**c) thus indicating a

contiguous carbon matrix. This is of disadvantage for photocatalytic applications that depend on a porous structure to provide pathways for mass transport. **Figure 5.3**e and **Figure 5.3**f depict the TEM images of the copolymer-grafted system IV. The image (**Figure 5.3**e) reveals smaller grains that are transparent to the electron beam which indicates a reduced electron density within the material.

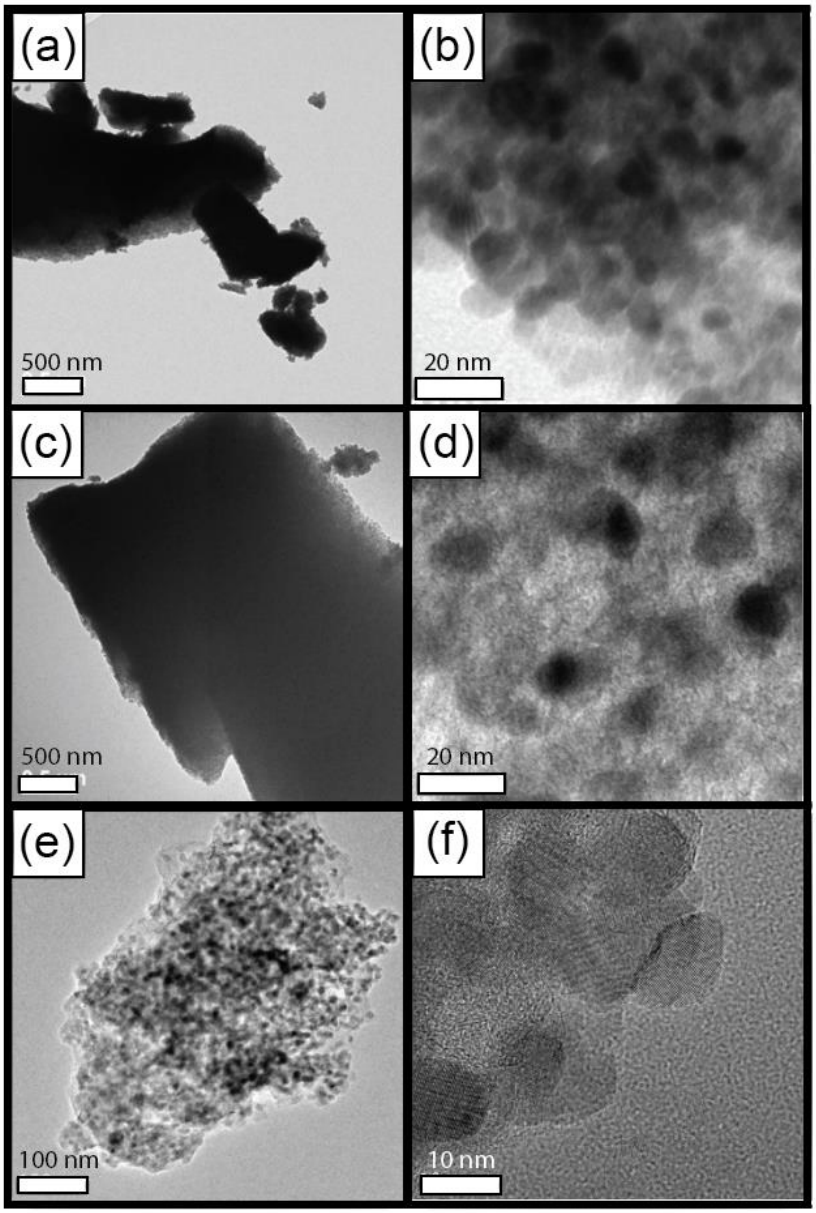

Figure 5.3. TEM images of ZnO-C composites, (a) and (b) ZnO-C_{LSAN} (system II); (c) and (d) ZnO-C_{SAN} (system III); (e) and (f) ZnO-$C_{SAN\text{-}S}$ (system IV).

To further understand the role of precursor morphology on the porosity of ZnO/C hybrids, the surface area, and porous structures were investigated by Brunauer-Emmett-Teller (BET) measurement. The hierarchically porous structure of ZnO-$C_{SAN\text{-}S}$ (system IV) was observed in the N_2 adsorption/desorption isothermal (**Figure 5.4**a). The uptake of N_2 at relative pressure (P/P_0) below 0.05, was attributed to the absorption in the micropores. The continuous increase in the absorbed volume of N_2 at P/P_0 between 0.05 and 0.8 was typical evidence of the presence of mesopores. Besides, the relatively flat region at P/P_0 above 0.8 indicated the lack of large mesopores and macropores. The N_2 absorption isothermal curve of ZnO-C_{SAN}, ZnO-C_{LSAN}, and ZnO is included in **Figure 5.4**a for comparison. In the case of the ZnO-C_{LSAN} (system II) and ZnO-C_{SAN} (system III), the relatively flat region at P/P_0 between 0.05 and 1 indicated that this sample has a very small amount of mesopores and macropores. The uptake of N_2 at P/P_0 below 0.05 was the result of the existence of micropores. For pure ZnO, the flat region at P/P_0 between 0 and 0.9 gives evidence of the lack of micropores and mesopores. The rapid increase in absorbed volume after that suggested the existence of large mesopores and macropores. These results were consistent with the pore size distribution of ZnO, ZnO-C_{LSAN}, ZnO-C_{SAN}, and ZnO-$C_{SAN\text{-}S}$, (see **Figure 5.4**b and **Figure 5.4**b inset).

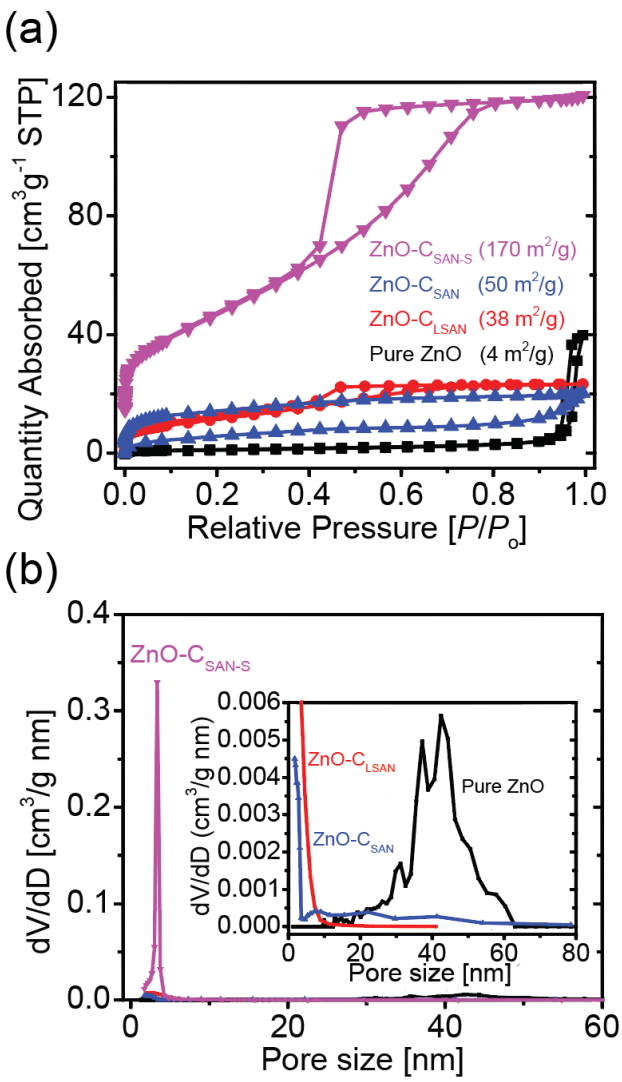

Figure 5.4. (a) Comparison of N_2 adsorption /desorption isothermal of pure ZnO (the system I), ZnO-C_{LSAN} (system II), ZnO-C_{SAN} (system III), and ZnO-$C_{SAN\text{-}S}$ (system IV); (b) pore size distribution of pure ZnO, ZnO-C_{LSAN}, ZnO-C_{SAN}, ZnO-$C_{SAN\text{-}S}$. Inset shows an enlarged plot of the pore size distribution of pure ZnO, ZnO-C_{LSAN} and ZnO-C_{SAN} (systems I-III).

Table 5.2 lists the specific surface areas of ZnO, ZnO-C_{LSAN}, ZnO-C_{SAN}, and ZnO-$C_{SAN\text{-}S}$ as 4 ± 1 m²/g, 38 ± 5 m²/g, 50 ± 5 m²/g, and 170 ± 10 m²/g, respectively. The comparatively low surface area of ZnO was due to the removal of the carbon coating layer during the annealing process in the air when the ZnO nanoparticles recrystallized to form large agglomerated particles.

Table 5.2. Summary of carbon-coated ZnO and pure ZnO characterization

Entry	ZnO Content (wt%)[a]	Specific Surface Area (m^2/g)[b]	Pore Size (nm)[b,c]
Pure ZnO (I)	100	4± 1	42
ZnO-C_{LSAN} (II)	86	38± 5	6
ZnO-C_{SAN} (III)	85	50± 5	4
ZnO-C_{SAN-S} (IV)	83	170 ± 10	2

a) inorganic content was determined by TGA; b) surface area was characterized by the Brunauer-Emmett-Teller (BET) method; c) pore size was reported as the peak value from the plots.

The large difference in surface areas between pure ZnO and carbon-ZnO composites implied that the high specific surface areas of ZnO-C_{LSAN}, ZnO-C_{SAN}, and ZnO-C_{SAN-S} mainly came from the outer carbon layers, which only occupied 14%, 15% and 17% of total mass, respectively. We thus conclude that the difference in surface area between ZnO-C_{LSAN}, ZnO-C_{SAN}, and ZnO was a result of a large number of accessible micropores in the carbon coating layer of ZnO-C_{LSAN} and ZnO-C_{SAN}. The significant increase in specific surface area (SSA) despite the similar volume fraction of inorganic suggests that interparticle crosslinking during the carbonization procedure was successfully suppressed by the PS ‘protective block’ thus resulting in more porous materials. This is an important observation since it can be expected that a more accessible porous structure in the composite should improve the dye transport and adsorption and benefit the photocatalytic performance of the material.

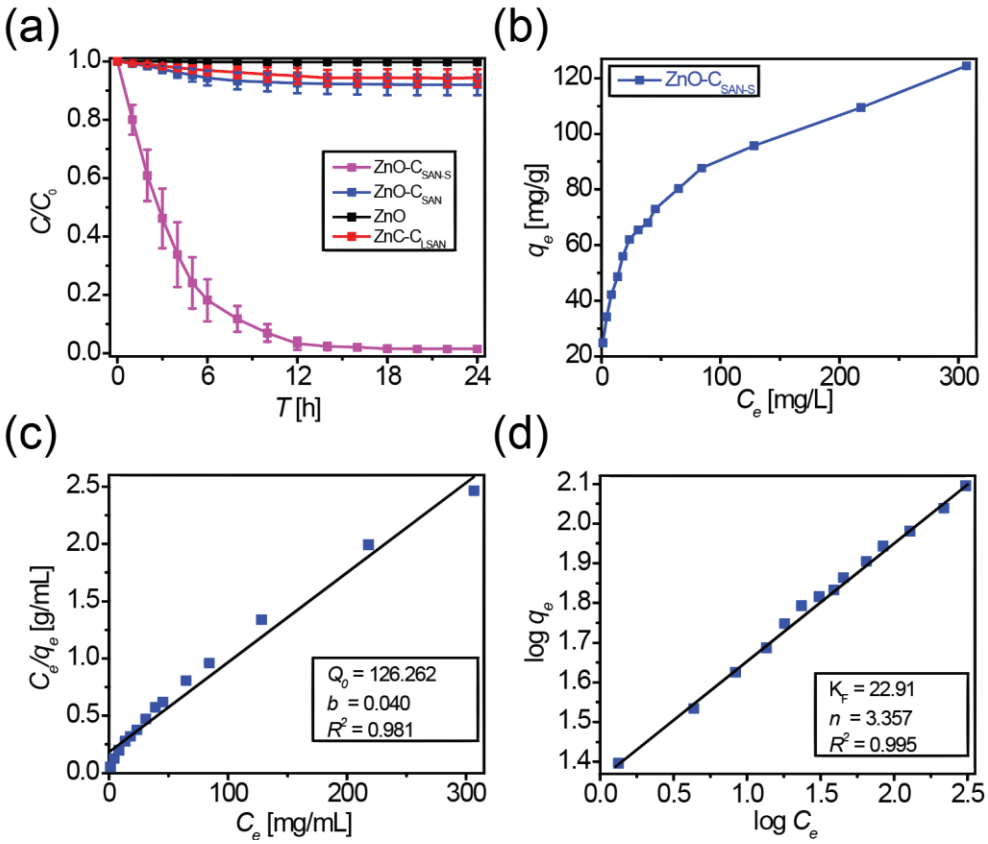

Figure 5.5. (a) Effect of contacting time on MB dye adsorption for pure ZnO (black), ZnO-C_{LSAN} (red), ZnO-C_{SAN} (blue) and ZnO-$C_{SAN\text{-}S}$ (magenta). (b) Adsorption isotherm for ZnO-$C_{SAN\text{-}S}$. (c) Langmuir adsorption isotherm of MB for ZnO-$C_{SAN\text{-}S}$. (d) Freundlich adsorption isotherm of MB for ZnO-$C_{SAN\text{-}S}$.

The photoactivity of three samples was evaluated by the degradation of methylene blue (MB), a common model dye to test the catalytic ability of photocatalysts.[51] In a typical dye degradation process, dye molecules would diffuse to, or near, the surface of photocatalyst and react with radicals.[52] Literature reported that the dye degradation rate of graphene- or carbon nanotube-based photocatalysts have benefited from their excellent dye adsorbability.[53-54] Porous carbon materials such as activated carbon with extraordinary dye adsorbability are widely used in the area of water treatment.[55-56] Hence, to reveal the adsorbability of ZnO/carbon nanocomposite before the photocatalytic activity measurement, the adsorption experiments were carried in MB solution with three samples in a dark room.

First, the time-dependent MB adsorption experiments were performed by measuring the dye concentration as a function of time after adding a 15 mg sample into 10 ml of a 0.2 mM MB solution. The effect of contact time on the adsorption of MB is shown in Figure 5a. For the ZnO-$C_{SAN\text{-}S}$ sample, it required around 18 h to reach equilibrium, 98.5% MB in the solution was adsorbed. The decrease in adsorption rate was the result of decreasing of vacant adsorbent sites and dye concentration. After equilibrium, the lack of active adsorbent prevented any further uptake. As a comparison, nearly no MB was adsorbed by the pure ZnO sample within 24 h, and only a small amount of MB was adsorbed by ZnO-C_{LSAN} and ZnO-C_{SAN}. The equilibrium was reached in the first 6 h. The adsorbability highly depended on the surface area and porous structure of the adsorbents. Compared to ZnO-$C_{SAN\text{-}S}$, the low specific surface areas of pure ZnO, ZnO-C_{LSAN} and ZnO-C_{SAN} particles limited their adsorbability.

To further understand each sample's adsorbability and surface nature, adsorption isotherm measurements were performed by measuring the equilibrium concentrations of three samples in solution with different initial concentrations (20~400 mg L^{-1}). **Figure 5.5**b shows the adsorption isotherm curve for ZnO-$C_{SAN\text{-}S}$. The adsorption isotherm provided information on the distribution of liquid molecules at the interface between the solid phase and liquid phase after equilibrium. The amount of dye adsorbed after equilibrium increased from 25 mg g^{-1} to 125 mg g^{-1} with increasing initial dye concentration from 20 mg L^{-1} to 0.4 g L^{-1}.

To better understand the nature of the adsorption characteristics of the materials, the experimental data were interpreted using the Langmuir and Freundlich isotherm models.[57] According to the Langmuir model, adsorption proceeds via the formation of a uniform monolayer of adsorbent on the surface without any transmigration. The linear equation of Langmuir isotherm model can be given as follow: $C_e/q_e = 1/Q_0b+C_e/Q_0$.[55] In this equation, C_e

represents the equilibrium concentration of the adsorbate (MB) (mg/L), q_e is the amount of adsorbate absorbed by per unit mass of sample; Q_0 and b are the Langmuir constants. On the other hand, the Freundlich isotherm model assumed the surface energy on the sample was not homogeneous. The linear equation of Freundlich isotherm model is: $\log q_e = \log K_F + (1/n) \log C_e$.[55] In analogy to the linear equation of Langmuir isotherm model, C_e is the equilibrium concentration of the adsorbate (MB) (mg L^{-1}), and q_e is the amount of adsorbate absorbed by per unit mass of sample. K_F and n are the Freundlich constants.

Table 5.3. Langmuir and Freundlich isotherm constants for MB at room temperature

Langmuir isotherm	
Q_0 [mg g^{-1}]	126.262
b [mg^{-1}]	0.040
R^2	0.981
Freundlich isotherm	
$1/n$	
K_F [(mg g^{-1})(mg^{-1})$^{1/n}$]	22.91
R^2	0.995

Figure 5.5c showed the Langmuir isotherm for ZnO-$C_{SAN\text{-}S}$ (system IV), where C_e/q_e is plotted as a function of C_e. After fitting the data point in **Figure 5.5**c with a straight line, the values of the Langmuir constants were calculated (**Table 5.3**). **Figure 5.5**d was the Freundlich isotherm for ZnO-$C_{SAN\text{-}S}$, where $\log q_e$ was plotted against $\log C_e$, giving a straight line with a slope of $(1/n)$ and intercept of $\log K_F$. Accordingly, Freundlich constants K_F and n were calculated (**Table 5.3**). Comparing the correlation coefficients for the two fitting models, the Freundlich isotherm model yielded a better fit which demonstrated the inhomogeneous nature of the surface of the ZnO-$C_{SAN\text{-}S}$ sample.

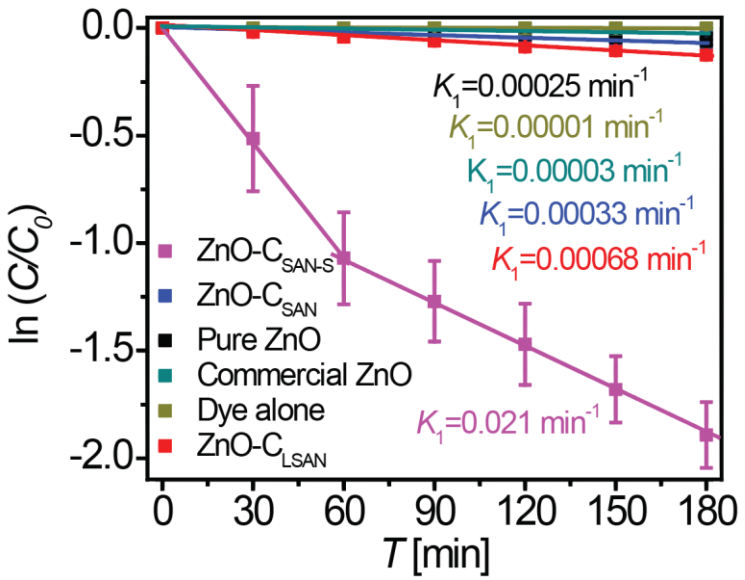

Figure 5.6. Methylene blue dye degradation for different sample materials. Black: pure ZnO (I); red: ZnO-C_{LSAN} (II); blue: ZnO-C_{SAN} (III); magenta: ZnO-$C_{SAN\text{-}S}$ (IV); dark cyan: commercial ZnO and dark yellow: pure dye.

The photocatalytic activity of the four samples was characterized by MB degradation overtime under visible light irradiation. The dye degradation rate for commercial ZnO was measured for comparison. The same measurement without any photocatalyst was performed as a blank control. Due to the huge difference of dye adsorbability between each sample, the starting dye concentration was adjusted for each sample to make sure the initial concentrations after equilibrium in the dark are the same. In **Figure 5.6**, to determine the dye degradation rate constant k, $\ln(C/C_0)$ was plotted as a function of time t, where C is a concentration of MB after a certain time of irradiation and C_0 is an initial concentration of MB after equilibrium. Based on equation $\ln(C/C_0) = -kt$,[57] a pseudo-first-order fitting model was used to calculate rate constant k. In **Figure 5.6**, there was almost no dye degradation when using sample ZnO-C_{SAN}, ZnO-C_{LSAN}, pure ZnO, commercial ZnO, and dye alone. The k values were 0.00033 min^{-1}, 0.00068 min^{-1}, 0.00025 min^{-1}, 0.00003 min^{-1}, and 0.00001 min^{-1} respectively. In contrast, the k value in the first hour of ZnO-$C_{SAN\text{-}S}$ was three orders of magnitude higher than the other samples, 0.021 min^{-1}. After the first hour, due to the decrease in the concentration of MB, it decreased to 0.0068 min^{-1}.

Later, the dye concentration decreased to a critical point when the diffusion of dye into the photocatalyst determined the reaction rate instead of the number of photocatalytic reaction sites. However, the *k* value of ZnO-C_{SAN-S} after the first hour was still significantly higher than the others. This is because the ZnO-C_{SAN-S} sample not only facilitated the degradation of the MB in solution but also the MB adsorbed in the composites during the equilibrium process. Meanwhile, this calculated *k* value can only show the degradation rate in the solution, plausibly the actual *k* value of ZnO-C_{SAN-S} was highly underestimated in the photocatalytic activity measurement.

The ZnO-C_{SAN-S} sample showed much higher visible-light photocatalytic activity than ZnO-C_{SAN}, ZnO-C_{LSAN} and pure ZnO samples that cannot be explained based on only increased SSA (170 m^2/g for system IV as compared to 4, 38, and 50 m^2/g for systems I-III). We hypothesize that the higher activity rather is a mutual effect of a 'narrowing' of the ZnO bandgap due to the carbon coating. The more narrow bandgap should result in a wider effective spectral range in the visible region and thus increase the photocatalytic efficacy. The second effect is believed to be the porous microstructure in system IV. Specifically, unlike systems II (ZnO-C_{LSAN}) and III (ZnO-C_{SAN}) sample, in which ZnO/C formed a dense contiguous structure, the structure of ZnO-C_{SAN-S} was highly porous. This should have two effects: first, it should increase the number of active sites on the surface of the ZnO. The higher specific surface area also increases dye adsorption for this sample and should promote dye diffusion. It is also conceivable that the carbon on the ZnO surface worked as a co-catalyst which can accelerate the separation of electrons and holes in the ZnO. Finally, the carbon layers between each ZnO particles prevented them from agglomeration. The ZnO particles maintained the size of around 10-15 nm in diameter even after 800 ºC pyrolysis. This provided ZnO high crystallinity while maintaining a short distance for excitons to diffuse to the surface.

5.5. Supporting Information

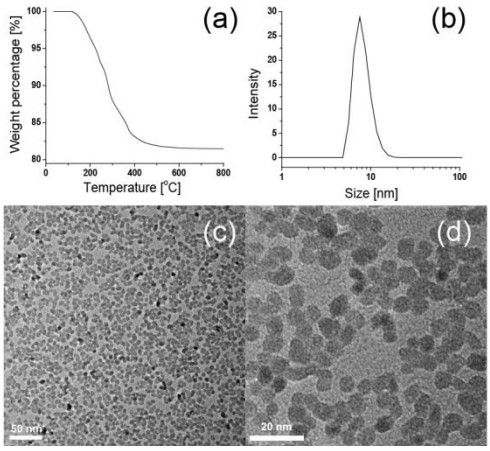

Figure S5.1. (a) TGA curve for OA capped ZnO NPs; (b) The size distribution of OA capped ZnO NPs measured by DLS measurements in THF; (c) and (d) TEM images of the OA capped ZnO NPs.

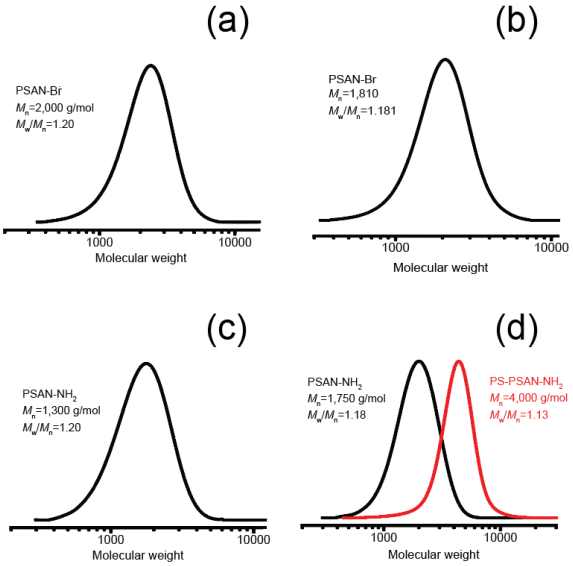

Figure S5.2. (a) SEC trace of PSAN-Br polymer ligand with M_n=2,000 and M_w/M_n=1.20; (a) SEC trace of PSAN-Br polymer ligand with M_n=1,800 and M_w/M_n=1.18; (c) SEC trace of PSAN-NH_2 polymer ligand with M_n=1,300 and M_w/M_n=1.20; (d) SEC trace of PS-PSAN-NH_2 polymer ligand with M_n=4,000 and M_w/M_n=1.13.

Table S5.1. Summary of ZnO-PSAN mixture (a and b) and ligand exchange reactions (c and d) of OA capped ZnO with PSAN/PS-b-PSAN-NH_2 polymer ligands

Entry	Ligands composition	M_n [b]	Mass (mg)	Inorganic fraction[c]
a	PSAN-Br	2000	1500	36.5%
b	PSAN-Br	1800	1500	40.0%
b	PSAN-NH_2	1300	300	47.0%
c	PS-b-PSAN-NH_2	4000	800	32.0%

Note: in all reactions, 1 g OA capped ZnO was added into the systems.

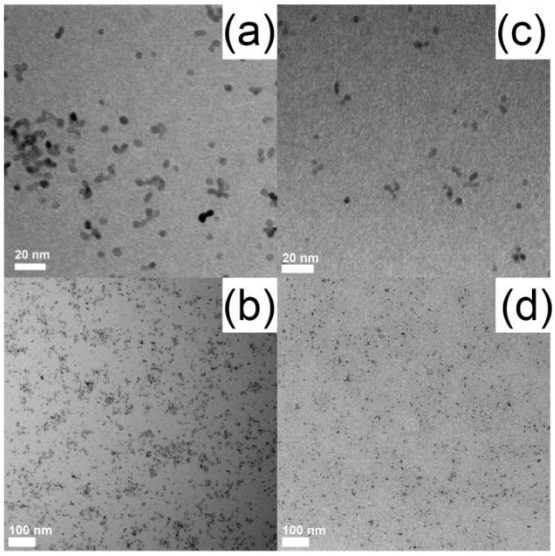

Figure S5.3. (a) and (b) TEM images of PSAN capped ZnO NPs with PSAN-NH_2 polymer ligands (M_n=1,300 and M_w/M_n=1.20); (c) and (d) TEM images of PS-b-PSAN capped ZnO NPs with PS-b-PSAN-NH_2 polymer ligands (M_n=4,000 and M_w/M_n=1.13).

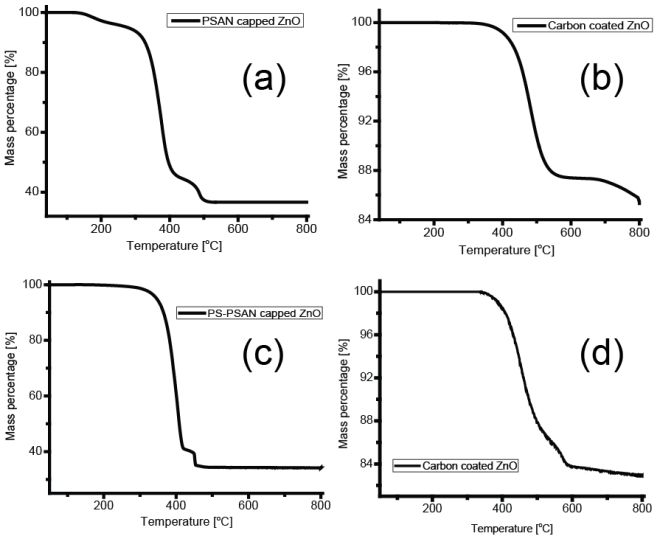

Figure S5.4. TGA measurements of (a), PSAN capped ZnO NPs; (b), carbon-coated ZnO NPs synthesized by PSAN capped ZnO NPs; (c), PS-b-PSAN capped ZnO NPs; (d), carbon-coated ZnO NPs synthesized by PS-b-PSAN capped ZnO NPs.

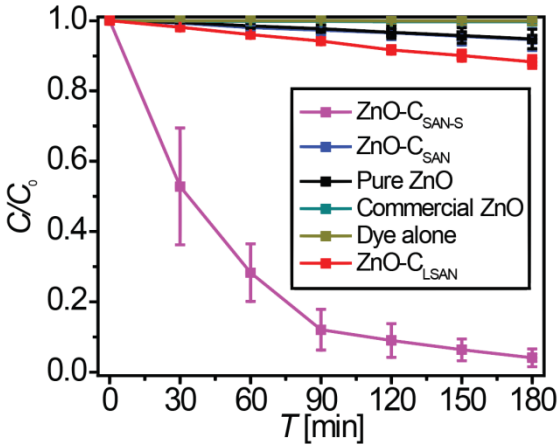

Figure S5.5. Methylene blue dye degradation for sample black: pure ZnO, red: ZnO-C_{LSAN}, blue: ZnO-C_{SAN}, magenta: ZnO-C_{SAN-S}, dark cyan: commercial ZnO and dark yellow: dye alone.

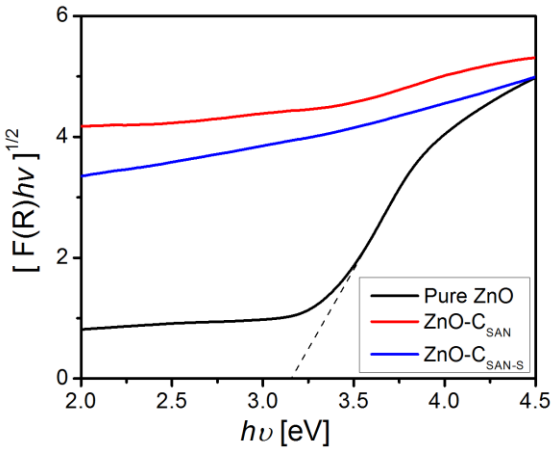

Figure S5.6. Tauc plot $[F(R)h\upsilon]^{1/2}$ versus photon energy (hυ) to estimate the absorption of edges of ZnO, ZnO-C_{SAN}, ZnO-C_{SAN-S}.

Table S5.2. Summary of K constants for MB dye degradation

Sample	k constant (min^{-1})
ZnO-C_{SAN-S}	0.02104
ZnO-C_{SAN}	0.00033
ZnO-C_{LSAN}	0.00068
Pure ZnO	0.00025
Dye alone	0.00001
Commercial ZnO	0.00003

Table S5.3. Comparisons of photocatalytic performances of ZnO/carbon composites

Materials	Light Power Source	Light Range	Dye	Rate Constant [min^{-1}]	Ref.
ZnO/Nanoporous carbon	300 W, Hg	420 ~ 1200 nm	Methylene Blue	0.02104	This work
ZnO/Carbon nanotube	Nature sunlight	-	Rhodamine B	0.00996	ref 1[1]
ZnO/rGraphene Oxide	500 W, Halogen	Visible	Methylene Blue	0.01155	ref 2[2]
ZnO/Graphene	400 W, Halogen	Visible	Methyl Orange	0.00851	ref 3[3]
Mn-ZnO/Graphene	400 W, Halogen	Visible	Methylene Blue	0.00594	ref 4[4]
ZnO	125 W, Hg	Visible	Methylene Blue	0.00683	ref 5[5]
MWCNT/ZnO	Solar simulator	-	Methylene Blue	0.01446	ref 6[6]
g-C_3N_4/ZnO	300 W, Xe	> 400 nm	Methylene Blue	0.01340	ref 7[7]
ZnO_{1-x}/Graphene	175 W, Halide	> 420 nm	Methylene Blue	0.01010	ref 8[8]
ZnO/Carbon quantum dots	8 W	Visible	Benzene gas	0.01254	ref 9[9]
Carbon doped ZnO	-	Visible	Rhodamine B	0.00833	ref 10[10]
C, N-doped ZnO	300 W, Xe	Visible	Methylene Blue	0.05365	ref 11[11]
ZnO/Carbon Dandelions	6 W, Xe	UV light	Methylene Blue	0.23026	ref 12[12]
ZnO-Carbon composite	250 W, GY-250	UV light	Methylene Blue	0.09163	ref 13[13]
ZnO/Graphene oxide/gold NPs	110 mW cm^{-2}, UV spot light	UV light	Rhodamine B	0.02878	ref 14[14]
Carbon-doped ZnO	500 W. Halide	> 420 nm	Methylene Blue	0.02015	ref 15[15]
Carbon/ZnO@ZnS nanotube	125 W, Mercury	UV light	Methyl Orange	0.03584	ref 16[16]
ZnO/Graphite carbon	8 W, Xe	UV light	Methylene Blue	0.03070	ref 17[17]
ZnO-carbon nanofiber	50 W, Mercury	313 nm	Rhodamine B	0.07533	ref 18[18]

1. M. Ahmad, E. Ahmed, Z. L. Hong, W. Ahmed, A. Elhissi and N. R. Khalid, *Ultrasonics Sonochemistry*, 2014, **21**, 761-773.
2. M. Azarang, A. Shuhaimi, R. Yousefi, A. Moradi Golsheikh, and M. Sookhakian, *Ceramics International*, 2014, **40**, 10217-10221.

3. M. Ahmad, E. Ahmed, Z. L. Hong, J. F. Xu, N. R. Khalid, A. Elhissi and W. Ahmed, *Applied Surface Science*, 2013, **274**, 273-281.
4. M. Ahmad, E. Ahmed, W. Ahmed, A. Elhissi, Z. L. Hong and N. R. Khalid, *Ceramics International*, 2014, **40**, 10085-10097.
5. Y. Li, W. Xie, X. Hu, G. Shen, X. Zhou, Y. Xiang, X. Zhao, and P. Fang, *Langmuir*, 2010, **26**, 591-597.
6. M. Samadi, H. A. Shivaee, M. Zanetti, A. Pourjavadi and A. Moshfegh, *Journal of Molecular Catalysis A: Chemical*, 2012, **359**, 42-48.
7. Y.-P. Zhu, M. Li, Y.-L. Liu, T.-Z. Ren and Z.-Y. Yuan, *The Journal of Physical Chemistry C*, 2014, **118**, 10963-10971.
8. X. Bai, L. Wang, R. Zong, Y. Lv, Y. Sun and Y. Zhu, *Langmuir*, 2013, **29**, 3097-3105.
9. H. Yu, H. Zhang, H. Huang, Y. Liu, H. Li, H. Ming, and Z. Kang, *New Journal of Chemistry*, 2012, **36**, 1031-1035.
10. S. A. Ansari, S. G. Ansari, H. Foaud and M. H. Cho, *New Journal of Chemistry*, 2017, **41**, 9314-9320.
11. P. Liang, C. Zhang, H. Sun, S. Liu, M. Tade and S. Wang, *RSC Advances*, 2016, **6**, 95903-95909.
12. X. Wang, P. Hu, Y. Fangli and L. Yu, *The Journal of Physical Chemistry C*, 2007, **111**, 6706-6712.
13. J. Xue, S. Ma, Y. Zhou and Z. Zhang, *New Journal of Chemistry*, 2015, **39**, 1852-1857.
14. K. Bramhaiah, V. N. Singh and N. S. John, *Physical Chemistry Chemical Physics*, 2016, **18**, 1478-1486.
15. X. Zhang, J. Qin, R. Hao, L. Wang, X. Shen, R. Yu, S. Limpanart, M. Ma and R. Liu, *The Journal of Physical Chemistry C*, 2015, **119**, 20544-20554.
16. Z. Shami and N. Sharifi-Sanjani, *CrystEngComm*, 2014, **16**, 910-921.
17. L. Zhang, H. Cheng, R. Zong and Y. Zhu, *The Journal of Physical Chemistry C*, 2009, **113**, 2368-2374.
18. J. Mu, C. Shao, Z. Guo, Z. Zhang, M. Zhang, P. Zhang, B. Chen and Y. Liu, *ACS Applied Materials & Interfaces*, 2011, **3**, 590-596.

5.6. Conclusion

The tethering of block copolymer grafts in which the outer block is designed to prevent crosslinking of carbon shells during the pyrolysis of ZnO/PSAN is shown to provide a strategy towards ZnO/C hybrid materials that combine fine ZnO particle dispersion within a high porosity carbon matrix. For the specific case of PS-*b*-PSAN-capped ZnO precursors, the resulting ZnO/C hybrids exhibited a specific surface area of 170 m^2/g and a rate constant of 0.021 min^{-1} for the photocatalytic degradation of methylene blue under visible light. The increase in photocatalytic efficacy is believed to be the result of several contributing factors: first, the increased porosity

that raises the dye adsorption within the material and also enables more effective mass transport. Second, the narrowing of the ZnO bandgap (via the presence of carbon shells) that increases the effective spectral range for photodegradation. Benefits of the synthetic approach (using PSAN-derived block copolymer tethered nanoparticle precursors) include the possible extension to other inorganic compositions as well as the potential scalability (since the different synthetic processes such as high-temperature pyrolysis or controlled radical polymerization are already being applied in industrial processes). Future research will have to better understand the role of copolymer degree of polymerization as well as composition on the attainable structure and performance of materials.

5.7. References

(1) Behnajady, M. A.; Modirshahla, N.; Hamzavi, R., Kinetic study on photocatalytic degradation of C.I. Acid Yellow 23 by ZnO photocatalyst. *Journal of Hazardous Materials* **2006,** *133* (1–3), 226-232.

(2) Hess, E. V., Environmental chemicals and autoimmune disease: cause and effect. *Toxicology* **2002,** *181–182*, 65-70.

(3) Sun, J.-H.; Dong, S.-Y.; Wang, Y.-K.; Sun, S.-P., Preparation and photocatalytic property of a novel dumbbell-shaped ZnO microcrystal photocatalyst. *Journal of Hazardous Materials* **2009,** *172* (2–3), 1520-1526.

(4) Yang, N.; Liu, Y.; Wen, H.; Tang, Z.; Zhao, H.; Li, Y.; Wang, D., Photocatalytic Properties of Graphdiyne and Graphene Modified TiO2: From Theory to Experiment. *ACS Nano* **2013,** *7* (2), 1504-1512.

(5) An, C.; Peng, S.; Sun, Y., Facile Synthesis of Sunlight-Driven AgCl: Ag Plasmonic Nanophotocatalyst. *Advanced Materials* **2010,** *22* (23), 2570-2574.

(6) Bai, X.; Wang, L.; Zhu, Y., Visible Photocatalytic Activity Enhancement of ZnWO4 by Graphene Hybridization. *ACS Catalysis* **2012,** *2* (12), 2769-2778.

(7) Ajmal, A.; Majeed, I.; Malik, R. N.; Idriss, H.; Nadeem, M. A., Principles and mechanisms of photocatalytic dye degradation on TiO2 based photocatalysts: a comparative overview. *RSC Advances* **2014,** *4* (70), 37003-37026.

(8) Fox, M. A.; Dulay, M. T., Heterogeneous photocatalysis. *Chemical Reviews* **1993,** *93* (1), 341-357.

(9) Barnes, R. J.; Molina, R.; Xu, J.; Dobson, P. J.; Thompson, I. P., Comparison of TiO2 and ZnO nanoparticles for photocatalytic degradation of methylene blue and the correlated inactivation of gram-positive and gram-negative bacteria. *Journal of Nanoparticle Research* **2013,** *15* (2), 1432.

(10) Wang, Y.; Shi, R.; Lin, J.; Zhu, Y., Enhancement of photocurrent and photocatalytic activity of ZnO hybridized with graphite-like C3N4. *Energy & Environmental Science* **2011,** *4* (8), 2922-2929.
(11) Maeda, K.; Domen, K., Solid Solution of GaN and ZnO as a Stable Photocatalyst for Overall Water Splitting under Visible Light. *Chemistry of Materials* **2010,** *22* (3), 612-623.
(12) Bai, X.; Wang, L.; Zong, R.; Lv, Y.; Sun, Y.; Zhu, Y., Performance Enhancement of ZnO Photocatalyst via Synergic Effect of Surface Oxygen Defect and Graphene Hybridization. *Langmuir* **2013,** *29* (9), 3097-3105.
(13) Li, Y.; Zhang, B.-P.; Zhao, J.-X.; Ge, Z.-H.; Zhao, X.-K.; Zou, L., ZnO/carbon quantum dots heterostructure with enhanced photocatalytic properties. *Applied Surface Science* **2013,** *279*, 367-373.
(14) Subash, B.; Krishnakumar, B.; Swaminathan, M.; Shanthi, M., Highly Efficient, Solar Active, and Reusable Photocatalyst: Zr-Loaded Ag–ZnO for Reactive Red 120 Dye Degradation with Synergistic Effect and Dye-Sensitized Mechanism. *Langmuir* **2013,** *29* (3), 939-949.
(15) Kudo, S.; Maki, T.; Miura, K.; Mae, K., High porous carbon with Cu/ZnO nanoparticles made by the pyrolysis of carbon material as a catalyst for steam reforming of methanol and dimethyl ether. *Carbon* **2010,** *48* (4), 1186-1195.
(16) Wu, D.; Liang, Y.; Yang, X.; Zou, C.; Li, Z.; Lv, G.; Zeng, X.; Fu, R., Preparation of Activated Ordered Mesoporous Carbons with a Channel Structure. *Langmuir* **2008,** *24* (7), 2967-2969.
(17) Punetha, V. D.; Rana, S.; Yoo, H. J.; Chaurasia, A.; McLeskey Jr, J. T.; Ramasamy, M. S.; Sahoo, N. G.; Cho, J. W., Functionalization of carbon nanomaterials for advanced polymer nanocomposites: A comparison study between CNT and graphene. *Progress in Polymer Science* **2017,** *67*, 1-47.
(18) Wu, D.; Xu, F.; Sun, B.; Fu, R.; He, H.; Matyjaszewski, K., Design, and Preparation of Porous Polymers. *Chemical Reviews* **2012,** *112* (7), 3959-4015.
(19) Kongkanand, A.; Kamat, P. V., Electron Storage in Single-Wall Carbon Nanotubes. Fermi Level Equilibration in Semiconductor–SWCNT Suspensions. *ACS Nano* **2007,** *1* (1), 13-21.
(20) Lee, W. J.; Lee, J. M.; Kochuveedu, S. T.; Han, T. H.; Jeong, H. Y.; Park, M.; Yun, J. M.; Kwon, J.; No, K.; Kim, D. H.; Kim, S. O., Biomineralized N-Doped CNT/TiO2 Core/Shell Nanowires for Visible Light Photocatalysis. *ACS Nano* **2012,** *6* (1), 935-943.
(21) Park, H.-A.; Liu, S.; Oh, Y.; Salvador, P. A.; Rohrer, G. S.; Islam, M. F., Nano-Photoelectrochemical Cell Arrays with Spatially Isolated Oxidation and Reduction Channels. *ACS Nano* **2017,** *11* (2), 2150-2159.
(22) Han, C.; Yang, M.-Q.; Weng, B.; Xu, Y.-J., Improving the photocatalytic activity and anti-photo corrosion of semiconductor ZnO by coupling with versatile carbon. *Physical Chemistry Chemical Physics* **2014,** *16* (32), 16891-16903.
(23) Fu, H.; Xu, T.; Zhu, S.; Zhu, Y., Photocorrosion Inhibition and Enhancement of Photocatalytic Activity for ZnO via Hybridization with C60. *Environmental Science & Technology* **2008,** *42* (21), 8064-8069.
(24) Mu, J.; Shao, C.; Guo, Z.; Zhang, Z.; Zhang, M.; Zhang, P.; Chen, B.; Liu, Y., High Photocatalytic Activity of ZnO−Carbon Nanofiber Heteroarchitectures. *ACS Applied Materials & Interfaces* **2011,** *3* (2), 590-596.

(25) Zhu, Y.-P.; Li, M.; Liu, Y.-L.; Ren, T.-Z.; Yuan, Z.-Y., Carbon-Doped ZnO Hybridized Homogeneously with Graphitic Carbon Nitride Nanocomposites for Photocatalysis. *The Journal of Physical Chemistry C* **2014,** *118* (20), 10963-10971.
(26) Yu, H.; Zhang, H.; Huang, H.; Liu, Y.; Li, H.; Ming, H.; Kang, Z., ZnO/carbon quantum dots nanocomposites: one-step fabrication and the superior photocatalytic ability for toxic gas degradation under visible light at room temperature. *New Journal of Chemistry* **2012,** *36* (4), 1031-1035.
(27) Shami, Z.; Sharifi-Sanjani, N., A well-designed three-dimensional ternary hierarchical co-axial ZnO@ZnS heteroarchitecture decorated electrospun carbon hollow tube nanofibrous mat: improved ultraviolet-light photocatalytic performance. *CrystEngComm* **2014,** *16* (5), 910-921.
(28) Liang, P.; Zhang, C.; Sun, H.; Liu, S.; Tade, M.; Wang, S., Photocatalysis of C, N-doped ZnO derived from ZIF-8 for dye degradation and water oxidation. *RSC Advances* **2016,** *6* (98), 95903-95909.
(29) Bramhaiah, K.; Singh, V. N.; John, N. S., Hybrid materials of ZnO nanostructures with reduced graphene oxide and gold nanoparticles: enhanced photodegradation rates concerning their composition and morphology. *Physical Chemistry Chemical Physics* **2016,** *18* (3), 1478-1486.
(30) Zhang, X.; Qin, J.; Hao, R.; Wang, L.; Shen, X.; Yu, R.; Limpanart, S.; Ma, M.; Liu, R., Carbon-Doped ZnO Nanostructures: Facile Synthesis and Visible Light Photocatalytic Applications. *The Journal of Physical Chemistry C* **2015,** *119* (35), 20544-20554.
(31) Wang, X.; Hu, P.; Fangli, Y.; Yu, L., Preparation and Characterization of ZnO Hollow Spheres and ZnO−Carbon Composite Materials Using Colloidal Carbon Spheres as Templates. *The Journal of Physical Chemistry C* **2007,** *111* (18), 6706-6712.
(32) Li, W.; Liu, J.; Zhao, D., Mesoporous materials for energy conversion and storage devices. **2016,** *1*, 16023.
(33) Zhong, M.; Kim, E. K.; McGann, J. P.; Chun, S.-E.; Whitacre, J. F.; Jaroniec, M.; Matyjaszewski, K.; Kowalewski, T., Electrochemically Active Nitrogen-Enriched Nano carbons with Well-Defined Morphology Synthesized by Pyrolysis of Self-Assembled Block Copolymer. *Journal of the American Chemical Society* **2012,** *134* (36), 14846-14857.
(34) Kruk, M.; Dufour, B.; Celer, E. B.; Kowalewski, T.; Jaroniec, M.; Matyjaszewski, K., Well-Defined Poly(ethylene oxide)−Polyacrylonitrile Diblock Copolymers as Templates for Mesoporous Silicas and Precursors for Mesoporous Carbons. *Chemistry of Materials* **2006,** *18* (6), 1417-1424.
(35) Wu, D.; Li, Z.; Zhong, M.; Kowalewski, T.; Matyjaszewski, K., Templated Synthesis of Nitrogen-Enriched Nanoporous Carbon Materials from Porogenic Organic Precursors Prepared by ATRP. *Angewandte Chemie International Edition* **2014,** *53* (15), 3957-3960.
(36) Wu, D.; Dong, H.; Pietrasik, J.; Kim, E. K.; Hui, C. M.; Zhong, M.; Jaroniec, M.; Kowalewski, T.; Matyjaszewski, K., Novel Nanoporous Carbons from Well-Defined Poly(styrene-co-acrylonitrile)-Grafted Silica Nanoparticles. *Chemistry of Materials* **2011,** *23* (8), 2024-2026.
(37) Jun, S.; Joo, S. H.; Ryoo, R.; Kruk, M.; Jaroniec, M.; Liu, Z.; Ohsuna, T.; Terasaki, O., Synthesis of New, Nanoporous Carbon with Hexagonally Ordered Mesostructure. *Journal of the American Chemical Society* **2000,** *122* (43), 10712-10713.

(38) Choi, J.; Hui, C. M.; Pietrasik, J.; Dong, H.; Matyjaszewski, K.; Bockstaller, M. R., Toughening fragile matter: mechanical properties of particle solids assembled from polymer-grafted hybrid particles synthesized by ATRP. *Soft Matter* **2012,** *8* (15), 4072-4082.
(39) Hui, C. M.; Pietrasik, J.; Schmitt, M.; Mahoney, C.; Choi, J.; Bockstaller, M. R.; Matyjaszewski, K., Surface-Initiated Polymerization as an Enabling Tool for Multifunctional (Nano-)Engineered Hybrid Materials. *Chemistry of Materials* **2014,** *26* (1), 745-762.
(40) Schmitt, M.; Choi, J.; Min Hui, C.; Chen, B.; Korkmaz, E.; Yan, J.; Margel, S.; Burak Ozdoganlar, O.; Matyjaszewski, K.; Bockstaller, M. R., Processing fragile matter: effect of polymer graft modification on the mechanical properties and processibility of (nano-) particulate solids. *Soft Matter* **2016,** *12* (15), 3527-3537.
(41) Wang, Z.; Mahoney, C.; Yan, J.; Lu, Z.; Ferebee, R.; Luo, D.; Bockstaller, M. R.; Matyjaszewski, K., Preparation of Well-Defined Poly(styrene-co-acrylonitrile)/ZnO Hybrid Nanoparticles by an Efficient Ligand Exchange Strategy. *Langmuir* **2016,** *32* (49), 13207-13213.
(42) Wang, Z.; Lu, Z.; Mahoney, C.; Yan, J.; Ferebee, R.; Luo, D.; Matyjaszewski, K.; Bockstaller, M. R., Transparent and High Refractive Index Thermoplastic Polymer Glasses Using Evaporative Ligand Exchange of Hybrid Particle Fillers. *ACS Applied Materials & Interfaces* **2017,** *9* (8), 7515-7522.
(43) Epifani, M.; Arbiol, J.; Díaz, R.; Perálvarez, M. J.; Siciliano, P.; Morante, J. R., Synthesis of SnO2 and ZnO Colloidal Nanocrystals from the Decomposition of Tin(II) 2-Ethylhexanoate and Zinc(II) 2-Ethylhexanoate. *Chemistry of Materials* **2005,** *17* (25), 6468-6472.
(44) Weber, D.; Botnaras, S.; Pham, D. V.; Steiger, J.; De Cola, L., Functionalized ZnO nanoparticles for thin-film transistors: support of ligand removal by non-thermal methods. *Journal of Materials Chemistry C* **2013,** *1* (18), 3098-3103.
(45) Ojha, S.; Dang, A.; Hui, C. M.; Mahoney, C.; Matyjaszewski, K.; Bockstaller, M. R., Strategies for the Synthesis of Thermoplastic Polymer Nanocomposite Materials with High Inorganic Filling Fraction. *Langmuir* **2013,** *29* (28), 8989-8996.
(46) Pietrasik, J.; Dong, H.; Matyjaszewski, K., Synthesis of High Molecular Weight Poly(styrene-co-acrylonitrile) Copolymers with Controlled Architecture. *Macromolecules* **2006,** *39* (19), 6384-6390.
(47) Plichta, A.; Zhong, M.; Li, W.; Elsen, A. M.; Matyjaszewski, K., Tuning Dispersity in Diblock Copolymers Using ARGET ATRP. *Macromolecular Chemistry and Physics* **2012,** *213* (24), 2659-2668.
(48) Matyjaszewski, K., Atom Transfer Radical Polymerization (ATRP): Current Status and Future Perspectives. *Macromolecules* **2012,** *45* (10), 4015-4039.
(49) Matyjaszewski, K.; Xia, J., Atom Transfer Radical Polymerization. *Chemical Reviews* **2001,** *101* (9), 2921-2990.
(50) Pan, X.; Tasdelen, M. A.; Laun, J.; Junkers, T.; Yagci, Y.; Matyjaszewski, K., Photomediated controlled radical polymerization. *Progress in Polymer Science* **2016,** *62*, 73-125.
(51) He, X.; Male, K. B.; Nesterenko, P. N.; Brabazon, D.; Paull, B.; Luong, J. H. T., Adsorption and Desorption of Methylene Blue on Porous Carbon Monoliths and Nanocrystalline Cellulose. *ACS Applied Materials & Interfaces* **2013,** *5* (17), 8796-8804.
(52) Chen, C.; Ma, W.; Zhao, J., Semiconductor-mediated photodegradation of pollutants under visible-light irradiation. *Chemical Society Reviews* **2010,** *39* (11), 4206-4219.
(53) Zhang, H.; Lv, X.; Li, Y.; Wang, Y.; Li, J., P25-Graphene Composite as a High-Performance Photocatalyst. *ACS Nano* **2010,** *4* (1), 380-386.

(54) Park, H.-A.; Liu, S.; Salvador, P. A.; Rohrer, G. S.; Islam, M. F., High visible-light photochemical activity of titania decorated on single-wall carbon nanotube aerogels. *RSC Advances* **2016,** *6* (27), 22285-22294.
(55) Hameed, B. H.; Din, A. T. M.; Ahmad, A. L., Adsorption of methylene blue onto bamboo-based activated carbon: Kinetics and equilibrium studies. *Journal of Hazardous Materials* **2007,** *141* (3), 819-825.
(56) Tan, I. A. W.; Ahmad, A. L.; Hameed, B. H., Adsorption of basic dye on high-surface-area activated carbon prepared from coconut husk: Equilibrium, kinetic and thermodynamic studies. *Journal of Hazardous Materials* **2008,** *154* (1–3), 337-346.
(57) Tang, W. Z.; Huren, A., UV/TiO2 photocatalytic oxidation of commercial dyes in aqueous solutions. *Chemosphere* **1995,** *31* (9), 4157-4170.

Chapter 6 ZnO/carbon Hybrids Derived from Polymer Nanocomposite Precursor Materials for Pseuocapacitor Electrodes with High Cycling Stability

6.1. Preface

A facile new route for fabricating carbon/zinc oxide composite materials suitable for pseudocapacitor electrodes with high cycling stability is presented. ZnO/carbon nanocomposites were successfully synthesized by pyrolysis of mixtures of octylamine (OA)-capped ZnO nanoparticles and poly(styrene-*r*-acrylonitrile) (PSAN) random copolymers. PSAN copolymers with two different chain lengths were prepared to reveal the effect of chain length on the structure and properties of the composites. For all cases, the pyrolysis of ZnO-OA/PSAN precursor blends resulted in the formation of dispersing ZnO/carbon core-shell hybrid structures. The accessible surface area was found to increase with the molecular weight of matrix chains. The ZnO/carbon composites exhibited a specific capacitance of 145 F/g at the scan rate of 2 mV s^{-1}. Besides, 91% of the initial capacitance was obtained after 10000 charge/discharge cycles. The versatility of the synthetic process should render the presented method attractive for the fabrication of a wide range of carbon/transition metal oxide hybrid materials.

In this chapter, the synthesis of ZnO/carbon hybrids used as a supercapacitor is discussed. I performed all synthetic work and part of the characterization in the project. I would like to thank especially my collaborators, Yepin Zhao for his hard and creative work on the design and performance characterization of the supercapacitors. Rui Yuan, Yu Lin, Jiajun Yan, Jianan Zhang, Zhaolu and Danli Luo assisted in the characterization work. Professor Matyjaszewski and Professor Bockstaller conceived and organized the project and together with Yepin and I wrote the manuscript.

This project was published in *Polymer*, (Yepin Zhao, **Zongyu Wang**, Rui Yuan, Yu Lin, Jiajun Yan, Jianan Zhang, Zhao Lu, Danli Luo, Joanna Pietrasik, Michael R Bockstaller, Krzysztof Matyjaszewski, "ZnO/carbon hybrids derived from polymer nanocomposite precursor materials for pseudocapacitor electrodes with high cycling stability", *Polymer*, **2018**, 137, 370-377).

This work was supported by NSF (Grants DMR 1501324 and CMMI 1663305), as well as the Scott Institute for Energy Technologies at Carnegie Mellon University.

6.2. Introduction

The combination of climate change coupled with rapidly increasing global energy consumption has generated a critical environmental issue that must be resolved.[1-4] This environmental challenge has made the development of efficient energy storage systems a high priority to make efficient use of the electricity generated from renewable resources. Electrochemical capacitors (ECs) are among the key technological systems that define the state of the art in electrical energy storage systems.[1-6] Electric double-layer capacitors (EDLCs), also known as supercapacitors, have garnered particular interest. This is because they offer high

power density (1-2 orders of magnitude higher than that of batteries), fast charging and discharging, short response time, superior cycle lifetime (2-3 orders of magnitude better than that of batteries), and high reliability.[1-7] A sign of the reliability and utility of supercapacitors is their use in a variety of applications, including portable consumer electronics, computer memory backup systems, power for the next generation all-electric vehicles, industrial-scale power, and energy management.[8] However, a major bottleneck that limits the acceptance of existing supercapacitors in many high-value applications, including energy storage devices, is their low energy storage density, generally an order of magnitude lower than that of batteries. Therefore, improving the energy density, while maintaining the high power density and cycling stability for supercapacitor devices, remains the primary challenge in the field.[3,9]

As another type of ECs, pseudocapacitors utilize fast and reversible redox reactions at the surface of the electroactive material for charge storage.[10-12] In fact, in addition to capacitive improvements, pseudocapacitive materials can provide much higher energy density than carbon-based materials in electric double-layer capacitors, resulting in increased interest in these systems.[10-12] Several active pseudocapacitive materials, including transition metal oxides and conducting redox polymers, have been developed.[13-20] Their high energy density along with fast and reversible redox reactions at the electrode surface can significantly enhance the specific capacitance.[18-19, 21] The ability of pseudocapacitors based on hybrid composite materials with a porous carbon structure to maintain high power density and the fast charge−discharge rate has drawn significant research attention. Recently, hybrid composites based on transition metal oxides, including iron oxide (Fe_2O_3),[22-23] cobalt oxide (CoO, Co_3O_4)[24,25] and manganese oxide (MnO_2),[26,27] have been evaluated as pseudocapacitor electrodes.[28] Unfortunately, most of these

specific metal oxides suffer poor cycling stability and reversibility during the charge−discharge process.

Zinc oxide has drawn interest as transition metal oxide for the fabrication of pseudocapacitors due to its low-cost, environmental friendliness, and ease of synthesis.[29-31] The integration of ZnO with other pseudocapacitive materials resulted in remarkable capacitance performance. However, existing materials were shown to suffer from poor cycling stability. One strategy to address this shortcoming is the integration of ZnO with materials that exhibit high cycling stability. In particular, ZnO/carbon hybrid materials have been pursued since carbon materials usually display excellent rate performances, reversibility, and stability, albeit the capacitance values are limited by the microstructures in the materials.[23, 32-42] Hence, although experiments on ZnO/carbon hybrids did show promising results, the cycling stability of tested materials was still not satisfactory because of the poor morphological control and phase separation in the hybrid material. Furthermore, although high capacitance values (>300 F g^{-1}) were reported for ZnO/carbon nanotubes[43] and ZnO/graphene nanofiber hybrids,[44] the cost and complexity of the synthesis limit the application of these materials.[28] Thus the development of effective strategies for the preparation of ZnO/carbon composites with high degree of morphological control for use as electrochemical capacitors remains an important goal.

Herein, we report a facile method to fabricate ZnO/carbon composites. Octylamine (OA) capped ZnO nanocrystals were prepared by thermal decomposition of zinc 2-ethylhexanoate in the presence of octylamine.[45-48] Poly(styrene-r-acrylonitrile) copolymers (PSAN) were synthesized through ARGET ATRP (Activator ReGenerated by Electron Transfer Atom Transfer Radical Polymerization).[49-56] The AN units in the copolymers can efficiently crosslink and form porous carbon structures.[57,58] The ZnO/PSAN precursors were prepared by mixing and drying of

dispersions of OA capped ZnO nanoparticles and PSAN polymers in THF followed by stabilization of the mixtures and pyrolysis to form carbon. The resulting ZnO/carbon nanocomposites were evaluated as electrode materials for the preparation of electrochemical capacitors. The electrochemical performance of the electrodes was studied in terms of specific capacitance and cycling stability. The gravimetric capacitance of 145 F g^{-1} was achieved and 91% of the initial capacitance was maintained after 10000 charge−discharge cycles. The viability of material synthesis and processing, along with the performance and lifetime of the materials in pseudocapacitor applications demonstrates the potential of these novel materials as candidates for electrochemical applications.

6.3. Experimental Section

Materials and Methods

Monomers: styrene (S, 99%, Aldrich) and acrylonitrile (AN, 99%, Aldrich) were purified by passing through a column filled with basic alumina to remove the inhibitor. Tris(2-dimethylaminoethyl)amine (Me_6TREN, 99%, Alfa), zinc 2-ethylhexanoate ($Zn(EH)_2$, 80% in mineral spirits, Alfa), anisole (99%, Aldrich), methylene chloride (DCM, 99.5%, Fisher), carbon black, acetylene (100% compressed, 99.9%, Alfa), *N*-methylpyrrolidone (NMP, 99.5%, Sigma-Aldrich), poly(vinylidene fluoride) (M_w~180,000, M_n~71,000, Aldrich), zinc oxide (ZnO, 18 nm, 99.95%), tetrahydrofuran (THF, 99%, VWR), methanol (99%, VWR), hexane (99%, VWR), acetone (99%, VWR), N,N-dimethylformamide (DMF, 99%, VWR), ethyl 2-bromoisobutyrate (EBiB, 98%, Aldrich), copper(II) bromide ($CuBr_2$, 99%, Aldrich), diphenyl ether (DPE, 99%, Aldrich), tin(II) 2-ethylhexanoate ($Sn(EH)_2$, 95%, Aldrich), and octylamine (OA, 99%, Aldrich) were used as received without further purification.

Synthesis of OA-capped ZnO nanoparticles

OA-capped ZnO NPs were synthesized as reported by Epifani and Weber,[45,46] by the procedure illustrated in **Scheme 6.1**. The resulting product was dispersed in THF and a stock solution was prepared for use in further experiments. ZnO NPs are stabilized by surfactant octylamine (OA) ligands.

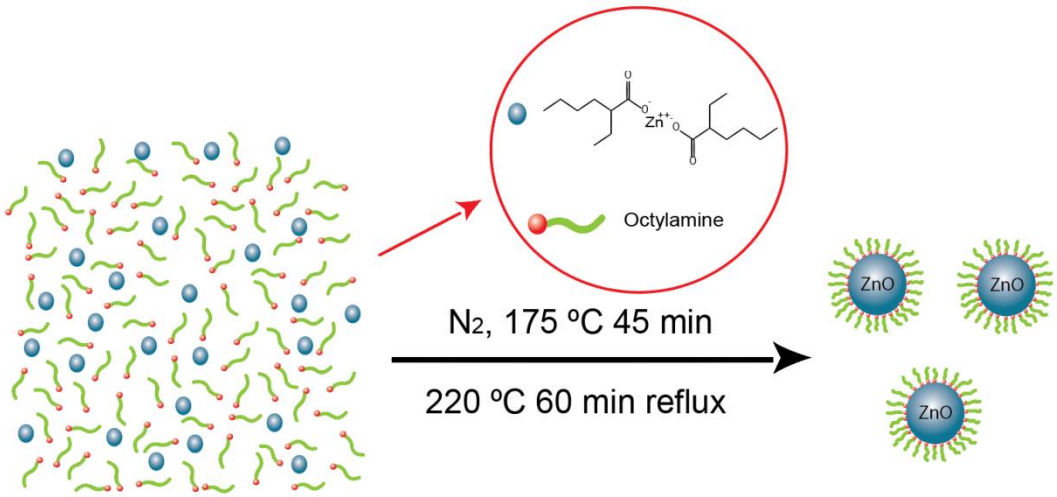

Scheme 6.1. Synthesis of OA-capped ZnO NPs.

Synthesis of PSAN copolymers

The copolymerization of St and AN by ATRP had been well studied in previous work.[56,59] Low molecular weight (MW) PSAN (M_n = 1800 with M_w/M_n = 1.18) and high MW PSAN (M_n = 8000 with M_w/M_n = 1.21) were synthesized via ARGET ATRP using EBiB as an initiator, $CuBr_2/Me_6TREN$ as precursor of the catalytic complex and $Sn(EH)_2$ as reducing agent using the following general procedure. Styrene (S) (16 mL, 139.85 mmol), acrylonitrile (AN) (5.5 mL, 83.91 mmol), Me_6TREN (0.075 mL, 0.28 mmol), anisole (7.2 mL), EBiB(1.37 mL, 9.32 mmol), and 0.03 mol L-1 solution of $CuBr_2$ in DMF (0.5 mL, 0.015 mmol) were added to a dry 50 mL Schlenk flask. After the flask was sealed, the resulting solution was bubbled with N_2 for 30 minutes. Then, 300 mM of $Sn(EH)_2$ solution in anisole (1 mL, 0.30 mmol) was slowly added to the flask to reduce a fraction of the $CuBr_2$ and activate the polymerization. The flask was

subsequently placed in an oil bath set at 60 ºC, and the reaction mixture was kept at that temperature for the desired time. Then the reaction mixture was exposed to air to stop the polymerization and the product was precipitated by the addition of the solution to cold hexane, filtered and dried in air.

The synthesis of the copolymers with different molecular weights was similar to the procedure described above, but with different targeted degrees of polymerization, as reported previously.[56, 59, 60]

Synthesis of ZnO/carbon nanocomposites

A typical procedure for synthesizing ZnO/carbon composite precursors consisted of dissolving PSAN copolymers and of OA-Capped ZnO NPs in 100 mL THF in a 200 mL beaker. To achieve uniform and homogenous solid powder mixtures, the beaker was covered with Al foil with pinholes on the top allowing the THF solvent to slowly evaporate under ambient condition over 2 days. The mixture was then transferred to a vacuum oven set at 100 ºC for 2 days to remove all residual solvent. Yellow powders were obtained for use in further experiments. The intimate mixture of PSAN/OA-capped ZnO powders was pyrolyzed in a tube furnace at 800 ºC for 3 hours under N_2 flow with a 10 ºC min^{-1} heating rate. Nanocomposite mixtures with a distinct molecular weight of the polymer matrix were compared. PSAN with M_n = 8000 was identified as the ideal polymer molecular weight to enable both dispersion of ZnO and material integrity during pyrolysis.

The typical procedure for the synthesis of a ZnO/carbon nanocomposites is illustrated in **Scheme 6.2**. The final products were prepared by pyrolysis of mixtures with different compositions of ZnO and PSAN, which were named by ZnO-C_{2k-4} (synthesized by 4 g of M_n~2000 PSAN), ZnO-C_{8k-2} (synthesized by 2 g of M_n~8000 PSAN), ZnO-$C_{8k-2.5}$ (synthesized

by 2.5 g of M_n~8000 PSAN), respectively, are listed in **Table 6.1**. A pure carbon sample was prepared by pyrolysis of M_n~8000 PSAN under the same condition for comparison.

Table 6.1. Preparation of nanocomposites from OA-capped ZnO and PSAN precursors

Entry	OA capped ZnO (g)	PSAN (g)	M_n, [a]	M_w/M_n [a]
ZnO-C$_{2k-4}$	3 g	4 g	1800	1.18
ZnO-C$_{8k-2}$	3 g	2 g	8000	1.21
ZnO-C$_{8k-2.5}$	3 g	2.5 g	8000	1.21

a) Number-average molecular weights (M_n) and molecular weight distributions (M_w/M_n) of the polymer ligands were measured by SEC.

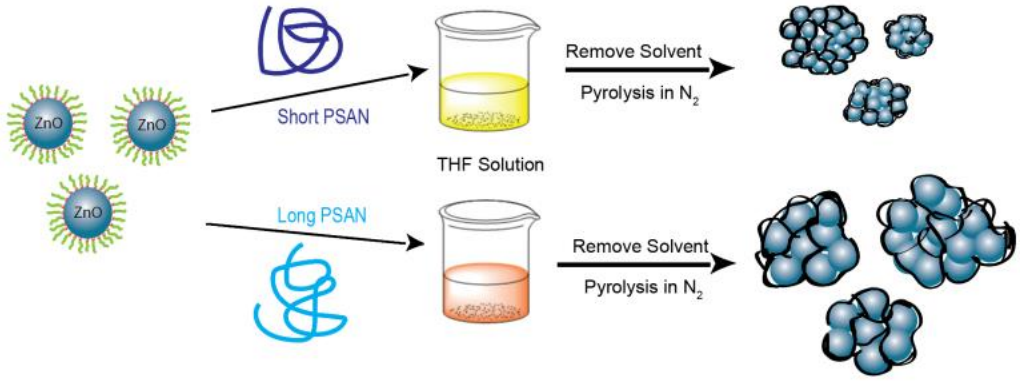

Scheme 6.2. Synthesis of ZnO/carbon nanocomposites

Characterization

Transmission electron microscopy (TEM) was carried out using a JEOL 2000 EX electron microscope operated at 200 kV. A scanning electron microscope (SEM) was carried out using a quanta 600 environmental scanning electron microscope. The average sizes of the ZnO NPs were determined from statistical analysis of TEM micrographs using ImageJ software. Dynamic light scattering (DLS) using a Malvern Zetasizer Nano ZS was performed to confirm the results obtained from TEM analysis. It was also employed to determine volume-weighted average hydrodynamic diameters and distribution. A Philips X'Pert (Philips Analytical, Netherlands) X-ray diffractometer (XRD) (Cu Kα radiation) was operated at 45 kV and 40 mA in grazing incidence mode to characterize the structure and crystallinity of the formed composite

materials. Thermogravimetric analysis (TGA) with TA Instruments 2950 was used to measure the fraction of ZnO in the hybrids. The data were analyzed with TA Universal Analysis. The TGA plots were normalized to the total weight after holding the samples at 120 ºC. The copolymers were characterized by size exclusion chromatography (SEC) and nuclear magnetic resonance (NMR) spectroscopy, the glass transition temperature (T_g) of PSAN polymers with different molecular weight were measured by differential scanning calorimetry (DSC) with TA Instrument QA-2000, the same procedure was run three times, each involving the following steps: (1) hold at 25 ºC for 2 min, (2) heat to 160 ºC at a rate of 10 ºC/min, (3) hold for 2 min, and (4) cool to 25 ºC, the DSC data were analyzed with a TA Universal Analysis instrument, and T_g was directly acquired, the detailed information is included in the Supporting Information. Surface areas of ZnO/carbon nanocomposite were measured by a Brunauer-Emmett-Teller (BET) Gemini VII 2390 Surface Area Analyzer.

Electrochemical Measurements

The symmetric two-electrode system was applied in the electrochemical tests. The electrodes were prepared by mixing 85 wt% of the ZnO/carbon samples, 5 wt% acetylene black as a conductive additive, and 10 wt% of poly(vinylidene fluoride) as a binder. The mixture was homogenized in *N*-methyl pyrrolidone (NMP) by sonication for 10 min and the slurry was deposited on carbon paper with a diameter of 13 mm and dried at 100 ºC in a vacuum oven over 24 h. For comparison, ZnO-C_{8k-2}, ZnO-$C_{8k-2.5}$, and ZnO-C_{8k-2} were made into electrodes. And to determine the contribution of ZnO and C and synergistic effect of the composite, ZnO nanoparticles and carbon made from PSAN polymers were made into electrodes separately. Electrochemical cells were prepared using a Teflon Swagelok. 1 M KOH was used as an

electrolyte and a porous polyolefin separator (Celgard Inc.) was soaked with KOH electrolyte and placed between the electrodes.

The electrochemical measurements were carried out on a potentiostat (Biologic SP-300). The cyclic voltammetry (CV) curves were obtained at various scan rates from 2 mV s^{-1} to 2000 mV s^{-1} in the range of 0 to 1 V. Galvanostatic charge-discharge (GCD) curves were obtained at various current densities from 0.1 A g^{-1} to 20 A g^{-1}. Electrochemical impedance spectroscopy (EIS) measurements were performed in the frequency range of 0.1 Hz to 800 kHz with a sinusoidal signal of 10 mV. For each sample, 10 measurements were repeated to confirm its reproducibility.[61]

For samples containing ZnO, the possible mechanisms of pseudocapacitance come from redox reactions which are mainly governed by the intercalation and deintercalation of K^+ from the electrolyte into ZnO: $ZnO + K^+ + e^- \leftrightarrow ZnOK$

The gravimetric capacitance of each electrode, C_{sp}, from the cyclic voltammetry (CV) is then determined via the following equation:

$$C_{sp} = \frac{\int IdV}{vmV} \qquad (1)$$

The gravimetric capacitance of each electrode, C_{sp}, from the galvanostatic charge-discharge (GCD) curves is determined *via* equation 2:

$$C_{sp} = \frac{2I\Delta t}{mV} \qquad (2)$$

In the equations, $\int IdV$ is the integration of CV curves; v (V s^{-1}) is the voltage scan rate; Δt (s) is the discharge time; I/m is the scan rate (A g^{-1}) where m (g) is the mass of each electrode; V (V) is the voltage window.

6.4. Results and Discussion

ZnO/carbon composites were prepared by the pyrolysis of a mixture of OA-capped ZnO nanoparticles and PSAN copolymer. The OA-capped ZnO nanoparticles were synthesized by the thermal decomposition of zinc 2-ethylhexanoate in a mixture of OA and diphenyl ether at 220 ºC. The resulted ZnO nanoparticles have narrow particle size distribution and good solubility in tetrahydrofuran (THF) or hexane, **Figure. S6.2**. Polyacrylonitrile (PAN) can be used as a precursor for carbon composite materials.[62,63] However, PAN polymers are not soluble in non-polar solvents, such as THF or hexane, which are good solvents for OA-capped ZnO nanoparticles. Therefore, THF soluble PSAN copolymers, which were synthesized by ARGET ATRP, were used as the carbon precursors instead of PAN, so those solvent cast methods could be applied to obtain well-dispersed ZnO/polymer mixtures suitable as a precursor of the desired hybrid carbon materials. Two different copolymers with narrow molecular weight distributions were prepared, one with M_n = 1,800 and another with M_n = 8000 to evaluate the role of matrix molecular weight on structure formation during pyrolysis (see **Figure. S6.1**). Three dilute THF solutions, with different polymers and compositions, were prepared and the ratios are listed in **Table 6.1**. After removing all solvent by atmospheric evaporation followed by vacuum annealing, yellow powders for low molecular weight (MW) PSAN-based mixtures and films for higher MW PSAN were obtained, which were further characterized by TGA. The three ZnO/carbon composite samples had similar carbon contents, between 7.6 to 8.4 wt%, **Figure. S6.3**.

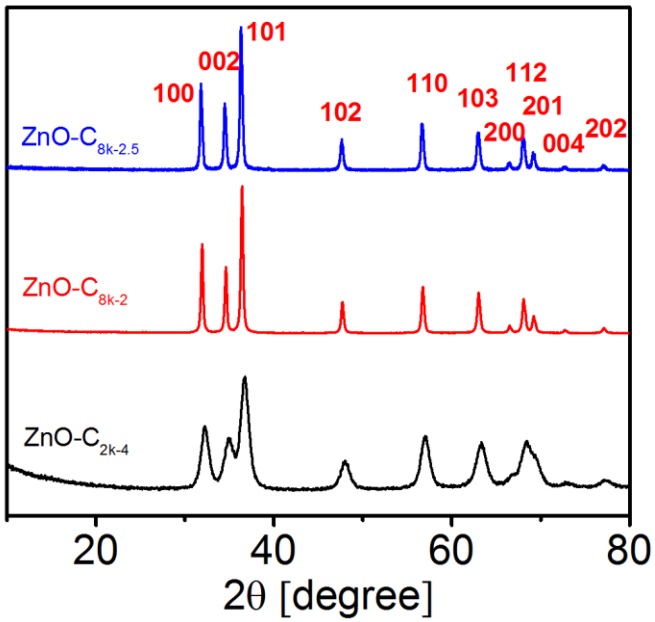

Figure. 6.1. XRD patterns of ZnO/carbon nanocomposites. The patterns reveal characteristic ZnO Wurtzite structure (JCPDS No. 36–1451). The increasing peak width indicates a decrease of the crystallite dimension for samples prepared from lower molecular weight PSAN precursor (ZnO-C_{2k-4}).

Carbothermic reduction of metal extraction, using carbon as a sacrificial agent has been used since ancient times. S-M Lee and his coworkers have reported that the carbothermic reduction of ZnO deposited on cotton textile under 1000 ºC enables them to prepare carbon textile electrodes for high-performance supercapacitors.[64,65] In our work, the pyrolysis temperature was significantly lower than 1000 ºC, therefore no certain reduction of ZnO was observed. The presence and crystallized structure of ZnO were characterized by XRD. XRD patterns of ZnO/carbon nanocomposite samples from the different precursors are shown in **Figure. 6.1**. Similar XRD patterns were obtained from ZnO-C_{2k-4}, ZnO-C_{8k-2}, and ZnO-$C_{8k-2.5}$. The patterns demonstrate the presence of a Wurtzite structure for the ZnO (JCPDS No. 36–1451) with no diffraction peak attributable to the carbon species. The well-fitted ZnO peaks in the patterns demonstrate that carbon formation does not influence the crystal structure of the ZnO. However, ZnO-C_{2k-4} exhibited much broader peaks than those observed from ZnO-C_{8k-2} and ZnO-$C_{8k-2.5}$. We can estimate the crystallite size *D* of ZnO-C_{2k-4}, ZnO-C_{8k-2} and ZnO-$C_{8k-2.5}$

particles from the (110) plane diffraction peak ($2\theta = 56.6°$), by using the Scherrer equation $D = 0.9(\lambda/\beta)\cos\theta$ (where $\lambda = 0.154$ nm is the wavelength of X-rays and β is the true half peak width of the X-ray diffraction lines). Following to this process, the sizes of the ZnO nanoparticles follow to be 5 nm, 25 nm, and 23 nm for ZnO-C_{2k-4}, ZnO-C_{8k-2}, and ZnO-$C_{8k-2.5}$, respectively.[42] Since all OA-capped ZnO nanoparticles precursors had the same size, the different sizes have to be attributed to changes of crystal size during the calcination process. Specifically, we hypothesize that the different dimensions of particles in the pyrolyzed products reflect different levels of aggregation of OA-capped ZnO particles in the polymer matrix. The results thus suggest that a low molecular weight matrix supports the stable dispersion of OA-capped ZnO particles and thus reduces aggregation and crystal coarsening during the pyrolysis process (although it should be noted that the lower particle concentration in the ZnO-C_{2k-4} system could also contribute to the reduced aggregation).

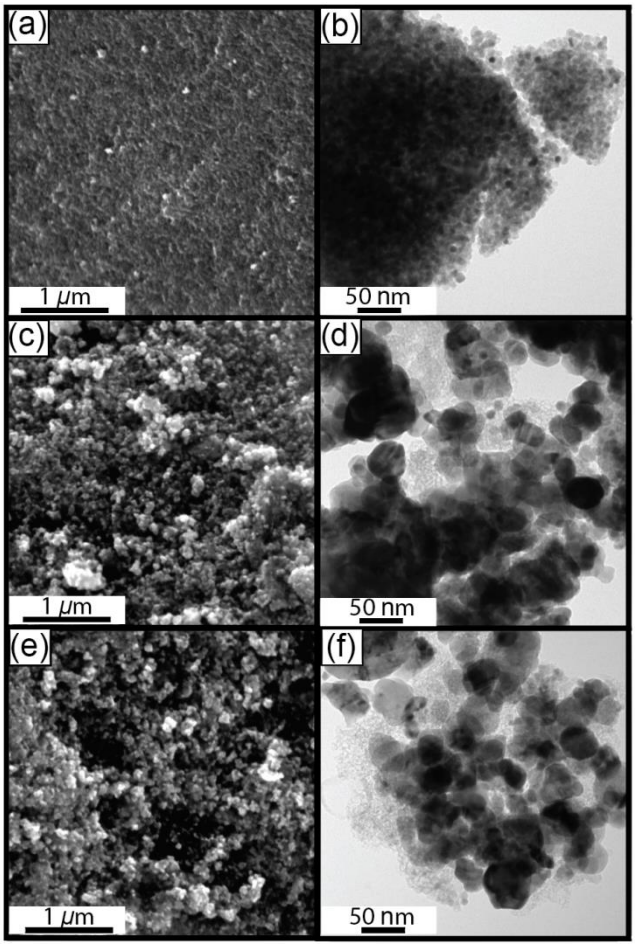

Figure. 6.2. Microstructural characterization of ZnO/carbon nanocomposites. SEM images (a), (c), and (e) showing non-porous surface of ZnO-C_{2k-4} (a); porous structure of ZnO-C_{8k-2} (c) and porous structure of ZnO-$C_{8k-2.5}$ (e). TEM images (b), (d), and (f) showing small size of particles with non-porous carbon shell in ZnO-C_{2k-4} (b); large size of particles with porous carbon shell in ZnO-C_{8k-2}, but still some non-porous components exist (d); large size of particles with porous carbon shell in ZnO-$C_{8k-2.5}$ (f).

Scanning and transmission electron microscopy (SEM and TEM) were used to further elucidate the microstructure of ZnO-C_{2k-4}, ZnO-C_{8k-2}, and ZnO-$C_{8k-2.5}$ composite materials. SEM images (**Figure. 6.2**a, **Figure. 6.2**c, and **Figure. 6.2**e) reveal a distinctive difference in the surface morphology of the three material systems. Specifically, the SEM image of ZnO-C_{2k-4} (see **Figure. 6.2**a) reveals a more contiguous film with a smooth non-porous surface. Such a structure is not expected to benefit applications as supercapacitor electrodes due to the reduced accessible surface area. In contrast, ZnO-C_{8k-2} and ZnO-$C_{8k-2.5}$ (see **Figure. 6.2**c and **Figure. 6.2**e) exhibited a coarse particulate morphology, which indicates the formation of a more porous

carbon matrix during the pyrolysis. TEM images (**Figure. 6.2**b, **Figure. 6.2**d, and **Figure. 6.2**f) further confirmed the differences in carbon morphology between low and high MW matrix materials. TEM images for low MW ZnO-C_{2k-4} (see **Figure. 6.2**b) reveal a particle size of 4-7 nm for ZnO particles (*i.e.* approximately equal to the pristine OA-capped ZnO). Particles appear uniformly distributed within a dense carbon matrix. In contrast, TEM images of high MW systems ZnO-C_{8k-2} and ZnO-$C_{8k-2.5}$ (see **Figure. 6.2**d and **Figure. 6.2**f) displayed a distinctively larger particle size of 25-35 nm. These results agree with the values obtained from the calculation based on XRD patterns (see **Figure. 6.1**) and thus confirm the more pronounced particle aggregation in the high MW matrix. Particle aggregation also induces a distinctive change in the morphology of the ZnO/carbon composite. With similar carbon contents, the ZnO-C_{8k-2} and ZnO-$C_{8k-2.5}$ samples exhibited a more porous microstructure (see **Figure. 6.2**d and **Figure. 6.2**f).

To rationalize the effect of molecular weight on morphology we note that the lower MW PSAN polymer, M_n = 1,800, has lower glass transition temperature ($T_{g,Mn\text{-}1800}$ ~ 58 ºC, $T_{g,Mn\text{-}8000}$ ~ 92 ºC), and also has greater mobility above its T_g, since the diffusion coefficient scales with the inverse of the molecular weight below the entanglement limit (see **Figure. S6.6**).[66] Furthermore, the entropy gain associated with particle dispersion is expected to increase within a lower molecular weight matrix. We, therefore, hypothesize that in the heating process, the better dispersion of OA-ZnO in low molecular PSAN was more effective in preventing the aggregation or recrystallization of ZnO.

Brunauer-Emmett-Teller (BET) and Barrett-Joyner-Halenda (BJH) methods were also applied to compare specific surface area and pore volume of ZnO/carbon nanocomposites. A type IV isotherm with hysteresis loops at $P/P_0 > 0.4$ was obtained for ZnO-C_{8k-2} and ZnO-$C_{8k-2.5}$,

as shown in **Figure. 6.3**a. This indicates the existence of a large number of mesopores inside the matrix of the ZnO/carbon nanocomposites.[67] The specific surface areas of ZnO-C_{2k-4}, ZnO-C_{8k-2}, ZnO-$C_{8k-2.5}$, pure ZnO and pure carbon were 40 m^2 g-1, 105 m^2 g^{-1}, 170 m^2 g^{-1}, 5 m^2 g^{-1}, and 244 m^2 g^{-1}respectively. Although pure carbon showed a relatively high specific surface area, it does not contain any ZnO particles which composed over 90% of the weight of ZnO/carbon composites. Since ZnO particles barely contribute to the specific surface area, if we only consider the specific surface areas from porous carbon structure, remarkably high values of 482 m^2 g^{-1}, 1382 m^2 g^{-1}, and 2024 m^2 g^{-1} can be obtained from ZnO-C_{8k-4}, ZnO-$C_{8k-2,}$ and ZnO-$C_{8k-2.5}$, respectively.

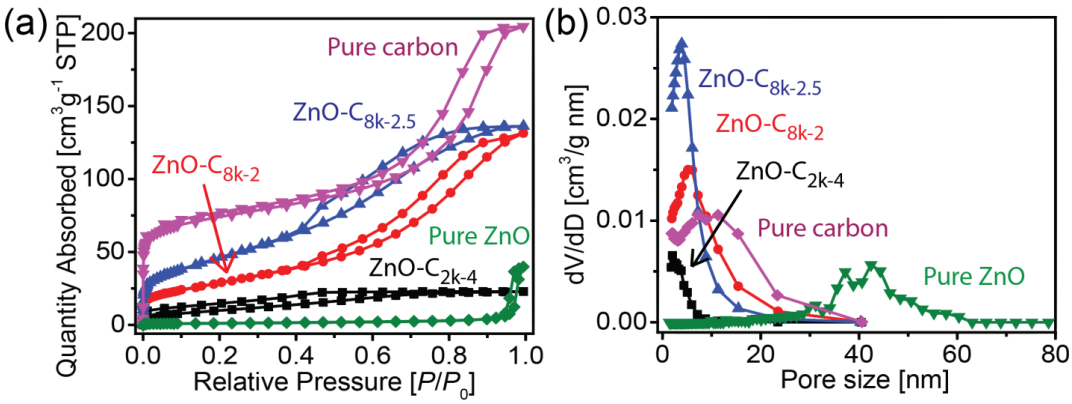

Figure. 6.3. (a) Comparison of N_2 absorption−desorption isothermal of ZnO-C_{2k-4}, ZnO-C_{8k-2}, ZnO-$C_{8k-2.5}$, pure ZnO and pure carbon, (b) pore size distribution of ZnO-C_{2k-4}, ZnO-$C_{8k-2,}$ ZnO-$C_{8k-2.5}$, pure ZnO and pure carbon.

These differences corroborate the expectations based on the distinct microstructure within the ZnO/carbon nanocomposites. Besides, BJH pore size distribution illustrated the presence of a large number of mesopores (with diameter from 2 nm to 50 nm) and nanopores (with a diameter lower than 2 nm) in the carbon formed from ZnO-$C_{8k-2.5}$. These mesopores could act as electrolyte reservoirs during the electrochemical tests which should lead to better capacitive performance. For both pure ZnO and pure carbon samples, the specific volumes of nanopores were distinctly lower than ZnO/carbon composites. For ZnO, it is because of the lack of porous

carbon to keep particles from aggregation, which leads to an unporous structure. For pure carbon, the absence of ZnO particles as hard temples hindered the formation of the nanoporous carbon structure.

Table 6.2. Summary of ZnO/carbon composites characterization

Entry	ZnO contents (wt%)[a]	Carbon contents (wt%)[a]	Surface area (m^2 g^{-1})[b]
ZnO-C_{2k-4}	91.7	8.3	40
ZnO-C_{8k-2}	92.4	7.6	105
ZnO-$C_{8k-2.5}$	91.6	8.4	170
Pure ZnO	100	0	5
Pure carbon	0	100	244

a) inorganic content was determined by TGA; b) surface area was characterized by BET.

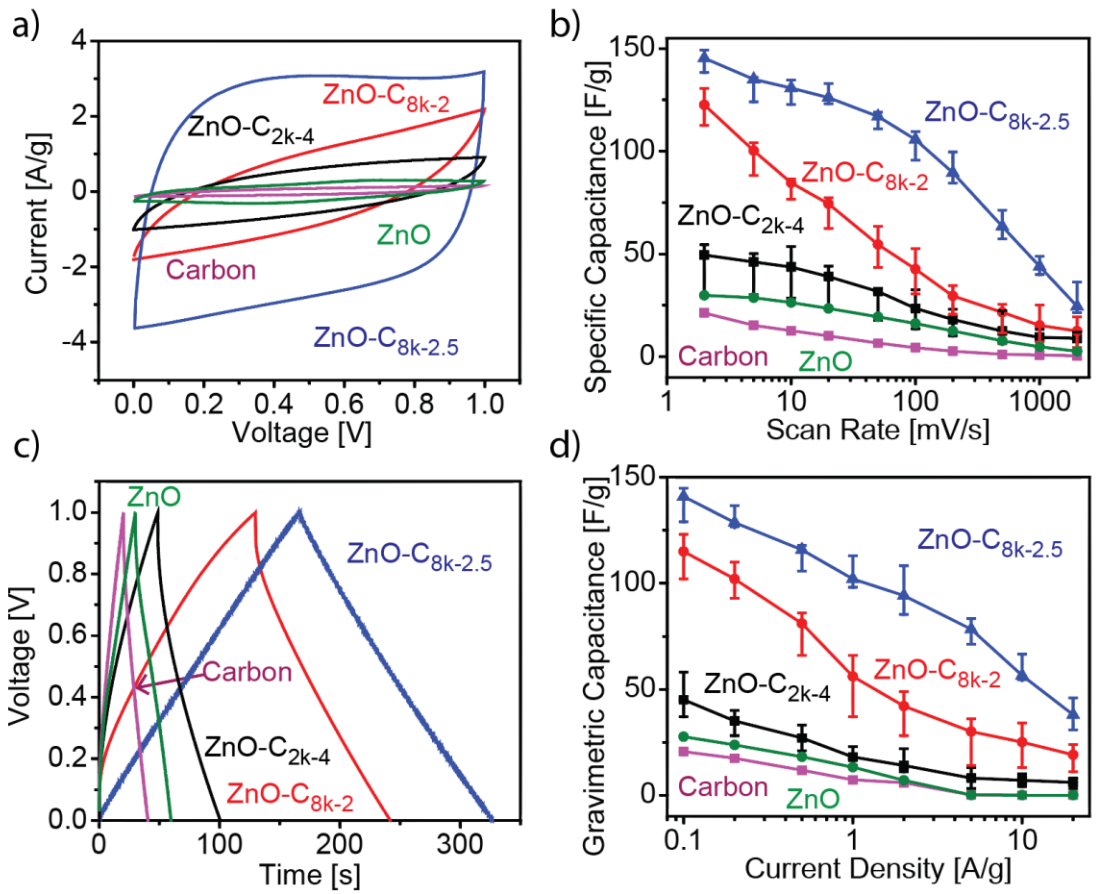

Figure. 6.4. (a) CV curves of samples ZnO-C_{2k-4}, ZnO-C_{8k-2}, ZnO-$C_{8k-2.5}$, pure ZnO nanoparticles and pure carbon from PSAN at 100 mV s^{-1} compared with electrodes with ZnO and porous carbon; (b) Comparison of specific capacitance from CV curves from 2 mV s^{-1} to 2000 mV s^{-1}; (c) GCD curves of samples ZnO-C_{2k-4}, ZnO-C_{8k-2}, ZnO-$C_{8k-2.5}$, pure ZnO nanoparticles and pure carbon from PSAN at current density of 0.2 A g^{-1}; (d) Comparison of specific capacitance from GCD curves from 0.1 A g^{-1} to 20 A g^{-1}.

Highly porous, conductive structures are particularly suitable for the preparation of pseudocapacitor electrodes. The electrochemical performance of ZnO/carbon nanocomposites was determined using a two-electrode system and the results are shown in **Figure. 6.4**. The results were also compared with electrodes with ZnO and porous carbon separately. In **Figure. 6.4**a, the CV curves were compared at a scan rate of 100 mV s^{-1}. Compared with ZnO-C_{2k-4}, ZnO-C_{8k-2}, sample ZnO-$C_{8k-2.5}$ shows symmetric rectangular CV curves. This was attributed to the lower internal resistance of ZnO-$C_{8k-2.5}$. By the comparison of specific capacitances at different scan rates, it is distinct that higher specific capacitance and better rate performance were obtained with ZnO-$C_{8k-2.5}$ (**Figure. 6.4**b).). At 2 mV s^{-1}, the mean specific capacitance of electrodes from samples ZnO-C_{2k-4}, ZnO-C_{8k-2}, and ZnO-$C_{8k-2.5}$ reached 49 F g^{-1}, 123 F g^{-1}, and 145 F g^{-1}, respectively. Presumably, the main reason for this difference in performance is the presence of a more developed contact area between ZnO and electrolyte and a larger specific surface area of electrodes prepared from ZnO-$C_{8k-2.5}$. Besides, the presence of mesopores inside the ZnO/carbon structure leads to better ionic diffusion by acting as reservoirs for the electrolyte.[6] Pure ZnO showed low capacitance (30 F g^{-1} at 2 mV s^{-1}) which is due to high internal resistance and aggregation of ZnO particles without porous carbon structure which leads to low contact area with electrolyte and long diffusion lengths for ions. Also, the pure carbon from PSAN exhibited low specific capacitance as 21 F g^{-1} at 2 mV s^{-1} though its relatively high specific area compared with other samples (as shown in **Figure. 6.3**). It results from the lack of pseudocapacitance from ZnO. Also without ZnO nanoparticles as a temple, pure carbon samples suffered from a shortage of nanopores to adhere to ions efficiently.

Galvanostatic charge−discharge (GCD) tests were applied to evaluate the performance and cycle-life of materials. The GCD performances of ZnO-C_{2k-4}, ZnO-$C_{8k-2,}$ and ZnO-$C_{8k-2.5}$

were compared with a current density of 0.2 A g^{-1} (see **Figure. 6.4**c). The electrode based on ZnO-C_{2k-4} displayed a larger IR drop than ZnO-C_{8k-2} and ZnO-$C_{8k-2.5}$ which demonstrated the larger internal resistance of the electrodes. This is interpreted as a consequence of the increased fraction of the amorphous component and non-porous structure of the carbon that essentially blocked the ionic and electrical transportation. The GCD behavior of the ZnO-$C_{8k-2.5}$-based electrode showed symmetric curves from 0.1 A g^{-1} to 20 A g^{-1}, illustrating ideal capacitive properties. The reason for the higher capacitance of ZnO-$C_{8k-2.5}$ is attributable to the porous morphology, with a large number of nanospheres, which provided more active sites for ion adsorption−desorption and faster ionic diffusion. The capacitance relationships of different electrodes were similar in GCD tests (**Figure. 6.4**d) as in CV tests. The mean specific capacitance ZnO-$C_{8k-2.5}$ reached 141 F g^{-1}, 102 F g^{-1}, and 38 F g^{-1} at a current density of 0.1 A g^{-1}, 1 A g^{-1} and 20 A g^{-1}, respectively. Low capacitance of electrodes with pure ZnO and pure carbon again confirmed the synergistic effect of the designed ZnO/Carbon composites.

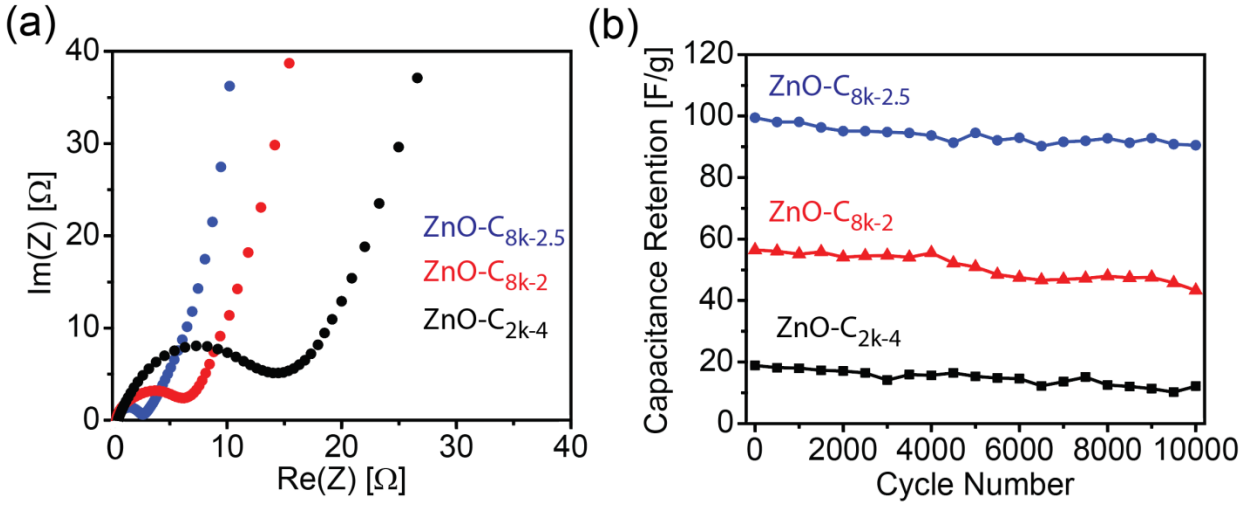

Figure. 6.5. (a) electrochemical impedance spectra (EIS) of samples ZnO-C_{2k-4}, ZnO-C_{8k-2}, ZnO-$C_{8k-2.5}$; (b) Lifetime tests of samples ZnO-C_{2k-4}, ZnO-C_{8k-2}, ZnO-$C_{8k-2.5}$ with a current density of 1 A g^{-1}.

Next, electrochemical impedance spectroscopy (EIS) was used to evaluate the electrical and ionic transport characteristics of the ZnO/carbon nanocomposites as seen in **Figure. 6.5**a.

The shape of EIS curves confirmed with our two-electrode configuration. In the high-frequency region, the curves showed negligible cells characteristic electrolyte resistance (R_S), lower than 0.2 Ω. The semicircles in the middle frequency region demonstrated differences in the internal resistances of electrodes prepared from ZnO-C_{2k-4} (15.9 Ω), ZnO-C_{8k-2} (6.4 Ω), to ZnO-$C_{8k-2.5}$ (2.0 Ω).[68] This difference should be attributed to mesoporous structure of the ZnO-$C_{8k-2.5}$ based carbon which led to higher conductivity and better ionic diffusion in the electrolyte. At low-frequency region, nearly vertical curve illustrated great ion diffusion of the ZnO-$C_{8k-2.5}$ electrodes in an electrolyte.

Finally, lifetime tests were applied with a current density of 1 A g^{-1} to access the durability of ZnO/carbon nanocomposites and electrodes based on ZnO-C_{2k-4}, ZnO-C_{8k-2} and ZnO-$C_{8k-2.5}$ and the samples maintained 64%, 77%, 91% of their initial capacitance after 10000 cycles, respectively (**Figure. 6.5**b). Compared with other ZnO based pseudocapacitors (**Table S6.1**), the retention of 91% after 10000 cycles is quite remarkable. This high stability is attached to stable carbon structures derived by copolymers and highly porous tunnels for ionic diffusion. As a critical indicator of capacitor performance, the high retention of sample ZnO-$C_{8k-2.5}$ suggested it was an ideal pseudocapacitance material for commercial utilization.

6.5. Supporting Information

Number average MW (M_n) and dispersity (M_w/M_n) were determined by GPC, conducted with a Waters 515 pump and Waters 2414 different refractometer using PSS columns (Styrogel 10^5,10^3, 10^2 A) in THF as an eluent (35 ºC, flow rate of 1 mL min^{-1}), using linear polystyrene (PS) and PMMA standards for calibration. ^{1}H NMR spectroscopy used for polymerization monitoring was performed using a Bruker Advance 300 MHz NMR spectrometer with $CDCl_3$ as

a solvent. The conversion was calculated by measuring the decrease of the monomer peak area relative to the peak area of the internal standards.

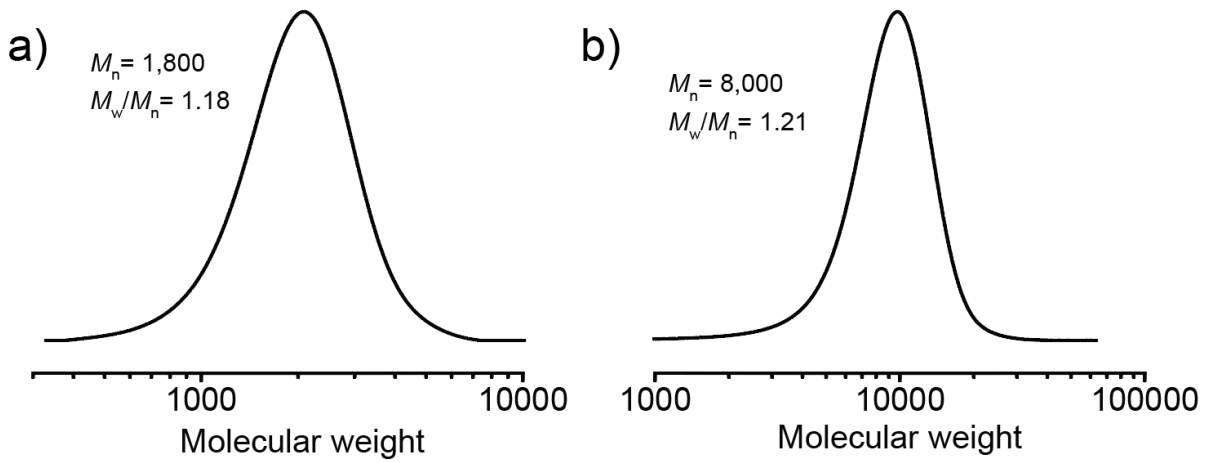

Figure S6.1. SEC trace of PSAN copolymer

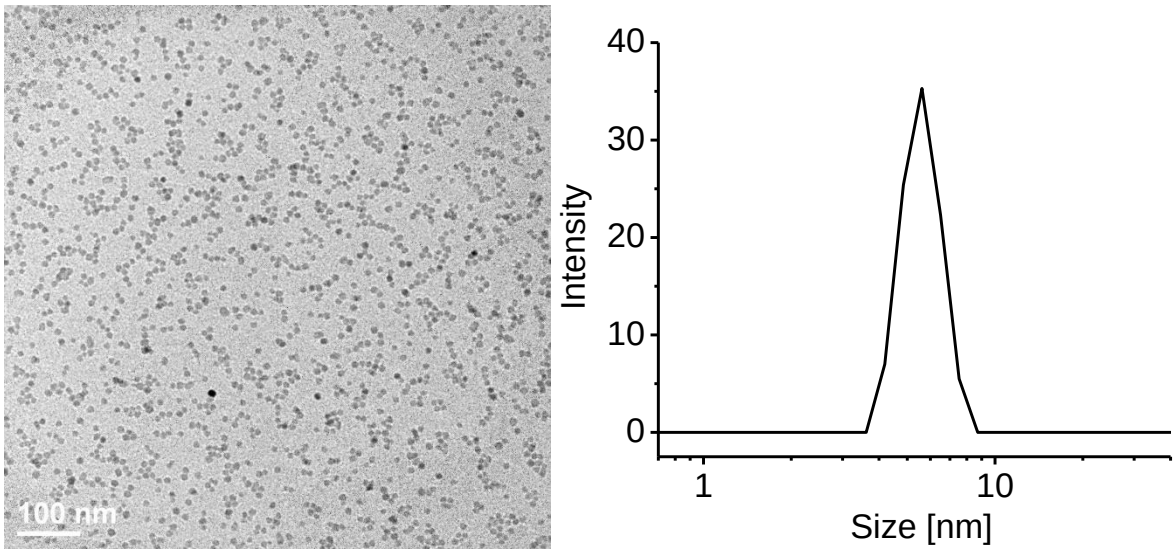

Figure S6.2. TEM images of OA capped ZnO nanocrystals and size distribution of OA capped ZnO NPs measured by dynamic light scattering (DLS) in the THF solution.

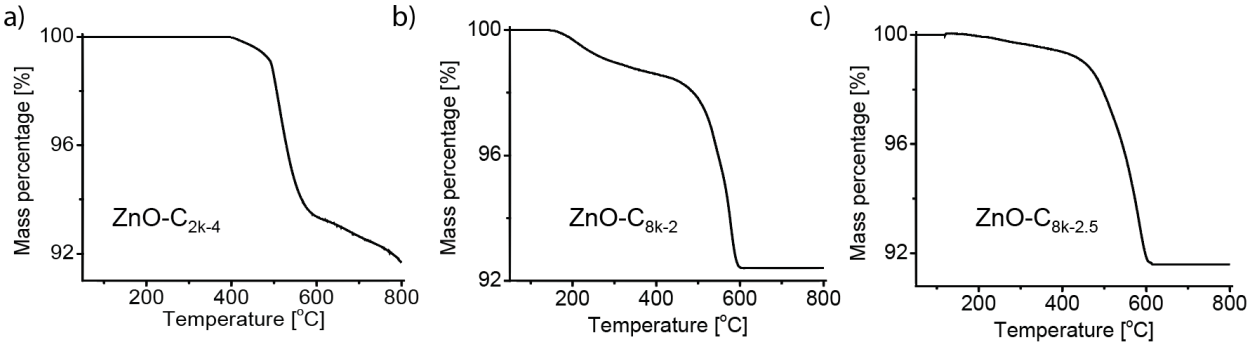

Figure S6.3. TGA curves of ZnO/carbon composite: (a) ZnO-C_{2k-4}; (b) ZnO-C_{8k-2}; (c) ZnO-$C_{8k-2.5}$.

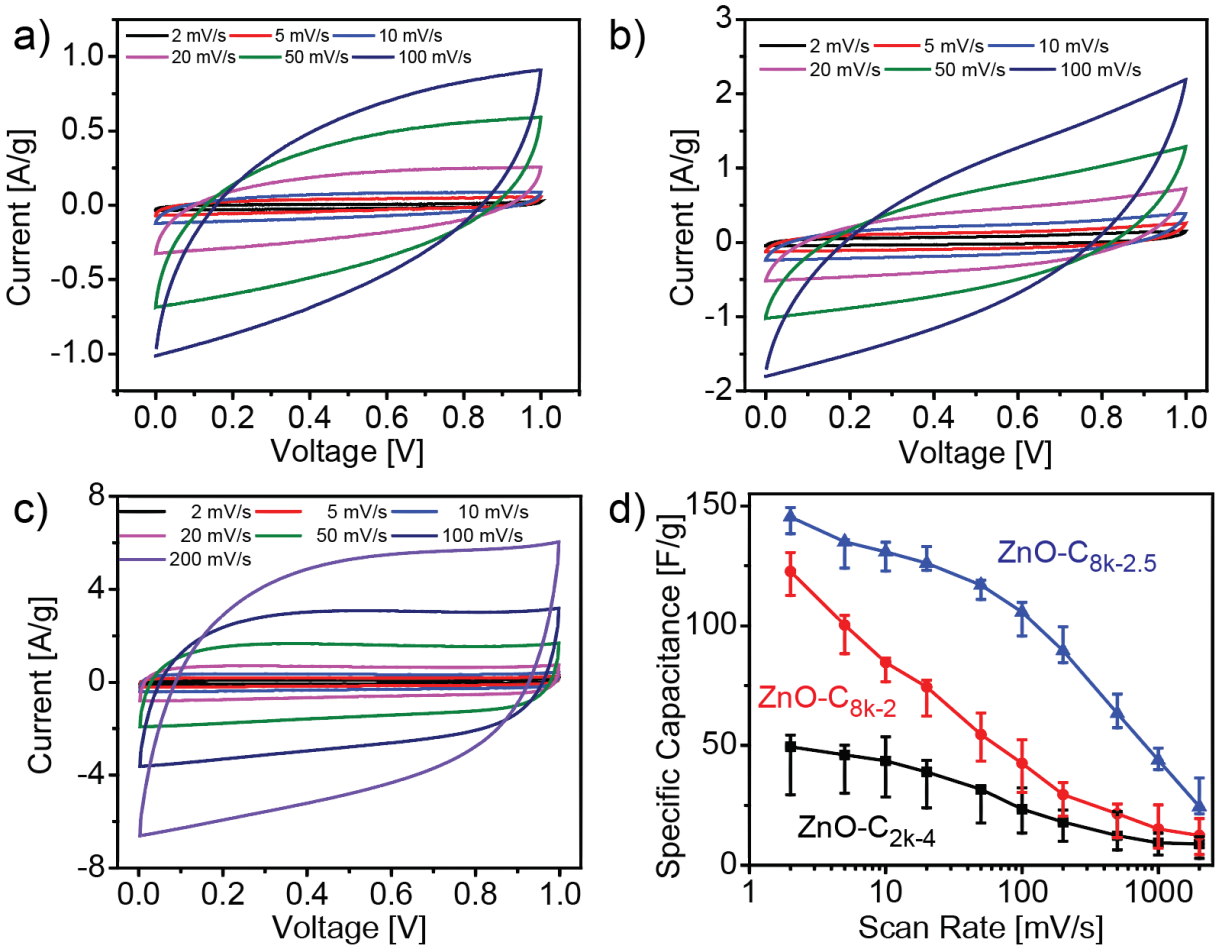

Figure S6.4. CV curves of ZnO/carbon composites: (a) ZnO-C_{2k-4}; (b) ZnO-C_{8k-2}; (c) ZnO-$C_{8k-2.5}$ at scan rates from 2 mV s^{-1} to 100 mV s^{-1}; (d) Comparison of capacitance from CV with scan rates from 2 mV s^{-1} to 2000 mV s^{-1}

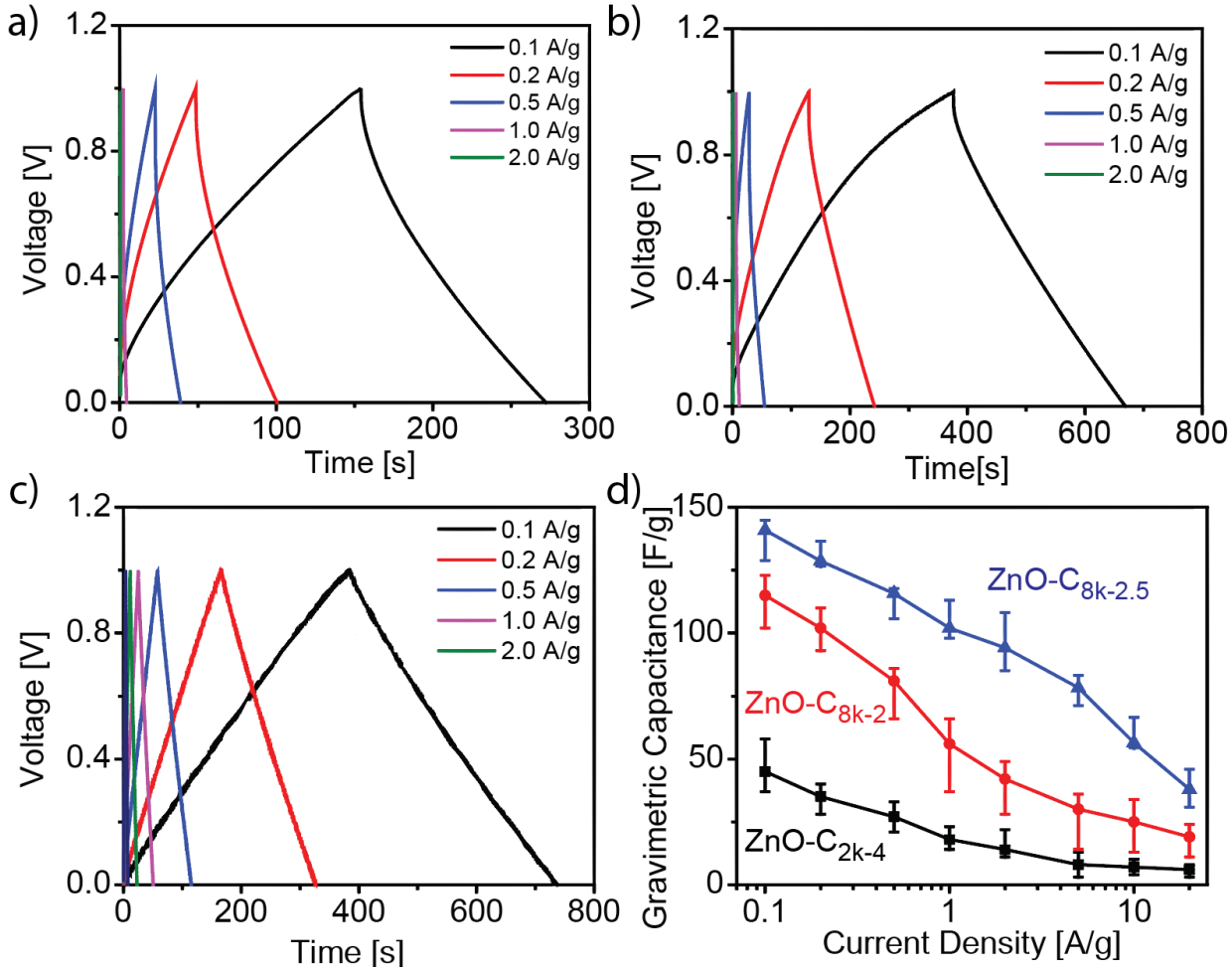

Figure S6.5. GCD curves of: (a) ZnO-C_{2k-4}; (b) ZnO-C_{8k-2}; (c) ZnO-$C_{8k-2.5}$ from 0.1 A g^{-1} to 2 A g^{-1}; (d) Comparison of capacitance from GCD with scan rates from 0.1 A g^{-1} to 20 A g^{-1}

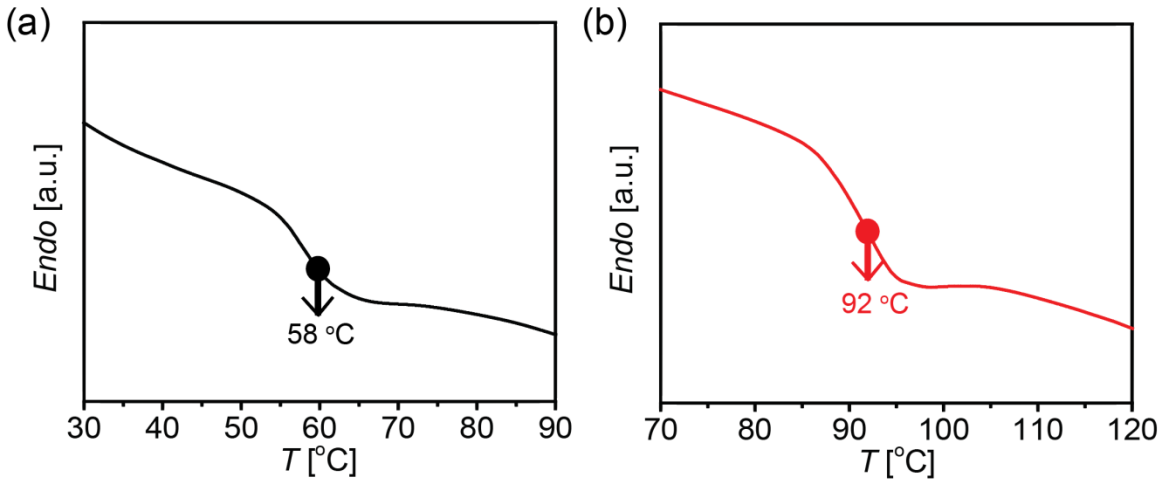

Figure S6.6. Heat flow curves of the PSAN polymers, T_g increased with increasing molecular weight. Black: M_n=1800, Red: M_n=8000.

Table S6.1. Comparisons of electrochemical performances of ZnO/carbon composites

Materials	Test system	Specific capacitance	A scan rate of current density	Electrolyte	Stability	Ref.
Carbon/ZnO Composites	Two-electrode	145 F g^{-1}	2 mV s^{-1}	1 M KOH	91% after 10000 cycles	This work
Carbon sphere@ ZnO core-shell nanocomposites	Three-electrode	630 F g^{-1}	2 A g^{-1}	6 M KOH	70.8% after 5000 cycles	ref 1
ZnO in Carbon nanotube/Graphene nanofiber	Three-electrode	306 F g^{-1}	10 mV s^{-1}	1 M H_2SO_4	99.4 % after 200 cycles	ref 2
Graphene/ZnO nanocomposites	Two-electrode	236 F g^{-1}	10 mV s^{-1}	1 M KOH	90 % after 200 cycles	ref 3
ZnO/Activated Carbon	Three-electrode	66 F g^{-1}	2 mV s^{-1}	500 ppm NaCl	N/A	ref 4
Graphene sheets anchored with ZnO nanocrystals	Three-electrode	231 F g^{-1}	50 mV s^{-1}	1 M H_2SO_4	99.5 % after 1000 cycles	ref 5
ZnO/Carbon nanotube nanocomposite	Two-electrode	48 F g^{-1}	5 mV s^{-1}	0.1 M TBAPC/DMF	104 % after 300 cycles	ref 6
ZnO/Reduced Graphene Oxide Composites	Three-electrode	308 F g^{-1}	1 A g^{-1}	0.1 M Na_2SO_4	93.5 % after 1500 cycles	ref 7
Graphene sheets/ZnO	Three-electrode	62.2 F g^{-1}	5 mV s^{-1}	1 M KOH	N/A	ref 8
Microwave-assisted synthesis of graphene–ZnO nanocomposite	Three-electrode	146 F g^{-1}	2 mV s^{-1}	1 M KCl	95% after 100 cycles	ref 9
Graphene–ZnO	Three-electrode	61.7 F g^{-1}	50 mV s^{-1}	1 M KCl	90% after 106 cycles	ref 10
Carbon nanotube-ZnO nanocomposite	Three-electrode	323.9 F g^{-1}	50 mV s^{-1}	1 M KCl	83% after 100 cycles	ref 11
ZnO/Carbon aerogel nanocomposite	Three-electrode	25 F g^{-1}	10 mV s^{-1}	6 M KOH	100% after 500 cycles	ref 12

1. Xiao, X.; Han, B.; Chen, G.; Wang, L.; Wang, Y., Preparation and electrochemical performances of carbon sphere@ ZnO core-shell nanocomposites for supercapacitor applications. *Scientific Reports* **2017,** *7*.
2. Ramli, N. I. T.; Rashid, S. A.; Mamat, M. S.; Sulaiman, Y.; Zobir, S. A.; Krishnan, S., Incorporation of Zinc Oxide into Carbon nanotube/Graphite nanofiber as a high-performance supercapacitor electrode. *Electrochimica Acta* **2017,** *228*, 259-267.
3. Ezeigwe, E. R.; Tan, M. T.; Khiew, P. S.; Siong, C. W., One-step green synthesis of graphene/ZnO nanocomposites for electrochemical capacitors. *Ceramics International* **2015,** *41* (1), 715-724.

4. Liu, J.; Lu, M.; Yang, J.; Cheng, J.; Cai, W., Capacitive desalination of ZnO/activated carbon asymmetric capacitor and mechanism analysis. *Electrochimica Acta* **2015,** *151*, 312-318.
5. Hsieh, C.-T.; Lin, J.-S.; Chen, Y.-F.; Lin, C.-Y.; Li, W.-Y., Graphene sheets anchored with ZnO nanocrystals as electrode materials for electrochemical capacitors. *Materials Chemistry and Physics* **2014,** *143* (2), 853-859.
6. Aravinda, L. S.; Nagaraja, K.; Nagaraja, H.; Bhat, K. U.; Bhat, B. R., ZnO/carbon nanotube nanocomposite for high energy density supercapacitors. *Electrochimica Acta* **2013,** *95*, 119-124.
7. Chen, Y.-L.; Hu, Z.-A.; Chang, Y.-Q.; Wang, H.-W.; Zhang, Z.-Y.; Yang, Y.-Y.; Wu, H.-Y., Zinc oxide/reduced graphene oxide composites and electrochemical capacitance enhanced by homogeneous incorporation of reduced graphene oxide sheets in zinc oxide matrix. *The Journal of Physical Chemistry C* **2011,** *115* (5), 2563-2571.
8. Wang, J.; Gao, Z.; Li, Z.; Wang, B.; Yan, Y.; Liu, Q.; Mann, T.; Zhang, M.; Jiang, Z., Green synthesis of graphene nanosheets/ZnO composites and electrochemical properties. *Journal of Solid State Chemistry* **2011,** *184* (6), 1421-1427.
9. Lu, T.; Pan, L.; Li, H.; Zhu, G.; Lv, T.; Liu, X.; Sun, Z.; Chen, T.; Chua, D. H., Microwave-assisted synthesis of graphene–ZnO nanocomposite for electrochemical supercapacitors. *Journal of Alloys and Compounds* **2011,** *509* (18), 5488-5492.
10. Lu, T.; Zhang, Y.; Li, H.; Pan, L.; Li, Y.; Sun, Z., Electrochemical behaviors of graphene–ZnO, and graphene–SnO 2 composite films for supercapacitors. *Electrochimica Acta* **2010,** *55* (13), 4170-4173.
11. Zhang, Y.; Sun, X.; Pan, L.; Li, H.; Sun, Z.; Sun, C.; Tay, B. K., Carbon nanotube–zinc oxide electrode and gel polymer electrolyte for electrochemical supercapacitors. *Journal of Alloys and Compounds* **2009,** *480* (2), L17-L19.
12. Kalpana, D.; Omkumar, K.; Kumar, S. S.; Renganathan, N., A novel high power symmetric ZnO/carbon aerogel composite electrode for electrochemical supercapacitor. *Electrochimica Acta* **2006,** *52* (3), 1309-1315.

6.6. Conclusion

In summary, random co-polymerization of acrylonitrile (AN) and styrene (S) enables the solution to processing of ZnO/PSAN composite films that can be pyrolyzed to form ZnO/carbon hybrid materials. Structure formation during pyrolysis is found to be sensitive to the molecular weight of matrix polymers. More uniform microstructures are observed for lower MW matrix polymers while higher MW PSAN promotes the coarsening of ZnO crystalallites and the formation of more porous hybrid morphologies. Molecular weight thus provides a gauge to control the microstructure of ZnO/carbon hybrids. More porous structures are found to exhibit better performance in pseudocapacitor applications. ZnO/carbon composite electrodes derived

from high MW PSAN exhibited a maximum specific capacitance as high as 145 F g^{-1}, at the scan rate of 2 mV s^{-1} in the presence of a KOH electrolyte. Furthermore, the specific capacitance was maintained at 91% of its initial values after 10000 successive charge/discharge cycles, which demonstrated its outstanding cycling stability. The simple synthesis method, competitive electrochemical capacitance, and high stability indicated its promising prospect as a pseudocapacitor electrode. Finally, given the wide range of materials that are amenable to SI-ATRP, we expect the presented approach to be applicable to enable the synthesis of a wide range of transition metal oxide/carbon hybrids.[69,70]

6.7. References

(1) Simon, P.; Gogotsi, Y., Materials for electrochemical capacitors. *Nat. Mater.* **2008,** *7* (11), 845-854.

(2) Liu, C.; Li, F.; Ma, L. P.; Cheng, H. M., Advanced materials for energy storage. *Adv. Mater.* **2010,** *22* (8), E28-62.

(3) Wang, G.; Zhang, L.; Zhang, J., A review of electrode materials for electrochemical supercapacitors. *Chem. Soc. Rev.* **2012,** *41* (2), 797-828.

(4) Zhang, L. L.; Zhao, X., Carbon-based materials as supercapacitor electrodes. *Chem. Soc. Rev.* **2009,** *38* (9), 2520-2531.

(5) Yang, Z.; Zhang, J.; Kintner-Meyer, M. C. W.; Lu, X.; Choi, D.; Lemmon, J. P.; Liu, J., Electrochemical Energy Storage for Green Grid. *Chemical Reviews* **2011,** *111* (5), 3577-3613.

(6) Stoller, M. D.; Park, S.; Zhu, Y.; An, J.; Ruoff, R. S., Graphene-based ultracapacitors. *Nano Lett.* **2008,** *8* (10), 3498-3502.

(7) Wu, Z.-S.; Ren, W.; Wang, D.-W.; Li, F.; Liu, B.; Cheng, H.-M., High-Energy MnO2 Nanowire/Graphene and Graphene Asymmetric Electrochemical Capacitors. *ACS Nano* **2010,** *4* (10), 5835-5842.

(8) Jiang, J.; Li, Y.; Liu, J.; Huang, X.; Yuan, C.; Lou, X. W., Recent Advances in Metal Oxide-based Electrode Architecture Design for Electrochemical Energy Storage. *Advanced Materials* **2012,** *24* (38), 5166-5180.

(9) Zhao, Y.; Li, M. P.; Liu, S.; Islam, M. F., Superelastic Pseudocapacitors from Freestanding MnO2 Decorated Graphene-Coated Carbon Nanotube Aerogels. *ACS Appl. Mater. Interfaces* **2017**.

(10) Zhang, Y.; Feng, H.; Wu, X.; Wang, L.; Zhang, A.; Xia, T.; Dong, H.; Li, X.; Zhang, L., Progress of electrochemical capacitor electrode materials: A review. *Int. J. Hydrogen Energy* **2009,** *34* (11), 4889-4899.

(11) Vangari, M.; Pryor, T.; Jiang, L., Supercapacitors: review of materials and fabrication methods. *Journal of Energy Engineering* **2012,** *139* (2), 72-79.

(12) Augustyn, V.; Simon, P.; Dunn, B., Pseudocapacitive oxide materials for high-rate electrochemical energy storage. *Energy & Environmental Science* **2014,** *7* (5), 1597-1614.

(13) Wang, D.-W.; Li, F.; Cheng, H.-M., Hierarchical porous nickel oxide and carbon as electrode materials for asymmetric supercapacitor. *Journal of Power Sources* **2008,** *185* (2), 1563-1568.
(14) Mastragostino, M.; Arbizzani, C.; Soavi, F., Polymer-based supercapacitors. *Journal of Power Sources* **2001,** *97–98*, 812-815.
(15) Grover, S.; Goel, S.; Sahu, V.; Singh, G.; Sharma, R. K., Asymmetric supercapacitive characteristics of pani embedded holey graphene nanoribbons. *ACS Sustainable Chemistry & Engineering* **2015,** *3* (7), 1460-1469.
(16) Chen, W.; Rakhi, R.; Alshareef, H. N., Facile synthesis of polyaniline nanotubes using reactive oxide templates for high energy density pseudocapacitors. *Journal of Materials Chemistry A* **2013,** *1* (10), 3315-3324.
(17) Liu, T.; Finn, L.; Yu, M.; Wang, H.; Zhai, T.; Lu, X.; Tong, Y.; Li, Y., Polyaniline and polypyrrole pseudocapacitor electrodes with excellent cycling stability. *Nano Lett.* **2014,** *14* (5), 2522-2527.
(18) Cai, X.; Lim, S. H.; Poh, C. K.; Lai, L.; Lin, J.; Shen, Z., High-performance asymmetric pseudocapacitor cell based on cobalt hydroxide/graphene and polypyrrole/graphene electrodes. *J. Power Sources* **2015,** *275*, 298-304.
(19) Hou, Y.; Chen, L.; Zhang, L.; Kang, J.; Fujita, T.; Jiang, J.; Chen, M., Ultrahigh capacitance of nanoporous metal enhanced conductive polymer pseudocapacitors. *J. Power Sources* **2013,** *225*, 304-310.
(20) Han, J.; Wang, M.; Hu, Y.; Zhou, C.; Guo, R., Conducting polymer-noble metal nanoparticle hybrids: Synthesis mechanism application. *Prog. Polym. Sci.* **2017,** *70*, 52-91.
(21) Hu, L.; Choi, J. W.; Yang, Y.; Jeong, S.; La Mantia, F.; Cui, L.-F.; Cui, Y., Highly conductive paper for energy-storage devices. *Proceedings of the National Academy of Sciences* **2009,** *106* (51), 21490-21494.
(22) Wang, D.; Li, Y.; Wang, Q.; Wang, T., Nanostructured Fe2O3–graphene composite as a novel electrode material for supercapacitors. *J. Solid State Electrochem.* **2012,** *16* (6), 2095-2102.
(23) Liu, J.; Lu, M.; Yang, J.; Cheng, J.; Cai, W., Capacitive desalination of ZnO/activated carbon asymmetric capacitor and mechanism analysis. *Electrochim. Acta* **2015,** *151*, 312-318.
(24) Lan, D.; Chen, Y.; Chen, P.; Chen, X.; Wu, X.; Pu, X.; Zeng, Y.; Zhu, Z., Mesoporous CoO nanocubes@ continuous 3D porous carbon skeleton of rose-based electrode for high-performance supercapacitor. *ACS Appl. Mater. Interfaces* **2014,** *6* (15), 11839-11845.
(25) Xia, X.-H.; Tu, J.-P.; Wang, X.-L.; Gu, C.-D.; Zhao, X.-B., Mesoporous Co3O4 monolayer hollow-sphere array as electrochemical pseudocapacitor material. *Chem. Commun.* **2011,** *47* (20), 5786-5788.
(26) Hu, L.; Chen, W.; Xie, X.; Liu, N.; Yang, Y.; Wu, H.; Yao, Y.; Pasta, M.; Alshareef, H. N.; Cui, Y., Symmetrical MnO2–carbon nanotube–textile nanostructures for wearable pseudocapacitors with high mass loading. *Acs Nano* **2011,** *5* (11), 8904-8913.
(27) He, Y.; Chen, W.; Li, X.; Zhang, Z.; Fu, J.; Zhao, C.; Xie, E., Freestanding three-dimensional graphene/MnO2 composite networks as ultralight and flexible supercapacitor electrodes. *ACS nano* **2012,** *7* (1), 174-182.
(28) Punetha, V. D.; Rana, S.; Yoo, H. J.; Chaurasia, A.; McLeskey Jr, J. T.; Ramasamy, M. S.; Sahoo, N. G.; Cho, J. W., Functionalization of carbon nanomaterials for advanced polymer nanocomposites: A comparison study between CNT and graphene. *Prog. Polym. Sci.* **2017,** *67*, 1-47.

(29) Mu, J.; Shao, C.; Guo, Z.; Zhang, Z.; Zhang, M.; Zhang, P.; Chen, B.; Liu, Y., High Photocatalytic Activity of ZnO−Carbon Nanofiber Heteroarchitectures. *ACS Applied Materials & Interfaces* **2011,** *3* (2), 590-596.
(30) Pu, Z.; Liu, Q.; Qusti, A. H.; Asiri, A. M.; Al-Youbi, A. O.; Sun, X., Fabrication of Ni (OH) 2 coated ZnO array for high-rate pseudocapacitive energy storage. *Electrochim. Acta* **2013,** *109*, 252-255.
(31) Xing, Z.; Chu, Q.; Ren, X.; Ge, C.; Qusti, A. H.; Asiri, A. M.; Al-Youbi, A. O.; Sun, X., Ni 3 S 2 coated ZnO array for high-performance supercapacitors. *J. Power Sources* **2014,** *245*, 463-467.
(32) Kalpana, D.; Omkumar, K.; Kumar, S. S.; Renganathan, N., A novel high power symmetric ZnO/carbon aerogel composite electrode for electrochemical supercapacitor. *Electrochim. Acta* **2006,** *52* (3), 1309-1315.
(33) Jayalakshmi, M.; Palaniappa, M.; Balasubramanian, K., Single step solution combustion synthesis of ZnO/carbon composite and its electrochemical characterization for supercapacitor application. *Int. J. Electrochem. Sci* **2008,** *3*, 96-103.
(34) Zhang, Y.; Li, H.; Pan, L.; Lu, T.; Sun, Z., Capacitive behavior of graphene–ZnO composite film for supercapacitors. *J. Electroanal. Chem.* **2009,** *634* (1), 68-71.
(35) Zhang, Y.; Sun, X.; Pan, L.; Li, H.; Sun, Z.; Sun, C.; Tay, B. K., Carbon nanotube–zinc oxide electrode and gel polymer electrolyte for electrochemical supercapacitors. *J. Alloys Compd.* **2009,** *480* (2), L17-L19.
(36) Lu, T.; Zhang, Y.; Li, H.; Pan, L.; Li, Y.; Sun, Z., Electrochemical behaviors of graphene–ZnO and graphene–SnO 2 composite films for supercapacitors. *Electrochim. Acta* **2010,** *55* (13), 4170-4173.
(37) Lu, T.; Pan, L.; Li, H.; Zhu, G.; Lv, T.; Liu, X.; Sun, Z.; Chen, T.; Chua, D. H., Microwave-assisted synthesis of graphene–ZnO nanocomposite for electrochemical supercapacitors. *J. Alloys Compd.* **2011,** *509* (18), 5488-5492.
(38) Wang, J.; Gao, Z.; Li, Z.; Wang, B.; Yan, Y.; Liu, Q.; Mann, T.; Zhang, M.; Jiang, Z., Green synthesis of graphene nanosheets/ZnO composites and electrochemical properties. *J. Solid State Chem.* **2011,** *184* (6), 1421-1427.
(39) Chen, Y.-L.; Hu, Z.-A.; Chang, Y.-Q.; Wang, H.-W.; Zhang, Z.-Y.; Yang, Y.-Y.; Wu, H.-Y., Zinc oxide/reduced graphene oxide composites and electrochemical capacitance enhanced by homogeneous incorporation of reduced graphene oxide sheets in zinc oxide matrix. *J. Phys. Chem. C* **2011,** *115* (5), 2563-2571.
(40) Hsieh, C.-T.; Lin, J.-S.; Chen, Y.-F.; Lin, C.-Y.; Li, W.-Y., Graphene sheets anchored with ZnO nanocrystals as electrode materials for electrochemical capacitors. *Mater. Chem. Phys.* **2014,** *143* (2), 853-859.
(41) Ezeigwe, E. R.; Tan, M. T.; Khiew, P. S.; Siong, C. W., One-step green synthesis of graphene/ZnO nanocomposites for electrochemical capacitors. *Ceram. Int.* **2015,** *41* (1), 715-724.
(42) Xiao, X.; Han, B.; Chen, G.; Wang, L.; Wang, Y., Preparation and electrochemical performances of carbon sphere@ ZnO core-shell nanocomposites for supercapacitor applications. *Scientific Reports* **2017,** *7*.
(43) Zhang, Y.; Sun, X.; Pan, L.; Li, H.; Sun, Z.; Sun, C.; Tay, B. K., Carbon nanotube–ZnO nanocomposite electrodes for supercapacitors. *Solid State Ionics* **2009,** *180* (32), 1525-1528.

(44) Ramli, N. I. T.; Rashid, S. A.; Mamat, M. S.; Sulaiman, Y.; Zobir, S. A.; Krishnan, S., Incorporation of Zinc Oxide into Carbon nanotube/Graphite nanofiber as high performance supercapacitor electrode. *Electrochimica Acta* **2017,** *228* (Supplement C), 259-267.
(45) Epifani, M.; Arbiol, J.; Díaz, R.; Perálvarez, M. J.; Siciliano, P.; Morante, J. R., Synthesis of SnO2 and ZnO Colloidal Nanocrystals from the Decomposition of Tin(II) 2-Ethylhexanoate and Zinc(II) 2-Ethylhexanoate. *Chemistry of Materials* **2005,** *17* (25), 6468-6472.
(46) Weber, D.; Botnaras, S.; Pham, D. V.; Steiger, J.; De Cola, L., Functionalized ZnO nanoparticles for thin-film transistors: support of ligand removal by non-thermal methods. *Journal of Materials Chemistry C* **2013,** *1* (18), 3098-3103.
(47) Wang, Z.; Lu, Z.; Mahoney, C.; Yan, J.; Ferebee, R.; Luo, D.; Matyjaszewski, K.; Bockstaller, M. R., Transparent and High Refractive Index Thermoplastic Polymer Glasses Using Evaporative Ligand Exchange of Hybrid Particle Fillers. *ACS Applied Materials & Interfaces* **2017,** *9* (8), 7515-7522.
(48) Wang, Z.; Mahoney, C.; Yan, J.; Lu, Z.; Ferebee, R.; Luo, D.; Bockstaller, M. R.; Matyjaszewski, K., Preparation of Well-Defined Poly(styrene-co-acrylonitrile)/ZnO Hybrid Nanoparticles by an Efficient Ligand Exchange Strategy. *Langmuir* **2016,** *32* (49), 13207-13213.
(49) Jakubowski, W.; Min, K.; Matyjaszewski, K., Activators Regenerated by Electron Transfer for Atom Transfer Radical Polymerization of Styrene. *Macromolecules* **2006,** *39* (1), 39-45.
(50) Plichta, A.; Zhong, M.; Li, W.; Elsen, A. M.; Matyjaszewski, K., Tuning Dispersity in Diblock Copolymers Using ARGET ATRP. *Macromolecular Chemistry and Physics* **2012,** *213* (24), 2659-2668.
(51) Matyjaszewski, K., Atom Transfer Radical Polymerization (ATRP): Current Status and Future Perspectives. *Macromolecules* **2012,** *45* (10), 4015-4039.
(52) Chmielarz, P.; Fantin, M.; Park, S.; Isse, A. A.; Gennaro, A.; Magenau, A. J. D.; Sobkowiak, A.; Matyjaszewski, K., Electrochemically mediated atom transfer radical polymerization (eATRP). *Progress in Polymer Science* **2017,** *69* (Supplement C), 47-78.
(53) Pan, X.; Tasdelen, M. A.; Laun, J.; Junkers, T.; Yagci, Y.; Matyjaszewski, K., Photomediated controlled radical polymerization. *Progress in Polymer Science* **2016,** *62* (Supplement C), 73-125.
(54) Wu, D.; Li, Z.; Zhong, M.; Kowalewski, T.; Matyjaszewski, K., Templated Synthesis of Nitrogen-Enriched Nanoporous Carbon Materials from Porogenic Organic Precursors Prepared by ATRP. *Angewandte Chemie International Edition* **2014,** *53* (15), 3957-3960.
(55) Matyjaszewski, K.; Xia, J., Atom Transfer Radical Polymerization. *Chemical Reviews* **2001,** *101* (9), 2921-2990.
(56) Pietrasik, J.; Dong, H.; Matyjaszewski, K., Synthesis of High Molecular Weight Poly(styrene-co-acrylonitrile) Copolymers with Controlled Architecture. *Macromolecules* **2006,** *39* (19), 6384-6390.
(57) Wu, D.; Dong, H.; Pietrasik, J.; Kim, E. K.; Hui, C. M.; Zhong, M.; Jaroniec, M.; Kowalewski, T.; Matyjaszewski, K., Novel Nanoporous Carbons from Well-Defined Poly(styrene-co-acrylonitrile)-Grafted Silica Nanoparticles. *Chem. Mater.* **2011,** *23* (8), 2024-2026.
(58) Kruk, M.; Dufour, B.; Celer, E. B.; Kowalewski, T.; Jaroniec, M.; Matyjaszewski, K., Well-Defined Poly(ethylene oxide)−Polyacrylonitrile Diblock Copolymers as Templates for Mesoporous Silicas and Precursors for Mesoporous Carbons. *Chem. Mater.* **2006,** *18* (6), 1417-1424.

(59) Tsarevsky, N. V.; Sarbu, T.; Göbelt, B.; Matyjaszewski, K., Synthesis of Styrene−Acrylonitrile Copolymers and Related Block Copolymers by Atom Transfer Radical Polymerization. *Macromolecules* **2002,** *35* (16), 6142-6148.
(60) Sarkar, B.; Alexandridis, P., Block copolymer–nanoparticle composites: Structure, functional properties, and processing. *Prog. Polym. Sci.* **2015,** *40*, 33-62.
(61) Stoller, M. D.; Ruoff, R. S., Best practice methods for determining an electrode material's performance for ultracapacitors. *Energy & Environmental Science* **2010,** *3* (9), 1294-1301.
(62) Frank, E.; Steudle, L. M.; Ingildeev, D.; Spörl, J. M.; Buchmeiser, M. R., Carbon Fibers: Precursor Systems, Processing, Structure, and Properties. *Angew. Chem. Int. Ed.* **2014,** *53* (21), 5262-5298.
(63) Zhong, M.; Kim, E. K.; McGann, J. P.; Chun, S.-E.; Whitacre, J. F.; Jaroniec, M.; Matyjaszewski, K.; Kowalewski, T., Electrochemically Active Nitrogen-Enriched Nanocarbons with Well-Defined Morphology Synthesized by Pyrolysis of Self-Assembled Block Copolymer. *Journal of the American Chemical Society* **2012,** *134* (36), 14846-14857.
(64) Lam, D. V.; Jo, K.; Kim, C.-H.; Kim, J.-H.; Lee, H.-J.; Lee, S.-M., Activated Carbon Textile via Chemistry of Metal Extraction for Supercapacitors. *ACS Nano* **2016,** *10* (12), 11351-11359.
(65) Ellingham, H. J. T., Reducibility of oxides and sulphides in metallurgical processes. *J. Soc. Chem. Ind. (J. Chem. Technol. Biotechnol.)* **1944,** *10*, 125-133.
(66) Strobl, G. R., *The Physics of Polymers: Concepts for Understanding Their Structures and Behavior*. Springer Berlin Heidelberg: **2013**.
(67) Gregg, S., Mesoporous solids: the Type IV isotherm. *Adsorption, Surface Area and Porosity* **1982**, 137-143.
(68) Taberna, P.; Simon, P.; Fauvarque, J.-F., Electrochemical characteristics and impedance spectroscopy studies of carbon-carbon supercapacitors. *J. Electrochem. Soc.* **2003,** *150* (3), A292-A300.
(69) Hui, C. M.; Pietrasik, J.; Schmitt, M.; Mahoney, C.; Choi, J.; Bockstaller, M. R.; Matyjaszewski, K., Surface-Initiated Polymerization as an Enabling Tool for Multifunctional (Nano-)Engineered Hybrid Materials. *Chem. Mater.* **2014,** *26* (1), 745-762.
(70) Yan, J.; Pan, X.; Wang, Z.; Lu, Z.; Wang, Y.; Liu, L.; Zhang, J.; Ho, C.; Bockstaller, M. R.; Matyjaszewski, K., A Fatty Acid-Inspired Tetherable Initiator for Surface-Initiated Atom Transfer Radical Polymerization. *Chem. Mater.* **2017,** *29* (11), 4963-4969.

Chapter 7 Pushing the Limit: Synthesis of SiO_2-*g*-PMMA/PS Particle Brushes *via* ATRP with Very Low Concentration of Functionalized SiO_2-Br Nanoparticles

7.1. Preface

The kinetics and mechanism of the synthesis of SiO_2-*g*-poly(methyl methacrylate) (SiO_2-*g*-PMMA) and SiO_2-*g*-polystyrene (SiO_2-*g*-PS) nanoparticles was investigated through studies conducted at very low concentrations of the ATRP initiator functionalized silica particles (SiO_2-Br) in the presence of reducing agent (tin(II) 2-ethylhexanoate) and low ppm loadings of the Cu^{II} catalyst (25 ppm) complex. In the SiO_2-*g*-PMMA system, the grafting density decreased under very low concentrations (<100 ppm) of SiO_2-Br. However, in the SiO_2-*g*-PS system, the initiation efficiency, defined through the grafting density of polymer chains on the particle surface, decreased significantly for lower concentrations of the initiator SiO_2-Br. Besides, model systems with linear polymer chains (untethered) were studied to investigate the difference in initiation efficiency between polymers attached to nanoparticle surfaces and untethered chains. Due to the localization of initiation sites on the surface of nanoparticles and lower probabilities of collisions between nanoparticles, as compared to small initiator molecules, particle brush systems exhibited less inter-particle termination. This observation was employed to synthesize very high molecular weight (M_n> 500k) particle brushes with relatively narrow molecular weight distribution (M_w/M_n< 1.3).

In this chapter, the synthesis of SiO_2-*g*-PS/PMMA particle brushes with very low SiO_2-Br concentrations and its mechanism is discussed. I designed the entire project and performed all

synthetic work and the characterization in the project. I would like to thank especially my collaborators, Marco Fantin and Jiajun Yan for his extensive discussion and careful revision about the mechanism. Julian Sobieski, Zhenhua Wang, and Jiajun Yan assisted in the synthesis work. Jaejun Lee, Tong Liu, and Sipei Li assisted in the characterization work. Mateusz Olszewski helped to design the Scheme and Table of Contents. Professor Matyjaszewski and Professor Bockstaller conceived and organized the project and together with me wrote the manuscript.

This project was published in *Macromolecules*, (**Zongyu Wang**, Marco Fantin, Julian Sobieski, Zhenhua Wang, Jiajun Yan, Jaejun Lee, Tong Liu, Sipei Li, Mateusz Olszewski, Michael R Bockstaller, Krzysztof Matyjaszewski, "Pushing the Limit: Synthesis of SiO_2-*g*-PMMA/PS Particle Brushes via ATRP with Very Low Concentration of Functionalized SiO_2-Br Nanoparticles", *Macromolecules*, **2019**, 52, 22, 8713-8723).

This work was supported by NSF (DMR 1501324 and DMR 1410845), the Department of Energy (DE-EE0006702), as well as the Scott Institute for Energy Technologies at Carnegie Mellon University. Zhenhua Wang gratefully acknowledges financial support from the China Scholarship Council.

7.2. Introduction

Core-shell hybrids nanoparticles have attracted great interest as nanocomposites, components of catalysts systems, and as drug delivery systems.[1-6] Nanocomposites, inorganic particles with a grafted polymeric corona, can be used in the bulk state, and exhibit enhanced compatibility with polymer matrices.[7,8] Incorporation of nanometer-sized hybrid nanoparticles into a polymer matrix has led to the development of materials with new and exciting properties

that cannot be obtained using micrometer-sized fillers.[9-11] Nanocomposite fillers, with uniform distribution and minimal aggregation, can form polymer composites with increased thermal conductivity, enhanced thermal stability, higher refractive index and higher dielectric permittivity.[12-14]

To prepare a well-defined nanocomposite, the solid surface of the inorganic core can be covalently modified by using either a "grafting-onto" or a "grafting-from" technique.[15-17] In the "grafting-from" process, the polymer chains grow from inherent initiating sites or immobilized initiators on the surface of the particle. Consequently, the grafting density is higher than that prepared by the "grafting-onto" method, where preformed polymers have to diffuse to the surface and react with it.[18,19] Hence, in most cases, "grafting-from" is the preferred method for the preparation of nanocomposites.[20] A major driving force in the development of this field has been the advent of surface-initiated atom transfer radical polymerization (SI-ATRP) techniques.[21-23] SI-ATRP has revolutionized the fields of polymer chemistry and material science due to its high tolerance to functional groups, the ability to conduct the polymerization under a wide range of reactions conditions, and the precise control it offers over the molecular weight and architecture of tethered polymers.[16,21,23-26]

Traditional ATRP employed a high loading of low activity Cu-based redox catalysts to maintain a reasonable polymerization rate.[27-30] Consequently, the grafted substrates become colored and purification was necessary to remove the residual catalyst complex.[31] Alternative approaches to conduct ATRP were therefore developed including activators regenerated by electron transfer (ARGET) ATRP.[32-37] In ARGET ATRP, a pre-catalyst Cu^{II}/L is added, or formed *in situ*, at the beginning of the polymerization. A fraction of the stable Cu^{II} complex is continuously reduced to an active Cu^{I}/L species by a reducing agent.[38] The advantage of ARGET

ATRP is that the amount of copper in the polymerization can be significantly reduced, since Cu^{II}/L complexes formed via oxidation or radical termination are constantly transformed to active Cu^{I}/L species by the reducing agent.[39,40] Therefore only a few ppm of copper are required to mediate the polymerization. Besides, ARGET ATRP can be carried out in the presence of a large excess of the reducing agent, and as a result, the reaction can be conducted in the presence of limited amounts of air.[32,41] The use of low concentrations of a Cu catalyst in conjunction with a reducing agent can greatly improve particle brush synthesis by adjusting radical concentration during the polymerization process through control over the ratio of [Cu^{I}] to [Cu^{II}].[42] In typical ARGET ATRP, the concentration initiator is much higher than the concentration of Cu catalyst. The concentration of reducing agent is usually much higher than that of the catalyst to assure the catalyst regeneration. Additionally, the concentration of reducing agent is lower than that of the initiator to avoid termination of too many chains. Thus, ARGET ATRP with ppm Cu is best suited for the relatively high alkyl halides concentration and polymers with lower molecular weights, especially for slower polymerizing monomers such as styrene (S) or methyl methacrylate (MMA).

In this contribution, we investigated the mechanism for the synthesis of SiO_2-*g*-PMMA and SiO_2-*g*-PS nanoparticles utilizing low ppm levels of Cu catalyst in an SI-ATRP. Two parameters, the concentration of the reducing agent: tin(II) 2-ethylhexanoate [$Sn(EH)_2$] and the nanoparticle initiator [SiO_2-Br], were examined by measuring the grafting density, molecular weight, and dispersity of the polymer chains tethered to the silica nanoparticles. The targeted higher molecular weights presented a challenge because the concentration of alkyl halides was lower than both the reducing agent and Cu catalyst. The grafting density of the particle brush

strongly depended on the loading of the nanoparticle initiator SiO_2-Br, diminishing for low [SiO_2-Br].

The morphology and uniformity of the particles were studied by transmission electron microscopy (TEM) and dynamic light scattering (DLS) respectively, demonstrating the role of radical termination in particle brushes. Meanwhile, polymers grafted from particles were compared to linear polymers made in homogenous solutions. Compared to the small initiator molecules in a homogenous linear system, the localization of the initiator on the surface of nanoparticles lessens the chance of collisions between nanoparticles, which caused fewer terminations between particles. Therefore, the polymerization of SiO_2-*g*-PMMA particle brushes could be tuned to synthesize an ultra-high molecular weight particle brush with relatively narrow molecular weight distribution.

7.3. Experimental Section

Materials.

Monomers: styrene (S, 99%, Aldrich) and methyl methacrylate (MMA, 99%, Aldrich) were purified by passing through a column filled with basic alumina to remove the inhibitor. Tris(2-dimethylaminoethyl)amine (Me_6TREN, 99%, Alfa), anisole (99%, Aldrich), tetrahydrofuran (THF, 99%, VWR), methanol (99%, VWR), hexane (99%, VWR), acetone (99%, VWR), N,N-dimethylformamide (DMF, 99%, VWR), ethyl 2-bromoisobutyrate (EBiB, 98%, Aldrich), copper(II) bromide ($CuBr_2$, 99%, Aldrich), tin(II) 2-ethylhexanoate ($Sn(EH)_2$, 95%, Aldrich), hexane (Fluka), 48% hydrofluoric acid aqueous solution (HF, >99.99%, Aldrich), ammonium hydroxide aqueous solution (NH_4OH, 28.0-30.0%, Fisher), and anhydrous magnesium sulfate ($MgSO_4$, Fisher) were used as received without further purification. Silica

nanoparticles, 30 wt% solution in methyl isobutyl ketone (MIBK-ST), effective diameter d ≈ 15.8 nm, were kindly donated by Nissan Chemical Corp. and were used as received. The tethered ATRP initiator 1-(chlorodimethylsilyl)propyl-2-bromoisobutyrate and surface-modified silica (SiO_2-Br) were prepared using previously reported procedures.[16,43] It should be noted that the experiments in **Table 7.1** and **Table 7.2** were carried out with different batches of SiO_2-Br nanoparticles, which may, therefore, have slightly different grafting density of the initiator.

Procedures.

General procedure for SiO_2-g-PMMA/PS particle brushes synthesis via low Cu catalyst ATRP. Initiator (SiO_2-Br), monomers (MMA/S), solvents (anisole, DMF), $CuBr_2$, and Me_6TREN were mixed thoroughly in a sealed Schlenk flask. Meanwhile, a stock solution of $Sn(EH)_2$ in anisole was prepared. Both mixtures were degassed by nitrogen purging, then the $Sn(EH)_2$ solution was injected into the Schlenk flask to activate the catalyst complex and the flask was immediately placed into an oil bath set at 60 ºC. The conversion and molecular weight (MW) of the polymer were monitored by gravimetric analysis and size exclusion chromatography (SEC), respectively.

Procedures for the synthesis of linear PMMA and PS homopolymers via low Cu catalyst ATRP.

Initiator (EBiB), monomers (MMA/S), solvents (anisole, DMF), $CuBr_2$, and Me_6TREN were mixed thoroughly in a sealed Schlenk flask. A stock solution of $Sn(EH)_2$ in anisole was prepared. Both mixtures were degassed by nitrogen purging, then the $Sn(EH)_2$ solution was injected into the Schlenk flask to activate the catalyst complex and the flask was immediately placed into an oil bath. The conversion and MW of the polymer were monitored by gravimetric analysis and SEC, respectively.

Characterization.

Transmission electron microscopy (TEM). TEM was carried out using a JEOL 2000 EX electron microscope operated at 200 kV. The spatial distribution, radius and inter-particle distances of the SiO_2 nanoparticles were determined from statistical analysis of the TEM micrographs using ImageJ software. DLS, using a Malvern Zetasizer Nano ZS, was performed to confirm results obtained from TEM. It was also employed to determine volume-weighted average hydrodynamic diameters and distribution.

Thermogravimetric analysis (TGA). A TA Instruments 2950 was used to measure the fraction of SiO_2 in the hybrids by TGA. The data were analyzed using TA Universal Analysis. The heating procedure involved four steps: (1) jump to 120 ºC; (2) hold at 120 ºC for 10 min; (3) ramp up at a rate of 20 ºC/min to 800 ºC; (4) hold for 2 min. The TGA plots were normalized to the total weight after holding at 120 ºC.

Grafting density. Equation (1) was used to calculate the grafting density.

$$\sigma_{\mathrm{TGA}} = \frac{(1-f_{\mathrm{SiO2}})N_{\mathrm{Av}}\,\rho_{\mathrm{SiO2}}\,d}{6\,f_{\mathrm{SiO2}}\,M_n} \qquad (1)$$

where f_{SiO2} is the SiO_2 fraction (wt%) measured by TGA, N_{Av} is the Avogadro number, ρ_{SiO2} is the density of SiO_2 nanoparticles (2.2 g/cm^3), d is the average diameter of SiO_2 nanoparticles (15.8 nm), and M_n is the overall number-average MW of the cleaved polymer brushes.[44] It should be noted that eq. 1 underestimates grafting density in the event of substantial radical termination by coupling, which would cause M_n to increase—up to twice in the case of complete coupling. This can be relevant in the case of styrene polymerization. Also, grafting density could be

overestimated in the case of transfer or thermal self-initiation of styrene because some polymer chains are not attached to particles.

Polymer characterization. Number-average molecular weights (M_n) and molecular weight distributions (M_w/M_n) were determined by SEC. The SEC was conducted with a Waters 515 pump and Waters 410 differential refractometer using PSS columns (Styrogel 10^5, 10^3, 10^2 Å) in THF as an eluent at 35 ºC and a flow rate of 1 ml min^{-1}. Linear PS and PMMA standards were used for calibration. The conversion was calculated by gravimetric analysis.

Kinetic parameters calculation: Equations (2-4) were used to calculate the apparent rate of propagation (**k_p^{app}**) and the radical concentration [P•]. Equation (6) was used to calculate the dead chain fraction (DCF) of linear PMMA. Equation (7) was used to calculate the number of new chains introduced by the thermal self-initiation of S.

$$\ln\frac{[\mathrm{M}]}{[\mathrm{M}]_0} = -k_\mathrm{p}^{\mathrm{app}} \times t \quad (2)$$

$$k_\mathrm{p}^{app} = k_\mathrm{p} \times [\mathrm{P}^\bullet] \quad (3)$$

$$R_\mathrm{p} = k_\mathrm{p} \times [\mathrm{M}] \quad (4)$$

$$\mathrm{DCF}(\%) = 100\left(\frac{d\ln[\mathrm{M}]}{d_t}\right)\Delta\ln[\mathrm{M}]\,/[\mathrm{RX}]_0\left(\frac{k_\mathrm{t}}{k_\mathrm{p}^2}\right) \quad (5)$$

$$\mathrm{DCF} = \frac{2\mathrm{DP_T}k_\mathrm{t}[\ln(1-p)]^2}{[\mathrm{M}]_0 k_\mathrm{p}^2 t} \quad (6)^{45}$$

$$n_{\text{new chains}}\,(\mathrm{ppm}) = [\mathrm{EBiB}]_0(\mathrm{ppm}) \times \left(\frac{M_{\mathrm{n,theo}}}{M_{\mathrm{n,SEC}}} - 1\right) \quad (7)$$

where DP_T is the targeted degree of polymerization, k_p is the propagation rate constant, k_t is the termination rate constant, and p is conversion.

7.4. Results and Discussion

Effect of Reducing Agent Concentration in the Synthesis of SiO_2-g-PMMA/PS Particle Brushes

Figure 7.1 shows the effect of varying the concentration of the reducing agent [$Sn(EH)_2$] on the conversion profile, grafting density, and dispersity of the nanoparticle brushes synthesized with low ppm Cu catalyst ATRP using a fixed concentration of $CuBr_2$/Me_6TREN in 50% v/v solvent at 60 ºC. Computer simulations of ATRP suggested that a [Cu^{II}]/[R-X] ratio of 0.1 to 1 is appropriate for ARGET ATRP reactions,[46] therefore 25 ppm of $CuBr_2$ and 250 ppm of SiO_2-Br was used in the initial study. In ATRP, the concentration of reducing agent affects the radical concentration during the polymerization and the ratio of Cu^I/Cu^{II} catalyst. This technique is attractive for particle brush synthesis because it is possible to control radical concentration during an ARGET ATRP. **Figures 7.1**a and **Figures 7.1**b show the correlation of the reaction rate with the initial concentration of the reducing agent and indicate that the rate of polymerization is faster with a higher initial concentration of the reducing agent. The concentration of the reducing agent did not significantly affect the dispersity and initiation efficiency, i.e. the grafting density of the particle brush. The detailed results are presented in **Table 7.1** and show that M_w/M_n is in the range of 1.17 to 1.21 for SiO_2-*g*-PMMA and 1.29 to 1.47 for SiO_2-*g*-PS, while grafting density varies from 0.87 to 0.95 and 0.63 to 0.81 for SiO_2-*g*-PMMA and SiO_2-*g*-PS, respectively. It should be noted that, although the same SiO_2-Br nanoparticles were used in all reactions, the SiO_2-*g*-PMMA exhibited higher grafting density and narrower molecular weight distribution than the SiO_2-*g*-PS. Moreover, the plot of grafting density *vs.* [$Sn(EH)_2$] (**Figures 7.1**c) shows that [$Sn(EH)_2$] does not strongly affect initiation

efficiency. In summary, at relatively high concentration of the catalyst, the excess amount of reducing agent can be added to accelerate the reaction without reducing initiation efficiency (grafting density of the particle brush) or the control of the reactions (molecular weight distribution of the particle brush). The reaction kinetics was approximately 1/2 order in respect to $[Sn(EH)_2]$, as observed in other ARGET reactions.[15,32,34,37,47]

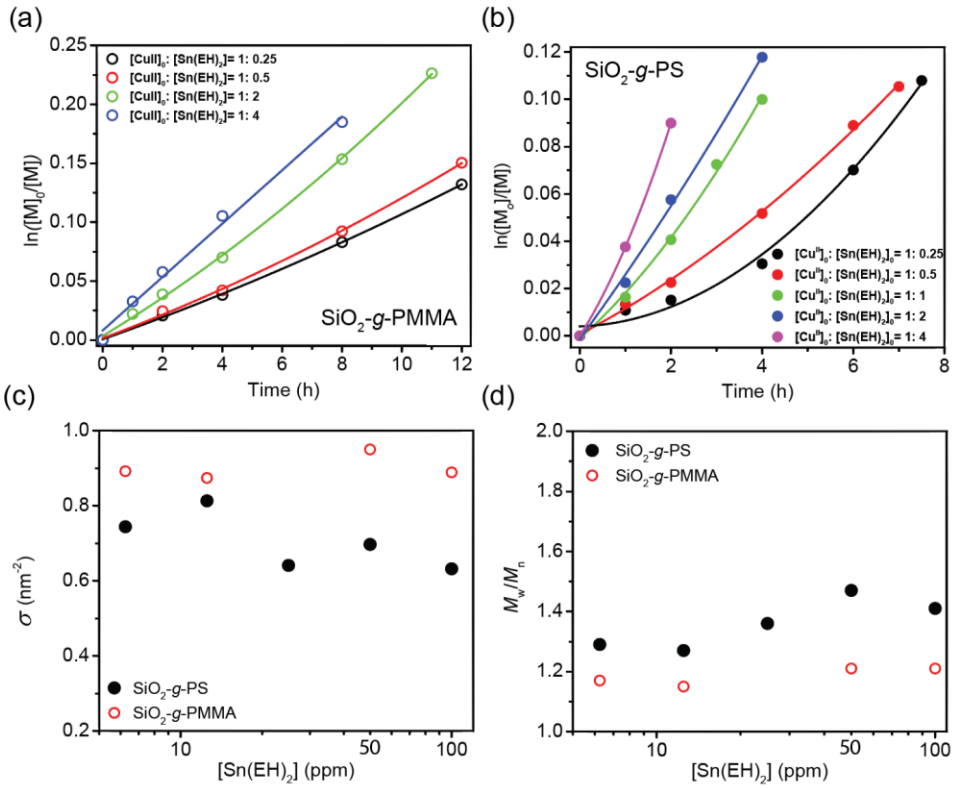

Figure 7.1. Polymerization of methyl methacrylate (MMA) and styrene (S) on SiO_2-Br nanoparticles by low Cu catalyst ATRP at different concentrations on reducing agent. Conditions: $[M]_0/[SiO_2\text{-}Br]_0/[CuBr_2]_0/[Me_6TREN]_0/[Sn(EH)_2]_0$ = 4000/1/0.1/1/x, with x = 0.025-0.4 as indicated in the figures. (a-b) Kinetics of SiO_2-*g*-PMMA/PS particle brushes synthesis and (c-d) plot of grafting density/MWD versus $[Sn(EH)_2]_0$. $[CuBr_2]_0$ = 25 ppm.

Table 7.1. Synthesis of SiO_2-*g*-PMMA/PS particle brushes with the different initial concentration of reducing agent

Entry[a]	Reaction conditions				M_n[d]	M_w/M_n[d]	f_{ino} (%)[e]	σ (nm^{-2})[f]
	$[SiO_2\text{-}Br]_0$ (ppm)[b]	time (h)	$[Sn(EH)_2]_0$ (ppm)[b]	conv (%)[c]				
PMMA-1	250	12	6.25	12.36	39,740	1.17	8.56	0.892
PMMA-2	250	12	12.5	13.96	46,730	1.15	7.51	0.874
PMMA-3	250	11	50	20.26	59,170	1.21	5.56	0.950
PMMA-4	250	8	100	16.88	52,770	1.21	6.61	0.889

PS-1	250	7.5	6.25	10.23	29,190	1.29	11.77	0.744
PS-2	250	7	12.5	10.00	28,789	1.27	10.24	0.813
PS-3	250	4	25	9.51	29,270	1.36	13.05	0.641
PS-4	250	4	50	11.11	30,010	1.47	12.81	0.697
PS-5	250	2	100	8.61	37,150	1.41	11.19	0.632

[a] Reaction conditions: $[M]_0/[SiO_2\text{-}Br]_0/[CuBr_2]_0/[Me_6TREN]_0/[Sn(EH)_2]_0$ = 4000/1/0.1/1/x, with x = 0.025-0.4. 50 vol% M in anisole: DMF= 9:1 at 60 ºC. $[MMA]_0$ = 4.7 M, $[S]_0$ = 4.3 M, $[CuBr_2]_0$ = 25 ppm. [b] Molar ratio *vs.* monomer. [c] Determined by gravimetric analysis. [d] Determined by SEC. [e] Fraction of inorganic content determined by TGA. [f] Calculated from Eq. 1 according to TGA data.

Effect of Initiator Concentration in the Synthesis of SiO_2-g-PMMA/PS Particle Brushes

Another critical parameter affecting the control of a low ppm catalyst ATRP reaction is the concentration of the initiator, [SiO_2-Br]. **Table 7.2** and **Figure 7.2** provide the results of the study on the influence of initial [SiO_2-Br] (which in turn affected the target DP) on the synthesis of particle brushes with 200 ppm of reducing agent added to the reactions. It should be noted that under these conditions the ratio of Cu complex concentration to alkyl halide concentration was varied from the previously used 0.1 to more than 1, which affected both polymerization rate and control.

Table 7.2. Synthesis of SiO_2-*g*-PMMA/PS particle brushes with different SiO_2-Br concentrations

	Reaction condition							
Entry[a]	$[SiO_2\text{-}Br]_0$ (ppm)[b]	Time (h)	$[Sn(EH)_2]_0$ (ppm)[b]	conv (%)[c]	**M_n**[d]	**M_w/M_n**[d]	**f_{ino} (%)**[e]	**σ (nm^{-2})**[f]
PMMA-5	400	3	200	7.77	24,300	1.21	21.2	0.541
PMMA-6	200	4.5	200	9.25	50,700	1.20	10.5	0.556
PMMA-7	100	5	200	8.58	87,300	1.25	6.47	0.548
PMMA-8	50	6	200	7.01	161,600	1.32	4.19	0.468
PMMA-9	25	6	200	3.65	258,200	1.24	5.53	0.219
PMMA-10	12.5	7.5	200	4.26	521,200	1.24	3.51	0.175
PS-6	400	4	200	4.87	18,720	1.19	28.81	0.437
PS-7	200	4	200	4.26	39,210	1.43	25.86	0.242
PS-8	100	6	200	4.72	37,890	1.67	28.87	0.215
PS-9	50	6	200	3.51	61,900	1.81	26.41	0.149
PS-10	25	6	200	2.03	103,584	1.92	21.47	0.117
PS-11	12.5	6	200	0.61	53,352	1.87	54.98	0.051

[a] Reaction conditions: $[M]_0/[SiO_2\text{-}Br]_0/[CuBr_2]_0/[Me_6TREN]_0/[Sn(EH)_2]_0$ = 4000/1/0.1/1/x, with x = 0.025-0.4. 50 vol% M in anisole: DMF= 9:1 at 60 ºC. $[MMA]_0$ = 4.7 M, $[S]_0$ = 4.3 M, $[CuBr_2]_0$ = 25 ppm. [b] Molar ratio *vs.* monomer. [c] Determined by gravimetric analysis. [d] Determined by SEC. [e] Fraction of inorganic content determined by TGA. [f] Calculated from Eq. 1 according to TGA data.

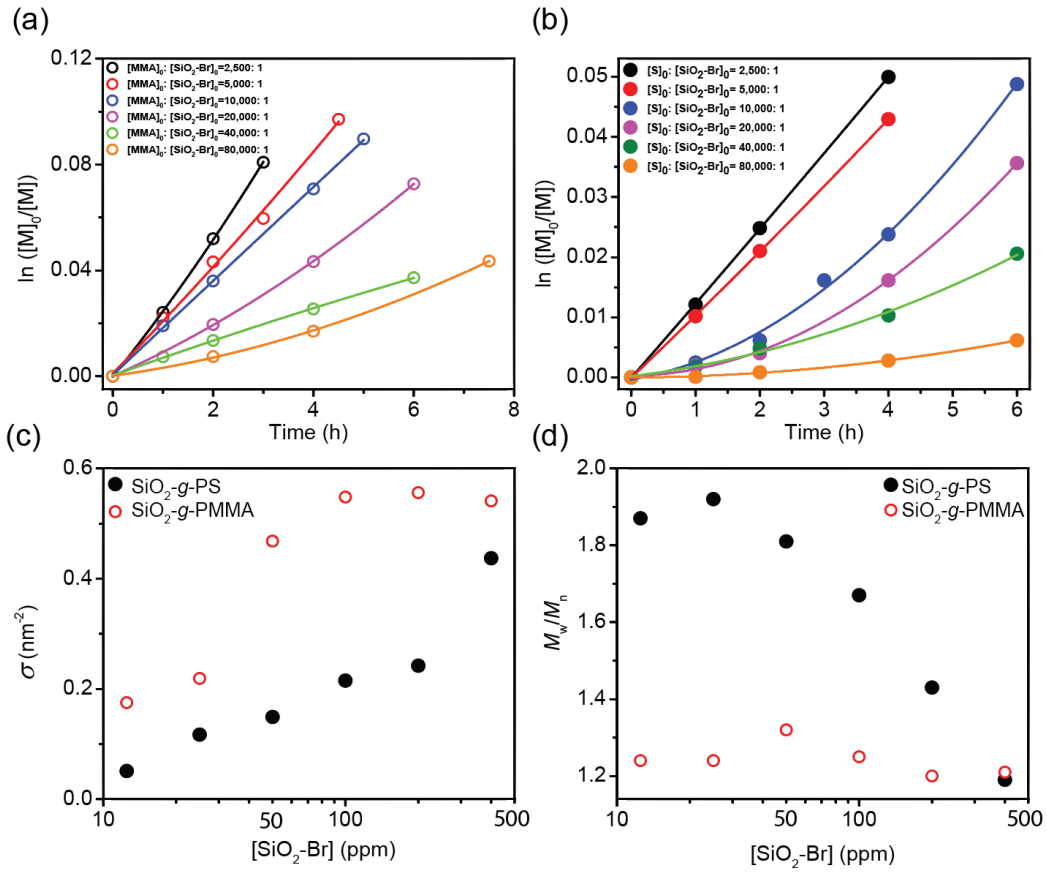

Figure 7.2. Polymerization of methyl methacrylate (MMA) and styrene (S) on SiO_2-Br nanoparticles by low Cu catalyst ATRP at different concentrations on SiO_2-Br. Conditions: $[M]_0/[SiO_2\text{-}Br]_0/[CuBr_2]_0/[Me_6TREN]_0/[Sn(EH)_2]_0$ = 4000/x/0.1/1/0.8, with x = 0.05-1.6 as indicated in the figures as $[M]_0/[SiO_2\text{-}Br]_0$ ratio. (a-b) Kinetics of SiO_2-*g*-PMMA/PS particle brushes synthesis and (c-d) plot of grafting density/MWD versus $[Sn(EH)_2]_0$.

Figure 7.2a and **Figure 7.2**b show the effect of different values of $[SiO_2\text{-}Br]_0$ on the rate of polymerization of particle brushes. The polymerization was faster when the initiator concentration increased, due to higher radical concentration (**Figure 7.2**a and **Figure 7.2**b). This is a peculiar behavior because the rates of an ARGET polymerization typically do not depend on initiator concentration, and it is further discussed below.[48]

Figure 7.2c shows that the grafting density decreased with decreasing $[SiO_2\text{-}Br]$. The effect was more pronounced for the SiO_2-*g*-PS system, for which the grafting density of the

particle brushes decreased to only 0.051 nm^{-2} when [SiO_2-Br] = 12.5 ppm. In contrast, the grafting density of SiO_2-*g*-PMMA remained stable at ~ 0.55 nm^{-2} for the highest [SiO_2-Br] and dropped only for [SiO_2-Br] < 100 ppm.

Not only grafting density, but also the uniformity of the grafted chains were affected by [SiO_2-Br]. For the SiO_2-*g*-PS system, dispersity increased with decreasing [SiO_2-Br] (**Figure 7.2**d). The dispersity of SiO_2-*g*-PMMA, however, was unaffected by the initiator loading.

Disproportionation and Coupling in the SiO_2-g-PMMA and SiO_2-g- PS Systems

Some of the differences between SiO_2-*g*-PMMA and SiO_2-*g*-PS particle brushes systems can be attributed to their termination mechanisms. As shown in **Scheme S7.1**, bimolecular radical termination can occur via combination or disproportionation.[49] According to literature,[50,51] at 60 ºC, the selectivity between disproportionation and combination (D/C) was 73/27 for methyl methacrylate polymerization and 14/86 for styrene polymerization. Therefore, more SiO_2-*g*-PS nanoparticles coupled. This termination caused an increase of the hydrodynamic size, as evidenced by the aggregation between nanoparticles detected in the TEM images (**Figure 7.3**c, d) and DLS traces (**Figure S7.3**), especially at the lowest SiO_2-Br concentrations (highest DP). On the other hand, few SiO_2-*g*-PMMA nanoparticles aggregated (**Figure 7.3**a, b). It should be mentioned that disproportionation fraction may increase in highly viscous media.[50]

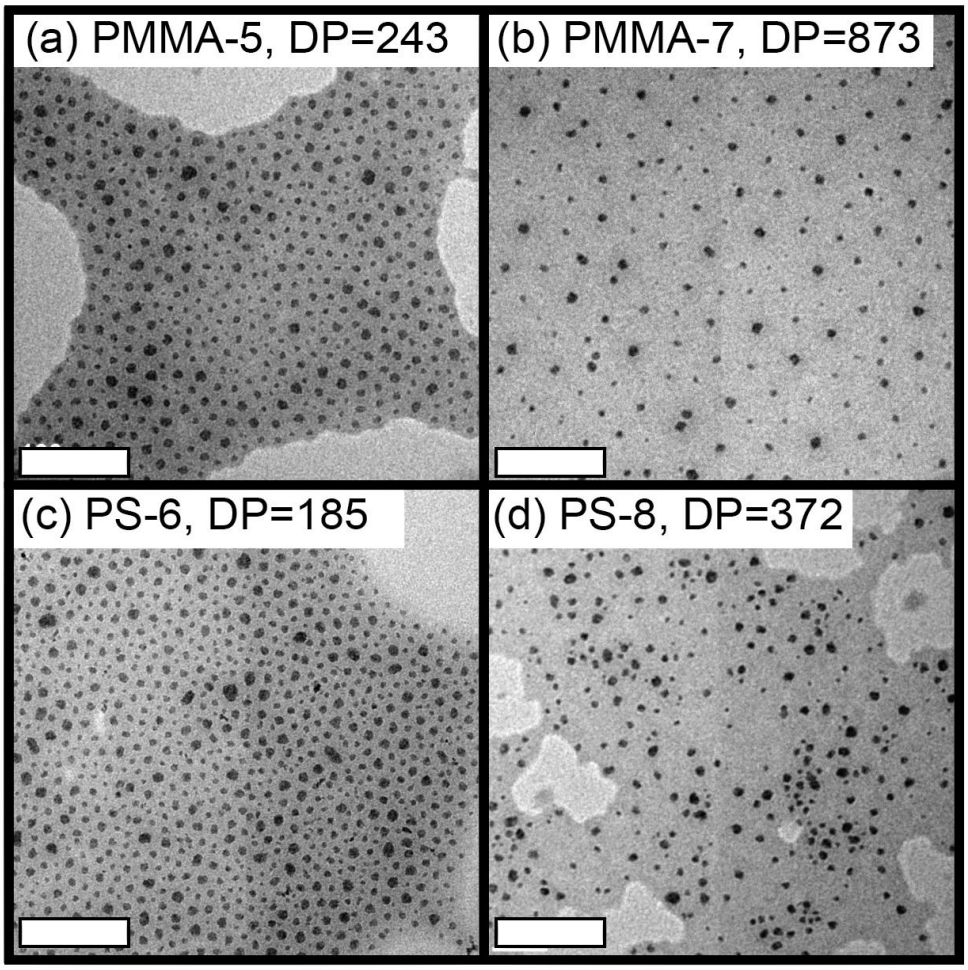

Figure 7.3. TEM images of monolayer films of SiO_2-*g*-PMMA particle brushes with different DP. (a) Entry PMMA-5, DP=243, M_w/M_n=1.21, σ=0.541 nm^{-1}, (b) Entry PMMA-7, DP=873, M_w/M_n=1.25, σ=0.548 nm^{-1}, (c) Entry PS-6, DP=185, M_w/M_n=1.19, σ=0.437 nm^{-1}, (d) EntryPS-8, DP=372, M_w/M_n=1.67, σ=0.215 nm^{-1}. Scale bar: 200 nm. Additional TEM images are presented in Figure S7.1.

Size of the Particle Brushes

The TEM images showed that the inter-particle distance increased as the DP of the grafted chains increased. The average particle core-*to*-core distance ($d_{\text{core-}to\text{-core}}$) is plotted versus DP in **Figure 7.4**a; for SiO_2-*g*-PMMA it increased linearly with the DP of the polymer brush. The $d_{\text{core-}to\text{-core}}$ could not be measured for the SiO_2-*g*-PS system because of excessive nanoparticle aggregation. The hydrodynamic volume (d_h) and the stability of the particle brush in solution were also evaluated by DLS in THF solutions (**Figure S7.3**). The intensity-weighted distribution of hydrodynamic sizes was measured in dilute solutions (1 mg/mL) to minimize hydrodynamic

interactions, which are negligible when the distance between adjacent particles is greater than the particle size.[52] **Figure 7.4**b depicts the correlation between the hydrodynamic size and DP. The hydrodynamic size is much larger than the particle core-*to*-core distance, which was measured in the solid-state where polymer chains collapse. Both TEM and DLS measurements reveal that SiO_2-*g*-PMMA samples are in semi-dilute particle brush (SDPB) regime, with slope of the diameter *vs.* DP of ~0.55 nm^{-2}.[53,54] It is noted that although the hydrodynamic size of SiO_2-*g*-PMMA particle brushes shows a clear linear trend with the DP, which agreed with the TEM analysis, the SiO_2-*g*-PS system shows poor correlation between hydrodynamic size and DP.

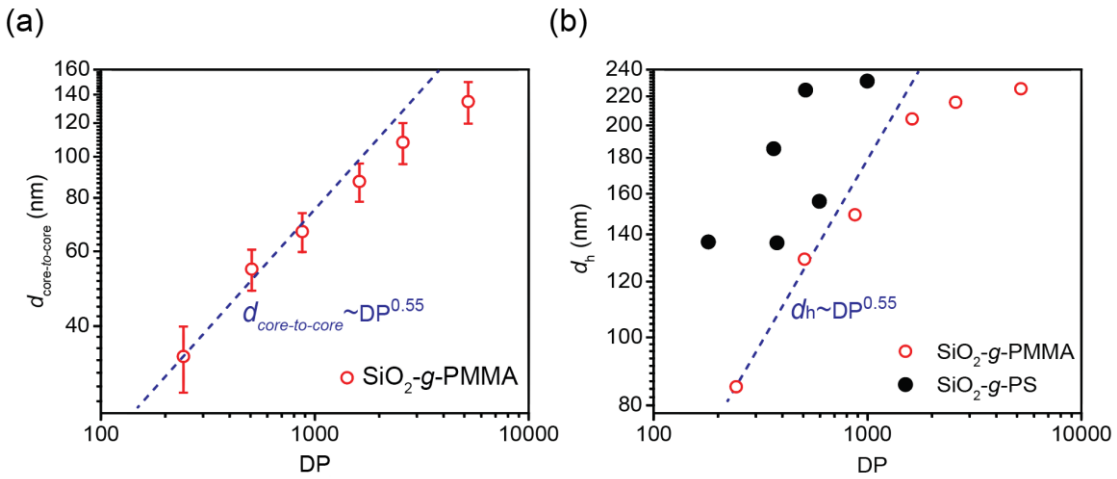

Figure 7.4. (a) Particle core-*to*-core distance of SiO_2-*g*-PMMA particle brushes versus DP, measured by TEM. (b) Hydrodynamic diameter (d_h) of SiO_2-*g*-PMMA/PS particle brushes versus DP, measured by DLS. The dashed lines represent a scaling with DP according to $d_h \sim DP^{0.55}$.

Model Linear Polymers Prepared at Different Initiator Concentrations

To further study the mechanism of polymerization of particle brushes at different initiator concentrations, a model polymerization system for linear homopolymers was investigated (**Table 7.3**). Linear PMMA and PS were prepared under the same conditions as used to prepare the SiO_2-grafted nanoparticles, except for the use of a small-molecule initiator, EBiB.

Figure 7.5a displays the semilogarithmic kinetic plots of model polymerization of methyl methacrylate at different initiator concentrations. When $[EBiB]_0$ was higher than 100 ppm, the plot was linear. However, conversion stopped after ca. 3h when $[EBiB]_0$ was lower than 100 ppm, suggesting that all chains terminated in this case. Further indicating the presence of a large fraction of terminated chains, dispersity increased with decreasing $[EBiB]_0$. Eq. 6 was used to estimate the percent of terminated chains, plotted in **Figure 7.5**d. As the $[EBiB]_0$ decreased, the dead PMMA chain fraction increased, reaching 100% for the lowest $[EBiB]_0$. The fraction of terminated chains was roughly inversely proportional to the initiator concentration. The polymerization of the corresponding SiO_2-*g*-PMMA was relatively slower (**Figure 7.2**a), thus the dead chain fraction is expected to be lower.

Table 7.3. Syntheses of Linear PMMA and PS

Entry[a]	[EBiB] (ppm)[b]	Time (h)	$[Sn(EH)_2]_0$ (ppm)[b]	conv (%)[c]	$M_{n,SEC}$[e]	M_w/M_n[e]	$M_{n,theo}$[e]	I_{eff} (%)	New Chains (ppm)
PMMA-L1	400	5	200	9.43	25,600	1.33	23,600	109	-
PMMA-L2	200	5	200	11.62	58,300	1.32	58,100	100	-
PMMA-L3	100	5	200	14.03	136,900	1.37	140,300	98	-
PMMA-L4	50	5	200	9.38	187300	1.39	187,600	100	-
PMMA-L5	25	5	200	6.86	249,300	1.89	274,400	91	-
PMMA-L6	12.5	5	200	5.23	392,000	2.11	418,400	94	-
PS-L1	400	8	200	5.52	12,800	1.23	14,352	111	44
PS-L2	200	8	200	4.87	21,500	1.22	25,300	118	36
PS-L3	100	8	200	4.95	37,800	1.24	51,480	136	36
PS-L4	50	8	200	6.49	84,000	1.39	135,000	161	31
PS-L5	25	8	200	3.76	52,800	1.26	156,400	297	49
PS-L6	12.5	8	200	5.06	99,700	1.52	421,000	422	40

[a] Reaction condition: $[M]_0/[EBiB]_0/[CuBr_2]_0/[Me_6TREN]_0/[Sn(EH)_2]_0$= 4000/x/0.1/1/0.8 with x = 0.05/0.1/0.2/0.4/0.8/1.6/3.2. 50 vol% M, 45 vol% anisole, 5 vol% DMF at 60 ºC. [b] Molar ratio *vs.* monomer. [c] Determined by gravimetric analysis. [d] $[S]_0$ = 4.3 M, $[MMA]_0$ = 4.7 M. [e] Determined by SEC.

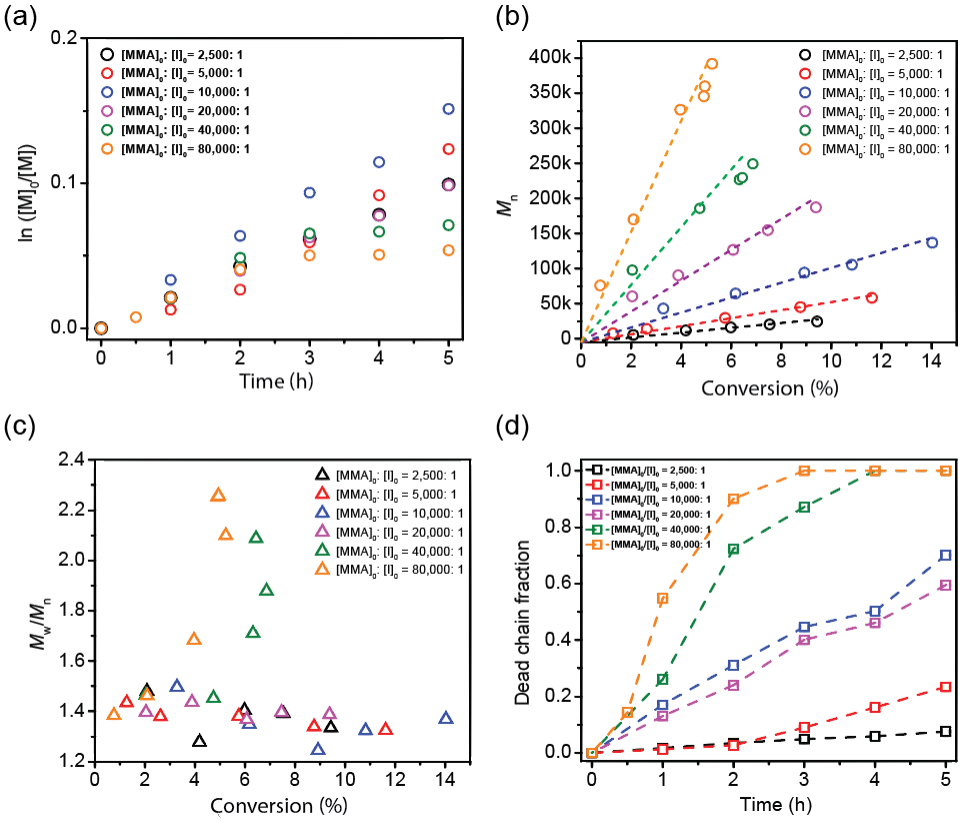

Figure 7.5. Results for linear homopolymer synthesis of methyl methacrylate (MMA) by low Cu catalyst ATRP under conditions $[MMA]_0/[EBiB]_0/[CuBr_2]_0/[Me_6TREN]_0/[Sn(EH)_2]_0$= 4000:x:0.1:1:0.8 with x = 0.05/0.1/0.2/0.4/0.8/1.6. 50 vol% MMA, 45 vol% anisole, 5 vol% DMF at 60 ºC. (a) Semilogarithmic kinetic plots for linear PMMA system, (b-c) number-average molecular weight and molecular weight distribution (M_w/M_n) for linear PMMA system, dash lines show the theoretical M_n *vs.* conversion plots and (d) plot of DCF vs. reaction time for linear homopolymer polymerization of MMA at 60 ºC. k_t = 9.0× $\mathbf{10^7}$ M^{-1} S^{-1} was obtained from the literature (Eq. 6). Only the DCF of the MMA system was analyzed because TSI prevented the use of Eq. 6 for styrene.

Table 7.3 and **Figure 7.6**a show that PS polymerizations reached lower conversions than PMMA because the rate constant of propagation of styrene (k_p = 341 M^{-1} s^{-1}) is smaller than that of methyl methacrylate (k_p = 833 M^{-1} s^{-1}) at 60 ºC.[51,55,56] As shown in **Figure 7.6**a, when the polymerization of styrene was targeting low DP, $[EBiB]_0$ >100 ppm, the kinetic plot was linear, and polymers with excellent control of molecular weight and low dispersity were obtained with

dispersity in the range 1.22~1.24. As the $[EBiB]_0$ was decreased below 100 ppm, the plot of M_n *vs.* conversion deviated from the linear trend. Moreover, dispersity was higher and M_n lower than $M_{n,theo}$ as conversion increased. Initiation efficiency increased as the initial [EBiB] decreased, **Table 7.3**, reaching apparent value as high as of 422% with 12.5 ppm $[EBiB]_0$. This value is so high because thermal-self initiation (TSI) of styrene introduces new chains (radicals) into the reaction, in addition to the radicals generated from the alkyl halide (**Scheme 7.1**).[57] The contribution of chain transfer to monomer is rather small for styrene and could be neglected.[58]

Scheme 7.1. Kinetic steps of radical generations in thermal self-initiated styrene polymerization

Themal-self initiation

$$3M \longrightarrow 2R^{\bullet}$$

Transfer

$$P_n^{\bullet} + M \longrightarrow D_t + P_l^{\bullet}$$

Previous studies have extensively explored the mechanisms for the self-initiation of both styrene and methyl methacrylate.[57,59,60] Pure styrene polymerizes at a rate of 0.1% per hour at 60 ºC.[61-63] For each styrene polymerization described in **Table 7.3**, the new chains generated by TSI were calculated from Eq.7. In each polymerization, TSI generated a roughly constant number of new chains, 39 ± 9 ppm in 8 h. These homopolymer impurities prevent good structure-property relationships in particle brush materials. They also indicate that the actual grafting density in brush particles could be even lower than estimated based on TGA and SEC data

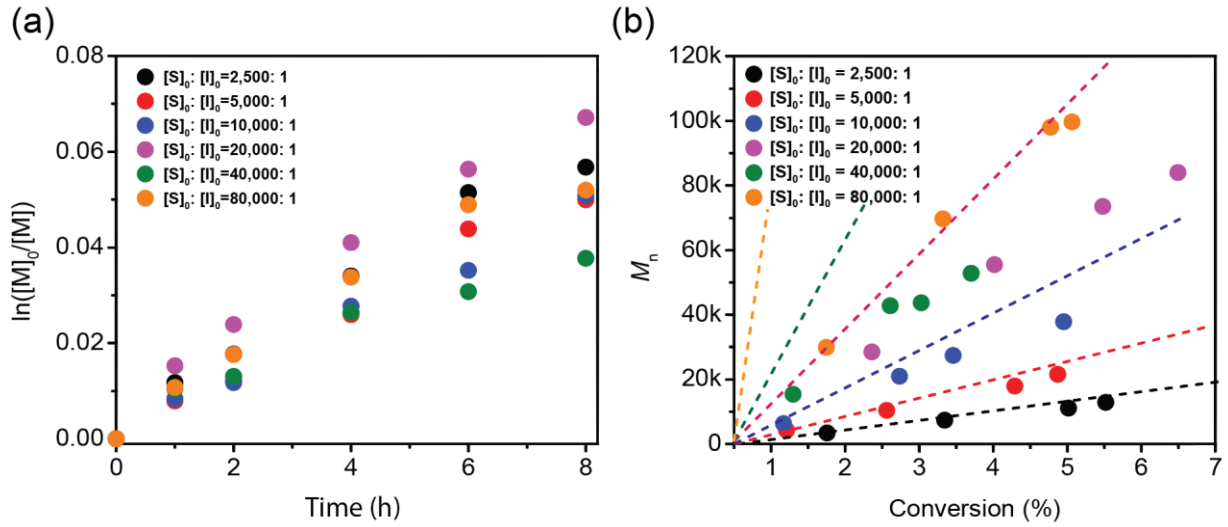

Figure 7.6. Results of polymerization of styrene (S) by low Cu catalyst ATRP under conditions $[S]_0/[EBiB]_0/[CuBr_2]_0/[Me_6TREN]_0/[Sn(EH)_2]_0$ = 4000:x:0.1:1:0.8 with x = 0.05/0.1/0.2/0.4/0.8/1.6. 50 vol% St, 45 vol% anisole, 5 vol% DMF at 60 ºC. (a) Semi-logarithmic kinetic plots for linear PS system and (b) number-average molecular weight for linear PS system, dash lines show the theoretical M_n *vs.* conversion plots.

Termination in Particle Brush vs. Linear Polymerization Systems

There are two main modes of termination in the polymer brush systems: (I) intraparticle and (II) interparticle (**Scheme 7.2**). For both the SiO_2-*g*-PS and SiO_2-*g*-PMMA systems, a large fraction of chains at low initiator concentration terminated. This degree of coupling should cause macroscopic gelation for multifunctional systems such as these nanoparticles that contains hundreds of initiating sites per particle. However, the polymerization solutions did not form a gel, and the TEM images showed little or no evidence of coupling, especially in the case of SiO_2-*g*-PMMA. This indicates that the particle brush system underwent mostly intraparticle termination (type I), with very limited interparticle termination (type II). Due to the size effect, the opportunity for two nanoparticles to collide and carry out bimolecular terminations is much lower than for two soluble low-molar-mass initiator molecules or linear chains. Moreover, the interparticle termination will be slower with increasing dilution of nanoparticles, while the intraparticle termination does not depend on the concentration of nanoparticles. Therefore,

compared to linear homopolymer systems, particle brush systems have fewer interparticle terminations which could be exploited to synthesize high molecular weight particle brushes.

Scheme 7.2. Terminations in SiO_2-*g*-PMMA and SiO_2-*g*-PS particle brush synthesis: orange dots represent C-Br chain ends.

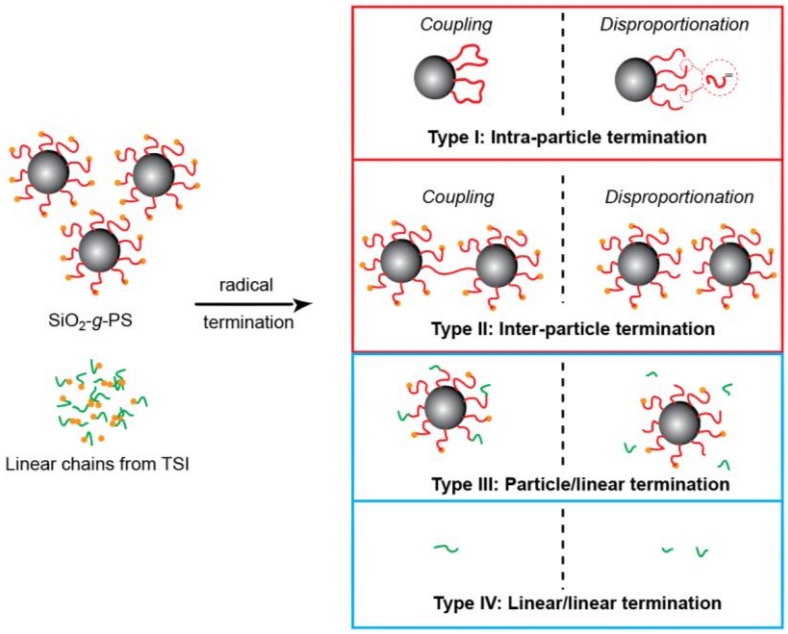

It should be noted that in the case of styrene, TSI introduces two additional possible termination pathways: (III) cross-termination between nanoparticles and small radicals/chains generated from TSI, and (IV) termination between two small radicals/chains generated from TSI (**Scheme 7.2**). Additionally, high viscosity may favor disproportionation.[50]

Grafting Density and Initiation Efficiency

The initiation efficiency/grafting density was different between the linear polymers (**Figure 7.5-7.6**a) and their particle brushes counterparts (**Figure 7.1-7.2**) prepared at progressively lower initiator concentrations. The initiation efficiency was ca. 100% for each linear polymerization with EBiB initiator, while the grafting density steeply diminished with [SiO_2-Br] in the particle-brush systems. This indicates that the diminished grafting density is a

peculiar property of the initiators localized on the particle surface. It is proposed that the change in grafting destiny is caused by the different localization of the ATRP initiators, which are dissolved in a solution for the linear system but grouped in the nanoparticle system. Such crowded initiators could respond differently to change of the chemical environment; in particular, they can be significantly affected by nearby tethered polymer chains. When diminishing the initiator concentration, longer and more uneven chains grow (dispersity increased in the linear model polymerizations as shown in **Table 7.3** and **Figure 7.5**c). Such longer and uneven chains shield neighboring initiating sites on the nanoparticle surface, thus causing the grafting to decrease.

The case of styrene is particularly interesting: molecular weights of linear PS are much lower than theoretical (i.e. >>100% I_{eff}), while they are much higher than theoretical in PS particle brushes (i.e. <<100% I_{eff} or grafting density). We ascribe both these peculiar behaviors to the effect of TSI. In the linear system, new radicals can efficiently initiate new chains. Conversely, in the nanoparticle system, new radicals introduce two new termination pathways (III and IV, **Scheme 7.2**) that are "faster" than particle-particle termination because they involve small radicals/chains. The short/small radicals generated by TSI will terminate the radicals on the surface, so the grafting density of nanoparticles will decrease. Additional investigations to calculate the extent of TSI-induced termination are underway in our laboratories.

Polymerization Rates

Typical kinetics of ARGET ATRP polymerization is limited by the reduction of Cu^{II}/L to Cu^{I}/L by the tin compounds (reducing agent, RA), which results in the polymerization following 1/2 order in both [RA] and [Cu^{II}].[47] Radical concentration can be expressed as follows:[46]

$$[R^{\bullet}] = \sqrt{\frac{k_{red}[RA][Cu^{II}/L]}{k_t}} \quad (8)$$

where k_{red} is the rate constant for the reduction of Cu^{II}/L by tin compounds. Both PMMA and PS particle brushes polymerization follow this reaction order in RA (**Figure 7.7**a), with slopes of 0.46 and 0.47, respectively. On the other hand, in ARGET reactions, the kinetics/rates should not depend on [RBr], since the activation of RBr by Cu^{I}/L should be faster than the rate of Cu^{II}/L reduction by RA. In this study, however, reactions with both particle brush and linear homopolymer synthesis were run at progressively lower [RBr], down to atypically low [RBr]. This has several consequences: first, when [RBr] < [Cu^{II}] << [RA], all chains can terminate; second, progressively decreasing of [RBr] can also change the rate-determining step, since activation of RBr by Cu^{I} or radical termination the may become slower than the reduction of Cu^{II}/L. Indeed, **Figure 7.7**b shows that rates start decreasing with [RBr] for all systems, except in the linear styrene polymerizations. In the linear PS system, rates do not drop because radical concentration is supplemented by thermal-self initiation.

The rates, however, drop significantly with decreasing [RBr] for both SiO_2-*g*-PS and SiO_2-*g*-PMMA (**Figure 7.7**b). This additional diminished polymerization rate could be caused by the different localization of radicals in the linear and nanoparticle systems. If we consider, for example, one linear and one particle brush system, at the same polymerization rate, the overall radical concentration is the same for the two systems, but the localization of radicals is different. For the linear polymers, the radical concentration diminishes uniformly in solution when targeting higher and higher DP. Conversely, the local radical concentration in the nanoparticle system is fixed by its grafting density. This “clustering” of radicals on the nanoparticle surface

could have the effect of increasing the local intraparticle termination rate, thus amplifying the reduction in polymerization rates (resulting in an artificially increased denominator in Eq. 8).

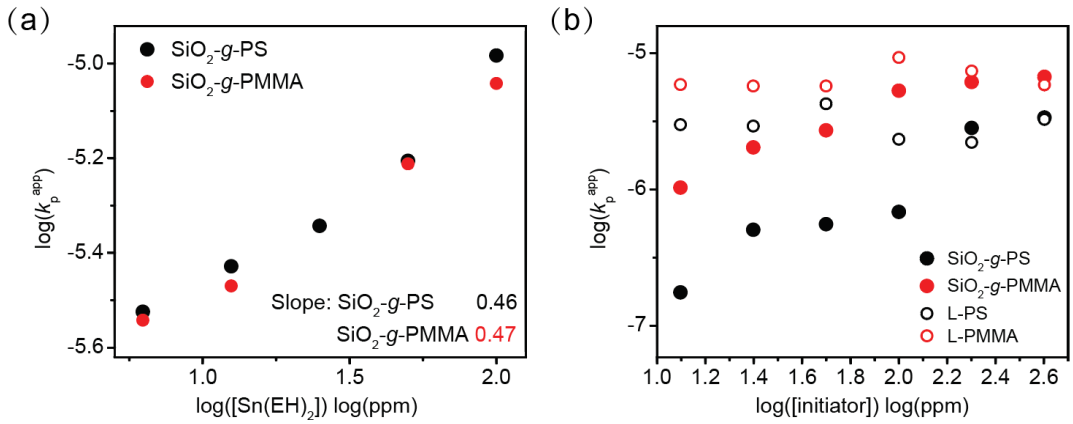

Figure 7.7. Kinetics study of SiO_2-*g*-PMMA/PS and linear PMMA/PS synthesis. (a) plot of log(k_{papp}) vs. log([Sn(EH)$_2$]); (b) plot of log(k_{papp}) vs. log([Initiator]), the first hour conversions were used to calculate k_p^{app}.

7.5. Supporting Information

Determining the density of the initiating site for SiO_2-Br nanoparticles

The concentration of initiating sites on the surface of silica nanoparticles was determined by model reactions (i.e. polymerization of SiO_2-*g*-PMMA, $[MMA]_0/[SiO_2\text{-}Br]_0/[CuBr_2]_0/[Me_6TREN]_0/[Sn(EH)_2]_0$=2000:1: 1:10:8 with 45 vol% anisole, 5 vol% DMF at 60 ºC) with certain amount of SiO_2-Br nanoparticles (e.g. with 100 mg). After purification, SEC and TGA were conducted to characterize the grafting density of the particle brushes. The particles used in the current study had grafting density ~ 0.95/0.65 nm^{-2}, the –Br (initiating site) concentration on the surface was assumed the same. Based on the average radius of nanoparticles, 7.9 nm, density of silica, 2.2 g/cm^3, the average molar mass of SiO_2-Br, are 3,670 g/mol (for PMMA1-4, PS-1-5), 5,370 g/mol (for PMMA-5-10 and PS-6-11).

Scheme S7.1. Synthesis of Polymer Grafted Particle Brushes with Low Catalyst Loadings ATRP

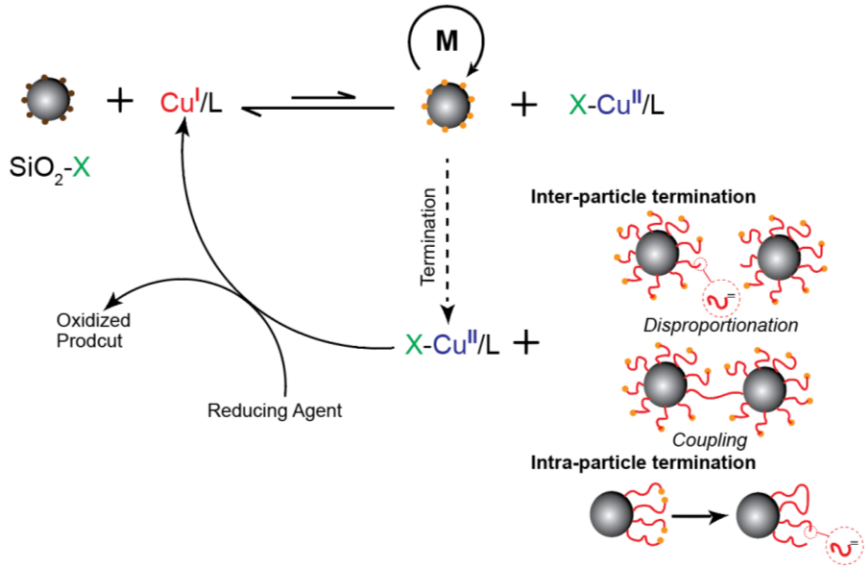

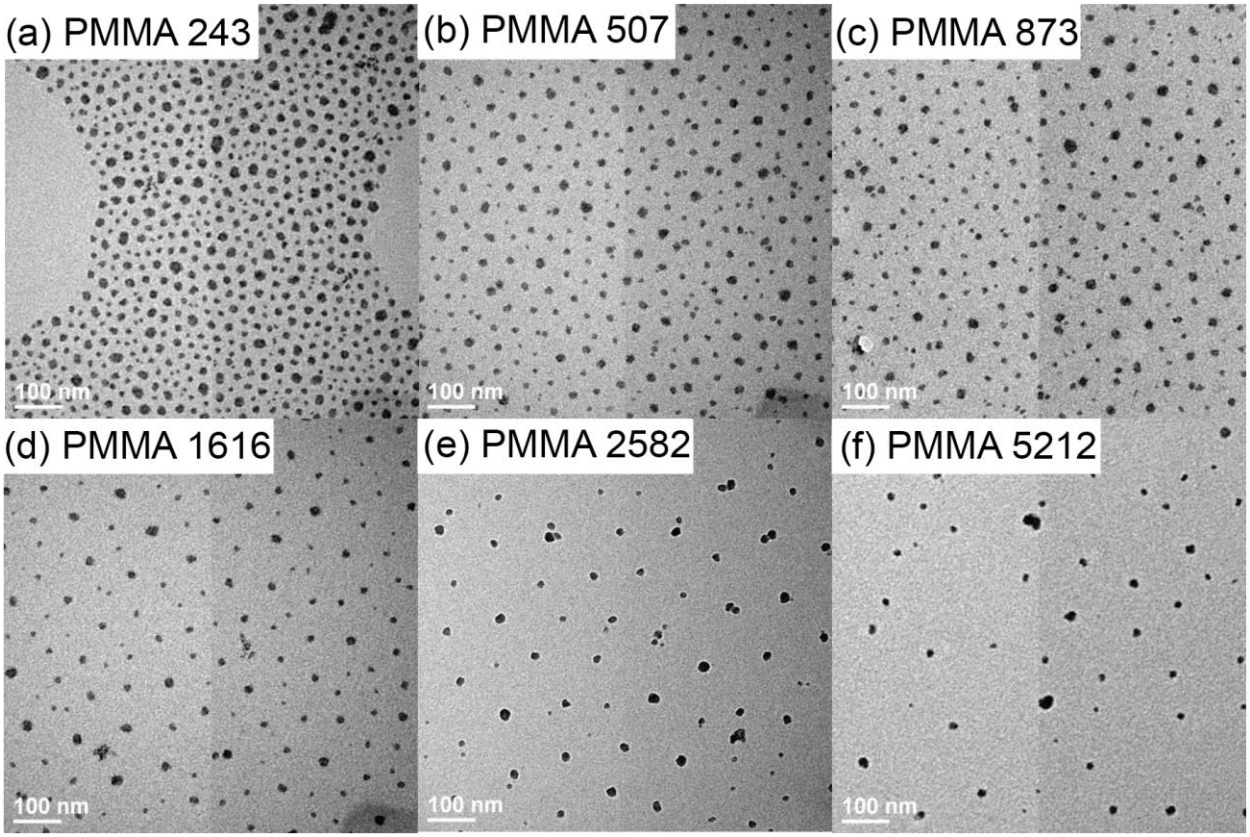

Figure S7.1. TEM images of SiO_2-*g*-PMMA particle brushes with various DP. (a) PMMA-5, DP=243, M_w/M_n=1.21, σ=0.541 nm^{-1}, (b) PMMA-6, DP=507, M_w/M_n=1.20, σ=0.556 nm^{-1}, (c) PMMA-7, DP=873, M_w/M_n=1.25, σ=0.548 nm^{-1}, (d) PMMA-8, DP=1616, M_w/M_n=1.32, σ=0.468 nm^{-1}, (e) PMMA-9, DP=2582, M_w/M_n=1.24, σ=0.219 nm^{-1}, (f) PMMA-10, DP=5212, M_w/M_n=1.24, σ=0.175 nm^{-1}.

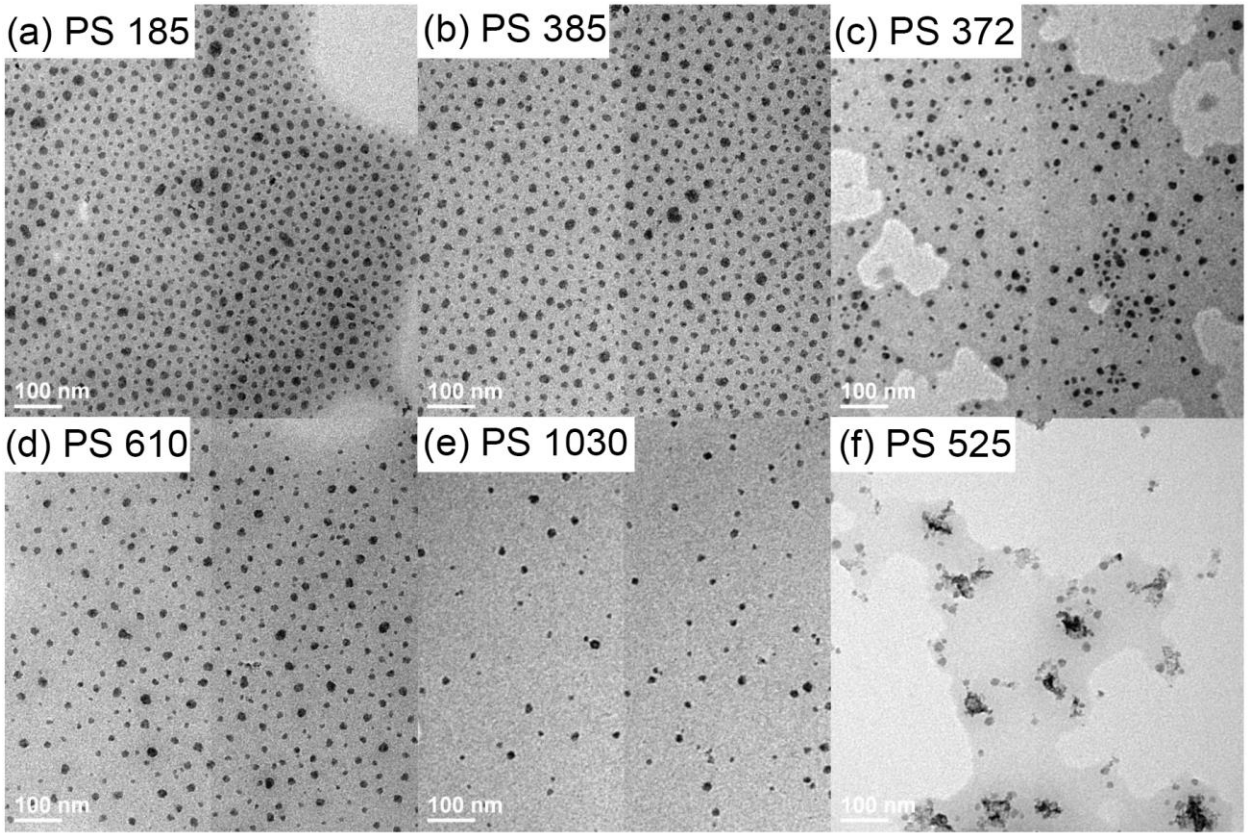

Figure S7.2. TEM images of SiO_2-*g*-PS particle brushes with different DP. (a) PS-6, DP=185, M_w/M_n=1.19, σ=0.437 nm^{-1}, (b) PS-7, DP=385, M_w/M_n=1.43, σ=0.242 nm^{-1}, (c) PS-8, DP=372, M_w/M_n=1.67, σ=0.215 nm^{-1}, (d) PS-9, DP=610, M_w/M_n=1.81, σ=0.149 nm^{-1}, (e) PS-10, DP=1030, M_w/M_n=1.92, σ=0.117 nm^{-1}, (f) PS-11, DP=525, M_w/M_n=1.87, σ=0.051 nm^{-1}.

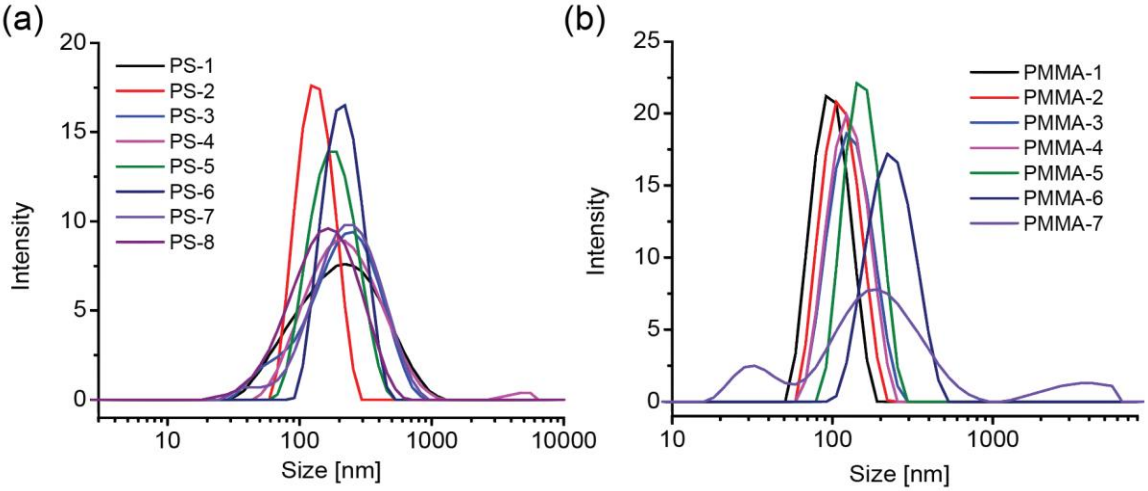

Figure S7.3. DLS traces (a) SiO_2-*g*-PS particle brushes, (b) SiO_2-*g*-PMMA particle brushes.

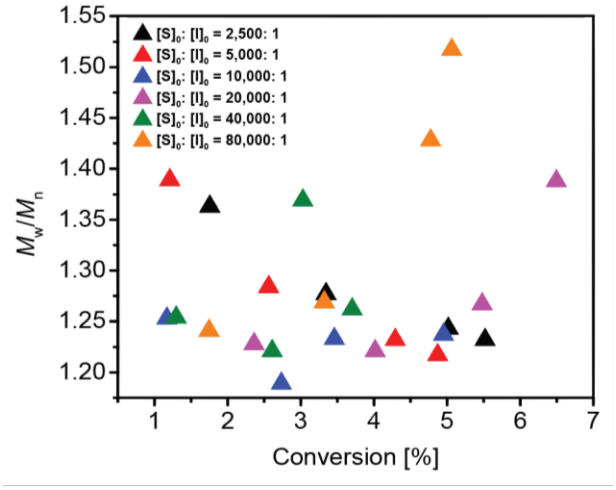

Figure S7.4. Plot of molecular weight distribution (M_w/M_n) vs. conversion for polymerization of styrene (S) by ARGET ATRP under conditions $[S]_0/[EBiB]_0/[CuBr_2]_0/[Me_6TREN]_0/[Sn(EH)_2]_0$=4000:0.05/0.1/0.2/0.4/0.8/1.6:0.1:1:0.8 with 45 vol% anisole, 5 vol% DMF at 60 ºC.

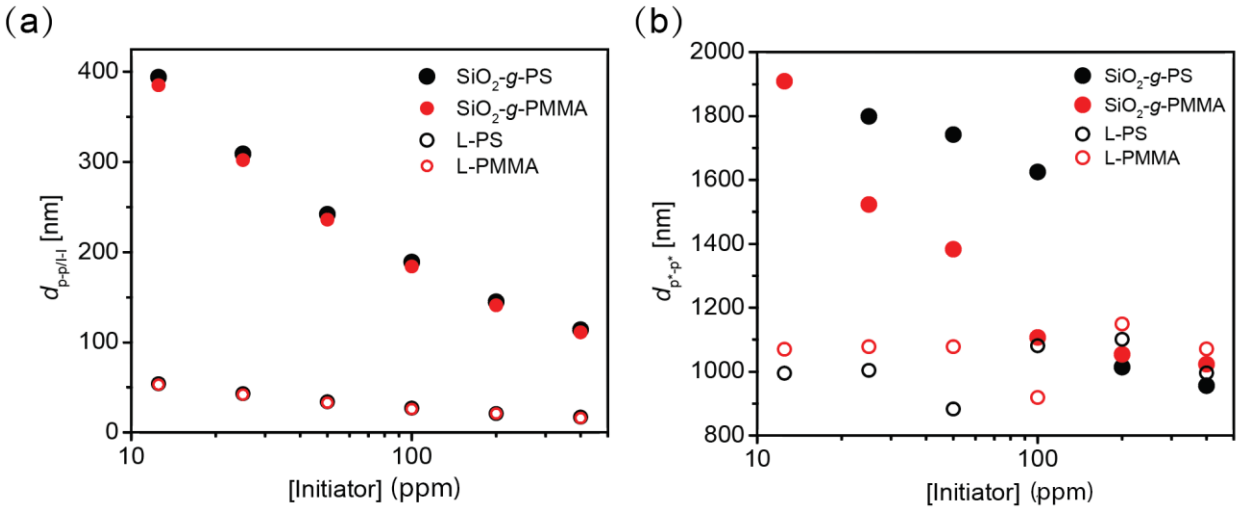

Figure S7.5. (a) the plot of the average distance of particle-*to*-particle/initiator-*to*-initiator to initiator concentration; (b) plot of the average distance of radical-*to*-radical to initiator concentration.

Table S7.1. Summary of kinetic parameters calculation

Particle Brushes

Entry	$[SiO_2\text{-}Br]_0$ (ppm)	$[SiO_2]_0$ (ppm)[a]	$[SiO_2]_0$ (M)[b]	k_p^{app}	$P^*(M)$[c]	$[P^*]/[RBr]$[d]	$d_{p\text{-}p}$ (nm)[e]	$d_{p^*\text{-}p^*}$ (nm)[f]
PMMA-1	250	0.34	1.59×10^{-6}	2.87×10^{-6}	3.44×10^{-9}	1.83×10^{-6}	161	1358
PMMA-2	250	0.34	1.59×10^{-6}	3.39×10^{-6}	4.07×10^{-9}	2.16×10^{-6}	161	1284
PMMA-3	250	0.34	1.59×10^{-6}	6.14×10^{-6}	7.36×10^{-9}	3.91×10^{-6}	161	1054
PMMA-4	250	0.34	1.59×10^{-6}	9.08×10^{-6}	1.09×10^{-8}	5.79×10^{-6}	161	925
PMMA-5	400	0.928	4.36×10^{-6}	6.69×10^{-6}	8.04×10^{-9}	4.28×10^{-6}	111	1023
PMMA-6	200	0.464	2.18×10^{-6}	6.13×10^{-6}	7.36×10^{-9}	7.83×10^{-6}	141	1054
PMMA-7	100	0.232	1.09×10^{-6}	5.29×10^{-6}	6.35×10^{-9}	1.35×10^{-5}	184	1107
PMMA-8	50	0.116	5.45×10^{-7}	2.71×10^{-6}	3.26×10^{-9}	1.39×10^{-5}	236	1383
PMMA-9	25	0.058	2.72×10^{-7}	2.03×10^{-6}	2.44×10^{-9}	2.07×10^{-5}	302	1523
PMMA-10	12.5	0.029	1.36×10^{-7}	1.03×10^{-6}	1.24×10^{-9}	2.11×10^{-5}	385	1909
PS-1	250	0.34	1.46×10^{-6}	2.99×10^{-6}	8.79×10^{-9}	5.11×10^{-6}	165	993
PS-2	250	0.34	1.46×10^{-6}	3.73×10^{-6}	1.09×10^{-8}	6.34×10^{-6}	165	925
PS-3	250	0.34	1.46×10^{-6}	4.54×10^{-6}	1.33×10^{-8}	7.73×10^{-6}	165	865
PS-4	250	0.34	1.46×10^{-6}	6.23×10^{-6}	1.83×10^{-8}	1.06×10^{-5}	165	778
PS-5	250	0.34	1.46×10^{-6}	1.04×10^{-5}	3.06×10^{-8}	1.78×10^{-5}	165	655
PS-6	400	0.928	3.99×10^{-6}	3.36×10^{-6}	9.85×10^{-9}	5.72×10^{-6}	114	956
PS-7	200	0.464	1.99×10^{-6}	2.82×10^{-6}	8.27×10^{-9}	9.61×10^{-6}	145	1014
PS-8	100	0.232	9.98×10^{-7}	6.83×10^{-7}	2.01×10^{-9}	4.67×10^{-6}	189	1625
PS-9	50	0.116	4.99×10^{-7}	5.55×10^{-7}	1.63×10^{-9}	7.58×10^{-6}	242	1742
PS-10	25	0.058	2.49×10^{-7}	5.05×10^{-7}	1.48×10^{-9}	1.38×10^{-5}	309	1799
PS-11	12.5	0.029	1.25×10^{-7}	$1.58*10^{-7}$	0.46×10^{-9}	1.51×10^{-6}	394	2662

Linear Homopolymers

Entry	$[I]_0$ (ppm)[a]	$[I]_0$ (M)[b]	k_p^{app}	$P^*(M)$[c]	$[P^*]/[RBr]$[d]	$d_{I\text{-}I}$ (nm)	$d_{p^*\text{-}p^*}$ (nm)[f]

						e	
PMMA-L1	400	1.88×10^{-3}	5.84×10^{-6}	7.01×10^{-9}	3.73×10^{-6}	16	1071
PMMA-L2	200	9.38×10^{-4}	3.69×10^{-6}	4.43×10^{-9}	4.72×10^{-6}	21	1149
PMMA-L3	100	4.69×10^{-4}	9.26×10^{-6}	1.11×10^{-8}	2.36×10^{-5}	26	919
PMMA-L4	50	2.34×10^{-4}	5.73×10^{-6}	6.87×10^{-9}	2.93×10^{-5}	33	1078
PMMA-L5	25	1.17×10^{-4}	5.73×10^{-6}	6.87×10^{-9}	5.87×10^{-5}	42	1078
PMMA-L6	12.5	5.86×10^{-5}	5.87×10^{-6}	7.04×10^{-9}	1.20×10^{-4}	53	1070
PS-L1	400	1.72×10^{-3}	3.26×10^{-6}	9.57×10^{-9}	5.56×10^{-6}	17	996
PS-L2	200	8.62×10^{-4}	2.21×10^{-6}	6.45×10^{-9}	7.51×10^{-6}	21	1101
PS-L3	100	4.31×10^{-4}	2.33×10^{-6}	6.83×10^{-9}	1.59×10^{-5}	27	1081
PS-L4	50	2.16×10^{-4}	4.24×10^{-6}	1.25×10^{-8}	5.81×10^{-5}	34	883
PS-L5	25	1.08×10^{-4}	2.91×10^{-6}	8.52×10^{-9}	7.93×10^{-5}	43	1004
PS-L6	12.5	5.39×10^{-5}	2.98×10^{-6}	8.75×10^{-9}	1.63×10^{-4}	54	995

[a] silica NPs or EBiB initiator's concentration in reaction solutions, unit in ppm. [b] silica NPs or EBiB initiator's concentration in reaction solutions, unit in M. [c] radical concentration. [d] ratio between radical concentration and initial initiator concentration. [e] average particle-*to*-particle or initiator-*to*-initiator distance in solution, calculated by Eq.(a). [f] average radical-*to*-radical distance in reaction solutions, calculated by Eq.(b).

Kinetic Parameters Calculation Procedures:

$[SiO_2]_0$ (silica nanoparticles concentration)

$[SiO_2\text{-}Br]$ (unit in ppm) is the concentration of NP initiators, $[SiO_2]_0$ (unit in ppm) is the concentration of SiO_2 NPs, which was calculated by $[SiO_2]_0 = \frac{[SiO_2-Br]_0}{\sigma\times4\pi r^2}$. σ is the maximum grafting density of the particle brushes (0.95 chains/nm^2 for PMMA1-4, PS-1-5, and 0.65 chains/nm^2 for PMMA-5-10 and PS-6-11), r is the radius of silica NPs (7.9 nm).

$[SiO_2]_0(unit\ in\ M) = [SiO_2]_0(unit\ in\ ppm) \times [MMA/S]_0 \times 10^{-6}$, $[MMA/S]_0$ is the monomer (MMA or S) concentration (unit in M), $[MMA]_0$=4.7 M, $[S]_0$=4.3 M.

k_p^{app} and P*

k_p^{app} and P* (radical concentration) were calculated by equations below by using first-hour conversion data points from kinetic plots (Figure 1a, 1b, 2a, 2b, 5a, and 6a).

$$\ln \frac{[\mathrm{M}]}{[\mathrm{M}]_0} = -k_{\mathrm{p}}^{\mathrm{app}} \times t$$

$$k_{\mathrm{p}}^{app} = k_{\mathrm{p}} \times [\mathrm{P}^{\bullet}]$$

$d_{p\text{-}p/I\text{-}I}$ and $d_{p^*\text{-}p^*}$

$d_{p\text{-}p/I\text{-}I}$ (average particle-*to*-particle or initiator-*to*-initiator distance, unit in nm) and $d_{p^*\text{-}p^*}$ (average radical-*to*-radical distance in reaction solutions, unit in nm) were calculated by equations below.

$$d_{p-p} = \sqrt{3} \times \sqrt[3]{\left(1.67 / [SiO_2]_0 (unit\ in\ M)\right)}\ ,\ d_{I-I} = \sqrt{3} \times \sqrt[3]{\left(1.67 / [I]_0 (unit\ in\ M)\right)} \qquad \text{(a)}$$

$$d_{p*-p*} = \sqrt{3} \times \sqrt[3]{\left(1.67 / [p*] (unit\ in\ M)\right)} \qquad \text{(b)}$$

Note:

1. The average volume (V, nm^3) of the space each particle/radical occupied is $1.67/[I]_0$ and $1.67/[P^*]_0$, unit of $[I]_0$ and $[P^*]_0$ is M.
2. For simplification, we assume the space each particle/radical occupied is cubic, the diagonal ($\sqrt{3} \times \sqrt[3]{V}$) of the cube is the average particle-*to*-particle/radical-*to*-radical distance.

7.6. Conclusions

SiO_2-*g*-PMMA and SiO_2-*g*-PS particle brushes were prepared by low Cu catalyst ATRP at different concentrations of reducing agent and $[SiO_2\text{-}Br]_0$ initiators. Increasing [RA] has the

expected effect of increasing polymerization rate while maintaining good polymerization control and high grafting density of the polymer brushes. The tethered polymer brushes have narrow molecular weight distributions.

On the other hand, decreasing $[SiO_2\text{-}Br]_0$ to target high degrees of polymerization has drastic effects on both particle morphology and polymerization kinetics. Reducing initiator concentration increases the impact of termination; the fraction terminated chains are inversely proportional to $[SiO_2\text{-}Br]_0$. This resulted in substantial nanoparticle aggregation, especially in the case of SiO_2-*g*-PS. It appears that the differences between SiO_2-*g*-PMMA and SiO_2-*g*-PS are due to their different termination mechanisms, with a larger fraction of the polystyrene chains terminating by bimolecular coupling. In the particle brush system, the increased inter-particle coupling will lead to the formation of clusters and ultimately particle aggregation.

The results of the synthesis of linear PMMA and PS homopolymers suggest that particle brush systems have less interparticle coupling termination due to the localization of initiation sites on the surface of nanoparticles and lower opportunities of collisions between nanoparticles compared to small initiator molecules. Decreased interparticle coupling could be exploited to synthesize high molecular weight (M_n> 500k) and low dispersity particle brushes without gelation.

Grafting density decreases with decreasing $[SiO_2\text{-}Br]_0$. SiO_2-*g*-PMMA particle brushes had a higher grafting density than SiO_2-*g*-PS. The new chains generated from thermal-self initiation of styrene would possibly result in cross-termination with radicals on nanoparticles resulting in a reduction in grafting density.

The polymerization rate diminished with initiator concentration, unlike in typical ARGET ATRP that does not depend on initiator concentration. The kinetic study suggests that when initiator concentration is very low (< 100 ppm), the rate-determining step was not the reduction by RA, as typical in ARGET ATRP. This is especially magnified for particle brush systems due to the localized initiators and propagating radicals on the particle surfaces.

7.7. References

(1) Schadler, L. S.; Kumar, S. K.; Benicewicz, B. C.; Lewis, S. L.; Harton, S. E., Designed Interfaces in Polymer Nanocomposites: A Fundamental Viewpoint, *MRS Bulletin* **2011**, *32*, 335-340.

(2) Lu, Y.; Mei, Y.; Drechsler, M.; Ballauff, M., Thermosensitive Core-Shell Particles as Carriers for Ag Nanoparticles: Modulating the Catalytic Activity by a Phase Transition in Networks, *Angewandte Chemie International Edition* **2006**, *45*, 813-816.

(3) Rösler, A.; Vandermeulen, G. W. M.; Klok, H.-A., Advanced drug delivery devices via self-assembly of amphiphilic block copolymers, *Advanced Drug Delivery Reviews* **2001**, *53*, 95-108.

(4) Gan, L.; Heggen, M.; Rudi, S.; Strasser, P., Core-Shell Compositional Fine Structures of Dealloyed PtxNi1–x Nanoparticles and Their Impact on Oxygen Reduction Catalysis, *Nano Letters* **2012**, *12*, 5423-5430.

(5) Ghosh, B.; Sahu, S.; Pal, A. J., Core−Shell Nanoparticles: An Approach to Enhance Electrical Bistability, *The Journal of Physical Chemistry C* **2008**, *112*, 11290-11294.

(6) Zhang, X.; Zhao, X.; Luckanagul, J. A.; Yan, J.; Nie, Y.; Lee, L. A.; Wang, Q., Polymer–Protein Core-Shell Nanoparticles for Enhanced Antigen Immunogenicity, *ACS Macro Letters* **2017**, *6*, 442-446.

(7) Askar, S.; Li, L.; Torkelson, J. M., Polystyrene-Grafted Silica Nanoparticles: Investigating the Molecular Weight Dependence of Glass Transition and Fragility Behavior, *Macromolecules* **2017**, *50*, 1589-1598.

(8) Vaia, R. A.; Maguire, J. F., Polymer Nanocomposites with Prescribed Morphology: Going beyond Nanoparticle-Filled Polymers, *Chemistry of Materials* **2007**, *19*, 2736-2751.

(9) Bockstaller, M. R.; Mickiewicz, R. A.; Thomas, E. L., Block Copolymer Nanocomposites: Perspectives for Tailored Functional Materials, *Advanced Materials* **2005**, *17*, 1331-1349.

(10) Smith, G. D.; Bedrov, D., Dispersing Nanoparticles in a Polymer Matrix: Are Long, Dense Polymer Tethers Necessary? *Langmuir* **2009**, *25*, 11239-11243.

(11) Lin, C.-C.; Ohno, K.; Clarke, N.; Winey, K. I.; Composto, R. J., Macromolecular Diffusion through a Polymer Matrix with Polymer-Grafted Chained Nanoparticles, *Macromolecules* **2014**, *47*, 5357-5364.

(12) Kumar, S. K.; Jouault, N.; Benicewicz, B.; Neely, T., Nanocomposites with Polymer Grafted Nanoparticles, *Macromolecules* **2013**, *46*, 3199-3214.

(13) Tchoul, M. N.; Fillery, S. P.; Koerner, H.; Drummy, L. F.; Oyerokun, F. T.; Mirau, P. A.; Durstock, M. F.; Vaia, R. A., Assemblies of Titanium Dioxide-Polystyrene Hybrid Nanoparticles for Dielectric Applications, *Chemistry of Materials* **2010**, *22*, 1749-1759.
(14) Lü, C.; Guan, C.; Liu, Y.; Cheng, Y.; Yang, B., PbS/Polymer Nanocomposite Optical Materials with High Refractive Index, *Chemistry of Materials* **2005**, *17*, 2448-2454.
(15) Matyjaszewski, K.; Dong, H.; Jakubowski, W.; Pietrasik, J.; Kusumo, A., Grafting from Surfaces for "Everyone": ARGET ATRP in the Presence of Air, *Langmuir* **2007**, *23*, 4528-4531.
(16) Matyjaszewski, K.; Miller, P. J.; Shukla, N.; Immaraporn, B.; Gelman, A.; Luokala, B. B.; Siclovan, T. M.; Kickelbick, G.; Vallant, T.; Hoffmann, H.; Pakula, T., Polymers at Interfaces: Using Atom Transfer Radical Polymerization in the Controlled Growth of Homopolymers and Block Copolymers from Silicon Surfaces in the Absence of Untethered Sacrificial Initiator, *Macromolecules* **1999**, *32*, 8716-8724.
(17) Goncalves, G.; Marques, P. A. A. P.; Barros-Timmons, A.; Bdkin, I.; Singh, M. K.; Emami, N.; Gracio, J., Graphene oxide modified with PMMA via ATRP as a reinforcement filler, *Journal of Materials Chemistry* **2010**, *20*, 9927-9934.
(18) Berger, S.; Synytska, A.; Ionov, L.; Eichhorn, K.-J.; Stamm, M., Stimuli-Responsive Bicomponent Polymer Janus Particles by "Grafting from"/"Grafting to" Approaches, *Macromolecules* **2008**, *41*, 9669-9676.
(19) Liu, Y.; Klep, V.; Zdyrko, B.; Luzinov, I., Polymer Grafting via ATRP Initiated from Macroinitiator Synthesized on Surface, *Langmuir* **2004**, *20*, 6710-6718.
(20) Krishnamoorti, R.; Vaia, R. A.; Giannelis, E. P., Structure, and Dynamics of Polymer-Layered Silicate Nanocomposites, *Chemistry of Materials* **1996**, *8*, 1728-1734.
(21) Hui, C. M.; Pietrasik, J.; Schmitt, M.; Mahoney, C.; Choi, J.; Bockstaller, M. R.; Matyjaszewski, K., Surface-Initiated Polymerization as an Enabling Tool for Multifunctional (Nano-)Engineered Hybrid Materials, *Chemistry of Materials* **2014**, *26*, 745-762.
(22) Khabibullin, A.; Mastan, E.; Matyjaszewski, K.; Zhu, S., *Surface-Initiated Atom Transfer Radical Polymerization*; In *Controlled Radical Polymerization at and from Solid Surfaces*; Vana, P., Ed.; Springer International Publishing: Cham, 2016; pp 29-76.
(23) Tsujii, Y.; Ohno, K.; Yamamoto, S.; Goto, A.; Fukuda, T., *Structure, and Properties of High-Density Polymer Brushes Prepared by Surface-InitiatedLiving Radical Polymerization*; In *Surface-Initiated Polymerization I*; Jordan, R., Ed.; Springer Berlin Heidelberg: Berlin, Heidelberg, 2006; pp 1-45.
(24) Zoppe, J. O.; Ataman, N. C.; Mocny, P.; Wang, J.; Moraes, J.; Klok, H.-A., Surface-Initiated Controlled Radical Polymerization: State-of-the-Art, Opportunities, and Challenges in Surface and Interface Engineering with Polymer Brushes, *Chemical Reviews* **2017**, *117*, 1105-1318.
(25) Barbey, R.; Lavanant, L.; Paripovic, D.; Schüwer, N.; Sugnaux, C.; Tugulu, S.; Klok, H.-A., Polymer Brushes via Surface-Initiated Controlled Radical Polymerization: Synthesis, Characterization, Properties, and Applications, *Chemical Reviews* **2009**, *109*, 5437-5527.
(26) Boyer, C.; Corrigan, N. A.; Jung, K.; Nguyen, D.; Nguyen, T.-K.; Adnan, N. N. M.; Oliver, S.; Shanmugam, S.; Yeow, J., Copper-Mediated Living Radical Polymerization (Atom Transfer Radical Polymerization and Copper(0) Mediated Polymerization): From Fundamentals to Bioapplications, *Chemical Reviews* **2016**, *116*, 1803-1949.
(27) Matyjaszewski, K.; Xia, J., Atom Transfer Radical Polymerization, *Chemical Reviews* **2001**, *101*, 2921-2990.

(28) Kamigaito, M.; Ando, T.; Sawamoto, M., Metal-Catalyzed Living Radical Polymerization, *Chemical Reviews* **2001**, *101*, 3689-3746.
(29) Matyjaszewski, K., Atom Transfer Radical Polymerization (ATRP): Current Status and Future Perspectives, *Macromolecules* **2012**, *45*, 4015-4039.
(30) Wang, J.-S.; Matyjaszewski, K., Controlled/"living" radical polymerization. atom transfer radical polymerization in the presence of transition-metal complexes, *Journal of the American Chemical Society* **1995**, *117*, 5614-5615.
(31) Mueller, L.; Matyjaszewski, K., Reducing Copper Concentration in Polymers Prepared via Atom Transfer Radical Polymerization, *Macromolecular Reaction Engineering* **2010**, *4*, 180-185.
(32) Kwak, Y.; Magenau, A. J. D.; Matyjaszewski, K., ARGET ATRP of Methyl Acrylate with Inexpensive Ligands and ppm Concentrations of Catalyst, *Macromolecules* **2011**, *44*, 811-819.
(33) Tsarevsky, N. V.; Jakubowski, W., Atom transfer radical polymerization of functional monomers employing Cu ‐ based catalysts at low concentration: Polymerization of glycidyl methacrylate, *Journal of Polymer Science Part A: Polymer Chemistry* **2011**, *49*, 918-925.
(34) Jakubowski, W.; Min, K.; Matyjaszewski, K., Activators Regenerated by Electron Transfer for Atom Transfer Radical Polymerization of Styrene, *Macromolecules* **2006**, *39*, 39-45.
(35) Tsarevsky, N. V.; Matyjaszewski, K., “Green” Atom Transfer Radical Polymerization: From Process Design to Preparation of Well-Defined Environmentally Friendly Polymeric Materials, *Chemical Reviews* **2007**, *107*, 2270-2299.
(36) Matyjaszewski, K.; Jakubowski, W.; Min, K.; Tang, W.; Huang, J.; Braunecker, W. A.; Tsarevsky, N. V., Diminishing catalyst concentration in atom transfer radical polymerization with reducing agents, *Proceedings of the National Academy of Sciences* **2006**, *103*, 15309-15314.
(37) Jakubowski, W.; Matyjaszewski, K., Activators Regenerated by Electron Transfer for Atom-Transfer Radical Polymerization of (Meth)acrylates and Related Block Copolymers, *Angewandte Chemie International Edition* **2006**, *45*, 4482-4486.
(38) Ding, H.; Park, S.; Zhong, M.; Pan, X.; Pietrasik, J.; Bettinger, C. J.; Matyjaszewski, K., Facile Arm-First Synthesis of Star Block Copolymers via ARGET ATRP with ppm Amounts of Catalyst, *Macromolecules* **2016**, *49*, 6752-6760.
(39) Burdyńska, J.; Cho, H. Y.; Mueller, L.; Matyjaszewski, K., Synthesis of Star Polymers Using ARGET ATRP, *Macromolecules* **2010**, *43*, 9227-9229.
(40) Hansson, S.; Östmark, E.; Carlmark, A.; Malmström, E., ARGET ATRP for Versatile Grafting of Cellulose Using Various Monomers, *ACS Applied Materials & Interfaces* **2009**, *1*, 2651-2659.
(41) Jakubowski, W.; Matyjaszewski, K., Activators Regenerated by Electron Transfer for Atom ‐ Transfer Radical Polymerization of (Meth)acrylates and Related Block Copolymers, *Angewandte Chemie* **2006**, *118*, 4594-4598.
(42) Wang, Y.; Soerensen, N.; Zhong, M.; Schroeder, H.; Buback, M.; Matyjaszewski, K., Improving the “Livingness” of ATRP by Reducing Cu Catalyst Concentration, *Macromolecules* **2013**, *46*, 683-691.
(43) Pyun, J.; Jia, S.; Kowalewski, T.; Patterson, G. D.; Matyjaszewski, K., Synthesis and Characterization of Organic/Inorganic Hybrid Nanoparticles: Kinetics of Surface-Initiated Atom

Transfer Radical Polymerization and Morphology of Hybrid Nanoparticle Ultrathin Films, *Macromolecules* **2003**, *36*, 5094-5104.
(44) Turgman-Cohen, S.; Genzer, J., Simultaneous Bulk- and Surface-Initiated Controlled Radical Polymerization from Planar Substrates, *Journal of the American Chemical Society* **2011**, *133*, 17567-17569.
(45) Zhong, M.; Matyjaszewski, K., How Fast Can a CRP Be Conducted with Preserved Chain End Functionality?, *Macromolecules* **2011**, *44*, 2668-2677.
(46) Keating Iv, J. J.; Lee, A.; Belfort, G., Predictive Tool for Design and Analysis of ARGET ATRP Grafting Reactions, *Macromolecules* **2017**, *50*, 7930-7939.
(47) Li, X.; Wang, W.-J.; Li, B.-G.; Zhu, S., Kinetics and Modeling of Solution ARGET ATRP of Styrene, Butyl Acrylate, and Methyl Methacrylate, *Macromolecular Reaction Engineering* **2011**, *5*, 467-478.
(48) Jakubowski, W.; Matyjaszewski, K., Activator Generated by Electron Transfer for Atom Transfer Radical Polymerization, *Macromolecules* **2005**, *38*, 4139-4146.
(49) Ribelli, T. G.; Augustine, K. F.; Fantin, M.; Krys, P.; Poli, R.; Matyjaszewski, K., Disproportionation or Combination? The Termination of Acrylate Radicals in ATRP, *Macromolecules* **2017**, *50*, 7920-7929.
(50) Nakamura, Y.; Yamago, S., Termination Mechanism in the Radical Polymerization of Methyl Methacrylate and Styrene Determined by the Reaction of Structurally Well-Defined Polymer End Radicals, *Macromolecules* **2015**, *48*, 6450-6456.
(51) Buback, M.; Gilbert, R. G.; Hutchinson, R. A.; Klumperman, B.; Kuchta, F.; Manders, B. G.; O'Driscoll, K. F.; Russell, G. T.; Schweer, J., Critically evaluated rate coefficients for free‐radical polymerization, 1. Propagation rate coefficient for styrene, *Macromolecular Chemistry and Physics* **1995**, *196*, 3267-3280.
(52) Finkenauer, L. R.; Lu, Q.; Hakem, I. F.; Majidi, C.; Bockstaller, M. R., Analysis of the Efficiency of Surfactant-Mediated Stabilization Reactions of EGaIn Nanodroplets, *Langmuir* **2017**, *33*, 9703-9710.
(53) Daoud, M.; Cotton, J. P., Star-shaped polymers: a model for the conformation and its concentration dependence, *Journal de Physique* **1982**, *43*, 531-538.
(54) Choi, J.; Dong, H.; Matyjaszewski, K.; Bockstaller, M. R., Flexible Particle Array Structures by Controlling Polymer Graft Architecture, *Journal of the American Chemical Society* **2010**, *132*, 12537-12539.
(55) Buback, M.; Kurz, C. H.; Schmaltz, C., the Pressure dependence of propagation rate coefficients in free-radical homopolymerizations of methyl acrylate and dodecyl acrylate, *Macromolecular Chemistry and Physics* **1998**, *199*, 1721-1727.
(56) Beuermann, S.; Buback, M.; Davis, T. P.; García, N.; Gilbert, R. G.; Hutchinson, R. A.; Kajiwara, A.; Kamachi, M.; Lacík, I.; Russell, G. T., Critically Evaluated Rate Coefficients for Free‐Radical Polymerization, 4, *Macromolecular Chemistry and Physics* **2003**, *204*, 1338-1350.
(57) Tchoul, M. N.; Dalton, M.; Tan, L.-S.; Dong, H.; Hui, C. M.; Matyjaszewski, K.; Vaia, R. A., Enhancing the fraction of grafted polystyrene on silica hybrid nanoparticles, *Polymer* **2012**, *53*, 79-86.
(58) Lutz, J.-F.; Matyjaszewski, K., Nuclear magnetic resonance monitoring of chain-end functionality in the atom transfer radical polymerization of styrene, *Journal of Polymer Science Part A: Polymer Chemistry* **2005**, *43*, 897-910.

(59) Russell, K. E.; Tobolsky, A. V., Thermal Initiation of Styrene Polymerization, *Journal of the American Chemical Society* **1953**, *75*, 5052-5054.
(60) Walling, C.; Briggs, E. R., The Thermal Polymerization of Methyl Methacrylate, *Journal of the American Chemical Society* **1946**, *68*, 1141-1145.
(61) Srinivasan, S.; Lee, M. W.; Grady, M. C.; Soroush, M.; Rappe, A. M., Computational Evidence for Self-Initiation in Spontaneous High-Temperature Polymerization of Methyl Methacrylate, *The Journal of Physical Chemistry A* **2011**, *115*, 1125-1132.
(62) Breitenbach, J. W.; Raff, R., Über den Wand‐Einfluß bei der thermischen Polymerisation ungesättigter Ester, *Berichte der Deutschen Chemische Gesellschaft (A and B Series)* **1936**, *69*, 1107-1110.
(63) Khuong, K. S.; Jones, W. H.; Pryor, W. A.; Houk, K. N., The Mechanism of the Self-Initiated Thermal Polymerization of Styrene. Theoretical Solution of a Classic Problem, *Journal of the American Chemical Society* **2005**, *127*, 1265-1277.

Chapter 8 Control of Dispersity and Grafting Density of Particle Brushes by Variation of ATRP Catalyst Concentration

8.1. Preface

Silica particles with grafted poly(methyl methacrylate) brushes, SiO_2-*g*-PMMA, were prepared *via* activator regeneration by electron transfer (ARGET) atom transfer radical polymerization (ATRP). The grafting density and dispersity of the polymer brushes were tuned by the initial ATRP catalyst concentration ($[Cu^{II}/L]_0$). Sparsely grafted particle brushes, which also displayed an anisotropic string-like structure in TEM images, were obtained at very low catalyst concentrations, $[Cu^{II}/L]_0 < 1$ ppm. The effect of the initial catalyst concentration on dispersity and initiation efficiency in the particle brush system was similar to that observed in the synthesis of linear PMMA homopolymers. The kinetic study revealed a transition from controlled radical polymerization to a less controlled process at low monomer conversion, when the $[Cu^{II}/L]_0$ decreased below ca. 10 ppm.

In this chapter, the effect of Cu^{II} catalyst concentration on the dispersity of PMMA polymer ligands on the SiO_2-*g*-PMMA particle brushes is discussed. I performed all synthetic work and the characterization in the project. I would like to thank especially my collaborators, Jiajun Yan for his intellectual contribution at the initial stage of this project. Tong Liu, Qiangbing Wei, Julian Sobieski, and Marco Fantin assisted in the synthesis work. Sipei Li and Jianing Wu assisted in the characterization work. Mateusz Olszewski helped to design the Scheme and Table of Contents. Professor Matyjaszewski and Professor Bockstaller conceived and organized the project and together with Jiajun and I wrote the manuscript.

This project was published in *ACS Macro Letters*, (**Zongyu Wang**, Jiajun Yan, Tong Liu, Qiangbing Wei, Sipei Li, Mateusz Olszewski, Jianing Wu, Julian Sobieski, Marco Fantin, Michael R Bockstaller, Krzysztof Matyjaszewski, "Control of Dispersity and Grafting Density of Particle Brushes by Variation of ATRP Catalyst Concentration", *ACS Macro Letters*, **2019**, 8, 859-864.).

This work was supported by NSF (DMR 1501324 and DMR 1410845), the Department of Energy (DE-EE0006702), as well as the Scott Institute for Energy Technologies at Carnegie Mellon University.

8.2. Introduction

Polymer brushes have been extensively investigated over the past 50 years because they are effective particle/surface modifiers.[1-6] Brushes are dense layers of polymer chains with a chain end attached to a surface. Both theory and simulations were used to understand how to brush heights and grafting densities affect properties of the nanocomposite hybrid materials.[7] The preparation of "monodisperse" brushes (brushes with a very narrow molecular weight

distribution), requires well-controlled synthetic methods. Atom transfer radical polymerization (ATRP), a powerful controlled radical polymerization technique, has produced a vast array of polymeric materials with excellent control over topologies, compositions, microstructures, and functionalities over the past two decades.[3, 5, 8-10] Recently, concentration of Cu-based catalysts can be diminished to the ppm level with the use of a reducing agents and rational selection of suitable Cu-complexing ligands in activator regeneration by electron transfer (ARGET) ATRP technique.[11-14]

Graft density and uniformity of polymer chains can significantly affect the conformation of polymer brushes and the properties of composite systems.[15] Theoretical studies showed that polymer brushes exhibit a relaxation of chain extended conformation with increasing molecular weight. Also, higher dispersity can stabilize dispersions, even if the average graft molecular weight is lower than the matrix molecular weight.[16] Moreover, simulations demonstrated that dispersity may affect the adhesion of microscale particles by enhancing interparticle entanglement.[16-18] Brushes with higher dispersity may significantly improve the ability and efficacy of smart coatings, as compared to monodisperse brushes.[19-20] Recent reports demonstrated that particle brushes with bimodal molecular weight distribution (MWD) showed superior mechanical properties and significantly improved interparticle and particle-matrix interactions.[21-25] However, some conventional approaches to broaden MWD might be complicated and difficult to perform. In this contribution, we report the synthesis of SiO_2-*g*-PMMA particle brushes with controlled dispersity and grafting density using a facile scalable approach consisting of simple tuning the initial ATRP catalyst concentration, top scheme in **Figure 8.1**. A similar approach was used for liner chains in ARGET ATRP.[26-28]

8.3. Results and Discussion

The effect of varying the initial concentration of catalyst $[Cu^{II}/L]_0$ on the grafting density and dispersity of SiO_2-*g*-PMMA particle brushes synthesized with ARGET ATRP was studied. A fixed concentration of initiating sites on SiO_2-Br particles (200 ppm) and wide range of catalyst ($CuBr_2/Me_6TREN$) concentrations ($[Cu^{II}/L]_0$ = 0.01~400 ppm) in 50% v/v solvent (anisole) at 60 °C was applied and the results are provided in **Table 8.1**. Because of the possible gelation of the reaction medium due to interparticle coupling, reactions were carried out for a relatively short time (< 2 h) to diminish coupling between nanoparticles (NPs). **Figure 8.2**a and **Figure 8.2**b show the correlation of the grafting density and dispersity with the initial concentration of the catalyst ($[Cu^{II}/L]_0$). The results indicate that the dispersity of the grafted brushes increased with the decreasing initial concentration of the catalyst, from 1.18 to 2.11. On the other hand, the grafting density, which is an indication of the initiation efficiency of the reaction was relatively steady at high catalyst concentrations (>25 ppm), but dropped significantly with lower initial catalyst concentrations at < 10 ppm conditions, from 0.71 to 0.012 chain/nm^2. Such an observation agreed with the previous theoretical study on the correlation between grafting density and dispersity.[29] After polymerization, the products were precipitated by addition to cold methanol to remove the catalyst ($CuBr_2/Me_6TREN$), solvent, unreacted monomer, and NPs.

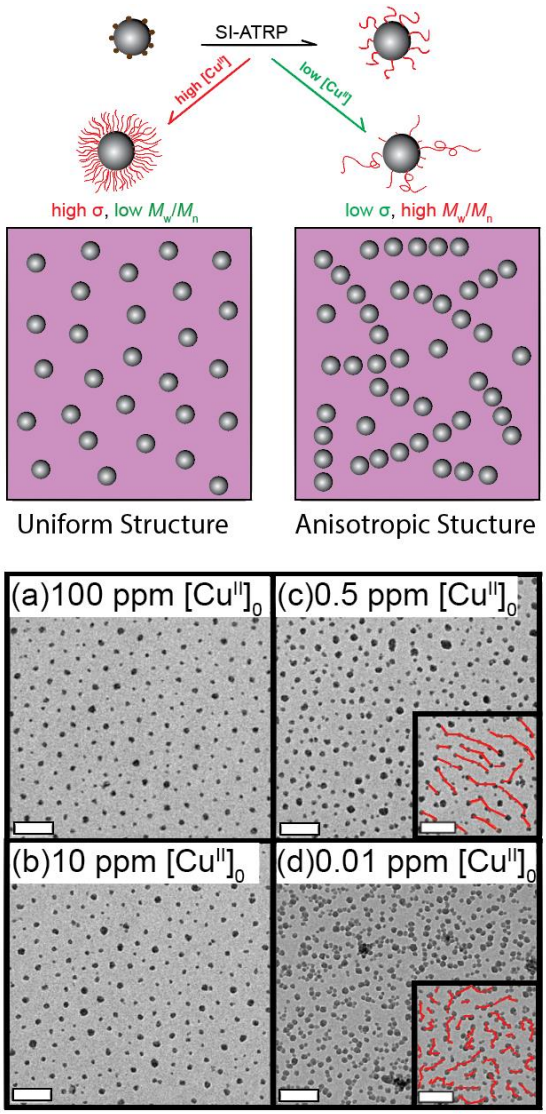

Figure 8.1. Schematic graph of the synthesis of SiO_2-*g*-PMMA particle brushes with different initial catalyst concentrations and TEM images of monolayer films of SiO_2-*g*-PMMA particle brushes with different DP and grafting densities. (a) PMMA-3, DP = 600, M_w/M_n = 1.16, σ = 0.65 nm^{-2}, (b) PMMA-6, DP = 787, M_w/M_n = 1.46, σ = 0.15 nm^{-2}, (c) PMMA-10, DP = 2,471, M_w/M_n = 1.90, σ = 0.049 nm^{-2}, (d) PMMA-15, DP = 1,972, M_w/M_n=2.06, σ =0.015 nm^{-2}. Red lines highlight the string structures in (c) and (d) insets. Scale bar: 100 nm.

Due to the significant decrease of the grafting density at low catalyst concentrations, it is necessary to verify if the polymer chains were initiated from the surface of silica NPs or via side-reactions in the solution (e.g. thermal self-initiation).[30-32] Therefore, we characterized the samples by TEM to confirm the attachment of polymer brushes to the surface of the NPs. TEM images showed that no obvious free homopolymers were present after polymerization, and all

particle brushes were well-dispersed on the Cu grids without aggregations, even with catalyst concentration > 0.1 ppm, **Figure 8.1** (cf. also **Figure S8.6**). It should be noted that as the grafting density diminished with the decreasing initial catalyst concentration, the morphologies of particle brushes changed. Above 10 ppm $[Cu^{II}/L]_0$, isotropic and uniform structures were observed (**Figure 8.1**a and **Figure 8.1**b). On the other hand, as the $[Cu^{II}/L]_0$ decreased below 10 ppm, the grafting density dropped to < 0.15 chains/nm^2, and an anisotropic structure was observed in the TEM images, **Figure 8.1**c. This trend further evolved with the decreasing $[Cu^{II}/L]_0$ and grafting density, **Figure 8.1**d. These string-like structures, the top scheme in **Figure 8.1**, were previously reported and studied in sparsely grafted particle systems.[33-35] The driving force to form this self-assembled structure was the attraction between patches of bare surfaces of NPs.[36-38]

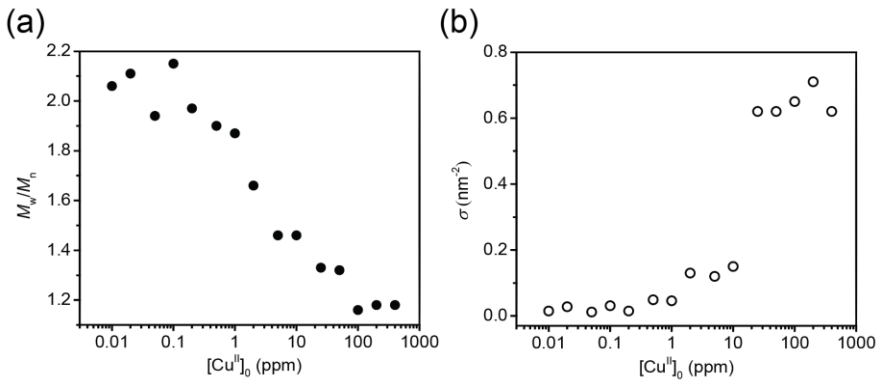

Figure 8.2. Reaction characteristics in the synthesis of SiO_2-*g*-PMMA particle brushes by ARGET ATRP with different $[Cu^{II}]_0$: (a) dispersity (M_w/M_n) *vs.* $[Cu^{II}]_0$, (b) grafting density (σ) *vs.* $[Cu^{II}]_0$.

Table 8.1. Result of syntheses of SiO_2-*g*-PMMA particle brushes

Entry[a]	Reaction condition			M_n[d]	M_w/M_n[d]	f_{ino} (%)[e]	σ (nm^{-2})[f]
	$[CuBr_2]_0$ (ppm)[b]	Reaction time (h)	Conv (%)[c]				
PMMA-1	400	2	7.9	42,090	1.18	11.2	0.62
PMMA-2	200	2	9.0	41,950	1.18	9.9	0.71
PMMA-3	100	2	11.8	60,050	1.16	7.8	0.65
PMMA-4	50	1	7.2	38,190	1.32	12.2	0.62
PMMA-5	25	1.5	10.7	56,750	1.33	8.6	0.62
PMMA-6	10	1.5	3.7	78,710	1.46	21.4	0.15
PMMA-7	5	1	3.9	108,100	1.46	20.2	0.12
PMMA-8	2	1	3.4	86,810	1.66	22.5	0.13
PMMA-9	1	1	2.5	181,000	1.87	28.3	0.046

PMMA-10	0.5	1	3.7	247,100	1.90	21.4	0.049
PMMA-11	0.2	1	1.3	296,200	1.97	42.6	0.015
PMMA-12	0.1	1.5	2.2	229,500	2.15	31.5	0.031
PMMA-13	0.05	1	0.55	149,300	1.94	64.3	0.012
PMMA-14	0.02	1.5	1.9	223,400	2.11	34.6	0.028
PMMA-15	0.01	1	1	197,200	2.06	52.5	0.015

[a] Reaction condition: PMMA-1~15: $[MMA]_0/[SiO_2\text{-}Br]_0/[CuBr_2]_0/[Me_6TREN]_0:[Sn(EH)_2]_0$=5000:1:x:10x:2.5, x = 2/1/0.5/0.25/0.125/0.05/0.025/0.01/0.005/0.0025/0.001/0.0005/0.00025/0.0001/0.00005 with 50 vol% anisole, at 60 ºC, $[MMA]_0$ = 4.7 M. [b] Molar ratio *vs.* monomer. [c] Determined by gravimetric analysis. [d] Determined by SEC. [e] Fraction of inorganic content determined by TGA. [f] Calculated from Eq. S1 according to TGA data.

Due to short reaction time (1 h), and relatively low conversion (~ 1%) in several reactions, accurate kinetic plots could not be obtained. Therefore, we conducted a series of homopolymerizations of linear model systems with similar initial catalyst concentrations to study the reaction kinetics. Linear PMMA samples were prepared under the same conditions used to prepare the SiO_2-*g*-PMMA particle brushes, except for the use of a small-molecule initiator, ethyl 2-bromoisobutyrate (EBiB), and the results are reported in **Table 8.2**.

The key factors dominating the dispersity of model linear ATRP reactions can be summarized in the following equation (if the contribution of termination is small).[39-41]

$$\frac{M_\mathrm{w}}{M_\mathrm{n}} = 1 + \frac{[\mathrm{RX}]k_\mathrm{p}}{k_\mathrm{d}[\mathrm{Cu^{II}}]}\left(\frac{2}{p} - 1\right) \quad (1)$$

where [RX] and $[Cu^{II}]$ are the concentrations of the alkyl halide chain end and the Cu^{II} species, respectively; k_p and k_d are the rate constants of propagation and deactivation, respectively; p is the conversion. $[Cu^{I}]/[Cu^{II}]$ ratio can be estimated based on the apparent rate constants (**Figure S8.1**) of polymerization and the ATRP equilibrium constant, K_{ATRP}, using the following equation.[42]

$$k_\mathrm{p}^\mathrm{app} = k_\mathrm{p} K_\mathrm{ATRP} \frac{[\mathrm{RX}][\mathrm{Cu^I}]}{[\mathrm{Cu^{II}}]} \quad (2)$$

Table 8.2 and **Figure 8.3** show the correlation between dispersity/initiation efficiency and the initial catalyst concentration in the polymerization of linear PMMA homopolymers. Similar trends to those observed in the particle brush system were obtained. In the linear model system control of polymerization decreased with the initial concentration of catalyst. Also, the initiation efficiency was relatively constant above a certain initial catalyst concentration (10 ppm), and below this threshold concentration, the initiation efficiency dropped with decreasing catalyst concentrations.

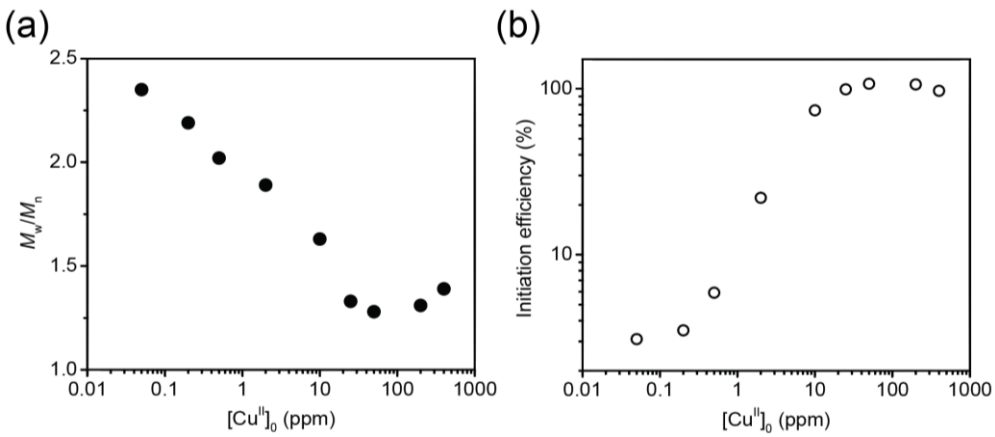

Figure 8.3. Reaction characteristics in the synthesis of linear PMMA homopolymers by ARGET ATRP with different $[Cu^{II}]_0$: (a) dispersity (M_w/M_n) *vs.* $[Cu^{II}]_0$, (b) initiation efficiency *vs.* $[Cu^{II}]_0$.

Table 8.2. Result of syntheses of linear PMMA

Entry[a]	Reaction condition			$M_{n,SEC}$[d]	M_w/M_n[d]	$M_{n,theo}$[e]	Efficiency (%)[f]
	$[CuBr_2]_0$ (ppm)[b]	Reaction time (h)	Conv (%)[c]				
PMMA-L1	400	3	27.43	141,700	1.39	137,150	97
PMMA-L2	200	3	20.21	94,640	1.31	101,050	107
PMMA-L3	50	5	25.64	118,950	1.28	128,200	108
PMMA-L4	25	5	18.44	87,350	1.33	92,200	106
PMMA-L5	10	5	11.85	80,980	1.63	59,250	73
PMMA-L6	2	5	4.61	103,800	1.89	23,050	22
PMMA-L7	0.5	5	3.1	262,200	2.02	15,500	5.9
PMMA-L8	0.2	5	2.3	325,300	2.19	11,550	3.6
PMMA-L9	0.05	5	1.6	267,000	2.35	8,050	3.1

[a] Reaction condition: PMMA-L1~9: $[MMA]_0/[EBiB]_0/[CuBr_2]_0/[Me_6TREN]_0:[Sn(EH)_2]_0$=5000:1:x:10x:0.25, x = 2/1/0.25/0.125/0.05/0.01/0.0025/0.001/0.00025 with 50 vol% anisole, at 60 ºC, $[MMA]_0$=4.7 M. [b] Molar ratio *vs.* monomer. [c] Determined by gravimetric analysis. [d] Determined by SEC. [e] Determined by conversion and target DP. [f] Initiation efficiency was calculated by $M_{n,theo}/M_{n,SEC}$.

Figure 8.4a displays the semilogarithmic kinetic plots of model polymerization for linear MMA at different initial catalyst concentrations and indicates that the rate of polymerization is faster with a higher initial catalyst concentration. The apparent rate constant of polymerization, k_p^{app}, was calculated by Eq. S2 and a trend between the rate and the initial catalyst concentration is shown in **Figure S8.1**, the literature values of propagation rate constant $k_{p,\,MMA}$ = 833 M^{-1} s^{-1} at 60 °C was used to calculate the radical concentration, **Figure S8.2**.[43-44] The polymerization rate of a classic ARGET ATRP reaction is defined by the ratio of the rates of reduction of Cu^{II}/L to Cu^{I}/L and radical termination. Thus, the overall rate should obey 1/2 order in both [RA] and [Cu^{II}/L].[41, 45] **Figure S8.1** shows PMMA particle brushes polymerization rate indeed follows the ARGET kinetics and the reaction order in Cu^{II}/L has a slope of 0.47. The initial concentration of the catalyst also significantly affected the dispersity (control) of polymers formed in the reactions. The dispersity (M_w/M_n) increased with decreasing [Cu^{II}/L]$_0$, up to 2.35, **Figure S8.3**. **Figure 8.4**b shows the correlations between number-average molecular weight and conversion with selected initial catalyst concentrations. An approximation of typical living polymerization features was observed for conditions with catalyst concentrations between 200 ppm and 25 ppm [Cu^{II}/L]$_0$, and molecular weight showed a good correlation with the theoretical value. However, when [Cu^{II}/L]$_0$ was decreased below 10 ppm, **Figure 8.2**b inset, control of polymerization was lost, as the relations between the molecular weight and conversion were no longer monotonically increasing. The 10 ppm [Cu^{II}/L]$_0$ concentration was also the transition point to a lower initiation efficiency.

The PMMA chains generated in a linear homopolymer system were initiated from ATRP initiator EBiB which is consistent with the observations for the SiO_2-*g*-PMMA particle brush system. To confirm this, three control experiments were conducted. A Cu-free system ([Cu^{II}/L]$_0$

= 0 ppm, $[EBiB]_0$ = 200 ppm, $[Sn(EH)_2]_0$ = 400 ppm), an initiator-free system ($[Cu^{II}/L]_0$ = 200 ppm, $[EBiB]_0$ = 0 ppm, $[Sn(EH)_2]_0$ = 400 ppm), and the one with a Cu-and-initiator-free system ($[Cu^{II}/L]_0$ = 0 ppm, $[EBiB]_0$ = 0 ppm, $[Sn(EH)_2]_0$ = 400 ppm). Kinetic studies, **Figure S8.4**, show that no polymerization occurred under the initiator-free and the initiator-and-Cu-free conditions, but a slow uncontrolled polymerization proceeded under the Cu-free condition. Therefore, the mechanism of the polymerization of linear PMMA with different catalyst concentration can be summarized as predominantly a controlled radical polymerization above the critical initial catalyst concentration 10 ppm $[Cu^{II}/L]_0$, for the current study conditions. The reactions showed good control, while the initiation efficiencies were high and independent of reaction time. When the initial catalyst concentration was below the critical threshold of 10 ppm, the reactions showed non-linear correlations of M_n *vs.* conversion and a slow initiation, due to insufficient deactivation, **Figure S8.5**. Specifically, in this linear polymerization study, the initiation efficiency was observed to decrease with decreasing initial catalyst concentration at the same reaction time. This mechanism is believed to apply also to the particle brush system.

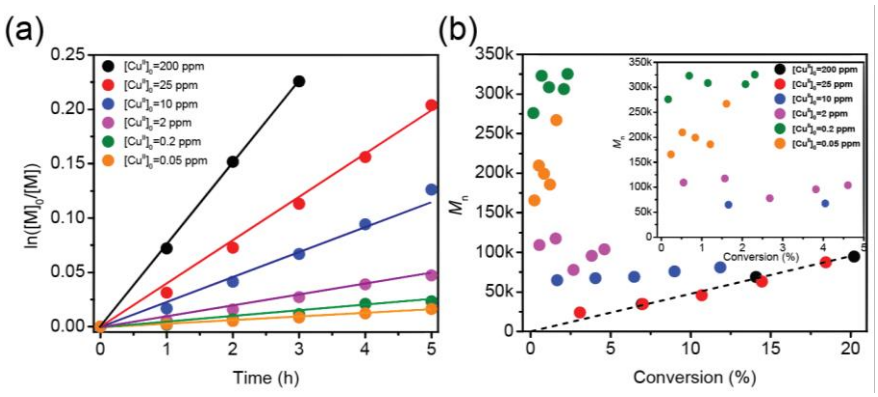

Figure 8.4. Results for linear homopolymer polymerization of methyl methacrylate (MMA) by ARGET ATRP under reaction condition: $[MMA]_0/[EBiB]_0/[CuBr_2]_0/[Me_6TREN]_0:[Sn(EH)_2]_0$=5000:1:x:10x:2.5, x = 1/0.125/0.05/0.01/0.001/0.00025, with 50 vol% anisole, at 60 ºC. (a) Semilogarithmic kinetic plots for linear PMMA system, (b) Number-average molecular weight (M_n) *vs.* conversion of linear PMMA, dash line in (b) show the theoretical M_n vs. conversion plots under high $[Cu^{II}/L]_0$ conditions.

8.4. Supporting Information

Materials.

Methyl methacrylate (MMA, 99%, Aldrich) was purified by passing through a column filled with basic alumina to remove the inhibitor. Tris(2-dimethylaminoethyl)amine (Me_6TREN, 99%, Alfa), anisole (99%, Aldrich), tetrahydrofuran (THF, 99%, VWR), methanol (99%, VWR), *N*,*N*-dimethylformamide (DMF, 99%, VWR), ethyl 2-bromoisobutyrate (EBiB, 98%, Aldrich), copper(II) bromide ($CuBr_2$, 99%, Aldrich), tin(II) 2-ethylhexanoate ($Sn(EH)_2$, 95%, Aldrich), 48% hydrofluoric acid aqueous solution (HF, >99.99%, Aldrich), ammonium hydroxide aqueous solution (NH_4OH, 28.0-30.0%, Fisher), and anhydrous magnesium sulfate ($MgSO_4$, Fisher) were used as received without further purification. Silica NPs, 30 wt% solution in methyl isobutyl ketone (MIBK-ST), effective diameter $d \approx 15.8$ nm, were kindly donated by Nissan Chemical Corp. and were used as received. The tethered ATRP initiator 1-(chlorodimethylsilyl)propyl α-bromoisobutyrate and surface-modified silica (SiO_2-Br) were prepared using previously reported procedures.

Procedures. General procedure for the synthesis of SiO_2-g-PMMA particle brushes via ARGET ATRP.

The initiator (SiO_2-Br), monomer (MMA), solvents (anisole, DMF), $CuBr_2$, and Me_6TREN were mixed thoroughly in a sealed Schlenk flask. Meanwhile, a stock solution of $Sn(EH)_2$ in anisole was prepared. Both mixtures were degassed by nitrogen purging, then the $Sn(EH)_2$ solution was injected into the Schlenk flask to activate the catalyst complex and the flask was immediately placed into an oil bath set at 60 ºC. The conversion and molecular weight

(MW) of the polymer were monitored by gravimetric analysis and size exclusion chromatography (SEC), respectively.

Procedure for synthesis of linear PMMA homopolymers via ARGET ATRP. Initiator (EBiB), MMA, solvents (anisole, DMF), $CuBr_2$, and Me_6TREN were mixed thoroughly in a sealed Schlenk flask. A stock solution of $Sn(EH)_2$ in anisole was prepared. Both mixtures were degassed by nitrogen purging, then the $Sn(EH)_2$ solution was injected into the Schlenk flask to activate the catalyst complex and the flask was immediately placed into an oil bath. The conversion and MW of the polymer were monitored by gravimetric analysis and SEC, respectively.

Characterization. Transmission electron microscopy (TEM). TEM was carried out using a JEOL 2000 EX electron microscope operated at 200 kV. The spatial distribution, radius and inter-particle distances of the SiO_2 NPs were determined from statistical analysis of the TEM micrographs using ImageJ software. DLS, using a Malvern Zetasizer Nano ZS, was performed to confirm results obtained from TEM. It was also employed to determine volume-weighted average hydrodynamic diameters and distribution.

Thermogravimetric analysis (TGA). A TA Instruments 2950 was used to measure the fraction of SiO_2 in the hybrids by TGA. The data were analyzed with TA Universal Analysis. The heating procedure involved four steps: (1) jump to 120 ºC; (2) hold at 120 ºC for 10 min; (3) ramp up at a rate of 20 ºC/min to 800 ºC; (4) hold for 2 min. The TGA plots were normalized to the total weight after holding at 120 ºC.

Grafting density. Equation (S1) was used to calculate the grafting density.

$$\sigma_{\mathrm{TGA}} = \frac{(1-f_{\mathrm{SiO2}})N_{\mathrm{Av}}\,\rho_{\mathrm{SiO2}}\,d}{6\,f_{\mathrm{SiO2}}\,M_n} \qquad \text{(S1)}$$

where f_{SiO2} is the SiO_2 fraction (wt%) measured by TGA, N_{Av} is the Avogadro number, ρ_{SiO2} is the density of SiO_2 NPs (2.2 g/cm^3), d is the average diameter of SiO_2 NPs (15.8 nm), and M_n is the overall number-average MW of the cleaved polymer brushes.[3]

Polymer characterization. Number-average molecular weights (M_n) and molecular weight distributions (MWDs) were determined by SEC. The SEC was conducted with a Waters 515 pump and Waters 410 differential refractometer using PSS columns (Styrogel 10^5, 10^3, 10^2 Å) in THF as an eluent at 35 ºC and a flow rate of 1 ml min^{-1}. Linear PS and PMMA standards were used for calibration. The conversion was calculated by gravimetric analysis.

Kinetic parameters calculation: Equations (S2-4) were used to calculate the apparent rate of propagation **(**k_p^{app}) and the radical concentration [P$^\bullet$].

$$\ln\frac{[\mathrm{M}]}{[\mathrm{M}]_0} = -k_{\mathrm{p}}^{\mathrm{app}} \times t \qquad \text{(S2)}$$

$$k_{\mathrm{p}}^{app} = k_{\mathrm{p}} \times [\mathrm{P}^\bullet] \qquad \text{(S3)}$$

$$R_{\mathrm{p}} = k_{\mathrm{p}} \times [\mathrm{M}] \qquad \text{(S4)}$$

where k_p is the propagation rate constant, k_t is the termination rate constant, and p is conversion.

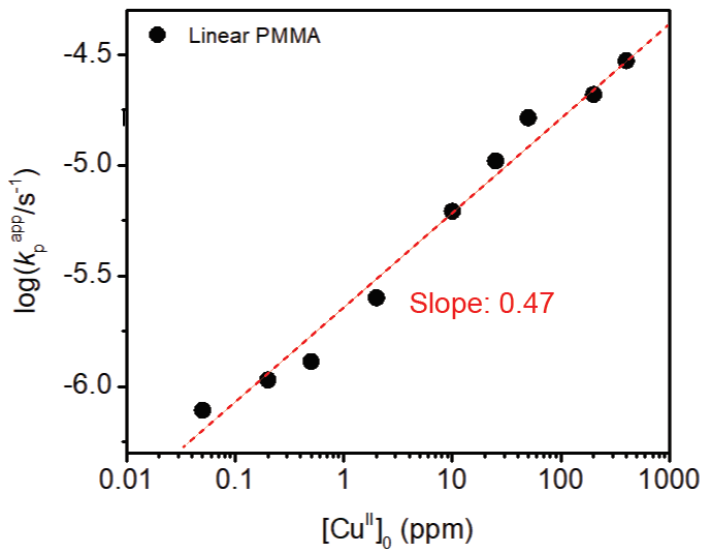

Figure S8.1. Plot of log(k_p^{app}/s^{-1}) *vs.* [$CuBr_2$]$_0$, $k_{p,MMA}$ = 833 M^{-1} s^{-1} at 60 °C.

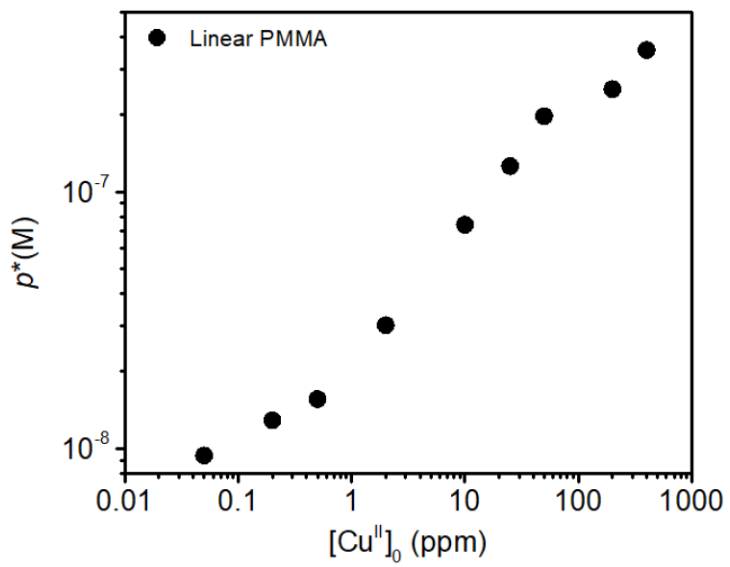

Figure S8.2. The plot of radical concentration *vs*. initial catalyst concentration in linear PMMA polymerization

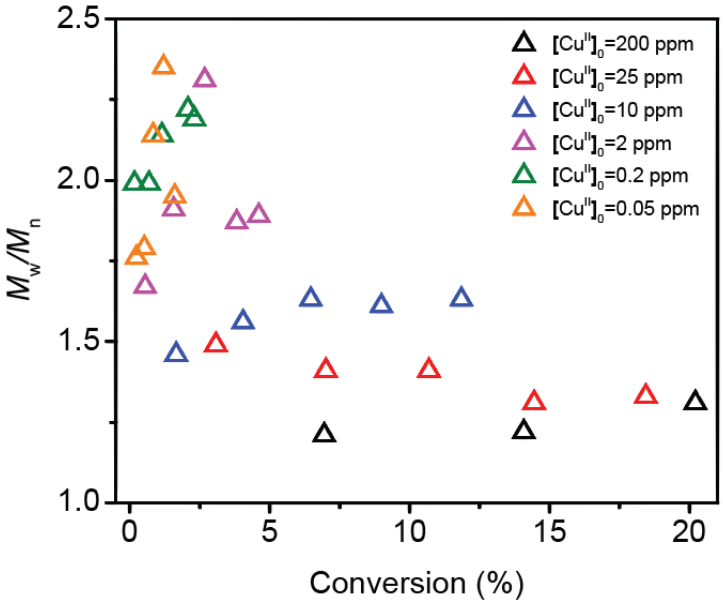

Figure S8.3. Dispersity (M_w/M_n) *vs.* conversion of linear PMMA

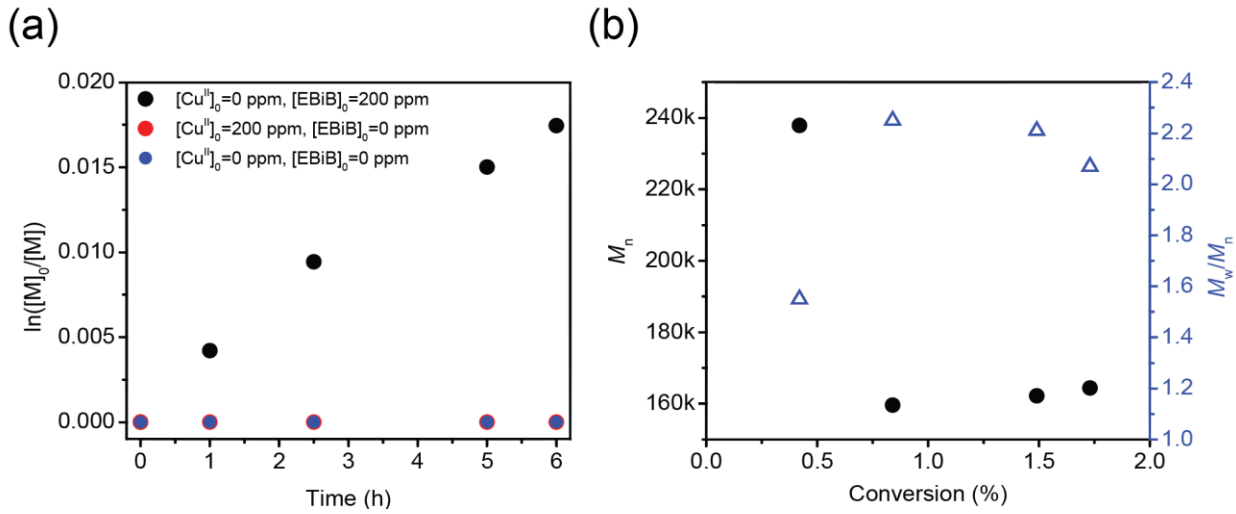

Figure S8.4. Results for linear homopolymer polymerization of methyl methacrylate (MMA) by ARGET ATRP under reaction condition: $[MMA]_0/[EBiB]_0/[CuBr_2]_0/[Me_6TREN]_0:[Sn(EH)_2]_0$=5000:1/0/0:0/1/0:10:2.5, with 50 vol% anisole, at 60 ºC. (a) Semi-logarithmic kinetic plots for linear PMMA system, (b) Number-average molecular weight and molecular weight distribution (M_w/M_n) for linear PMMA system with $[Cu^{II}/L]_0$=0 ppm, and $[EBiB]_0$=200 ppm condition.

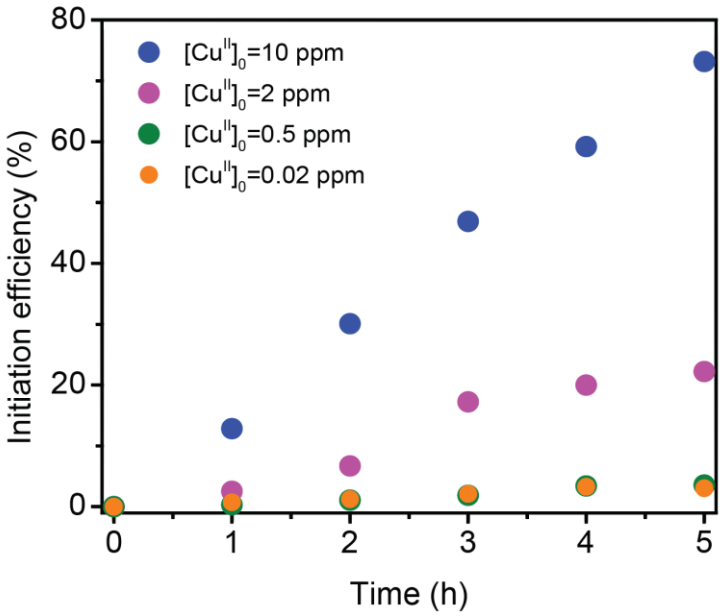

Figure S8.5. The plot of initiation efficiency *vs.* time in linear PMMA polymerization under low $[Cu^{II}/L]_0$ conditions

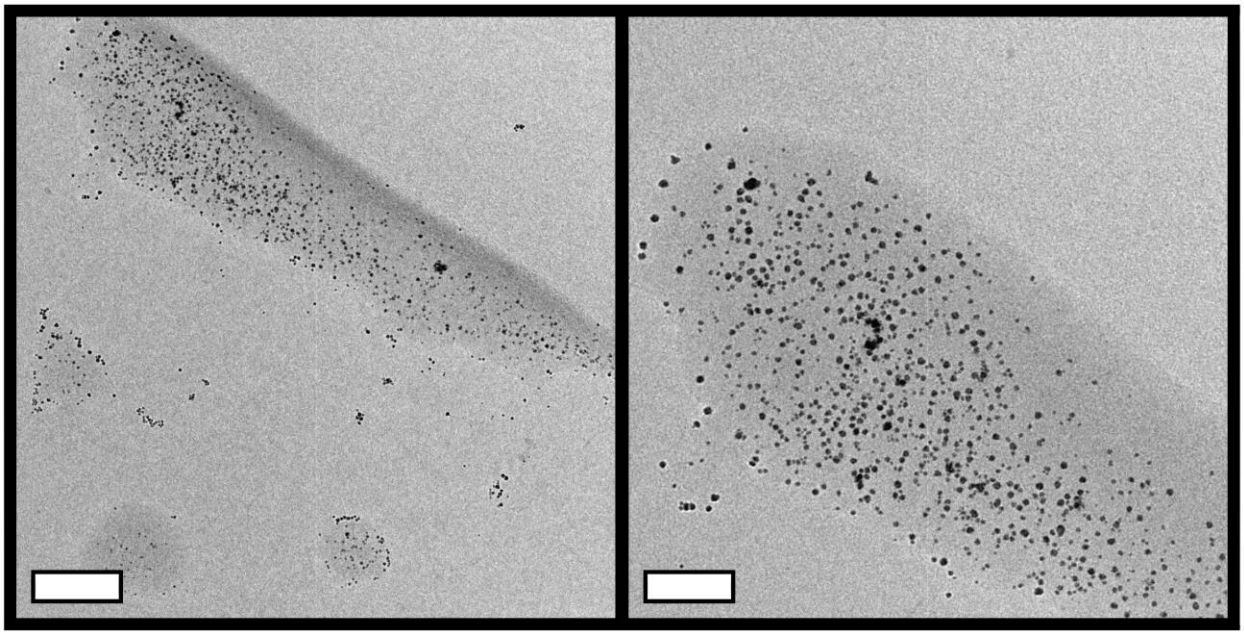

Figure S8.6. TEM images of a mixture of SiO_2-*g*-PMMA particle brush (PMMA-15) with linear homopolymers (sample: PMMA-L1), mass ratio=1:1. Scale bar: left: 500 nm, right: 200 nm.

8.5. Conclusions

In conclusion, SiO_2-*g*-PMMA particle brushes were synthesized *via* ARGET ATRP with different initial catalyst concentrations and provided facile control of dispersity and grafting

density. Under high catalyst concentration conditions (>10 ppm), the high grafting densities of the products were observed with uniform structures and the molecular weight distribution increased with decreasing $[Cu^{II}/L]_0$. When the initial catalyst concentration decreased to < 10 ppm, the dispersity further increased, up to 2.3, and the grafting density dropped significantly, to as low as 0.012 chain/nm^2. Sparsely grafted particle brushes with large dispersity were obtained under these conditions, resulting in anisotropic string-like structures for the final product. The results of linear polymerization of MMA showed very similar trends in the initiation efficiency and the dispersity *vs.* $[Cu^{II}/L]_0$. A transition from controlled to uncontrolled radical polymerization was revealed at initial catalyst concentrations below 10 ppm. Distinctly different types of control over the polymerization were observed above and below this critical concentration. Such observations demonstrated polymer brushes with a wide selection of MWD are accessible *via* tuned catalyst concentrations. This enables applications of these polymer brushes where a broad transition among polymer brush interactions is needed, such as antifouling, mechanical reinforcement, sensing, and separations.

8.6. References

(1) Qi, S.; Klushin, L. I.; Skvortsov, A. M.; Schmid, F., Polydisperse Polymer Brushes: Internal Structure, Critical Behavior, and Interaction with Flow. *Macromolecules* **2016,** *49* (24), 9665-9683.

(2) Bixler, G. D.; Bhushan, B., Biofouling: lessons from nature. *Philosophical Transactions of the Royal Society A: Mathematical, Physical and Engineering Sciences* **2012,** *370* (1967), 2381-2417.

(3) Hui, C. M.; Pietrasik, J.; Schmitt, M.; Mahoney, C.; Choi, J.; Bockstaller, M. R.; Matyjaszewski, K., Surface-Initiated Polymerization as an Enabling Tool for Multifunctional (Nano-)Engineered Hybrid Materials. *Chem. Mater.* **2014,** *26* (1), 745-762.

(4) Zoppe, J. O.; Ataman, N. C.; Mocny, P.; Wang, J.; Moraes, J.; Klok, H.-A., Surface-Initiated Controlled Radical Polymerization: State-of-the-Art, Opportunities, and Challenges in Surface and Interface Engineering with Polymer Brushes. *Chem. Rev.* **2017,** *117* (3), 1105-1318.

(5) Barbey, R.; Lavanant, L.; Paripovic, D.; Schüwer, N.; Sugnaux, C.; Tugulu, S.; Klok, H.-A., Polymer Brushes via Surface-Initiated Controlled Radical Polymerization: Synthesis, Characterization, Properties, and Applications. *Chem. Rev.* **2009,** *109* (11), 5437-5527.

(6) Kumar, S. K.; Benicewicz, B. C.; Vaia, R. A.; Winey, K. I., 50th Anniversary Perspective: Are Polymer Nanocomposites Practical for Applications? *Macromolecules* **2017,** *50* (3), 714-731.
(7) Romeis, D.; Merlitz, H.; Sommer, J. U., A new numerical approach to dense polymer brushes and surface instabilities. *The Journal of Chemical Physics* **2012,** *136* (4), 044903.
(8) Matyjaszewski, K.; Xia, J., Atom Transfer Radical Polymerization. *Chem. Rev.* **2001,** *101* (9), 2921-2990.
(9) Matyjaszewski, K., Advanced Materials by Atom Transfer Radical Polymerization. *Adv. Mater.* **2018,** *30* (23), 1706441.
(10) Matyjaszewski, K., Atom Transfer Radical Polymerization (ATRP): Current Status and Future Perspectives. *Macromolecules* **2012,** *45* (10), 4015-4039.
(11) Jakubowski, W.; Min, K.; Matyjaszewski, K., Activators Regenerated by Electron Transfer for Atom Transfer Radical Polymerization of Styrene. *Macromolecules* **2006,** *39* (1), 39-45.
(12) Matyjaszewski, K.; Jakubowski, W.; Min, K.; Tang, W.; Huang, J.; Braunecker, W. A.; Tsarevsky, N. V., Diminishing catalyst concentration in atom transfer radical polymerization with reducing agents. *Proc. Nat. Acad. Sci.* **2006,** *103* (42), 15309-15314.
(13) Tsarevsky, N. V.; Matyjaszewski, K., "Green" Atom Transfer Radical Polymerization: From Process Design to Preparation of Well-Defined Environmentally Friendly Polymeric Materials. *Chem. Rev.* **2007,** *107* (6), 2270-2299.
(14) Pan, X.; Fantin, M.; Yuan, F.; Matyjaszewski, K., Externally controlled atom transfer radical polymerization. *Chem. Soc. Rev.* **2018,** *47* (14), 5457-5490.
(15) Milner, S. T.; Witten, T. A.; Cates, M. E., Effects of polydispersity in the end-grafted polymer brush. *Macromolecules* **1989,** *22* (2), 853-861.
(16) Martin, T. B.; Dodd, P. M.; Jayaraman, A., Polydispersity for Tuning the Potential of Mean Force between Polymer Grafted Nanoparticles in a Polymer Matrix. *Phys. Rev. Lett.* **2013,** *110* (1), 018301.
(17) de Vos, W. M.; Leermakers, F. A. M., Modeling the structure of a polydisperse polymer brush. *Polymer* **2009,** *50* (1), 305-316.
(18) de Vos, W. M.; Leermakers, F. A. M.; de Keizer, A.; Kleijn, J. M.; Cohen Stuart, M. A., Interaction of Particles with a Polydisperse Brush: A Self-Consistent-Field Analysis. *Macromolecules* **2009,** *42* (15), 5881-5891.
(19) Liu, X.; Wang, C.-G.; Goto, A., Polymer Dispersity Control by Organocatalyzed Living Radical Polymerization. *Angew. Chem. Int. Ed.* **2019,** *0* (0).
(20) Yadav, V.; Jaimes-Lizcano, Y. A.; Dewangan, N. K.; Park, N.; Li, T.-H.; Robertson, M. L.; Conrad, J. C., Tuning Bacterial Attachment and Detachment via the Thickness and Dispersity of a pH-Responsive Polymer Brush. *ACS Appl. Mater. Interfaces* **2017,** *9* (51), 44900-44910.
(21) Yan, J.; Kristufek, T.; Schmitt, M.; Wang, Z.; Xie, G.; Dang, A.; Hui, C. M.; Pietrasik, J.; Bockstaller, M. R.; Matyjaszewski, K., Matrix-free Particle Brush System with Bimodal Molecular Weight Distribution Prepared by SI-ATRP. *Macromolecules* **2015,** *48* (22), 8208-8218.
(22) Nair, N.; Wentzel, N.; Jayaraman, A., Effect of bidispersity in grafted chain length on grafted chain conformations and potential of mean force between polymer grafted nanoparticles in a homopolymer matrix. *The Journal of Chemical Physics* **2011,** *134* (19), 194906.

(23) Rungta, A.; Natarajan, B.; Neely, T.; Dukes, D.; Schadler, L. S.; Benicewicz, B. C., Grafting Bimodal Polymer Brushes on Nanoparticles Using Controlled Radical Polymerization. *Macromolecules* **2012,** *45* (23), 9303-9311.
(24) Natarajan, B.; Neely, T.; Rungta, A.; Benicewicz, B. C.; Schadler, L. S., Thermomechanical Properties of Bimodal Brush Modified Nanoparticle Composites. *Macromolecules* **2013,** *46* (12), 4909-4918.
(25) Li, Y.; Krentz, T. M.; Wang, L.; Benicewicz, B. C.; Schadler, L. S., Ligand Engineering of Polymer Nanocomposites: From the Simple to the Complex. *ACS Appl. Mater. Interfaces* **2014,** *6* (9), 6005-6021.
(26) Jakubowski, W.; Matyjaszewski, K., Activators Regenerated by Electron Transfer for Atom-Transfer Radical Polymerization of (Meth)acrylates and Related Block Copolymers. *Angew. Chem. Int. Ed.* **2006,** *45* (27), 4482-4486.
(27) Lamson, M.; Kopeć, M.; Ding, H.; Zhong, M.; Matyjaszewski, K., Synthesis of well-defined polyacrylonitrile by ICAR ATRP with low concentrations of catalyst. *J. Polym. Sci., Part A: Polym. Chem.* **2016,** *54* (13), 1961-1968.
(28) Listak, J.; Jakubowski, W.; Mueller, L.; Plichta, A.; Matyjaszewski, K.; Bockstaller, M. R., Effect of Symmetry of Molecular Weight Distribution in Block Copolymers on Formation of "Metastable" Morphologies. *Macromolecules* **2008,** *41* (15), 5919-5927.
(29) Mastan, E.; Xi, L.; Zhu, S., Factors Affecting Grafting Density in surface-initiated ATRP: A Simulation Study. *Macromol. Theory Simul.* **2016,** *25* (3), 220-228.
(30) Riazi, H.; A. Shamsabadi, A.; Grady, M. C.; Rappe, A. M.; Soroush, M., Experimental and Theoretical Study of the Self-Initiation Reaction of Methyl Acrylate in Free-Radical Polymerization. *Industrial & Engineering Chemistry Research* **2018,** *57* (2), 532-539.
(31) Srinivasan, S.; Lee, M. W.; Grady, M. C.; Soroush, M.; Rappe, A. M., Self-Initiation Mechanism in Spontaneous Thermal Polymerization of Ethyl and n-Butyl Acrylate: A Theoretical Study. *The Journal of Physical Chemistry A* **2010,** *114* (30), 7975-7983.
(32) Hui, C. M.; Dang, A.; Chen, B.; Yan, J.; Konkolewicz, D.; He, H.; Ferebee, R.; Bockstaller, M. R.; Matyjaszewski, K., Effect of Thermal Self-Initiation on the Synthesis, Composition, and Properties of Particle Brush Materials. *Macromolecules* **2014,** *47* (16), 5501-5508.
(33) Jiao, Y.; Tibbits, A.; Gillman, A.; Hsiao, M.-S.; Buskohl, P.; Drummy, L. F.; Vaia, R. A., Deformation Behavior of Polystyrene-Grafted Nanoparticle Assemblies with Low Grafting Density. *Macromolecules* **2018,** *51* (18), 7257-7265.
(34) Jiao, Y.; Parra, J.; Akcora, P., Effect of Ionic Groups on Polymer-Grafted Magnetic Nanoparticle Assemblies. *Macromolecules* **2014,** *47* (6), 2030-2036.
(35) Liu, S.; Senses, E.; Jiao, Y.; Narayanan, S.; Akcora, P., Structure and Entanglement Factors on Dynamics of Polymer-Grafted Nanoparticles. *ACS Macro Lett.* **2016,** *5* (5), 569-573.
(36) Akcora, P.; Liu, H.; Kumar, S. K.; Moll, J.; Li, Y.; Benicewicz, B. C.; Schadler, L. S.; Acehan, D.; Panagiotopoulos, A. Z.; Pryamitsyn, V.; Ganesan, V.; Ilavsky, J.; Thiyagarajan, P.; Colby, R. H.; Douglas, J. F., Anisotropic self-assembly of spherical polymer-grafted nanoparticles. *Nat. Mater.* **2009,** *8*, 354.
(37) Zhao, D.; Di Nicola, M.; Khani, M. M.; Jestin, J.; Benicewicz, B. C.; Kumar, S. K., Self-Assembly of Monodisperse versus Bidisperse Polymer-Grafted Nanoparticles. *ACS Macro Lett.* **2016,** *5* (7), 790-795.

(38) Zheng, Y.; Huang, Y.; Abbas, Z. M.; Benicewicz, B. C., One-pot synthesis of inorganic nanoparticle vesicles via surface-initiated polymerization-induced self-assembly. *Polym. Chem.* **2017,** *8* (2), 370-374.
(39) Matyjaszewski, K., The importance of exchange reactions in controlled/living radical polymerization in the presence of alkoxyamines and transition metals. *Macromolecular Symposia* **1996,** *111* (1), 47-61.
(40) Krys, P.; Matyjaszewski, K., Kinetics of Atom Transfer Radical Polymerization. *Eur. Polym. J.* **2017,** *89*, 482-523.
(41) Li, X.; Wang, W.-J.; Li, B.-G.; Zhu, S., Kinetics and Modeling of Solution ARGET ATRP of Styrene, Butyl Acrylate, and Methyl Methacrylate. *Macromolecular Reaction Engineering* **2011,** *5* (9-10), 467-478.
(42) Shipp, D. A.; Matyjaszewski, K., Kinetic Analysis of Controlled/"Living" Radical Polymerizations by Simulations. 2. Apparent External Orders of Reactants in Atom Transfer Radical Polymerization. *Macromolecules* **2000,** *33* (5), 1553-1559.
(43) Zhong, M.; Matyjaszewski, K., How Fast Can a CRP Be Conducted with Preserved Chain End Functionality? *Macromolecules* **2011,** *44* (8), 2668-2677.
(44) Buback, M.; Kurz, C. H.; Schmaltz, C., the Pressure dependence of propagation rate coefficients in free-radical homopolymerizations of methyl acrylate and dodecyl acrylate. *Macromol. Chem. Phys.* **1998,** *199* (8), 1721-1727.
(45) Keating Iv, J. J.; Lee, A.; Belfort, G., Predictive Tool for Design and Analysis of ARGET ATRP Grafting Reactions. *Macromolecules* **2017,** *50* (20), 7930-7939.

Chapter 9 Synthesis of Ultra-high Molecular Weight SiO_2-*g*-PMMA Particle Brushes

9.1. Preface

A simple route to synthesize ultra-high molecular weight particle brushes by surface-initiated atom transfer radical polymerization (SI-ATRP) from silica nanoparticles was developed. SiO_2-*g*-PMMA and SiO_2-*g*-PS particle brushes were prepared with different [SiO_2-Br]$_0$ concentration of initiating sites on the surface of the nanoparticles. Ultra-high MW (>10^6) SiO_2-*g*-PMMA particle brushes with narrow molecular weight distribution (<1.3) and different grafting densities were synthesized. The grafting density of SiO_2-*g*-PMMA particle brushes decreased with an increasing target degree of polymerization. The same conditions were applied to the synthesis of SiO_2-*g*-PS particle brushes. However, due to the lower propagation rate

constant of styrene, the coupling between SiO_2-*g*-PS particle brushes occurred and also some fraction of unattached homopolystyrene was generated by the thermal self- initiation of styrene, preventing the successful synthesis of ultra-high MW SiO_2-*g*-PS particle brushes.

In this chapter, the synthesis of ultra-high molecular weight SiO_2-*g*-PMMA particle brushes is discussed. I performed all synthetic work and the characterization in the project. Tong Liu, Jiajun Yan, Julian Sobieski, and Kevin C. Lin assisted in the synthesis and characterization work. Mateusz Olszewski helped to design the Scheme and Table of Contents. Professor Matyjaszewski and Professor Bockstaller conceived and organized the project and together with me wrote the manuscript.

This project was published in *Journal of Inorganic and Organometallic Polymers and Materials*, (**Zongyu Wang**, Tong Liu, Kevin C. Lin, Sipei Li, Jiajun Yan, Mateusz Olszewski, Julian Sobieski, Joanna Pietrasik, Michael R Bockstaller, Krzysztof Matyjaszewski, "Synthesis of Ultra-high Molecular Weight SiO_2-*g*-PMMA Particle Brushes", *Journal of Inorganic and Organometallic Polymers and Materials*, **2019**, 1-8.).

This work was supported by NSF (DMR 1501324 and DMR 1410845), the Department of Energy (DE-EE0006702), the National Science Center (grant UMO-2014/14/A/ST5/00204), as well as the Scott Institute for Energy Technologies at Carnegie Mellon University.

9.2. Introduction

Conventional radical polymerizations provide high molecular weight polymers, but slow initiation and fast termination limit access to polymers with predetermined molecular weights, narrow molecular weight distributions (MWDs), retained chain-end functionality, or block copolymers.[1-3] Conversely, reversible deactivation radical polymerization (RDRP) procedures

allow for excellent control of molecular weight, and enables the synthesis of polymers with diverse architecture, including hyperbranched, star, brush, and block copolymers, while also providing polymers with narrow and tunable MWDs.[4-12] However, procedures for the preparation of polymer nanocomposites with controlled molecular weights, well-defined architectures, and avenues to ultra-high molecular weight materials are limited. The relatively low molecular weights of the typical controlled radical polymerization products (<150,000) result in poor mechanical properties for the resulting hybrid materials. Applying RDRP techniques to achieve extraordinarily high chain lengths is challenging. The unavoidable side reactions generate a significant fraction of dead chains when the targeted molecular weights exceed 100,000. However, polymerizations targeting ultra-high molecular weight, defined here as molecular weight greater than $1x10^6$, have been achieved through atom transfer radical polymerization (ATRP), and reversible addition-fragmentation chain transfer (RAFT) polymerization.[13,14] Some previous efforts targeting high molecular weight polymers employed very high pressure,[15-18] long reaction times, heterogeneous conditions (i.e. emulsion polymerization),[19-23] low monomer conversion, and could be accompanied by a loss of control over the molecular weight distribution. In this contribution, we reveal a simple, low ATRP catalyst concentration route to prepare polymer grafted silica nanoparticles with degrees of polymerization (DPs) above 10,000.

9.3. Experimental Section

Materials

Monomers: styrene (S, 99%, Aldrich), methyl methacrylate (MMA, 99%, Aldrich) were purified by passing through a column filled with basic alumina to remove the inhibitor. Tris(2-dimethylaminoethyl)amine (Me_6TREN, 99%, Alfa), 4,4'-dinonyl-2,2'-bipyridyne (dNbpy, 97%,

Aldrich), anisole (99%, Aldrich), tetrahydrofuran (THF, 99%, VWR), methanol (99%, VWR), hexane (99%, VWR), acetone (99%, VWR), *N*,*N*-dimethylformamide (DMF, 99%, VWR), copper(II) bromide ($CuBr_2$, 99%, Aldrich), copper(II) chloride ($CuCl_2$, 99%, Aldrich),), tin(II) 2-ethylhexanoate ($Sn(EH)_2$, 95%, Aldrich), hexane (Fluka), 48% hydrofluoric acid aqueous solution (HF, >99.99%, Aldrich), ammonium hydroxide aqueous solution (NH_4OH, 28.0-30.0%, Fisher), anhydrous magnesium sulfate ($MgSO_4$, Fisher) were used as received without further purification. Copper (I) bromide (CuBr, 98%, Acros), was washed with glacial acetic acid to remove any soluble oxidized species, filtered, washed twice with anhydrous ethyl ether, dried and kept under vacuum. Silica nanoparticles, 30 wt % solution in methyl isobutyl ketone (MIBK-ST), effective diameter $d \approx 15.8$ nm, were kindly donated by Nissan Chemical Corp. and used as received. The tethered ATRP initiator 1-(chlorodimethylsilyl)propyl 2-bromoisobutyrate and surface-modified silica (SiO_2-Br) were prepared using previously reported procedures.[24,25] The surface initiator densities are moderated with a "dummy" initiator chlorotrimethylsilane (99%, Aldrich).

Synthesis

Procedure for synthesis of SiO_2-*g*-PMMA/PS particle brushes *via* activators regenerated by electron transfer (ARGET) ATRP.

Initiator (SiO_2-Br nanoparticles), monomer (MMA/S), solvents (anisole, DMF), $CuBr_2$, and Me_6TREN were mixed thoroughly in a sealed Schlenk flask. A stock solution of $Sn(EH)_2$ in anisole was prepared. Both mixtures were degassed by nitrogen purging, then the $Sn(EH)_2$ solution was injected into the Schlenk flask to activate the catalyst complex and the flask was immediately put into an oil bath. The MW of the polymer was measured by SEC.

Characterization

Transmission electron microscopy (TEM) was carried out using a JEOL 2000 EX electron microscope operated at 200 kV. The spatial distribution, radius and inter-particle distances of the SiO_2 nanoparticles were determined from statistical analysis of the TEM micrographs using ImageJ software.

Thermogravimetric analysis (TGA) with TA Instruments 2950 was used to measure the fraction of SiO_2 in the hybrids. The data were analyzed with TA Universal Analysis. The heating procedure involved four steps: (1) jump to 120 ºC; (2) hold at 120 ºC for 10 min; (3) ramp up at a rate of 20 ºC/min to 800 ºC; (4) hold for 2 min. The TGA plots were normalized to the total weight after holding at 120 ºC.

Dynamic light scattering (DLS). DLS, using a Malvern Zetasizer Nano ZS, was performed to confirm results obtained from TEM. It was also employed to determine volume-weighted average hydrodynamic diameters and distribution.

The grafting density was calculated using formula (1)[26-28].

$$\sigma_{\mathrm{TGA}} = \frac{(1-f_{\mathrm{SiO2}})N_{\mathrm{Av}}\,\rho_{\mathrm{SiO2}}\,d}{6\,f_{\mathrm{SiO2}}\,M_n} \qquad (1)$$

where f_{SiO2} is the SiO_2 fraction measured by TGA, N_{Av} is the Avogadro number, ρ_{SiO2} is the density of SiO_2 nanoparticles (2.2 g/cm^3), d is the average diameter of SiO_2 nanoparticles (15.8 nm), M_n is the overall number-average MW of the cleaved polymer brushes.

Number-average molecular weights (M_n) and MWDs were determined by size exclusion chromatography (SEC). The SEC was conducted with a Waters 515 pump and Waters 410

differential refractometer using PSS columns (Styrogel 10^5, 10^3, 10^2 Å) in THF as an eluent at 35 ºC and a flow rate of 1 ml min^{-1}. Linear PS and PMMA standards were used for calibration. The conversion was calculated by gravimetric analysis.

Determining the density of the initiating site for SiO_2-Br nanoparticles

The concentration of initiating sites on the surface of silica nanoparticles was determined by model reactions (i.e. polymerization of SiO_2-*g*-PMMA, $[MMA]_0/[SiO_2\text{-}Br]_0/[CuBr_2]_0/[Me_6TREN]_0/[Sn(EH)_2]_0$=2000:1: 1:10:8 with 45 vol% anisole, 5 vol% DMF at 60 ºC) with certain amount of SiO_2-Br nanoparticles (e.g. with 100 mg). After purification, SEC and TGA were conducted to characterize the grafting density of the particle brushes. The particles used in the current study had grafting density ~ 0.45/0.15/0.052 nm^{-2}, the –Br (initiating site) concentration on the surface was assumed the same. Based on the average radius of nanoparticles, 7.9 nm, density of silica, 2.2 g/cm^3, the average molar mass of SiO_2-Br, are 6,470 g/mol (high grafting density), 19,420 g/mol (medium grafting density), and 56,000 g/mol (low grafting density).

Determining the initiation efficiency of the reactions

The initiation efficiency was determined by two methods.

Efficiency-1 was calculated by eq.2

$$Efficieny_1 = {M_{n,theo}}/{M_{n,SEC}} \qquad (2)$$

Efficiency-2 was calculated by eq.3

$$Efficieny_2 = {\sigma}/{\sigma_0} \qquad (3)$$

where σ is the grafting density of particle brushes, σ_0 is the concentration of initiating sites on the surface of SiO_2-Br nanoparticles, which are 0.45 nm^{-2} (high grafting density), 0.15 nm^{-2} (medium grafting density), 0.052 nm^{-2}, (low grafting density), respectively.

9.4. Results and Discussion

15 nm SiO_2 nanoparticles were surface modified with an ATRP initiator, 1-(chlorodimethylsilyl)propyl 2-bromoisobutyrate, using previously reported procedures.[29] Moderating the concentration of initiator on the particle surface was accomplished by use of a "dummy" initiator chlorotrimethylsilane, to provide SiO_2-Br nanoparticles with three different grafting densities, 0.45/0.15/0.052 chain/nm^2, i.e. densely/intermediately/sparsely grafted. A low concentration catalyst system (25 ppm Cu^{II}/Me_6TREN) was chosen to carry out ARGET ATRP. In ARGET ATRP, a pre-catalyst Cu^{II}/L is added, or formed *in situ*, at the beginning of the polymerization. A fraction of the stable Cu^{II} complex is continuously reduced to an active Cu^{I}/L species by a reducing agent.[30] The advantage of ARGET ATRP is that the amount of copper in the polymerization can be significantly reduced, since Cu^{II}/L complexes formed *via* oxidation or *via* radical termination are constantly transformed to active Cu^{I}/L species by the reducing agent.[31-35] Tuning the targeted molecular weight and reaction times was expected to provide particle brushes with ultra-high molecular weight and different grafting densities (**Figure. 9.1**).

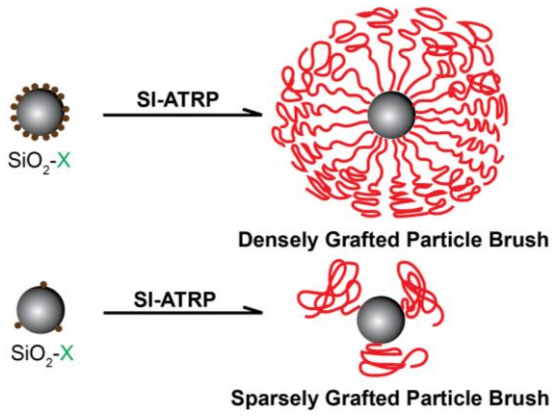

Figure. 9.1 Particle brush synthesis with different grafting densities

As shown in **Figure. 9.2**, compared to a linear homopolymer system with the same concentration of initiators in the system, localization of initiator sites on the surface of nanoparticles significantly alter the homogeneity of the reaction solutions, as the higher the grafting density of the particle brushes introduces a greater heterogeneity to the system. Termination in ATRP is a bimolecular reaction, which requires the collision between two radicals.[36,37] Due to the placement of the initiators on a particle, the size, and viscosity effects, the probability of collision between particle brushes (nanoparticles) is much lower than between linear homopolymers (small initiator molecules). Less termination could lead to the preparation of higher molecular weight polymer ligands.

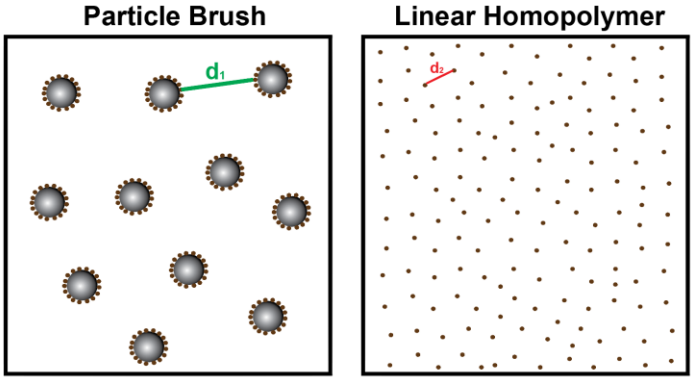

Figure. 9.2. Same initiator concentration with linear homopolymer and particle brushes

Controlled polymerization of methyl methacrylate (MMA) from the surfaces of SiO_2 nanoparticles was conducted using a low Cu catalyst ATRP procedure with different initiating sites densities and different $[SiO_2\text{-}Br]_0$, where SiO_2-Br served as the initiator and $CuBr_2/Me_6TREN$ as the catalyst. The polymerizations produced PMMA brushes with low dispersity (**Table 9.1**). To avoid gelation of the particle brushes, the conversion of MMA was limited to below 10%. As shown in **Table 9.1**, the obtained M_n values were consistently higher than theoretically predicted values as the target molecular weight increased, which is due to

limited initiation efficiency. This also resulted in reduced grafting density of the particle brushes which diminished with the target degree of polymerization. The initiation efficiency of the reactions was calculated by both $M_{n,\,\mathrm{SEC}}$ *vs.* $M_{n,\mathrm{theo}}$ and grafting density *vs*. the concentration of initiating sites (**Table 9.1**), and the results were very close. Ultra-high molecular weight PMMA particle brushes with different grafting densities (M_n=1.7×10^6, $Đ$=1.31, 0.009 nm^{-2}, M_n =1.0×10^6, $Đ$ = 1.31, 0.016 nm^{-2}, M_n =1.1×10^6, $Đ$ = 1.24, 0.018 nm^{-2}) were successfully synthesized within 21 hours.

Table 9.1. Result of syntheses of SiO_2-*g*-PMMA particle brushes with different grafting densities

Entry[a]	[SiO_2-Br] (ppm)	Time (h)	Conv[b] (%)	M_n[c]	$M_{n,theo}$	M_w/M_n [c]	f_{ino} (%)[d]	σ (nm^{-2})[e]	Efficiency-1(%)[f]	Efficiency-2(%)[g]
HGM-1	100	3	7.01	84,290	70,100	1.39	9.11	0.392	83	87
HGM-2	50	6	3.54	125,200	70,800	1.51	9.01	0.267	56	59
HGM-3	25	12	2.45	726,500	98,000	1.53	6.51	0.065	13	14
HGM-4	12.5	24	4.05	1,744,000	324,000	1.31	1.97	0.094	18	20
MGM-1	100	3	6.01	76,220	60,100	1.37	26.54	0.121	78	81
MGM-2	50	6	5.23	135,400	104,600	1.56	15.23	0.136	77	91
MGM-3	25	12	5.42	757,400	216,800	1.48	7.36	0.055	28	37
MGM-4	12.5	24	1.21	1,054,000	96,800	1.31	16.55	0.016	9	11
LGM-1	100	3	9.82	109,200	98,200	1.33	42.57	0.055	90	106
LGM-2	50	6	5.41	188,500	108,200	1.32	36.96	0.031	57	60
LGM-3	25	12	4.03	304,700	161,200	1.47	25.95	0.031	53	60
LGM-4	12.5	24	4.24	1,114,000	339,200	1.24	14.09	0.018	30	35

[a] Reaction condition: $[MMA]_0/[SiO_2\text{-}Br]_0/[CuBr_2]_0/[Me_6TREN]_0/[Sn(EH)_2]_0$=40000:4/2/1/0.5: 1:10:8 with 45 vol% anisole, 5 vol% DMF at 60 ºC. [b] Monomer conversion was determined with gravimetric analysis. [c] Determined by SEC. [d] Determined by TGA. [e] Calculated according to TGA data. [f] Calculated by eq.2. [g] Calculated by eq.3.

TEM was applied to study the morphology of the particle brushes and **Figure. 9.3** confirmed successful grafting of PMMA from silica nanoparticles. In the densely grafted particle systems (**Figure. 9.3**a-d), no apparent aggregation/particle couplings were observed. On the other hand, clear aggregations were seen in intermediately/sparsely grafted particle systems (**Figure. 9.3**e-l), which indicated more inter-particle interactions in those reactions. Agglomeration/couplings between particles could result from termination between polymer

ligands or interactions between bare particle surfaces. The clear/non-agglomeration TEM images from densely grafted particle brushes system suggest large heterogeneity which was introduced by the localization of initiators on the surface of nanoparticles can efficiently reduce the terminations between particle brushes. As compared to linear homopolymers, in the particle brush system the probability of effective collisions (and radical termination) between particles is much lower than between linear homopolymer chains. The hydrodynamic sizes of the particle brushes in THF solutions were measured by DLS. **Figure. 9.4**a shows the DLS traces of SiO_2-*g*-PMMA particle brushes with different DP and grafting densities, where the increase in hydrodynamic size with DP and grafting density can be observed. **Figure. 9.4**b shows more detailed measurement results for each sample, the trend of hydrodynamic size increases with DP and can be observed for all three sets of samples. It should be noted that the increase of particle brush size with DP was not linear due to the change of grafting density.

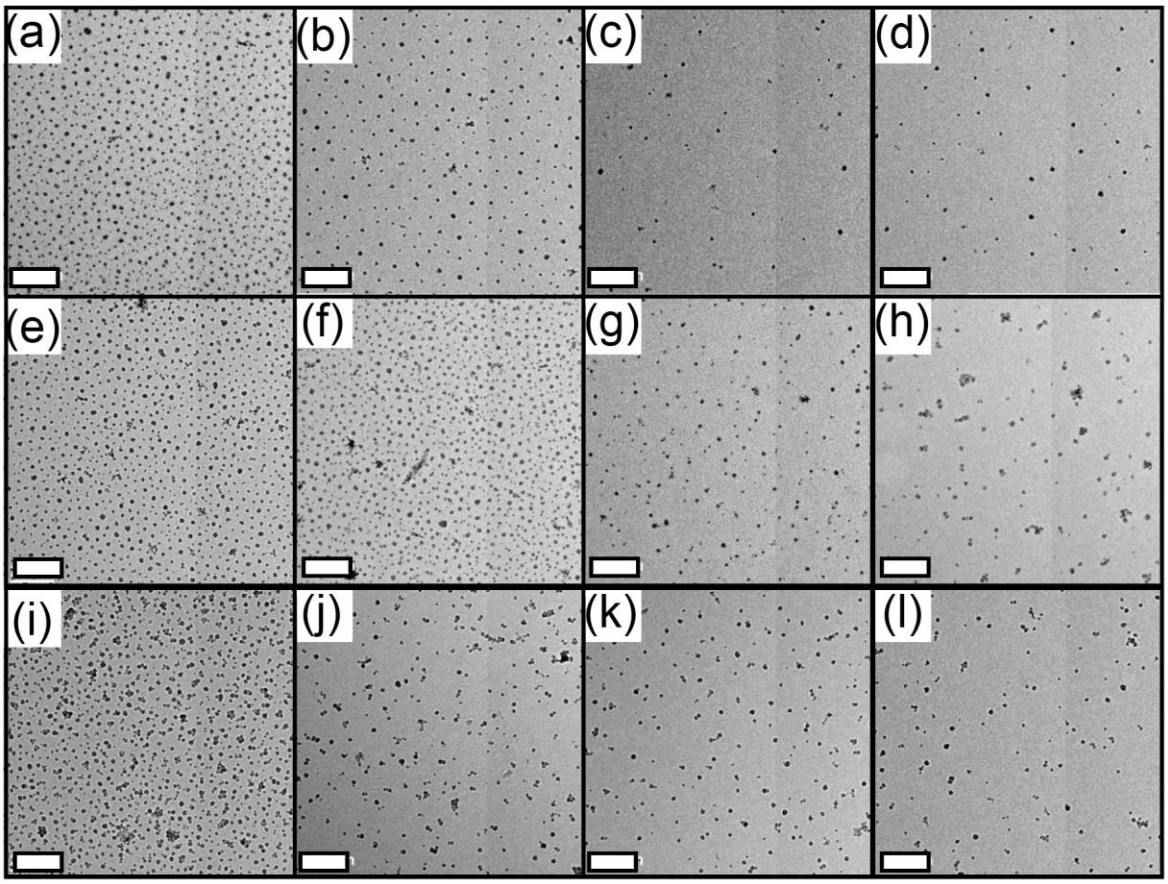

Figure. 9.3. TEM image of SiO_2-*g*-PMMA particle brushes: (a-d) HGM-1~4, (e-h) MGM-1~4, (i-l) LGM-1~4, scale bar 200 nm

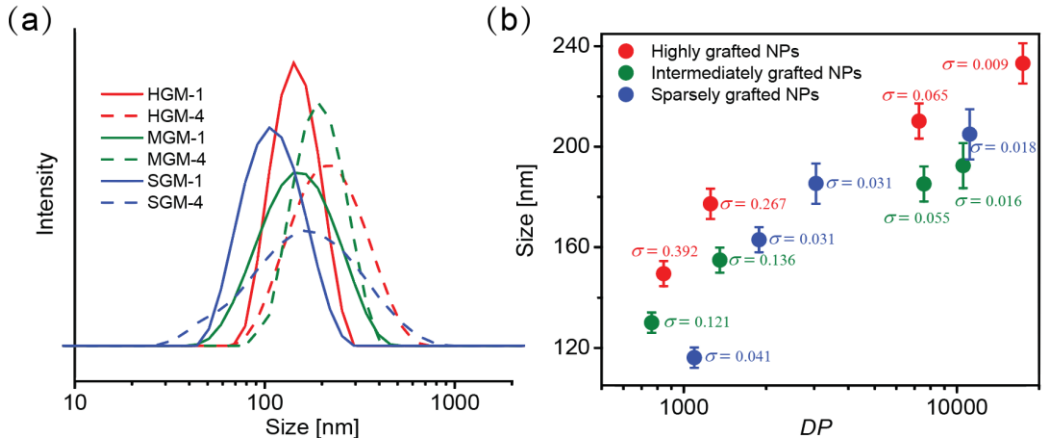

Figure. 9.4. DLS traces (a) SiO_2-*g*-PMMA particle brushes, (b) hydrodynamic diameter of SiO_2-*g*-PMMA particle brushes versus DP.

Table 9.2. Result of syntheses of SiO_2-*g*-PS particle brushes with different grafting densities

Entry[a]	[SiO_2-Br] (ppm)	Time (h)	Conv[b] (%)	M_n[c]	$M_{n,theo}$	M_w/M_n [c]	f_{ino} (%)[d]	σ (nm^{-2})[e]	efficiency(%) [f]	efficiency(%)[g]
HGS-1	100	3	2.37	50,940	24,600	1.49	16.55	0.328	48	73
HGS-2	50	6	1.41	39,010	29300	2.34	21.25	0.314	75	70

HGS-3	25	10	2.74	139,100	113,900	2.42	5.68	0.394	82	88
HGS-4	12.5	21	1.76	93,370	146,400	3.25	6.12	0.541	157	120
MGS-1	100	2	3.86	59,320	40,100	1.71	29.97	0.131	68	87
MGS-2	50	5	1.48	56,110	30,700	1.72	35.79	0.106	55	71
MGS-3	25	10	0.79	50,600	32,800	2.61	34.49	0.124	65	82
MGS-4	12.5	21	0.83	98,770	69,000	5.03	18.05	0.147	70	98
LGS-1	100	3	5.09	46,260	52,900	1.99	56.43	0.051	114	98
LGS-2	50	6	1.83	43,470	38,000	2.31	64.31	0.042	88	81
LGS-3	25	10	1.01	39,850	42,000	3.45	61.90	0.051	105	98
LGS-4	12.5	21	3.51	196,000	292,000	2.45	19.01	0.071	149	137

[a] Reaction condition: $[S]_0/[SiO_2\text{-}Br]_0/[CuBr_2]_0/[Me_6TREN]_0/[Sn(EH)_2]_0$=40000:4/2/1/0.5: 1:10:8 with 45 vol% anisole, 5 vol% DMF at 60 ºC. [b] Monomer conversion was determined with gravimetric analysis. [c] Determined by SEC. [d] Determined by TGA. [e] calculated according to TGA data. [f] Calculated by eq.S2. [g] Calculated by eq.S3.

SiO_2-*g*-PS particle brushes were prepared using the same method and same reaction conditions as developed for SiO_2-*g*-PMMA particle brushes (**Table 9.2**). The major differences between styrene (S) and methyl methacrylate (MMA) include: (i) a much lower k_p value for styrene than for MMA;[38-40] (ii) the termination mechanisms for MMA and S are different, i.e. in the former termination by disproportionation dominates, whereas in the latter combination dominates and coupling between particle brushes could lead to formation of aggregates and gelation;[41,42] and (iii) styrene undergoes spontaneous (thermal) polymerization.[43,44]

As shown in **Table 9.2**, ultra-high MW particle brushes cannot be obtained in a SiO_2-*g*-PS system under the same reaction conditions that were successful for SiO_2-*g*-PMMA. The highest M_n is around 200,000 and with high dispersity (M_w/M_n>2). This can be attributed to termination reactions and thermal-self initiation in the styrene system. Unlike SiO_2-*g*-PMMA, coupling in the SiO_2-*g*-PS system would cause non-uniform structures, agglomeration of particles and gelation, as shown in the TEM images (**Figure. 9.5**). The heterogeneity introduced by the agglomeration and increase of viscosity could lead to a further increase in the dispersity. One feature that was observed in the attempted synthesis of ultra-high MW SiO_2-*g*-PMMA particle brushes is that the grafting density of the particle brushes (initiation efficiency of the

reactions) decreased with the increasing target DP. However, in the SiO_2-*g*-PS system, the apparent grafting density/initiation efficiency first decreased but then increased with the target DP. The difference originates from the contribution of thermal-self initiation in styrene polymerization, which increases with reaction temperature and reaction time. The apparent high initiation efficiency (>100%, calculated from the entire polystyrene same. i.e. attached to the particles and unattached formed via self-initiation) shown in **Table 9.2** indicated the presence of a large amount of linear PS homopolymers in the systems.

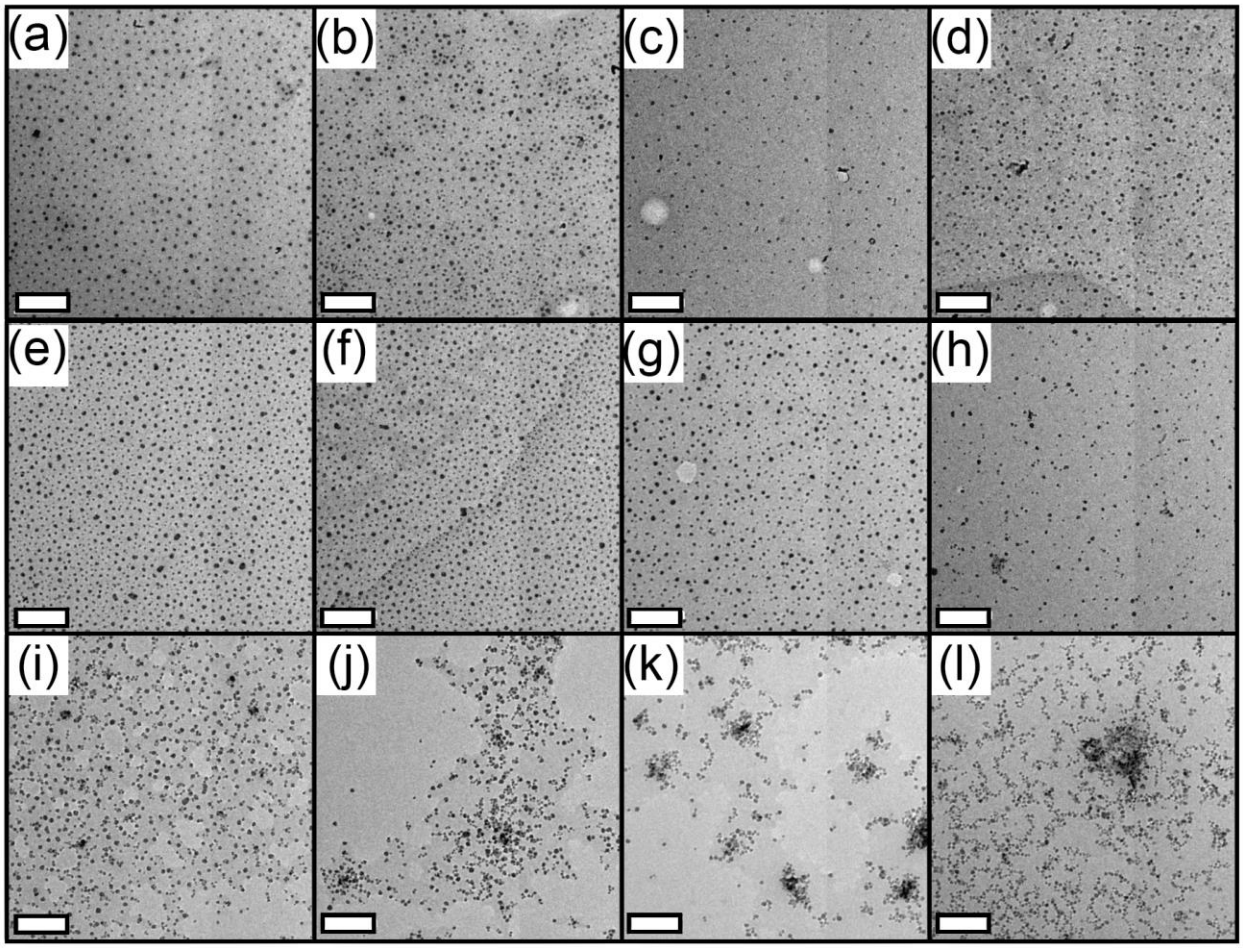

Figure. 9.5. TEM image of SiO_2-*g*-PS particle brushes: (a-d) HGS-1~4, (e-h) MGS-1~4, (i-l) LGS-1~4, scale bar 200 nm.

9.5. Conclusions

In conclusion, ultra-high MW (>10^6) SiO_2-*g*-PMMA with narrow molecular weight distribution (<1.3) and variable grafting densities of particle brushes were synthesized through ARGET-ATRP under low $[SiO_2\text{-}Br]_0$ condition within 21 hours. The grafting density of SiO_2-g-PMMA particle brushes decreased as the target DP was increased. The same conditions were applied to the synthesis of SiO_2-*g*-PS particle brushes; however, the ultra-high MW SiO_2-*g*-PS cannot be obtained. This is due to the lower propagation rate constant of styrene, more significant coupling between SiO_2-*g*-PS particle brushes and the unattached homopolymers formed by the self-thermal initiation of styrene.

9.6. References

[1] W.A. Braunecker, K. Matyjaszewski, Prog. Polym. Sci. 32, 93-146 (2007)
[2] R. Braslau, J. Am. Chem. Soc. 125, 3399-3400 (2003)
[3] K. Matyjaszewski, T.P. Davis In Handbook of Radical Polymerization, 2002, p 117-186.
[4] M. Husseman, E.E. Malmström, M. McNamara, M. Mate, D. Mecerreyes, D.G. Benoit, J.L. Hedrick, P. Mansky, E. Huang, T.P. Russell, C.J. Hawker, Macromolecules 32, 1424-1431 (1999)
[5] K. Matyjaszewski, J. Xia, Chem. Rev. 101, 2921-2990 (2001)
[6] K.Y. Choi, J.J. Han, B. He, S.B. Lee, J. Am. Chem. Soc. 130, 3920-3926 (2008)
[7] J.O. Zoppe, N.C. Ataman, P. Mocny, J. Wang, J. Moraes, H.-A. Klok, Chem. Rev. 117, 1105-1318 (2017)
[8] C.M. Hui, J. Pietrasik, M. Schmitt, C. Mahoney, J. Choi, M.R. Bockstaller, K. Matyjaszewski, Chem. Mater. 26, 745-762 (2014)
[9] K. Matyjaszewski, Macromolecules 45, 4015-4039 (2012)
[10] J.-S. Wang, K. Matyjaszewski, J. Am. Chem. Soc. 117, 5614-5615 (1995)
[11] J. Chiefari, Y.K. Chong, F. Ercole, J. Krstina, J. Jeffery, T.P.T. Le, R.T.A. Mayadunne, G.F. Meijs, C.L. Moad, G. Moad, E. Rizzardo, S.H. Thang, Macromolecules 31, 5559-5562 (1998)
[12] M. Kamigaito, T. Ando, M. Sawamoto, Chem. Rev. 101, 3689-3746 (2001)
[13] J.K.D. Mapas, T. Thomay, A.N. Cartwright, J. Ilavsky, J. Rzayev, Macromolecules 49, 3733-3738 (2016)
[14] R. Nicolaÿ, Y. Kwak, K. Matyjaszewski, Angew. Chem. Int. Ed. 49, 541-544 (2010)
[15] J. Rzayev, J. Penelle, Angew. Chem. Int. Ed. 43, 1691-1694 (2004)
[16] L. Mueller, W. Jakubowski, K. Matyjaszewski, J. Pietrasik, P. Kwiatkowski, W. Chaladaj, J. Jurczak, Eur. Polym. J. 47, 730-734 (2011)
[17] T. Arita, Y. Kayama, K. Ohno, Y. Tsujii, T. Fukuda, Polymer 49, 2426-2429 (2008)

[18] P. Kwiatkowski, J. Jurczak, J. Pietrasik, W. Jakubowski, L. Mueller, K. Matyjaszewski, Macromolecules 41, 1067-1069 (2008)
[19] R.W. Simms, M.F. Cunningham, Macromolecules 40, 860-866 (2007)
[20] D. Charmot, P. Corpart, H. Adam, S.Z. Zard, T. Biadatti, G. Bouhadir, Macromolecular Symposia 150, 23-32 (2000)
[21] X.-Y. Zhang, D.-M. Liu, X.-H. Lv, M. Sun, X.-L. Sun, W.-M. Wan, Macromol. Rapid Commun. 37, 1735-1741 (2016)
[22] P.B. Zetterlund, Y. Kagawa, M. Okubo, Chem. Rev. 108, 3747-3794 (2008)
[23] N.P. Truong, M.V. Dussert, M.R. Whittaker, J.F. Quinn, T.P. Davis, Polym. Chem. 6, 3865-3874 (2015)
[24] K. Matyjaszewski, P.J. Miller, N. Shukla, B. Immaraporn, A. Gelman, B.B. Luokala, T.M. Siclovan, G. Kickelbick, T. Vallant, H. Hoffmann, T. Pakula, Macromolecules 32, 8716-8724 (1999)
[25] J. Pyun, S. Jia, T. Kowalewski, G.D. Patterson, K. Matyjaszewski, Macromolecules 36, 5094-5104 (2003)
[26] C.C. Greenberg, M.D. Foster, C.M. Turner, S. Corona-Galvan, E. Cloutet, P.D. Butler, B. Hammouda, R.P. Quirk, Polymer 40, 4713-4716 (1999)
[27] S. Turgman-Cohen, J. Genzer, J. Am. Chem. Soc. 133, 17567-17569 (2011)
[28] M.J.A. Hore, J. Ford, K. Ohno, R.J. Composto, B. Hammouda, Macromolecules 46, 9341-9348 (2013)
[29] J. Yan, T. Kristufek, M. Schmitt, Z. Wang, G. Xie, A. Dang, C.M. Hui, J. Pietrasik, M.R. Bockstaller, K. Matyjaszewski, Macromolecules 48, 8208-8218 (2015)
[30] H. Ding, S. Park, M. Zhong, X. Pan, J. Pietrasik, C.J. Bettinger, K. Matyjaszewski, Macromolecules 49, 6752-6760 (2016)
[31] Y. Kwak, A.J.D. Magenau, K. Matyjaszewski, Macromolecules 44, 811-819 (2011)
[32] W. Jakubowski, K. Matyjaszewski, Angew. Chem. Int. Ed. 45, 4482-4486 (2006)
[33] K. Matyjaszewski, H. Dong, W. Jakubowski, J. Pietrasik, A. Kusumo, Langmuir 23, 4528-4531 (2007)
[34] W. Jakubowski, K. Min, K. Matyjaszewski, Macromolecules 39, 39-45 (2006)
[35] T.G. Ribelli, F. Lorandi, M. Fantin, K. Matyjaszewski, Macromol. Rapid Commun. 40, 1800616 (2019)
[36] J.C. Bevington, H.W. Melville, R.P. Taylor, J. Polym. Sci. 12, 449-459 (1954)
[37] G. Moad, D.H. Solomon In The Chemistry of Radical Polymerization (Second Edition), G. Moad, D.H. Solomon, Eds., Elsevier Science Ltd: Amsterdam, 2005, p 11-48.
[38] M. Buback, R.G. Gilbert, R.A. Hutchinson, B. Klumperman, F. Kuchta, B.G. Manders, K.F. O'Driscoll, G.T. Russell, J. Schweer, Macromol. Chem. Phys. 196, 3267-3280 (1995)
[39] X. Li, W.-J. Wang, B.-G. Li, S. Zhu, Macromolecular Reaction Engineering 5, 467-478 (2011)
[40] P. Krys, K. Matyjaszewski, Eur. Polym. J. 89, 482-523 (2017)
[41] Y. Nakamura, S. Yamago, Macromolecules 48, 6450-6456 (2015)
[42] M. Buback, F.D. Kuchta, Macromol. Chem. Phys. 198, 1455-1480 (1997)
[43] W.A. Pryor, J.H. Coco, Macromolecules 3, 500-508 (1970)
[44] M.N. Tchoul, M. Dalton, L.-S. Tan, H. Dong, C.M. Hui, K. Matyjaszewski, R.A. Vaia, Polymer 53, 79-86 (2012)

.

Chapter 10 Molecular Parameters Governing the Elastic Properties of Brush Particle Films

10.1. Preface

Elucidation of the mutual influence of the composition and architecture of polymer canopies on the assembly and mechanical properties of particle brush-based materials holds the promise of advancing the understanding of the governing parameters controlling interactions in hybrid materials and the development of novel functional materials. In this work, the elastic properties of three series of brush particle systems were investigated, differentiated by grafting density as dense, intermediate and sparse brush systems. Dense and intermediate systems displayed uniform microstructures; the degree of order (measured using Voronoi cell area analysis) increased with grafting density. For dense and intermediate brush particle systems, instrumented indentation analysis revealed an increase of the elastic modulus with the degree of polymerization of tethered chains. Furthermore, the effectiveness of ligands to enhance interactions increased with decreasing grafting density. The results are rationalized as a consequence of more pronounced brush interdigitation in the case of intermediate systems and the resulting increase of the dispersion interactions between ligands of adjacent particles. A reversed trend in modulus was observed in films of sparse brush particles that also featured the formation of string-like superstructures. Here, the elastic modulus was substantially increased for low molecular ligands and continuously decreased with increasing degree of polymerization of tethered chains along with a transition from string-like to uniform morphologies. Independent of grafting density, the elastic modulus of the pristine polymer was recovered in the limit if a high degree of polymerization of polymer ligands.

In this chapter, the mechanical properties of SiO_2-*g*-PMMA/PS particle brushes are discussed. I performed all synthetic work and parts of characterization in the project. I would like to thank especially my collaborators, Jaejun Lee for his extensive discussion and careful characterization work.

This project will be published in *Macromolecules*.

The financial support from the National Science Foundation (DMR 1501324, CMMI-1663305) and the Department of Energy (Basic Energy Sciences) via award DE-SC0018854 is gratefully acknowledged. The authors would like to further acknowledge the use of facilities at the Materials Characterization Facility at Carnegie Mellon University under grant MCF-677785 and the Colloids, Surfaces, and Polymer Laboratory under grant CMU 678083-769798.

10.2. Introduction

Recent advances in the field of surface-initiated reversible deactivation radical polymerization (SI-RDRP) enable the grafting of polymeric chains to the surface of nanoparticles with controlled grafting density, molecular weight, dispersity and composition.[1–6] The resulting brush (or 'hairy') particles have been pursued as building blocks for the fabrication of 'one-component hybrid materials' that are formed via the assembly of brush particles in the absence of an additional matrix polymer.[7–13] Interest in one-component hybrids is motivated by microstructural features that give rise to novel property characteristics.[14,15] Mean-field theory, computer simulations, and experiments have revealed that 'steric confinement' insufficiently dense brush materials give rise to a transition of chain conformation from more stretched (in the vicinity of the surface) to more relaxed at the sufficiently high degree of polymerization or low grafting density or particle size.[7–9, 11,13,16–23] Because physical properties of polymers are sensitive to orientation, this presents the prospect of realizing novel functionalities in brush particle hybrids by deliberate control of the orientation of tethered chains. For example, increasing chain orientation in dense brush systems has been argued to raise thermal transport,

to reduce dielectric breakdown, or to result in novel phonon transport characteristics of brush particle hybrids.[24–26] More relaxed (coiled) chain conformations were shown to promote chain entanglement, thus giving rise to polymer-like deformation properties and formability.[7–9] This was used to enable the fabrication of 'moldable colloidal crystals' as well as transparent high refractive index glasses or low-modulus hybrid elastomers that might find use in soft robotics.[8,12,27–29] As brush particles are assembled into films (these will be denoted 'particle solids' in the following), the constraints arising from the packing into ordered structures have been shown to induce further chain perturbation that has been harnessed, for example, for the fabrication of mesoporous membranes.[30]

As the density of tethered chains is reduced to values of about 0.05 nm^{-2} (the so-called 'sparse' grafting regime), distinctive differences in the assembly behavior of brush particles – such as the formation of anisotropic sheet and string structures – was observed.[20,31–35] The polarization of particle interactions was related to the segregation of tethered chains into the galley regions between particle strings. This breaking of symmetry is thought to minimize free energy by enabling more relaxed chain conformations and more effective particle core interactions.[31–35]

To understand the effect of brush architecture on material performance, research has focused on the thermomechanical and relaxation behavior of brush particle hybrids. Concerning mechanical properties of solid brush particle films, two quantities were of particular interest, *i.e.* the elastic (Young's) modulus and the fracture toughness.[36–38] The former is related to short-range interactions between constituents (and thus gives information about the relevant bonding interactions) while the latter gives insight into dissipative pathways within materials during fracture. The elasticity of particle brush solids was evaluated using a variety of techniques such as micro- and nanoindentation, uniaxial extension, buckling as well as non-contact Brillouin scattering.[7,8,20,26,31,39–43] Indentation experiments by Podsiadlo *et al*. (on films assembled from low molecular surfactant-coated semiconductor nanocrystals)

were the first to suggest the elastic response of particle solids to be determined by dispersion interactions between tethered ligands.[39] Nanoindentation in conjunction with tensile testing confirmed this conclusion for polymeric ligands.[7,8,20,43,44] These studies further revealed a toughening transition above a threshold molecular weight of polymeric tethers that was attributed to the onset of entanglement of tethered chains and the associated increase in ductility of particle brush hybrids. Experiments, theory, and simulations correlated this brittle-ductile transition to the more relaxed (coiled) chain conformations that are favored for a sufficiently large degree of polymerization.[7,16,18,19,45] In sparse grafted systems, mechanical analysis (using wrinkling and shear tests) have revealed a significant enhancement of elastic moduli.[20,31] This was interpreted to be a consequence of the organization of sparse brush particles into anisotropic string-like superstructures. Recent BLS experiments and simulations suggested that this 'strengthening effect' is caused by the concentration of polymer segments within 'interstitial spaces' between particle strings and the associated increase of the contribution of core-core interactions to the elastic modulus.[16,42]

Collectively, previous research illustrates the relevance of brush architecture on the properties of particle brush-based materials. A requisite for translating these results into opportunities for material design is a better understanding of the mutual influence of the various relevant characteristics of polymer canopies on performance. For example, while modulus and toughness have been shown to increase with a molecular weight of polymeric tethers, the associated reduction of inorganic content limits the practical use of the one-component hybrid approach for material design.[7–9,44] A concurrent reduction of the grafting density could alleviate this problem. This raises intriguing questions: Is there an optimum graft density to enhance the mechanical properties of particle brush materials? Can isotropic microstructures be retained in the limit of low grafting densities (which might be preferable for applications)? What is the role of graft composition (monomodal vs. multimodal) and chain dispersity (narrow vs. wide) on the interactions in brush particle materials? This contribution presents a systematic

evaluation of the effect of grafting density on the structure and elastic properties of narrow-dispersed and monomodal brush particle systems; the role of graft molecular weight distribution will be explored in a subsequent paper. Six series of particle brush model systems representing the dense, intermediate and sparse grafting regimes, respectively, were evaluated. In principle, the distinct grafting regimes could be distinguished based on the conformation of tethered chains that is predicted, for example, via the Daoud-Cotton (DC) model.[46–49] The latter ascribes a 'critical' radius $r_c = r_0\sigma_s^{1/2}/\nu$, where σ_s denotes the grafting density, r_0 the particle radius, and ν the excluded volume parameter, to indicate the transition between two conformational regimes. Segmental crowding in the limit of $r < r_c$ is predicted to induce stretched chain conformations (the concentrated polymer brush regime, CPB) whereas relaxed conformations are expected for a brush particle diameter $r > r_c$ (the semi-dilute polymer brush regime, SDPB). Conceptually, one might then distinguish dense, intermediate and sparse grafting regimes, like those corresponding to $r_0 < r_c$, $r_0 \sim r_c$, and $r_0 > r_c$, respectively. However, in the literature, the sparse grafting regime has been identified on an empirical basis as the regime in which grafting density is low enough to drive the formation of string-like superstructures.[32] The latter not only depends on the characteristics of tethered chains but also on geometrical features such as particle size or uniformity.[19,31] For this reason, in the following, a more 'ad hoc' definition of grafting regimes will be adopted that is based on the underlying initiator density and the observed behavior of brush particle assemblies. The material system consists of silica particles with radius $r_0 = 7.9 \pm 2.2$ nm tethered with polystyrene (PS) and poly(methyl methacrylate) (PMMA). Both polymers are glassy at room temperature for all tested molecular weights. This is a requisite for the present study as it simplifies the analysis of elastic properties and avoids convoluting influences of morphological features (such as crystallization) on structure-property relations. Dense, intermediate and sparse regimes are defined as grafting density in the range of 1, 0.3 and 0.05 nm^{-2} (the numbers correspond to the respective density of initiator sites, see below). While this definition is, by nature, specific for the present material system, the conclusions are

consistent with reported findings in the literature on diverse brush particle compositions.[8,20] We thus expect this classification to be useful as a basis for the more general categorization of brush particle systems. For brush particles with dense and intermediate grafting density, we find the effectiveness of ligands to enhance interactions (measured in terms of Young's modulus as a function of volume fraction of polymer repeat units) to increase with decreasing grafting density. This is interpreted as a consequence of increased brush interdigitation which raises interactions between ligands of adjacent particles. In this regime, the elastic modulus increases with the degree of polymerization of tethered chains, a trend that is captured by a model that attributes the effective brush particle interactions to the dispersion forces between segments of interdigitated chains. In contrast, the opposite trend in modulus is observed in films of sparse brush particles that feature the formation of string-like superstructures. Our results point to subtle relationships between brush architecture, interactions, and properties of brush particle films that could benefit material design and hence merit further investigation.

10.3. Experimental Section

Materials

Monomers (styrene (S, 99%, Aldrich) and methyl methacrylate (MMA, 99%, Aldrich)) were purified by passing through a column filled with basic alumina to remove the inhibitor. Tris(2-dimethylaminoethyl)amine (Me_6TREN, 99%, Alfa), 4,4'-dinonyl-2,2'-bipyridyne (dNbpy, 97%, Aldrich), anisole (99%, Aldrich), tetrahydrofuran (THF, 99%, VWR), methanol (99%, VWR), hexane (99%, VWR), acetone (99%, VWR), N,N-dimethylformamide (DMF, 99%, VWR), 2-bromoisobutyryl bromide (2BiB, Aldrich, 98%), triethylamine (TEA, Aldrich, 99.5%), copper(II) bromide ($CuBr_2$, 99%, Aldrich), copper(II) chloride ($CuCl_2$, 99%, Aldrich), copper(I) chloride (CuCl, 97%, Sigma-Aldrich), tin(II) 2-ethylhexanoate ($Sn(EH)_2$, 95%, Aldrich), hexane (Fluka), 48% hydrofluoric acid aqueous solution (HF, >99.99%, Aldrich), ammonium hydroxide aqueous solution (NH_4OH, 28.0-30.0%, Fisher),

anhydrous magnesium sulfate ($MgSO_4$, Fisher), hexamethyldisilazane (HMDZ, Aldrich, 99%) were used as received unless otherwise stated. Copper (I) bromide (CuBr, 98%, Acros), was washed with glacial acetic acid to remove any soluble oxidized species, filtered, washed twice with anhydrous ethyl ether, dried and kept in vacuum. Silica nanoparticles (SiO_2) 30 wt% dispersion in methyl isobutyl ketone (MIBK-ST), with an effective radius 7.9 ± 2.2 nm, measured by transmission electron microscopy (TEM), were donated by Nissan Chemical America Corp. The surface initiator densities are moderated with a dummy initiator chlorotrimethylsilane (99%, Aldrich).

Synthesis of tetherable initiator, 3-(Chlorodimethylsilyl)propyl 2-bromoisobutyrate (BiBSiCl)

18.6 mL (273 mmol) of allyl alcohol and 38.1 mL (273 mmol) of TEA were dissolved in 100 mL of dry THF in a round bottom flask and cooled down to 0 °C in an ice bath. 27.0 (218 mmol) mL of 2BiB was diluted with 50 mL of dry THF. The 2BiB solution was added dropwise to the reaction solution over 30 min while the reaction was stirred in the ice bath. The reaction mixture was then stirred at room temperature overnight. The resulting suspension was filtered and the residue washed with THF. The filtrate was diluted with 200 mL of ethyl ether and washed three times with deionized (DI) water, once with saturated $NaHCO_3$ solution and once with brine. The organic solution was dried over anhydrous Na_2SO_4. Upon removal of solvents in vacuo, allyl 2-bromoisobutyrate was obtained as a slightly yellow liquid. 1 H NMR (300 MHz, $CDCl_3$) δ: 5.94 (dt, J = 17.3, 10.5, 5.6 Hz, 1H), 5.39 (dq, J = 17.3, 1.5 Hz, 1H), 5.27 (dq, J = 10.5, 1.5 Hz, 1H), 4.67 (dt, J = 5.5, 1.4 Hz, 2H), 1.95 (s, 6H) ppm.

30.0 g (145 mmol) of allyl 2-bromoisobutyrate and 94.4 mL (869 mmol) of chlorodimethylsilane were mixed in a round bottom flask sealed with a rubber septum. The flask was placed in an ice bath and dry nitrogen was bubbled through the solution for 10 min. 1.2 mL of Karstedt's catalyst solution was added dropwise to the purged solution then the reaction solution was stirred for two days after returning to room temperature. The conversion was monitored by 1 H NMR. Unreacted silane was removed by

rotary evaporation. The platinum catalyst was precipitated when the crude product was cooled down to −18 ºC and was removed via filtration through a 450 nm PTFE syringe filter. The product was obtained as a yellow liquid. 1 H NMR (300 MHz, $CDCl_3$) δ: 4.18 (t, J = 6.7 Hz, 2H), 1.94 (s, 6H), 1.86-1.78 (m, 2H), 0.93-0.83 (m, 2H), 0.44 (s, 6H) ppm

Surface modification of silica NPs

Dry nitrogen was bubbled through 10 mL of dispersion of the silica particles (in MIBK-ST) for 5 min then 1.5 mL of a mixture of initiator and dummy initiator solutions was slowly injected into the dispersion. The reaction was stirred at 60 °C for 24 h then the flask was cooled down to room temperature and 1.1 mL (5.4 mmol) of HMDZ was slowly injected to the reaction. The pale brown dispersion was stirred at 35 °C for another 12 h. The modified nanoparticles were dialyzed against methanol three times and acetone twice.

SI-ATRP of PS-grafted silica NPs

Surface-modified NPs (SiO_2-Br), monomers (styrene, methyl methacrylate), solvents (anisole, DMF), $CuBr_2$, and Me_6TREN were mixed thoroughly in a sealed Schlenk flask. Meanwhile, a stock solution of $Sn(EH)_2$ in anisole was prepared. Both mixtures were degassed by nitrogen purging, then the $Sn(EH)_2$ solution was injected into the Schlenk flask to activate the catalyst complex and the flask was immediately put into an oil bath. For a detailed procedure, we followed the reference.[4] Characteristics of the polymer were monitored by gravimetric analysis and SEC, respectively.

Size exclusion chromatography (SEC)

Number-average molecular weights (M_n) and molecular weight distributions (MWDs) were determined by SEC. The SEC was conducted with a Waters 515 pump and Waters 410 differential

refractometer using PSS columns (Styrogel 105, 103, 102 Å) in THF as an eluent at 35 °C and a flow rate of 1 ml min^{-1}. Linear PS and PMMA standards were used for calibration.

Thermogravimetric Analysis (TGA)

TGA with TA Instruments 2950 was used to measure the fraction of SiO_2 in the hybrids. The data were analyzed with TA Universal Analysis. The heating procedure involved four steps: (1) jump to 120 °C; (2) hold at 120 ºC for 10 min; (3) ramp up at a rate of 20 °C/min to 800 °C; (4) hold for 2 min. The TGA plots were normalized to the total weight after holding at 120 °C.

Transmission Electron Microscopy (TEM)

Approximately monolayer films of all particle brush systems were prepared by drop-casting of dilute colloidal solutions (~ 1 mg/mL in THF) on a carbon-supported copper grid. The particulate film morphology and craze formation were studied using TEM with a JEOL EX2000 electron microscope operated at 200 kV. Images with amplitude and phase contrast were obtained by a Gatan Orius SC600 high-resolution camera.

Nanoindentation

Relatively thick films (> 20 μm) were prepared from concentrated solutions (~ 20 mg/mL) using PTFE molds. Elastic modulus and indentation hardness of films were characterized using an MTS nanoindenter XP with a Berkovich indenter of which the shape is tetrahedral. Displacement was under control to no more than 10% of the particulate film thickness to exclude any effect from substrates. Poisson's ratio of the material was calculated based on composition using the Voigt model for composite materials.[37] Details are shown in supporting information. At least nine locations were indented with a 500 nm depth limit, 5 nm/s displacement rate, 0.05 nm/s allowable drift rate and 10

seconds constant loading time before unloading for each sample. The standard deviation of the measurements was calculated as experimental error.

Atomic Force Microscopy (AFM)

The residual indentations from nanoindentation were visualized using AFM on an NT-MDT SolverNEXT system in semi-contact mode with silicon cantilevers (300 kHz resonance frequency, 40 N m^{-1} force constant) of small tip radius (< 10 nm). Samples were imaged in height and phase imaging modes to observe the indented surface.

Image analysis

Micrographs were analyzed using the combination of ImageJ and MATLAB. The particle-to-particle distance was manually measured with ImageJ, while Voronoi tessellation analysis was carried out by programming with MATLAB. See details in supporting information.

10.4. Results and Discussion

A library of silica particle (r_0 = 7.9 ± 2.2 nm) brush materials with systematically controlled degree of polymerization (*N*) of grafted polystyrene (PS) and poly(methyl methacrylate) (PMMA) chains as well as surface grafting density (σ_s) was synthesized *via* surface-initiated atom transfer radical polymerization (SI-ATRP) using established protocols[1,3,5,50,51]. The classification of brush particles into dense, intermediate, and sparse (sample ID: SiO_2-*d*/*i*/*s*-(S or MMA)*N*) is based on the respective composition of active and inactive sites of partially passivated silica particles as illustrated in **Figure 10.1**.

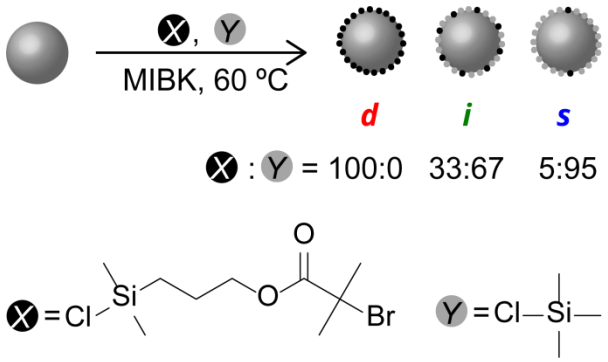

Figure 10.1. Synthesis and categorization of dense (*d*), intermediate (*i*), and sparse (*s*) brush particles. Control of grafting density is facilitated by silanization with the distinct ratio between an active initiator (*X*, black circle; 3-(chlorodimethylsilyl)propyl 2-bromoisobutyrate, BiBSiCl) and inactive (*Y*, gray circle; chlorotrimethylsilane) sites.

A summary of the relevant characteristics of PS- and PMMA brush particle systems is presented in **Table 10.1** and **Table 10.2**. Where possible, the results will be complemented with those of PMMA brush particles (~ 0.4 chains/nm^2) that were synthesized as part of a previous study (and hence present an independent reference) to strengthen the generalizability of the presented results. The compositional characteristics for these particles are tabulated in **Table S10.1**; data relating to these materials in figures are marked with asterisks.

Table 10.1. Molecular characteristics of polystyrene tethered SiO2-d/i/s-SN brush particles**.**

Sample ID	N	M_w/M_n	f_{org}	ϕ_{org}	σ_s (nm^{-2})
SiO_2-*d*-S120	120	1.17	0.75	0.86	0.78
SiO_2-*d*-S136	136	1.11	0.78	0.88	0.85
SiO_2-*d*-S204	204	1.10	0.83	0.91	0.74
SiO_2-*d*-S212	212	1.14	0.83	0.91	0.72
SiO_2-*d*-S226	226	1.11	0.84	0.92	0.74
SiO_2-*d*-S231	231	1.20	0.82	0.90	0.62
SiO_2-*d*-S231(2)	231	1.14	0.85	0.92	0.78
SiO_2-*d*-S355	355	1.10	0.87	0.94	0.61
SiO_2-*d*-S365	365	1.15	0.89	0.94	0.71
SiO_2-*d*-S365(2)	365	1.18	0.87	0.93	0.58
SiO_2-*d*-S400	400	1.22	0.88	0.94	0.61
SiO_2-*d*-S432	432	1.47	0.91	0.96	0.75
SiO_2-*d*-S549	549	1.25	0.89	0.94	0.46
SiO_2-*d*-S638	638	1.36	0.91	0.95	0.50
SiO_2-*d*-S762	762	1.35	0.92	0.96	0.49
SiO_2-*d*-S829	829	1.72	0.94	0.97	0.60
SiO_2-*d*-S841	841	1.18	0.93	0.96	0.48
SiO_2-*d*-S890	890	1.25	0.93	0.96	0.45
SiO_2-*d*-S1087	1087	1.28	0.92	0.96	0.33

SiO_2-*d*-S1777	1777	1.19	0.91	0.96	0.19
SiO_2-*d*-S1800	1800	1.42	0.93	0.96	0.22
SiO_2-*i*-S221	221	1.09	0.55	0.72	0.17
SiO_2-*i*-S255	255	1.11	0.49	0.66	0.12
SiO_2-*i*-S313	313	1.15	0.59	0.75	0.15
SiO_2-*i*-S328	328	1.14	0.62	0.77	0.16
SiO_2-*i*-S440	440	1.15	0.63	0.78	0.12
SiO_2-*i*-S758	758	1.10	0.71	0.84	0.10
SiO_2-*i*-S1103	1103	1.24	0.72	0.84	0.07
SiO_2-*s*-S432	432	1.21	0.31	0.48	0.03
SiO_2-*s*-S600	600	1.29	0.42	0.60	0.04
SiO_2-*s*-S954	954	1.33	0.45	0.63	0.03
SiO_2-*s*-S1576	1576	1.47	0.55	0.72	0.03

Variables represent the degree of polymerization of graft, N; dispersity index, M_w/M_n; weight fraction of polymer, f_{org}; volume fraction of polymer, ϕ_{org}; surface grafting density, σ_s.

Table 10.2. Molecular characteristics of poly(methyl methacrylate) tethered SiO_2-*d*/*i*/*s*-MMA*N* brush particles.

Sample ID	N	M_w/M_n	f_{org}	ϕ_{org}	σ_s (nm^{-2})
SiO_2-*d*-MMA188	188	1.21	0.80	0.88	0.71
SiO_2-*d*-MMA213	213	1.18	0.82	0.90	0.69
SiO_2-*d*-MMA250	250	1.25	0.84	0.91	0.69
SiO_2-*d*-MMA382	382	1.15	0.90	0.95	0.79
SiO_2-*d*-MMA405	405	1.18	0.89	0.94	0.68
SiO_2-*d*-MMA445	445	1.16	0.91	0.95	0.76
SiO_2-*d*-MMA460	460	1.18	0.92	0.96	0.80
SiO_2-*d*-MMA777	777	1.15	0.95	0.97	0.78
SiO_2-*i*-MMA206	206	1.35	0.49	0.65	0.16
SiO_2-*i*-MMA379	379	1.22	0.70	0.82	0.20
SiO_2-*i*-MMA563	563	1.13	0.74	0.84	0.17
SiO_2-*i*-MMA637	637	1.25	0.78	0.87	0.19
SiO_2-*i*-MMA732	732	1.13	0.83	0.90	0.22
SiO_2-*i*-MMA752	752	1.24	0.83	0.90	0.21
SiO_2-*s*-MMA232	232	1.23	0.23	0.36	0.04
SiO_2-*s*-MMA365	365	1.15	0.32	0.47	0.04
SiO_2-*s*-MMA401	401	1.17	0.38	0.54	0.05
SiO_2-*s*-MMA477	477	1.13	0.42	0.58	0.05
SiO_2-*s*-MMA798	798	1.07	0.53	0.68	0.05
SiO_2-*s*-MMA993	993	1.11	0.62	0.75	0.05
SiO_2-*s*-MMA1067	1067	1.25	0.65	0.78	0.06
SiO_2-*s*-MMA1147	1147	1.27	0.64	0.78	0.05
SiO_2-*s*-MMA1410	1410	1.11	0.70	0.82	0.05

Variables represent the degree of polymerization of graft, N; dispersity index, M_w/M_n; weight fraction of polymer, f_{org}; volume fraction of polymer, ϕ_{org}; surface grafting density, σ_s.

The structure of particle brush materials was characterized using transmission electron microscopy (TEM). **Figure 10.2** (and **Figure S10.1**) displays representative TEM images of PS (PMMA) brush materials in the respective grafting regime. Brush particles in the dense and intermediate

grafting regimes display uniform microstructures while sparse systems display the formation of string-like superstructures. To determine whether uniform or string-like structures are present, image analysis was performed on electron micrographs on particle monolayers (after vacuum annealing at T = 130 °C, 24 hours) to determine the distance between adjacent particles. Structures were considered 'uniform' if distance distributions were monomodal; in this case, the average distance was denoted d. In contrast, structures were considered 'string-like' if a bimodal distribution of particle distances was observed (**Figure S10.3** depicts an example of the analysis for the images shown in **Figure 10.2a, Figure 10.2b,** and **Figure 10.2c**). For dense and intermediate grafting densities, Voronoi cell analysis revealed that the degree of ordering (measured in terms of the variance of Voronoi cell area, see insets of **Figure 10.2**a and **Figure 10.2b** and similar **Figure S10.1** for PMMA systems) in particle brush films decreases with grafting density. Following to procedures established in the literature, a measure for the 'degree of order' was defined as 1–*FWHM* where *FWHM* is the full-width at half-maximum of the distribution of Voronoi cell areas, normalized by the average cell area.[44] **Figure 10.2d** displays 1–*FWHM* of PS-brush systems clearly revealing the trend towards a higher degree of structural order in films of dense brush systems (note that results are only shown for samples for which unambiguous analysis of electron micrographs could be performed). This is attributed to the more hard-sphere-type interaction potential in dense brush particle systems that support the formation of more ordered structures.[2,44,49,52–55]

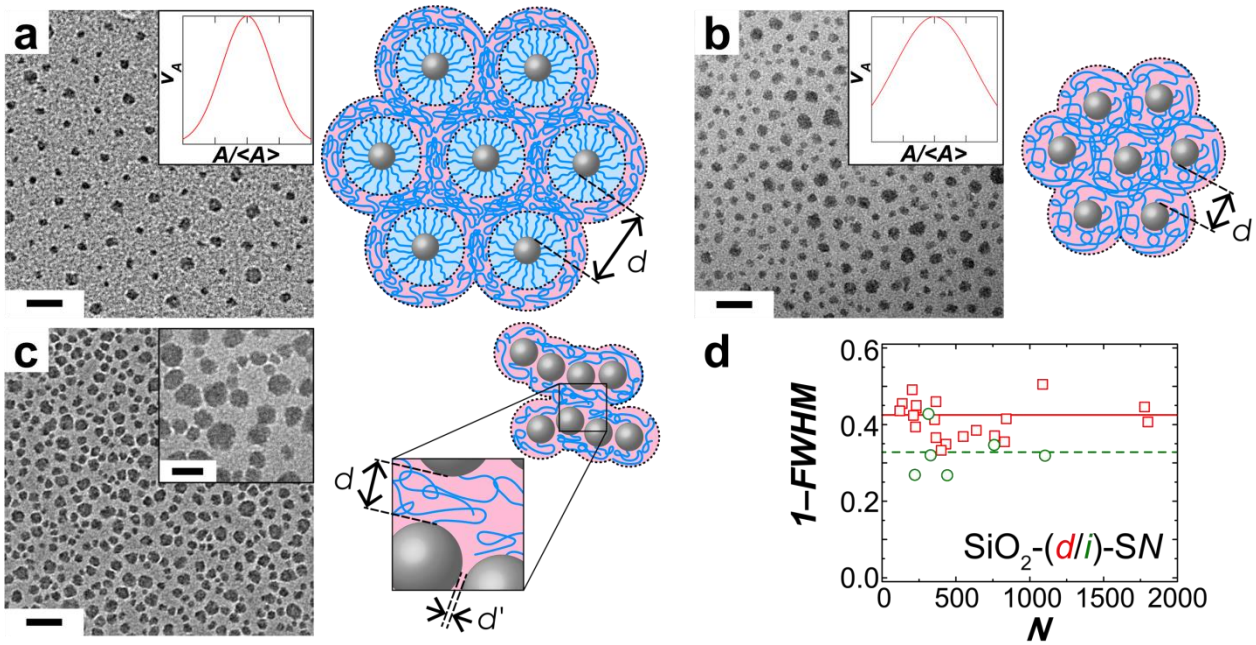

Figure 10.2. Representative bright-field transmission electron micrographs for (a) dense (SiO_2-*d*-S365), (b) intermediate (SiO_2-*i*-S328) and (c) sparse (SiO_2-*s*-S432) PS-brush systems with similar degrees of polymerization. Also shown are schematic illustrations of the corresponding microstructures. The characteristic distance *d* is defined as the inter-particle distance in dense and intermediate systems and as inter-string distance in the sparse system. The area distributions of Voronoi cell from the dense and the intermediate materials are shown as insets in (a) and (b). All scale bars are 50 nm (20 nm in insets). (d) Comparison of 1–*FWHM* for monolayer particle brush films of dense (red circles) and intermediate (green squares) systems. Larger values indicate a higher degree of order (for the case of close packing of spheres in a plane, a reference value of '1' is expected). For dense and intermediate brush systems an average degree of order $\langle 1\text{–}FWHM\rangle_{\text{dense}}$ = 0.422 and $\langle 1\text{–}FWHM\rangle_{\text{interm.}}$ = 0.325 is observed (indicated by red solid and green dashed lines respectively).

In agreement with literature reports, sparsely grafted systems were found to form string-like superstructures.[13,17,19,31,33,56,57] Hence, while dense and intermediate brush particle assemblies were described by one characteristic distance *d*, sparse systems were characterized by two distances that will in the following be denoted *d* (representing the inter-string particle distance) and *d′* (representing the intra-string particle distance; see also **Figure S10.3**). The inter-string distance was considered as the analog to *d* in dense/intermediate systems since it identifies the spacing between particles separated by polymeric ligands. The average number of particles per string of SiO_2-*s*-S432 determined from **Figure 10.2c** was approximately 23. We defined a string as a group of particles linked within 5 nm because *d′* was found less than this value in **Figure S10.3 (c)**. The structure formation of sparse systems will be discussed in more detail in a later part of this paper.

To discern the effect of grafting density on the conformation of tethered chains, the characteristic distance *d* was analyzed by electron imaging. **Figure 10.3** displays the dependence of interparticle distance on *N* for brush particles in the various grafting regimes. Dense brush systems (red symbols) reveal two distinct regimes with scaling exponents 0.8 and 0.5 thus indicating a transition from oriented to random chain conformation with an increasing degree of polymerization. This supports previous findings on dense brush particle systems that were analyzed using TEM and scattering analysis.[8,44,55,58,59] The transition between the two regimes occurs at a similar degree of polymerization ($N_{crit} \approx 300$) for PS and PMMA brush particles. This finding is attributed to the similar grafting density and comparable persistence length of both polymers.[47] In contrast, intermediate brush systems (green symbols) as well as the inter-string distance in the case of sparse brush particles (blue symbols) exhibit $N^{0.5}$ scaling for all (tested) values of *N*. This is consistent with the expectation that a reduction of chain crowding across the particle surface affords more relaxed chain conformations. For the case of sparse brush particle systems, we note that the $N^{0.5}$ scaling supports prior reports that attributed the formation of string structures in part to the increase of chain conformational entropy that is associated with the segregation of polymer chains to the galley regions between particle strings.[20,31,33] We also note that no effect of *N* on the intra-string distance *d*' was observed; however, the average 'length' of strings decreased with increasing *N* (this aspect will be further discussed below).

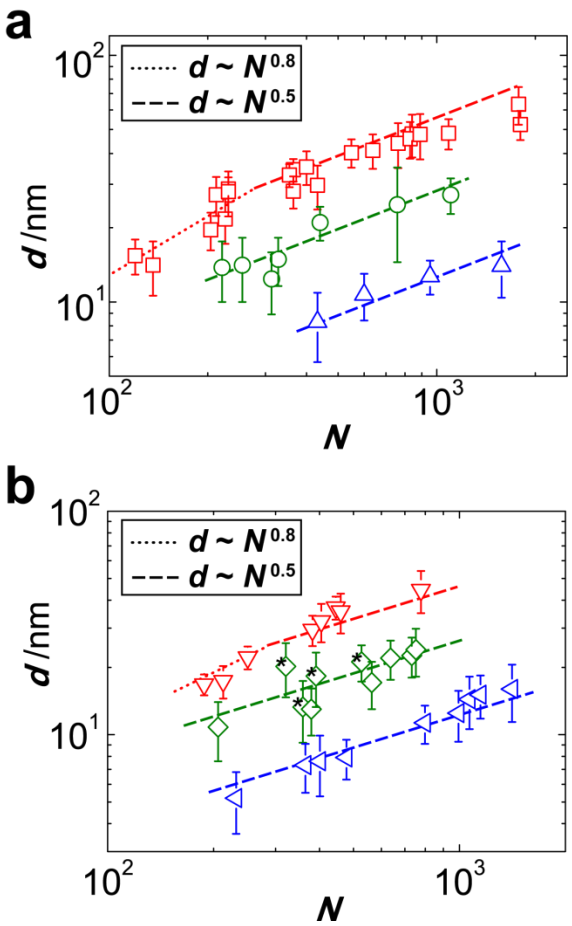

Figure 10.3. Dependence of the characteristic distance *d* (dense & intermediate: inter-particle distance, sparse: inter-string distance) on the degree of polymerization of PS (a) or PMMA (b) for all systems (red: dense, green: intermediate and blue: sparse system). The trend lines indicate corresponding brush regimes: CPB (dotted) and SDPB (dashed). Data points with asterisks indicate additional (intermediate dense) PMMA brush particles.

The elastic modulus (*E*) and hardness (*H*) of 20–60 μm thick brush particle films were measured using nanoindentation after thermal annealing in a vacuum (*T* = 130 °C, 24 hours). Representative load-displacement curves and images of residual indents are shown in **Figure S10.4**. Measurements were recorded at a displacement rate of 5 nm/s. Variation of the indentation rate in the range 1−25 nm/s was used to confirm the absence of viscoelastic contributions to the response of films.[7] This is important because our analysis of instrumented indentation results rests on the assumption of samples undergoing elastic-plastic deformation only. Indentation depths of 500 nm were chosen to ensure meaningful sampling of interactions (the test volume 20 μm^3 corresponds to > 1,000 brush particles). The elastic modulus was evaluated from load-displacement curves using the Oliver-Pharr method that has been

shown to yield results with satisfying accuracy for glassy polymeric materials.[60] Films were imaged (using AFM) after indentation to ensure the absence of excessive pile-up in the indent region. For each sample, more than nine independent measurements were evaluated. **Figure 10.4** depicts the resulting trends of *E* and *H* along with the respective standard deviations. In discussing the results, we will focus on the elastic modulus since it directly relates to constituent interactions in materials. However, because 'hardness' is a quantity that is directly determined from indentation measurements (as opposed to the elastic modulus, which is indirectly inferred from load-displacement curves), hardness values are shown in support. The common trend of *E* and *H* that is seen for all systems in **Figure 10.4** supports the validity of the analysis.

The elastic moduli (and hardness) of bare and initiator-tethered silica particle films were measured as a reference. The elastic modulus of initiated-tethered reference systems was determined to be 1.8 GPa (black symbols in **Figure 10.4**), regardless of the ratio of active initiator to inactive sites. We note that the total modification density (active and inactive sites) was identical for *d*/*i*/*s* – brush systems (~ 1 nm^{-2}); only the ratio of active and inactive surface groups changed accordingly for the different systems. This value was markedly less than the value for pristine silica particles that were found to be 5.5 GPa (not shown here). This result confirmed a previous report on the effect of organic ligand coatings on silica particle interactions and was rationalized as a consequence of the weaker cohesive interactions upon replacement of polar hydroxy-group functionalities with nonpolar low-molecular ligands (trichlorosilane or initiator) that interact predominantly through dispersion interactions.[39,61,62] The result thus further supported the assumption that brush particle interactions are dominated by ligand-ligand rather than core-core interactions. Increasing the degree of polymerization of tethered chains was found to exert two distinct effects, depending on the grafting density. For brush systems with dense and intermediate grafting density (**Figure 104a–4d**), the elastic modulus (and hardness) continuously increased and eventually leveled off at values similar to the respective bulk homopolymer

reference (E_{PS} = 3.9 GPa and E_{PMMA} = 3.8 GPa) which are indicated as dotted lines in Figure 4. We rationalized the threshold degree of polymerization for leveling-off as being related to a correlation length beyond which dispersion interactions become independent of chain length (an analogous argument applies to the molecular weight dependence of the elastic modulus of amorphous polymers in general[36]).

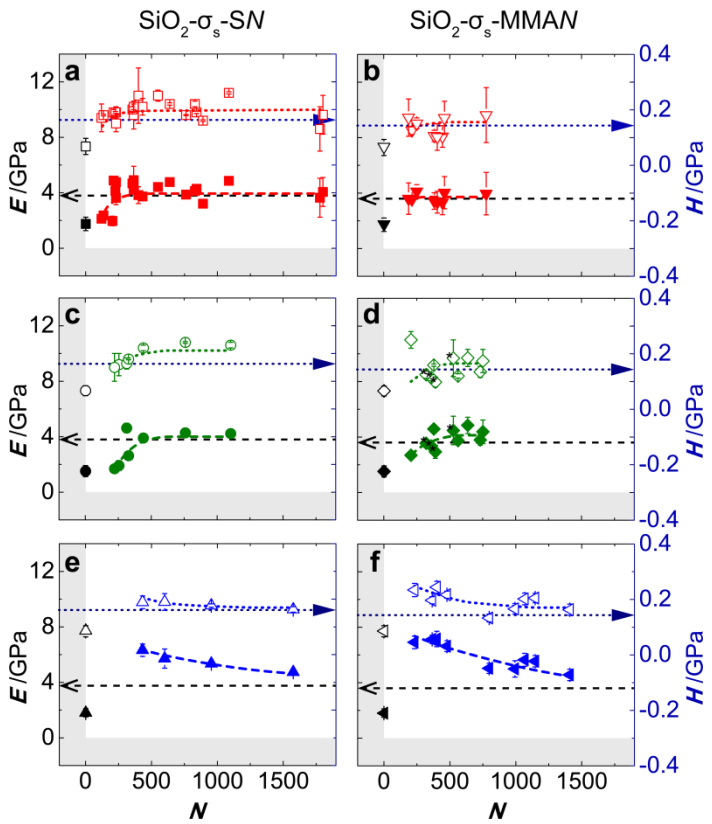

Figure. 10.4. Young's modulus (E, left y-axes, filled symbols) and hardness (H, right y-axes, open symbols) of PS-grafted (left column) and PMMA-grafted (right column) particle films in the (a, b) dense, (c, d) intermediate and (e, f) sparse systems measured by nanoindentation. Fitted lines from the data are exhibited as dotted (for H) and dashed (for E) lines with the same colors. The black and navy dashed lines indicate the elastic modulus and hardness (E_{PS} = 3.9 GPa, E_{PMMA} = 3.8 GPa, H_{PS} = 0.16 GPa, H_{PMMA} = 0.14 GPa) of bulk homopolymer reference systems with degree of polymerization N_{PS} = 500 and N_{PMMA} = 1200. The data points at N = 1 (black symbols) correspond to initiator-tethered nanoparticle films. Axis labels and titles in the intervening spaces are removed for convenience.

In stark contrast to dense and intermediate systems, sparse brush particle films displayed an opposite behavior (**Figure 10.4e** and **Figure 10.4f**). Here, the elastic modulus assumed a maximum value for the smallest N tested (6.3 GPa for PS with N = 432 and 6.9 GPa for PMMA with N = 232) and

subsequently decreased with increasing degree of polymerization. This trend was rationalized as a consequence of the anisotropic assembly structures in sparse brush particle films (see below).

To evaluate the role of graft architecture on the elastic modulus in dense and intermediate brush particle systems, **Figure 10.5** depicts the dependence of E on the organic volume fraction ϕ_{org} for the case of PS brush particles. Interestingly, the elastic modulus of intermediate brush systems increased at a distinctively lower threshold volume fraction of polymer component. Conversely, at an equal volume fraction of organic component, the elastic modulus of intermediate brush systems systematically exceeded the modulus of dense analogs. For example, sample SiO_2-*i*-S1103 (indicated by the green arrow in **Figure 10.5**) exhibited a modulus of E = 4.2 GPa while the dense analog, SiO_2-*d*-S120 (indicated by the red arrow in **Figure 10.5**) only displayed E = 2.1 GPa. The data thus revealed polymer repeat units to be more effective in raising brush interactions in the case of intermediate brush architectures.

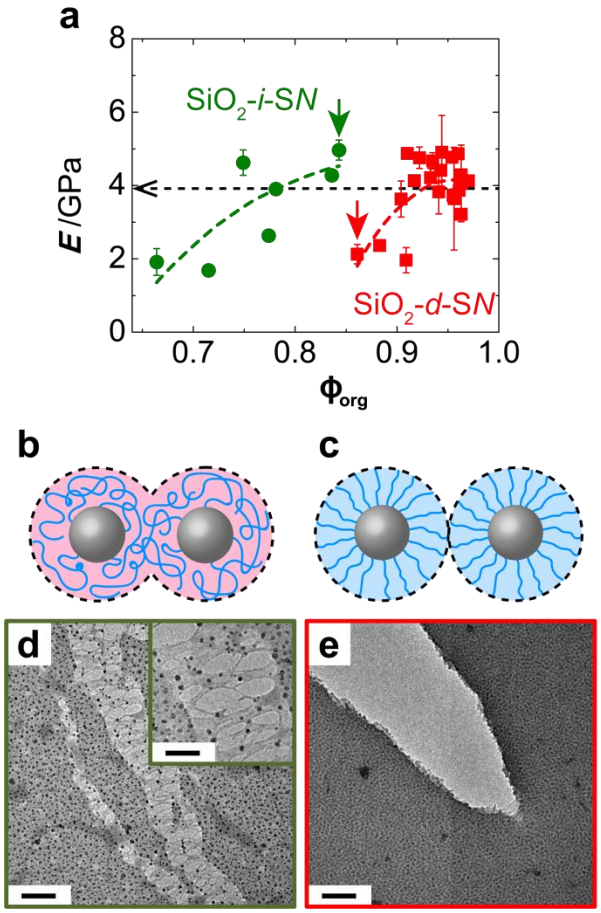

Figure 10.5. (a) Young's moduli of the dense (red squares) and intermediate (green circles) PS-grafted particle films as a function of the volume fraction of the polymer with trend lines. The black dashed line indicates the elastic modulus of bulk homopolymer reference (E_{PS} = 3.9 GPa). Arrows indicate systems with the comparable composition (green: SiO_2-*i*-S1103, red: SiO_2-*d*-S120) that were chosen for crack formation analysis. Panel (b) and (c) illustrate chain structures of intermediate (b) and dense (c) systems. Panel (d) and (e) show TEM micrographs of SiO_2-*i*-S1103 and SiO_2-*d*-S120. The inset in panel (d) is a magnified micrograph showing craze formation. Scale bars are 200 nm (100 nm in inset).

To rationalize this observation, we proposed that the relevant component of the total cohesive interactions concerning the measured elastic modulus in instrumented indentation analysis – at least in the case of dense and intermediate systems – is the dispersion interaction between ligands of adjacent particles. The latter should be sensitive to the interdigitation of brush layers between adjacent particles. We note that because of the pronounced distance dependence of dispersion interactions ($U(r) \sim r^{-6}$, where r is the distance between two molecules) 'side-on' orientation of ligands should contribute substantially more to the net bonding interactions as compared to 'end-on' alignment.[63] The reduced elastic modulus of dense brush systems could thus be interpreted as a consequence of the reduction of

cohesive interactions in non-interdigitating brush particle assemblies. This situation is schematically depicted in **Figure 10.5b** and **Figure 10.5c**. Indirect evidence for the reduced interdigitation in dense brush particle solids is provided in **Figure 10.5d** and **Figure 10.5e** that depict TEM images of cracks formed in approximately monolayer films of intermediate (SiO_2-*i*-S1103, **Figure 10.5d**) and dense (SiO_2-*d*-S120, **Figure 10.5e**) brush particle systems with near equal organic content. Craze formation that was observed in sample SiO_2-*i*-S1103 provided evidence for the interdigitation of chains while the smooth surface of cracks in the dense SiO_2-*d*-S120 system was indicative of brittle fracture (and hence the absence of significant chain entanglement). We note that the effect of graft architecture is expected to be reduced once the degree of polymerization is large enough to support sufficient brush interdigitation in dense systems – a trend that is indeed consistent with the data shown in **Figure 10.5a**.

To further support the interpretation of the effect of graft architecture, an analytical model was used to estimate the role of brush interpenetration on the cohesive energy density and effective elastic modulus of brush particle films. Only van der Waals interactions between nanoparticle cores and London dispersion interactions between ligands were considered; the system was assumed to consist of silica nanoparticles with uniform radius r_0 = 7.9 nm grafted with uniform PS chains of the degree of polymerization N (*i.e.* particle and polymer molecular weight dispersity is neglected). Van der Waals and ligand dispersion interactions in brush particle films were calculated based on pairwise interaction models published in the literature.[64,65] Comparison between ligand-ligand and core-core interactions (see **Figure S10.5**) revealed that the latter is negligible if the distance between particle cores exceeds about one nanometer, which is small compared to the experimental value of particle spacings for any of the (intermediate or dense) brush systems that were the subject of the present study (see **Figure 10.3**). Hence, in the following, the contribution of core-core interactions to the cohesive interactions in dense and intermediate brush particle materials was neglected. Our approach consisted of two steps: First, the *inter*particle cohesive energy density (*IPCED*) was calculated that accounts (only) for the dispersion

interactions contributed by chain segments that participate in interdigitation between adjacent brush particles (*i.e.* the interaction between ligands that are aligned end-on is neglected, see **Figure 10.6a** and **Figure 10.6b**). The dispersion interaction between two side-on oriented ligands was determined from Eq. 1 which was first provided by Salem *et al.* and later confirmed by numerous studies.

$$U_l(L) = -C_{\mathrm{PS}} \frac{3\pi L}{8\lambda^2 x^5} \tag{1}$$

where $C_{\mathrm{PS}} \sim 7.1\times10^{-79}$ J · m^6 is the interaction constant for PS, L is the length of overlap between two parallel (*i.e.* side-on aligned) chain segments, λ is the length of the monomer (~ 0.25 nm), and x is the intermolecular spacing between chains (~ 0.4 nm).[65–68] Note that we focused on the cohesive energy density contributed by interdigitating chain segments because it was expected to be the primary origin for the elastic forces resisting the perturbation of particle positions. In a second step, the effective elastic modulus was derived based on the *IPCED* and compared with the experimental data.

The *inter*particle cohesive energy density was calculated as the sum of all dispersion interactions between interpenetrated ligands per material volume. To calculate *IPCED*, a cubic close-packed (face-centered cubic; fcc) microstructure of brush particle films was assumed.[2,39,47,53,69] The assumption of a lattice structure simplifies the estimation of the cohesive energy density because it reduces the relevant volume element to the respective Wigner-Seitz (WS) cell of the structure (for example, a rhombic-dodecahedron in the case of fcc). Cubic close-packed structures have indeed been observed in films of dense brush particles and were rationalized as a consequence of hard-sphere-type interactions between dense brush particles.[26,49,52] For brush systems with intermediate graft density (or dense systems with a sufficiently high degree of polymerization of polymer tethers) the assumption of close packing is an

approximation. However, since the errors associated with non-close packing were estimated to be within 15% of the result, fcc packing was assumed for all brush particle systems. Since the volume associated with each WS cell $V_{\mathrm{WS}}(d) = (2r_0 + d)^3/\sqrt{2}$ is determined by the distance *d* between particle cores (*d* was known from TEM analysis, **Figure 10.3**) and since the volume fraction of organic component was known from TGA characterization, the cohesive energy density of brush particle films could be estimated by summation of ligand dispersion interactions across each WS cell and subsequent normalization by the cell volume. To estimate the number of polymer repeat units contributing to the *IPCED* (*i.e.* the number of polymer repeat units that are part of interdigitating segments), the assumption was made that only segments in the semi-dilute brush region (SDPB) participate in interdigitation. This restriction is motivated by prior reports demonstrating dense brush layers to allow for onlan y limited overlap of polymer canopies both in the solution[47,66] and solid state[7,8,31,52]. For the dense brush particle series (SiO_2-*d*-S*N*), the CPB-SDPB transition was determined by evaluating the experimental scaling behavior $d \sim N^x$ (with x = 0.8 in the CPB and x = 0.5 in the SDPB regime, see **Figure 10.3**). Following this process, the *IPCED* could be expressed as

$$IPCED = U_l(L)\frac{\lambda}{L}\rho_S\left[\frac{\sqrt{2}}{2}(2r_0 + BN^{0.5})^3 - \frac{4}{3}\pi(r_0 + \frac{A}{2}N_c^{0.8})^3\right] / \left[\frac{\sqrt{2}}{2}(2r_0 + BN^{0.5})^3\right] \qquad (2)$$

where *A* and *B* are constants experimentally determined from **Figure 10.3a** (A = 0.335 nm, B = 0.907 nm), $L = N_{\mathrm{SDPB}}\lambda$ is the length of side-on overlap among chains in the SDPB regime and $\rho_S = 6.07\times10^{27}$ m^{-3} is the number density of the repeat units (which was assumed to be independent of chain orientation). For brush systems with intermediate grafting density, the length of chain segments participating in interdigitation was assumed to be equal to the contour length of tethered chains. The resulting trend of *IPCED* for dense and intermediate brush particle systems is shown in **Figure 10.6**.

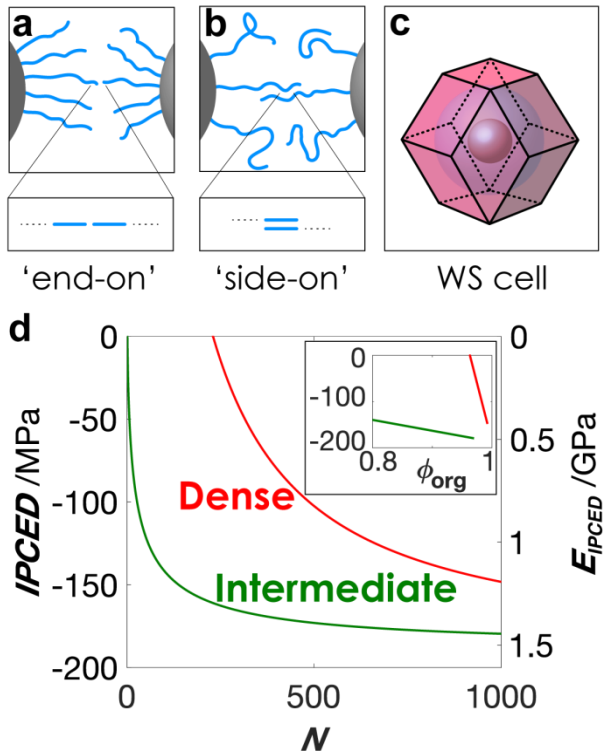

Figure 10.6. Illustrations of (a) end-on arrangement of densely tethered ligands, and (b) side-on arrangement of interdigitated tethered ligands. Panel (c) shows a scheme of the Wigner-Seitz (WS) cell of particle brush (blue inner shell: CPB; red outer shell: SDPB). Panel (d) depicts a plot of the *inter*particle cohesive energy density (*IPCED*) in dense and intermediate brush particles as functions of degree of polymerization along with the corresponding values of elastic modulus (see text for more detail). Inset shows *IPCED* as a function of organic volume fraction.

Since for materials undergoing only elastic-plastic deformation the stored elastic energy upon deformation is directly related to the corresponding change in cohesive energy density (*CED*), the elastic modulus of brush particle films could be determined from the calculated *IPCED*. Specifically, Willbourn *et al.* demonstrated the empirical relation $E \simeq 8.04\ CED$ to apply to a wide range of polymers.[67] The resulting prediction of Young's moduli is depicted in **Figure 10.6**. Note that the predicted trend of E_{ICPED} confirmed the initial increase and following level-off with increasing degree of polymerization. Discrepancies from the experimental result (a more rapid increase of modulus in the intermediate system and increase of modulus in dense system arising from N_{crit}) might be attributable to the contribution of *inter*particle interaction between CPB-regime ligands to the total cohesive interaction, which is not considered in the calculation. Interestingly, despite the approximations made by the model, the resulting absolute values of Young's modulus are captured within a factor of about two.

In contrast to dense and intermediate bush particle systems, sparse analogs displayed a systematic decrease of the elastic modulus with an increasing degree of polymerization of polymeric tethers, eventually leveling out at values of *E* corresponding to the reference homopolymer (see **Figure 10.4**). We attribute this opposing trend to the characteristic difference in microstructure in sparse brush particle films, specifically the formation of string-like aggregate structures. As discussed above, van der Waals interactions between particle cores increase when particles are close (less than about 0.5 nm). This is also confirmed by recent molecular dynamics simulation by Midya *et al.* that have shown core interactions to dominate other interactions in sparse brush particle architectures.[42] Qualitatively, the increased core-core interactions raise the *IPCED* of sparse brush materials and hence raise the elastic modulus. The mechanical properties of sparse brush particle hybrid materials might be better described by effective medium models for anisotropic filler shapes, such as the Cox short fiber model.[70] However, more quantitative information about the interactions within string aggregate structures would be required to test the applicability of effective medium models. Interestingly, the number of particles within aggregates (*i.e.* the string length) in SiO_2-*s*-S*N* systems decreases with increasing degree of polymerization. The corresponding reduction of core-core contacts rationalizes the observed decrease of *E* with increasing *N* that is observed in SiO_2-*s*-S*N* systems. This situation is illustrated in **Figure 10.7**.

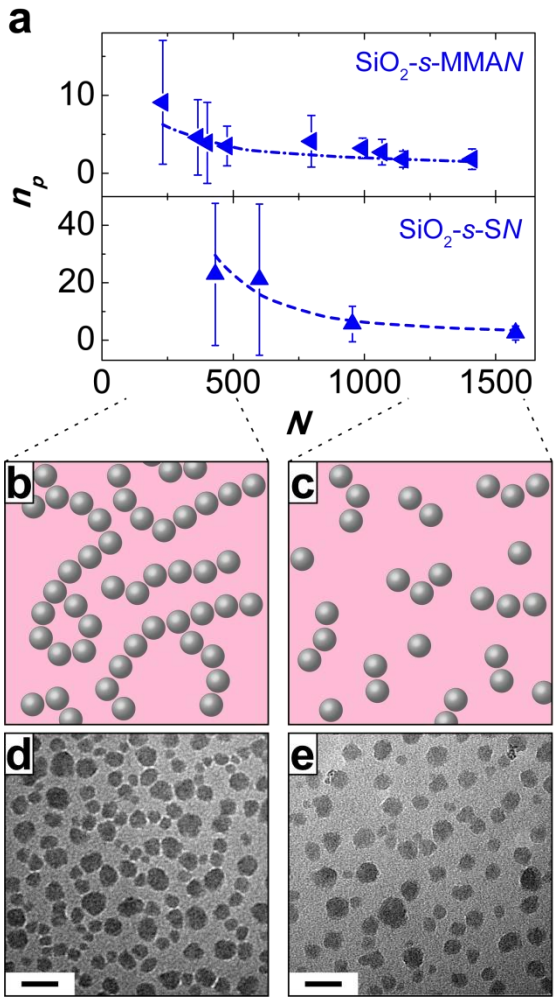

Figure 10.7. Structural transition in sparsely grafted particle films. The number of particles per string as a function of the degree of polymerization in PMMA analog (top) and PS analog (bottom) is plotted in a. Schematic illustrations of string formation in sparse brush particles when brushes are short (b) and long (c) are shown. Panel d and e show corresponding electron micrographs for short (d: SiO_2-*s*-S432) and long tethered chains (e: SiO_2-*s*-S1576). Scale bars are 30 nm.

The above discussion centered on the interpretation of the elastic modulus of particle brush films. This was motivated by the direct relation between the cohesive energy density and the elastic modulus that enables the interpretation of modulus changes based on the interactions between constituents. However, as explained above, the determination of elastic moduli from instrumented indentation experiments is subject to assumptions about parameters such as Poisson's ratio that are difficult to determine experimentally. A more directly accessible – but less readily interpretable – quantity is the material's hardness that directly follows from the peak loading during indentation. **Figure 10.8** displays an Ashby chart correlating the elastic modulus and hardness for all tested brush materials.

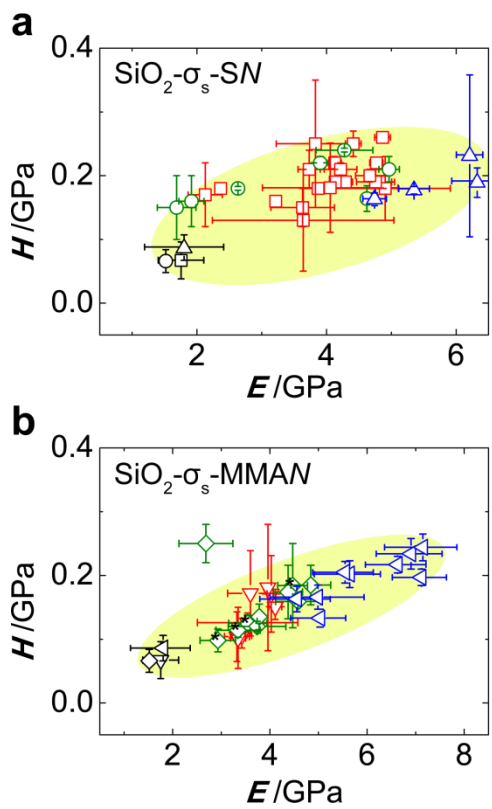

Figure 10.8. Indentation hardness (*H*) *vs* Young's modulus (*E*) plots of PS materials (a) and PMMA materials (b) (red: dense, green: intermediate, blue: sparse, black: initiator-tethered nanoparticles; symbols are matched up with the corresponding system). Trends are highlighted in yellow.

The linear trend in the *E*–*H* plots that are observed in the figure reveals that both quantities were correlated and hence obeyed similar structure-property relations. This suggests that hardness measurements might provide a versatile alternative to evaluate structure and interactions in brush particle solids. **Figure 10.8** also might find use as 'design guideline' for the synthesis of particle brush materials with desired properties. For high modulus and hardness, brush systems with reduced grafting density are preferable, depending on the constraints on the targeted microstructure.

10.5. Supporting Information

Calculation of surface grafting density

Graft densities were calculated using the following equation:

$$\sigma_s = \frac{(1 - f_{SiO_2}) N_A \rho_{SiO_2} d}{6 f_{SiO_2} M_n} \quad (1)$$

The value of f_{SiO_2}, in the equation, is the weight fraction of silica measured by TGA after exclusion of any residual solvent; N_A is the Avogadro number; ρ_{SiO_2} is the density of silica NPs; d is the average diameter of silica NPs; M_n is the number average MW of polymer brushes.

Calculation of Poisson's ratio of composite materials

Poisson's ratio of brush particle materials was calculated using the Voigt model for composite materials[1]:

$$\nu = \nu_{org}\phi_{org} + \nu_{SiO_2}\phi_{SiO_2} \quad (2)$$

where ν_i is the Poisson's ratio of component i and ϕ_i is the volume fraction of component i.

Table S10.1. Additional material information of (intermediate dense) poly(methyl methacrylate) brush particles.

Sample ID	N	M_w/M_n	f_{org}	ϕ_{org}	σ_s (nm^{-2})
SiO_2-*i*-MMA321*	321	1.20	0.81	0.89	0.44
SiO_2-*i*-MMA359*	359	1.15	0.82	0.90	0.42
SiO_2-*i*-MMA391*	391	1.23	0.85	0.91	0.46
SiO_2-*i*-MMA527*	527	1.21	0.87	0.93	0.43

Variables represent the degree of polymerization of graft, N; dispersity index, M_w/M_n; weight fraction of polymer, f_{org}; volume fraction of polymer, ϕ_{org}; surface grafting density, σ_s. Sample ID: SiO_2-(σ_s regime: *d* (dense) /*i* (intermediate) /*s* (sparse))-(monomer)*N*.

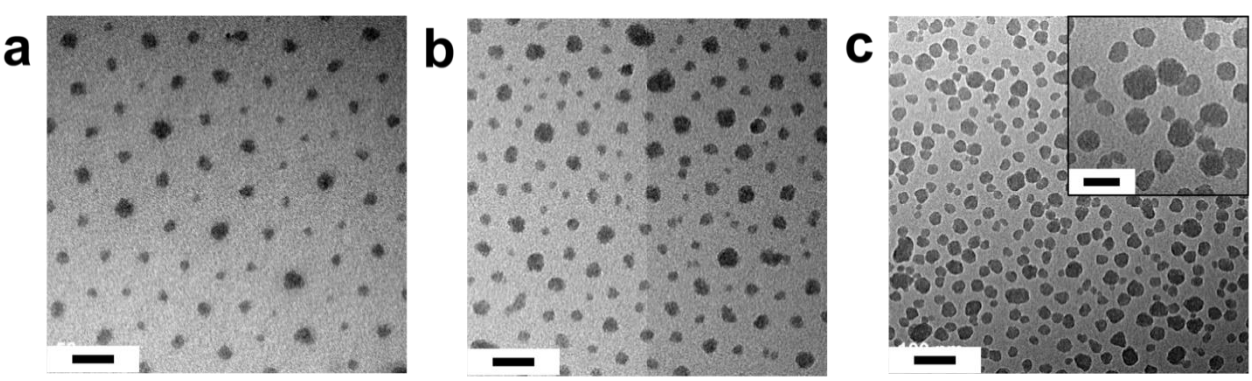

Figure S10.1. Representative bright-field transmission electron micrographs and corresponding schemes of structure for the (a) dense (SiO_2-*d*-MMA445), (b) intermediate (SiO_2-*i*-MMA563) and (c) sparse (SiO_2-*s*-MMA365) PMMA-brush systems with similar degrees of polymerization. All scale bars are 50 nm (20 nm in inset).

Quantitative analysis of domain structure using TEM micrographs

A quantitative analysis of TEM micrographs following systematic processing was conducted using Matlab. A sequence for the analysis is shading correction – blurring – dilation – erosion – particle recognition – tessellation. A bandpass filter was applied to correct shading. As the next step, the combination of dilation and erosion was exploited to separate merged (neighboring) domains. Gaussian blurring is necessary to reduce detail for better recognition. Given that unstained TEM images provide 3 distinct contrast levels (dark (silica particles) and bright (polymer brush)), each domain was mapped by binarization. Then, the particle domain was recognized, followed by Voronoi tessellation using centroid information. The results at each step are shown in **Figure S10.2**.

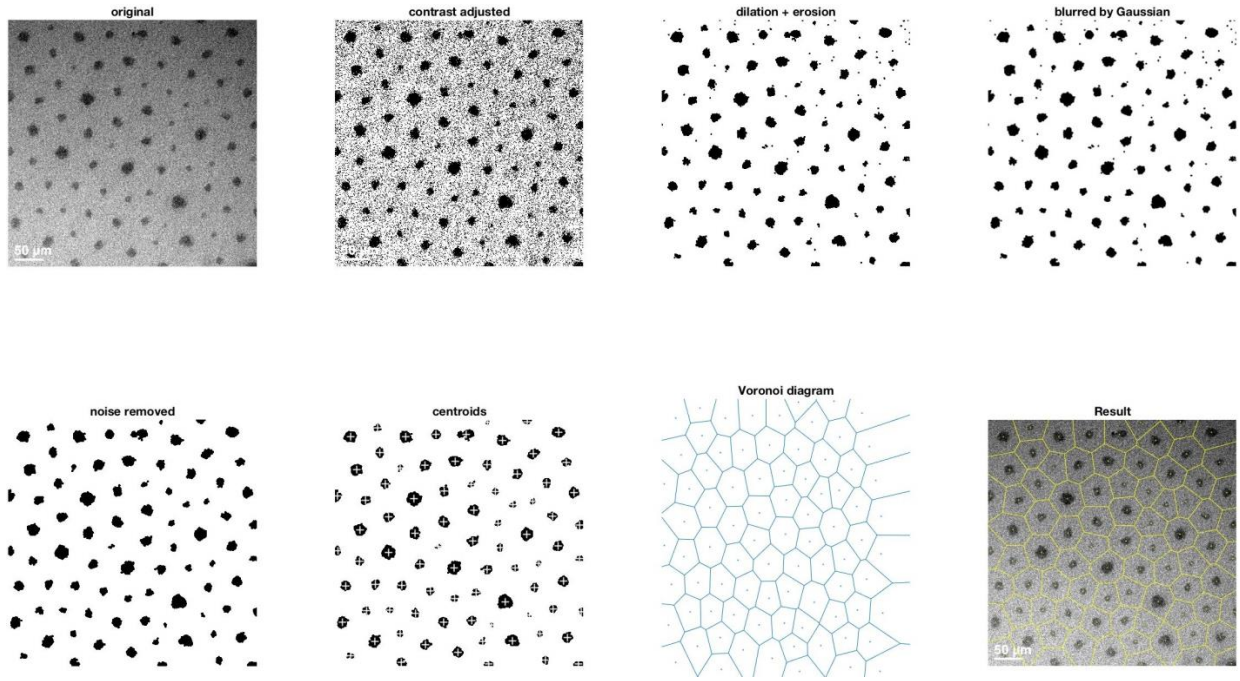

Figure S10.2. A representative image processing of a TEM micrograph (SiO_2-*d*-MMA445) for Voronoi tessellation.

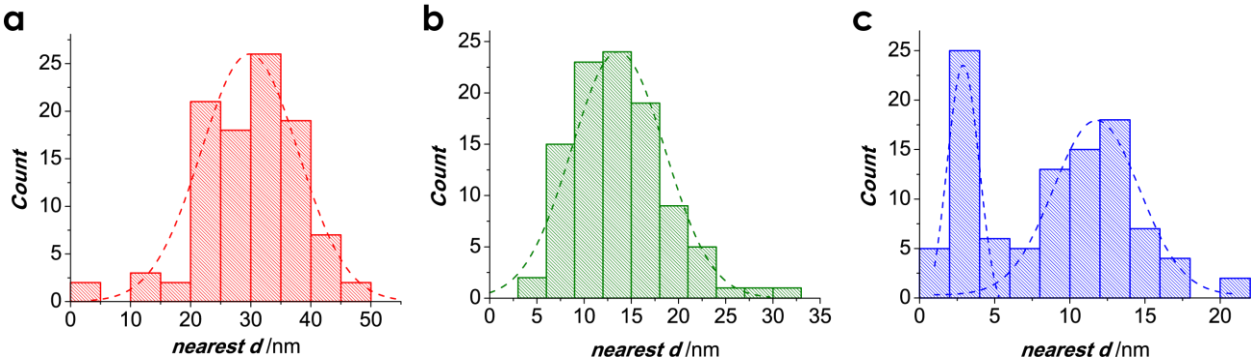

Figure S10.3. Histograms of spacing between adjacent particle cores in dense (a: SiO_2-*d*-S365), intermediate (b: SiO_2-*i*-S328) and sparse (c: SiO_2-*s*-S432) systems. Monomodal distributions in the dense and intermediate materials indicate 'isotropic' microstructure while bimodal distribution in the sparse brush particles demonstrates an 'anisotropic' structure.

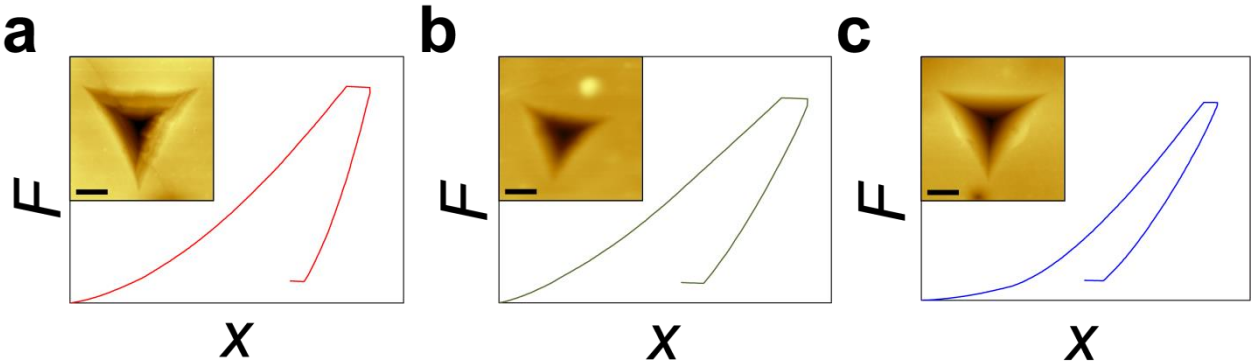

Figure S10.4. Representative load-displacement curves of (a) dense (SiO_2-*d*-S890), (b) intermediate (SiO_2-*i*-S328) and (c) sparse (SiO_2-*s*-S432) brush particulate films during nanoindentation measurements. Insets are corresponding topographs taken by AFM. All scale bars are 1 μm.

Comparison of cohesive energy contributed from core-core interaction and ligand-ligand interaction

A quantitative analysis of the effect of interpenetration between ligands is carried out. Herein we assume that there are only van der Waals interactions between nanoparticle cores and London dispersion interactions between ligands. The model system we adopt for the estimation is silica nanoparticles (r_0 = 7.5 nm) grafted by PS chains. We also assumed the additivity of interactions to simplify the estimation.

First, the van der Waals interactions between two identical hard spheres[2] are:

$$U_c(d) = -\frac{A_{SiO_2}}{6}\left\{\frac{2{r_0}^2}{(4r_0+d)d} + \frac{2{r_0}^2}{(2r_0+d)^2} + ln\frac{(4r_0+d)d}{(2r_0+d)^2}\right\} \quad (2)$$

where, $A_{\mathrm{SiO_2}}$ is the Hamaker constant of silica in PS medium (~ 3.3×10^{-21} J), r_0 is the radius of spherical particles, and d is the distance between particles. This cohesive energy is considerable when particles are very closely located. Otherwise, it is negligible.

The other interaction we consider is between overlapped (side-on) ligands. Dispersion interactions between end-on chains are insignificant as mentioned above. The interaction between two parallel ligands [3] is:

$$U_l(L) = -C_{\mathrm{PS}}\frac{3\pi L}{8\lambda^2 x^5} \tag{3}$$

where C_{PS} ~ 7.1×10^{-79} J·m^6 is the interaction constant, L is the length of overlap between two parallel chains, λ is the contour length of the repeat unit (~ 0.252 nm), x is the intermolecular spacing between chains (~ 0.4 nm).[4] We then extended the two interactions to our system. Assemblies of particle brush with relatively high grafting density have been known to form the close-packed structure in 2D[5–10] and face-centered cubic (FCC) or hexagonal close-packed (HCP) structure in 3D.[8–10] Hence, each particle core is considered to the neighbor with 12 cores at the closest distance with a polymer buffer layer and forms a rhombic-dodecahedral unit cell. Similarly, each polymeric chain has 6 neighboring chains when closely packed. Under an assumption that densely grafted particles form a closely packed structure and are separated by a distance, d, the core-core interaction, U_{cc}, and the total ligand-ligand interaction, U_{ll}, per unit cell can be estimated as follows:

$$U_{cc}(d) = 12U_c(d) = -2A_{\mathrm{SiO_2}}\left\{\frac{2{r_0}^2}{(4r_0+d)d} + \frac{2{r_0}^2}{(2r_0+d)^2} + ln\frac{(4r_0+d)d}{(2r_0+d)^2}\right\} \tag{4}$$

$$U_{ll}(d) = 6U_l(L)\frac{\lambda}{L}\rho_{St}V(d) = -6C_{\mathrm{PS}}\frac{3\pi}{8\lambda x^5}\rho_{St}\left\{\frac{\sqrt{2}}{2}(2r_0+d)^3 - \frac{4}{3}\pi{r_0}^3\right\} \tag{5}$$

As shown in **Figure S10.4**, U_{ll} is much stronger except for extremely short separations (< 1 Å). For this reason, the core-core interaction is not considered when calculating effective cohesive energy, U_{eff}, in particle brush assembly.

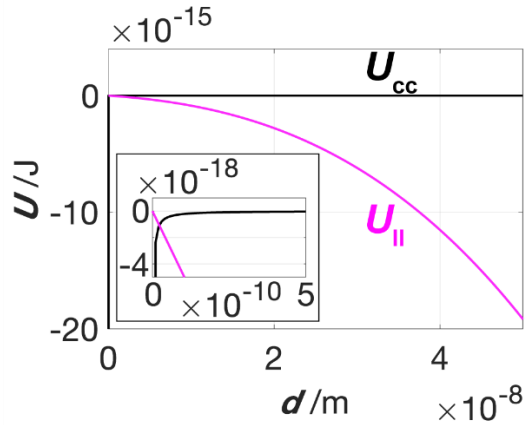

Figure S10.5. Comparison of interactions between inter-core, U_{cc}, and inter-ligand, U_{ll}. The inter-ligand dispersion interactions are dominant except for contact.

(1) Ward, I. M.; Sweeney, J. *An Introduction to the Mechanical Properties of Solid Polymers*, 2nd ed.; Wiley, 2004.
(2) Israelachvili, J. *Intermolecular and Surface Forces*, 3rd ed.; Acedemic Press, 2011. https://doi.org/10.1016/C2009-0-21560-1.
(3) Salem, L. Attractive Forces between Long Saturated Chains at Short Distances. *J. Chem. Phys.* **1962**, *37* (9), 2100. https://doi.org/10.1063/1.1733431.
(4) Gedde, U. W. *Polymer Physics*; Springer Science & Business Media, 1995. https://doi.org/10.1007/978-94-011-0543-9.
(5) Hui, C. M.; Pietrasik, J.; Schmitt, M.; Mahoney, C.; Choi, J.; Bockstaller, M. R.; Matyjaszewski, K. Surface-Initiated Polymerization as an Enabling Tool for Multifunctional (Nano-)Engineered Hybrid Materials. *Chem. Mater.* **2014**, *26* (1), 745–762. https://doi.org/10.1021/cm4023634.
(6) Choi, J.; Hui, C. M.; Pietrasik, J.; Dong, H.; Matyjaszewski, K.; Bockstaller, M. R.; Hui, M.; Pietrasik, J.; Dong, H.; Hui, C. M.; et al. Toughening Fragile Matter: Mechanical Properties of Particle Solids Assembled from Polymer-Grafted Hybrid Particles Synthesized by ATRP. *Soft Matter* **2012**, *8* (15), 4072. https://doi.org/10.1039/c2sm06915f.
(7) Schmitt, M.; Choi, J.; Hui, C. M.; Chen, B.; Korkmaz, E.; Yan, J.; Margel, S.; Ozdoganlar, O. B.; Matyjaszewski, K.; Bockstaller, M. R. Processing Fragile Matter: Effect of Polymer Graft Modification on the Mechanical Properties and Processibility of (Nano-) Particulate Solids. *Soft Matter* **2016**, *12* (15), 3527–3537. https://doi.org/10.1039/C6SM00095A.
(8) Goel, V.; Pietrasik, J.; Dong, H.; Sharma, J.; Matyjaszewski, K.; Krishnamoorti, R. Structure of Polymer Tethered Highly Grafted Nanoparticles. *Macromolecules* **2011**, *44* (20), 8129–8135. https://doi.org/10.1021/ma200621r.
(9) Morinaga, T.; Ohno, K.; Tsujii, Y.; Fukuda, T. Structural Analysis of "Semisoft" Colloidal Crystals by Confocal Laser Scanning Microscopy. *Macromolecules* **2008**, *41* (10), 3620–3626. https://doi.org/10.1021/ma7028665.
(10) Podsiadlo, P.; Krylova, G.; Lee, B.; Critchley, K.; Gosztola, D. J.; Talapin, D. V.; Ashby, P. D.; Shevchenko, E. V. The Role of Order, Nanocrystal Size, and Capping Ligands in the Collective Mechanical Response of Three-Dimensional Nanocrystal Solids. *J. Am. Chem. Soc.* **2010**, *132* (26), 8953–8960. https://doi.org/10.1021/ja100464a.

10.6. Conclusions

In this work, three series of brush particle systems were investigated, differentiated by grafting density as dense (~ 1 nm^{-2}), intermediate (~ 0.3 nm^{-2}) and sparse (~ 0.05 nm^{-2}) brush systems. The

density of tethered polymer chains exerted a pronounced effect on both structure and elastic modulus of films assembled from brush particles. Dense and intermediate systems displayed uniform microstructures while sparse systems formed string-like superstructures. For dense and intermediate systems, the elastic modulus – measured through instrumented indentation analysis – increased with an increasing degree of polymerization of tethered chains. At a given volume fraction of organic component, the increase was found to be more pronounced for lower graft densities. This trend indicated that the restoring forces resisting elastic deformation are due to dispersion interactions between segments of interdigitated chains of adjacent brush particles. A reverse trend was observed in the case of materials that were assembled from sparse brush particles. Here, Young's modulus continuously decreased with increasing degree of polymerization of tethered chains – a trend that correlated with a decreasing number of particles per string.

We expect our results to be relevant in the context of mutual property optimization in particle brush-based hybrid materials. For example, if maximum reinforcement is to be achieved at high inorganic fractions and the formation of particle strings is to be avoided (such as in applications that require high dielectric breakdown strength) then our results suggest that brush particles with intermediate grafting density can be advantageous. Open questions that warrant further investigation include the better understanding of the mechanism of reinforcement in case of sparse particle brush assemblies. While the argument of increased contributions of core-core interactions is compelling, it is not clear why particle solids assembled from sparse initiator-capped particles (*i.e.* in the absence of any polymer) do not show a similar enhancement. We hypothesize that the lower modulus in the case of pristine initiator-capped particles might be, in part, caused by void spaces in the microstructure that are not present in the case of polymer tethered systems, however, this issue remains to be clarified. A second question relates to the role experimental methodology. Complementary techniques such as Brillouin scattering (which probes the propagation of acoustic waves and hence gives information on

both the bulk and the elastic modulus) could provide additional insight into the relevant modes of interaction in particle brush systems. An interesting question also concerns the role of chain length dispersity which was not considered in the present study. In particular, the deliberate control of the fraction of long to short chains could provide additional means to concurrently improve the modulus and fracture toughness of brush particle solids while maintaining high inorganic content in the hybrid material.

10.7. References

(1) J Emmerling, S. G.; N Langer, L. B.; Pihan, S. A.; Lellig, P.; Gutmann, J. S. Patterning of a Surface Immobilized ATRP Initiator with an Inkjet Printer. *Macromolecules* **2010**, *43* (11), 5033–5042. https://doi.org/10.1021/ma902836n.

(2) Ohno, K.; Morinaga, T.; Takeno, S.; Tsujii, Y.; Fukuda, T. Suspensions of Silica Particles Grafted with Concentrated Polymer Brush: A New Family of Colloidal Crystals. *Macromolecules* **2006**, *39* (3), 1245–1249. https://doi.org/10.1021/MA0521708.

(3) Yan, J.; Pan, X.; Schmitt, M.; Wang, Z.; Bockstaller, M. R.; Matyjaszewski, K. Enhancing Initiation Efficiency in Metal-Free Surface-Initiated Atom Transfer Radical Polymerization (SI-ATRP). *ACS Macro Lett.* **2016**, *5*, 661–665. https://doi.org/10.1021/acsmacrolett.6b00295.

(4) Pyun, J.; Matyjaszewski, K. Synthesis of Nanocomposite Organic/Inorganic Hybrid Materials Using Controlled/"living" Radical Polymerization. *Chem. Mater.* **2001**, *13* (10), 3436–3448. https://doi.org/10.1021/cm011065j.

(5) Hui, C. M.; Pietrasik, J.; Schmitt, M.; Mahoney, C.; Choi, J.; Bockstaller, M. R.; Matyjaszewski, K. Surface-Initiated Polymerization as an Enabling Tool for Multifunctional (Nano-)Engineered Hybrid Materials. *Chem. Mater.* **2014**, *26* (1), 745–762. https://doi.org/10.1021/cm4023634.

(6) Barbey, R. R.; Lavanant, L.; Paripovic, D.; Schüwer, N.; Sugnaux, C.; Tugulu, S.; Klok, H.-A. A. Polymer Brushes via Surface-Initiated Controlled Radical Polymerization: Synthesis, Characterization, Properties, and Applications. *Chem. Rev.* **2009**, *109* (11), 5437–5527. https://doi.org/10.1021/cr900045a.

(7) Choi, J.; Hui, C. M.; Pietrasik, J.; Dong, H.; Matyjaszewski, K.; Bockstaller, M. R.; Hui, M.; Pietrasik, J.; Dong, H.; Hui, C. M.; et al. Toughening Fragile Matter: Mechanical Properties of Particle Solids Assembled from Polymer-Grafted Hybrid Particles Synthesized by ATRP. *Soft Matter* **2012**, *8* (15), 4072. https://doi.org/10.1039/c2sm06915f.

(8) Schmitt, M.; Choi, J.; Hui, C. M.; Chen, B.; Korkmaz, E.; Yan, J.; Margel, S.; Ozdoganlar, O. B.; Matyjaszewski, K.; Bockstaller, M. R. Processing Fragile Matter: Effect of Polymer Graft Modification on the Mechanical Properties and Processibility of (Nano-) Particulate Solids. *Soft Matter* **2016**, *12* (15), 3527–3537. https://doi.org/10.1039/C6SM00095A.

(9) Choi, J.; Dong, H.; Matyjaszewski, K.; Bockstaller, M. R. Flexible Particle Array Structures by Controlling Polymer Graft Architecture. *J. Am. Chem. Soc.* **2010**, *132* (36), 12537–12539. https://doi.org/10.1021/ja105189s.

(10) Tchoul, M. N.; Fillery, S. P.; Koerner, H.; Drummy, L. F.; Oyerokun, F. T.; Mirau, P. A.; Durstock, M. F.; Vaia, R. A. Assemblies of Titanium Dioxide-Polystyrene Hybrid Nanoparticles for Dielectric Applications. *Chem. Mater.* **2010**, *22*, 1749. https://doi.org/10.1021/cm903182n.

(11) Huang, Y.; Zheng, Y.; Sarkar, A.; Xu, Y.; Stefik, M.; Benicewicz, B. C. Matrix-Free Polymer Nanocomposite Thermoplastic Elastomers. *Macromolecules* **2017**, *50* (12), 4742–4753. https://doi.org/10.1021/acs.macromol.7b00873.
(12) Bilchak, C. R.; Huang, Y.; Benicewicz, B. C.; Durning, C. J.; Kumar, S. K. High-Frequency Mechanical Behavior of Pure Polymer-Grafted Nanoparticle Constructs. *ACS Macro Lett.* **2019**, *8*, 294–298. https://doi.org/10.1021/acsmacrolett.8b00981.
(13) Ginzburg, V. V. Modeling the Morphology and Phase Behavior of One-Component Polymer-Grafted Nanoparticle Systems. *Macromolecules* **2017**, *50* (23), 9445–9455. https://doi.org/10.1021/acs.macromol.7b01922.
(14) Hore, M. J. A. Polymers on Nanoparticles: Structure & Dynamics. *Soft Matter* **2019**, *15* (6), 1120–1134. https://doi.org/10.1039/c8sm02110d.
(15) Fernandes, N. J.; Koerner, H.; Giannelis, E. P.; Vaia, R. A. Hairy Nanoparticle Assemblies as One-Component Functional Polymer Nanocomposites: Opportunities and Challenges. *MRS Commun.* **2013**, *3* (1), 13–29. https://doi.org/10.1557/mrc.2013.9.
(16) Ethier, J. G.; Hall, L. M. Structure and Entanglement Network of Model Polymer-Grafted Nanoparticle Monolayers. *Macromolecules* **2018**, *51*, 9878−9889. https://doi.org/10.1021/acs.macromol.8b01373.
(17) Ethier, J. G.; Hall, L. M. Modeling Individual and Pairs of Adsorbed Polymer-Grafted Nanoparticles: Structure and Entanglements. *Soft Matter* **2018**, *14* (4), 643–652. https://doi.org/10.1039/C7SM02116J.
(18) Hansoge, N. K.; Huang, T.; Sinko, R.; Xia, W.; Chen, W.; Keten, S. Materials by Design for Stiff and Tough Hairy Nanoparticle Assemblies. *ACS Nano* **2018**, *12*, 7946–7958. https://doi.org/10.1021/acsnano.8b02454.
(19) Kravchenko, V. S.; Potemkin, I. I. Self-Assembly of Rarely Polymer-Grafted Nanoparticles in Dilute Solutions and on a Surface: From Non-Spherical Vesicles to Graphene-like Sheets. *Polymer (Guildf).* **2018**, *142*, 23–32. https://doi.org/10.1016/j.polymer.2018.03.019.
(20) Jiao, Y.; Tibbits, A.; Gillman, A.; Hsiao, M. S.; Buskohl, P.; Drummy, L. F.; Vaia, R. A. Deformation Behavior of Polystyrene-Grafted Nanoparticle Assemblies with Low Grafting Density. *Macromolecules* **2018**, *51* (18), 7257–7265. https://doi.org/10.1021/acs.macromol.8b01524.
(21) Cang, Y.; Reuss, A. N.; Lee, J.; Yan, J.; Zhang, J.; Alonso-Redondo, E.; Sainidou, R.; Rembert, P.; Matyjaszewski, K.; Bockstaller, M. R.; et al. Thermomechanical Properties and Glass Dynamics of Polymer-Tethered Colloidal Particles and Films. *Macromolecules* **2017**, *50* (21), 8658–8669. https://doi.org/10.1021/acs.macromol.7b01752.
(22) Asai, M.; Cacciuto, A.; Kumar, S. K. Surface Fluctuations Dominate the Slow Glassy Dynamics of Polymer-Grafted Colloid Assemblies. *ACS Cent. Sci.* **2018**, *4*, 1179–1184. https://doi.org/10.1021/acscentsci.8b00352.
(23) Zhang; Horsch, M. A.; Lamm, M. H.; Glotzer, S. C. Tethered Nano Building Blocks: Toward a Conceptual Framework for Nanoparticle Self-Assembly. *Nano Lett.* **2003**, *3* (10), 1341–1346. https://doi.org/10.1021/nl034454g.
(24) Mahoney, C.; Hui, C. M.; Majumdar, S.; Wang, Z.; Malen, J. A.; N. Tchoul, M.; Matyjaszewski, K.; Bockstaller, M. R. Enhancing Thermal Transport in Nanocomposites by Polymer-Graft Modification of Particle Fillers. *Polymer (Guildf).* **2016**, *93*, 72–77. https://doi.org/10.1016/J.POLYMER.2016.04.014.
(25) Grabowski, C. A.; Koerner, H.; Meth, J. S.; Dang, A.; Hui, C. M.; Matyjaszewski, K.; Bockstaller, M. R.; Durstock, M. F.; Vaia, R. A. Performance of Dielectric Nanocomposites: Matrix-Free, Hairy Nanoparticle Assemblies and Amorphous Polymer-Nanoparticle Blends. *ACS Appl. Mater. Interfaces* **2014**, *6* (23), 21500–21509. https://doi.org/10.1021/am506521r.

(26) Alonso-Redondo, E.; Schmitt, M.; Urbach, Z.; Hui, C. M.; Sainidou, R.; Rembert, P.; Matyjaszewski, K.; Bockstaller, M. R.; Fytas, G. A New Class of Tunable Hypersonic Phononic Crystals Based on Polymer-Tethered Colloids. *Nat. Commun.* **2015**, *6*, 1–8. https://doi.org/10.1038/ncomms9309.
(27) Wang, Z.; Lu, Z.; Mahoney, C.; Yan, J.; Ferebee, R.; Luo, D.; Matyjaszewski, K.; Bockstaller, M. R. Transparent and High Refractive Index Thermoplastic Polymer Glasses Using Evaporative Ligand Exchange of Hybrid Particle Fillers. *ACS Appl. Mater. Interfaces* **2017**, *9* (8), 7515–7522. https://doi.org/10.1021/acsami.6b12666.
(28) Yan, J.; Malakooti, M. H.; Lu, Z.; Wang, Z.; Kazem, N.; Pan, C.; Bockstaller, M. R.; Majidi, C.; Matyjaszewski, K. Solution Processable Liquid Metal Nanodroplets by Surface-Initiated Atom Transfer Radical Polymerization. *Nat. Nanotechnol.* **2019**, *14* (7), 684–690. https://doi.org/10.1038/s41565-019-0454-6.
(29) Mbanga, B. L.; Iyer, B. V. S.; Yashin, V. V.; Balazs, A. C. Tuning the Mechanical Properties of Polymer-Grafted Nanoparticle Networks through the Use of Biomimetic Catch Bonds. *Macromolecules* **2016**, *49* (4), 1353–1361. https://doi.org/10.1021/acs.macromol.5b02455.
(30) Bilchak, C. R.; Buenning, E.; Asai, M.; Zhang, K.; Durning, C. J.; Kumar, S. K.; Huang, Y.; Benicewicz, B. C.; Gidley, D. W.; Cheng, S.; et al. Polymer-Grafted Nanoparticle Membranes with Controllable Free Volume. *Macromolecules* **2017**, *50* (18), 7111–7120. https://doi.org/10.1021/acs.macromol.7b01428.
(31) Akcora, P.; Liu, H.; Kumar, S. K.; Moll, J.; Li, Y.; Benicewicz, B. C.; Schadler, L. S.; Acehan, D.; Panagiotopoulos, A. Z.; Pryamitsyn, V.; et al. Anisotropic Self-Assembly of Spherical Polymer-Grafted Nanoparticles. *Nat. Mater.* **2009**, *8* (4), 354–359. https://doi.org/10.1038/nmat2404.
(32) Jiao, Y.; Akcora, P. Assembly of Polymer-Grafted Magnetic Nanoparticles in Polymer Melts. *Macromolecules* **2012**, *45*, 3463–3470. https://doi.org/10.1021/ma3000576.
(33) Liu, S.; Senses, E.; Jiao, Y.; Narayanan, S.; Akcora, P. Structure and Entanglement Factors on Dynamics of Polymer-Grafted Nanoparticles. *ACS Macro Lett.* **2016**, *5* (5), 569–573. https://doi.org/10.1021/acsmacrolett.6b00089.
(34) Bianchi, E.; Blaak, R.; Likos, C. N. Patchy Colloids: State of the Art and Perspectives. *Phys. Chem. Chem. Phys.* **2011**, *13* (14), 6397. https://doi.org/10.1039/c0cp02296a.
(35) Chao, H.; Riggleman, R. A. Inverse Design of Grafted Nanoparticles for Targeted Self-Assembly. *Mol. Syst. Des. Eng.* **2018**, *3* (1), 214–222. https://doi.org/10.1039/C7ME00081B.
(36) Nielsen, L. E.; Landel, R. F. *Mechanical Properties of Polymers and Composites*; CRC press, 1994.
(37) Ward, I. M.; Sweeney, J. *An Introduction to the Mechanical Properties of Solid Polymers*, 2nd ed.; Wiley, 2004.
(38) Tobolsky, A. V. *Properties and Structure of Polymers*; Wiley, 1960. https://doi.org/10.1149/1.2427514.
(39) Podsiadlo, P.; Krylova, G.; Lee, B.; Critchley, K.; Gosztola, D. J.; Talapin, D. V.; Ashby, P. D.; Shevchenko, E. V. The Role of Order, Nanocrystal Size, and Capping Ligands in the Collective Mechanical Response of Three-Dimensional Nanocrystal Solids. *J. Am. Chem. Soc.* **2010**, *132* (26), 8953–8960. https://doi.org/10.1021/ja100464a.
(40) Gu, X. W.; Ye, X.; Koshy, D. M.; Vachhani, S.; Hosemann, P.; Alivisatos, A. P. Tolerance to Structural Disorder and Tunable Mechanical Behavior in Self-Assembled Superlattices of Polymer-Grafted Nanocrystals. *Proc. Natl. Acad. Sci.* **2017**, *114* (11), 2836–2841. https://doi.org/10.1073/pnas.1618508114.
(41) Hilburg, S. L.; Elder, A. N.; Chung, H.; Ferebee, R. L.; Bockstaller, M. R.; Washburn, N. R. A Universal Route towards Thermoplastic Lignin Composites with Improved Mechanical

Properties. *Polymer (Guildf).* **2014**, *55* (4), 995–1003. https://doi.org/10.1016/j.polymer.2013.12.070.
(42) Midya, J.; Cang, Y.; Egorov, S. A.; Matyjaszewski, K.; Bockstaller, M. R.; Nikoubashman, A.; Fytas, G. Disentangling the Role of Chain Conformation on the Mechanics of Polymer Tethered Particle Materials. *Nano Lett.* **2019**, *19* (4), 2715–2722. https://doi.org/10.1021/acs.nanolett.9b00817.
(43) Giovino, M.; Pribyl, J.; Benicewicz, B.; Bucinell, R.; Schadler, L. Mechanical Properties of Polymer Grafted Nanoparticle Composites. *Nanocomposites* **2018**, *4* (4), 244–252. https://doi.org/10.1080/20550324.2018.1560988.
(44) Choi, J.; Hui, C. M.; Schmitt, M.; Pietrasik, J.; Margel, S.; Matyjazsewski, K.; Bockstaller, M. R. Effect of Polymer-Graft Modification on the Order Formation in Particle Assembly Structures. *Langmuir* **2013**, *29*, 6452–6459.
(45) Askar, S.; Li, L.; Torkelson, J. M. Polystyrene-Grafted Silica Nanoparticles: Investigating the Molecular Weight Dependence of Glass Transition and Fragility Behavior. *Macromolecules* **2017**, *50* (4), 1589–1598. https://doi.org/10.1021/acs.macromol.7b00079.
(46) Daoud, M.; Cotton, J. P. Star Shaped Polymers : A Model for the Conformation and Its Concentration Dependence. *J. Phys.* **1982**, *43* (3), 531–538. https://doi.org/10.1051/jphys:01982004303053100.
(47) Ohno, K.; Morinaga, T.; Takeno, S.; Tsujii, Y.; Fukuda, T. Suspensions of Silica Particles Grafted with Concentrated Polymer Brush: Effects of Graft Chain Length on Brush Layer Thickness and Colloidal Crystallization. *Macromolecules* **2007**, *40* (25), 9143–9150. https://doi.org/10.1021/ma071770z.
(48) Mongcopa, K. I. S.; Poling-Skutvik, R.; Ashkar, R.; Butler, P.; Krishnamoorti, R. Conformational Change and Suppression of the Θ -Temperature for Solutions of Polymer-Grafted Nanoparticles. *Soft Matter* **2018**, *14*, 6102–6108. https://doi.org/10.1039/C8SM00929E.
(49) Chen, J.; Fasoli, A.; Cushen, J. D.; Wan, L.; Ruiz, R. Self-Assembly and Directed Assembly of Polymer Grafted Nanocrystals via Solvent Annealing. *Macromolecules* **2017**, *50*, 9636–9646. https://doi.org/10.1021/acs.macromol.7b01921.
(50) Ohno, K.; Morinaga, T.; Koh, K.; Tsujii, Y.; Fukuda, T. Synthesis of Monodisperse Silica Particles Coated with Well-Defined, High-Density Polymer Brushes by Surface-Initiated Atom Transfer Radical Polymerization. *Macromolecules* **2005**, *38*, 2137–2142. https://doi.org/10.1021/ma048011q.
(51) Wang, Z.; Yan, J.; Liu, T.; Wei, Q.; Li, S.; Olszewski, M.; Wu, J.; Sobieski, J.; Fantin, M.; Bockstaller, M. R.; et al. Control of Dispersity and Grafting Density of Particle Brushes by Variation of ATRP Catalyst Concentration. *ACS Macro Lett.* **2019**, *8*, 859–864. https://doi.org/10.1021/acsmacrolett.9b00405.
(52) Voudouris, P.; Choi, J.; Dong, H.; Bockstaller, M. R.; Matyjaszewski, K.; Fytas, G. Effect of Shell Architecture on the Static and Dynamic Properties of Polymer-Coated Particles in Solution. *Macromolecules* **2009**, *42* (7), 2721–2728. https://doi.org/10.1021/ma802878r.
(53) Morinaga, T.; Ohno, K.; Tsujii, Y.; Fukuda, T. Structural Analysis of "Semisoft" Colloidal Crystals by Confocal Laser Scanning Microscopy. *Macromolecules* **2008**, *41* (10), 3620–3626. https://doi.org/10.1021/ma7028665.
(54) Ohno, K.; Koh, K.; Tsujii, Y.; Fukuda, T. Fabrication of Ordered Arrays of Gold Nanoparticles Coated with High-Density Polymer Brushes. *Angew. Chemie Int. Ed.* **2003**, *42* (24), 2751–2754. https://doi.org/10.1002/anie.200250850.
(55) Nakanishi, Y.; Ishige, R.; Ogawa, H.; Sakakibara, K.; Ohno, K.; Morinaga, T.; Sato, T.; Kanaya, T.; Tsujii, Y. USAXS Analysis of Concentration-Dependent Self-Assembling of Polymer-Brush-Modified Nanoparticles in Ionic Liquid: [I] Concentrated-Brush Regime. *J. Chem. Phys.* **2018**,

148 (12). https://doi.org/10.1063/1.5017552.
(56) Bachhar, N.; Jiao, Y.; Asai, M.; Akcora, P.; Bandyopadhyaya, R.; Kumar, S. K. Impact of the Distributions of Core Size and Grafting Density on the Self-Assembly of Polymer Grafted Nanoparticles. *Macromolecules* **2017**, *50* (19), 7730–7738. https://doi.org/10.1021/acs.macromol.7b01093.
(57) Hickey, R. J.; Seo, M.; Luo, Q.; Park, S. J. Directional Self-Assembly of Ligand-Stabilized Gold Nanoparticles into Hollow Vesicles through Dynamic Ligand Rearrangement. *Langmuir* **2015**, *31* (14), 4299–4304. https://doi.org/10.1021/la503903n.
(58) Choi, J.; Hore, M. J. A.; Clarke, N.; Winey, K. I.; Composto, R. J. Nanoparticle Brush Architecture Controls Polymer Diffusion in Nanocomposites. *Macromolecules* **2014**, *47*, 2404–2410. https://doi.org/10.1021/ma500235v.
(59) Chevigny, C. E.; Gigmes, D.; Bertin, D.; Jestin, J.; Bou, F. Polystyrene Grafting from Silica Nanoparticles via Nitroxide-Mediated Polymerization (NMP): Synthesis and SANS Analysis with the Contrast Variation Method. *Soft Matter* **2009**, *5*, 3741–3753. https://doi.org/10.1039/b906754j.
(60) Oliver, W. C.; Pharr, G. M. Measurement of Hardness and Elastic Modulus by Instrumented Indentation: Advances in Understanding and Refinements to Methodology. *J. Mater. Res.* **2004**, *19* (1), 3–20. https://doi.org/10.1557/jmr.2004.19.1.3.
(61) Avice, J.; Boscher, C.; Vaudel, G.; Brotons, G.; Juvé, V.; Edely, M.; Méthivier, C.; Gusev, V. E.; Belleville, P.; Piombini, H.; et al. Controlling the Nanocontact Nature and the Mechanical Properties of a Silica Nanoparticle Assembly. *J. Phys. Chem. C* **2017**, *121* (42), 23769–23776. https://doi.org/10.1021/acs.jpcc.7b08404.
(62) Griesemer, S. D.; You, S. S.; Kanjanaboos, P.; Calabro, M.; Jaeger, H. M.; Rice, S. A.; Lin, B. The Role of Ligands in the Mechanical Properties of Langmuir Nanoparticle Films. *Soft Matter* **2017**, *13* (17), 3125–3133. https://doi.org/10.1039/c7sm00319f.
(63) Ghosh, S. K.; Cherstvy, A. G.; Petrov, E. P.; Metzler, R. Interactions of Rod-like Particles on Responsive Elastic Sheets. *Soft Matter* **2016**, *12* (38), 7908–7919. https://doi.org/10.1039/c6sm01522k.
(64) Israelachvili, J. *Intermolecular and Surface Forces*, 3rd ed.; Acedemic Press, 2011. https://doi.org/10.1016/C2009-0-21560-1.
(65) Salem, L. Attractive Forces between Long Saturated Chains at Short Distances. *J. Chem. Phys.* **1962**, *37* (9), 2100. https://doi.org/10.1063/1.1733431.
(66) Boles, M. A.; Talapin, D. V. Many-Body Effects in Nanocrystal Superlattices: Departure from Sphere Packing Explains Stability of Binary Phases. *J. Am. Chem. Soc.* **2015**, *137* (13), 4494–4502. https://doi.org/10.1021/jacs.5b00839.
(67) Willbourn, A. H. Molecular Design of Polymers. *Polymer (Guildf).* **1976**, *17* (11), 965–976. https://doi.org/10.1016/0032-3861(76)90172-5.
(68) Gedde, U. W. *Polymer Physics*; Springer Science & Business Media, 1995. https://doi.org/10.1007/978-94-011-0543-9.
(69) Zhang, H.; Wang, W.; Akinc, M.; Mallapragada, S.; Travesset, A.; Vaknin, D. Assembling and Ordering Polymer-Grafted Nanoparticles in Three Dimensions. *Nanoscale* **2017**, *9* (25), 8710–8715. https://doi.org/10.1039/C7NR00787F.
(70) Cox, H. L. The Elasticity and Strength of Paper and Other Fibrous Materials. *Br. J. Appl. Phys.* **1952**, *3*, 72–79. https://doi.org/10.1088/0508-3443/3/3/302.

Chapter 11 Tunable Assembly of Block Copolymer Tethered Particle Brushes by SI-ATRP

11.1. Preface

A strategy to synthesize SiO_2-*g*-PMMA/PMMA-*b*-PS bimodal block copolymer particle brushes by surface-initiated atom transfer radical polymerization (SI-ATRP) from silica particles was developed. The initial tethered PMMA blocks were prepared by normal ATRP with different degrees of polymerizations (DPs) and grafting densities. The second PS block was synthesized through a low-ppm Cu catalyst ATRP chain extension. The chain composition/bimodality of the particle brushes (PMMA-*b*-PS fraction) was tuned by changing the concentration of the SiO_2-*g*-PMMA-Br macroinitiator in the reactions. Size-exclusion chromatography (SEC) and transmission electron microscopy (TEM) were used to study the chain composition and morphology of the products. Particles distributed or formed aggregated network structures such as strings and clusters, strongly depending on the chain architecture and the composition. These hierarchical architectures are promising in approaching the synthesis of novel functional materials.

In this chapter, the synthesis of SiO_2-*g*-PMMA-*b*-PS particle brushes and their self-assembly behavior is discussed. I designed the entire project and performed all synthetic work and characterization. I would like to thank especially my collaborators, Jaejun Lee for his extensive discussion and careful characterization work.

This project will be published in *ACS Macro Letters*.

This work was supported by NSF (DMR 1501324 and DMR 1410845), the Department of Energy (DE-SC0018784), the National Science Center (grant UMO-2014/14/A/ST5/00204), as well as the Scott Institute for Energy Technologies at Carnegie Mellon University. M.R. Bockstaller further

acknowledges the support by the National Science Foundation *via* grants CMMI-1663305 and DMR-1709344. Zhenhua Wang gratefully acknowledges financial support from the China Scholarship Council.

11.2. Introduction

The dispersion of nanoparticles in polymers, metals, or ceramic matrixes can dramatically improve the properties of the composite material.[1-3] Inorganic nanoparticles can be added to polymer matrices as nanofillers to tune a material's the mechanical properties.[4-5] Controlling the dispersion of unmodified nanoparticles into polymer matrices is a significant challenge facing achievement of the proclaimed property improvements promised by polymer nanocomposites,[6] as inorganic particles are typically immiscible with an organic phase.[7-8] Polymer nanocomposites formed by one-component polymer grafted nanoparticles, which are also referred to as matrix-free nanocomposites, overcome this "demixing" issue in traditional nanoparticles filled matrix systems.[9-11]

An interesting property of polymer grafted nanoparticles is their tendency to self-assemble into various well-defined structures in solution, or in a polymer matrix, including assembly into sheets and strings.[12-13] The dispersion of nanoparticles in polymer nanocomposites mainly depends on polymer graft density and the ratio of the molecular weights of the grafted polymer to the matrix polymer. Generally, co-assembly of nanoparticles and block copolymer (BCP) has been considered to be an efficient way of forming hybrid aggregates with controlled morphology and nanoparticles distribution.[14] This property arises from mesoscopic phase separation between inorganic and polymer parts of the nanoparticles and resembles the self-assembly characteristics of a BCP.[15] Nanoparticles can alter the orientation of BCP microdomains and tailor the morphology of the nanocomposite.[16-17] Theory predicts the formation of various structures by the self-assembly of particles with few attached polymer chains,[18] depending on the particle size, molecular weight of attached polymers and chain grafting density. These structures, which include lamellae, cylinders, and lattices, exhibit unique properties.[19-21] Analogous to

the mesostructure formation in phase-separated diblock/triblock copolymers, the morphology of these hybrid nanoparticles could be highly sensitive to even a small fraction of unattached free polymer chains, therefore, a precise knowledge of the structure and composition of materials based on hybrid particles is of paramount importance for the successful design of bottom-up composites.[22]

While uniform nanoparticle spatial distribution is usually the focus of hybrid particle synthesis and dispersion procedures, many situations take advantage of spatially non-uniform, anisotropic nanoparticle organization.[23-24] There has been significantly fascination with the self-assembling behavior of amphiphilic chain-like molecules that range from short surfactants to long diblock copolymers.[25-27] The self-organization of amphiphiles with more complex architectures can lead to a stunning variety of complex morphologies. Due to the difficulty and complication of synthesis, most studies of the self-assembly and aggregation behaviors of nanoparticles in hybrid assemblies made from block copolymer tethered nanoparticles are accomplished by simulation and computations work, for example, the modeling of nanoparticle-coil tadpole macromolecules,[28] the giant surfactant systems formed by tethering a single AB diblock copolymer onto nanoparticle,[29] the tethered nanoparticle telechelic system in where immiscible nanoparticle spheres tethered to one another by one polymer chain.[30] The complex phases (micelle in-network, gyroid, etc) and morphologies (spheres, rings, rod-like, and disk-like micelles, vesicles) are found which are highly affected by particle size and size distribution, chain architecture, arm numbers, and the interaction between nanoparticle and block copolymers.[31-34]

One key advantage of atom transfer radical polymerization (ATRP) over conventional radical polymerization is the possibility to prepare BCPs.[35-36] The ability to control both the length scale and the spatial organization of BCP brush morphologies on nanoparticles makes these materials particularly attractive as scaffolds for the engineering of nanostructures.[37-39] The grafting density of the polymer

brushes and fraction of free self-initiated polymer can be changed by altering the targeted degree of polymerization (DP) of SiO_2-*g*-PS particle brush, hence changing the $[SiO_2\text{-}Br]_0$.[22] The interdependence of grafting density, initiation efficiency and initiator concentration can be used to prepare particle brushes with PMMA-*b*-PS BCPs through simple chain extension reactions from pre-synthesized SiO_2-*g*-PMMA particle brushes. When nanoparticles are sparsely grafted with hydrophobic polymer chains, some parts of the particle surface area covered by the grafted chains while the other unmodified hydrophilic parts are exposed, resulting in the formation of anisotropic self-assembled morphologies, e.g. strings, sheets.[40-42]

Scheme 11.1. Synthesis of SiO_2-*g*-PMMA particle brushes with different grafting densities

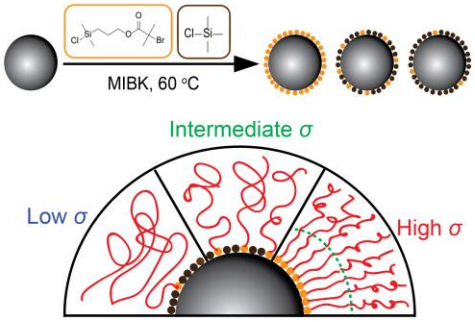

In this contribution, a system based on bimodal polymer grafted nanoparticles was examined. The synthesis of SiO_2-*g*-PMMA-*b*-PS particle brushes was accomplished using surface-initiated atom transfer radical polymerization (SI-ATRP).[43-46] First, PMMA blocks were "grafted from" the surface of the SiO_2 particles by normal SI-ATRP. Three SiO_2-Br nanoparticles were prepared for initial grafting of PMMA chains with controlled grafting densities (**Table 11.11, Scheme 11.11**). The grafting density was tuned by altering the ratio between tetherable ATRP initiator ((chlorodimethylsilyl)propyl-2-bromoisobutyrate) and "dummy" initiator (chlorotrimethylsilane).[21] The second PS blocks were formed using a low-ppm Cu catalyst ATRP procedure comprising of catalyst complexes with highly activating ligands.

11.3. Experimental Section

Materials.

Monomers: styrene (S, 99%, Aldrich), methyl methacrylate (MMA, 99%, Aldrich) were purified by passing through a column filled with basic alumina to remove the inhibitor. Tris(2-dimethylaminoethyl)amine (Me_6TREN, 99%, Alfa), 4,4'-dinonyl-2,2'-bipyridyne (dNbpy, 97%, Aldrich), anisole (99%, Aldrich), tetrahydrofuran (THF, 99%, VWR), methanol (99%, VWR), hexane (99%, VWR), acetone (99%, VWR), N,N-dimethylformamide (DMF, 99%, VWR), copper(II) bromide ($CuBr_2$, 99%, Aldrich), copper(II) chloride ($CuCl_2$, 99%, Aldrich), copper(I) chloride (CuCl, 97%, Sigma-Aldrich), tin(II) 2-ethylhexanoate ($Sn(EH)_2$, 95%, Aldrich), hexane (Fluka), 48% hydrofluoric acid aqueous solution (HF, >99.99%, Aldrich), ammonium hydroxide aqueous solution (NH_4OH, 28.0-30.0%, Fisher), anhydrous magnesium sulfate ($MgSO_4$, Fisher) were used as received without further purification. Copper (I) bromide (CuBr, 98%, Acros), was washed with glacial acetic acid to remove any soluble oxidized species, filtered, washed twice with anhydrous ethyl ether, dried and kept under vacuum. Silica nanoparticles, 30 wt % solution in methyl isobutyl ketone (MIBK-ST), effective diameter d ≈ 15.8 nm, were kindly donated by Nissan Chemical Corp. and used as received. The tethered ATRP initiator 1-(chlorodimethylsilyl)propyl-2-bromoisobutyrate and surface-modified silica (SiO_2-Br) were prepared using previously reported procedures. The surface initiator densities are moderated with a "dummy" initiator chlorotrimethylsilane (99%, Aldrich).

Procedures. Procedures for the synthesis of bimodal SiO_2-g-PMMA-b-PS particle brushes via ARGET ATRP.

SiO_2-g-PMMA particle brushes synthesis.

Initiator (SiO_2-Br), monomer (MMA), solvents (anisole, DMF), $CuCl_2$, and dNbpy (molar ratio shown as a subscript of **Table 11.1**) were mixed thoroughly in a sealed Schlenk flask. The mixture was

degassed by bubbling with nitrogen. Then, the mixture was flash-frozen by immersion in liquid nitrogen under continuous nitrogen purge and CuCl was immediately added. Another 10 min of nitrogen purge removed residual air from the flask. The reaction mixture was thawed by immersing the flask in water then subsequently placed in an oil bath set at the desired temperature. The conversion and molecular weight (MW) of polymer were monitored by gravimetric analysis and SEC, respectively.

Chain extension with styrene by ARGET ATRP.

Initiator (SiO_2-*g*-PMMA-Br particle brushes), monomer (S), solvents (anisole, DMF), $CuBr_2$, and Me_6TREN were mixed thoroughly in a sealed Schlenk flask. A stock solution of $Sn(EH)_2$ in anisole was prepared. Both mixtures were degassed by nitrogen purging, then the $Sn(EH)_2$ solution was injected into the Schlenk flask to activate the catalyst complex and the flask was immediately put into an oil bath. The MW of the polymer was measured by SEC.

Characterization.

Transmission electron microscopy (TEM) was carried out using a JEOL 2000 EX electron microscope operated at 200 kV. The spatial distribution, radius and inter-particle distances of the SiO_2 nanoparticles were determined from statistical analysis of the TEM micrographs using ImageJ software.

Thermogravimetric analysis (TGA) with TA Instruments 2950 was used to measure the fraction of SiO_2 in the hybrids. The data were analyzed with TA Universal Analysis. The heating procedure involved four steps: (1) jump to 120 ºC; (2) hold at 120 ºC for 10 min; (3) ramp up at a rate of 20 ºC/min to 800 ºC; (4) hold for 2 min. The TGA plots were normalized to the total weight after holding at 120 ºC.

The grafting density was calculated using the formula (S1).

$$\sigma_{\mathrm{TGA}} = \frac{(1-f_{\mathrm{SiO2}})N_{\mathrm{Av}}\,\rho_{\mathrm{SiO2}}\,d}{6\,f_{\mathrm{SiO2}}\,M_n} \qquad \text{(S1)}$$

where f_{SiO2} is the SiO_2 fraction measured by TGA, N_{Av} is the Avogadro number, ρ_{SiO2} is the density of SiO_2 nanoparticles (2.2 g/cm^3), d is the average diameter of SiO_2 nanoparticles (15.8 nm), M_n is the overall number-average MW of the cleaved polymer brushes.

Number-average molecular weights (M_n) and MWDs were determined by size exclusion chromatography (SEC). The SEC was conducted with a Waters 515 pump and Waters 410 differential refractometer using PSS columns (Styrogel 10^5, 10^3, 10^2 Å) in THF as an eluent at 35 ºC and a flow rate of 1 ml min^{-1}. Linear PS and PMMA standards were used for calibration. The conversion was calculated by gravimetric analysis. The fraction of short PMMA and long PS-*b*-PMMA long brushes were calculated by deconvolution of differential refractive index (dRI) *vs* elution volume (V_e), in Origin 9.0 assuming both of the polymer signals follow Gaussian distribution.

11.4. Results and Discussion

Compared to the high and medium grafting density systems, the sparsely grafted SiO_2 particle brushes showed more unique self-assembly behaviors. To investigate the synthesis of bimodal copolymer particle brush with low grafting density, we utilized our findings that the bimodality of the particle brushes and the population of conjugated PS blocks can be easily tuned by altering the concentration of the pre-synthesized SiO_2-*g*-PMMA particle brush macro-initiators in the reaction. The chain composition strongly influences the morphology and aggregation states of the block hybrid particles in bulk and solution. Single particles and cluster string-like structures were observed, the top scheme in **Figure 11.1**. These hierarchical architectures present a promising approach to prepare novel functional materials.

Table 11.1. Result of syntheses of sparsely grafted SiO_2-*g*-PMMA/PMMA-*b*-PS particle brushes

Entry[a]	M_n[b]	M_w/M_n[b]	f_{ino} (%)[c]	σ (nm^{-2})[d]
PMMA-L1	133,500	1.18	35.1	0.046
M-b-S-1	209,400	2.66	24.52	0.049
M-b-S-2	241,800	2.11	24.15	0.044

PMMA-L2	23,200	1.23	77.2	0.042
M-b-S-3	206,800	3.17	27.52	0.042
M-b-S-4	80,600	1.68	21.98	0.043

[a] Reaction condition: M-*b*-S-1~2: $[S]_0/[SiO_2\text{-}g\text{-}PMMA\text{-}Br]_0/[CuBr_2]_0/[Me_6TREN]_0/[Sn(EH)_2]_0$=50000:1/2:5:50:5; M-*b*-S-3~4: $[S]/_0[SiO_2\text{-}g\text{-}PMMA\text{-}Br]_0/[CuBr_2]_0/[Me_6TREN]_0/[Sn(EH)_2]_0$=5000:1/2:0.5:5:0.5; PMMA-L1-2: $[MMA]_0/[SiO_2\text{-}Br]_0/[CuCl_2]_0/[dNbpy]_0/CuCl]_0$ = 3000:1/4:0.4:8:3.6 with 45 vol% anisole, 5 vol% DMF at 60 ºC. [b] Determined by SEC. [c] f_{ino} (inorganic content), determined by TGA. [d] σ (grafting density), calculated according to TGA data.

Table 11.1 shows the compositions of two sparsely grafted SiO_2-*g*-PMMA NPs synthesized by normal ATRP, PMMA-L1 with DP = 1335, grafting density 0.046 chains/nm^2 and PMMA-L2 with DP = 232, grafting density 0.042 chains/nm^2, respectively. To achieve bimodal structures, low initiator concentrations of 20 and 40 ppm were used, for chain extension experiments with styrene monomers, samples M-*b*-S-1/2. After polymerization and purification, the samples were characterized by TEM and SEC. SEC traces of polymers cleaved from nanoparticles indicated clear bimodal features (**Figures S11.5** and **Figures S11.6**). The number-averaged molecular weight (M_n), dispersity and PMMA/PMMA-*b*-PS chain fractions were calculated by deconvolution of SEC traces. As shown in **Table S11.3**, under high target DP conditions, 50,000 and 25,000, only 7% and 11% of PMMA-Br chains were chains extended. Constant grafting density values before and after chain extensions suggested that the amount of new chains, which are free homo-polymers generated from thermal-self initiation of styrene monomers, is negligible.

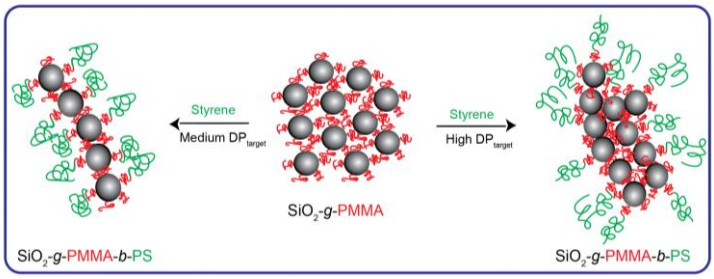

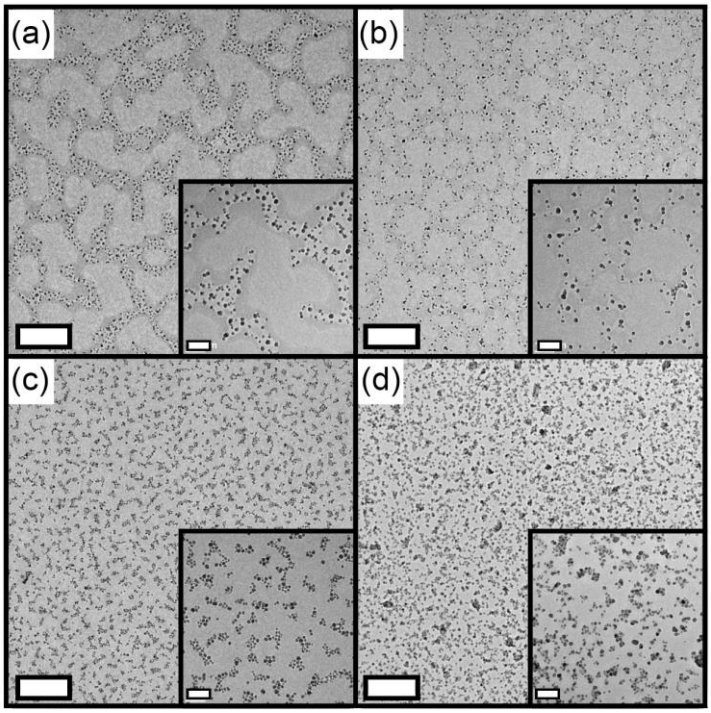

Figure 11.1. Schematic graph of the synthesis and assembly of bimodal SiO_2-g-PMMA/PMMA-*b*-PS particle brushes and TEM images of SiO_2-*g*-PMMA-*b*-PS particle brushes. (a) M-*b*-S-1, (b) M-*b*-S-2: (c) M-*b*-S-3: (d) M-*b*-S-4. Scale bar: 500 nm, inset scale bar: 100 nm.

TEM was used to investigate the morphology of the particle brush assemblies. Representative images are shown in **Figure 11.1**. Figures 1a-b shows that PMMA-*g*-SiO_2 particles were well-dispersed on the grid. Sparsely grafted particle brushes have low grafting density and tend to self-assemble to anisotropic string-like structures, which can be observed in the higher magnification TEM image, **Figure 11.1**b(inset). This tendency of the particles to link directionally is due to limited numbers of chains distributed on the surface of nanoparticles. Even after partial chain extension with a PS block, the low grafting density SiO_2-*g*-PMMA particles remained connected and formed a predominately one-dimensional short string composed of several particles, **Figure 11.1**b. A decrease of BCP chain fraction to 6.9% resulted in the formation of a more elaborately branched and thicker network structure, accompanied by interpenetrating higher DP chains at the junction points (**Figure 11.1**a). The basis for the self-assembly process is illustrated in the top scheme of **Figure 11.1**. The images show that the nanoparticles are not in direct contact with each other since there is an average 15-30 nm gap between

each nanoparticle pair along the string orientation. This gap represents the presence of a shell formed by the collapsed PMMA domains. It is important to note that the self-assembly mechanism of these bimodal polymers grafted particle brushes is different from most of the polymer-directed colloidal assemblies previously reported. In this case, sparsely grafted homopolymer/BCP brushes result in direct anisotropic assembly, which originates from the phase separation of immiscible polymer brushes without the need of any post-polymerization procedures. It is noted that due to the self-assembly of particle brush to a string-like structure, some void spaces are observed in TEM images of the monolayer sample films (**Figure 11.1**a-b), which confirm the ligand-induced self-assembly behavior and also the absence of free PS polymers from thermal-self initiation. The volume of the void space can be diminished when the DP of PS blocks is increased.

PMMA-L2, SiO_2-*g*-PMMA hybrid particles with shorter PMMA chains were prepared to confirm the mechanism of self-assembly of bimodal BCP particle brushes. As shown in **Figures 11.1**c-d, the inter-particle distance decreased considerably for the bimodal BCP particle brushes with similar grafting density, but lower DP (DP = 232), due to the shrinkage of the collapsed PMMA polymer shell. The self-assembly of sparsely grafted nanoparticles can no longer be observed in TEM images (**Figure S11.13**b). This also leads to a thinner PMMA phase in the BCP particle brushes (M-*b*-S-3~4) after chain extension. Lower target DPs, 10,000 and 5,000, were also examined in the chain extension reactions with the expectation of forming a higher fraction of PMMA-*b*-PS in the products. SEC traces, **Figures 11.1**c and **Figures 11.1**d, showed that when compared to samples M-*b*-S-1~2, the PMMA peaks in M-*b*-S-3~4 were much smaller, implying higher PMMA-*b*-PS fractions. After deconvolution of the traces, the chain compositions of the PMMA-*b*-PS fractions were 55% and 80%, respectively. Although no clear string-like structures were observed in the images of the SiO_2-*g*-PMMA samples before chain extension, and no obvious PMMA phase was found in TEM images after chain extension, the images from the PMMA-*b*-PS sample with a higher block fraction of 80%, displayed a string-like structure

(**Figures 11.1**d). On the other hand, some clusters structures were observed in **Figure 11.1**c with only 55% of PMMA-*b*-PS.

Block copolymers can self-assemble into various morphologies after annealing.[15, 47-49] In contrast to linear block copolymers, self-assembly of block copolymer particle brushes are not only affected by polymer chain composition but are also strongly associated with the grafting density of polymer ligands on the surface of the nanoparticles. Three SiO_2-*g*-PMMA-*b*-PS particle brush systems were investigated to study the effect of chain composition and grafting density on the self-assembly of block copolymer particle brushes. First, three SiO_2-*g*-PMMA particle brushes (PMMA-H1/M1/L3) with different grafting densities (high: 0.75 nm^{-2}, medium: 0.15 nm^{-2}, low: 0.05 nm^{-2}) but with a similar degree of polymerizations (DP~450-550) were prepared, **Table 11.2**. Before chain extension, the morphologies of SiO_2-*g*-PMMA particle brushes were characterized by TEM, **Figure S11.14**, which showed that the decreased distance between particle cores with decreasing grafting density. The outer PS blocks were prepared by ARGET ATRP chain extension with the same initial macro-initiator concentration ($[SiO_2$-*g*-PMMA-Br$]_0$), (50 ppm). Polymer ligands were characterized by SEC after etching the SiO_2 cores, the bimodal features and high dispersity values from the SEC traces (**Figures S11.9-S11.11**) indicated only a partial chain extension from the tethered PMMA blocks. After deconvolution of the SEC traces, the composition of polymer ligands (PMMA and PMMA-*b*-PS) are listed in **Table S11.3**, which shows that the fraction of PMMA-*b*-PS ligands prepared under these conditions was 30% to 45%， which is also the re-initiation efficiency for the chain extension reaction of PS blocks. (**Scheme 11.2**)

Table 11.2. Result of syntheses of SiO_2-*g*-PMMA nanoparticles with different grafting density

Entry[a]	**M_n**[b]	**M_w/M_n**[b]	**f_{ino} (%)**[c]	**σ (nm^{-2})**[d]
PMMA-H1	44,500	1.16	8.9	0.763
M-b-S-5	97,100	2.46	5.3	0.609
PMMA-	56,300	1.12	26.2	0.165

M1				
M-b-S-6	113,000	1.93	15.8	0.156
PMMA-L3	47,700	1.13	57.7	0.051
M-b-S-7	152,400	4.41	36.7	0.038

[a] Reaction condition: M-*b*-S-5~7: $[S]_0/[SiO_2\text{-}g\text{-}PMMA\text{-}Br]_0/[CuBr_2]_0/[Me_6TREN]_0/[Sn(EH)_2]_0$=10000:1:2:20:2; PMMA-H1/M1/L3: $[MMA]_0/[SiO_2\text{-}Br]_0/[CuCl_2]_0/[dNbpy]_0/CuCl]_0$ = 4000:1:0.4:8:3.6 with 45 vol% anisole, 5 vol% DMF at 60 ºC. [b] Determined by SEC. [c] f_{ino} (inorganic content), determined by TGA. [d] σ (grafting density), calculated according to TGA data.

Scheme 11.2. Synthesis of bimodal SiO_2-g-PMMA/PMMA-*b*-PS particle brushes with different grafting densities

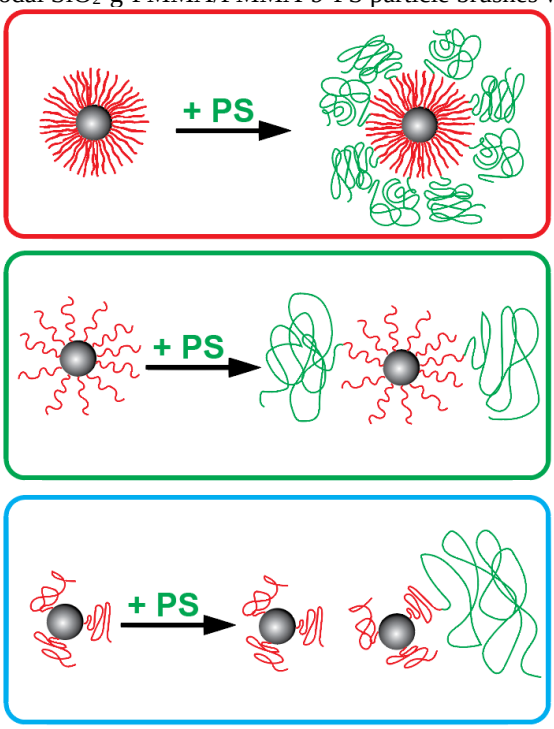

Although the three-block copolymer particle brushes (M-*b*-S-5~7) have comparable ligand compositions, i.e. similar PMMA blocks and block copolymer ligand fractions, their morphologies are dramatically different. **Figure 11.2** shows the TEM images of M-*b*-S-5~7 particle brushes with the same magnification. The high grafting density particle brush (M-*b*-S-5) showed a relatively uniform structure with partially string-like features in the monolayer film on Cu grids, **Figures 11.2a-b** and **Figure S11.22** (after staining with RuO_4). On the other hand, the medium grafting density and low grafting density samples exhibited strongly anisotropic morphological features, as connecting strings (M-*b*-S-6, **Figures 11.2c-d**) and continuous cluster networks (M-*b*-S-7, **Figures 11.2e-f**), respectively. These unique assembly behaviors are attributed to the different grafting densities and resulting chain

conformations of polymer ligands on the silica nanoparticles surfaces. The apparent grafting densities (σ_2) of PMMA-*b*-PS block, which are calculated using the grafting density of SiO_2-*g*-PMMA particle brush (σ, **Table 11.2**) and the fraction of block copolymer ligands after chain extension are listed in **Table S11.3**. In the case of high grafting density particle brush, the grafting density of PMMA-*b*-PS ligands is 0.192 nm^{-2}, which is still in the medium and high grafting density region. With sufficient PS outer layers, this leads to a relatively uniform structure.

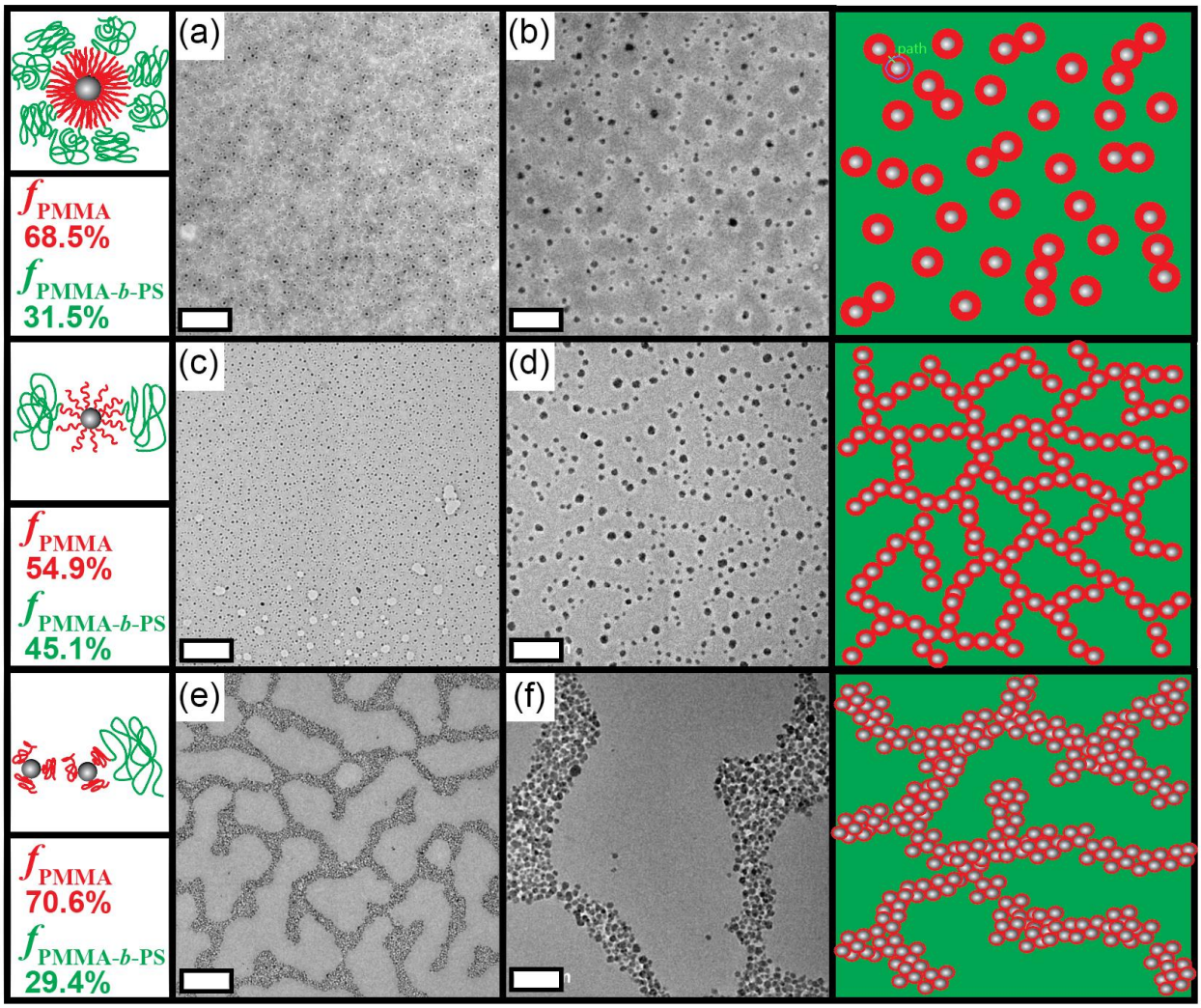

Figure 11.2. TEM images of SiO_2-*g*-PMMA-*b*-PS particle brushes. (a-b) M-*b*-S-5, (c-d) M-*b*-S-6: (e-f) M-*b*-S-7. Scale bar, (a), (c), (e): 500 nm, (b), (d), (f), 100 nm.

Meanwhile, the grafting density of block copolymer ligands in the intermediately grafted particle brush (M-*b*-S-6) is 0.07 nm^{-2}, which falls into the typical sparsely grafted particle brush region. The medium grafting density system displays a connected single SiO_2-*g*-PMMA particle brush domain covered with PS outer shell structure, which agrees with the composition of the ligand. The grafting density of PMMA-*b*-PS chains in the sparsely grafted particle brush sample is only 0.01 nm^{-2}, and the surface area of a 15 nm silica nanoparticle is around 700 nm^2, giving an average of 7 BCP chains per particle. According to an estimation based on a kinetic analysis in literature,[50] a fair proportion of particle brush in the system will be nearly bare SiO_2-*g*-PMMA (5 extended chains or less: 29.6%; 7 or less: 59.5%, **Figure 11.3**a), possibly explaining the "cluster" structure in the SiO_2-*g*-PMMA domain due to the strong particle-particle attraction. Although quantitative analysis of the TEM images (**Figure 11.2**e-f) was difficult because of the visual overlapping of particles within the images, the aforementioned fractions of 29.6% and 59.5% roughly correspond to the percentages of particles lying within the cluster and on the surface. The schematic illustrations of block copolymer particle brush structures and monolayer film morphologies are shown in the scheme of **Figure 11.2**.

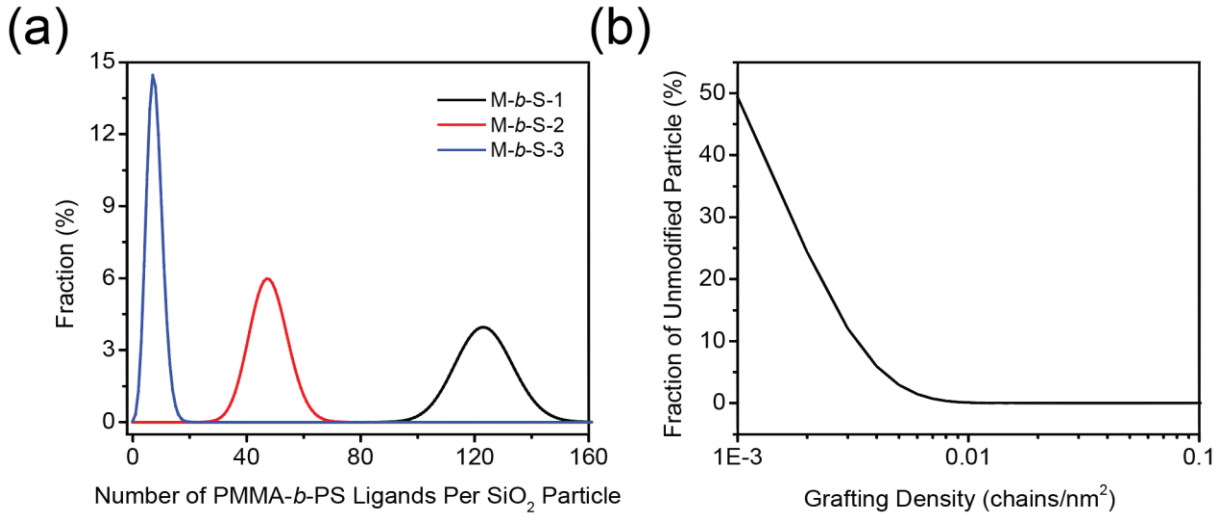

Figure 11.3. Plots of (a) particle fraction (number-average) *vs.* the number of ligands in SiO_2-*g*-PMMA-*b*-PS particle brushes, (b) fraction of unmodified particle as a function of grafting density.

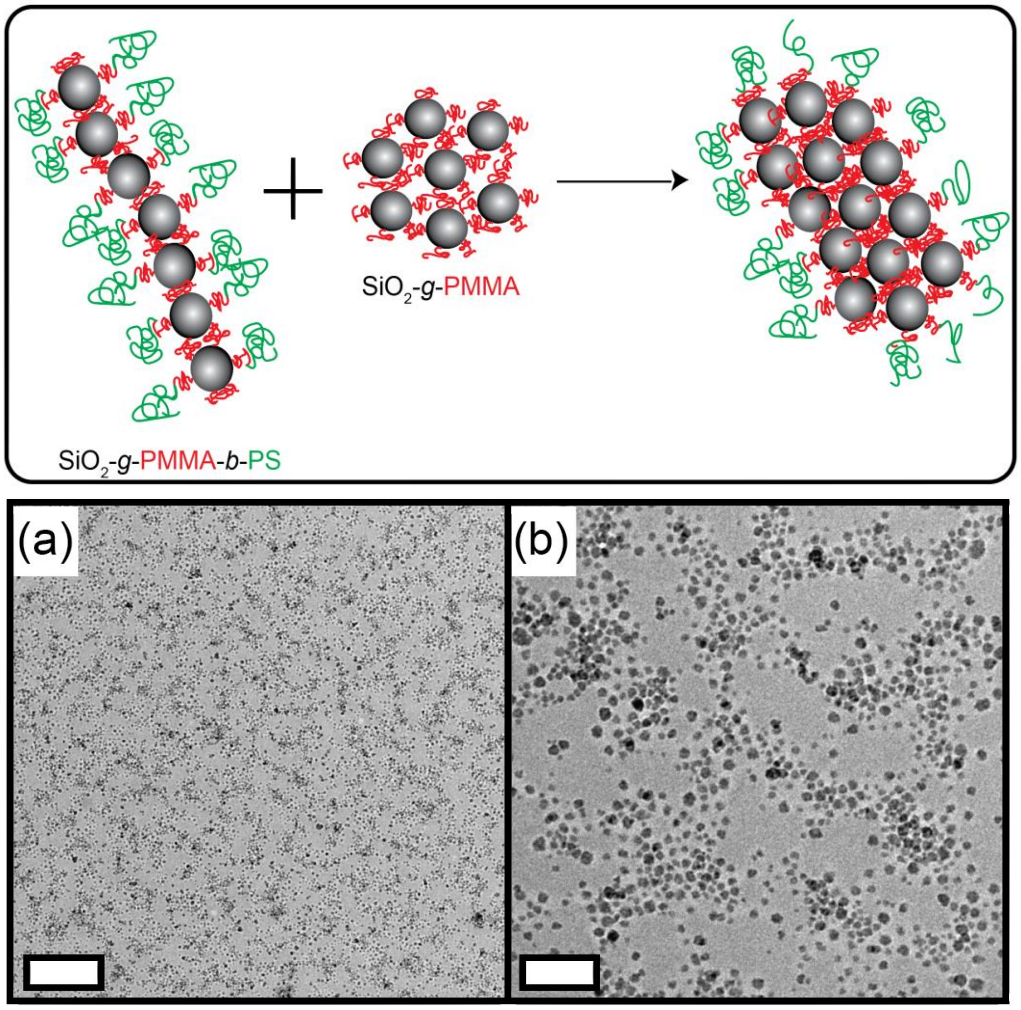

Figure 11.4. Schematic graph of the assembly of bimodal SiO_2-g-PMMA/PMMA-*b*-PS and SiO_2-*g*-PMMA particle brushes mixtures and TEM images of a mixture of SiO_2-*g*-PMMA-*b*-PS and SiO_2-*g*-PMMA particle brushes. (a-b) M-*b*-S-6 with PMMA-L2, mass ratio=1:4, scale bar: (a) 500 nm, (b) 100 nm.

To further investigate if the self-assembly mechanism of non-chain-extended SiO_2-*g*-PMMA particle brushes would form a "cluster-like" structure, which is surrounded by SiO_2-*g*-PMMA-*b*-PS particle brushes, sparsely grafted SiO_2-*g*-PMMA particle brushes (PMMA-L2) were mixed with two SiO_2-*g*-PMMA-*b*-PS particle brushes (M-*b*-S-6 and M-*b*-S-4) separately in THF solution, with a mass ratio of 4:1. The morphology of the mixtures was studied by TEM. As shown in **Figure 11.4**, after adding a large amount of SiO_2-*g*-PMMA particle brushes, the "string-like" structure of M-*b*-S-6 (**Figure 11.4**b) evolved to a "cluster-string" structure. Due to the lower grafting density of the adding particle brushes, PMMA-L2, it is easy to distinguish the two distinct PMMA regions, one where the SiO_2-*g*-

PMMA-*b*-PS particle brushes are located outside of the cluster and another where the SiO_2-*g*-PMMA particle brushes are inside the clusters. A similar evolution can be observed in a sparsely grafted bimodal copolymer particle brush system (M-*b*-S-4) with a smaller PMMA phase (**Figure S11.24**). These observations not only confirm the self-assembly mechanism we proposed but also show that adding PMMA-*g*-SiO_2 particle brushes can enrich the PMMA phase in the system, overall enhancing the design and fabrication of unique and elaborate network structures.

11.5. Supporting Information

Example of the deconvolution of PMMA-b-PS SEC traces

1. Intensity vs. Elution time plot

The example PMMA-*b*-PS sample was first characterized by SEC with PMMA standard calibration.

The M_n of PMMA macro-initiator is 133,500, with M_w/M_n=1.18

The M_n of PMMA-*b*-PS is 241,800, with M_w/M_n=2.11.

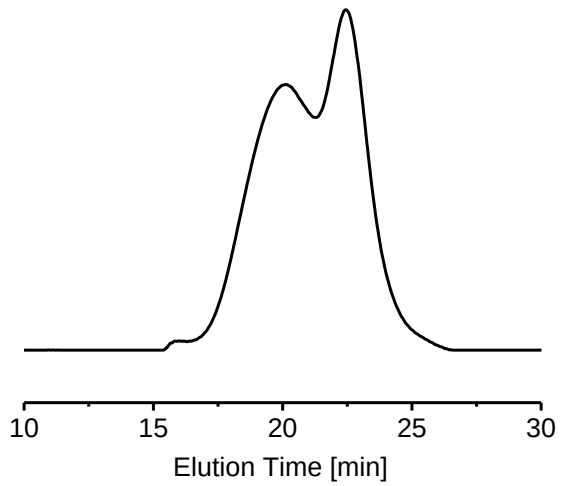

Figure S11.1. SEC traces of PMMA-*b*-PS polymer ligand (intensity vs. elution time)

Raw data were obtained from SEC, intensity vs. elution time graph was plotted as shown in Figure S1. A clear bimodal feature was observed.

2. Fitting to obtain different peaks in Origin 9.0

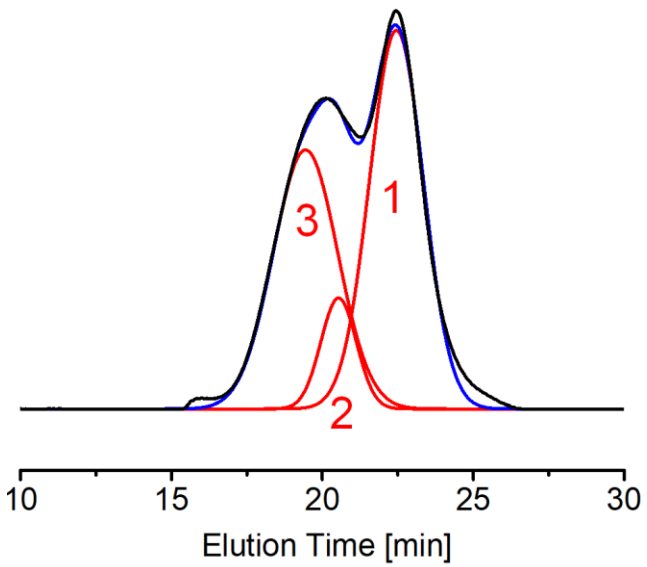

Figure S11.2. Fitting plots of SEC traces by Origin 9.0, black curve: raw data, blue: added fitting curves, red: three different unimodal curves.

It was assumed that all of the polymer signals follow Gaussian distribution. As shown in **Figure S11.2**, after fitting in Origin 9.0, three curves (red) were obtained. The added curve (blue) has great overlap with the original curve, which suggested the fitting's good accuracy.

3. Fit data into two PMMA and PMMA-*b*-PS curves

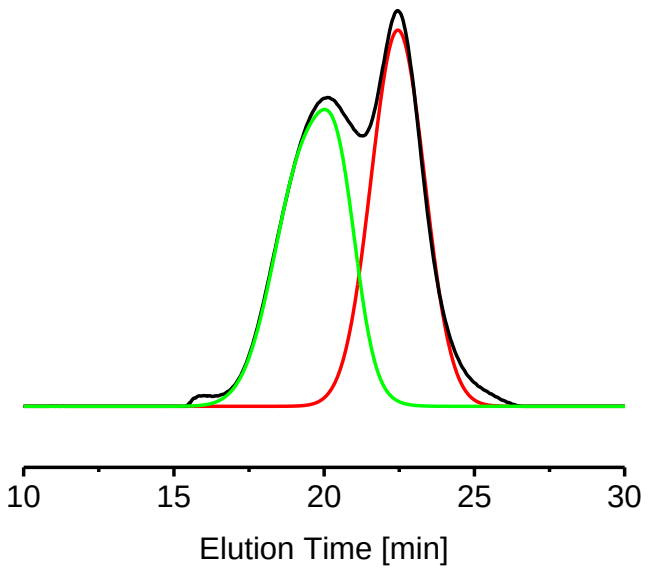

Figure S11.3. Added fitting curve, red: PMMA, green: PMMA-*b*-PS, black: original curve.

According to the mechanism reported, curve 1 in **Figure S11.2** corresponds to un-extended PMMA polymer ligands. The green curve in **Figure S11.3** is the sum of curve 2 and curve 3 in **Figure S11.2**, which corresponds to PMMA-*b*-PS.

4. Calculation of the M_n and M_w/M_n of two fitting curves and their chain compositions

Each time in elution time plot corresponds to a molar mass and after calculation in the raw data; the data obtained are summarized in **Table S11.1** and shows the M_n and M_w/M_n of two fitting curves and their chain compositions.

Table S11.1. Summary of PMMA/PMMA-*b*-PS molecular weight and fractions

Entry	**PMMA**		**PMMA-b-PS**		f_{PMMA}[c]	$f_{PMMA\text{-}b\text{-}PS}$[c]
	M_n	M_w/M_n	M_n	M_w/M_n	**(%)**	**(%)**
PMMA-b-PS[a]	**145,000**	**1.22**	**773,000**	**1.35**	**79.6**	**20.4**
PMMA[b]	133,500	1.18			100	0

[a] Fitting curve and deconvolution data, [b] Original PMMA-Br marco-initiator data as comparison, [c] mol% fraction of PMMA and PMMA-*b*-PS.

5. Normalization with $d_n/d_{c(eff)}$

The refractive indexes of PMMA (1.4813) and PS (1.5717) under wavelength 1.052 μm are very different. The d_n/d_c values used in SEC for PMMA and PS are 0.09 and 0.18, respectively, which leads to different signal intensities in the same curve. Therefore, to achieve more accurate chain composition, normalization to provide d_n/d_c(eff) for PMMA-*b*-PS blocks is necessary.

$$\boldsymbol{d_n/d_c(eff)} = \frac{\boldsymbol{M_n(PMMA)}}{\boldsymbol{M_n(PMMA-b-PS)}} \times \boldsymbol{d_n/d_c(PMMA)} + \frac{\boldsymbol{M_n(PMMA-b-PS)-M_n(PMMA)}}{\boldsymbol{M_n(PMMA-b-PS)}} \times \boldsymbol{d_n/d_c(PS)} \quad \text{(S2)}$$

Equation (S2) was used to calculate the $d_n/d_{c(eff)}$ for PMMA-*b*-PS blocks, where $M_{n(PMMA)}$ and $M_{n(PMMA\text{-}b\text{-}PS)}$ were obtained from **Table S11.1**. After calculation, we have the $d_n/d_{c(eff)}$ = 0.163 for PMMA-*b*-PS blocks. In **Figure S11.3**, the d_n/d_c value for PMMA-*b*-PS was assumed to be the same as PMMA. After normalization with new $d_n/d_{c(eff)}$, **Figure S11.4** was plotted, with new PMMA-*b*-PS in the green dash curve, which is much less intense than the previous one. The peak values didn't move, which means the M_n of PMMA-*b*-PS would not change after normalization. The intensity decrease leads to a lower fraction of PMMA-*b*-PS. (**Table S11.2**)

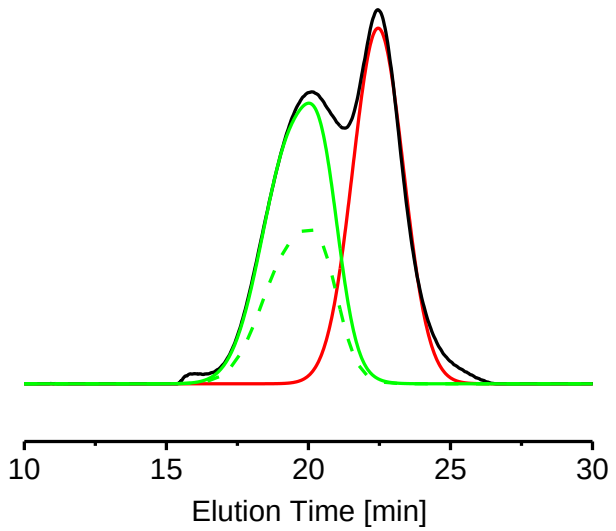

Figure S11.4. SEC trace after normalization with d_n/d_c(eff) for PMMA-*b*-PS blocks, black: Original curve, red: PMMA curve, green solid: PMMA-*b*-PS curve with $d_n/d_{c(PMMA)}$, green dash: PMMA-*b*-PS curve with $d_n/d_{c(eff)}$.

Table S11.2. Summary **of PMMA/PMMA-b-PS molecular weight and fractions after normalization**

Entry	**PMMA**		**PMMA-b-PS**		f_{PMMA}[c]	$f_{PMMA\text{-}b\text{-}PS}$[c]
	M_n	M_w/M_n	M_n	M_w/M_n	**(%)**	**(%)**
PMMA-b-PS[a]	**145,000**	**1.22**	**773,000**	**1.35**	**79.6**	**20.4**
PMMA-b-PS[b]	**145,000**	**1.22**	**773,000**	**1.35**	**88.6**	**11.4**
PMMA[c]	133,500	1.18			100	0

[a] Fitting curve and deconvolution data, [b] Original PMMA-Br macro-initiator data as a comparison, [b] PMMA-*b*-PS M_n and fractions after normalization, [b] Original PMMA-Br macro-initiator data as a comparison, [c] mol% fraction of PMMA and PMMA-*b*-PS.

As shown in **Table S11.2**, after normalization, the M_n and M_w/M_n for PMMA-*b*-PS did not change. However, the molar compositions changed significantly.

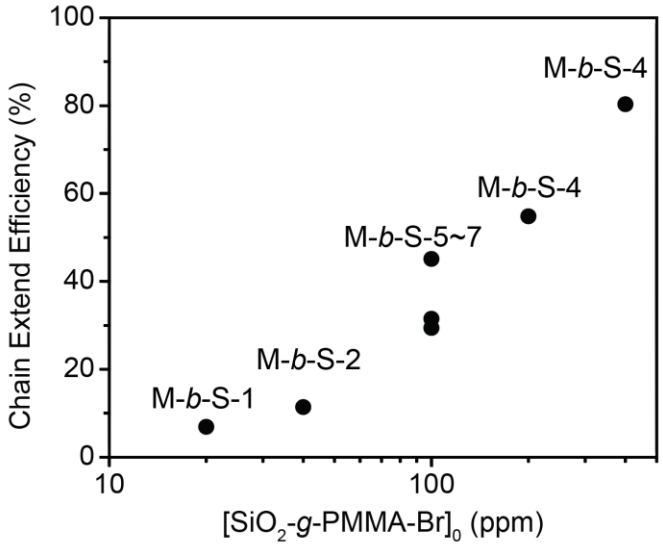

Figure S11.5. The plot of chain extension efficiency of PS block *vs.* the concentration of macro-initiators SiO_2-*g*-PMMA-Br ([SiO_2-*g*-PMMA-Br]$_0$)

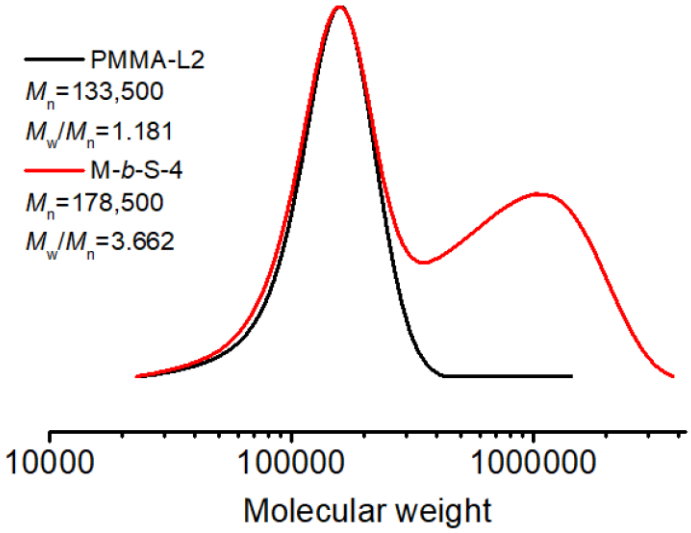

Figure S11.6. SEC trace of PMMA-L1 and M-*b*-S-1

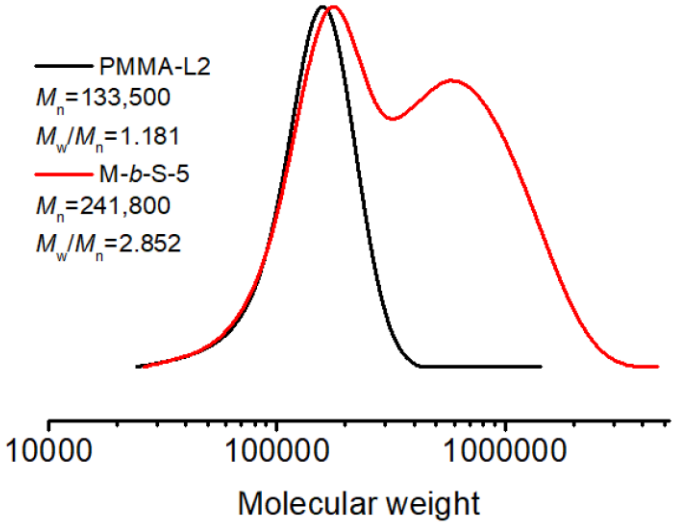

Figure S11.7. SEC trace of PMMA-L1 and M-*b*-S-2

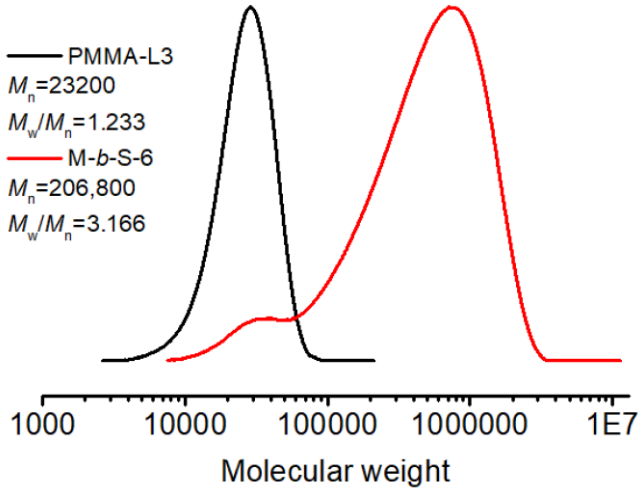

Figure S11.8. SEC trace of PMMA-L2 and M-*b*-S-3

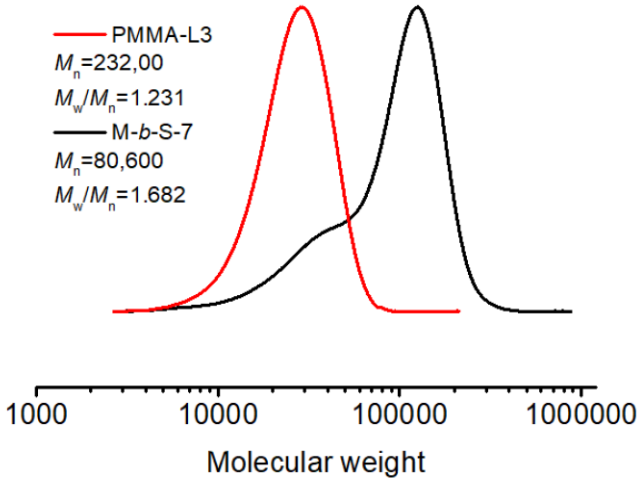

Figure S11.9. SEC trace of PMMA-L2 and M-*b*-S-4

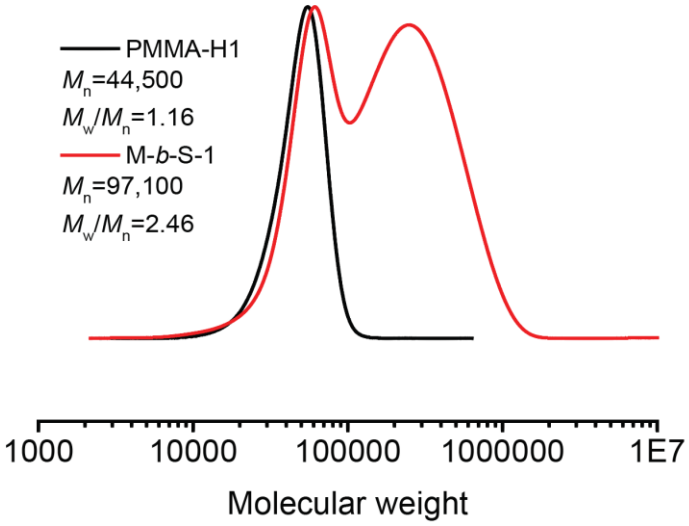

Figure S11.10. SEC trace of PMMA-H1 and M-*b*-S-5

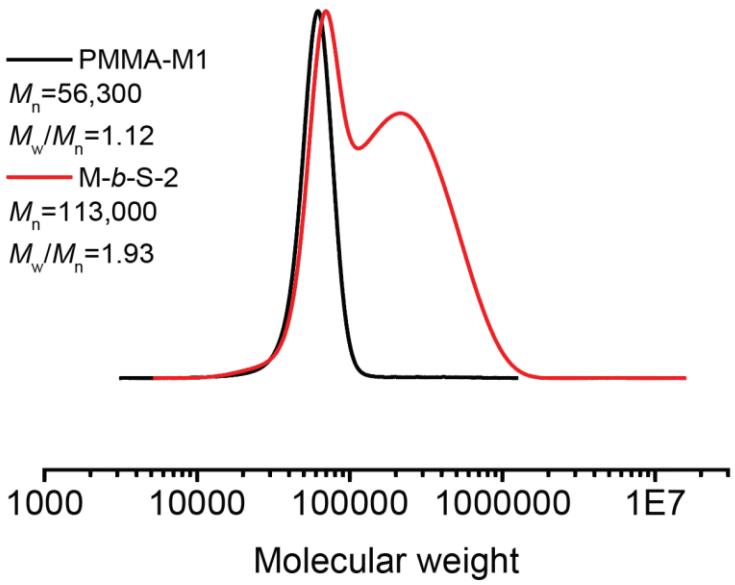

Figure S11.11. SEC trace of PMMA-M1 and M-*b*-S-6

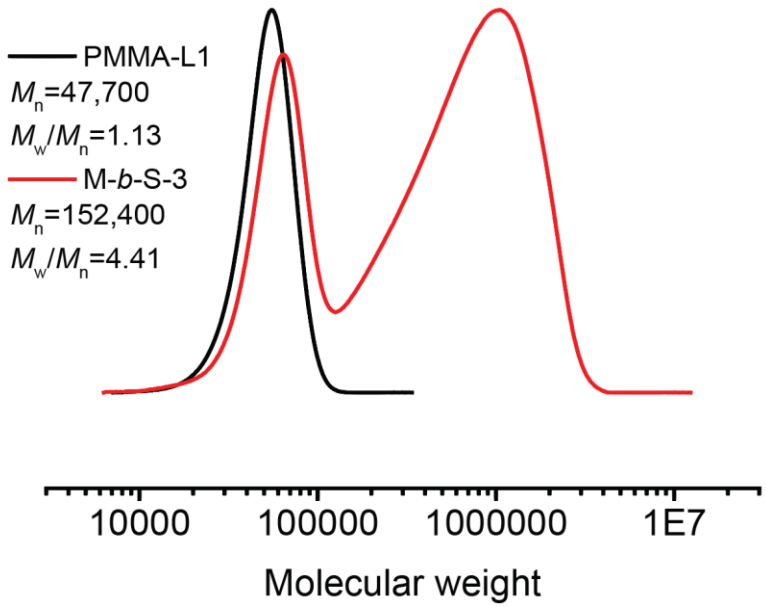

Figure S11.12. SEC trace of PMMA-L3 and M-*b*-S-7

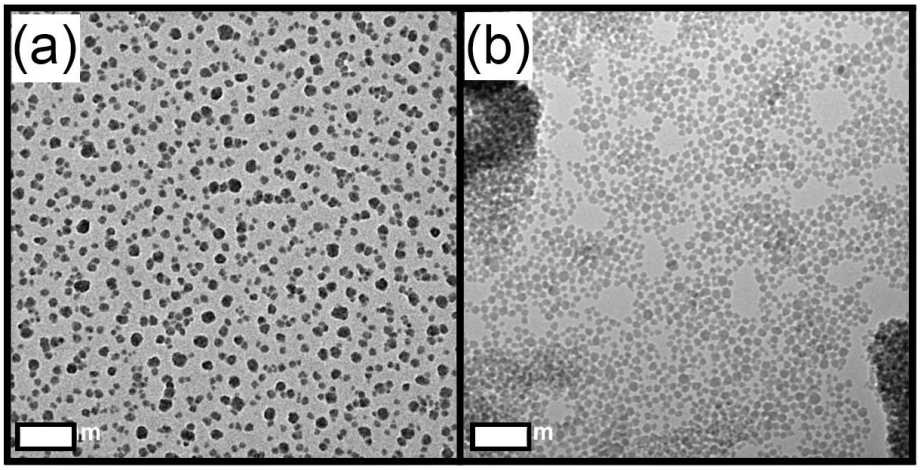

Figure S11.13. TEM image of SiO_2-*g*-PMMA particle brushes: (a) PMMA-L1, (b) PMMA-L2, scale bar: 100 nm.

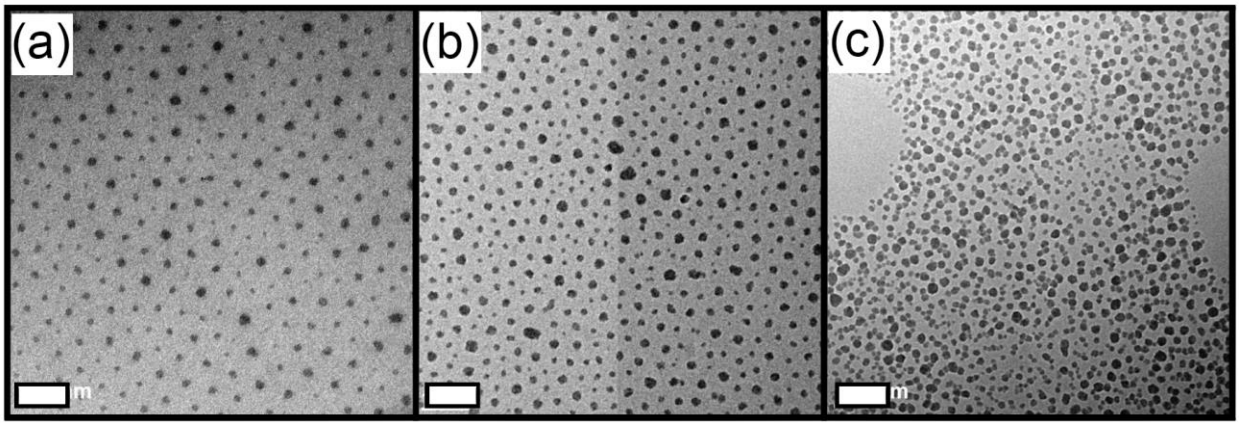

Figure S11.14. TEM image of SiO_2-*g*-PMMA particle brushes: (a) PMMA-H1, (b) PMMA-M1, (c) PMMA-L3, scale bar: 100 nm.

Quantitative analysis of domain structure using TEM micrographs

A quantitative analysis of TEM micrographs following systematic processing was conducted. A sequence for the analysis is shading correction – blurring – dilation – erosion – domain mapping. A bandpass filter was applied to correct shading. Gaussian blurring is necessary to reduce detail for better recognition. As the next step, the combination of dilation and erosion was exploited to separate merged (neighboring) domains. Given that unstained TEM images provide 3 distinct contrast levels (dark: silica, intermediate: PS, and bright: PMMA), each domain was mapped by binarization. The results at each step are shown in **Figure S11.14** – **Figure S11.20**.

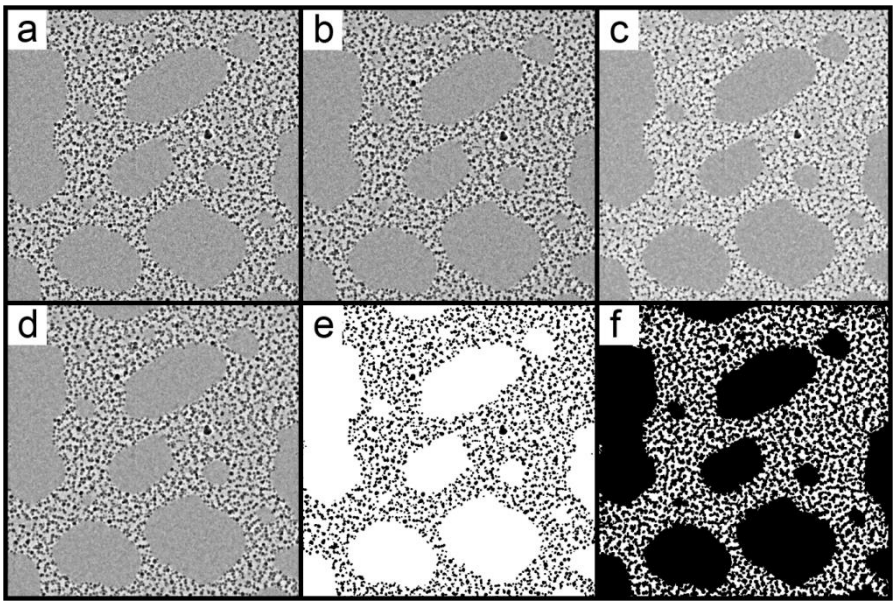

Figure S11.15. Image analysis of M-*b*-S-1 (a) shading-corrected, (b) blurred, (c) dilated, (d) eroded, (e) particle domain recognized, and (f) PS+particle domain recognized images.

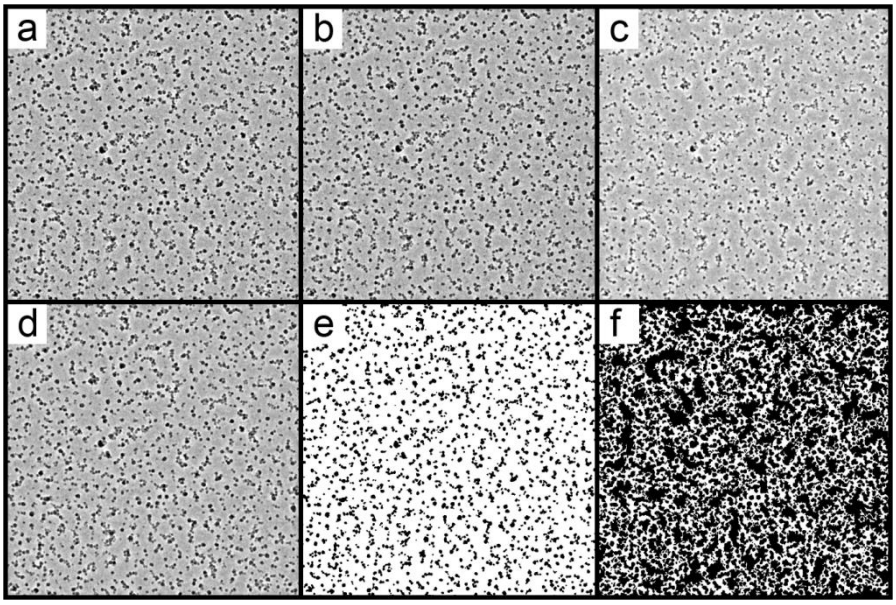

Figure S11.16. Image analysis of M-*b*-S-2 (a) shading-corrected, (b) blurred, (c) dilated, (d) eroded, (e) particle domain recognized, and (f) PS+particle domain recognized images.

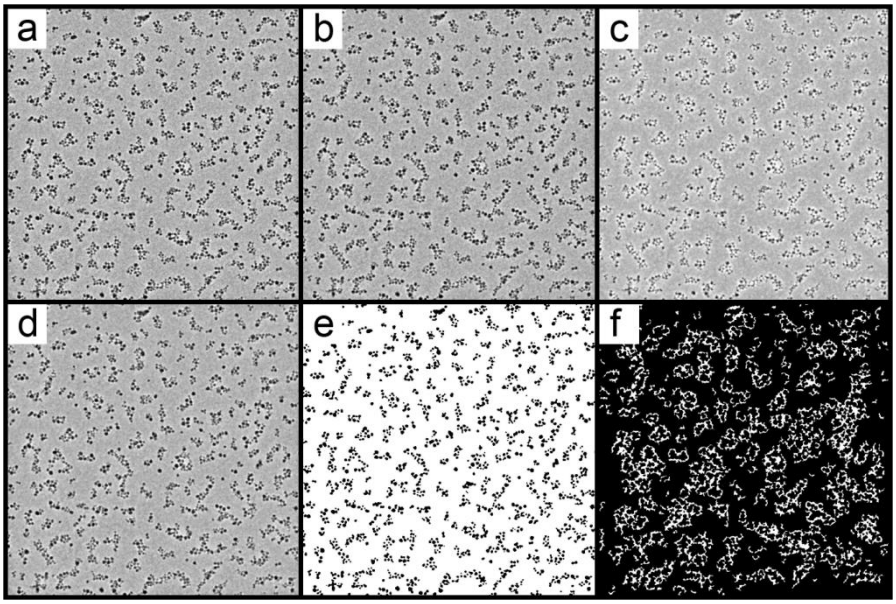

Figure S11.17. Image analysis of M-*b*-S-3 (a) shading-corrected, (b) blurred, (c) dilated, (d) eroded, (e) particle domain recognized, and (f) PS+particle domain recognized images.

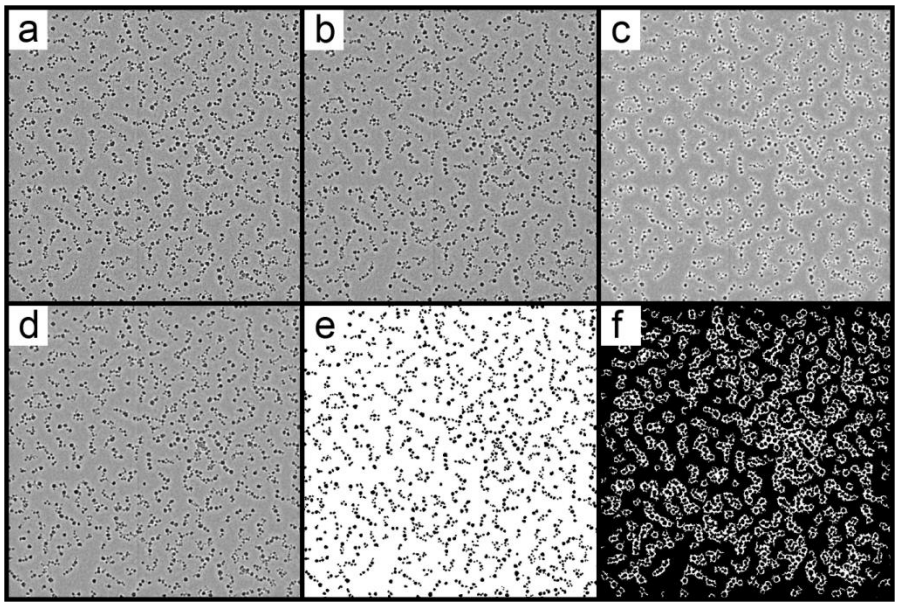

Figure S11.18. Image analysis of M-*b*-S-4 (a) shading-corrected, (b) blurred, (c) dilated, (d) eroded, (e) particle domain recognized, and (f) PS+particle domain recognized images.

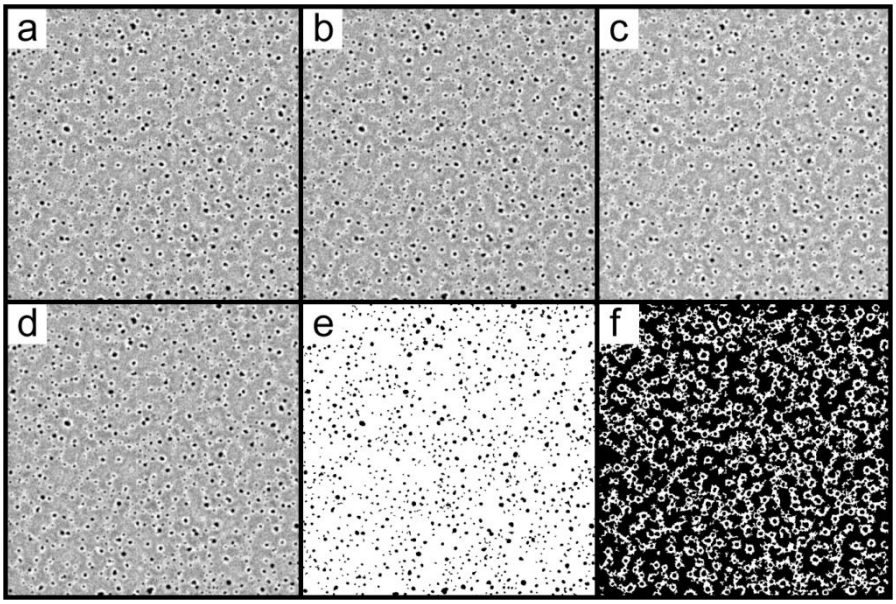

Figure S11.19. Image analysis of M-*b*-S-5 (a) shading-corrected, (b) blurred, (c) dilated, (d) eroded, (e) particle domain recognized, and (f) PS+particle domain recognized images.

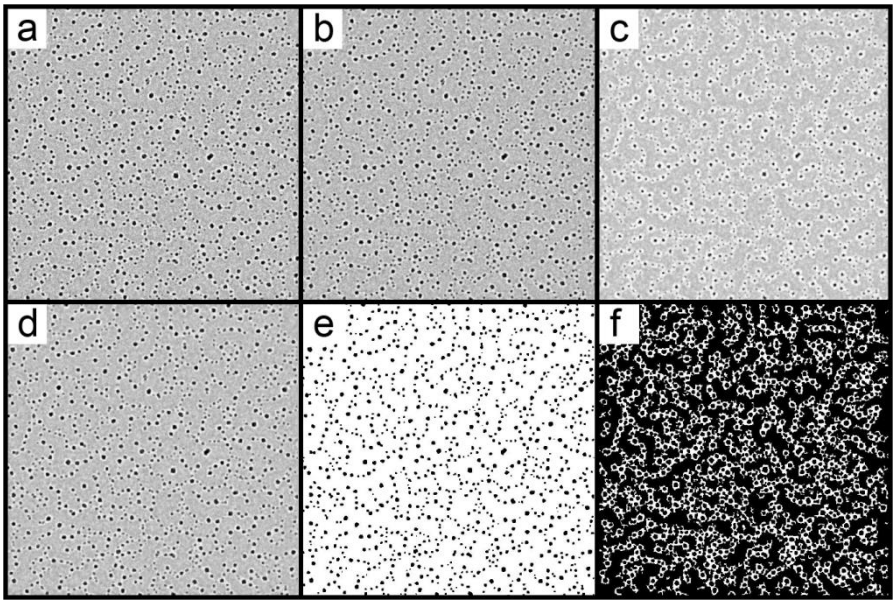

Figure S11.20. Image analysis of M-*b*-S-6 (a) shading-corrected, (b) blurred, (c) dilated, (d) eroded, (e) particle domain recognized, and (f) PS+particle domain recognized images.

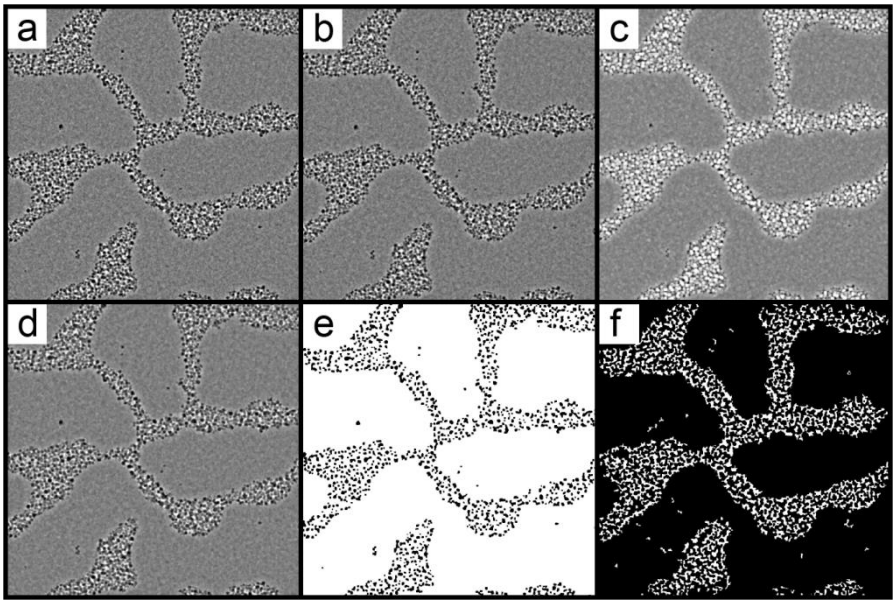

Figure S11.21. Image analysis of M-*b*-S-7 (a) shading-corrected, (b) blurred, (c) dilated, (d) eroded, (e) particle domain recognized, and (f) PS+particle domain recognized images.

Table S11.3. Deconvolution results of SiO_2-*g*-PMMA/PMMA-*b*-PS SEC traces

Entry	PMMA		PMMA-b-PS		f_{PMMA}[b] (%)	σ_1 (nm^{-2})[a]	$f_{PMMA-b-PS}$[b] (%)	σ_2 (nm^{-2})[a]
	M_n	M_w/M_n	M_n	M_w/M_n				
M-b-S-1	142,000	1.41	1,150,000	1.85	93.1	0.043	6.9	0.003
M-b-S-2	145,000	1.22	773,000	1.75	88.6	0.039	11.4	0.005
M-b-S-3	36,200	1.34	503,000	1.81	45.2	0.019	54.8	0.023
M-b-S-4	24,100	1.35	121,000	2.04	19.7	0.008	80.3	0.035
M-b-S-5	46,000	1.32	141,000	1.75	68.5	0.417	31.5	0.192
M-b-S-6	50,200	1.35	168,000	1.85	54.9	0.086	45.1	0.070
M-b-S-7	47,900	1.28	395,000	2.02	70.6	0.027	29.4	0.011

[a] Calculated according to TGA data, $\sigma=\sigma_1+\sigma_2$, [b] mol% fraction.

Table S11.4. Composition analysis of SiO_2-*g*-PMMA/PMMA-*b*-PS particle brushes

Entry	F_{PMMA} (vol%)[a]	F_{PS} (vol%)[a]	F_{SiO2} (vol%)[a]	S_{PMMA} (vol%)[b]	S_{PS} (vol%)[b]	S_{SiO2} (vol%)[b]
M-b-S-1	50.9	38.1	11	29.1	53.8	17.1
M-b-S-2	48.2	40.9	10.9	38.9	46.0	15.1
M-b-S-3	7.3	80.2	12.5	14.3	74.5	11.2
M-b-S-4	12.9	77.1	10	18.7	70.9	10.4
M-b-S-5	46.8	50.8	2.4	29.6	63.6	6.8
M-b-S-6	32.9	59.7	7.2	25.6	65.6	8.8
M-b-S-7	16.8	66.5	16.7	13.4	77.8	8.8

[a] Determined by SEC traces, and calculated by Eq S3-S8, F_{PMMA} is the volume fraction of PMMA, F_{PS} is the volume fraction of PS, F_{SiO2} is the volume fraction of SiO_2 nanoparticles. [b] Determined by image analysis from TEM images using a Matlab script, S_{PMMA} is the area fraction of the PMMA domain, S_{PS} is the area fraction of the PS domain, S_{SiO2} is the area fraction of SiO_2 domain.

$$F_{PMMA}^{**} = \frac{f_{PMMA}\times M_{w,PMMA}}{f_{PMMA}\times M_{w,PMMA}+f_{PMMA-b-PS}\times M_{w,PMMA-b-PS}} + \frac{M_{w,PMMA}}{M_{w,PMMA-b-PS}} \times \frac{f_{PMMA-b-PS}\times M_{w,PMMA-b-PS}}{f_{PMMA}\times M_{w,PMMA}+f_{PMMA-b-PS}\times M_{w,PMMA-b-PS}} \quad \text{(S3)}$$

$$F_{PMMA}^{*}(vol\%) = \frac{F_{PMMA}^{**}/1.18}{F_{PMMA}^{**}/1.18+\left(1-F_{PMMA}^{*}\right)/1.05} \times 100 \quad \text{(S4)}$$

$$F_{PS}^{*}(vol\%) = 100 - F_{PMMA}^{*} \quad \text{(S5)}$$

$$F_{SiO2}(vol\%) = f_{SiO2}/\rho_{SiO2} \quad \text{(S6)}$$

$$F_{PMMA}(vol\%) = F^{*}_{PMMA} \times (100 - F_{SiO2})/100 \qquad \text{(S7)}$$

$$F_{PS}(vol\%) = 100 - F_{SiO2} - F_{PMMA} \qquad \text{(S8)}$$

Eq. S3 calculated the weight fraction of PMMA (F_{PMMA}**) in the polymer ligands, which includes the PMMA ligands and the PMMA blocks in the PMMA-*b*-PS ligands.

Eq. S4 normalized the volume fraction of PMMA with the density of bulk PMMA (1.18 g/cm^3) and bulk PS (1.05 g/cm^3).

Eq. S7 normalized the volume fraction of PMMA after considering the volume fraction of SiO_2 nanoparticles.

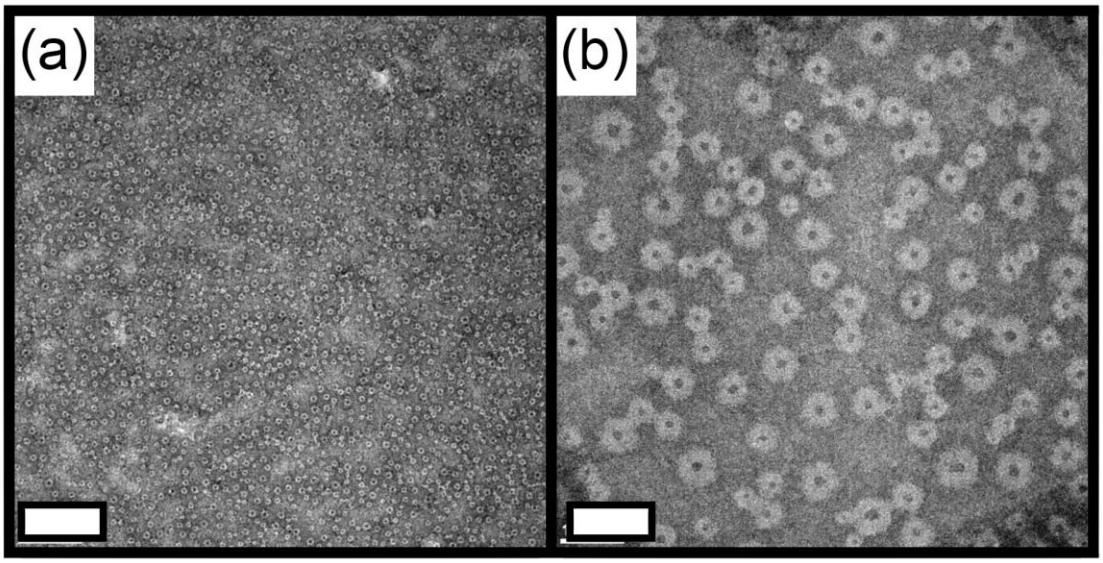

Figure S11.22. TEM images of M-*b*-S-5 particle brushes after staining by RuO_4. Scale bar: left: 500 nm, right: 100 nm.

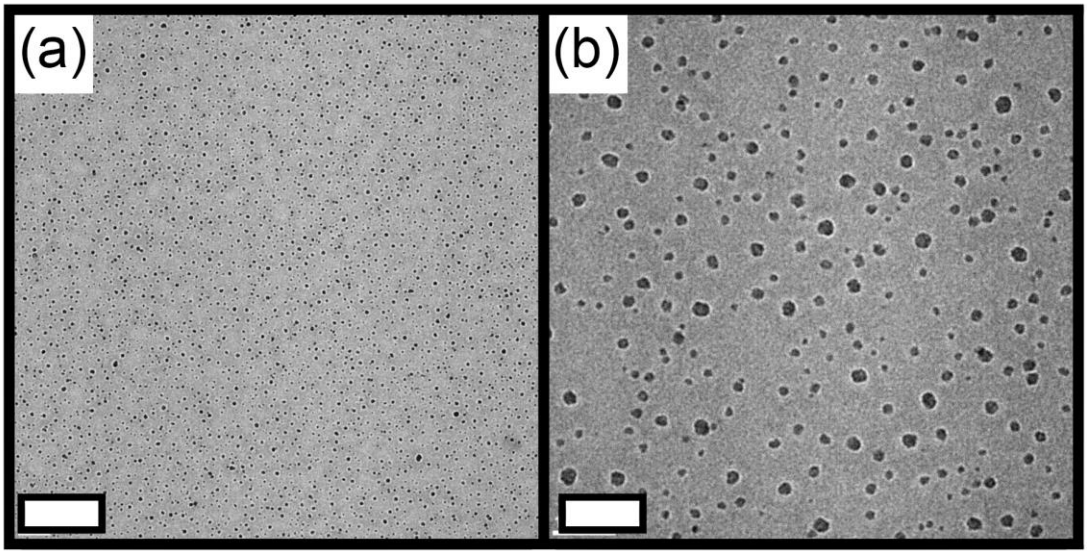

Figure S11.23. TEM images of M-*b*-S-6 particle brushes after staining by RuO_4. Scale bar: left: 500 nm, right: 100 nm.

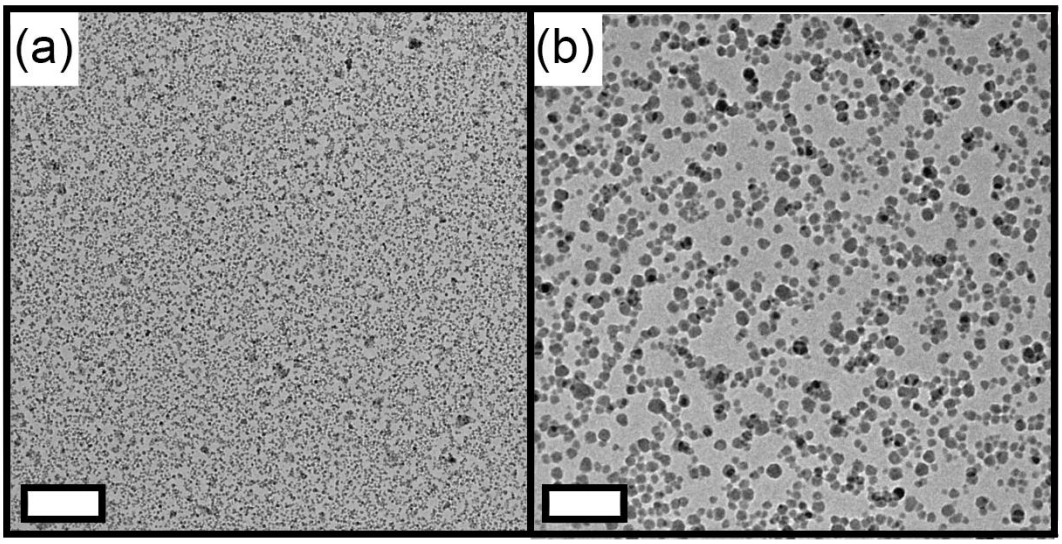

Figure S11.24. TEM images of a mixture of SiO_2-*g*-PMMA-*b*-PS and SiO_2-*g*-PMMA particle brushes. (a-b) M-*b*-S-4 with PMMA-L1, mass ratio=1:4. scale bar: (a) 500 nm, (b) 100 nm.

Estimation of the graft number distribution

Understanding the statistical characteristics of the grafts are especially critical in sparsely tethered cases because the proportion of (completely or nearly) bare particles is not negligible. Hakem *et al*. successfully derived a model to describe incomplete chemical modification using kinetic analysis.[4] The statistical expression is applied to estimate the distribution of the number of grafts per particle as follows.

$$v(g) = \binom{g_{max}}{g} e^{-g_{max}f}(e^f - 1)^g \qquad \text{(S9)}$$

where g is the number of grafted chains, ν is the fraction of particles grafted with g chains, g_{max} is the initial number of reactive sites on a particle (*i.e.*, the maximum number of grafts), and f is the ratio of reacted sites at the time to g_{max}. The maximum grafting density is assumed 1.00 nm^{-2}, thus g_{max} is approximately 700 since the surface area of a 15 nm (diameter) spherical particle is ~700 nm^2. The ratio of reacted sites to the total sites is 0.01 in the sparse system. Figure 3a blue curve shows the anticipated distribution of graft number in M-*b*-S-7. It is found that 30% of the particle surface is nearly bare (5 chains or less), which leads to structures displaying clusters or string-like structure formation.

(1) Matyjaszewski, K.; Miller, P. J.; Shukla, N.; Immaraporn, B.; Gelman, A.; Luokala, B. B.; Siclovan, T. M.; Kickelbick, G.; Vallant, T.; Hoffmann, H.; Pakula, T., Polymers at Interfaces: Using Atom Transfer Radical Polymerization in the Controlled Growth of Homopolymers and Block Copolymers from Silicon Surfaces in the Absence of Untethered Sacrificial Initiator. *Macromolecules* **1999,** *32* (26), 8716-8724.
(2) Pyun, J.; Jia, S.; Kowalewski, T.; Patterson, G. D.; Matyjaszewski, K., Synthesis, and Characterization of Organic/Inorganic Hybrid Nanoparticles: Kinetics of Surface-Initiated Atom Transfer Radical Polymerization and Morphology of Hybrid Nanoparticle Ultrathin Films. *Macromolecules* **2003,** *36* (14), 5094-5104.
(3) Tung, L. H.; Runyon, J. R., Calibration of instrumental spreading for GPC. *Journal of Applied Polymer Science* **1969,** *13* (11), 2397-2409
(4) Hakem, I. F.; Leech, A. M.; Johnson, J. D.; Donahue, S. J.; Walker, J. P.; Bockstaller, M. R., Understanding Ligand Distributions in Modified Particle and Particlelike Systems. *J. Am. Chem. Soc.* **2010,** *132* (46), 16593-16598.

11.6. Conclusions

Our results demonstrate that in the presence of a copper catalyst formed with highly activating ligands under a low ppm catalyst loading condition, SiO_2-*g*-PMMA/PMMA-*b*-PS particle brushes were successfully synthesized by SI-ATRP. By altering the grafting density and concentration of the hybrid initiator, SiO_2-*g*-PMMA-Br, predesigned bimodality chain compositions were achieved. Bimodal homo-/block copolymer particle brushes were obtained through simple chain extensions from PMMA grafted silica particle brushes that formed anisotropic string-like and continuous cluster network morphologies. The self-assembly of BCPs grafted from strategically designed nanocomposites provides a new route toward hierarchically ordered quasi-one component materials as a result of the morphology of the grafted homo-/block copolymer brushes. This provides new perspectives for engineering high-performance composite materials that require localized or specifically oriented particles, ultimately allowing for efficient capitalization of these materials' distinct properties.

11.7. References

(1) Maillard, D.; Kumar, S. K.; Fragneaud, B.; Kysar, J. W.; Rungta, A.; Benicewicz, B. C.; Deng, H.; Brinson, L. C.; Douglas, J. F., Mechanical Properties of Thin Glassy Polymer Films Filled with Spherical Polymer-Grafted Nanoparticles. *Nano Letters* **2012,** *12* (8), 3909-3914.

(2) Kumar, S. K.; Benicewicz, B. C.; Vaia, R. A.; Winey, K. I., 50th Anniversary Perspective: Are Polymer Nanocomposites Practical for Applications? *Macromolecules* **2017,** *50* (3), 714-731.
(3) Jancar, J.; Douglas, J. F.; Starr, F. W.; Kumar, S. K.; Cassagnau, P.; Lesser, A. J.; Sternstein, S. S.; Buehler, M. J., Current issues in research on structure-property relationships in polymer nanocomposites. *Polymer* **2010,** *51* (15), 3321-3343.
(4) Kumar, S. K.; Krishnamoorti, R., Nanocomposites: Structure, Phase Behavior, and Properties. *Annual Review of Chemical and Biomolecular Engineering* **2010,** *1* (1), 37-58.
(5) Zou, H.; Wu, S.; Shen, J., Polymer/Silica Nanocomposites: Preparation, Characterization, Properties, and Applications. *Chemical Reviews* **2008,** *108* (9), 3893-3957.
(6) Krishnamoorti, R.; Vaia, R. A., Polymer nanocomposites. *Journal of Polymer Science Part B: Polymer Physics* **2007,** *45* (24), 3252-3256.
(7) Bansal, A.; Yang, H.; Li, C.; Cho, K.; Benicewicz, B. C.; Kumar, S. K.; Schadler, L. S., Quantitative equivalence between polymer nanocomposites and thin polymer films. *Nature Materials* **2005,** *4*, 693.
(8) Mackay, M. E.; Tuteja, A.; Duxbury, P. M.; Hawker, C. J.; Van Horn, B.; Guan, Z.; Chen, G.; Krishnan, R. S., General Strategies for Nanoparticle Dispersion. *Science* **2006,** *311* (5768), 1740-1743.
(9) Fernandes, N. J.; Koerner, H.; Giannelis, E. P.; Vaia, R. A., Hairy nanoparticle assemblies as one-component functional polymer nanocomposites: opportunities and challenges. *MRS Communications* **2013,** *3* (1), 13-29.
(10) Guo, Y.; Harirchian-Saei, S.; Izumi, C. M. S.; Moffitt, M. G., Block Copolymer Mimetic Self-Assembly of Inorganic Nanoparticles. *ACS Nano* **2011,** *5* (4), 3309-3318.
(11) Huang, Y.; Zheng, Y.; Sarkar, A.; Xu, Y.; Stefik, M.; Benicewicz, B. C., Matrix-Free Polymer Nanocomposite Thermoplastic Elastomers. *Macromolecules* **2017,** *50* (12), 4742-4753.
(12) Bockstaller, M. R.; Lapetnikov, Y.; Margel, S.; Thomas, E. L., Size-Selective Organization of Enthalpic Compatibilized Nanocrystals in Ternary Block Copolymer/Particle Mixtures. *Journal of the American Chemical Society* **2003,** *125* (18), 5276-5277.
(13) Lin, Y.; Böker, A.; He, J.; Sill, K.; Xiang, H.; Abetz, C.; Li, X.; Wang, J.; Emrick, T.; Long, S.; Wang, Q.; Balazs, A.; Russell, T. P., Self-directed self-assembly of nanoparticle/copolymer mixtures. *Nature* **2005,** *434*, 55.
(14) Liang, R.; Xu, J.; Li, W.; Liao, Y.; Wang, K.; You, J.; Zhu, J.; Jiang, W., Precise Localization of Inorganic Nanoparticles in Block Copolymer Micellar Aggregates: From Center to Interface. *Macromolecules* **2015,** *48* (1), 256-263.
(15) Sarkar, B.; Alexandridis, P., Block copolymer–nanoparticle composites: Structure, functional properties, and processing. *Progress in Polymer Science* **2015,** *40*, 33-62.
(16) Balazs, A. C., Economy at the nanoscale. *Nature Materials* **2007,** *6*, 94.
(17) Tang, S.; Horton, J. M.; Zhao, B.; Zhu, L., Self-organization of homopolymer brush- and mixed homopolymer brush-grafted silica nanoparticles in block copolymers and polymer blends. *Polymer* **2016,** *90*, 9-17.
(18) Zhang; Horsch, M. A.; Lamm, M. H.; Glotzer, S. C., Tethered Nano Building Blocks: Toward a Conceptual Framework for Nanoparticle Self-Assembly. *Nano Letters* **2003,** *3* (10), 1341-1346.
(19) Vaia, R. A.; Maguire, J. F., Polymer Nanocomposites with Prescribed Morphology: Going beyond Nanoparticle-Filled Polymers. *Chemistry of Materials* **2007,** *19* (11), 2736-2751.
(20) Bockstaller, M. R.; Mickiewicz, R. A.; Thomas, E. L., Block Copolymer Nanocomposites: Perspectives for Tailored Functional Materials. *Advanced Materials* **2005,** *17* (11), 1331-1349.
(21) Bombalski, L.; Dong, H.; Listak, J.; Matyjaszewsk, K.; Bockstaller, M. R., Null-Scattering Hybrid Particles Using Controlled Radical Polymerization. *Adv. Mater.* **2007,** *19* (24), 4486-4490.

(22) Tchoul, M. N.; Dalton, M.; Tan, L.-S.; Dong, H.; Hui, C. M.; Matyjaszewski, K.; Vaia, R. A., Enhancing the fraction of grafted polystyrene on silica hybrid nanoparticles. *Polymer* **2012,** *53* (1), 79-86.
(23) Cersonsky, R. K.; van Anders, G.; Dodd, P. M.; Glotzer, S. C., Relevance of packing to colloidal self-assembly. *Proc. Nat. Acad. Sci.* **2018,** *115* (7), 1439-1444.
(24) Zhang, T.; Fu, C.; Yang, Y.; Qiu, F., Phase Behaviors and Bridging Properties of Bolaform Tethered Nanoparticles. *Macromolecules* **2018,** *51* (5), 1654-1665.
(25) Thompson, R. B.; Ginzburg, V. V.; Matsen, M. W.; Balazs, A. C., Block Copolymer-Directed Assembly of Nanoparticles: Forming Mesoscopically Ordered Hybrid Materials. *Macromolecules* **2002,** *35* (3), 1060-1071.
(26) Yue, K.; Huang, M.; Marson, R. L.; He, J.; Huang, J.; Zhou, Z.; Wang, J.; Liu, C.; Yan, X.; Wu, K.; Guo, Z.; Liu, H.; Zhang, W.; Ni, P.; Wesdemiotis, C.; Zhang, W.-B.; Glotzer, S. C.; Cheng, S. Z. D., Geometry induced sequence of nanoscale Frank–Kasper and quasicrystal mesophases in giant surfactants. *Proc. Nat. Acad. Sci.* **2016,** *113* (50), 14195-14200.
(27) Santos, P. J.; Cheung, T. C.; Macfarlane, R. J., Assembling Ordered Crystals with Disperse Building Blocks. *Nano Lett.* **2019,** *19* (8), 5774-5780.
(28) Lee, J. Y.; Balazs, A. C.; Thompson, R. B.; Hill, R. M., Self-Assembly of Amphiphilic Nanoparticle−Coil "Tadpole" Macromolecules. *Macromolecules* **2004,** *37* (10), 3536-3539.
(29) Wang, Y.; Cui, J.; Han, Y.; Jiang, W., Effect of Chain Architecture on Phase Behavior of Giant Surfactant Constructed from Nanoparticle Monotethered by Single Diblock Copolymer Chain. *Langmuir* **2019,** *35* (2), 468-477.
(30) Marson, R. L.; Phillips, C. L.; Anderson, J. A.; Glotzer, S. C., Phase Behavior and Complex Crystal Structures of Self-Assembled Tethered Nanoparticle Telechelics. *Nano Lett.* **2014,** *14* (4), 2071-2078.
(31) Ma, S.; Hu, Y.; Wang, R., Amphiphilic Block Copolymer Aided Design of Hybrid Assemblies of Nanoparticles: Nanowire, Nano ring, and Nanocluster. *Macromolecules* **2016,** *49* (9), 3535-3541.
(32) Li, Q.; Wang, Z.; Yin, Y.; Jiang, R.; Li, B., Self-Assembly of Giant Amphiphiles Based on Polymer-Tethered Nanoparticle in Selective Solvents. *Macromolecules* **2018,** *51* (8), 3050-3058.
(33) Ma, S.; Qi, D.; Xiao, M.; Wang, R., Controlling the localization of nanoparticles in assemblies of amphiphilic diblock copolymers. *Soft Matter* **2014,** *10* (45), 9090-9097.
(34) Phillips, C. L.; Glotzer, S. C., Effect of nanoparticle polydispersity on the self-assembly of polymer tethered nanospheres. *The Journal of Chemical Physics* **2012,** *137* (10), 104901.
(35) Matyjaszewski, K.; Xia, J., Atom Transfer Radical Polymerization. *Chemical Reviews* **2001,** *101* (9), 2921-2990.
(36) Matyjaszewski, K., Atom Transfer Radical Polymerization (ATRP): Current Status and Future Perspectives. *Macromolecules* **2012,** *45* (10), 4015-4039.
(37) Zheng, Y.; Huang, Y.; Abbas, Z. M.; Benicewicz, B. C., One-pot synthesis of inorganic nanoparticle vesicles via surface-initiated polymerization-induced self-assembly. *Polym. Chem.* **2017,** *8* (2), 370-374.
(38) Pyun, J.; Kowalewski, T.; Matyjaszewski, K., Synthesis of Polymer Brushes Using Atom Transfer Radical Polymerization. *Macromolecular Rapid Communications* **2003,** *24* (18), 1043-1059.
(39) Pietrasik, J.; Hui, C. M.; Chaladaj, W.; Dong, H.; Choi, J.; Jurczak, J.; Bockstaller, M. R.; Matyjaszewski, K., Silica-Polymethacrylate Hybrid Particles Synthesized Using High-Pressure Atom Transfer Radical Polymerization. *Macromolecular Rapid Communications* **2011,** *32* (3), 295-301.
(40) Zhao, D.; Di Nicola, M.; Khani, M. M.; Jestin, J.; Benicewicz, B. C.; Kumar, S. K., Self-Assembly of Monodisperse versus Bidisperse Polymer-Grafted Nanoparticles. *ACS Macro Lett.* **2016,** *5* (7), 790-795.

(41) Bozorgui, B.; Meng, D.; Kumar, S. K.; Chakravarty, C.; Cacciuto, A., Fluctuation-Driven Anisotropic Assembly in Nanoscale Systems. *Nano Letters* **2013,** *13* (6), 2732-2737.
(42) Kravchenko, V. S.; Potemkin, I. I., Self-assembly of rarely polymer-grafted nanoparticles in dilute solutions and on a surface: From non-spherical vesicles to graphene-like sheets. *Polymer* **2018,** *142*, 23-32.
(43) Hui, C. M.; Pietrasik, J.; Schmitt, M.; Mahoney, C.; Choi, J.; Bockstaller, M. R.; Matyjaszewski, K., Surface-Initiated Polymerization as an Enabling Tool for Multifunctional (Nano-)Engineered Hybrid Materials. *Chemistry of Materials* **2014,** *26* (1), 745-762.
(44) Matyjaszewski, K.; Miller, P. J.; Shukla, N.; Immaraporn, B.; Gelman, A.; Luokala, B. B.; Siclovan, T. M.; Kickelbick, G.; Vallant, T.; Hoffmann, H.; Pakula, T., Polymers at Interfaces: Using Atom Transfer Radical Polymerization in the Controlled Growth of Homopolymers and Block Copolymers from Silicon Surfaces in the Absence of Untethered Sacrificial Initiator. *Macromolecules* **1999,** *32* (26), 8716-8724.
(45) Tsujii, Y.; Ohno, K.; Yamamoto, S.; Goto, A.; Fukuda, T., Structure, and Properties of High-Density Polymer Brushes Prepared by Surface-Initiated Living Radical Polymerization. In *Surface-Initiated Polymerization I*, Jordan, R., Ed. Springer Berlin Heidelberg: Berlin, Heidelberg, **2006**, pp 1-45.
(46) Ohno, K.; Morinaga, T.; Koh, K.; Tsujii, Y.; Fukuda, T., Synthesis of Monodisperse Silica Particles Coated with Well-Defined, High-Density Polymer Brushes by Surface-Initiated Atom Transfer Radical Polymerization. *Macromolecules* **2005,** *38* (6), 2137-2142.
(47) Sundrani, D.; Darling, S. B.; Sibener, S. J., Guiding Polymers to Perfection: Macroscopic Alignment of Nanoscale Domains. *Nano Lett.* **2004,** *4* (2), 273-276.
(48) Choi, J.; Gunkel, I.; Li, Y.; Sun, Z.; Liu, F.; Kim, H.; Carter, K. R.; Russell, T. P., Macroscopically ordered hexagonal arrays by directed self-assembly of block copolymers with minimal topographic patterns. *Nanoscale* **2017,** *9* (39), 14888-14896.
(49) Berry, B. C.; Bosse, A. W.; Douglas, J. F.; Jones, R. L.; Karim, A., Orientational Order in Block Copolymer Films Zone Annealed below the Order−Disorder Transition Temperature. *Nano Lett.* **2007,** *7* (9), 2789-2794.
(50) Hakem, I. F.; Leech, A. M.; Johnson, J. D.; Donahue, S. J.; Walker, J. P.; Bockstaller, M. R., Understanding Ligand Distributions in Modified Particle and Particlelike Systems. *J. Am. Chem. Soc.* **2010,** *132* (46), 16593-16598.

Chapter 12 Synthesis of Gradient Copolymer Grafted Particle Brushes by ATRP

12.1. Preface

Linear poly(*n*-butyl acrylate)-*gradient*-poly(methyl methacrylate) (PBA-*grad*-PMMA) copolymers and SiO_2-*g*-PBA-*grad*-PMMA particle brushes were synthesized by activator regenerated by electron transfer (ARGET) atom transfer radical polymerization (ATRP) *via* a semi-batch copolymerization method, in which methyl methacrylate (MMA) monomer was slowly fed to the

polymerizing *n*-butyl acrylate (BA) solutions. The effect of initial BA concentration and the MMA feeding rate on the polymerization were investigated. Controlled gradient compositions were achieved at relatively low conversion, <20%. Two gradient copolymer particle brushes, with grafting density: 0.55/0.126 nm^{-2}, and one linear gradient copolymer were prepared with the same composition. Significant changes were observed after attaching the gradient copolymer ligands onto the surface of SiO_2 nanoparticles, in both thermal and mechanical properties. Greater heterogeneity and microphase separation were introduced after the addition of SiO_2 nanoparticles and the nanocomposites displayed more complex glass transition temperatures (T_gs) behavior and a broader T_g range. Improvement in mechanical properties (strength and stiffness) was observed as the SiO_2 nanoparticle content increased in gradient copolymer particle brushes, however, the damping property was compromised with the increased stiffness of the materials, especially under low-frequency conditions.

In this chapter, the synthesis of gradient copolymer particle brushes is discussed. I designed the entire project and performed all synthetic work and part of the characterization in the project. I would like to thank especially my collaborators, Tong Liu for extensive discussion and the help with ^{1}H-NMR characterization.

This project will be published on *Macromolecules*.

This work was supported by NSF (DMR 1501324 and DMR 1410845), the Department of Energy (DE-EE0006702), as well as the Scott Institute for Energy Technologies at Carnegie Mellon University.

12.2. Introduction

Controlled radical polymerization (CRP, also known as reversible-deactivation radical polymerization, RDRP) processes such as atom transfer radical polymerization (ATRP) allow the synthesis of various copolymers with well-controlled molecular weights, narrow molecular weight

distribution, and defined architectures.[1-7] ATRP shows a high tolerance to a variety of functional groups for a broad spectrum of monomers.[8-11] An additional feature of RDRP is the ability to copolymerize monomer pairs, enabling the synthesis of random, block and gradient copolymers.[12-15] In particular, gradient copolymers form a class of copolymers in which the comonomer composition gradually varies along the chain length, which cannot be accomplished in a conventional radical system where the polymer chains are continuously initiated and terminated. They can be easily synthesized by ATRP.[16-19]

One of the main motivations for the investigation of gradient copolymers is the possibility that gradient copolymers could have considerably different physical properties from those of random or block copolymers with analogous compositions. Various composition distributions of specifically interacting comonomers along the copolymer chain should lead to a variety of possibilities and scales of the spatial organization of comonomers and, consequently, to unique properties.[12, 20] Because of their unusual molecular structures, gradient copolymers are efficient stabilizers for emulsions, cosmetic additives, immiscible blends compatibilizers, nanocomposite filler dispersants, and acoustic damping materials.[21-26]

Nanofillers are commonly blended in neat polymers to prepare nanocomposites with enhanced optical, thermal, electric and mechanical properties.[27-39] One approach to improve particle dispersion in a matrix polymer involves utilizing polymer grafted nanoparticles, which can exhibit enhanced compatibility with the surrounding polymer matrix.[40-44] Many of the property enhancements, associated with nanocomposites, have been explained as arising from that the interphase regions of the polymers located close to the interfaces of nanofillers which are perturbed by the nanofillers.[45-52] When polymer ligands are confined to nanoscale dimensions, such interfacial perturbations can originate from confinement effects.[53] Bulk polymer grafted nanoparticles have exhibited enhanced mechanical properties and interesting self-healing behavior.[37, 54, 55]

To the best of our knowledge, there is no published report on the synthesis and properties of particle brushes with grafted gradient copolymers. In this contribution, linear PBA-*grad*-PMMA and SiO_2-*g*-PBA-*grad*-PMMA particle brushes synthesized by ARGET ATRP were studied. To avoid gelation in the particle brush system during synthesis, reactions were conducted under relatively low conversion conditions, <20%. A well-controlled copolymer displaying a significant gradient was achieved by using a semi-batch copolymerization method, in which the MMA monomer was slowly fed into BA solutions undergoing an ATRP. The thermal properties and T_g values of the products were studied by DSC.

A major part of this investigation was to explore the effect of nanofillers' loading on the mechanical properties of the gradient copolymer nanocomposites. Therefore, a linear gradient copolymer and two-particle brushes with different grafting densities were prepared, in which the polymer ligands and linear copolymers have the same composition and the same gradient sequence. The mechanical strength, Young's modulus and damping properties of the materials were studied by DMA and nanoindentation.

Gradient copolymers can be prepared either by simultaneous copolymerization (batch copolymerization) or by feeding one monomer into the reaction mixture (semi-batch copolymerization).[12, 56] In the former case, the living copolymerization of monomers with different reactivity ratios lead to a continuous change in monomer concentrations in the reaction mixture, which results in a continuous compositional change along each polymer chain. In the latter case, comonomers with similar reactivity ratios can be used, but a change of composition in the polymer chains is accomplished by continuous addition of one comonomer into the active polymerization.[57]

12.3. Experimental Section

Materials.

Monomers: n-butyl acrylate (BA, 99%, Aldrich), methyl methacrylate (MMA, 99%, Aldrich) were purified by passing through a column filled with basic alumina to remove the inhibitor. Tris(2-dimethylaminoethyl)amine (Me_6TREN, 99%, Alfa), anisole (99%, Aldrich), tetrahydrofuran (THF, 99%, VWR), methanol (99%, VWR), hexane (99%, VWR), acetone (99%, VWR), N,N-dimethylformamide (DMF, 99%, VWR), copper(II) bromide ($CuBr_2$, 99%, Aldrich), ethyl α-bromoisobutyrate (EBiB, 98%, Sigma Aldrich), tin(II) 2-ethylhexanoate ($Sn(EH)_2$, 95%, Aldrich), 48% hydrofluoric acid aqueous solution (HF, >99.99%, Aldrich), ammonium hydroxide aqueous solution (NH_4OH, 28.0-30.0%, Fisher), anhydrous magnesium sulfate ($MgSO_4$, Fisher) were used as received without further purification. Silica nanoparticles, 30 wt % solution in methyl isobutyl ketone (MIBK-ST), effective diameter d ≈ 15.8 nm, were kindly donated by Nissan Chemical Corp. and used as received. The tethered ATRP initiator 1-(chlorodimethylsilyl)propyl-2-bromoisobutyrate and surface-modified silica (SiO_2-Br) were prepared using previously reported procedures.[1-2] The surface initiator densities were moderated with a "dummy" initiator chlorotrimethylsilane (99%, Aldrich).

Procedures. Procedures for the synthesis of linear PBA-grad-PMMA gradient copolymers via ARGET ATRP.

Linear PBA-grad-PMMA copolymer synthesis.

Initiator (EBiB), monomer (BA), solvents (anisole, DMF), $CuBr_2$, and Me_6TREN (molar ratio shown as a subscript of Table 1) were mixed thoroughly in a sealed Schlenk flask. The mixture was degassed by bubbling with nitrogen. A stock solution of $Sn(EH)_2$ in anisole was prepared. Both mixtures and 20 mL MMA monomers were degassed by nitrogen purging respectively, then the $Sn(EH)_2$ solution was injected into the Schlenk flask to activate the catalyst complex and the flask was immediately put into an oil bath. MMA monomer was injected into the reaction by a syringe pump at a certain feeding rate (shown as a subscript of Table 1). Samples of the polymerization mixture were

withdrawn at periodic intervals, and conversion was determined by ^{1}H NMR spectroscopy, while molecular weights were determined by SEC calibrated with PMMA standards. The final polymer obtained was soluble in THF, precipitated in methanol/water (v/v=3/1), and the resulting solid was isolated by vacuum filtration and dried for 48 h under vacuum.

Procedures for the synthesis of SiO_2-g-PBA-grad-PMMA particle brushes via ARGET ATRP.

SiO_2-g-PBA-grad-PMMA particle brushes synthesis.

Initiator (SiO_2-Br), monomer (BA), solvents (anisole, DMF), $CuBr_2$, and Me_6TREN (molar ratio shown as a subscript of Table 2) were mixed thoroughly in a sealed Schlenk flask. The mixture was degassed by bubbling with nitrogen. A stock solution of $Sn(EH)_2$ in anisole was prepared. Both mixtures and 20 mL MMA monomers were degassed by nitrogen purging respectively, then the $Sn(EH)_2$ solution was injected into the Schlenk flask to activate the catalyst complex and the flask was immediately put into an oil bath. Meanwhile, the MMA monomer was injected into the reaction by a syringe pump at a certain feeding rate (shown as a subscript of Table 2). The conversion and molecular weight (MW) of the polymer were monitored by ^{1}H-NMR and SEC, respectively. The final particle brushes obtained was soluble and stored in THF.

Procedures for bulk film fabrication.

The linear PBA-*grad*-PMMA gradient copolymers (L10) and SiO_2-*g*-PBA-*grad*-PMMA particle brushes (PB-HG/PB-LG) were dispersed in THF *via* sonication. After the solution was stirred for 24 h, the bulk dispersions were transferred into 15 mm × 5 mm rectangular Teflon molds. After the solvent was slowly evaporated over 48 h at room temperature, transparent nanocomposite films with a thickness of 0.06-0.1 mm were formed. The residual solvent was removed from the bulk films by transferring it to a vacuum oven and slowly increasing the temperature at the rate of 10 °C per 24 h to 120 °C. At least

five specific bulk films were investigated to systematically study the thermo-mechanical properties of the nanocomposite films.

Characterization.

Nuclear Magnetic Resonance Spectroscopy (NMR). Conversion of polymerization was monitored by ^{1}H NMR on a Bruker Advance 500 MHz NMR instrument in $CDCl_3$ at room temperature.

Size Exclusion Chromatography (SEC). Number-average molecular weights (M_n) and molecular weight distributions (MWD) of PBA-grad-PMMA samples were determined by size exclusion chromatography (SEC). The SEC was conducted with an Agilent 1260 Iso pump and Waters 410 differential refractometer using PSS columns (Styragel 10^5, 10^3, 10^2 Å) with THF as an eluent at 35 ºC and a flow rate of 1 ml min^{-1}. Linear PMMA standards were used for calibration. Diphenylethylene and toluene were used as internal standards for the system.

Transmission Electron Microscopy (TEM). TEM was carried out using a JEOL 2000 EX electron microscope operated at 200 kV. The spatial distribution, radius and inter-particle distances of the SiO_2 nanoparticles were determined from statistical analysis of the TEM micrographs using ImageJ software.

Dynamic Light Scattering (DLS). DLS using a Malvern Zetasizer Nano ZS was employed to determine volume-weighted average hydrodynamic radius and distribution. The particle brushes were suspended in filtered THF (450 nm PTFE filter) at low concentrations.

Thermogravimetric Analysis (TGA). TGA with TA Instruments 2950 was used to measure the fraction of SiO_2 in the hybrids. The data were analyzed with TA Universal Analysis. The heating procedure involved four steps: (1) jump to 120 ºC; (2) hold at 120 ºC for 10 min; (3) ramp up at a rate of 20 ºC/min to 800 ºC; (4) hold for 2 min. The TGA plots were normalized to the total weight after holding at 120 ºC.

The grafting density was calculated using the formula (S1).

$$\sigma_{\mathrm{TGA}} = \frac{(1-f_{\mathrm{SiO2}})N_{\mathrm{Av}}\,\rho_{\mathrm{SiO2}}\,d}{6\,f_{\mathrm{SiO2}}\,M_n} \qquad \text{(S1)}$$

where f_{SiO2} is the SiO_2 fraction measured by TGA, N_{Av} is the Avogadro number, ρ_{SiO2} is the density of SiO_2 nanoparticles (2.2 g/cm^3), d is the average diameter of SiO_2 nanoparticles (15.8 nm), M_n is the overall number-average MW of the cleaved polymer brushes.

Differential Scanning Calorimetry (DSC). The glass transition temperature (T_g) of linear PBA-*grad*-PMMA and SiO_2-*g*-PBA-*grad*-PMMA particle brushes were measured by differential scanning calorimetry (DSC) with TA Instrument QA-2000. The same procedure was run three times, each involving the following steps: (1) Equilibrate at 25.00 °C, (2) Isothermal for 1.00 min, (3) Ramp 20.00 °C/min to -70.00 °C, (4) Isothermal for 1.00 min, (5) Ramp 20.00 °C/min to 160.00 °C, (6) Isothermal for 1.00 min, (7) Ramp 20.00 °C/min to -70.00 °C, (8) Isothermal for 1.00 min, (9) Ramp 20.00 °C/min to 160.00 °C, (10) Isothermal for 1.00 min, (11) Ramp 20.00 °C/min to -70.00 °C, (12) Isothermal for 1.00 min, (13) Ramp 20.00 °C/min to 160.00 °C, (14) Isothermal for 1.00 min, (15) Jump to 25.00 °C. The DSC data were analyzed with a TA Universal Analysis instrument, and T_g was directly acquired.

Dynamic Mechanical Analysis (DMA).

Tensile test: the linear PBA-grad-PMMA gradient copolymers (L10) and SiO_2-*g*-PBA-*grad*-PMMA particle brushes (PB-HG/PB-LG) bulk films are tested in the tensile mode by using DMA (TA RSA-G2). The film thickness was between 60-100 μm. The samples were stretched at a constant tensile rate of 0.005 mm/s at room temperature.

Glass transition temperature measurement: The glass transition temperature was also measured through dynamic mechanical analysis (DMA, TA RSA-G2) at a constant frequency (1 Hz) in a temperature range of -50 ℃ to 150 ℃, with a heating rate of 3 ℃/min, and application of 0.1% strain.

Damping property measurement: The damping property was measured through dynamic mechanical analysis (DMA, TA RSA-G2) in a frequency range of 0.1-100 Hz at room temperature, with the application of 0.1% strain. All the samples were tested at least three times for consistency.

Nanoindentation. The mechanical properties (elastic modulus, hardness) of the bulk films were measured using MTS Nanoindenter XP with a nanoscopic diamond-based Berkovich tip under displacement control to no more than ∼10% of the nanocrystal film thickness. Experimental data for particle brush samples were obtained from at least 25 indentations per sample, and the standard deviation of the measurements was calculated as experimental error. The displacement rate during the indentation of the particle brush samples was 5 nm s^{-1} to a maximum load followed by constant load indentation for 10 s by depth control to a depth of 2 μm.

Determination of the cumulative and instantaneous compositions in gradient copolymers.

The cumulative and instantaneous compositions of MMA are calculated from equation (S2) and (S3), respectively.

$$\boldsymbol{F_{cum,MMA}} = \frac{(\%\boldsymbol{conv})_{\boldsymbol{MMA}} \times [\boldsymbol{M_{MMA}}]_0}{(\%\boldsymbol{conv})_{\boldsymbol{MMA}} \times [\boldsymbol{M_{MMA}}]_0 + (\%\boldsymbol{conv})_{\boldsymbol{BA}} \times [\boldsymbol{M_{BA}}]_0} \qquad \text{(S2)}$$

$$\boldsymbol{F_{inst,MMA}} = \boldsymbol{F_{cum,MMA}} + (\%\boldsymbol{conv}) \times \frac{\Delta \boldsymbol{F_{cum,MMA}}}{\Delta(\%\boldsymbol{conv})} \qquad \text{(S3)}$$

where $(\%conv)_{MMA}$ denotes the conversion of MMA monomer and $[M_{MMA}]_0$ denotes the initial concentration of MMA monomer.

12.4. Results and Discussion

The formation of gradient copolymers with a sufficiently strong spontaneous gradient requires high conversions of both comonomers. However, to prevent gelation in systems with hundreds of chains

growing from each nanoparticle, the conversion was limited to <20%.[58, 59] Therefore, linear PBA-*grad*-PMMA copolymer and SiO_2-*g*-PBA-*grad*-PMMA particle brushes were synthesized by the "semi-batch copolymerization" method. Due to the large difference in reactivity ratios between methyl methacrylate and *n*-butyl acrylate (r_1 = 2.07, r_2 = 0.35),[60] MMA monomer was slowly fed into the reaction mixture (Scheme 1).[61, 62] Compared to batch copolymerization which forms a spontaneous gradient in the copolymers employing different reactivity ratios between the comonomers, continuously addition of one comonomer to a copolymerization can add to form a more significant compositional gradient along the chain. In addition to temperature and catalysts, two main factors, initial BA concentration ($[BA]_0$) and the feeding rate of MMA monomers (v_{MMA}), significantly affected the compositional gradient of the formed copolymers. The effects caused by differences in reactivity ratios can be compensated through appropriate rates and order of addition of one monomer to the other.

Scheme 12.1. Synthesis of linear PBA-grad-PMMA and SiO_2-*g*-PBA-*grad*-PMMA particle brushes

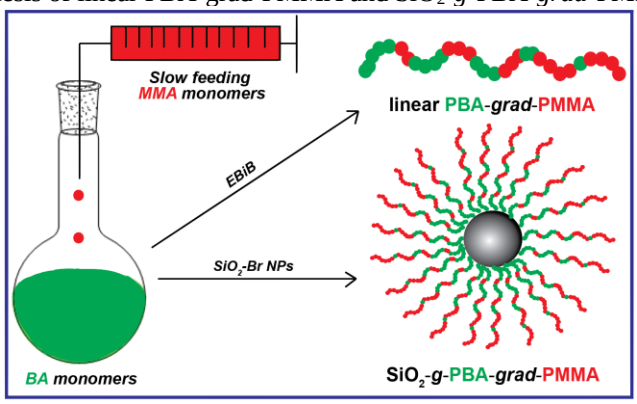

Linear gradient copolymers

Various $[BA]_0$ and v_{MMA} were studied in the synthesis of linear PBA-*grad*-PMMA copolymers, as shown in **Table 12.1**. The chain length, composition, and sequence of the gradient copolymers were monitored by SEC and NMR. The control of the compositional gradient through the use of controlled monomer addition was demonstrated for the ATRP of BA and MMA. The conversion of monomers was

maintained below 20%, comparable to the highest conversion attained before gelation in the synthesis of particle brushes.

Table 12.1. Syntheses of linear PMMA-*grad*-PBA copolymers

Entry[a]	Reaction conditions				M_n[d]	M_w/M_n[d]	T_g[e] (°C)
	$[BA]_0$ (M)[b]	Feeding rate (mL/h)	Comp, $_{BA}$ (mol%)[c]	Comp,$_{MMA}$ (mol%)[c]			
L-1	2.3	1	45.8	54.2	13,430	1.42	-5
L-2	3.5	1	59.8	40.2	23,360	1.21	-8
L-3	4.2	1	64.5	35.5	24,250	1.22	-22
L-4	2.3	2	33.2	66.8	13,490	1.49	5
L-5	3.5	2	45.8	54.2	23,370	1.42	-5
L-6	4.2	2	49.1	50.9	29,960	1.29	-9
L-7	2.3	3	21.6	78.4	17,400	1.51	18
L-8	3.5	3	35.5	64.5	19,950	1.59	10
L-9	4.2	3	44.8	55.2	25,530	1.45	-3

[a] Reaction conditions: $[BA]_0$:$[EBiB]_0$:$[CuBr_2]_0$:$[Me_6TREN]_0$:$[Sn(EH)_2]_0$=260/520/780:1:0.7:7:3.5, at 45 ºC with 10 mL anisole, V_0(BA) = 5/10/15 mL, total [BA]: [MMA]=260/520/780: 350/700/1050. [b] Monomer concentration. [c] Composition of PBA/PMMA in isolated copolymers, which was determined by ^{1}H nuclear magnetic resonance (^{1}H NMR) spectroscopy. [d] Determined by SEC. [e] Glass transition temperatures determined by DSC.

Figure 12.1 illustrates the effect of initial $[BA]_0$ on the polymerization of linear PBA-*grad*-PMMA by ARGET ATRP using $CuBr_2$/Me_6TREN as the catalyst at 45 ºC. Figure 1a shows the effect of different values of $[BA]_0$ on the rate of polymerization of the gradient copolymers. The addition of MMA into the reaction reduced the polymerization rate of BA and increased the rate of incorporation of MMA. A higher initial BA concentration leads to a faster polymerization of BA and slower incorporation of MMA. Figure 1b displays the plot of M_n vs. total conversion of the polymerization, in where the experimental data have excellent agreement with theoretical values, showing controlled polymerization features in ATRP The cumulative and instantaneous composition of copolymer prepared through the semi-batch copolymerization of BA and MMA, with the same MMA feeding rate but different BA initial monomer feed ratios, are illustrated in **Figure 12.1**c and **Figure 12.1**d, demonstrating that a significant compositional gradient was achieved using the technique of controlled monomer addition (**Table 12.1**).

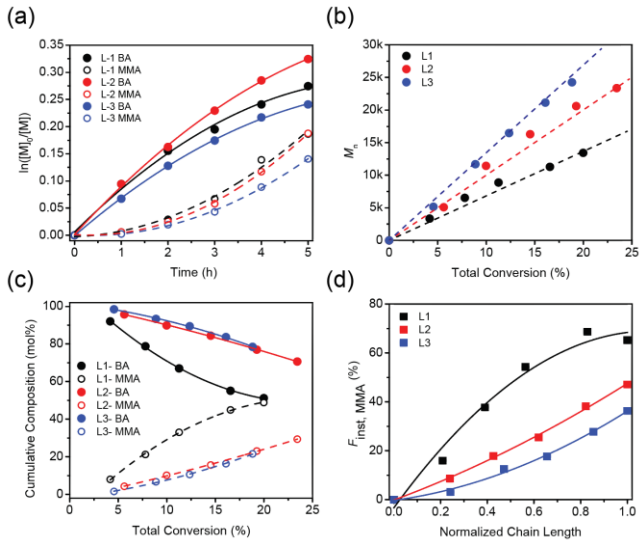

Figure 12.1. Results for effect of initial BA concentration on the polymerization of linear PBA-*grad*-PMMA by ARGET ATRP under reaction condition: $[BA]_0$:$[EBiB]_0$:$[CuBr_2]_0$:$[Me_6TREN]_0$: $[Sn(EH)_2]_0$=260/520/780:1:0.7:7:3.5, at 45 ºC with 10 mL anisole, V_0(BA) = 5/10/15 mL, MMA feeding rate=1 mL/h, total [BA]: [MMA]=260/520/780: 350. (a) Semilogarithmic kinetic plots for linear PBA-*grad*-PMMA system, (b) Number-average molecular weight (M_n) *vs.* conversion of linear PBA-*grad*-PMMA, dash lines in (b) show the theoretical M_n vs. conversion plots, (c) Cumulative composition *vs.* conversion for linear PBA-*grad*-PMMA system, (d) Instantaneous MMA composition *vs.* normalized chain length for linear PBA-*grad*-PMMA system.

The initial BA concentration and the MMA feeding rate (v_{MMA}) have a similar effect on the polymerization of linear PBA-*grad*-PMMA gradient copolymers. **Figure 12.2** shows that the shape and significance of the composition gradient can be manipulated by altering the rate of MMA monomer addition. Due to the higher reactivity ratio of MMA, under high feeding rate conditions, 3 mL/h, within the same reaction time, the MMA fraction in the copolymers dramatically increased, 80%, **Figure 12.2**c. The above results confirm that semi-batch copolymerization can allow the formation of gradient copolymers with MMA and BA comonomers. The shape and variation of the composition of the copolymers can be tuned by changing the $[BA]_0$ and v_{MMA}. Thus, significantly different gradient copolymers were prepared while maintaining monomer conversion below 20%. Analogous initial BA concentration and MMA feeding rate conditions were then used in the synthesis of gradient copolymer particle brushes systems.

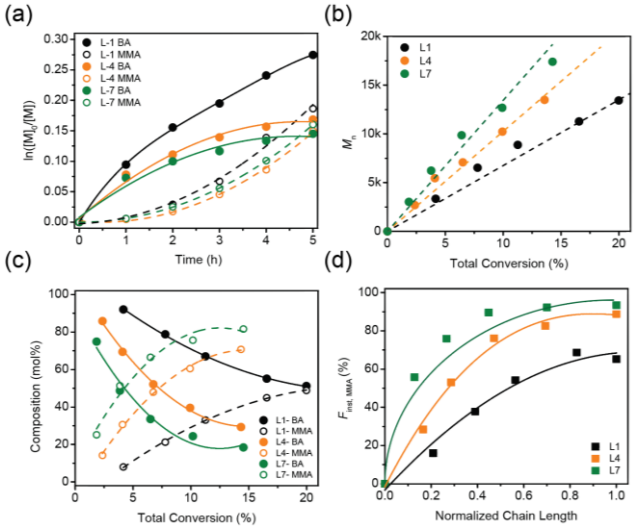
(a)
L-1 BA
L-1 MMA
L-4 BA
L-4 MMA
L-7 BA
L-7 MMA
ln([M]0/[M])
Time (h)
(b)
L1
L4
L7
Mn
Total Conversion (%)
(c)
L1- BA
L1- MMA
L4- BA
L4- MMA
L7- BA
L7- MMA
Composition (mol%)
Total Conversion (%)
(d)
L1
L4
L7
Finst, MMA (%)
Normalized Chain Length

Figure 12.2. Results for effect of MMA feeding rate on the polymerization of linear PBA-*grad*-PMMA by ARGET ATRP under reaction condition: $[BA]_0$:$[EBiB]_0$:$[CuBr_2]_0$:$[Me_6TREN]_0$: $[Sn(EH)_2]_0$=260:1:0.7:7:3.5, at 45 ºC with 10 mL anisole, V_0(BA) = 5 mL, MMA feeding rate=1/2/3 mL/h, total [BA]: [MMA]=260: 350/700/1050. (a) Semilogarithmic kinetic plots for linear PBA-*grad*-PMMA system, (b) Number-average molecular weight (M_n) *vs.* conversion of linear PBA-*grad*-PMMA, dash line in (b) show the theoretical M_n vs. conversion plots, (c) Cumulative composition *vs.* conversion for linear PBA-*grad*-PMMA system, (d) Instantaneous MMA composition *vs.* normalized chain length for linear PBA-*grad*-PMMA system.

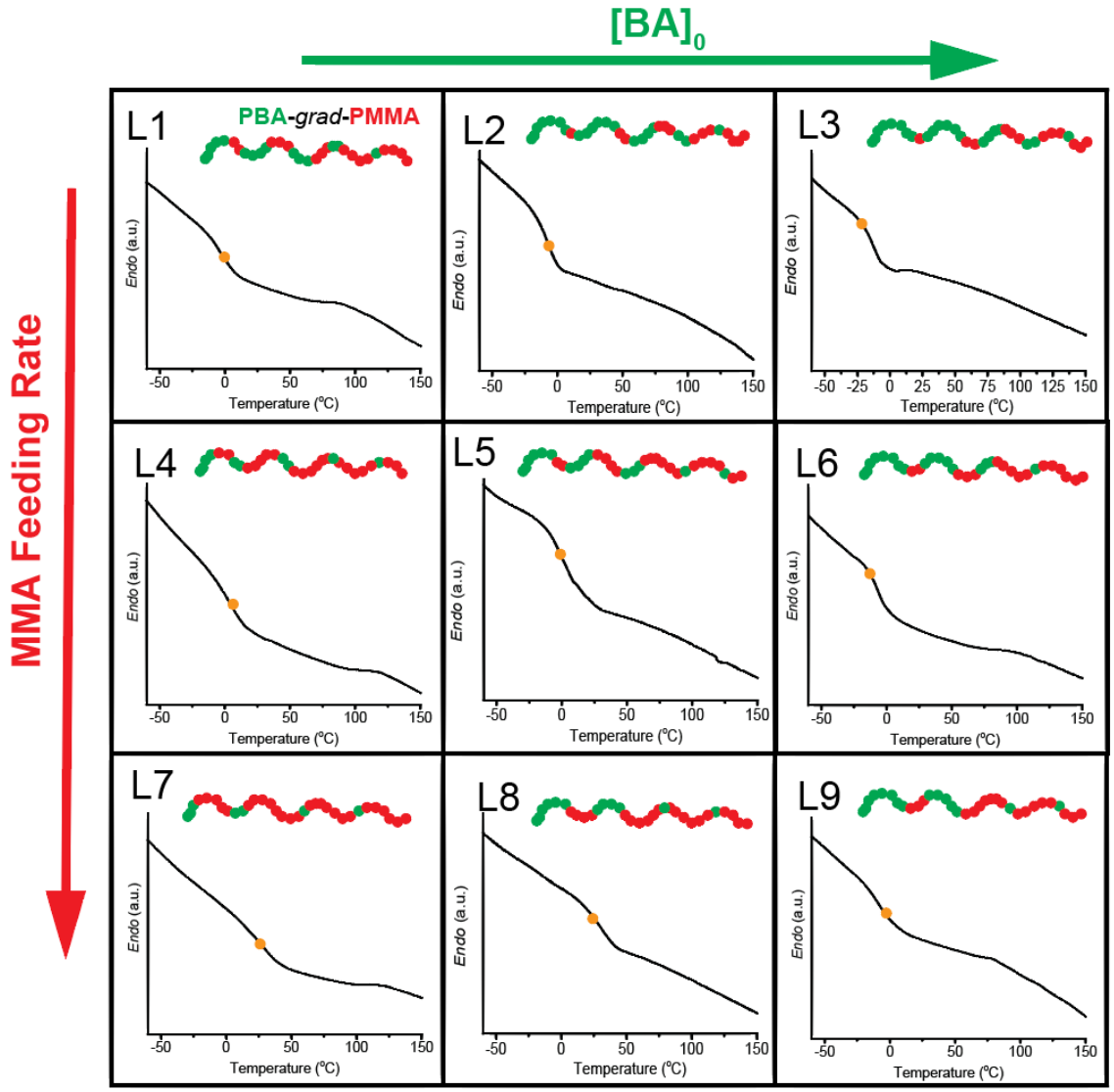

Figure 12.3. DSC curves for linear PBA-*grad*-PMMA gradient copolymers, orange dots highlighted the major T_g in each sample, which was determined from the plots of deriv. heat flow *vs.* temperature **(Figure S12.1-S12.9).**

One of the main benefits of gradient copolymers is their unique physical properties, which differ from those of random or block copolymers with similar overall compositions. The level of compositional heterogeneity of nano-phase separated gradient copolymers can be highly tuned and consequently act as an exquisite means for controlling the glass transition response.[12] DSC measurements, and application of the derivative analysis method can serve as a simple means for

qualitative evaluation of gradient copolymer nano-phase separation. The uniqueness of the thermal properties of linear-gradient copolymers is illustrated in the DSC thermograms shown in **Figure 12.3**. They show the schematic representations of the copolymer composition with the variation of $[BA]_0$ and v_{MMA}. To facilitate the comparison of the T_g among various polymer systems, the first derivatives of DSC heating curves concerning temperature were plotted in *Figures S12.1-S12.9*. Because these gradient copolymers were synthesized in semi-batch reactions, in which MMA comonomer was added at a constant rate to BA, L1-L9, the copolymers have one chain end that was a nearly very pure BA. However, the other chain end, while containing much more MMA units than BA units, does not contain pure MMA units.[23] This is because the BA concentration in the monomers mixture never reaches zero even at the latest stage of the reaction. Thus, samples L1-L9 exhibit T_gs below room temperature, in the range from -22 ºC to 18 ºC, which is influenced by the $[BA]_0$ and v_{MMA}, **Table 12.1**. It should be noted that, as the MMA feeding rate increased, a high PMMA fraction composition was obtained, **Figure 12.2**d. In this case, high values of T_g were observed in the DSC curves (**Figure S12.7-S12.9**). Moreover, according to DSC heating curves and their first derivatives plots, slower feeding could lead to a more subtle and complicated gradient in the gradient copolymers, which resulted in higher T_gs and the broader T_g ranges in the DSC curves.

Silica nanoparticles with gradient brush copolymers

Silica particle brushes with grafted gradient copolymers were synthesized by SI-ATRP from functionalized SiO_2-Br nanoparticles with different concentrations of initiating sites. Particle brushes with high and low grafting densities were prepared (PB-HG, PB-LG). For comparison, a linear gradient copolymer (L-10) was prepared using the same reaction conditions, **Table 12.2**.

Table 12.2. Result of syntheses of SiO_2-*g*-PMMA-*grad*-PBA particle brushes

Entry[a]	Comp, BA (mol%)[b]	Comp,MMA (mol%)[b]	M_n[c]	M_w/M_n[c]	f_{ino} (%)[d]	σ (nm^{-2})[e]	T_g[f] (ºC)

L-10	38	62	23,070	1.27	-	-	5, 25
PB-HG	36	64	29,500	1.25	16.93	0.551	-45, 5, 35, 105
PB-LG	33	67	31,850	1.51	44.71	0.128	-50, 3, 35, 110

[a] Reaction conditions: $[BA]_0$:$[EBiB/SiO_2\text{-}Br]_0$:$[CuBr_2]_0$:$[Me_6TREN]_0$:$[Sn(EH)_2]_0$=680:1:1.8:18:9, at 50 ºC with 20 mL anisole, $V_0(BA)$ = 5 mL, MMA feeding rate: 1 mL/h, reaction time: 5 h. [b] Composition of PBA/PMMA in isolated particle brushes, which was determined by ^{1}H nuclear magnetic resonance (^{1}H NMR) spectroscopy. [c] Determined by SEC. [d] Fraction of inorganic content determined by TGA. [e] Calculated from Eq. S1 according to TGA. [f] Glass transition temperatures determined by DSC.

A relatively slow MMA feeding rate (1 mL/h) was applied to generate a steeper gradient. Since the same initiator and catalyst concentrations were applied to all reactions, similar gradients and compositions were obtained from the three systems, which was confirmed by the kinetic studies, **Figure 12.4**. The overlaps of the three curves in the cumulative and instantaneous composition plots, **Figure 12.4**c and **Figure 12.4**d, indicate a similar sequence and compositions for the linear copolymers and the copolymers grafted from the surface of nanoparticles. Additionally, it is noted that under the same conditions, linear copolymer synthesis resulted in a lower molecular weight, M_n=23,000 *vs.* 29,000, which could be attributed to the higher solution viscosity in the particle brush system and diminished radical termination.

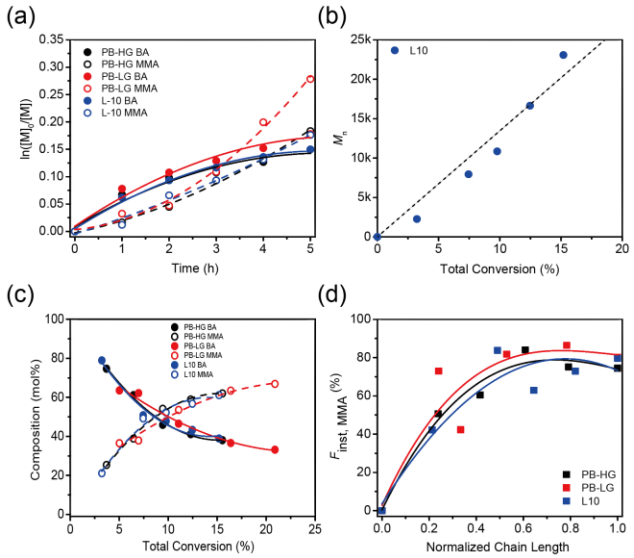

Figure 12.4. Results of polymerization of linear PBA-*grad*-PMMA and SiO_2-*g*-PBA-*grad*-PMMA particle brushes by ARGET ATRP under the same reaction condition: $[BA]_0$:$[EBiB]_0$:$[CuBr_2]_0$:$[Me_6TREN]_0$:$[Sn(EH)_2]_0$=680:1:1.8:18:9, at 50 ºC with 20 mL anisole, V_0(BA) = 5 mL, MMA feeding rate: 1 mL/h, reaction time: 5 h. (a) Semilogarithmic kinetic plots, (b) Plot of number-average molecular weight (M_n) *vs.* conversion, dash line in (b) show the theoretical M_n vs. conversion plots, (c) Cumulative composition *vs.* conversion, (d) Instantaneous MMA composition *vs.* normalized chain length.

The gradient copolymer particle brushes were first studied by TEM and DLS. The densely grafted particle brush (PB-HG) has a grafting density, ~0.55 chain/nm^2 and the intermediately grafted particle brush (PB-LG) has a lower grafting density, ~0.13 chain/nm^2. The nanocomposite with lower grafting density provides a higher inorganic content, **Figure 12.5**c. The low grafting density particle brushes, with the same chain length of polymer ligands, exhibit a shorter interparticle distance from TEM images (**Figure 12.5**a and **Figure 12.5**b) and a smaller hydrodynamic size in THF solution by DLS (**Figure 12.5**d).

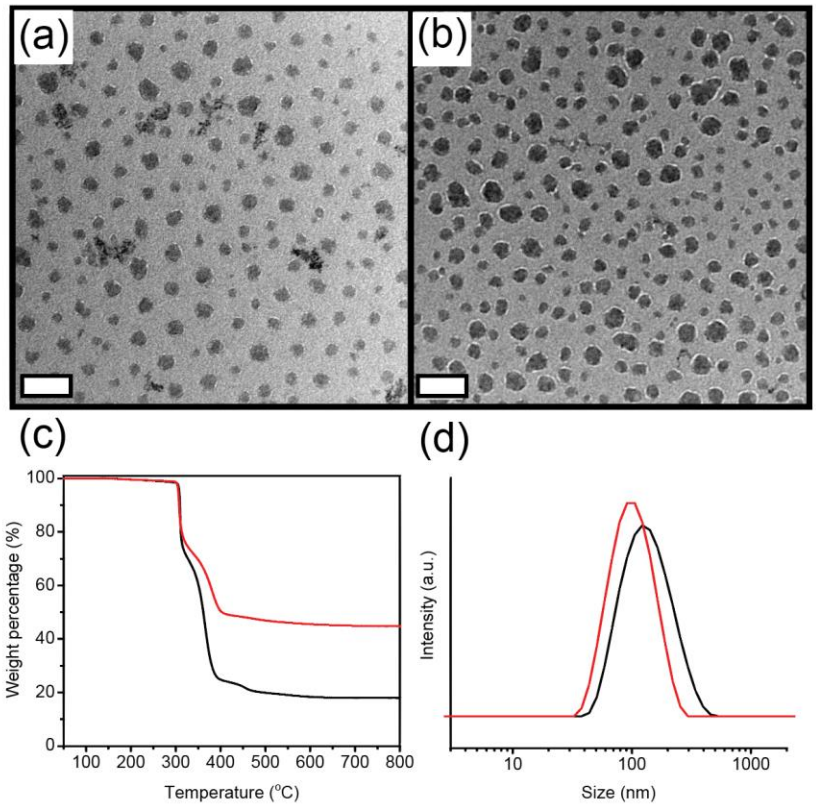

Figure 12.5. SiO_2-*g*-PBA-*grad*-PMMA particle brushes. (a-b) TEM images of gradient copolymer grafted particle brushes: (a) PB-HG, (b) PB-LG, Scale bar: 50 nm; (c) TGA curves (d) DLS curves of gradient copolymer grafted particle brushes: black line: PB-HG, red line: PB-LG.

The thermal and mechanical properties of the linear gradient copolymer and gradient copolymer particle brushes were studied by DSC and DMA. The stress and solvent residuals were removed by a 24 hours thermal annealing process. **Figure 12.6**a shows the DSC curves of these three systems and a more distinct glass transition which is corresponded to a larger T_g breadth can be observed in the linear copolymer system. More detailed and accurate T_g values were determined from the first derivative of DSC heating curves, **Figures S12.10-12.12**, which are listed in **Table 12.2**. Since the linear gradient copolymer and the polymer ligands on the surface of silica nanoparticle have similar composition and chain length, similar T_g values and thermal behaviors are expected. However, although two T_g values, 3-5 ºC, and 25-35 ºC, were present in all three samples, two additional T_gs (-45/-50 ºC and 105/110 ºC) were detected in particle brushes systems, which correspond to the T_g of bulk PBA and PMMA, respectively. One possible explanation for this could be the result of microphase separation in the particle brushes induced by the attachments of all PBA-rich chain ends to the surfaces of SiO_2 nanoparticles. As shown in the most significant peaks in Figure **S12.10-12.12**, particle brushes display a higher T_g compared to linear copolymer, which comes from the effect that the covalent bonds between SiO_2 nanoparticles and polymer ligands restrict the molecular motion and lead to an increase in T_g.[63] Moreover, it should be noted that the breadth of the T_g region in the particle brush system, ~50 ºC, measured from **Figure S12.11-12.12**, is significantly larger than in the linear gradient copolymer system, ~25 ºC, shown in Figure S10. The broadening of the glass transition region is attributed to the increased heterogeneity, which is introduced by the added SiO_2 nanofillers (**Scheme S12.1**). In addition to direct T_g measurements from DSC, the thermal properties of the three samples were confirmed by DMA, which are shown in **Figure 12.6**b. **Figure S12.13** shows the dependency of storage modulus obtained from oscillatory tension deformation. The storage modulus provides information regarding how much energy can be stored in material, its stiffness and its elastic nature. **Figure S12.13** shows the same glass transition behaviors of three samples as shown in DSC measurement. Due to the softening of specimens

under high temperatures, the measurements were limited to the range between -50 ºC to 80 ºC, where two similar T_g values (5-10 ºC and 45-55 ºC) as in DSC measurements were observed (**Figure 12.6**b and **Figure S12.13**).

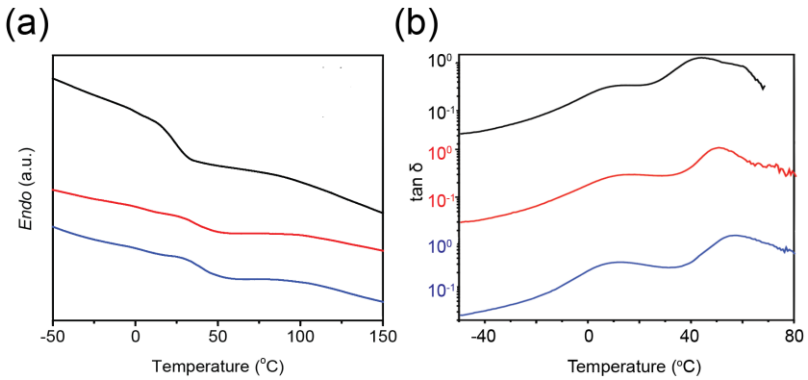

Figure 12.6. (a) DSC curves, (b) time-dependent *tan δ* variation for linear-gradient copolymers (L-10, black) and gradient copolymer particle brushes (PB-HG, red, PB-LG, blue).

Mechanical property measurements examine the reinforcing effect of nanofillers. Typical stress-strain curves of linear-gradient copolymer and gradient copolymer grafted nanoparticle composites are shown in **Figure S12.14**. Highly transparent bulk films were fabricated through the solvent casting method from THF solutions (**Figure 12.7** inset). The Young's modulus and fragile toughness of each sample are shown in **Figure 12.7**. As expected, both tensile strength and modulus at a given strain increase with the increase in SiO_2 nanoparticle loading. This enhancement reveals the very good reinforcing effect of SiO_2 nanoparticle and thereby the strong surface bonding between the SiO_2 nanoparticles and the polymer ligands. Tensile strength increased with SiO_2 nanoparticles loading and reached up to a value of 17 MPa (PB-LG) from 2.8 MPa (L-10), an improvement of ~600% over the linear gradient copolymer. The presence of polymer ligands on the surfaces of the SiO_2 nanoparticles aided the dispersion and results in better load transfer from the composites to the SiO_2 nanoparticles, causing an even stress distribution thereby minimizing the presence of concentrated stress. The Young's modulus values of linear-gradient copolymer L-10 is around 75 MPa, and 44.7 wt% loading of SiO_2 nanoparticles leads to Young's modulus value around 883 MPa due to the addition of stiff material to

the nanocomposite. The stiffening effect without sacrificing the strength of the composite is a result of the strong chemical bonding between nanofillers and polymer ligands. The same trend was also observed, and confirmed, in Young's modulus and hardness measurements by nanoindentation, **Figure S12.15** and **Figure S12.16**. Toughness can be estimated *via* the integrating of tensile strain-stress curves. As shown in Figure 7, PB-HG has the highest toughness (365 MJ/m^3), which was ~27% and ~453% higher than L-10 (287 MJ/m^3) and PB-LG (103 MJ/m^3). The high loading of SiO_2 nanoparticles enhanced the stiffness but meanwhile led to a low fracture strain, which illustrated the lowest toughness in PB-LG.

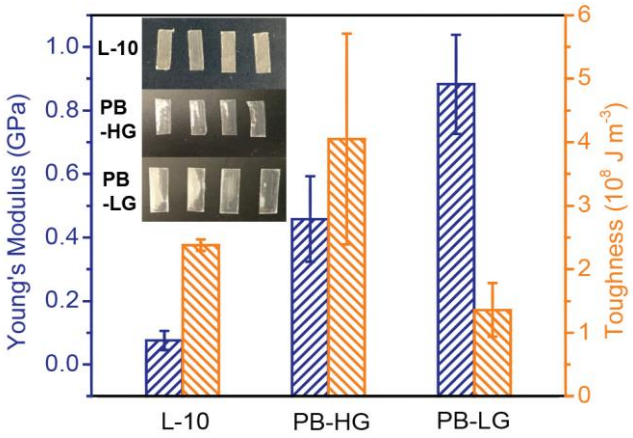

Figure 12.7. Young's modulus and toughness of linear-gradient copolymer (L-10) and gradient copolymer particle brushes (PB-HG, PB-LG) from DMA measurement, inset: photographs of linear-gradient copolymers and gradient copolymer particle brushes bulk films

Damping behavior was evaluated through dynamic mechanical analysis (DMA) over the frequency range of 0.1-100 Hz with 0.1% strain oscillation. A clear improvement in stiffness compared to linear-gradient copolymer is observed as the SiO_2 nanoparticle content increases in gradient copolymer particle brushes, **Figure 12.8**a and **Figure S12.17**. Viscoelastic polymers dissipate energy by shear deformation, and this may be enhanced by altering the microarchitecture of the composites, to achieve localized high energy dissipation regions. The damping of the linear-gradient copolymer and gradient copolymer grafted particle brushes is expressed as "*tan δ*", which is the phase lag between the force applied and displacement obtained. Improvement in stiffness due to the addition of stiffer

nanoparticles is usually associated with a reduction in damping, which seen in **Figure 12.8**b.[64] Both PB-HG and PB-LG show significant changes in damping behavior with frequency. Damping reaches a peak in PB-HG at ~50 Hz and ~10 Hz in PB-LG. On the contrary, damping continues to decrease with the frequency for linear-gradient copolymer up to 100 Hz, Figure 8b. These observations indicate the dominating influence of the frequency on the damping behavior. Thus particle brushes show a similar trend in damping behavior. The nanocomposite becomes brittle, and damping decreases significantly with an increased SiO_2 volume fraction.

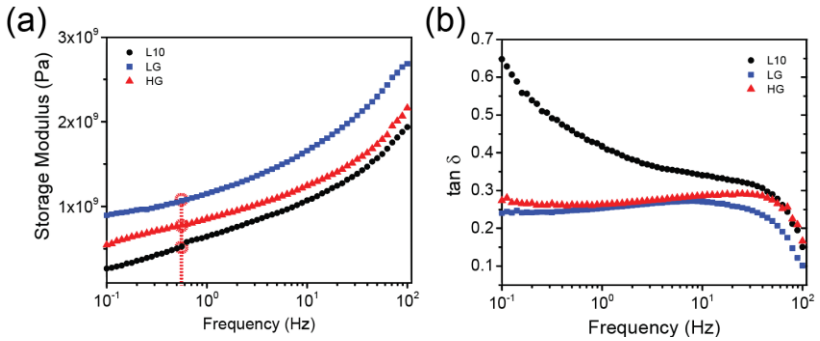

Figure 12.8. (a) Frequency-dependent storage modulus variation, red dash line highlighted the storage modulus at frequency 0.56 Hz of each sample which is shown in **Figure S12.17**, (b) frequency-dependent *tan δ* variation for linear-gradient copolymers and gradient copolymer particle brushes.

12.5. Supporting Information

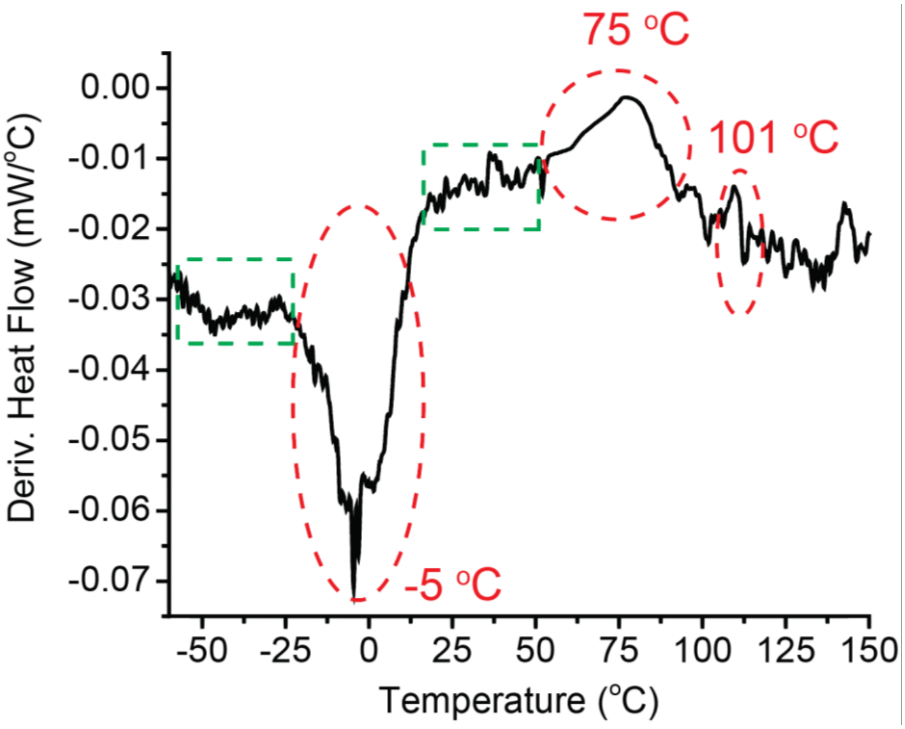

Figure S12.1. The plot of deriv. heat flow *vs*. temperature: sample L1.

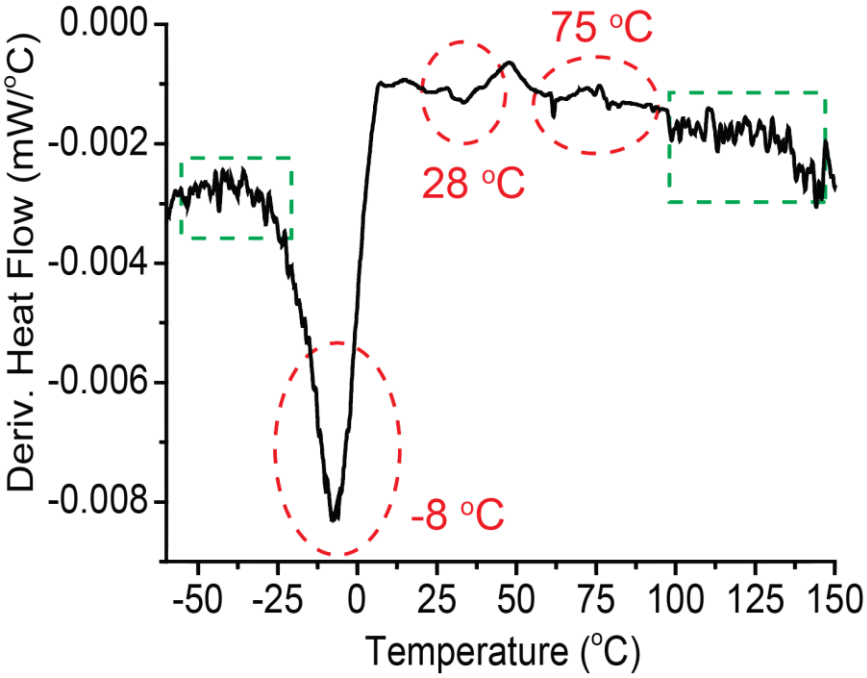

Figure S12.2. The plot of deriv. heat flow *vs.* temperature: sample L2.

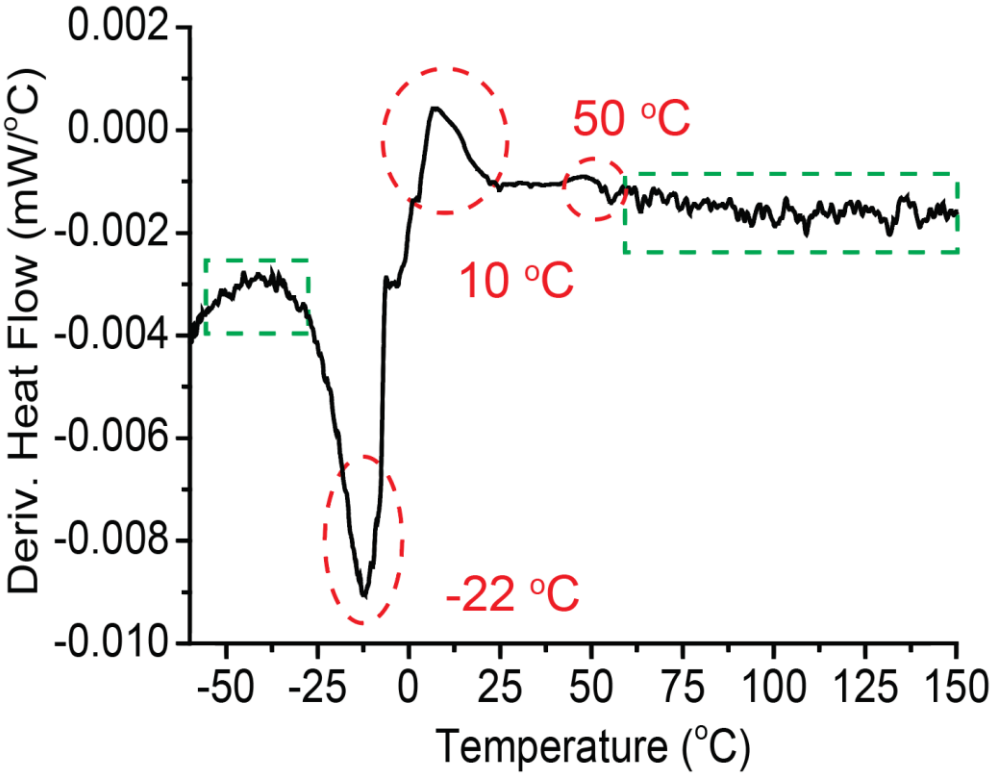

Figure S12.3. The plot of deriv. heat flow *vs.* temperature: sample L3.

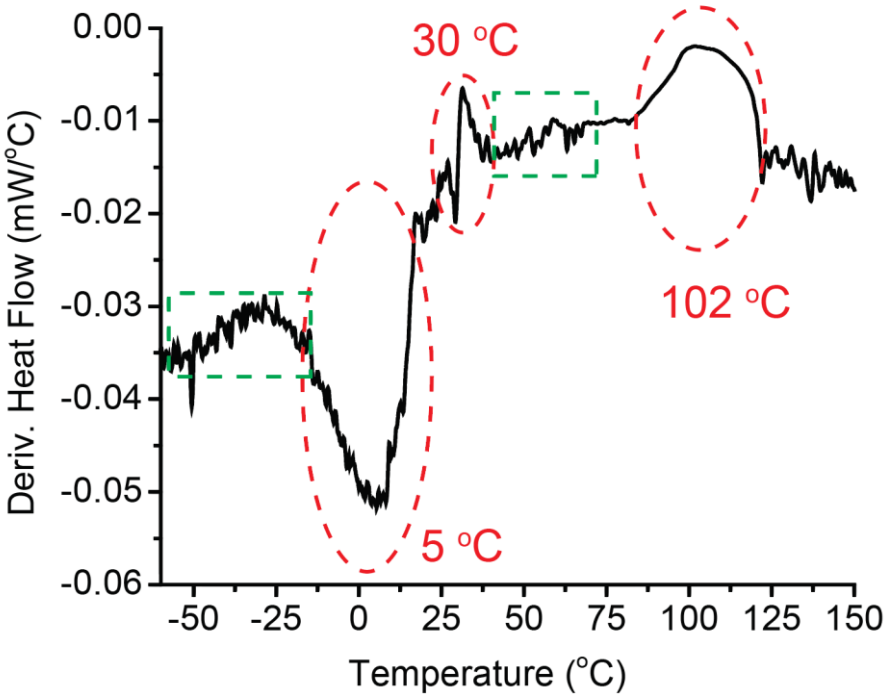

Figure S12.4. The plot of deriv. heat flow *vs.* temperature: sample L4.

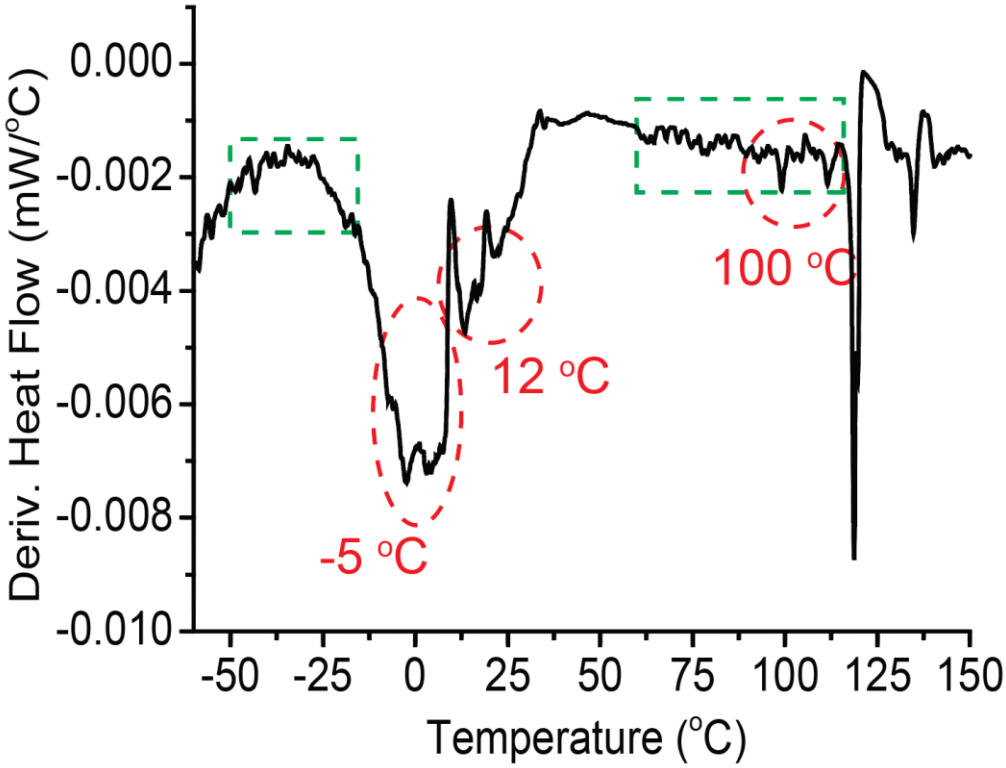

Figure S12.5. The plot of deriv. heat flow *vs.* temperature: sample L5.

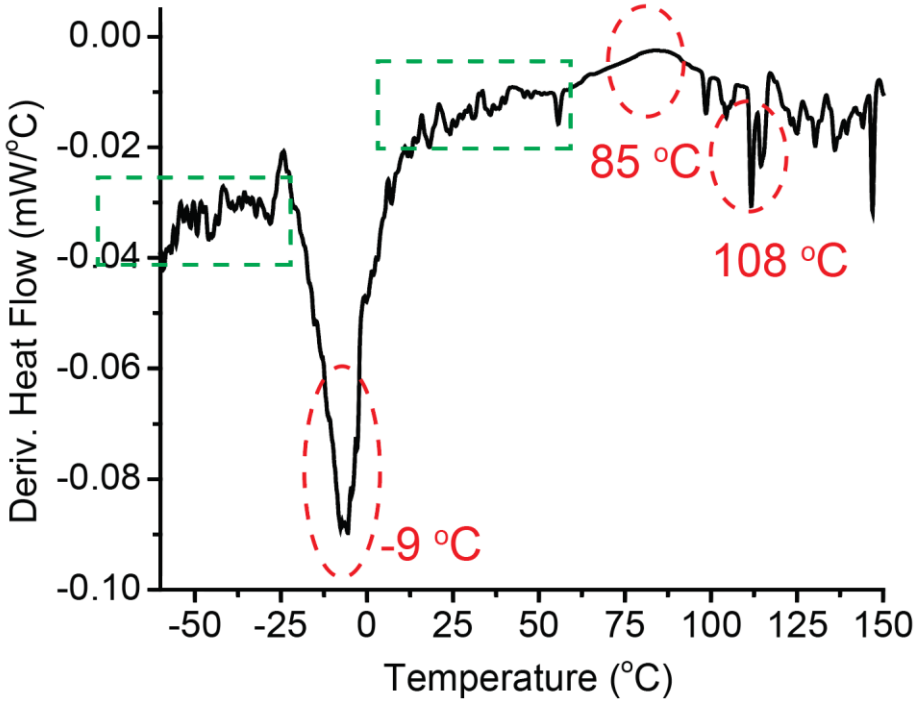

Figure S12.6. The plot of deriv. heat flow *vs.* temperature: sample L6.

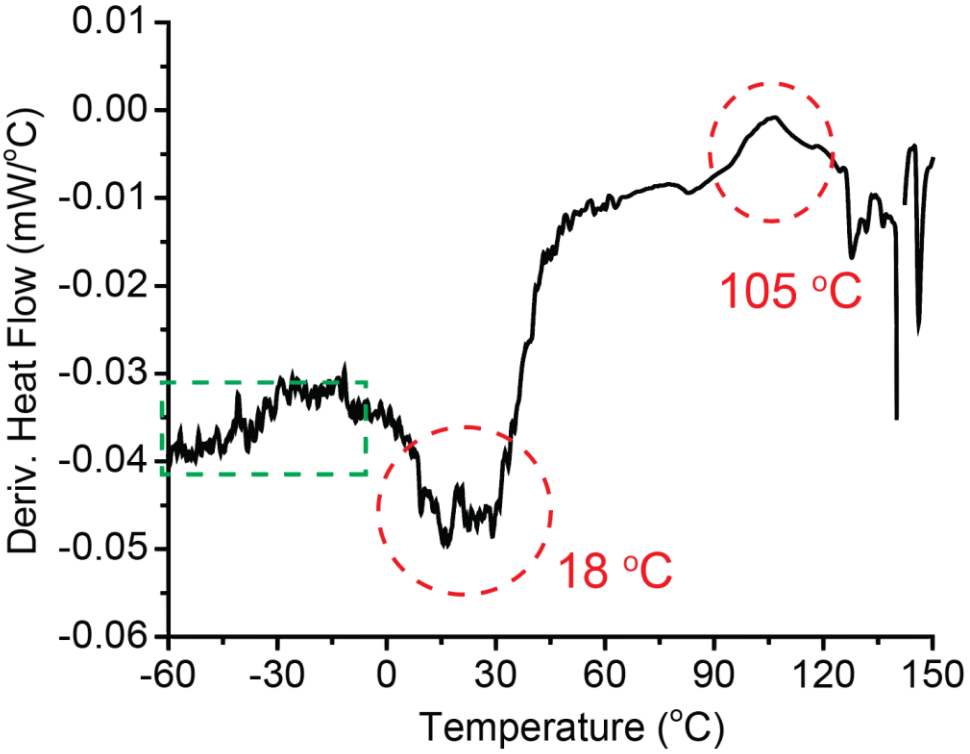

Figure S12.7. The plot of deriv. heat flow *vs.* temperature: sample L7.

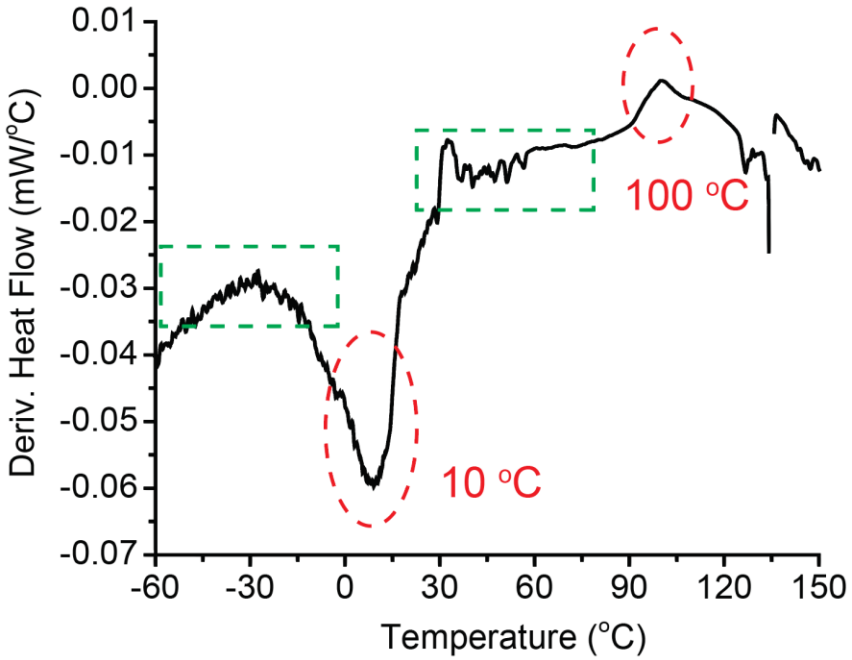

Figure S12.8. The plot of deriv. heat flow *vs.* temperature: sample L8.

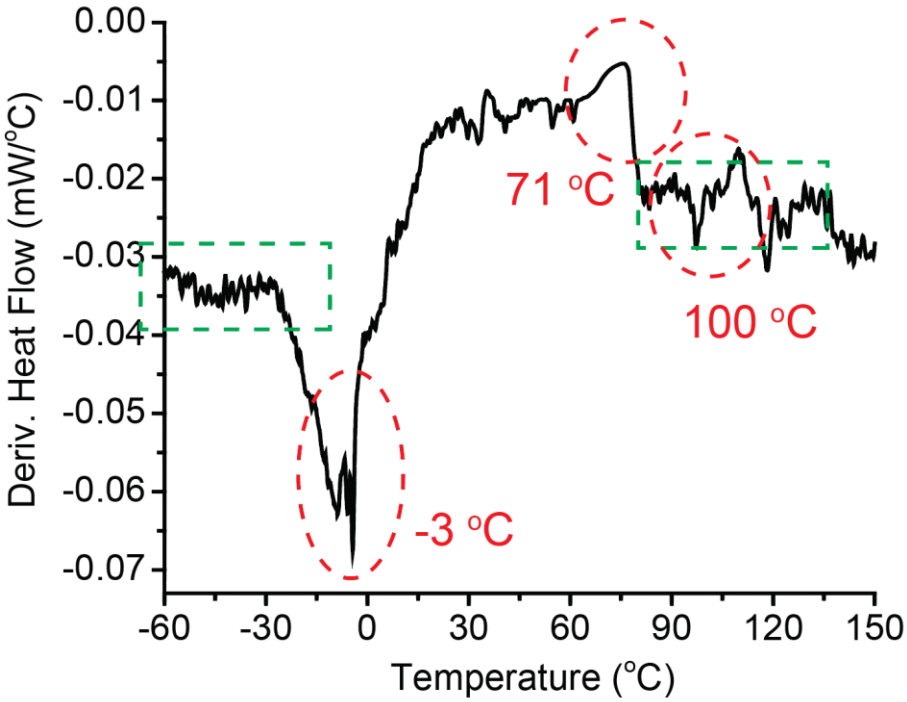

Figure S12.9. The plot of deriv. heat flow *vs.* temperature: sample L9.

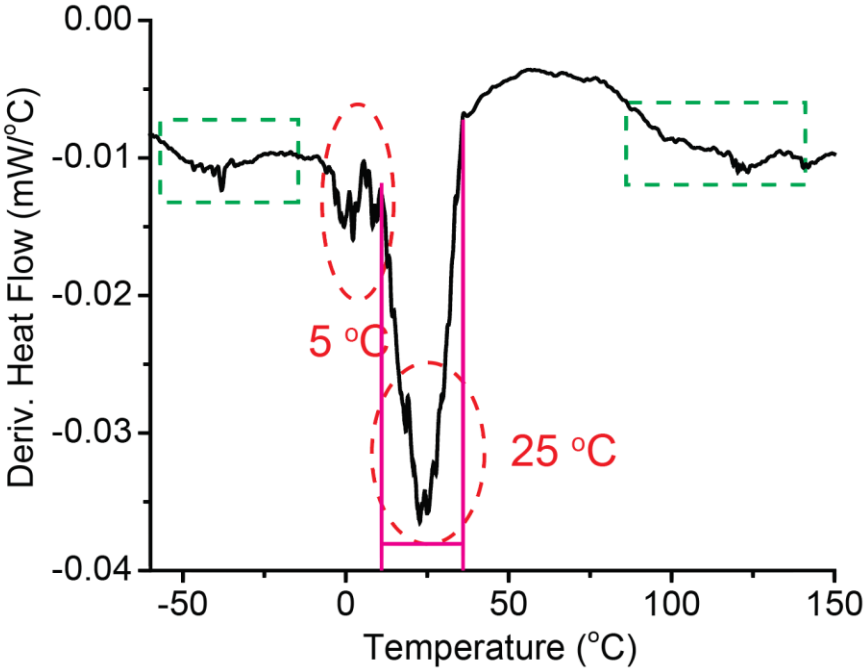

Figure S12.10. The plot of deriv. heat flow *vs.* temperature: sample L10.

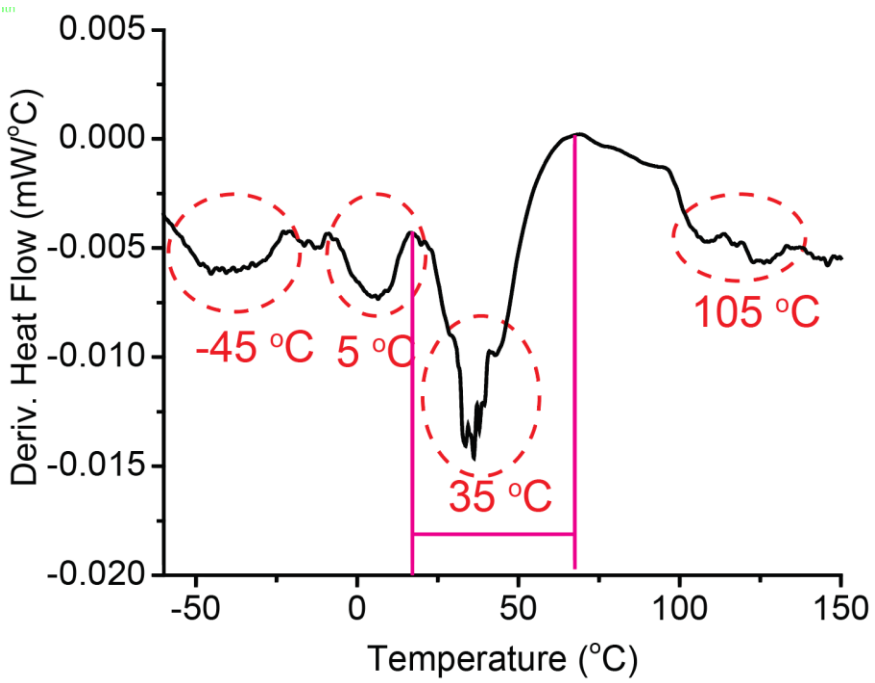

Figure S12.11. The plot of deriv. heat flow *vs*. temperature: sample PB-HG.

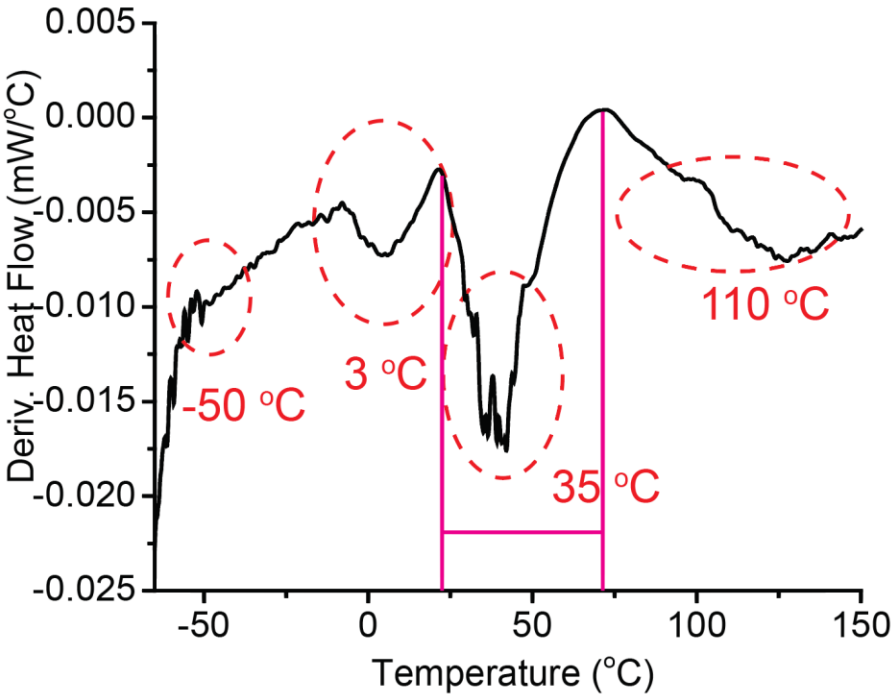

Figure S12.12. The plot of deriv. heat flow *vs*. temperature: sample PB-LG.

Scheme S12.1. Schematic graphs of linear PBA-grad-PMMA copolymers and SiO2-g-PBA-grad-PMMA particle brushes

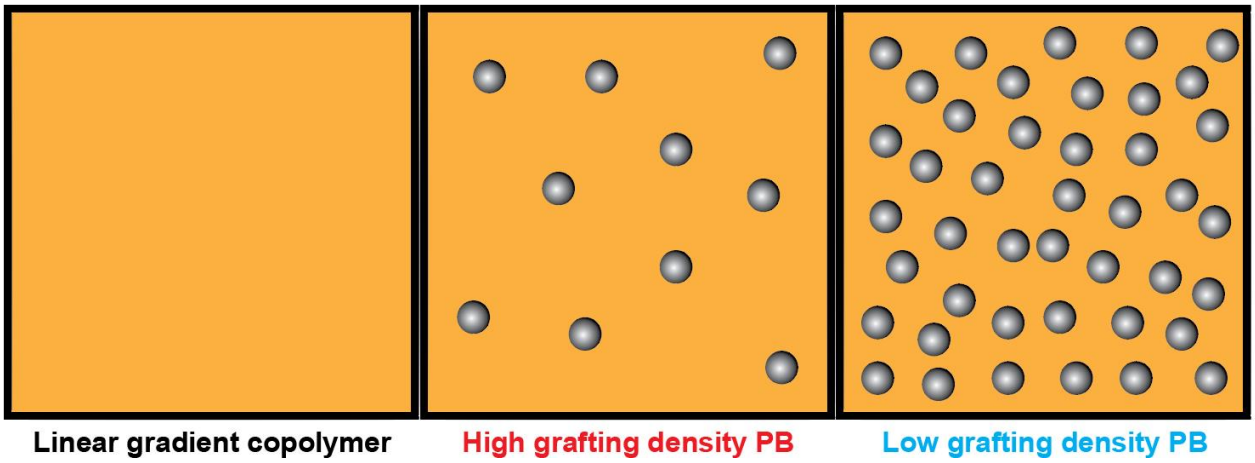

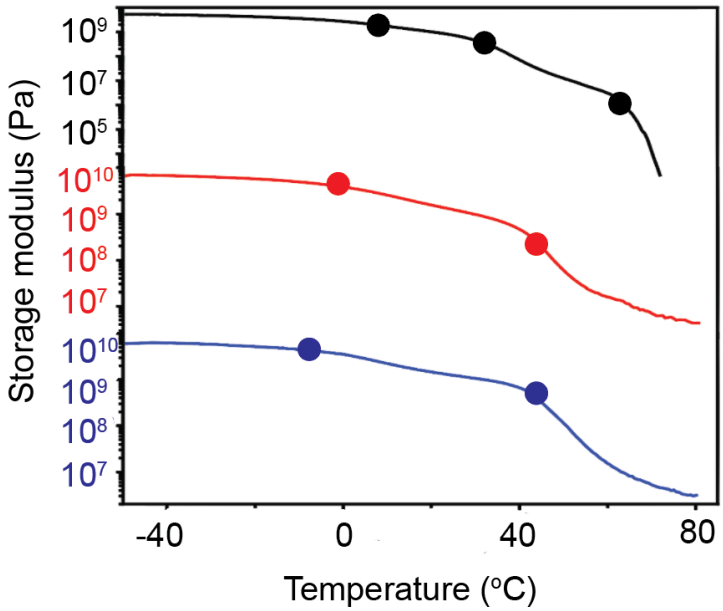

Figure S12.13. Time-dependent storage modulus variation for linear-gradient copolymers (L-10, black) and gradient copolymer particle brushes (PB-HG, red, PB-LG, blue).

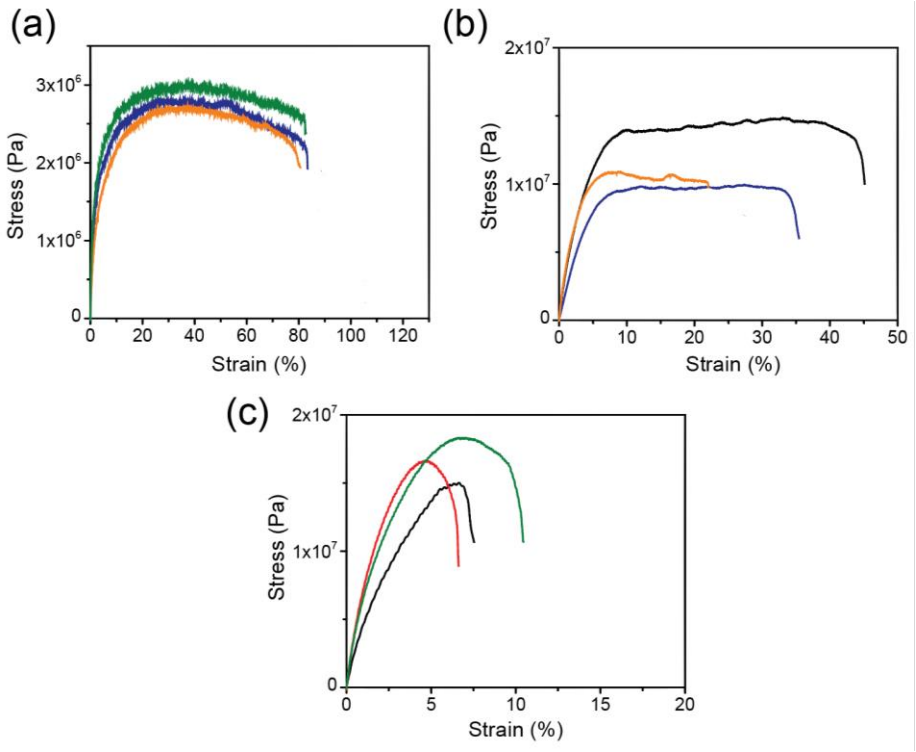

Figure S12.14. Stress-strain response for (a) linear gradient copolymer L-10, (b) gradient copolymer particle brushes PB-HG, (c) gradient copolymer particle brush PB-LG.

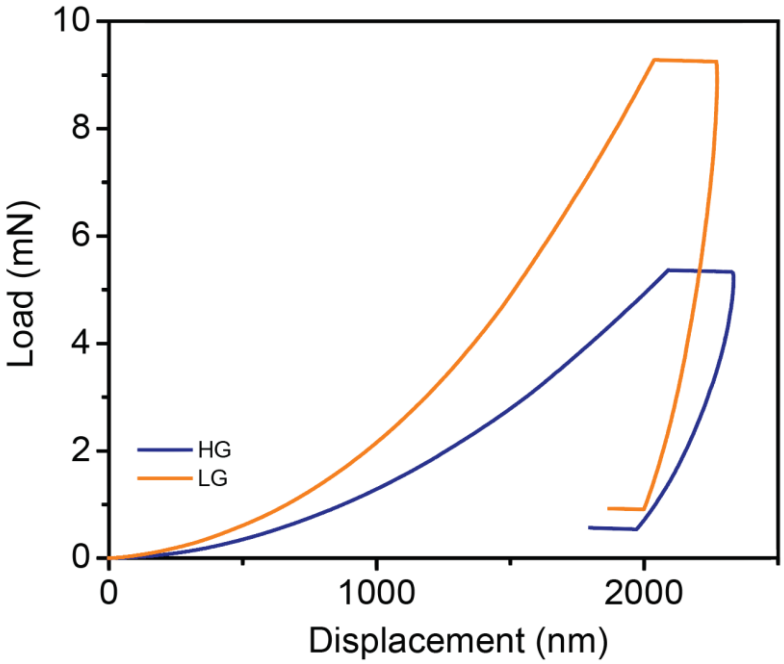

Figure S12.15. Characteristic load-displacement curves for sample PB-HG (orange) and PB-LG (blue) from nanoindentation.

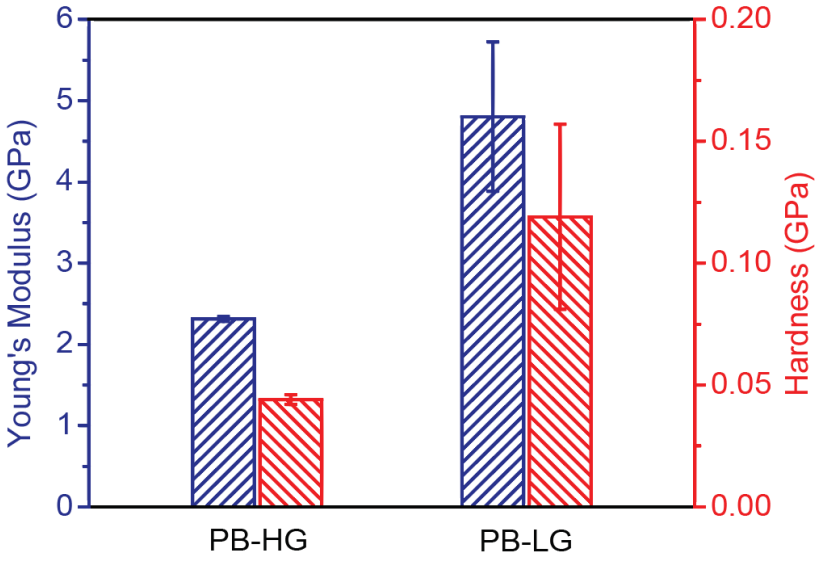

Figure S12.16. Young's modulus, and hardness of gradient copolymer particle brushes (PB-HG, PB-LG) under nanoindentation.

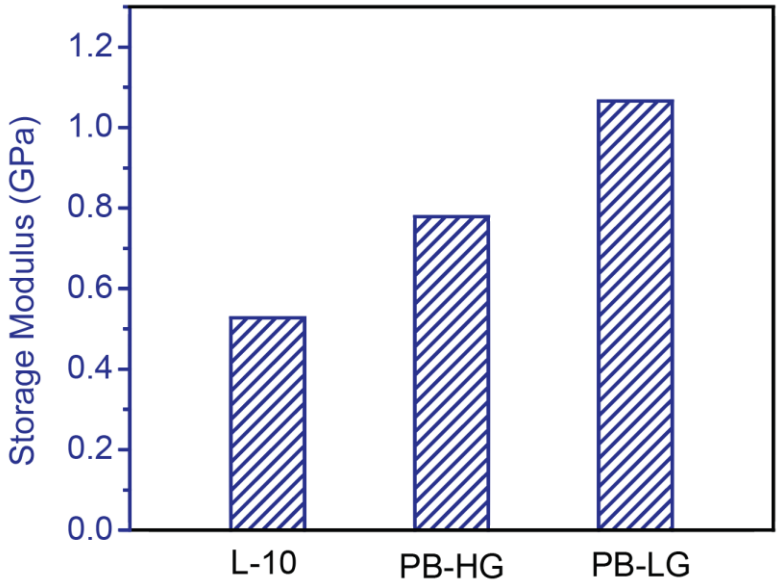

Figure S12.17. Storage modulus at frequency 0.56 Hz for gradient copolymer and gradient copolymer grafted particle brushes**.**

12.6. Conclusions

This study demonstrated a new route to synthesize linear-gradient copolymers and gradient copolymer particle brushes through a "semi-batch" ATRP method. By slow feeding of

MMA monomer to BA reaction solutions, well-defined copolymers with a significant gradient in composition were obtained at relatively low monomer conversions, <20%. The chain length, composition, and sequence of the polymer ligands can be tuned by the initial BA monomer concentration and the feeding rate of the MMA monomer. Gradient copolymer particle brushes with the same ligand composition, but different grafting densities (0.55/0.126 nm^{-2}), were prepared and compared to a linear gradient copolymer with the same composition. Dramatic changes were observed in both thermal and mechanical properties after grafting the gradient copolymer from the surface of SiO_2 nanoparticles. Increased heterogeneity and microphase separation were introduced to the matrix of the nanocomposites after the addition of SiO_2 nanoparticles, which resulted in a more complexed T_gs and a wider T_g range. A clear improvement in mechanical properties (strength, stiffness) compared to linear-gradient copolymer is observed as the SiO_2 nanoparticle content increases in gradient copolymer particle brushes, however, the damping property was compromised as the increasing stiffness of the materials, especially at low-frequency condition. This work could pave the way for using gradient copolymer as shock reservoirs to design impact-sensitive materials.

12.7. References

1. Wang, J.-S.; Matyjaszewski, K., Controlled/"living" radical polymerization. atom transfer radical polymerization in the presence of transition-metal complexes. *J. Am. Chem. Soc.* **1995,** 117, (20), 5614-5615.
2. Kamigaito, M.; Ando, T.; Sawamoto, M., Metal-Catalyzed Living Radical Polymerization. *Chem. Rev.* **2001,** 101, (12), 3689-3746.
3. Matyjaszewski, K.; Xia, J., Atom Transfer Radical Polymerization. *Chem. Rev.* **2001,** 101, (9), 2921-2990.
4. Kato, M.; Kamigaito, M.; Sawamoto, M.; Higashimura, T., Polymerization of Methyl Methacrylate with the Carbon Tetrachloride/Dichlorotris-(triphenylphosphine)ruthenium(II)/Methylaluminum Bis(2,6-di-tert-butylphenoxide) Initiating System: Possibility of Living Radical Polymerization. *Macromolecules* **1995,** 28, (5), 1721-1723.

5. Matyjaszewski, K.; Spanswick, J., Controlled/living radical polymerization. *Mater. Today* **2005,** 8, (3), 26-33.
6. Patten, T. E.; Xia, J.; Abernathy, T.; Matyjaszewski, K., Polymers with Very Low Polydispersities from Atom Transfer Radical Polymerization. *Science* **1996,** 272, (5263), 866-868.
7. Matyjaszewski, K.; Tsarevsky, N. V., Nanostructured functional materials prepared by atom transfer radical polymerization. *Nat. Chem.* **2009,** 1, 276.
8. Patten, T. E.; Matyjaszewski, K., Atom Transfer Radical Polymerization and the Synthesis of Polymeric Materials. *Adv. Mater.* **1998,** 10, (12), 901-915.
9. Teodorescu, M.; Matyjaszewski*, K., Controlled polymerization of (meth)acrylamides by atom transfer radical polymerization. *Macromol. Rapid Commun.* **2000,** 21, (4), 190-194.
10. Coessens, V.; Pintauer, T.; Matyjaszewski, K., Functional polymers by atom transfer radical polymerization. *Prog. Polym. Sci.* **2001,** 26, (3), 337-377.
11. Matyjaszewski, K., Advanced Materials by Atom Transfer Radical Polymerization. *Adv. Mater.* **2018,** 30, (23), 1706441.
12. Matyjaszewski, K.; Ziegler, M. J.; Arehart, S. V.; Greszta, D.; Pakula, T., Gradient copolymers by atom transfer radical copolymerization. *J. Phys. Org. Chem.* **2000,** 13, (12), 775-786.
13. Noda, T.; Grice, A. J.; Levere, M. E.; Haddleton, D. M., Continuous process for ATRP: Synthesis of homo and block copolymers. *Eur. Polym. J.* **2007,** 43, (6), 2321-2330.
14. Dervaux, B.; Junkers, T.; Barner-Kowollik, C.; Du Prez, F. E., Continuous ATRP Synthesis of Block-Like Copolymers via Column Reactors: Design and Validation of a Kinetic Model. *Macromolecular Reaction Engineering* **2009,** 3, (9), 529-538.
15. Davis, K. A.; Matyjaszewski, K., Statistical, Gradient, Block, and Graft Copolymers by Controlled/Living Radical Polymerizations. In *Statistical, Gradient, Block and Graft Copolymers by Controlled/Living Radical Polymerizations*, Springer Berlin Heidelberg: Berlin, Heidelberg, 2002; pp 1-13.
16. Lee, H.-i.; Matyjaszewski, K.; Yu, S.; Sheiko, S. S., Molecular Brushes with Spontaneous Gradient by Atom Transfer Radical Polymerization. *Macromolecules* **2005,** 38, (20), 8264-8271.
17. Min, K.; Li, M.; Matyjaszewski, K., Preparation of gradient copolymers via ATRP using a simultaneous reverse and normal initiation process. I. Spontaneous gradient. *J. Polym. Sci., Part A: Polym. Chem.* **2005,** 43, (16), 3616-3622.
18. Lutz, J.-F.; Pakula, T.; Matyjaszewski, K., Synthesis and Properties of Copolymers with Tailored Sequence Distribution by Controlled/Living Radical Polymerization. In *Advances in Controlled/Living Radical Polymerization*, American Chemical Society: 2003; Vol. 854, pp 268-282.
19. Nakatani, K.; Ogura, Y.; Koda, Y.; Terashima, T.; Sawamoto, M., Sequence-Regulated Copolymers via Tandem Catalysis of Living Radical Polymerization and In Situ Transesterification. *J. Am. Chem. Soc.* **2012,** 134, (9), 4373-4383.
20. Pakula, T.; Matyjaszewski, K., Copolymers with controlled distribution of comonomers along the chain, 1. Structure, thermodynamics and dynamic properties of gradient copolymers. Computer simulation. *Macromol. Theory Simul.* **1996,** 5, (5), 987-1006.
21. Lefay, C.; Charleux, B.; Save, M.; Chassenieux, C.; Guerret, O.; Magnet, S., Amphiphilic gradient poly(styrene-co-acrylic acid) copolymer prepared via nitroxide-mediated solution

polymerization. Synthesis, characterization in aqueous solution and evaluation as emulsion polymerization stabilizer. *Polymer* **2006,** 47, (6), 1935-1945.
22. Mok, M. M.; Kim, J.; Torkelson, J. M., Gradient copolymers with broad glass transition temperature regions: Design of purely interphase compositions for damping applications. *J. Polym. Sci., Part B: Polym. Phys.* **2008,** 46, (1), 48-58.
23. Kim, J.; Mok, M. M.; Sandoval, R. W.; Woo, D. J.; Torkelson, J. M., Uniquely Broad Glass Transition Temperatures of Gradient Copolymers Relative to Random and Block Copolymers Containing Repulsive Comonomers. *Macromolecules* **2006,** 39, (18), 6152-6160.
24. Wong, C. L. H.; Kim, J.; Roth, C. B.; Torkelson, J. M., Comparison of Critical Micelle Concentrations of Gradient Copolymer and Block Copolymer in Homopolymer: Novel Characterization by Intrinsic Fluorescence. *Macromolecules* **2007,** 40, (16), 5631-5633.
25. Dettmer, C. M.; Gray, M. K.; Torkelson, J. M.; Nguyen, S. T., Synthesis and Functionalization of ROMP-Based Gradient Copolymers of 5-Substituted Norbornenes. *Macromolecules* **2004,** 37, (15), 5504-5512.
26. Urban, M. W.; Davydovich, D.; Yang, Y.; Demir, T.; Zhang, Y.; Casabianca, L., Key-and-lock commodity self-healing copolymers. *Science* **2018,** 362, (6411), 220-225.
27. Askar, S.; Li, L.; Torkelson, J. M., Polystyrene-Grafted Silica Nanoparticles: Investigating the Molecular Weight Dependence of Glass Transition and Fragility Behavior. *Macromolecules* **2017,** 50, (4), 1589-1598.
28. Bockstaller, M. R.; Mickiewicz, R. A.; Thomas, E. L., Block Copolymer Nanocomposites: Perspectives for Tailored Functional Materials. *Adv. Mater.* **2005,** 17, (11), 1331-1349.
29. Krishnamoorti, R.; Vaia, R. A.; Giannelis, E. P., Structure and Dynamics of Polymer-Layered Silicate Nanocomposites. *Chem. Mater.* **1996,** 8, (8), 1728-1734.
30. Lin, Y.; Böker, A.; He, J.; Sill, K.; Xiang, H.; Abetz, C.; Li, X.; Wang, J.; Emrick, T.; Long, S.; Wang, Q.; Balazs, A.; Russell, T. P., Self-directed self-assembly of nanoparticle/copolymer mixtures. *Nature* **2005,** 434, (7029), 55-59.
31. Kumar, S. K.; Jouault, N.; Benicewicz, B.; Neely, T., Nanocomposites with Polymer Grafted Nanoparticles. *Macromolecules* **2013,** 46, (9), 3199-3214.
32. Ndoro, T. V. M.; Voyiatzis, E.; Ghanbari, A.; Theodorou, D. N.; Böhm, M. C.; Müller-Plathe, F., Interface of Grafted and Ungrafted Silica Nanoparticles with a Polystyrene Matrix: Atomistic Molecular Dynamics Simulations. *Macromolecules* **2011,** 44, (7), 2316-2327.
33. Song, G.; Zhang, L.; He, C.; Fang, D.-C.; Whitten, P. G.; Wang, H., Facile Fabrication of Tough Hydrogels Physically Cross-Linked by Strong Cooperative Hydrogen Bonding. *Macromolecules* **2013,** 46, (18), 7423-7435.
34. Hu, Y.; Du, Z.; Deng, X.; Wang, T.; Yang, Z.; Zhou, W.; Wang, C., Dual Physically Cross-Linked Hydrogels with High Stretchability, Toughness, and Good Self-Recoverability. *Macromolecules* **2016,** 49, (15), 5660-5668.
35. Kango, S.; Kalia, S.; Celli, A.; Njuguna, J.; Habibi, Y.; Kumar, R., Surface modification of inorganic nanoparticles for development of organic–inorganic nanocomposites—A review. *Prog. Polym. Sci.* **2013,** 38, (8), 1232-1261.
36. Hui, C. M.; Pietrasik, J.; Schmitt, M.; Mahoney, C.; Choi, J.; Bockstaller, M. R.; Matyjaszewski, K., Surface-Initiated Polymerization as an Enabling Tool for Multifunctional (Nano-)Engineered Hybrid Materials. *Chem. Mater.* **2014,** 26, (1), 745-762.

37. Choi, J.; Hui, C. M.; Pietrasik, J.; Dong, H.; Matyjaszewski, K.; Bockstaller, M. R., Toughening fragile matter: mechanical properties of particle solids assembled from polymer-grafted hybrid particles synthesized by ATRP. *Soft Matter* **2012,** 8, (15), 4072-4082.
38. Bombalski, L.; Dong, H.; Listak, J.; Matyjaszewsk, K.; Bockstaller, M. R., Null-Scattering Hybrid Particles Using Controlled Radical Polymerization. *Adv. Mater.* **2007,** 19, (24), 4486-4490.
39. Alonso-Redondo, E.; Schmitt, M.; Urbach, Z.; Hui, C. M.; Sainidou, R.; Rembert, P.; Matyjaszewski, K.; Bockstaller, M. R.; Fytas, G., A new class of tunable hypersonic phononic crystals based on polymer-tethered colloids. *Nat. Commun.* **2015,** 6, 8309.
40. Rong, M. Z.; Zhang, M. Q.; Ruan, W. H., Surface modification of nanoscale fillers for improving properties of polymer nanocomposites: a review. *Mater. Sci. Technol.* **2006,** 22, (7), 787-796.
41. Akcora, P.; Liu, H.; Kumar, S. K.; Moll, J.; Li, Y.; Benicewicz, B. C.; Schadler, L. S.; Acehan, D.; Panagiotopoulos, A. Z.; Pryamitsyn, V.; Ganesan, V.; Ilavsky, J.; Thiyagarajan, P.; Colby, R. H.; Douglas, J. F., Anisotropic self-assembly of spherical polymer-grafted nanoparticles. *Nat. Mater.* **2009,** 8, 354.
42. Kim, S. A.; Mangal, R.; Archer, L. A., Relaxation Dynamics of Nanoparticle-Tethered Polymer Chains. *Macromolecules* **2015,** 48, (17), 6280-6293.
43. Fernandes, N. J.; Wallin, T. J.; Vaia, R. A.; Koerner, H.; Giannelis, E. P., Nanoscale Ionic Materials. *Chem. Mater.* **2014,** 26, (1), 84-96.
44. Voudouris, P.; Choi, J.; Gomopoulos, N.; Sainidou, R.; Dong, H.; Matyjaszewski, K.; Bockstaller, M. R.; Fytas, G., Anisotropic Elasticity of Quasi-One-Component Polymer Nanocomposites. *ACS Nano* **2011,** 5, (7), 5746-5754.
45. Porter, C. E.; Blum, F. D., Thermal Characterization of Adsorbed Polystyrene Using Modulated Differential Scanning Calorimetry. *Macromolecules* **2002,** 35, (19), 7448-7452.
46. Cheng, S.; Holt, A. P.; Wang, H.; Fan, F.; Bocharova, V.; Martin, H.; Etampawala, T.; White, B. T.; Saito, T.; Kang, N.-G.; Dadmun, M. D.; Mays, J. W.; Sokolov, A. P., Unexpected Molecular Weight Effect in Polymer Nanocomposites. *Phys. Rev. Lett.* **2016,** 116, (3), 038302.
47. Harton, S. E.; Kumar, S. K.; Yang, H.; Koga, T.; Hicks, K.; Lee, H.; Mijovic, J.; Liu, M.; Vallery, R. S.; Gidley, D. W., Immobilized Polymer Layers on Spherical Nanoparticles. *Macromolecules* **2010,** 43, (7), 3415-3421.
48. Holt, A. P.; Sangoro, J. R.; Wang, Y.; Agapov, A. L.; Sokolov, A. P., Chain and Segmental Dynamics of Poly(2-vinylpyridine) Nanocomposites. *Macromolecules* **2013,** 46, (10), 4168-4173.
49. Mutiso, R. M.; Winey, K. I., Electrical properties of polymer nanocomposites containing rod-like nanofillers. *Prog. Polym. Sci.* **2015,** 40, 63-84.
50. Hu, Z.; Shao, Q.; Moloney, M. G.; Xu, X.; Zhang, D.; Li, J.; Zhang, C.; Huang, Y., Nondestructive Functionalization of Graphene by Surface-Initiated Atom Transfer Radical Polymerization: An Ideal Nanofiller for Poly(p-phenylene benzobisoxazole) Fibers. *Macromolecules* **2017,** 50, (4), 1422-1429.
51. Ahn, C.; Kim, S.-M.; Jung, J.-W.; Park, J.; Kim, T.; Lee, S. E.; Jang, D.; Hong, J.-W.; Han, S. M.; Jeon, S., Multifunctional Polymer Nanocomposites Reinforced by 3D Continuous Ceramic Nanofillers. *ACS Nano* **2018,** 12, (9), 9126-9133.
52. Su, R.; Luo, Z.; Zhang, D.; Liu, Y.; Wang, Z.; Li, J.; Bian, J.; Li, Y.; Hu, X.; Gao, J.; Yang, Y., High Energy Density Performance of Polymer Nanocomposites Induced by Designed

Formation of BaTiO3@sheet-likeTiO2 Hybrid Nanofillers. *J. Phys. Chem. C* **2016,** 120, (22), 11769-11776.
53. Tan, A. W.; Torkelson, J. M., Poly(methyl methacrylate) nanotubes in AAO templates: Designing nanotube thickness and characterizing the Tg-confinement effect by DSC. *Polymer* **2016,** 82, 327-336.
54. Williams, G. A.; Ishige, R.; Cromwell, O. R.; Chung, J.; Takahara, A.; Guan, Z., Mechanically Robust and Self-Healable Superlattice Nanocomposites by Self-Assembly of Single-Component "Sticky" Polymer-Grafted Nanoparticles. *Adv. Mater.* **2015,** 27, (26), 3934-3941.
55. Dreyer, A.; Feld, A.; Kornowski, A.; Yilmaz, E. D.; Noei, H.; Meyer, A.; Krekeler, T.; Jiao, C.; Stierle, A.; Abetz, V.; Weller, H.; Schneider, G. A., Organically linked iron oxide nanoparticle supercrystals with exceptional isotropic mechanical properties. *Nat. Mater.* **2016,** 15, 522.
56. Börner, H. G.; Duran, D.; Matyjaszewski, K.; da Silva, M.; Sheiko, S. S., Synthesis of Molecular Brushes with Gradient in Grafting Density by Atom Transfer Polymerization. *Macromolecules* **2002,** 35, (9), 3387-3394.
57. Arehart, S. V.; Matyjaszewski, K., Atom Transfer Radical Copolymerization of Styrene and n-Butyl Acrylate. *Macromolecules* **1999,** 32, (7), 2221-2231.
58. Zhou, D.; Gao, X.; Wang, W.-j.; Zhu, S., Termination of Surface Radicals and Kinetic Modeling of ATRP Grafting from Flat Surfaces by Addition of Deactivator. *Macromolecules* **2012,** 45, (3), 1198-1207.
59. Khabibullin, A.; Mastan, E.; Matyjaszewski, K.; Zhu, S., Surface-Initiated Atom Transfer Radical Polymerization. In *Controlled Radical Polymerization at and from Solid Surfaces*, Vana, P., Ed. Springer International Publishing: Cham, 2016; pp 29-76.
60. Roos, S. G.; Müller, A. H. E.; Matyjaszewski, K., Copolymerization of n-Butyl Acrylate with Methyl Methacrylate and PMMA Macromonomers: Comparison of Reactivity Ratios in Conventional and Atom Transfer Radical Copolymerization. *Macromolecules* **1999,** 32, (25), 8331-8335.
61. Ziegler, M. J.; Matyjaszewski, K., Atom Transfer Radical Copolymerization of Methyl Methacrylate and n-Butyl Acrylate. *Macromolecules* **2001,** 34, (3), 415-424.
62. Van Steenberge, P. H. M.; D'hooge, D. R.; Wang, Y.; Zhong, M.; Reyniers, M.-F.; Konkolewicz, D.; Matyjaszewski, K.; Marin, G. B., Linear Gradient Quality of ATRP Copolymers. *Macromolecules* **2012,** 45, (21), 8519-8531.
63. Abraham, J.; Thomas, J.; Kalarikkal, N.; George, S. C.; Thomas, S., Static and Dynamic Mechanical Characteristics of Ionic Liquid Modified MWCNT-SBR Composites: Theoretical Perspectives for the Nanoscale Reinforcement Mechanism. *J. Phys. Chem. B* **2018,** 122, (4), 1525-1536.
64. Meaud, J.; Sain, T.; Yeom, B.; Park, S. J.; Shoultz, A. B.; Hulbert, G.; Ma, Z.-D.; Kotov, N. A.; Hart, A. J.; Arruda, E. M.; Waas, A. M., Simultaneously High Stiffness and Damping in Nanoengineered Microtruss Composites. *ACS Nano* **2014,** 8, (4), 3468-3475.

Chapter 13 Mechanically Robust and Self-healable Gradient Copolymer Particle Brushes

13.1. Preface

Remarkable mechanical properties and excellent self-healing ability are difficult to combine in one polymer nanocomposite. Here we report a facile synthetic route to synthesize SiO_2-*g*-poly(methyl methacrylate)(PMMA)-*grad*-poly(*n*-butyl acrylate)(PBA) gradient copolymer particle brushes through semi-batch copolymerization by surface-initiated atom transfer radical polymerization (SI-ATRP). Two series of samples with different grafting densities (0.55/0.15 chains/nm^2) were prepared. The BA/MMA composition in the polymer ligands was tuned by altering the MMA feeding rate. DSC and DMA were applied to investigate the thermal and mechanical properties of the nanocomposites. It was determined that the properties are not only affected by the composition of polymer ligands but also the featured structures (multiple "core-shell coronas") formed in the bulk composite materials. Self-healing tests were conducted at different temperatures, 50/80/120 ºC, provided by external heat, and a high compositional sensitivity was observed only in the samples with BA composition 50-55% in the gradient copolymer polymers. These samples exhibited good self-healing behaviors.

In this chapter, the self-healing of gradient copolymer particle brushes is discussed. I designed the entire project and performed all synthetic work and part of the characterization in the project. I would like to thank especially my collaborators, Yuqi Zhao for extensive discussion and the help with self-healing test.

This project will be published in *Chemistry of Materials*.

This work was supported by NSF (DMR 1501324 and DMR 1410845), the Department of Energy (DE-EE0006702), as well as the Scott Institute for Energy Technologies at Carnegie Mellon University.

13.2. Introduction

Synthetic materials are often susceptible to degradation, fracture or damage by external factors, leading to a limitation to their lifetime.[1-5] However, the fraction of polymeric materials that are recycled remains low.[6-7] Numerous studies, inspired by nature, have been conducted in the past few decades that were dedicated to the development of self-healing and sustainable materials and stand out for their simplicity and potential scalability.[8-16] Self-healing polymeric materials can retain the desired properties, including mechanical and electrical functions, after damage using the resources inherently, automatically, available in the materials or with the assistance of external stimuli.[9, 17-25] Currently, most approaches to synthetic self-healing materials require the input of external energy in the form of heat,[26-28] light,[15, 29-30] incorporation of additional healing reagents,[5, 31] solvent (substantial solvation)[14, 32] or plasticizers.[33-34] These soft and rubbery materials are usually composed of soft polymer blocks and organic components. The reversible and dynamic nature of the non-covalent interactions and dynamic bonds tends to produce soft materials with high mobility to facilitate the healing process.[34-36] However, the incorporation of moieties, that for example can form dynamic covalent or non-covalent bonds,[37-39] or can chelate metals with the necessary affinity and concentration, to produce robust materials with efficient healing often requires additional synthetic steps or the design of polymers that are considerably different in expense and chemical makeup from common commercial commodity materials.[5, 40-43] The poor mechanical properties of current efficient self-healing materials will

limit their potential applications.[44] The synthesis of stiff material with intrinsic self-healing ability remains a key challenge.[45]

A major goal in the field of self-healing materials is to combine robust mechanical and efficient healing properties.[46] The dispersion nanoparticles in a matrix of polymers can enhance the stability and mechanical properties of the formed nanocomposites.[47-49] Surface functionalization with small molecules ligands,[1-5] has been successfully used to assemble nanoparticle into several 2D and 3D crystalline morphologies,[50-54] and the self-assembly of single component polymer-grafted nanoparticles is a promising approach because it offers many advantages.[55-56] Such hybrid nanoparticles can combine the functional properties of the nanoparticle core with the processability and mechanical properties of the grafted polymer in one system. The covalent linkage between the polymer grafts and nanoparticles in such single-component systems intrinsically avoids phase demixing and aggregation and allows for versatile processing options such as extrusion, molding, roll-to-roll manufacturing, and 3D printing.

13.3. Experimental Section

Materials.

Monomers: butyl acrylate (BA, 99%, Aldrich), methyl methacrylate (MMA, 99%, Aldrich) were purified by passing through a column filled with basic alumina to remove the inhibitor. Tris(2-dimethylaminoethyl)amine (Me_6TREN, 99%, Alfa), anisole (99%, Aldrich), tetrahydrofuran (THF, 99%, VWR), methanol (99%, VWR), hexane (99%, VWR), acetone (99%, VWR), N,N-dimethylformamide (DMF, 99%, VWR), copper(II) bromide ($CuBr_2$, 99%, Aldrich), tin(II) 2-ethylhexanoate ($Sn(EH)_2$, 95%, Aldrich), 48% hydrofluoric acid aqueous solution (HF, >99.99%, Aldrich), ammonium hydroxide aqueous solution (NH_4OH, 28.0-30.0%, Fisher),

anhydrous magnesium sulfate ($MgSO_4$, Fisher) were used as received without further purification. Silica nanoparticles, 30 wt % solution in methyl isobutyl ketone (MIBK-ST), effective diameter d ≈ 15.8 nm, were kindly donated by Nissan Chemical Corp. and used as received. The tetherable ATRP initiator 1-(chlorodimethylsilyl)propyl-2-bromoisobutyrate and surface-modified silica (SiO_2-Br) were prepared using previously reported procedures.[1-2] The surface initiator densities are moderated with a "dummy" initiator chlorotrimethylsilane (99%, Aldrich).

Procedures.

Procedures for the synthesis of SiO_2-g-PBA-grad-PMMA particle brushes via ARGET ATRP.

Synthesis of SiO_2-g-PBA-grad-PMMA particle brushes.

Initiator (SiO_2-Br), monomer (BA), solvents (anisole, DMF), $CuBr_2$, and Me_6TREN, molar ratios shown as a subscript in Table 1, were mixed thoroughly in a sealed Schlenk flask. The mixture was degassed by bubbling with nitrogen. A stock solution of $Sn(EH)_2$ in anisole was prepared. Both mixtures and 20 mL MMA monomers were degassed by nitrogen purging respectively, then the $Sn(EH)_2$ solution was injected into the Schlenk flask to activate the catalyst complex and the flask was immediately put into an oil bath set at the desired temperature. Meanwhile, the MMA monomer was injected into the reaction by a syringe pump at the specific feeding rate shown as a subscript of Table 1. The conversion and molecular weight (MW) of the polymer were monitored by ^{1}H-NMR and SEC, respectively. The final particle brushes were soluble and stored in THF.

Procedures for the fabrication of a bulk film.

SiO_2-*g*-PBA-*grad*-PMMA particle brushes (HG-1~6/LG-1~6) were dispersed in THF *via* sonication. After the solution was stirred for 24 h, the bulk dispersions were transferred into 15 mm × 5 mm rectangular Teflon molds. The solvent was slowly evaporated over 48 h at room temperature generating transparent nanocomposite films with a thickness of 0.06-0.1 mm. The residual solvent was removed from the bulk films by transferring them to a vacuum oven and slowly increasing the temperature at the rate of 10 °C per 24 h to 120 °C. At least five specific bulk films of the same composition were investigated to systematically study the thermo-mechanical properties of the nanocomposite films.

Determining the density of the initiating site for SiO_2-Br nanoparticles

The concentration of initiating sites on the surface of the silica nanoparticles was determined by model reactions: i.e. polymerization of SiO_2-*g*-PMMA, conducted with a mole ration of $[MMA]_0/[SiO_2\text{-}Br]_0/[CuBr_2]_0/[Me_6TREN]_0/[Sn(EH)_2]_0$ = 2000:1:1:10:8 with 45 vol% anisole, 5 vol% DMF at 60 ºC) with certain amount of SiO_2-Br nanoparticles (e.g. with 100 mg). After purification, SEC and TGA were conducted to characterize the grafting density of the particle brushes. The particles used in the current study had a grafting density ~ 0.55/0.15 nm^{-2}, and the –Br (initiating site) concentration on the surface was assumed to be the same. Based on the average radius of nanoparticles, 7.9 nm, density of silica, 2.2 g/cm^3, the average molar mass of SiO_2-Br, are 6,340 g/mol (high grafting density), 23,240 g/mol (low grafting density).

Characterization.

Nuclear Magnetic Resonance Spectroscopy (NMR). Conversion of polymerization was monitored by ^{1}H NMR on a Bruker Advance 500 MHz NMR instrument in $CDCl_3$ at room temperature.

Size Exclusion Chromatography (SEC). Number-average molecular weights (M_n) and molecular weight distributions (MWD) of PBA-*grad*-PMMA samples were determined by size exclusion chromatography (SEC). The SEC was conducted with an Agilent 1260 Iso pump and Waters 410 differential refractometer using PSS columns (Styragel 10^5, 10^3, 10^2 Ǻ) with THF as an eluent at 35 ºC and a flow rate of 1 ml min^{-1}. Linear PMMA standards were used for calibration. Diphenylethylene and toluene were used as internal standards for the system.

Transmission Electron Microscopy (TEM). TEM was carried out using a JEOL 2000 EX electron microscope operated at 200 kV. The spatial distribution, radius and inter-particle distances of the SiO_2 nanoparticles were determined from statistical analysis of the TEM micrographs using ImageJ software.

Dynamic Light Scattering (DLS). DLS using a Malvern Zetasizer Nano ZS was employed to determine volume-weighted average hydrodynamic radius and distribution. The particle brushes were suspended in filtered THF (450 nm PTFE filter) at low concentrations.

Thermogravimetric Analysis (TGA). TGA with TA Instruments 2950 was used to measure the fraction of SiO_2 in the hybrids. The data were analyzed with TA Universal Analysis. The heating procedure involved four steps: (1) jump to 120 ºC; (2) hold at 120 ºC for 10 min; (3) ramp up at a rate of 20 ºC/min to 800 ºC; (4) hold for 2 min. The TGA plots were normalized to the total weight after holding at 120 ºC.

The grafting density was calculated using the formula (S1).

$$\sigma_{\mathrm{TGA}} = \frac{(1-f_{\mathrm{SiO2}})N_{\mathrm{Av}}\,\rho_{\mathrm{SiO2}}\,d}{6\,f_{\mathrm{SiO2}}\,M_n} \qquad \text{(S1)}$$

where f_{SiO2} is the SiO_2 fraction measured by TGA, N_{Av} is the Avogadro number, ρ_{SiO2} is the density of SiO_2 nanoparticles (2.2 g/cm^3), d is the average diameter of SiO_2 nanoparticles (15.8 nm), M_n is the overall number-average MW of the cleaved polymer brushes.

Differential Scanning Calorimetry (DSC). The glass transition temperature (T_g) of linear PBA-*grad*-PMMA and SiO_2-*g*-PBA-*grad*-PMMA particle brushes were measured by differential scanning calorimetry (DSC) with TA Instrument QA-2000. The same procedure was run three times, each involving the following steps: (1) Equilibrate at 25.00 °C, (2) Isothermal for 1.00 min, (3) Ramp 20.00 °C/min to -70.00 °C, (4) Isothermal for 1.00 min, (5) Ramp 20.00 °C/min to 160.00 °C, (6) Isothermal for 1.00 min, (7) Ramp 20.00 °C/min to -70.00 °C, (8) Isothermal for 1.00 min, (9) Ramp 20.00 °C/min to 160.00 °C, (10) Isothermal for 1.00 min, (11) Ramp 20.00 °C/min to -70.00 °C, (12) Isothermal for 1.00 min, (13) Ramp 20.00 °C/min to 160.00 °C, (14) Isothermal for 1.00 min, (15) Jump to 250.00 °C. The DSC data were analyzed with a TA Universal Analysis instrument, and T_g was directly acquired.

Dynamic Mechanical Analysis (DMA).

Tensile test: the SiO_2-*g*-PBA-*grad*-PMMA particle brushes (HG-1~6/LG-1~6) bulk films are tested in the tensile mode by using DMA (TA RSA-G2). The film thickness was between 60-100 μm. The samples were stretched at a constant tensile rate of 0.005 mm/s at room temperature.

Glass transition temperature measurement: The glass transition temperature was also measured through dynamic mechanical analysis (DMA, TA RSA-G2) at a constant frequency (1 Hz) in a

temperature range of -50 ℃ to 150 ℃, with a heating rate of 3 ℃/min, and application of 0.1% strain.

Damping property measurement: The damping property was measured through dynamic mechanical analysis (DMA, TA RSA-G2) in a frequency range of 0.1-100 Hz at room temperature, with the application of 0.1% strain. All the samples were tested at least three times for consistency.

Self-healing Test.

For self-healing test, bulk films with the same dimensions as fabricated before were cut by stainless-steel razor blade into two completely separate parts. Subsequently, the two cut interfaces were gently reattached for 1 minute, leaving them on the PTFE film substrate, and allowed to self-heal under room temperature, around 20 ℃, 50 ℃, 80 ℃, and 120 ℃. At least 5 samples for different entries under a specific temperature were tested for consistency.

13.4. Results and Discussion

Scheme 13.1. Self-healing of gradient copolymer particle brush bulk films

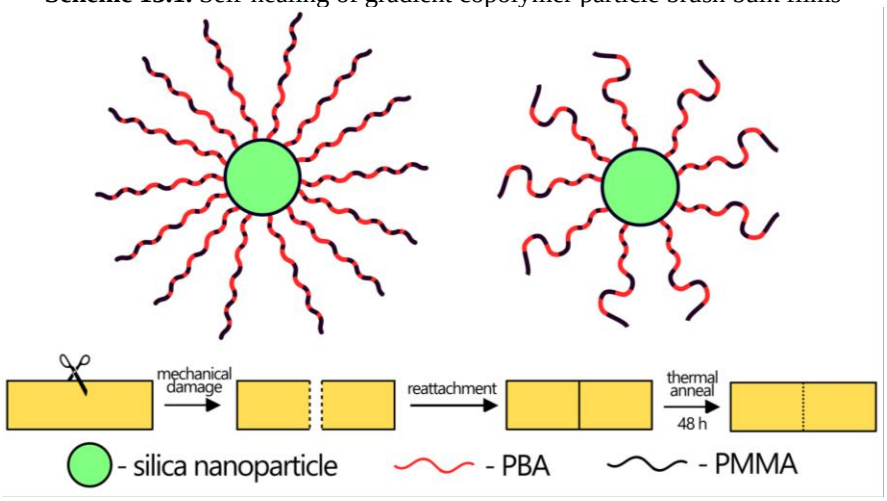

In our previous work, we reported the synthesis of SiO_2-*g*-PBA-*grad*-PMMA particle brushes with different grafting densities using a semi-batch copolymerization activator regenerated by electron transfer (ARGET) surface-initiated atom transfer radical polymerization (SI-ATRP). The bulk polymer grafted silica nanoparticle composites exhibited enhanced mechanical properties. In this contribution, two series of SiO_2-*g*-PBA-*grad*-PMMA particle brushes with systematic MMA/BA gradient compositions were prepared, and their thermal, mechanical and self-healing properties were systemically investigated. Self-healing in PBA-*grad*-PMMA gradient copolymers relies on non-covalent Van der Waals interactions (VdW), without any added healing agents or functional anchors. Compared with hydrogen bonding, VdW interactions are present essentially in all materials. Although relatively weak, they are particularly important in polymeric materials because their small attractive forces are summed up over the length of chains that contains hundreds of thousands of units.[31]

Precise synthesis of particle brushes by SI-ATRP offers extraordinary control over the resulting morphology, spanning length scales, chain sequence and defined architectures.[57-62] Two series of SiO_2-*g*-PBA-*grad*-PMMA particle brushes with various MMA/BA compositions were synthesized by changing the MMA feeding rate to the ongoing polymerization. The grafting densities were tuned by mixing a "dummy" initiator with the ATRP initiator during the surface modification step.[63-64] As shown in **Table 13.1**, for both high grafting density (HG) and low grafting density (LG) particle brushes, the molecular weights of polymer ligands increased with a higher MMA feeding rate, which leads to an increase in the PMMA composition in the gradient copolymer ligands, except for samples HG-6 and LG-6.

The overall PBA/PMMA compositions of the polymer ligands were confirmed by 1H-NMR after etching the silica core by HF aqueous solutions. The drop in molecular weight in

samples HG/LG-6 can be attributed to over dilution of the reaction solutions by the addition of MMA monomers, which results in a decrease in the polymerization rates and thus the final molecular weights. The corresponding inorganic fractions and comparable grafting density values were obtained by TGA. The morphology and structure of the particle brush in the solution and solid-state were investigated by DLS and TEM. With comparable grafting density in the same sample series, a strong correlation between particle brush morphology and molecular weight was observed, in which the interparticle distance and hydrodynamic size increased with increasing molecular weight, **Figure S13.1-S13.3**.

Table 13.1. Result of syntheses of SiO_2-*g*-PBA-*grad*-PMMA particle brushes

Entry[a]	Comp, $_{BA}$ (mol%)[b]	Comp, $_{MMA}$ (mol%)[b]	M_n[c]	M_w/M_n[c]	f_{ino} (%)[d]	σ (nm^2)[e]	$T_{g,1}$[f](°C)
HG-1	67.3	32.7	21,040	1.47	20.59	0.608	-20
HG-2*	56.3	43.7	23,150	1.55	21.41	0.526	3
HG-3*	50.4	49.5	36,700	1.37	12.37	0.639	10
HG-4	48.1	51.9	44,350	1.41	12.96	0.502	23
HG-5	45.5	54.5	54,470	1.39	8.94	0.619	38
HG-6	38.4	61.6	49,960	1.42	10.14	0.587	41
LG-1	58.7	41.3	16,480	1.29	57.19	0.151	-21
LG-2*	54.1	45.9	26,080	1.36	43.95	0.162	0
LG-3	48.5	51.5	28,210	1.32	51.65	0.109	6
LG-4	43.6	56.4	32,670	1.37	44.38	0.127	25
LG-5	39.1	60.9	44,010	1.36	30.86	0.168	36
LG-6	32.8	67.2	36,620	1.43	36.02	0.161	47

[a] Reaction conditions: $[BA]_0$:$[SiO_2\text{-}Br]_0$:$[CuBr_2]_0$:$[Me_6TREN]_0$:$[Sn(EH)_2]_0$=5000:1:0.5:5:5, at 50 ºC with 25 vol% anisole, V_0(BA) = 15 mL, MMA feeding rate = 0.5/1/1.5/2/2.5/3 mL/h, total [BA]: [MMA]=5000: 1500/3000/4500/6000/7500/9000. [b] Determined by ^{1}HNMR. [c] Determined by SEC. [d] Determined by TGA. [d] Calculated by Eq. S1. [f] The major glass transition temperature determined by DSC. * The stars in the table highlight the samples which show self-healable properties.

The thermal properties and mechanical properties of polymer nanocomposites are strongly associated with their composition, molecular weight, and sequence distribution.[65] The heat flow curves of high and low grafting density gradient copolymer particle brushes are shown in **Figure 13.1**a and **Figure 13.1**b, which were obtained by DSC. Despite the different molecular weights among samples in the same series, a clear trend in which the major T_g increases with

higher PMMA contents in polymer ligands is observed in both high/low grafting density particle brush systems. Moreover, although the low grafting density particle brushes have much higher silica content, as fewer polymer ligands are attached to the surfaces, with the same BA/MMA compositions, they have very close T_gs to those determined for high grafting density particle brushes, which are listed in **Table 13.1**. The thermal behavior of the gradient copolymer particle brushes was also investigated by a DMA oscillation test on the bulk films. Standard bulk films of gradient copolymer particle brushes, 15 mm × 5 mm, were fabricated through a solvent-casting method in Teflon molds, **Figure S13.4**. Due to the over-softening of the samples under high temperature, the test conditions were limited to the temperature range from -50 to 80 ºC. The same trend as shown in DSC plots was observed in the DMA measurements, where the T_gs can be obtained from the plot of time-dependent tanδ *vs.* temperature. Generally, with higher PMMA fractions in the polymer ligands, a higher T_g and greater strength of the polymer composite can be expected.

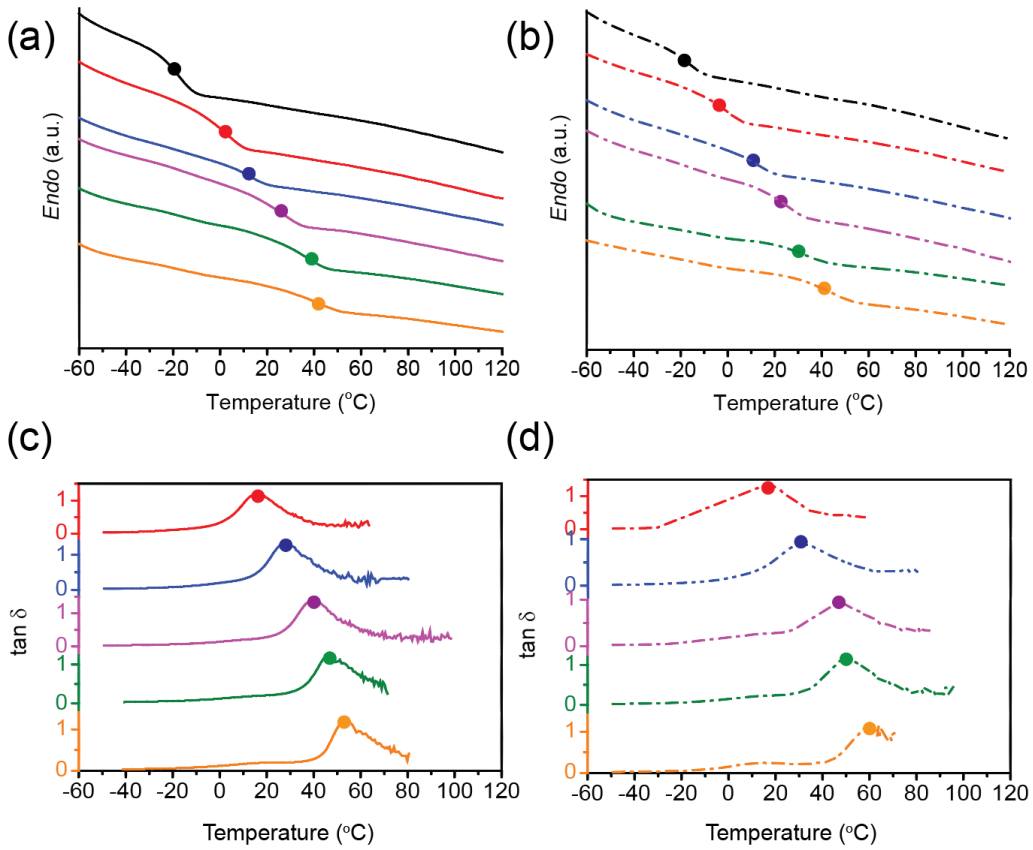

Figure 13.1. (a) DSC curves for high grafting density gradient copolymer particle brushes (HG-1: black, HG-2: red, HG-3: blue, HG-4: magenta, HG-5: olive, HG-6: orange), (b) DSC curves for low grafting density gradient copolymer particle brushes (LG-1: black, LG-2: red, LG-3: blue, LG-4: magenta, LG-5: olive, LG-6: orange), (c) time-dependent *tan δ* variation for high grafting density gradient copolymer particle brushes (HG-2: red, HG-3: blue, HG-4: magenta, HG-5: olive, HG-6: orange), (d) time-dependent *tan δ* variation for low grafting density gradient copolymer particle brushes (LG-2: red, LG-3: blue, LG-4: magenta, LG-5: olive, LG-6: orange). The T_gs are highlighted with solid points in the figures.

In order to better understand the chain conformation and architecture in the gradient copolymer particle brushes, the first derivatives of DSC heating curves with respect to temperature were plotted in **Figure 13.2**a and **Figure 13.2**b, which can facilitate the comparison of the T_g among the various systems and provide more detailed information about morphological changes in the polymer chains.[66] In contrast to the single T_g shown in heat flow curves, more complicated features are observed in the first derivatives of heating curves, which are marked in the plots. Compared to HG/LG-1~3, two featured peaks around -30 ºC and 100 ºC were observed

in HG-5~6 and LG-4-6, (**Figure S13.4-5**), which corresponded to the formation of BA/PMMA-rich regimes in the samples, **Scheme 13.2**. This is can be attributed to the increase of chain length and more significant gradient sequence in the polymer ligands that resulted from the acceleration of PMMA feeding rate. The formation of "multiple core-shell coronas" structure (PBA-rich inner shell, and PMMA-rich outer shell) would not only influence the thermal behavior but also dramatically affect the mechanical properties of the polymer nanocomposite.

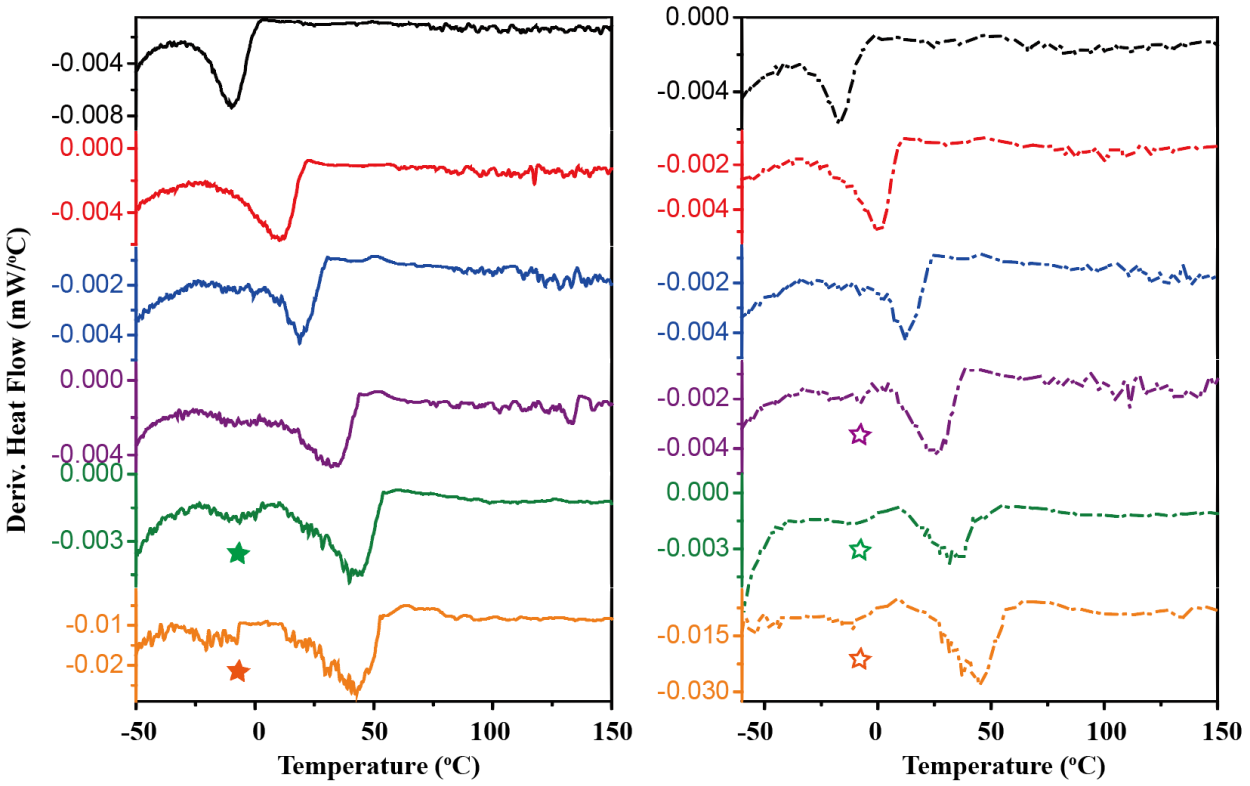

Figure 13.2. (a) plot of deriv. heat flow *vs.* temperature of high grafting density gradient copolymer particle brushes (HG-1: black, HG-2: red, HG-3: blue, HG-4: magenta, HG-5: olive, HG-6: orange), (b) plot of deriv. heat flow *vs.* temperature of low grafting density gradient copolymer particle brushes (LG-1: black, LG-2: red, LG-3: blue, LG-4: magenta, LG-5: olive, LG-6: orange). The stars in the plots highlight the minor T_gs in the samples which have PBA/PMMA-rich regimes.

Scheme 13.2. "Multiple core-shell coronas" structure in gradient copolymer particle brushes

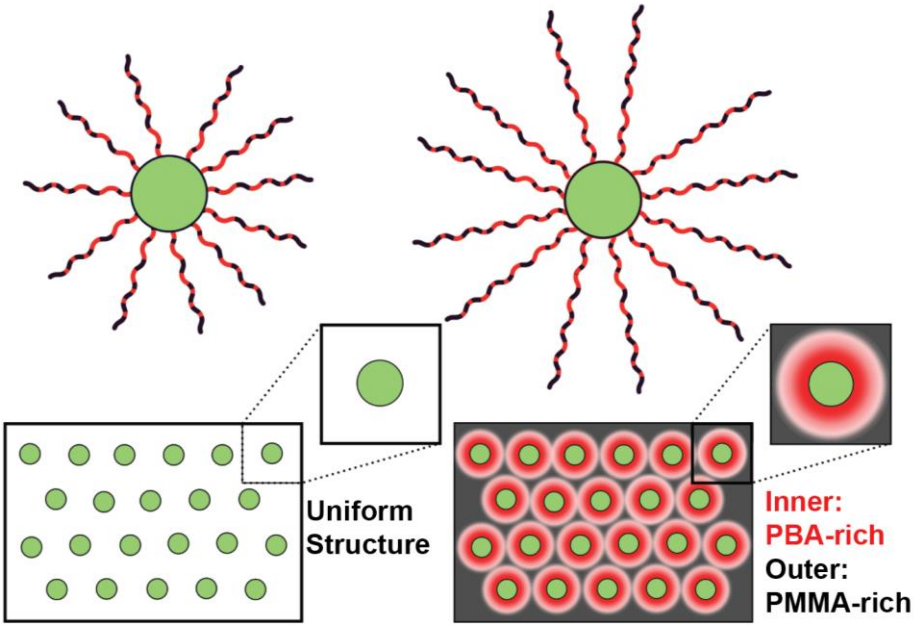

Young's modulus and toughness were first examined *via* uniaxial tensile test at a constant tensile rate of 0.005 mm/s at room temperature to study the mechanical properties of the gradient copolymer particle brushes. The detailed strain-stress curves are shown in **Figure S13.7** and **Figure S13.8**, and the corresponded Young's modulus and toughness were calculated from the incipient linear slope and integrating the area under curves, which are summarized in the bar graphs, **Figure 13.3**a and **Figure 13.3**b. The absence of the LG-1 measurement in the plot is due to the low molecular weight of LG-1 polymer ligands, which results in less entanglement among the chains and makes a coherent film fabrication impossible. As shown in **Figures 13.3**a and **Figure 13.3**b, Young's modulus of gradient copolymer particle brushes increased from HG-1 to HG-6 (LG-2 to LG-6), and dramatic enhancements are displayed for samples HG-4 (52.0 MPa) to HG-5 (521.0 MPa) and from LG-3 (47.1 MPa) to LG-4 (332.1 MPa), around a 9-fold and a 6-fold increase, respectively. The improvement in the strength of the materials could be attributed to the introduction of the silica nanofillers and the increasing fraction of PMMA compositions.

To further study these effects, plots of the dependence of Young's modulus with SiO_2 fraction and PMMA fraction are shown in **Figure S13.11**. Unexpectedly, instead of increasing, the modulus decreased with the increasing silica content, **Figure S13.11**a and **Figure S13.11**b, on the other hand, a positive correlation between Young's modulus of the bulk films and the PMMA composition was observed, **Figure S13.11**c and **Figure S13.11**d. It should be noted that the sharp enhancement of Young's modulus in the sample series, HG-5/LG-4, can be attributed to the formation of localized PMMA-rich shell regimes, which was earlier illustrated in the derivative heat flow curves. Benefits from the high uniformity of the particle brushes and precise control of the chain confirmation/architecture by SI-ATRP, the more rigid interpenetrating PMMA-rich shells were homogeneously distributed over the bulk films, which significantly improve the stiffness of the materials. The toughness of high and low grafting density particle brushes are shown in **Figure 13.3**a and **Figure 13.3**b. As observed in Young's modulus, a similar trend that the toughness increased with increasing PMMA fractions was expected. However, as is well-known for brittle materials, there is a tradeoff, as constantly increasing the PMMA composition indeed enhances the strength of the materials but decreases the toughness, which is shown the sharp drops from HG-5 ($5.15\times 10^9\, J\cdot m^3$) to HG-6 ($2.42\times 10^9\, J\cdot m^3$) and LG-5 ($2.33\times 10^9\, J\cdot m^3$) to LG-6 ($0.16\times 10^9\, J\cdot m^3$) in the plots.

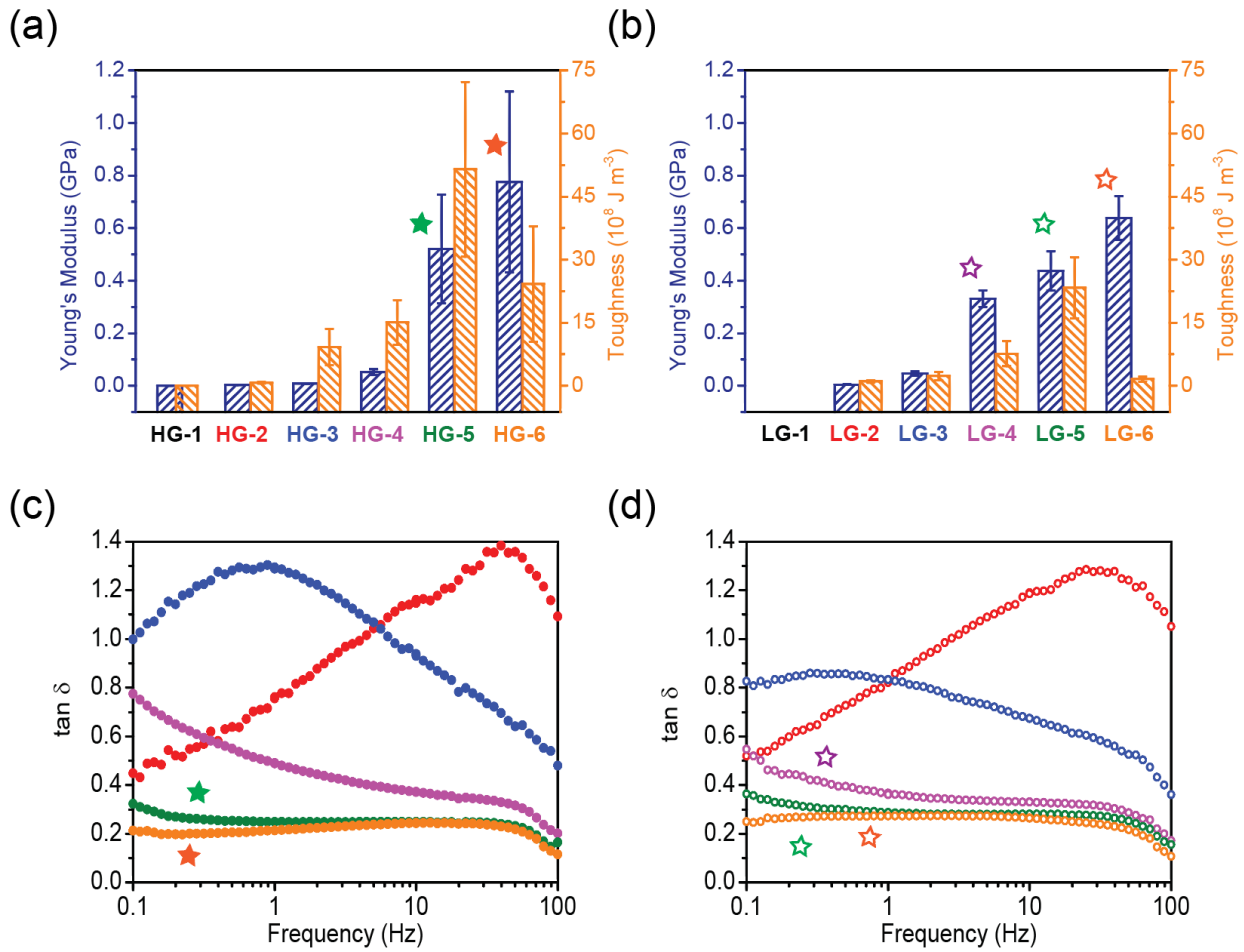

Figure 13.3. (a) Young's modulus and toughness of high grafting density gradient copolymer particle brushes from DMA measurement, (b) Young's modulus and toughness of low grafting density gradient copolymer particle brushes from DMA measurement, (c) frequency-dependent *tan δ* variation for high grafting density gradient copolymer particle brushes: HG-2: red, HG-3: blue, HG-4: magenta, HG-5: olive, HG-6: orange, (d) frequency-dependent *tan δ* variation for low grafting density gradient copolymer particle brushes: LG-2: red, LG-3: blue, LG-4: magenta, LG-5: olive, LG-6: orange. The stars in the plots highlight the sudden changes of the mechanical properties which are corresponded to the formation of multiple "core-shell coronas" structures in the samples.

One of the major advantages of combining PMMA and PBA in the gradient copolymers is the incorporation of PMMA's superior mechanical strength and the excellent damping property of PBA, which is as known as the ability to dissipate energy. The damping property of the gradient copolymer particle brush bulk films was studied *via* DMA over the frequency range of 0.1-100 Hz with 0.1% strain oscillation. The plots of tan *δ vs*. frequency are shown in **Figure 13.3**c and **Figure 13.3**d. The absence of HG-1 in the plots is due to the over-softness of the bulk

films. Soft materials have a better ability to dissipate energy, however, HG-2 and LG-2 at low frequency, which corresponded to high temperature, exhibited liquid-like properties which lead to a poor damping property. Comparing the tan δ curves of HG-2 with HG-3 (LG-2 with LG-3), the peak damping property frequency response is shifted from a high-frequency regime to a low-frequency regime, which is associated with the increasing PMMA fraction in the system. On the other hand, the sudden drops in the plots between HG-4(LG-3) to HG-5(LG-4) can be explained by the increase in the heterogeneity in the samples resulting from the introduction of sole-composition-rich regimes to the system.

Integration of self-healing ability and mechanical robustness is challenging in the fabrication of bulk films for applications.[67] After the detailed investigation of the thermal and mechanical properties of the composite materials, a series of self-healing experiments were designed. For this purpose, each bulk film was cut into two separate parts and gently reattached for about 1 minute, this was followed by thermally annealed the films on a PTFE film substrate under specific temperatures: ca. 20 ºC (room temperature), 50 ºC, 80 ºC, 120 ºC and 150 ºC for the self-healing tests. After 48 hours, the films were characterized by conducting uniaxial tensile tests to investigate the recovery efficiency in strain to fracture, as shown in **Figure S13.12**, **Figure S13.13** and **Table S13.1**. Only in 3 samples show the occurrence of self-repair; samples HG-2, HG-3 and LG-3, each of which possess a narrow BA/MMA compositional range, between 57/43 to 50/50. As shown in **Figure 13.4**, the tensile test curves of the after-healing samples were compared with the undamaged samples. Under the 120 ºC and 48 hours treatment condition, the recovery ratios of high grafting density particle brush HG-2 and HG-3 are 82% and 75%, respectively. However, once the treatment temperature was decreased to 80 ºC, recovery efficiency dropped to 65% and 35%, moreover, no self-healing behaviors were achieved below

50 ºC and room temperature conditions. A similar phenomenon was observed in low grafting density particle brush sample LG-3, as the self-healing efficiency exhibited as 40% for 120 ºC and 15% for 80 ºC. These highly compositional-sensitive self-healing behaviors were reported by Urban and his coworker in linear random/alternating PBA/PMMA copolymers, where the bulk films can self-repair at room temperature within a short time.[6]

The healing observed in gradient copolymer particle brush systems was attributed to molecular interdiffusion across the interface, facilitated by close contact between two surfaces at a temperature higher than T_g, where the molecular chain entanglement would ensure the interdiffusion process along with the completion of the repairing process, leading to a release of the surface energy, a disappearance of the interface and an increase in mechanical strength.[68] To rationalize the highly compositional-sensitive self-healing behavior, Urban and his coworkers raised a hypothesis that the induced dipole interaction between PBA and PMMA segments in the copolymers was envisioned to afford the self-healing properties to the polymeric composites.[6] Compared to the linear copolymers, the similar polymeric compositions' gradient copolymer particle brushes cannot undergo self-repair except under heating conditions, 80/120 ºC. Besides the difference of chain orientation between random/alternating and gradient copolymers, reasonable explanations for these observations could include: 1) the relatively high inorganic fraction of silica nanoparticles, which result is a much lower graft chain mobility compared to free polymer chains, 2) the immobilization of the polymer ligands on the surface of the nanoparticles, which tremendously slow the movements of the chains and affect the chain conformation and orientation of the gradient copolymers ligands.

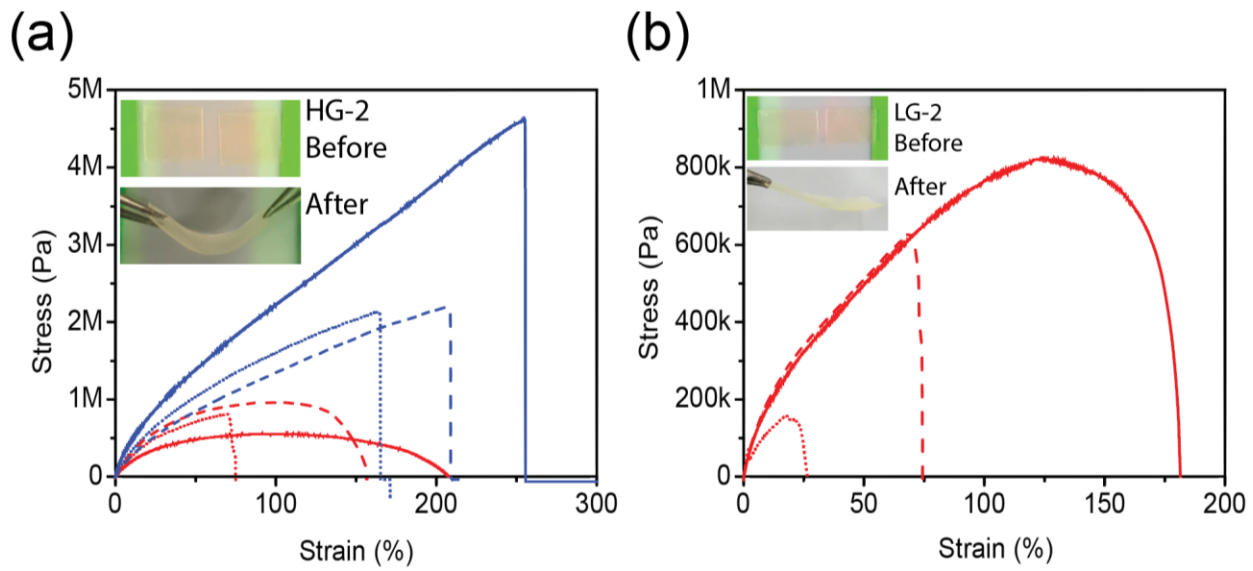

Figure 13.4. Self-healing of gradient copolymer particle brushes: (a) high grafting density gradient copolymer particle brush (solid red: HG-2 before self-healing, dash red: HG-2 self-healing under 120 ºC for 48 hours, dot red: HG-2 self-healing under 80 ºC for 48 hours, solid blue: HG-3 before self-healing, dash blue: HG-3 self-healing under 120 ºC for 48 hours, dot blue: HG-3 self-healing under 80 ºC for 48 hours), inset: photographs of HG-2 gradient copolymer particle brushes bulk film before and after thermal annealing under 80 ºC for 48 hours; (b) low grafting density gradient copolymer particle brush (solid red: LG-2 before self-healing, dash red: LG-2 self-healing under 120 ºC for 48 hours, dot red: LG-2 self-healing under 80 ºC for 48 hours), inset: photographs of LG-2 gradient copolymer particle brushes bulk film before and after thermal annealing under 80 ºC for 48 hours.

13.5. Supporting Information

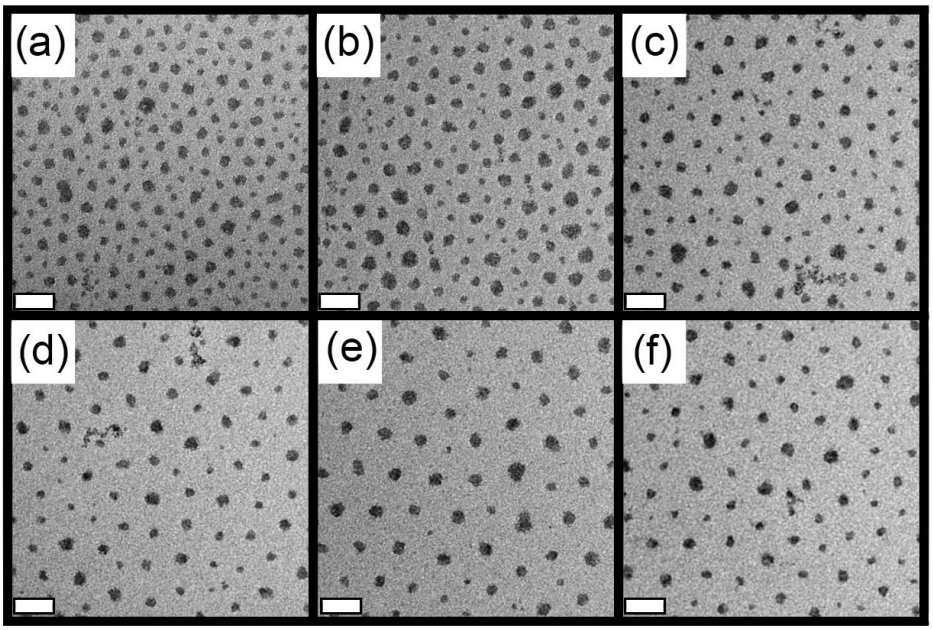

Figure S13.1. TEM images of high grafting density gradient copolymer particle brushes: (a) HG-1, (b) HG-2, (c) HG-3, (d) HG-4, (e) HG-5, (f) HG-6, scale bar: 50 nm.

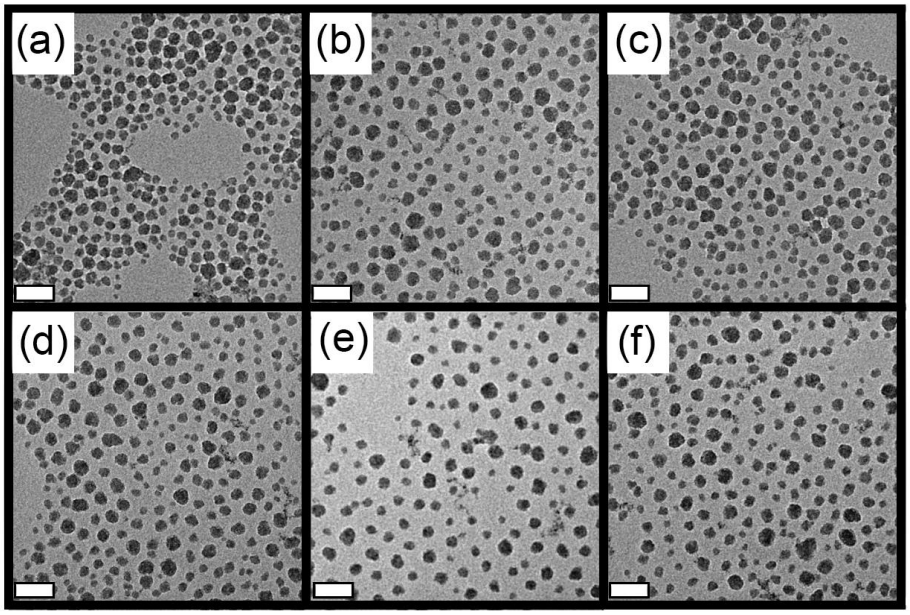

Figure S13.2. TEM images of low grafting density gradient copolymer particle brushes: (a) LG-1, (b) LG-2, (c) LG-3, (d) LG-4, (e) LG-5, (f) LG-6, scale bar: 50 nm.

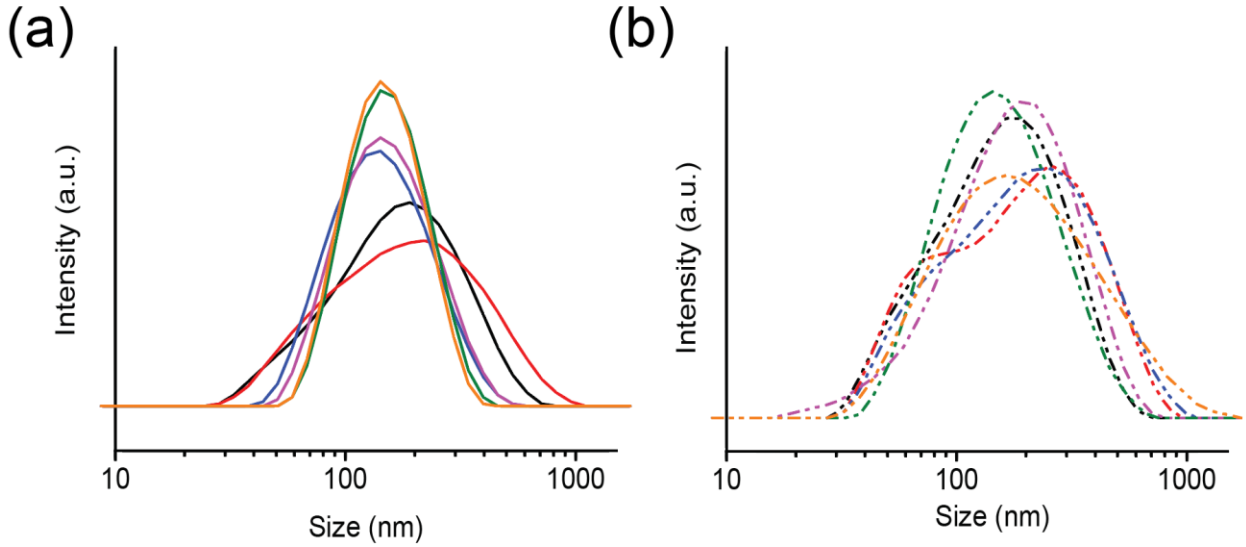

Figure S13.3. DLS traces of (a) high grafting density gradient copolymer particle brushes (HG-1: black, HG-2: red, HG-3: blue, HG-4: magenta, HG-5: olive, HG-6: orange), (b) low grafting density gradient copolymer particle brushes (LG-1: black, LG-2: red, LG-3: blue, LG-4: magenta, LG-5: olive, LG-6: orange)

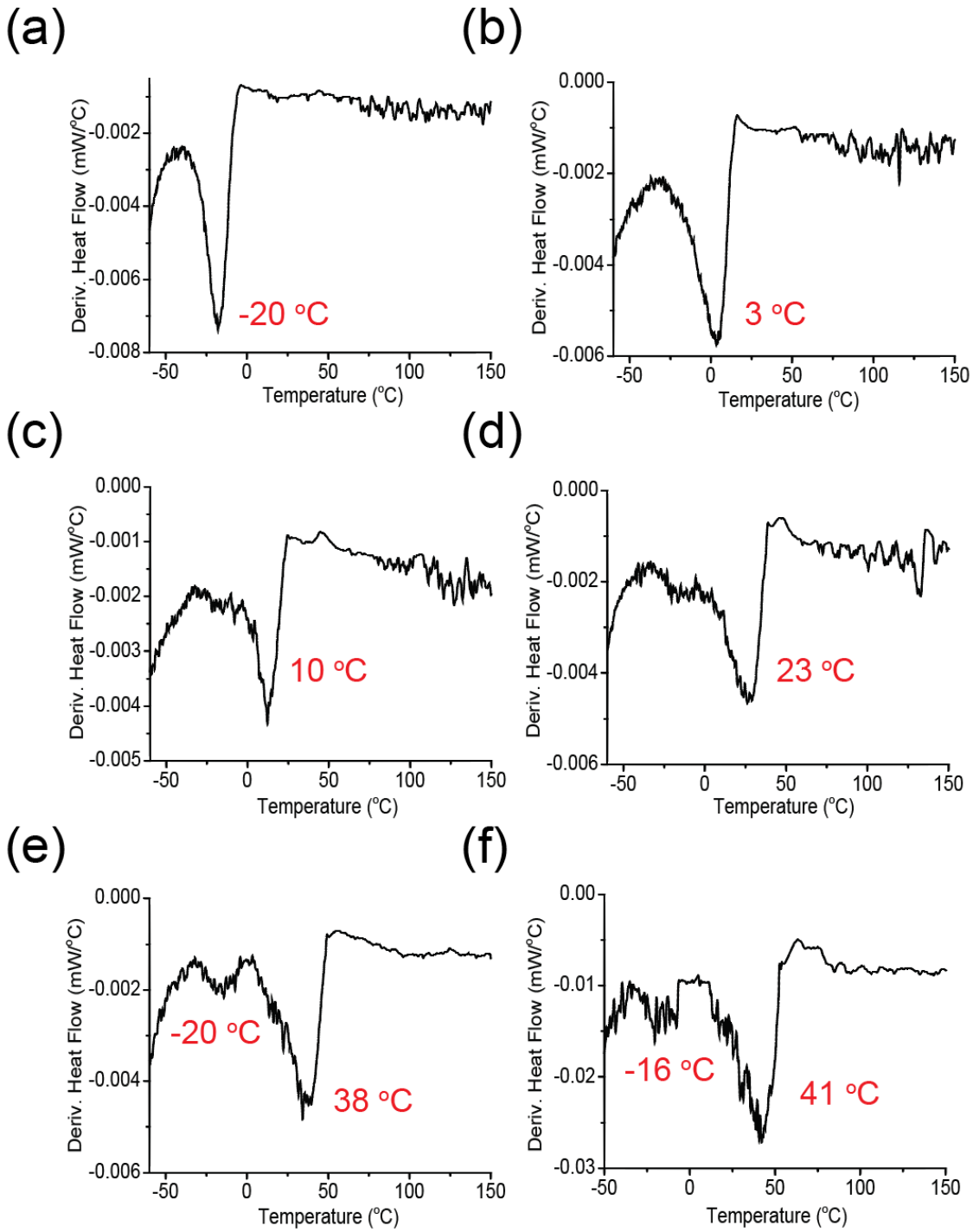

Figure S13.4. The plot of deriv. heat flow *vs*. temperature of high grafting density gradient copolymer particle brushes: (a) HG-1, (b) HG-2, (c) HG-3, (d) HG-4, (e) HG-5, (f) HG-6.

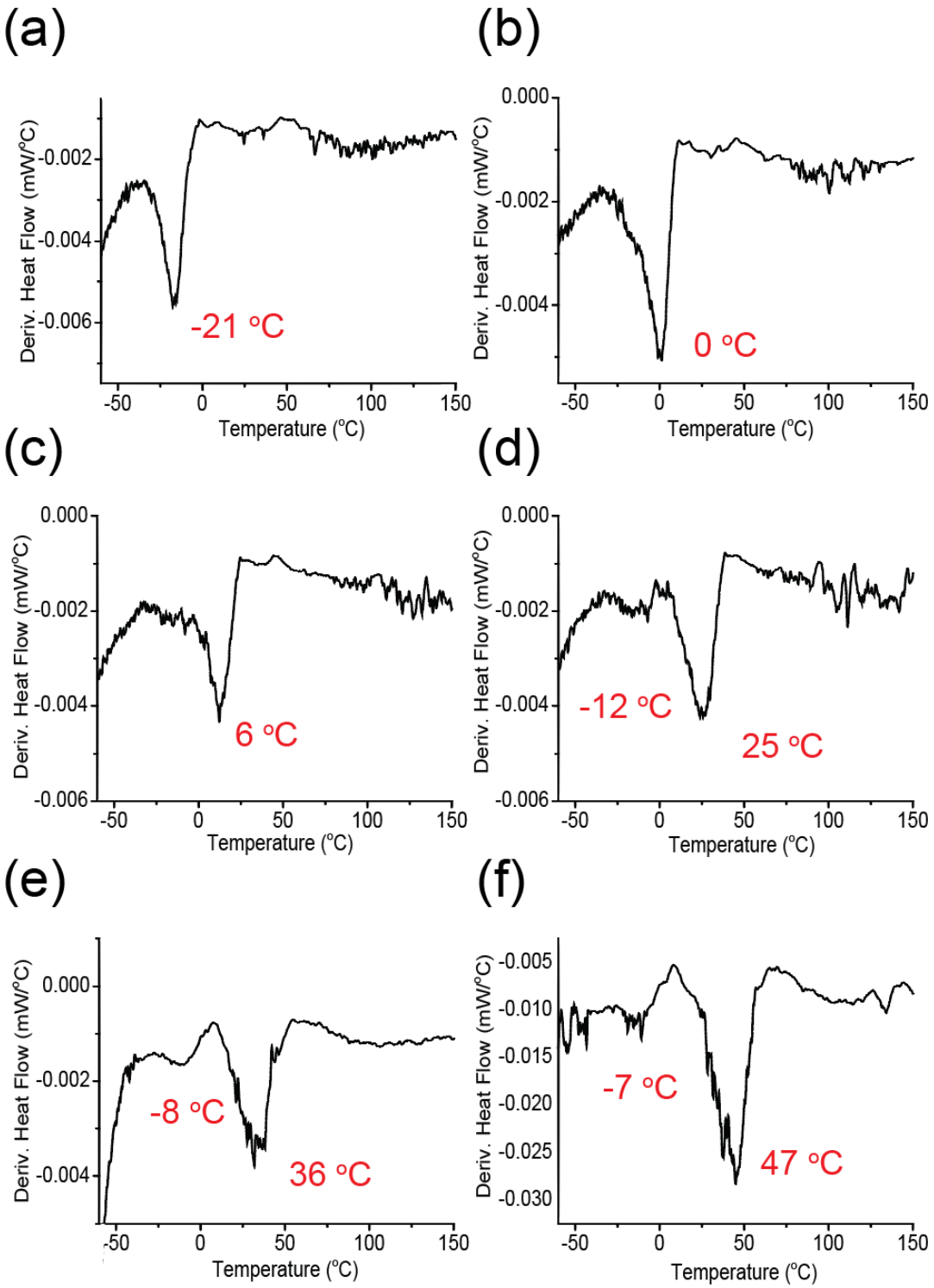

Figure S13.5. Plot of deriv. heat flow *vs*. temperature of low grafting density gradient copolymer particle brushes: (a) LG-1, (b) LG-2, (c) LG-3, (d) LG-4, (e) LG-5, (f) LG-6**.**

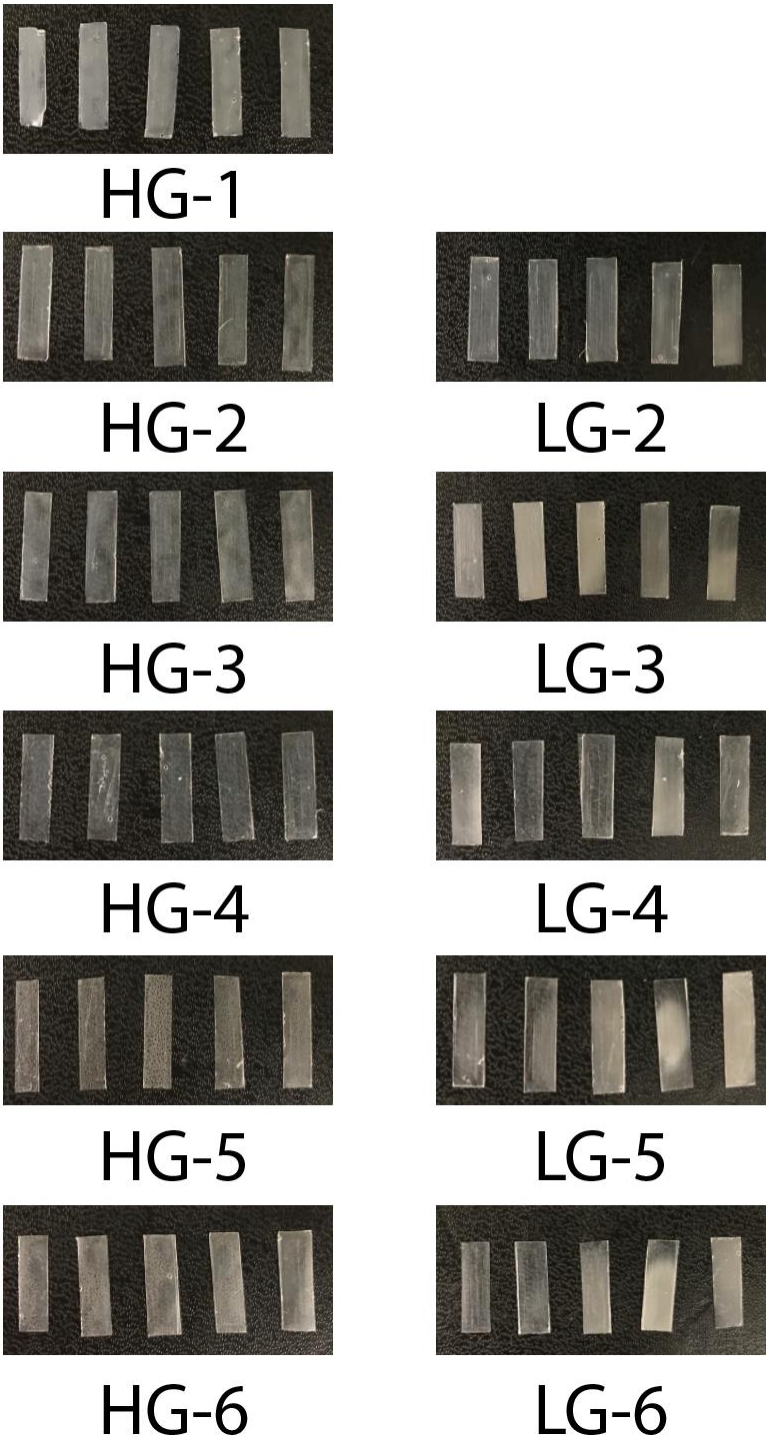

Figure S13.6. Photographs of high and low grafting density gradient copolymer particle brush bulk films, film size: 5×5 mm with thickness ~ 50 to100 μm.

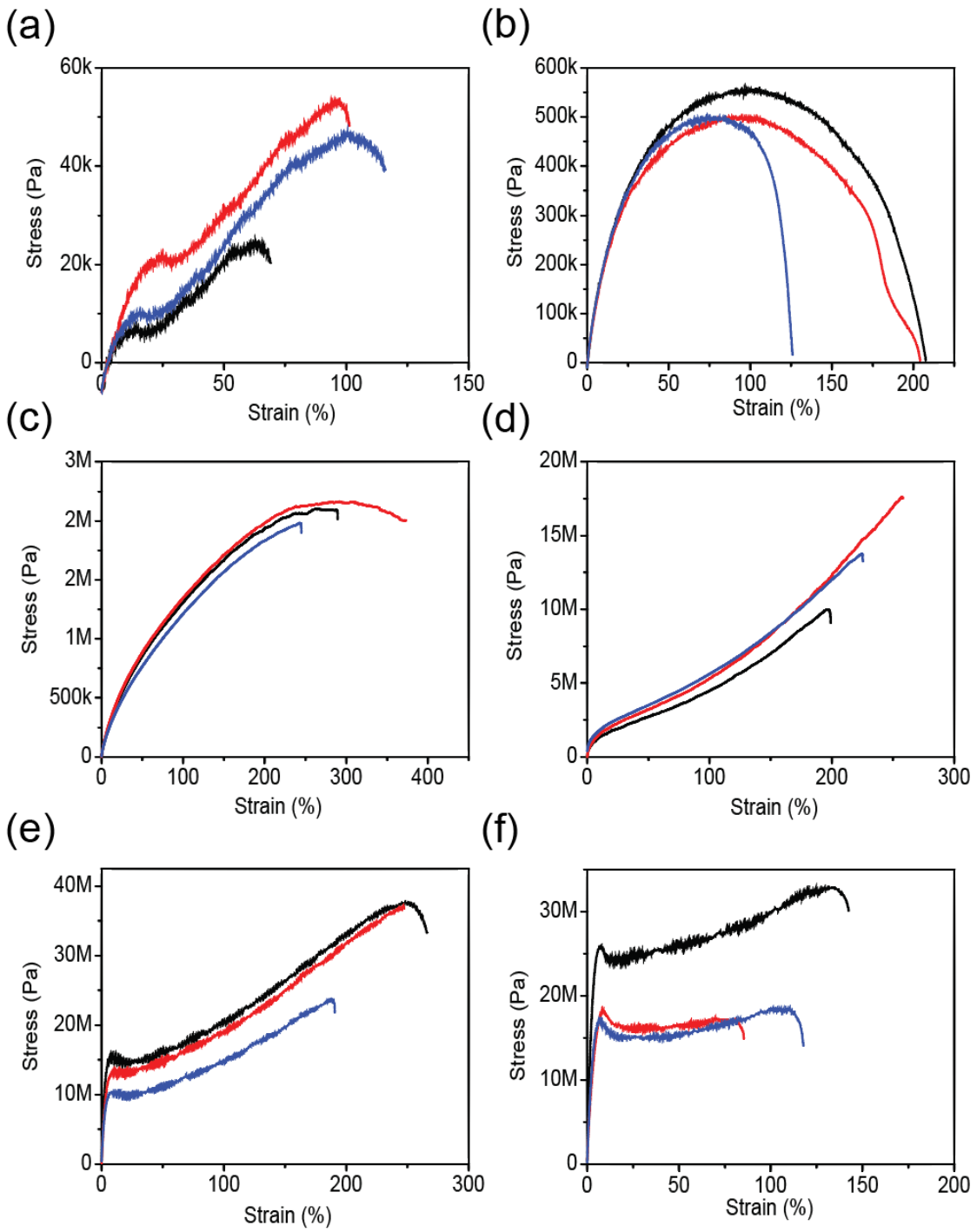

Figure S13.7. Strain-stress curves of high grafting density gradient copolymer particle brushes: (a) HG-1, (b) HG-2, (c) HG-3, (d) HG-4, (e) HG-5, (f) HG-6.

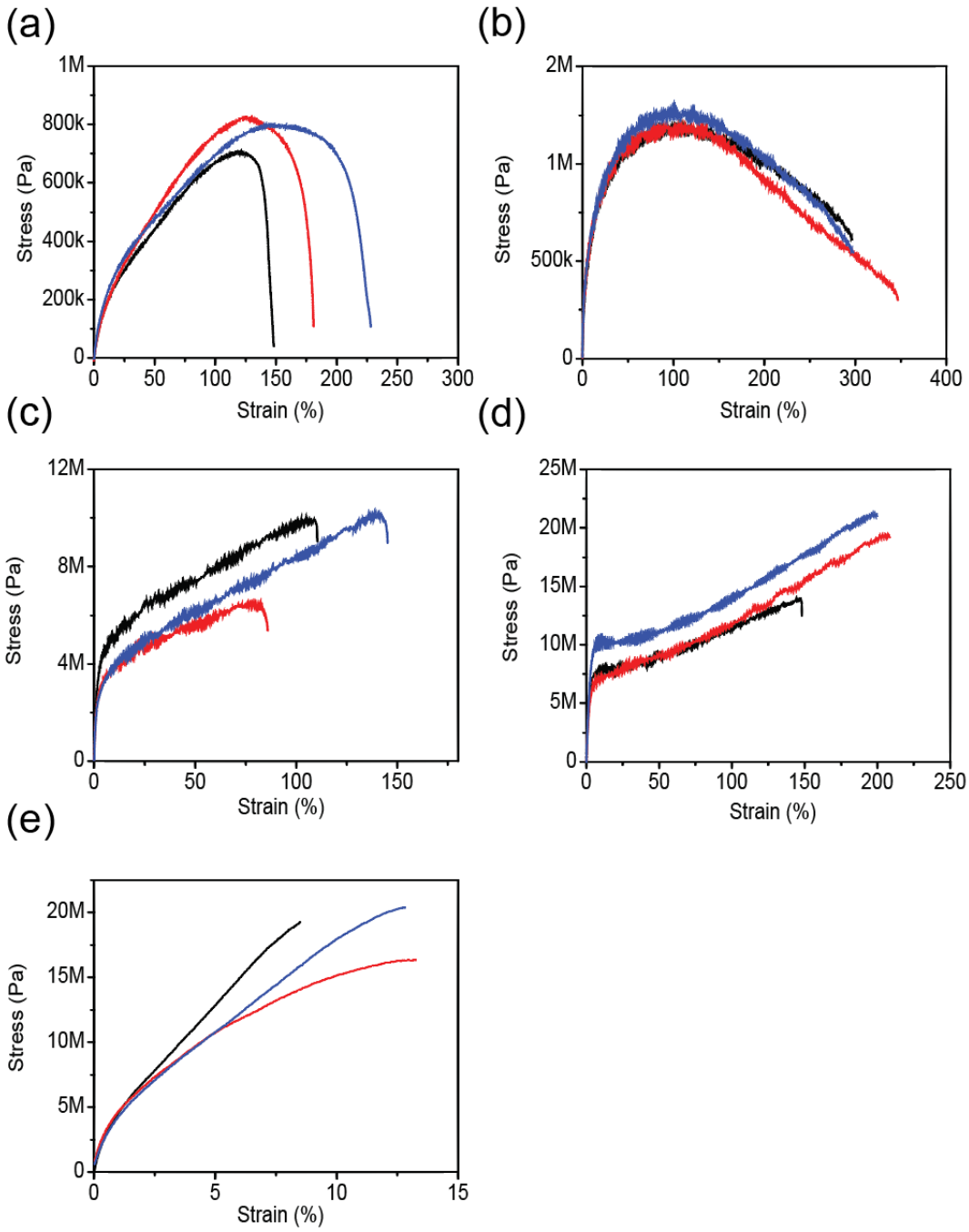

Figure S13.8. Strain-stress curves of low grafting density gradient copolymer particle brushes: (a) LG-2, (b) LG-3, (c) LG-4, (d) LG-5, (e) LG-6.

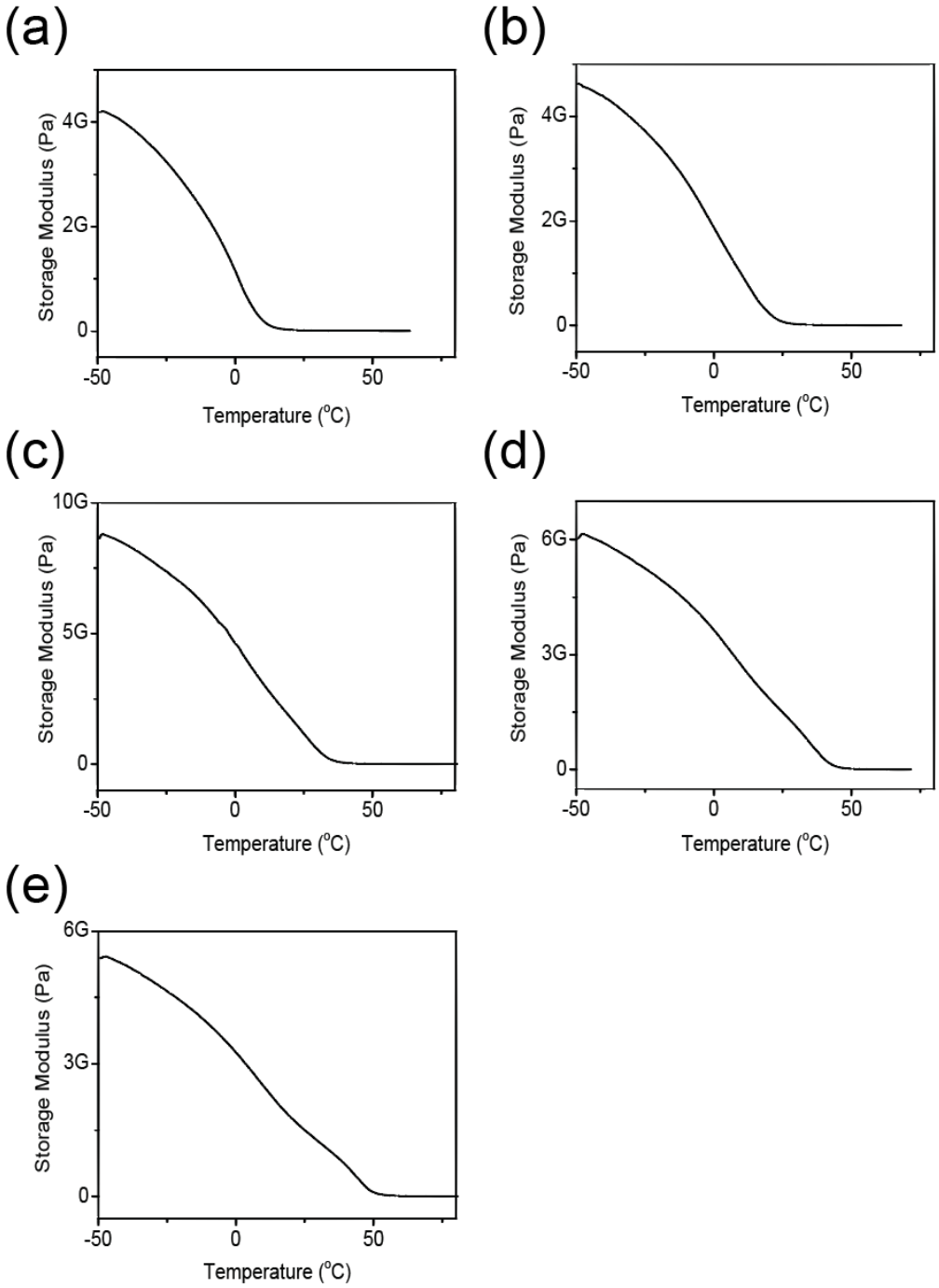

Figure S13.9. Time-dependent storage modulus variation for high grafting density gradient copolymers: (a) HG-2, (b) HG-3, (c) HG-4, (d) HG-5, (e) HG-6.

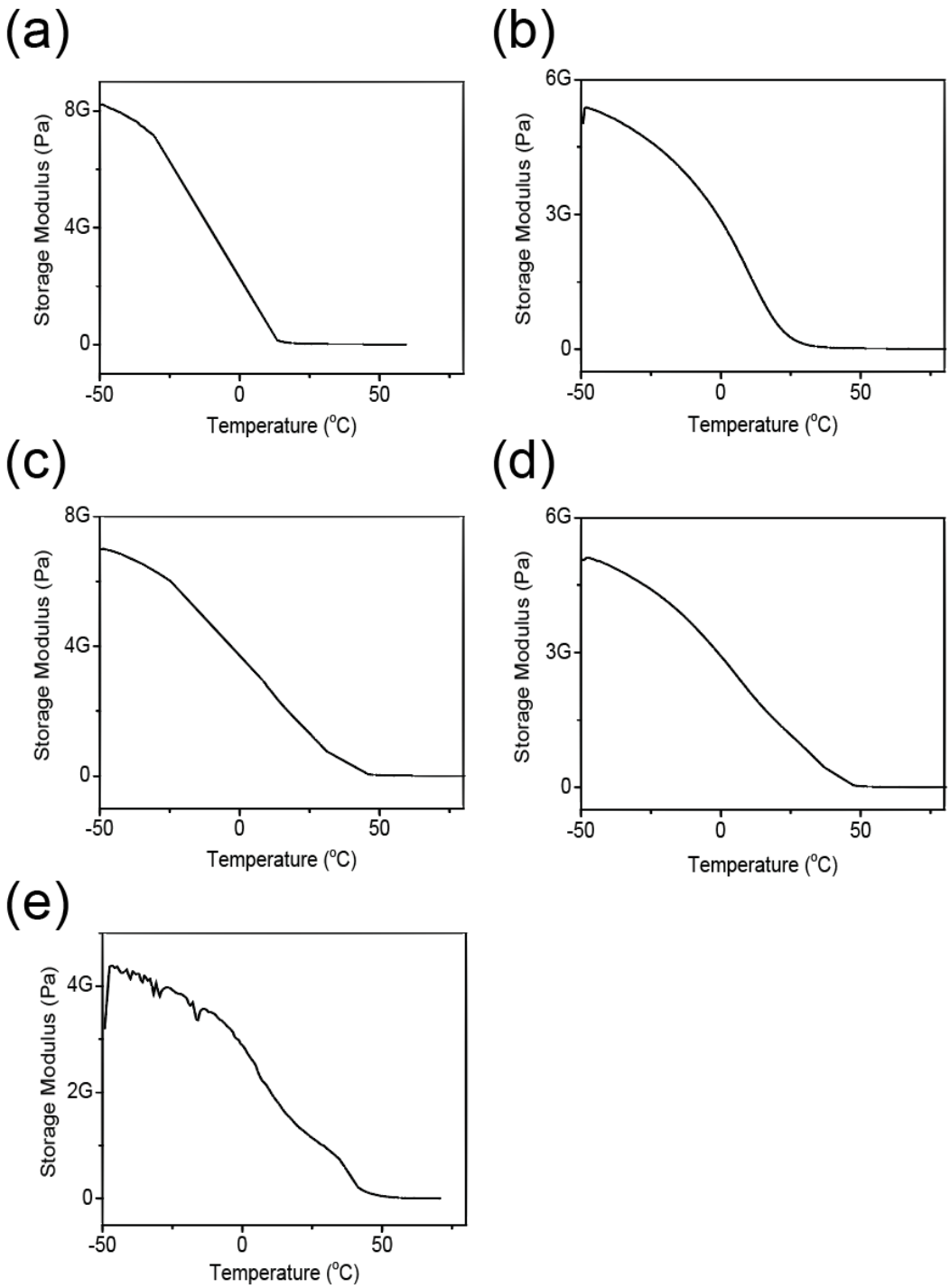

Figure S13.10. Time-dependent storage modulus variation for high grafting density gradient copolymers: (a) LG-2, (b) LG-3, (c) LG-4, (d) LG-5, (e) LG-6.

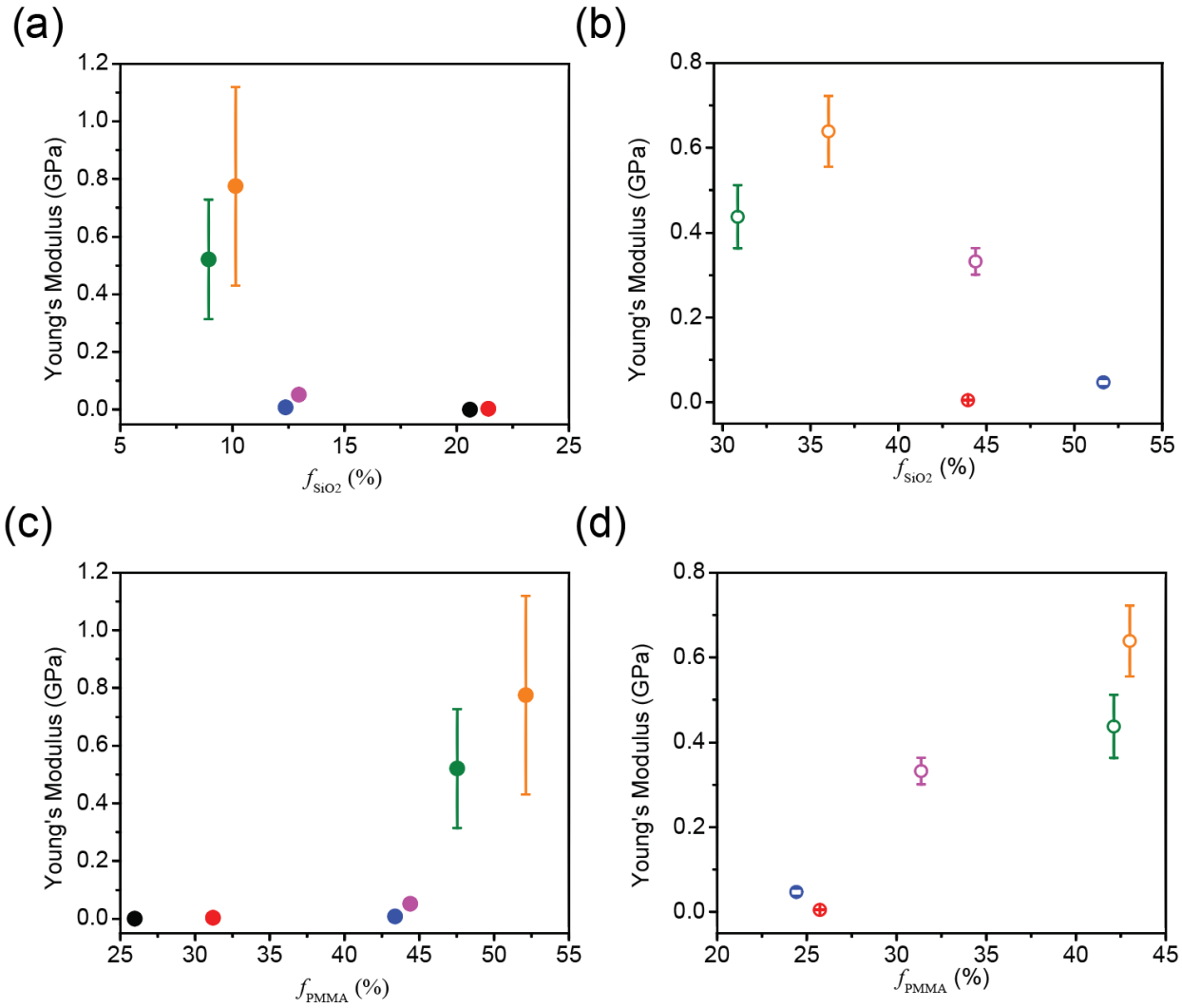

Figure S13.11. (a) Plot of Young's modulus *vs.* f_{SiO2} for high grafting density particle brushes (HG-1: black, HG-2: red, HG-3: blue, HG-4: magenta, HG-5: olive, HG-6: orange), (b) Plot of Young's modulus *vs.* f_{SiO2} for low grafting density particle brushes (LG-2: red, LG-3: blue, LG-4: magenta, LG-5: olive, LG-6: orange), (c) Plot of Young's modulus *vs.* f_{PMMA} for high grafting density particle brushes (HG-1: black, HG-2: red, HG-3: blue, HG-4: magenta, HG-5: olive, HG-6: orange), (d) Plot of Young's modulus *vs.* f_{PMMA} for low grafting density particle brushes (LG-2: red, LG-3: blue, LG-4: magenta, LG-5: olive, LG-6: orange).

Table S13.1. Result of self-healing tests

Entry	Self-healing temperature			
	r.t. (20 ºC)	50 ºC	80 ºC	120 ºC
HG-1	-	-	-	-
HG-2	-	-	65	82
HG-3	-	-	35	75
HG-4	-	-	-	-
HG-5	-	-	-	-
HG-6	-	-	-	-
LG-2	-	-	15	40
LG-3	-	-	-	-
LG-4	-	-	-	-
LG-5	-	-	-	-
LG-6	-	-	-	-

-

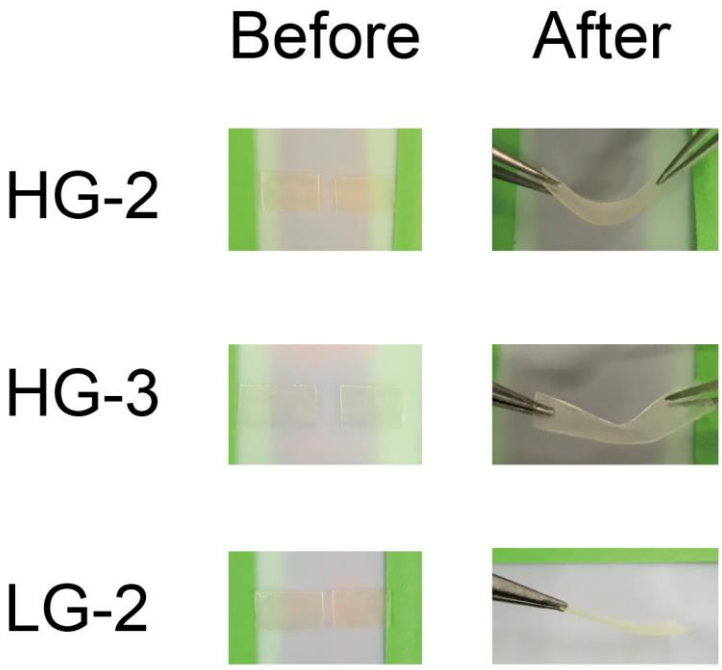

Figure S13.12. Photographs of HG-2 and HG-3 gradient copolymer particle brushes bulk films before and after thermal annealing under 80 ºC for 48 hours.

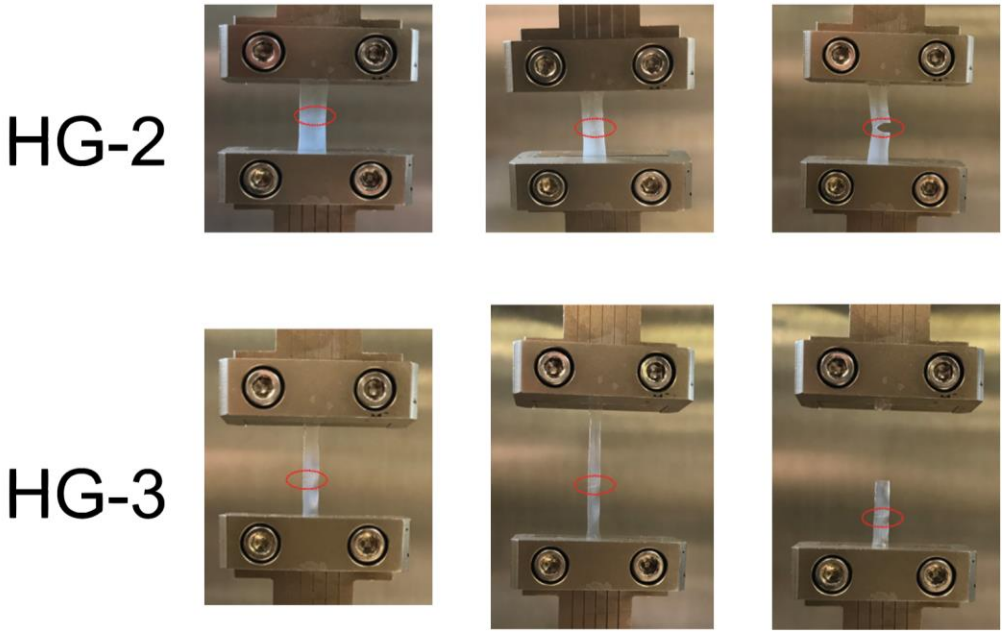

Figure S13.13. Photographs of the tensile tests of HG-2 and HG-3 gradient copolymer particle brushes bulk films after thermal annealing under 80 ºC for 48 hours.

13.6. Conclusions

In conclusion, a facile synthetic route to prepare a series of SiO_2-*g*-PBA-*grad*-PMMA gradient copolymer particle brushes and the fabrication of healable, mechanically strong polymeric nanocomposite bulk films are demonstrated. The concentration of initiating sites' on the functionalized SiO_2-Br particles was controlled by mixing a "dummy" initiator with the ATRP initiator anchors during the functionalization step; two grafting densities of particle brushes were prepared, 0.55 and 0.15 chains/nm^2. The BA/MMA composition in the tethered gradient copolymer ligands was tuned by altering the MMA feeding rate during an ARGET ATRP copolymerization. The morphologies, mechanical robustness and self-healing ability of the gradient copolymer particle brush composites were investigated. The thermal and mechanical properties are not only strongly associated with the composition changes in the polymer ligands, but also the morphological changes induced by the chain length and shape of the gradient, for

example, the necessity for formation of multiple "core-shell" coronas in high MMA composition and high molecular weight particle brushes. Moreover, highly compositional sensitive self-healing behavior was observed, with external heat 80/120 ºC, wherein only the samples with BA contents between 50-55% exhibited self-healing. The selectivity of composition was reported in the literature, which was explained by the induced dipole molecular interaction between PBA and PMMA sections. The requirement of external heat in the current work is mainly attributed to the introduction of high silica loading and localization of chain-ends of the polymer ligands on the surface of the solid nanoparticles. Given the simplicity and scalability, this gradient copolymer grafted nanoparticle approach could be a general method for preparing various self-healable nanocomposites as robust and dynamic functional materials with enhanced life time and durability.

13.7. References

(1) Thangavel, G.; Tan, M. W. M.; Lee, P. S., Advances in self-healing supramolecular soft materials and nanocomposites. *Nano Convergence* **2019,** *6* (1), 29.

(2) Hoogenboom, R., Hard Autonomous Self-Healing Supramolecular Materials—A Contradiction in Terms? *Angew. Chem. Int. Ed.* **2012,** *51* (48), 11942-11944.

(3) Wojtecki, R. J.; Meador, M. A.; Rowan, S. J., Using the dynamic bond to access macroscopically responsive structurally dynamic polymers. *Nat. Mater.* **2011,** *10* (1), 14-27.

(4) Wool, R. P., Self-healing materials: a review. *Soft Matter* **2008,** *4* (3), 400-418.

(5) Toohey, K. S.; Sottos, N. R.; Lewis, J. A.; Moore, J. S.; White, S. R., Self-healing materials with microvascular networks. *Nat. Mater.* **2007,** *6* (8), 581-585.

(6) Urban, M. W.; Davydovich, D.; Yang, Y.; Demir, T.; Zhang, Y.; Casabianca, L., Key-and-lock commodity self-healing copolymers. *Science* **2018,** *362* (6411), 220-225.

(7) Sumerlin, B. S., Next-generation self-healing materials. *Science* **2018,** *362* (6411), 150-151.

(8) Murphy, E. B.; Wudl, F., The world of smart healable materials. *Prog. Polym. Sci.* **2010,** *35* (1), 223-251.

(9) Hager, M. D.; Greil, P.; Leyens, C.; van der Zwaag, S.; Schubert, U. S., Self-Healing Materials. *Adv. Mater.* **2010,** *22* (47), 5424-5430.

(10) Guo, H.; Fang, X.; Zhang, L.; Sun, J., Facile Fabrication of Room-Temperature Self-Healing, Mechanically Robust, Highly Stretchable, and Tough Polymers Using Dual Dynamic Cross-Linked Polymer Complexes. *ACS Appl. Mater. Interfaces* **2019,** *11* (36), 33356-33363.

(11) Patrick, J. F.; Robb, M. J.; Sottos, N. R.; Moore, J. S.; White, S. R., Polymers with autonomous life-cycle control. *Nature* **2016,** *540*, 363.
(12) Yanagisawa, Y.; Nan, Y.; Okuro, K.; Aida, T., Mechanically robust, readily repairable polymers via tailored noncovalent cross-linking. *Science* **2018,** *359* (6371), 72-76.
(13) Chen, Y.; Kushner, A. M.; Williams, G. A.; Guan, Z., Multiphase design of autonomic self-healing thermoplastic elastomers. *Nat. Chem.* **2012,** *4* (6), 467-472.
(14) South, A. B.; Lyon, L. A., Autonomic Self-Healing of Hydrogel Thin Films. *Angew. Chem. Int. Ed.* **2010,** *49* (4), 767-771.
(15) Burnworth, M.; Tang, L.; Kumpfer, J. R.; Duncan, A. J.; Beyer, F. L.; Fiore, G. L.; Rowan, S. J.; Weder, C., Optically healable supramolecular polymers. *Nature* **2011,** *472* (7343), 334-337.
(16) Montarnal, D.; Capelot, M.; Tournilhac, F.; Leibler, L., Silica-Like Malleable Materials from Permanent Organic Networks. *Science* **2011,** *334* (6058), 965-968.
(17) Schneiderman, D. K.; Hillmyer, M. A., 50th Anniversary Perspective: There Is a Great Future in Sustainable Polymers. *Macromolecules* **2017,** *50* (10), 3733-3749.
(18) Yang, Y.; Davydovich, D.; Hornat, C. C.; Liu, X.; Urban, M. W., Leaf-Inspired Self-Healing Polymers. *Chem* **2018,** *4* (8), 1928-1936.
(19) Burattini, S.; Colquhoun, H. M.; Fox, J. D.; Friedmann, D.; Greenland, B. W.; Harris, P. J. F.; Hayes, W.; Mackay, M. E.; Rowan, S. J., A self-repairing, supramolecular polymer system: healability as a consequence of donor–acceptor π–π stacking interactions. *Chem. Commun.* **2009,** (44), 6717-6719.
(20) Shchukin, D. G.; Möhwald, H., Self-Repairing Coatings Containing Active Nanoreservoirs. *Small* **2007,** *3* (6), 926-943.
(21) Blaiszik, B. J.; Kramer, S. L. B.; Olugebefola, S. C.; Moore, J. S.; Sottos, N. R.; White, S. R., Self-Healing Polymers and Composites. *Annual Review of Materials Research* **2010,** *40* (1), 179-211.
(22) Burattini, S.; Greenland, B. W.; Chappell, D.; Colquhoun, H. M.; Hayes, W., Healable polymeric materials: a tutorial review. *Chem. Soc. Rev.* **2010,** *39* (6), 1973-1985.
(23) Mauldin, T. C.; Kessler, M. R., Self-healing polymers and composites. *Int. Mater. Rev.* **2010,** *55* (6), 317-346.
(24) Yang, Y.; Urban, M. W., Self-healing polymeric materials. *Chem. Soc. Rev.* **2013,** *42* (17), 7446-7467.
(25) Ahner, J.; Pretzel, D.; Enke, M.; Geitner, R.; Zechel, S.; Popp, J.; Schubert, U. S.; Hager, M. D., Conjugated Oligomers as Fluorescence Marker for the Determination of the Self-Healing Efficiency in Mussel-Inspired Polymers. *Chem. Mater.* **2018,** *30* (8), 2791-2799.
(26) Chen, X.; Dam, M. A.; Ono, K.; Mal, A.; Shen, H.; Nutt, S. R.; Sheran, K.; Wudl, F., A Thermally Re-mendable Cross-Linked Polymeric Material. *Science* **2002,** *295* (5560), 1698-1702.
(27) Burattini, S.; Greenland, B. W.; Merino, D. H.; Weng, W.; Seppala, J.; Colquhoun, H. M.; Hayes, W.; Mackay, M. E.; Hamley, I. W.; Rowan, S. J., A Healable Supramolecular Polymer Blend Based on Aromatic π–π Stacking and Hydrogen-Bonding Interactions. *J. Am. Chem. Soc.* **2010,** *132* (34), 12051-12058.
(28) Klukovich, H. M.; Kean, Z. S.; Iacono, S. T.; Craig, S. L., Mechanically Induced Scission and Subsequent Thermal Remending of Perfluorocyclobutane Polymers. *J. Am. Chem. Soc.* **2011,** *133* (44), 17882-17888.

(29) Amamoto, Y.; Kamada, J.; Otsuka, H.; Takahara, A.; Matyjaszewski, K., Repeatable Photoinduced Self-Healing of Covalently Cross-Linked Polymers through Reshuffling of Trithiocarbonate Units. *Angew. Chem. Int. Ed.* **2011,** *50* (7), 1660-1663.
(30) Ghosh, B.; Urban, M. W., Self-Repairing Oxetane-Substituted Chitosan Polyurethane Networks. *Science* **2009,** *323* (5920), 1458-1460.
(31) White, S. R.; Sottos, N. R.; Geubelle, P. H.; Moore, J. S.; Kessler, M. R.; Sriram, S. R.; Brown, E. N.; Viswanathan, S., Autonomic healing of polymer composites. *Nature* **2001,** *409* (6822), 794-797.
(32) Wang, Q.; Mynar, J. L.; Yoshida, M.; Lee, E.; Lee, M.; Okuro, K.; Kinbara, K.; Aida, T., High-water-content mouldable hydrogels by mixing clay and a dendritic molecular binder. *Nature* **2010,** *463* (7279), 339-343.
(33) Montarnal, D.; Tournilhac, F.; Hidalgo, M.; Couturier, J.-L.; Leibler, L., Versatile One-Pot Synthesis of Supramolecular Plastics and Self-Healing Rubbers. *J. Am. Chem. Soc.* **2009,** *131* (23), 7966-7967.
(34) Cordier, P.; Tournilhac, F.; Soulié-Ziakovic, C.; Leibler, L., Self-healing and thermoreversible rubber from supramolecular assembly. *Nature* **2008,** *451* (7181), 977-980.
(35) Appel, E. A.; Biedermann, F.; Rauwald, U.; Jones, S. T.; Zayed, J. M.; Scherman, O. A., Supramolecular Cross-Linked Networks via Host−Guest Complexation with Cucurbit[8]uril. *J. Am. Chem. Soc.* **2010,** *132* (40), 14251-14260.
(36) Lu, Y.-X.; Guan, Z., Olefin Metathesis for Effective Polymer Healing via Dynamic Exchange of Strong Carbon–Carbon Double Bonds. *J. Am. Chem. Soc.* **2012,** *134* (34), 14226-14231.
(37) Bergman, S. D.; Wudl, F., Mendable polymers. *J. Mater. Chem.* **2008,** *18* (1), 41-62.
(38) Liu, K.; Kang, Y.; Wang, Z.; Zhang, X., 25th Anniversary Article: Reversible and Adaptive Functional Supramolecular Materials: "Noncovalent Interaction" Matters. *Adv. Mater.* **2013,** *25* (39), 5530-5548.
(39) Yamaguchi, H.; Kobayashi, Y.; Kobayashi, R.; Takashima, Y.; Hashidzume, A.; Harada, A., Photoswitchable gel assembly based on molecular recognition. *Nat. Commun.* **2012,** *3* (1), 603.
(40) Noda, Y.; Hayashi, Y.; Ito, K., From topological gels to slide-ring materials. *J. Appl. Polym. Sci.* **2014,** *131* (15).
(41) Yang, R.; Peng, S.; Wan, W.; Hughes, T. C., Azobenzene based multistimuli responsive supramolecular hydrogels. *J. Mater. Chem. C* **2014,** *2* (43), 9122-9131.
(42) Ogawa, Y.; Yoshiyama, C.; Kitaoka, T., Helical Assembly of Azobenzene-Conjugated Carbohydrate Hydrogelators with Specific Affinity for Lectins. *Langmuir* **2012,** *28* (9), 4404-4412.
(43) Deindörfer, P.; Eremin, A.; Stannarius, R.; Davis, R.; Zentel, R., Gelation of smectic liquid crystal phases with photosensitive gel forming agents. *Soft Matter* **2006,** *2* (8), 693-698.
(44) Capelot, M.; Montarnal, D.; Tournilhac, F.; Leibler, L., Metal-Catalyzed Transesterification for Healing and Assembling of Thermosets. *J. Am. Chem. Soc.* **2012,** *134* (18), 7664-7667.
(45) Sottos, N. R.; Moore, J. S., Spot-on healing. *Nature* **2011,** *472* (7343), 299-300.
(46) Neal, J. A.; Mozhdehi, D.; Guan, Z., Enhancing Mechanical Performance of a Covalent Self-Healing Material by Sacrificial Noncovalent Bonds. *J. Am. Chem. Soc.* **2015,** *137* (14), 4846-4850.

(47) Akcora, P.; Liu, H.; Kumar, S. K.; Moll, J.; Li, Y.; Benicewicz, B. C.; Schadler, L. S.; Acehan, D.; Panagiotopoulos, A. Z.; Pryamitsyn, V.; Ganesan, V.; Ilavsky, J.; Thiyagarajan, P.; Colby, R. H.; Douglas, J. F., Anisotropic self-assembly of spherical polymer-grafted nanoparticles. *Nat. Mater.* **2009,** *8* (4), 354-359.
(48) Kumar, S. K.; Jouault, N.; Benicewicz, B.; Neely, T., Nanocomposites with Polymer Grafted Nanoparticles. *Macromolecules* **2013,** *46* (9), 3199-3214.
(49) Lin, Y.; Böker, A.; He, J.; Sill, K.; Xiang, H.; Abetz, C.; Li, X.; Wang, J.; Emrick, T.; Long, S.; Wang, Q.; Balazs, A.; Russell, T. P., Self-directed self-assembly of nanoparticle/copolymer mixtures. *Nature* **2005,** *434* (7029), 55-59.
(50) Klajn, R.; Bishop, K. J. M.; Fialkowski, M.; Paszewski, M.; Campbell, C. J.; Gray, T. P.; Grzybowski, B. A., Plastic and Moldable Metals by Self-Assembly of Sticky Nanoparticle Aggregates. *Science* **2007,** *316* (5822), 261-264.
(51) Murray, C. B.; Kagan, C. R.; Bawendi, M. G., Self-Organization of CdSe Nanocrystallites into Three-Dimensional Quantum Dot Superlattices. *Science* **1995,** *270* (5240), 1335-1338.
(52) Kalsin, A. M.; Fialkowski, M.; Paszewski, M.; Smoukov, S. K.; Bishop, K. J. M.; Grzybowski, B. A., Electrostatic Self-Assembly of Binary Nanoparticle Crystals with a Diamond-Like Lattice. *Science* **2006,** *312* (5772), 420-424.
(53) Mueggenburg, K. E.; Lin, X.-M.; Goldsmith, R. H.; Jaeger, H. M., Elastic membranes of close-packed nanoparticle arrays. *Nat. Mater.* **2007,** *6* (9), 656-660.
(54) Bigioni, T. P.; Lin, X.-M.; Nguyen, T. T.; Corwin, E. I.; Witten, T. A.; Jaeger, H. M., Kinetically driven self assembly of highly ordered nanoparticle monolayers. *Nat. Mater.* **2006,** *5* (4), 265-270.
(55) Choi, J.; Dong, H.; Matyjaszewski, K.; Bockstaller, M. R., Flexible Particle Array Structures by Controlling Polymer Graft Architecture. *J. Am. Chem. Soc.* **2010,** *132* (36), 12537-12539.
(56) Fernandes, N. J.; Koerner, H.; Giannelis, E. P.; Vaia, R. A., Hairy nanoparticle assemblies as one-component functional polymer nanocomposites: opportunities and challenges. *MRS Communications* **2013,** *3* (1), 13-29.
(57) Wang, J.-S.; Matyjaszewski, K., Controlled/"living" radical polymerization. atom transfer radical polymerization in the presence of transition-metal complexes. *J. Am. Chem. Soc.* **1995,** *117* (20), 5614-5615.
(58) Matyjaszewski, K.; Xia, J., Atom Transfer Radical Polymerization. *Chem. Rev.* **2001,** *101* (9), 2921-2990.
(59) Kamigaito, M.; Ando, T.; Sawamoto, M., Metal-Catalyzed Living Radical Polymerization. *Chem. Rev.* **2001,** *101* (12), 3689-3746.
(60) Kato, M.; Kamigaito, M.; Sawamoto, M.; Higashimura, T., Polymerization of Methyl Methacrylate with the Carbon Tetrachloride/Dichlorotris-(triphenylphosphine)ruthenium(II)/Methylaluminum Bis(2,6-di-tert-butylphenoxide) Initiating System: Possibility of Living Radical Polymerization. *Macromolecules* **1995,** *28* (5), 1721-1723.
(61) Matyjaszewski, K.; Tsarevsky, N. V., Nanostructured functional materials prepared by atom transfer radical polymerization. *Nat. Chem.* **2009,** *1* (4), 276-288.
(62) Hui, C. M.; Pietrasik, J.; Schmitt, M.; Mahoney, C.; Choi, J.; Bockstaller, M. R.; Matyjaszewski, K., Surface-Initiated Polymerization as an Enabling Tool for Multifunctional (Nano-)Engineered Hybrid Materials. *Chem. Mater.* **2014,** *26* (1), 745-762.

(63) Pyun, J.; Jia, S.; Kowalewski, T.; Patterson, G. D.; Matyjaszewski, K., Synthesis and Characterization of Organic/Inorganic Hybrid Nanoparticles: Kinetics of Surface-Initiated Atom Transfer Radical Polymerization and Morphology of Hybrid Nanoparticle Ultrathin Films. *Macromolecules* **2003,** *36* (14), 5094-5104.
(64) Wang, Z.; Liu, T.; Lin, K. C.; Li, S.; Yan, J.; Olszewski, M.; Sobieski, J.; Pietrasik, J.; Bockstaller, M. R.; Matyjaszewski, K., Synthesis of Ultra-high Molecular Weight SiO2-g-PMMA Particle Brushes. *Journal of Inorganic and Organometallic Polymers and Materials* **2019**.
(65) Cui, J.; Ma, Z.; Pan, L.; An, C.-H.; Liu, J.; Zhou, Y.-F.; Li, Y.-S., Self-healable gradient copolymers. *Materials Chemistry Frontiers* **2019,** *3* (3), 464-471.
(66) Matyjaszewski, K.; Ziegler, M. J.; Arehart, S. V.; Greszta, D.; Pakula, T., Gradient copolymers by atom transfer radical copolymerization. *J. Phys. Org. Chem.* **2000,** *13* (12), 775-786.
(67) Li, Y.; Chen, S.; Li, X.; Wu, M.; Sun, J., Highly Transparent, Nanofiller-Reinforced Scratch-Resistant Polymeric Composite Films Capable of Healing Scratches. *ACS Nano* **2015,** *9* (10), 10055-10065.
(68) Tyagi, P.; Deratani, A.; Quemener, D., Self-Healing Dynamic Polymeric Systems. *Isr. J. Chem.* **2013,** *53* (1-2), 53-60.

Chapter 14 Summary and Outlook

14.1 Summary

ZnO, a widely studied metal oxide semiconductor, has been extensively investigated concerning its potential use in bio-sensor, solid-state energy storage, food industry, optics, and medical fields. However, due to the inert surface feature of ZnO, modification of the ZnO nanoparticles with polymer ligands has been challenging. **Chapter 2** introduces a facile synthetic route to synthesize polymer capped ZnO nanocrystals through the “ligand exchange” method. The low boiling point surfactant octylamine was replaced with thermally stable functionalized polymer ligands (PSAN-NH_2) at high temperatures. Controlled radical polymerization has been used to synthesize the polymer ligands with well-defined molecular weight and architectures. The obtained ZnO/polymer hybrids significantly improved the dispersibility of ZnO nanoparticles in polymer matrix or solutions, which can be used as nanofillers to improve the

optical/thermal/electrical properties of the matrix materials (**Chapter 4**). Besides, the **Chapter 5-6** discussed by using the PSAN capped ZnO as precursors, where the PAN acts as the carbon source, to prepare ZnO/carbon materials, which significantly increased the photocatalytic efficiency and electrochemical property of ZnO nanoparticles.

Compared to the ZnO/polymer nanocomposite, SiO_2-*g*-polymer particle brushes were synthesized by SI-ATRP. With the strong covalent bonding between polymer ligands and the surface of a silica nanoparticle, the particle brushes are more suitable for morphological and self-assembled behavior studies. The synthesis of particle brushes was explored in **Chapter 7-9**. The mechanical property and self-assembly of particle brush were discussed in **Chapter 10-11**, especially the sparsely grafted silica particle brushes show very unique anisotropic features. Combing different particle and polymer ligands, novel polymer nanocomposites like self-healable gradient copolymer particle brushes (**Chapter 12-13**) and organoSiO_2 particle brush (**Appendix 2**) were designed and prepared.

The continuously growing interest in novel inorganic/polymer hybrid materials will lead to a better understanding of their synthesis, morphology and self-assembled features.

14.2 Outlook

Octylamine capped ZnO nanocrystals have small particle size and very narrow size distribution. It is an excellent starting material to prepare polymer/ZnO hybrid nanocomposite through “ligand exchange”. In our previous work, we tried to use ZnO nanoparticles as fillers to enhance the thermal conductivity of the polymer matrix. However, before the thermal conductivity measurement, we found that the synthesized PSAN capped ZnO nanoparticles have a very poor photo and thermal stabilities, which is attributed to the highly reactive halogen chain-

ends. The future work could focus on improving the stability of polymer capped ZnO nanoparticles by replacing the chain-ends to less reactive groups and continuing the thermal conductivity measurements. What's more, during the previous research, we observed that OA capped ZnO nanocrystals can be directly mixed with poly(dimethylsiloxane) (PDMS) matrix which is made of short-chain length dimethylsiloxane precursors ($M_n \sim 500$). A trial sample that was made of 120 nm silica nanoparticles and OA capped ZnO nanocrystals in the PDMS matrix can maintain high transparency with high inorganic contents loading. Zhao Lu and Yuqi Zhao can continue and finish this work with a more detailed and systematic study. Another potential work with ZnO nanoparticles is the utilization of ZnO as the catalyst in the crosslinking of rubbers. OA capped ZnO nanocrystals can be directly added into the rubber matrix by the solvent casting method (toluene as solvent). Compared to the commercialized ZnO nanoparticles, the OA capped ZnO nanocrystals have much smaller particle size and larger surface area even after partial agglomeration in the rubber matrix.

Although the self-assembly behaviors of block copolymers have been well-established, the phase separations of block copolymer tethered particle brushes are still difficult to be predicted. As shown in this thesis, the density of bulk PS and PMMA, as well as the molar mass of styrene and MMA monomers are very similar, which makes them the excellent candidates for the study of block copolymers phase separation. A very interesting phenomenon has been shown in our previous work, which is the formation of the anisotropic structure in the bimodal block copolymer tethered particle brushes (**Chapter 11**). However, the successful synthesis of unimodal block copolymer tethered particle brushes remains challenging due to the low initiation efficiency of PS blocks (**Chapter 7**). The future work could focus on the chain extension of SiO_2-*g*-PMMA with another monomer with full initiation efficiency. At last, the continuation of

gradient copolymer grafted particle brushes, which is carried on by Rongguan Yin and Yuqi Zhao, would focus on investigating the effect of the shape of the gradient on the mechanical properties of the materials and also the detailed self-healing mechanism of PBA-*grad*-PMMA block copolymer and SiO_2-*g*-PBA-*grad*-PMMA particle brushes.

Appendix 1 Polymerization-induced self-assembly of acrylonitrile via ICAR ATRP

A 1.1. Preface

Polymerization-induced self-assembly (PISA) has attracted growing interest as a facile fabrication process of polymer-based nanomaterials. However, PISA of acrylonitrile(AN) by atom transfer radical polymerization (ATRP) has remained an outstanding challenge due to the high activity of AN and poor solubility of polyacrylonitrile (PAN) in AN monomer. Herein, the application of PISA by using initiators for continuous activator regeneration (ICAR) ATRP for the synthesis of PAN-based nano-objects is demonstrated. A highly active ATRP macroinitiator, methoxy-poly(ethylene oxide) 2-bromo-2-phenylacetate (*m*PEO-BPA) was synthesized by esterification and used also as a stabilizer. The molecular weight of the macroinitiator was found to determine the structure of self-assembled nano-objects. The high molecular macroinitiator (*m*PEO_{113}-BPA) formed nano-objects with spherical or worm-like morphology, while the lower molecular weight analog (*m*PEO_{45}-BPA) resulted in precipitation in most cases due to insufficient stabilization of the nano-objects.

In this chapter, the synthesis and self-assembly of PAN via ICAR ATRP are discussed. I helped with part of the synthetic work and the imaging work in the project. I would like to thank especially my collaborator, Guowei Wang, to have the opportunity to work together in this project. Bongjoon Lee, Rui Yuan, Zhao Lu, Jiajun Yan, Xiangcheng Pan, and Yang Song assisted in the synthesis and characterization work.

This project was published in *Polymer*, (Guowei Wang, Zongyu Wang, Bongjoon Lee, Rui Yuan, Zhao Lu, Jiajun Yan, Xiangcheng Pan, Yang Song, Michael R Bockstaller, Krzysztof Matyjaszewski, "Polymerization-induced self-assembly of acrylonitrile via ICAR ATRP", *Polymer*, 2017,129, 57-67.).

We thank the NSF (via DMR 1501324, DMR-1410845, and DMR-1709344) for financial assistance. Wang, G. W. thanks the China Scholarship Council (CSC) for a fellowship.

A 1.2. Introduction

Polyacrylonitrile (PAN)-containing polymers are attracting increasing attention as precursors to nanofibres and carbon nanomaterials.[1-9] The PAN-based carbon nanomaterials can be used as fillers, templates, probes and sensors, electronic devices, or materials for energy and gas storage.[1] Three synthetic strategies can be employed to manipulate the nanoscale morphology,[10-12] The first strategy is realized by the pyrolysis of organic precursors under an inert atmosphere. Although carbon nanomaterials can be readily prepared on a large scale by this strategy, structural control is limited. The second strategy utilizes physical/chemical vapor deposition. This process is characterized by limited yield, complex equipment, and high cost thus preventing its practical applications. The third strategy, based on templating techniques, is

perhaps most promising. For example, diblock copolymer precursors containing a carbon-forming PAN block and a sacrificial poly(*n*-butyl acrylate) block were used.[4] Besides, various PAN-containing block copolymers,[13-16] brush copolymers,[17] silica-based hybrid copolymers,[18-21] and crosslinked spheres[22] were also developed as templates. Variation of the characteristics of precursors enables the tuning of the structure of nanocarbon. However, the technique requires processing in a good solvent for the PAN block, such as dimethylformamide (DMF), dimethylacetamide (DMAA), dimethyl sulfoxide (DMSO), *N*-methylpyrrolidone (NMP), or ethylene carbonate (EC).[23] These high boiling point solvents make the processing of templates more challenging and reduce the practical relevance of the templating process.[24-25] To simplify the process and increase control, the template technique was extended by self-assembling the precursor in a less expensive lower boiling point solvent (such as water).[26-27] However, control of the self-assembly of copolymers requires high dilution of the solution, which reduces the process efficiency. Thus, an efficient template technique to prepare carbon nanomaterials remains an outstanding challenge.

Recently, polymerization-induced self-assembly (PISA) has become an attractive method for preparing block copolymer nano-objects.[28-33] In a typical PISA process, a soluble polymer is simultaneously used as a macroinitiator and stabilizer, which can be chain-extended using a second monomer in a suitable solvent. At the initial stage, the macroinitiator and stabilizer can solubilize in the mixture of solvent and monomer, and a homogenous solution is featured. As the chain-extension proceeds, the self-assembly occurs concurrently with the polymerization as the growing second block gradually becomes insoluble, which drives *in situ* self-assembly of a diblock copolymer to form nano-objects with different morphologies. Similar to the conventional self-assembly procedure, various nano-objects such as spheres, worms/rods, lamellae, toroids,

and vesicles were prepared via PISA process.[28-33] The solids content in PISA can be increased up to 40-50% w/w, and the preparation can be easily realized in a one-pot manner rather than using a post-modification. Thus, the PISA process offers the potential to significantly improve the yield of the self-assembly process.[34-38]

Recent advancements in controlled/"living" polymerization techniques, such as reversible addition-fragmentation chain transfer (RAFT) polymerization,[28-40] atom transfer radical polymerization (ATRP),[41-45] nitroxide mediated polymerization (NMP),[46-51] and ring-opening metathesis polymerization (ROMP)[52] have driven the interest in developing PISA into a facile process for the synthesis of functional materials. Compared to the well-studied NMP PISA,[46-47] and RAFT PISA,2[8-32] the ATRP PISA is challenging because of its unique dual catalyst system consisting of both activator and deactivator.[45] In the past ten years, several modifications of the original ATRP process have been developed to reduce the catalyst concentration via regeneration of catalyst during the polymerization process.[53-61] Example include initiators for continuous activator regeneration (ICAR) ATRP,[62] activators regenerated by electron transfer (ARGET) ATRP,[63] supplemental activators and reducing agent (SARA) ATRP,[64] electrochemically mediated ATRP (*e*ATRP),[65-66] and photo-induced ATRP.[67-68] All these techniques can be conducted with a lower concentration of catalyst (ppm) and higher tolerance to impurities and air. For practical applications, the ICAR ATRP might be particularly favorable due to the ease of its implementation.[62] Typically, a source of conventional free radicals (such as azobisisobutyronitrile, AIBN) is employed to slowly and continuously regenerate the very low concentration of $Cu^{I}X$ activator, which is otherwise consumed in termination reactions. To avoid/reduce the possibility of poor temperature control, the rate of decomposition of the selected free radical initiator should be slow and could be used to mediate the rate of

polymerization. With the usage of several or tens of ppm copper catalyst, the removal or recycling of the catalyst complex would be unwarranted for many biomedical and industrial applications.

The objective of the present study was to evaluate the application of ICAR ATRP to enable further improvements to ATRP PISA process of AN-based polymer materials and to better understand the role of reaction parameters on the yield and morphology of the resulting products in a recently developed process for ICAR ATRP PISA of poly(oligo(ethylene oxide) methyl ether methacrylate) (POEOMA)-poly(benzyl methacrylate) (PB*n*MA) copolymers in ethanol using ppm copper catalyst concentration.[69] The second objective of this work was to overcome the challenge of the heterogeneous polymerization of acrylonitrile (AN) monomer. The controlled radical polymerization of AN under homogeneous conditions was successful using normal ATRP,[70] ARGET ATRP,[71] ICAR ATRP,[72] SARA ATRP,[73] metal-free ATRP,[74] and RAFT.[75] However, the controlled polymerization of AN was rarely examined in heterogeneous systems (such as the PISA process).

A 1.3. Experimental Section

Materials

Cupric bromide ($Cu^{II}Br_2$, 99%, Aldrich), azobisisobutyronitrile (AIBN, 98%, Aldrich), methoxy-poly(ethylene oxide) (*m*PEO-OH, average molecular weights 5000 and 2000, Aldrich), 4-(dimethylamino)pyridine (DMAP, 99%, Aldrich), dicyclohexylcarbodiimide (DCC, 99%, Aldrich), and α-bromophenylacetic acid (99%, Aldrich) were used as received. Acrylonitrile (AN, 99%, Aldrich) was passed over a column of basic alumina to

remove inhibitor before use. Tris(2-pyridylmethyl)amine (TPMA) was prepared as previously reported in literature.[76] All other chemicals were used as received unless otherwise specified.

*Synthesis of macroinitiator and stabilizer Methoxy-poly(ethylene oxide) 2-bromo-2-phenylacetate (*m*PEO-BPA)*

Using DMAP and DCC as catalysts, anhydrous dichloromethane (CH_2Cl_2) as the solvent, the macroinitiator, and stabilizer *m*PEO-BPA was prepared by esterification between *m*PEO-OH and α-bromophenylacetic acid. Typically, into a 500 mL round-bottom flask, 40.0 g (8.0 mmol, average molecular weight 5000) *m*PEO-OH was dissolved in 400 mL anhydrous CH_2Cl_2. After 1.6654 g (8.0 mmol) DCC and 0.1955 g (1.6 mmol) DMAP were added, 2.5800 g (12.0 mmol) α-bromophenylacetic acid was added in five batches in 30 min. After the reaction was continued for 24 h, the system was washed with water three times. The organic phase was dried over anhydrous magnesium sulfate ($MgSO_4$) and the CH_2Cl_2 was evaporated under reduced pressure. The *m*PEO-BPA was finally obtained by precipitation into ethyl ether for three times. ^{1}H NMR (DMSO-D_6), δ (ppm): 3.40 (C*H*$_3$O-), 3.50–3.90 (m, -C*H*$_2$C*H*$_2$O-), 4.35 (-CH_2C*H*$_2$OOC-), 5.40 (-C_6H_5C*H*Br), 7.35–7.60 (m, -C_6*H*$_5$).

Synthesis of diblock copolymer mPEO-PAN by ICAR ATRP PISA process

Using AN as the monomer, AIBN as activators, $Cu^{II}Br_2$ as catalyst and TPMA as the ligand, and the above *m*PEO-BPA as both macroinitiator and stabilizer, the diblock copolymer *m*PEO-PAN can be synthesized using a dispersed PISA process at 60 °C. Typically, 0.3000 g (6.00×10^{-2} mmol, average molecular weight 5000) *m*PEO-BPA, 0.0016 g (7.20×10^{-3}mmol) $Cu^{II}Br_2$, 0.0084 g (2.88×10^{-2}mmol) TPMA, 0.0059 g (3.60×10^{-2}mmol)

AIBN, 1.18 mL (18.0 mmol) AN, and 11.5 mL acetonitrile (MeCN) were sequentially added into a 25 mL Schlenk flask. After the system was degassed by three freeze-pump-thaw cycles, the flask was purged with nitrogen and placed in an oil bath set at 60 °C to start polymerization. The polymerization was quenched by exposure to air after 4 d. ^{1}H NMR (DMSO-D_6), δ (ppm): 2.10 (-CH_2CH(CN)-), 3.10 (-CH_2CH(CN)-), 3.50–3.90 (m, -CH_2CH_2O-).

Aliquots were periodically taken for kinetic studies and analysis by GPC and ^{1}H NMR measurements. The systematical variation of macroinitiator and stabilizer *m*PEO-BPA, targeted DP of PAN and solids content allowed different PISA systems to be realized.

Characterization

Molecular weight (MW) and molecular weight distribution (MWD) values were determined by gel permeation chromatography (GPC) system equipped with a Waters 515 HPLC pump, a Waters 2414 refractive index detector and PSS columns (Styragel 10^2, 10^3, 10^5 Å) with LiBr-containing DMF as the eluent at a flow rate of 1.0 mL/min at 50 °C. The linear PEO standards (M_n = 1420, 3810, 29760, 64300, 502000, 8075000) were used for calibration of polymers. ^{1}H Nuclear Magnetic Resonance (^{1}H NMR) measurement was performed on a Bruker Avance 300 MHz spectrometer using DMSO-d_6 as the solvent. Dynamic light scattering (DLS) using a Malvern Zetasizer Nano ZS was employed to determine the average hydrodynamic diameters and distribution. The scattered light was detected at an angle of 173°. Transmission electron microscopy (TEM) was performed using a JEOL 2000 EX electron microscope operated at 200 kV. The polymerization dispersions prepared at 60 °C was directly diluted with MeCN to give 0.02–0.20 wt% dispersions. After one drop of the dispersions was deposited onto the carbon-coated copper grid, the copper grid was dried in air for 24 h and further stained by

immersing into a container filled with the vapor of ruthenium tetroxide (RuO_4) for 10 min. The nano-objects were converted into nanocarbon materials through heating under air to 280 °C at a rate of 20 °C/min and maintaining at 280 °C for 1 h, subsequent heating under nitrogen to target temperature (600 °C) at a rate of 10 °C/min and keeping at this target temperature for 0.5 h and finally naturally cooling to room temperature. Tapping mode atomic force microscopy (AFM) measurement was taken using a Veeco Metrology Group Digital Instruments Dimension V with NanoScope V controller and NanoScope 7 software. A Veeco TESPA cantilever with a spring constant of 20–80 N/m and a resonance frequency of 320–375 kHz was used. The sample was spin-cast onto a freshly cleaved mica substrate, and then the solvent was evaporated at room temperature for 24 h.

A 1.4. Results and Discussion

To evaluate the governing parameters for the formation of PAN nano-objects by PISA, ICAR ATRP of AN in the presence of *m*PEO-BPA, a highly active ATRP initiator that was designed to act as both macroinitiator and stabilizer was performed. The process is illustrated in **Scheme A1.1**.

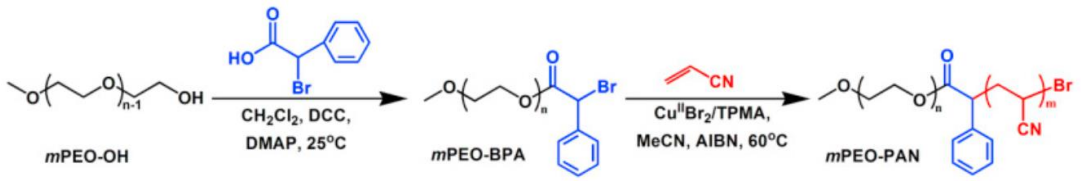

Scheme A1.1. The synthetic procedure for diblock copolymer *m*PEO-PAN by ICAR ATRP PISA process.

Synthesis and characterization of macroinitiator and stabilizer **m***PEO-BPA*

The macroinitiator and stabilizer *m*PEO-BPA was synthesized by the esterification of *m*PEO-OH with *α*-bromophenylacetic acid using DMAP and DCC as catalysts, and anhydrous CH_2Cl_2 as the solvent. To systematically study the effect of MW of *m*PEO-BPA on the PISA process in the following section, two *m*PEO-BPA with different MWs were synthesized and labeled as *m*PEO_{113}-BPA (M_n = 5000) and *m*PEO_{45}-BPA (M_n = 2000), respectively. The successful synthesis of *m*PEO_{113}-BPA was first evaluated by ^{1}H NMR measurement. **Figure SA1.1**(A) displayed the characteristic resonance signals of phenyl protons (-C_6H_5) at 7.35–7.60 ppm, methine proton connected to the phenyl and bromide group (-C_6H_5CHBr) at 5.40 ppm, methylene protons close to the ester bond (-CH_2CH_2OOC-) at 4.35 ppm. Also, the resonance signal of terminal methyl protons (CH_3O-) was discriminated at 3.40 ppm, and methylene protons (-CH_2CH_2O-) were found at 3.50–3.90 ppm. Comparison of the integrated resonance signal intensity at 7.35–7.60 ppm for the introduced α-bromophenyl protons with that at 3.50–3.90 ppm for the methylene protons on PEO chain indicated an esterification efficiency of 98%. To further confirm the high efficiency of functionalization, the *m*PEO_{113}-BPA was used as a macroinitiator to chain-extend with AN monomer by ICAR ATRP using DMSO as the solvent, $Cu^{II}Br_2$/TPMA as catalytic complex, and AIBN as radical initiator at 60 °C. Because DMSO is a good solvent for both PEO and PAN block, the polymerization proceeded homogeneously. As shown in **Figure A1.1**a, compared with the GPC trace for macroinitiator *m*PEO_{113}-BPA, the symmetrical GPC trace for block copolymer *m*PEO_{113}-PAN with increased MW (M_n = 18,900) and narrow MWD (M_w/M_n = 1.28) confirmed the successful synthesis of *m*PEO_{113}-BPA. Similarly, the esterification efficiency of *m*PEO_{45}-BPA was estimated as 99% by ^{1}H NMR measurement and a smooth chain-extended polymerization with AN monomer was conducted in DMSO.

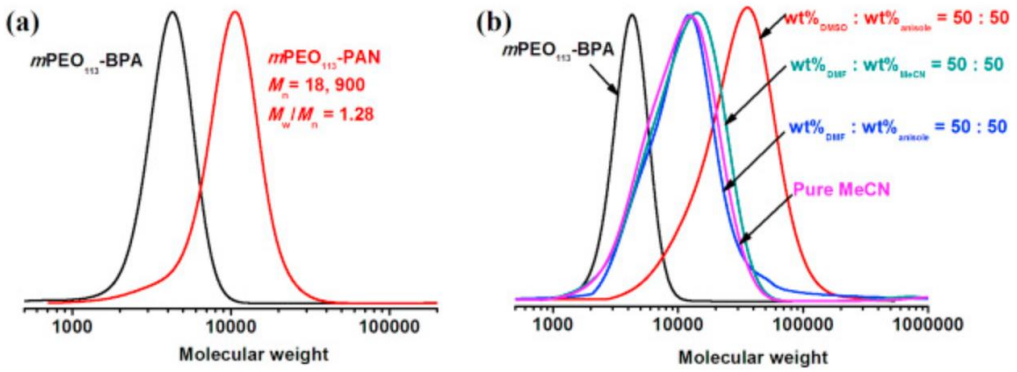

Figure 1.1. GPC traces for macroinitiator mPEO$_{113}$-BPA and diblock copolymer mPEO$_{113}$-PAN obtained by ICAR ATRP: (a) in DMSO ([mPEO$_{113}$-BPA]$_0$:[AN]$_0$:[Cu^{II}Br$_2$]$_0$:[TPMA]$_0$:[AIBN]$_0$ = 1:300:0.12:0.48:1.20, 10% w/w solids content, 60 °C, 24 h), and (b) in mixture solvents([mPEO$_{113}$-BPA]$_0$:[AN]$_0$:[Cu^{II}Br$_2$]$_0$:[TPMA]$_0$:[AIBN]$_0$ = 1:300:0.12:0.48:1.20, 10% w/w solids content, 60 °C, 4 d).

Optimization of ICAR ATRP PISA process

For a typical PISA process, the macroinitiator and stabilizer, core-forming block as well as monomer and solvent are the essential elements. Once the macroinitiator and stabilizer, core-forming block and monomer are selected based on certain practical applications, a proper solvent needs to be determined to guarantee the simultaneous self-assembly and polymerization. According to the principle of PISA, the mixture of solvent and monomer should be a good solvent for macroinitiator and, simultaneously, a poor solvent for core-forming block.[31-40] To enhance the ATRP efficiency, the selected solvent should also be sufficiently polar to allow the dissolution of the catalyst complex that is required for successful polymerization.[53-61] For example, the presently reported ATRP of AN monomer mostly proceeded in polar solvents of DMF, DMAA, DMSO, NMP, and EC, which are good solvents for PAN block.[70-81] Thus, considered the requirements both in the PISA process and ATRP mechanism, a solvent mixture containing DMF or DMSO was initially employed. As shown in **Figure A1.1**b and **Table SA1.1**, the solvent mixture of DMSO and anisole (wt%$_{DMSO}$: wt%$_{anisole}$ = 50: 50) led to a homogeneous polymerization throughout the whole process and no dispersion was formed. Meanwhile, the GPC of the obtained diblock copolymer mPEO$_{113}$-PAN showed symmetrical

trace with narrow MWD. However, in the solvent mixture consisting of DMF and anisole ($wt\%_{DMF}$: $wt\%_{anisole}$ = 50: 50) or DMF and MeCN ($wt\%_{DMF}$: $wt\%_{MeCN}$ = 50: 50), the formation of heterogeneous dispersion was observed. Correspondingly, the GPC traces for the obtained diblock copolymer *m*PEO_{113}-PAN displayed some tailings at the low MW region. Based on these results, we concluded that a proper mixture of DMF and a poor solvent for PAN block can realize a PISA process of AN. The failure of the PISA process in a solvent mixture of DMSO and anisole might be attributed to the better solvency of the PAN block in DMSO.[74] A further challenge regarding the use of solvent mixtures for PISA is that differences in the volatility of components might give rise to compositional changes. Because of these considerations, and because of the similarity in structure between MeCN and AN monomer, pure MeCN was selected as a solvent for the PISA process (**Table SA1.1**). Indeed, the system with pure MeCN led to a well-dispersed solution and gave similar GPC results like that from the mixture of DMF and anisole or DMF and MeCN (**Figure A1.1**b).

When aiming to improve the ATRP PISA process, the reduction of the usage of copper catalysts is the first important objective. As shown in **Table SA1.2** and **Figure A1.2**a, $[Cu^{II}Br_2]_0 \geq 400$ ppm can lead to a successful PISA process, while $[Cu^{II}Br_2]_0$ = 50, 100, and 200 ppm failed. This result is distinctly different from previous works on the ICAR ATRP of AN monomer in homogeneous solution,[72] where just 1.0 ppm copper catalyst was shown to provide a well-controlled polymerization. The reason can be attributed to the heterogeneous character of the PISA process, as well as its low solids content (10% w/w). According to the ICAR ATRP mechanism,[62] the molar ratio of $[AIBN]_0$:$[Cu^{II}Br_2]_0$ is important in modulating the rate of polymerization. As shown in **Table SA1.3** and **Figure A1.2**b, in the case of targeted DP = 300 of PAN, the molar ratio of $[AIBN]_0$:$[Cu^{II}Br_2]_0$ = 10 and 20 led to GPC traces with multimodal and

broad MWD, and the $[AIBN]_0:[Cu^{II}Br_2]_0 = 2.5$ and 5.0 resulted in a relatively controlled polymerization. The presence of excess AIBN initiator tended to provide a rapid polymerization since AIBN-derived radicals readily initiate homopolymerization of the highly reactive AN monomer.[72]

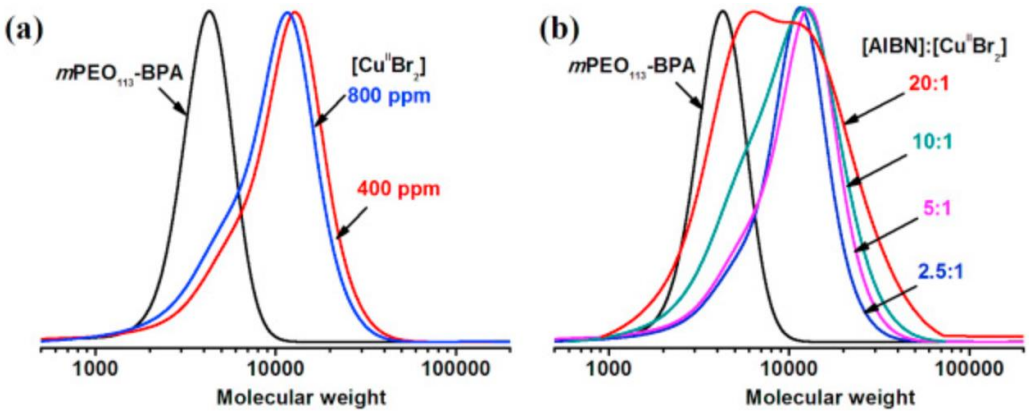

Figure A1.2. GPC traces for diblock copolymers mPEO$_{113}$-PAN obtained by ICAR ATRP in MeCN: (a) with different $[Cu^{II}Br_2]_0$ ($[m\text{PEO}_{113}\text{-BPA}]_0:[AN]_0:[Cu^{II}Br_2]_0:[TPMA]_0:[AIBN]_0 = 1:200:0.08\times:0.32\times:0.40\times$, x = 1 or 2, 10% w/w solid content, 60 °C, 4 d), and (b) with different molar ratio of $[AIBN]_0:[Cu^{II}Br_2]_0$ ($[m\text{PEO}_{113}\text{-BPA}]_0:[AN]_0:[Cu^{II}Br_2]_0:[TPMA]_0:[AIBN]_0 = 1:200:0.08:0.32:0.20\times$, x = 1, 2, 4, or 8, 10% w/w solid content, 60 °C, 4 d).

ICAR ATRP PISA process for diblock copolymer **m***PEO$_{45}$-PAN and* **m***PEO$_{113}$-PAN*

Using the optimized factors of $[Cu^{II}Br_2]_0 = 400$ ppm, and $[AIBN]_0$: $[Cu^{II}Br_2]_0 = 2.5$ and 5.0, the kinetics of ICAR ATRP PISA process were followed while targeting DP = 300 of PAN and solids content of 10% w/w and 20% w/w, respectively. Up to a reaction time of 4 d (96 h), the polymerization did display first-order kinetics (**Figure A1.3**a). With the increased monomer conversion, the MWs of diblock copolymers *m*PEO-*b*-PAN progressively increased and block copolymers *m*PEO-*b*-PAN with narrow MWDs were formed. The kinetics demonstrates that the ICAR ATRP proceeded in a controlled manner. After 4 d (96 h), the kinetic plots gradually became more curved and flattened. Correspondingly, at the higher MW region, the measured MWs of diblock copolymers *m*PEO-*b*-PAN deviated from the theoretical values, and the MWDs

gradually broadened (**Figure A1.3**b). Thus, to keep the ICAR ATRP PISA in a controlled manner, all the polymerizations in the following study were stopped after 96 h of reaction time. Unlike the previously reported three stages in the kinetic plot for a typical RAFT PISA process[28-31] and our ICAR ATRP process for B*n*MA monomer,[69] the curved and flattened kinetic plots imply that the ATRP of AN monomer in PISA process was gradually terminated and the radical species were continuously consumed until it resulted in termination of the polymerization. The premature ceasing of the polymerization can be attributed to several possible factors.[80-81] First, due to the poor solubility of PAN in AN monomer, the PAN segment in micelles formed a compact form in the nucleation stage, thus reducing the mobility of radicals that are required for the reaction. Second, the high activity and concentration of PAN radicals formed by the ATRP mechanism in micelles could increase termination reactions and hence decrease the concentration of radicals. Finally, the collapse of PAN segments within micelles might reduce the concentration of AN monomers. Besides, the solids content of 20% w/w tended to give a faster polymerization rate than that with 10% w/w due to the higher monomer concentration in the PISA process.

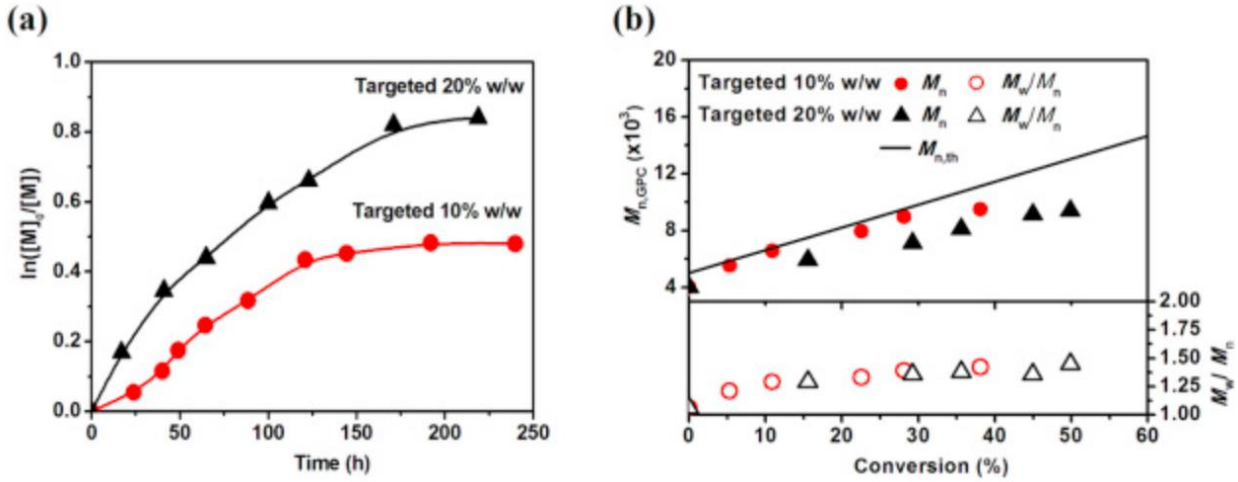

Figure. A1.3. (a) The semilogarithmic kinetic plots of ICAR ATRP PISA, and (b) the relationship of $M_{n,GPC}$ and M_w/M_n with monomer conversion in ICAR ATRP PISA (targeted 10% w/w, [*m*PEO$_{113}$-BPA]$_0$:[AN]$_0$:[Cu^{II}Br$_2$]$_0$:[TPMA]$_0$:[AIBN]$_0$ = 1:300:0.12:0.48:0.60, 60 °C; targeted 20% w/w, [*m*PEO$_{113}$-BPA]$_0$:[AN]$_0$:[Cu^{II}Br$_2$]$_0$:[TPMA]$_0$:[AIBN]$_0$ = 1:300:0.12:0.48:0.30, 60 °C).

When the macroinitiator and stabilizer were fixed as *m*PEO$_{113}$-BPA, different DPs of PAN were targeted in the case of a solids content of 10% w/w (**Table A1.1**). From **Figure A1.4**a, we can observe that the GPC traces gradually shifted to the higher MW region when the targeted DPs of PAN were increased. For the lower targeted DP = 50, and 100, the GPC traces were symmetrical with narrow MWDs. However, for the targeted DP ≥ 150, there were always shoulder peaks remaining at the lower MW region. In the case of *m*PEO$_{113}$-BPA and solids content of 20% w/w (**Figure A1.4**b), *m*PEO$_{45}$-BPA and solids content of 10% w/w (**Figure A1.5**a), *m*PEO$_{45}$-BPA and solids content of 20% w/w (**Figure A1.5**b), a similar evolution of GPC traces were observed. In **Figure SA1.1**(B), the characteristic resonance signal of methine proton (-C***H***(CN)CH$_2$-) for the PAN segment can be detected at 3.2 ppm, and signals of methylene and methine protons (C***H***$_2$=C***H***CN) of the unreacted AN monomer are at 5.90–6.40 ppm. Based on the integrated area at 3.10 ppm and those at 5.90–6.40 ppm, the monomer conversions, final solids content, final DP of PAN and molecular weight of block copolymer *m*PEO-*b*-PAN were calculated and listed in **Table A1.1**. The lower-than-target solids content and DP of PAN might be attributed to the incomplete monomer conversion (**Table A1.1**).

Table A1.1. The data for diblock copolymers mPEO$_{113}$-PAN and mPEO$_{45}$-PAN obtained by ICAR ATRP PISA.[a]

Entry	Sample	Targeted solids content (% w/w)	Targeted DP of PAN	[mPEO$_{113}$-BPA]$_0$:[AN]$_0$:[Cu^{II}Br$_2$]$_0$:[TPMA]$_0$:[AIBN]$_0$	Monomer conversion (%)[b]	$M_{n,GPC}$[c]	M_w/M_n[c]	Final solids content (% w/w)[d]	Final DP of PAN[e]	$M_{n,NMR}$[f]
1	mPEO$_{113}$-PAN$_{10}$	10	50	1:50:0.02:0.08:0.1	20	6200	1.13	7	10	5500
2	mPEO$_{113}$-PAN$_{29}$	10	100	1:100:0.04:0.16:0.2	29	7700	1.16	6	29	6500
3	mPEO$_{113}$-PAN$_{63}$	10	150	1:150:0.06:0.24:0.3	42	8600	1.26	6	63	8300
4	mPEO$_{113}$-PAN$_{78}$	10	200	1:200:0.08:0.32:0.4	39	9900	1.24	6	78	9100
5	mPEO$_{113}$-PAN$_{115}$	10	250	1:250:0.1:0.4:0.5	46	10,400	1.27	6	115	11095
6	mPEO$_{113}$-PAN$_{129}$	10	300	1:300:0.12:0.48:0.6	43	11,500	1.28	6	129	11800
7	mPEO$_{113}$-PAN$_{20}$	20	50	1:50:0.02:0.08:0.05	39	7300	1.14	16	20	6100
8	mPEO$_{113}$-PAN$_{46}$	20	100	1:100:0.04:0.16:0.1	46	8100	1.17	14	46	7400
9	mPEO$_{113}$-PAN$_{72}$	20	150	1:150:0.06:0.24:0.15	48	9500	1.19	14	72	8800
10	mPEO$_{113}$-PAN$_{104}$	20	200	1:200:0.08:0.32:0.2	52	10,200	1.23	13	104	10500
11	mPEO$_{113}$-PAN$_{120}$	20	250	1:250:0.1:0.4:0.25	48	12,100	1.26	12	120	11400
12	mPEO$_{113}$-PAN$_{138}$	20	300	1:300:0.12:0.48:0.3	46	11,900	1.21	12	138	12300
13	mPEO$_{45}$-PAN$_{5}$	10	50	1:50:0.02:0.08:0.1	21	3400	1.17	7	11	2600
14	mPEO$_{45}$-PAN$_{44}$	10	100	1:100:0.04:0.16:0.2	45	6500	1.19	7	44	4300
15	mPEO$_{45}$-PAN$_{77}$	10	150	1:150:0.06:0.24:0.3	51	8300	1.28	7	77	6100
15	mPEO$_{45}$-PAN$_{97}$	10	200	1:200:0.08:0.32:0.4	49	9200	1.34	7	97	7100
17	mPEO$_{45}$-PAN$_{100}$	10	250	1:250:0.1:0.4:0.5	40	9300	1.37	6	100	7300
18	mPEO$_{45}$-PAN$_{136}$	10	300	1:300:0.12:0.48:0.6	45	11,200	1.52	6	136	9200
19	mPEO$_{45}$-PAN$_{21}$	20	50	1:50:0.02:0.08:0.05	41	4000	1.16	16	21	3100
20	mPEO$_{45}$-PAN$_{51}$	20	100	1:100:0.04:0.16:0.1	51	7500	1.15	15	51	4700
21	mPEO$_{45}$-PAN$_{92}$	20	150	1:150:0.06:0.24:0.15	61	9600	1.29	15	92	6900
22	mPEO$_{45}$-PAN$_{115}$	20	200	1:200:0.08:0.32:0.2	58	10,200	1.33	14	115	8100
23	mPEO$_{45}$-PAN$_{152}$	20	250	1:250:0.1:0.4:0.25	61	13,100	1.35	14	152	10100
24	mPEO$_{45}$-PAN$_{51}$	20	300	1:300:0.12:0.48:0.3	50	13,300	1.41	12	151	10000

a Polymerization condition: 60 °C, 4d.
b Monomer conversion was measured by ^{1}H NMR according to the Formula S1.
c $M_{n,\,GPC}$ and M_w/M_n were determined by GPC instrument using LiBr-containing DMF as the eluent.
d Final solids contents (% w/w) were calculated according to the Formula S2.
e Final DPs of PAN were calculated according to the Formula S3.
f The $M_{n,\,NMR}$s were calculated according to the Formula S4.

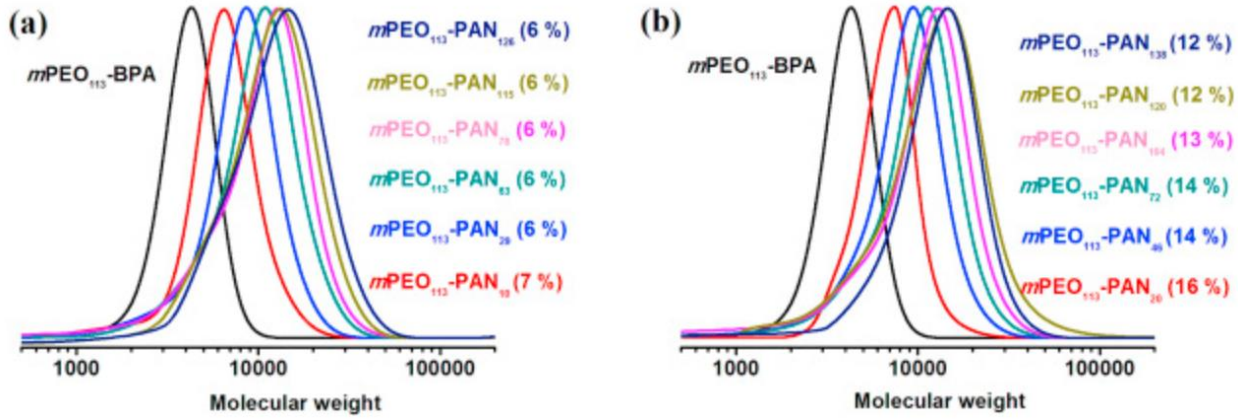

Figure A1.4. The GPC traces for diblock copolymers mPEO$_{113}$-PAN$_x$ obtained by ICAR ATRP PISA (Table A1.1) with different targeted DP of PAN (from 50 to 300) and targeted solids content: (a) 10% w/w, and (b) 20% w/w.

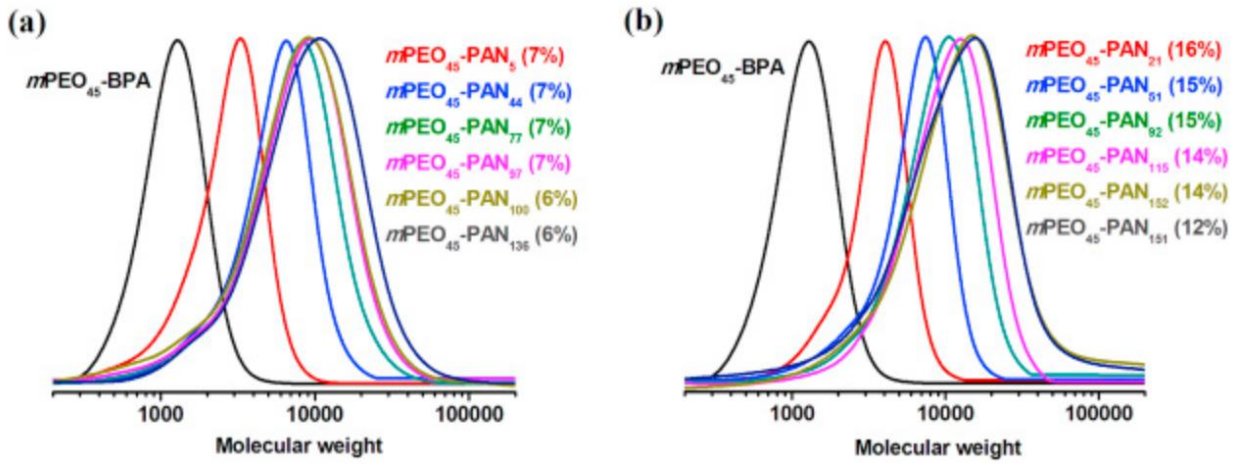

Figure A1.5. The GPC traces for diblock copolymers mPEO$_{45}$-PAN$_x$ obtained by ICAR ATRP PISA (Table A1.1) with different targeted DP of PAN (from 50 to 300) and targeted solids content: (a) 10% w/w, and (b) 20% w/w.

Evolution of morphology of the nano-objects formed in ICAR ATRP PISA process

Generally, the morphologies of nano-objects formed in a PISA process are determined by the solids content, DP of macroinitiator and stabilizer, and DP of core-forming block.[28-33] When the macroinitiator mPEO$_{113}$-BPA was used and the solids content was fixed at 10% w/w (**Table A1.1**), the morphological evolution was found to proceed as depicted in **Figure A1.6**. When the DP = 50 was targeted for PAN block, only 20% monomer conversion was reached and diblock copolymer mPEO$_{113}$-PAN$_{10}$ was achieved. The TEM image for mPEO$_{113}$-PAN$_{10}$ showed some nano-objects with irregular morphology (**Figure A1.6**a), which might be formed by dewetting on the copper grid, rather than the intrinsic morphology of the nano-objects in solution. The DLS results showed three populations of sizes of nano-objects with average diameters of 2 nm, 11 nm, 290 nm (**Figure A1.6**f), respectively, suggesting the coexistence of free chains next to self-assembled structures. When the DP = 100 was targeted for PAN block, copolymer mPEO$_{113}$-PAN$_{29}$ was formed and the TEM image revealed nano-objects with irregular morphology (**Figure A1.6**b). The DLS results suggest the presence of uniform and

large size nano-objects with an average diameter of 210 nm (**Figure A1.6**f). We can deduce that in the case of *m*PEO$_{113}$-PAN$_{29}$, all the diblock copolymers were aggregated into micelles. Similarly, when DP = 150, 200, 250, and 300 were targeted, the diblock copolymer *m*PEO$_{113}$-PAN with different lengths of the PAN block were prepared. The nano-objects with irregular but compacted morphology further evolved (**Figure A1.6**c, d, e). Correspondingly, the sizes of nano-objects by DLS measurement were gradually increased from 260 nm to 530 nm (**Figure A1.6**f), which was consistent with those from TEM images. In fact, with the increase of targeted DP of PAN, the PAN block with higher DP could be prepared. Once the PAN block was long enough, the *m*PEO block could not stabilize the initially formed micelles and the micelles tended to reorganize into large nano-objects.

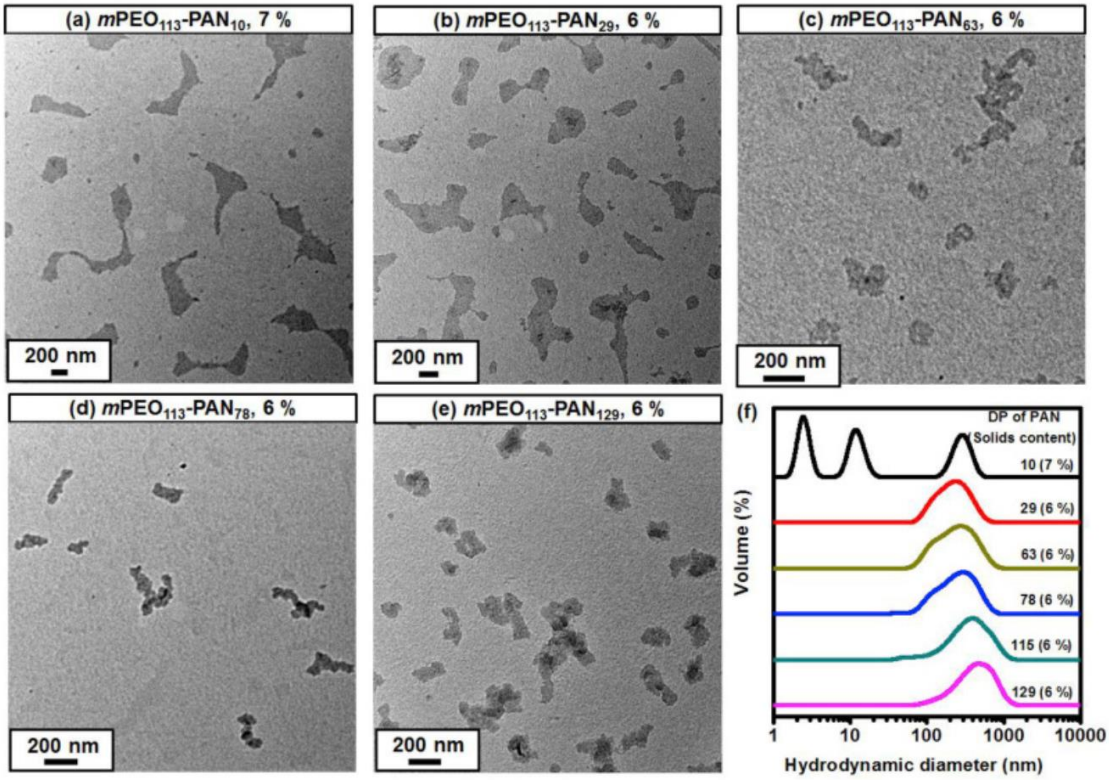

Figure A1.6. TEM images of the nano-objects formed from diblock copolymers *m*PEO$_{113}$-PAN$_x$ by ICAR ATRP PISA with different DP of PAN and solids content (a-e), and DLS results (f).

However, when the macroinitiator *m*PEO$_{113}$-BPA was used and 20% w/w solids content was targeted (**Table A1.1**), different morphologies and their changes were observed (**Figure A1.7**). As shown in **Figure A1.7**a, when DP = 50 was targeted for PAN block, the diblock copolymer *m*PEO$_{113}$-PAN$_{20}$ was formed. Similar to *m*PEO$_{113}$-PAN$_{10}$ with a solids content of 10% w/w, the TEM images showed some nano-objects with irregular and spherical morphology. The DLS results showed three populations with the average diameters of 3 nm, 30 nm and 100 nm (**Figure A1.7**f), respectively. When DP = 100 was targeted for the PAN block, diblock copolymer *m*PEO$_{113}$-PAN$_{46}$ was obtained. The irregular and spherical morphology gradually evolved into a worm-like morphology (**Figure A1.7**b). This trend continued when DP = 150 was targeted and the contour of the worm-like morphology become more clear. For DP = 200, 250, and 300, worm-like structures with a diameter of 30 nm and different lengths could be observed (**Figure A1.7**c, d, e). From the DLS results, the size of nano-objects changed from 75 nm–350 nm under the increasing targeted DP from 100 to 300 (**Figure A1.7**f). The TEM images were consistent with DLS results.

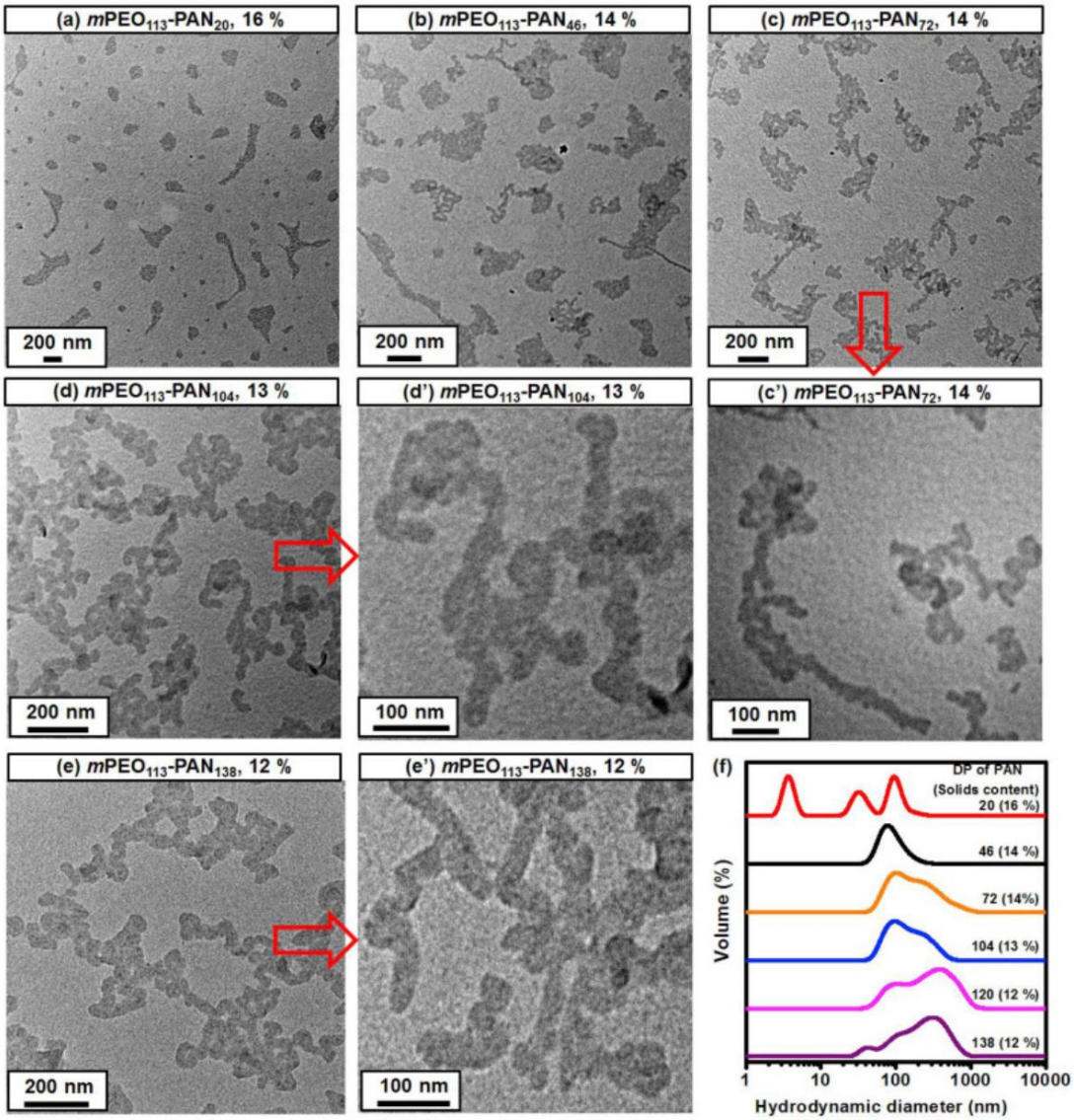

Figure A1.7. TEM images of the nano-objects formed from diblock copolymers mPEO$_{113}$-PAN$_x$ by ICAR ATRP PISA with different DP of PAN and solids content (a-e), and DLS results (f).

When the length of the macroinitiator mPEO$_{113}$-BPA was fixed, both the targeted solids content (10% w/w and 20% w/w) and targeted DPs of PAN affected the morphology evolution. According to a typical PISA process,[31-40] the micelles were gradually formed and some micelles were further fused with the growth of core-forming block. In the case of the lower targeted solids content of 10% w/w, the actual solids contents were close to 7% or 6% due to the incomplete conversion of AN monomer. In the target range of DP between 50 and 300, the lower solids

content did not help to fuse micelles and irregular morphologies were formed. In contrast, for the targeted solids content of 20% w/w, the relatively higher solids contents between 12 and 16% w/w were reached. With the targeted DP of PAN between 100 and 150, the irregular morphology gradually evolved into worm-like structures. With the target DP of PAN between 200 and 300, the fusion between the already formed nano-objects was pronounced and distinctive worm-like morphologies were observed. This result is consistent with our previous work[69] as well as literature reports.[28-31]

Some previous RAFT PISA reports showed that a lower DP of the macroinitiator and stabilizer should result in more ordered morphologies.[82-84] Thus, an alternative macroinitiator *m*PEO$_{45}$-BPA with lower DP was employed. For targeted solids content of 10% w/w and targeted DP = 50 of PAN block, a diblock copolymer *m*PEO$_{45}$-PAN$_{11}$ was formed and only some nano-objects with irregular morphology were observed. However, when DP ≥ 100 was targeted, the polymerization stopped with precipitation of the polymer. In the case of a targeted solids content of 20% w/w, some nano-objects with irregular and spherical morphology were formed for *m*PEO$_{45}$-PAN$_{21}$ when DP = 50 of PAN block was targeted (**Figure A1.8**a). Nano-objects with short worm-like morphology were formed for *m*PEO$_{45}$-PAN$_{51}$, when DP = 100 of PAN block was targeted (**Figure A1.8**b). The DLS results also showed the sizes of nano-objects with average diameters of 210 nm and 460 nm (**Figure A1.8**c). When DP > 100 of PAN was targeted, precipitation was again observed. We interpret these observations as an indication that in the case of *m*PEO$_{45}$-BPA as macroinitiator and stabilizer, the chain length was too short to stabilize nano-objects. Only a very narrow range of composition (20% solids content and targeted DP < 100) can be formulated for the spherical and short worm-like morphology.

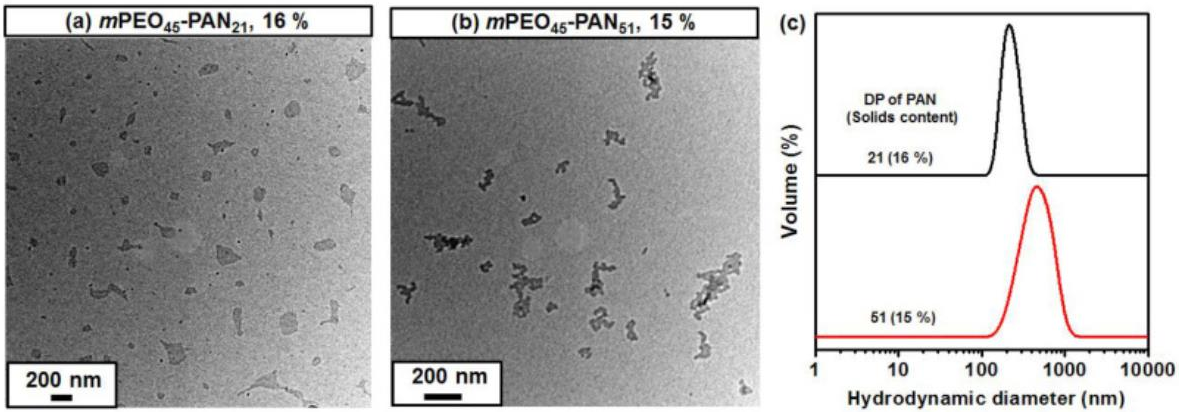

Figure A1.8. TEM images of the nano-objects formed from diblock copolymers mPEO$_{45}$-PAN$_x$ by ICAR ATRP PISA with different DP of PAN and solids content (a-b), and DLS results (c).

Furthermore, the nano-objects formed from diblock copolymer mPEO$_{113}$-PAN$_{104}$were observed by AFM measurement. Besides the dispersed spherical morphology, worm-like structures were also observed. The diameters of the spherical and worm-like morphologies were all close to 70 nm and the heights were measured as 10–30 nm (**Figure A1.9**a and **Figure A1.9**b). The diameters (70 nm) from AFM observation were rather different from those (30 nm) from the previous TEM image in **Figure. A1.7**d. Thus, combining the information from AFM and TEM images, we can deduce that the worm-like morphology of nano-objects from diblock copolymer mPEO$_{113}$-PAN$_{104}$was formed by the loose connection of spherical objects, rather than a true worm morphology. The difference between TEM and AFM observation can be attributed to the different procedures for sample preparation. For TEM, the dispersed solution was drop-cast on the copper grid and dried. However, for AFM, the dispersion solution was spin-cast onto mica substrates and certain stress might be exerted on the already formed worm-like morphology, which would induce the dissociation of the worm-like morphology.

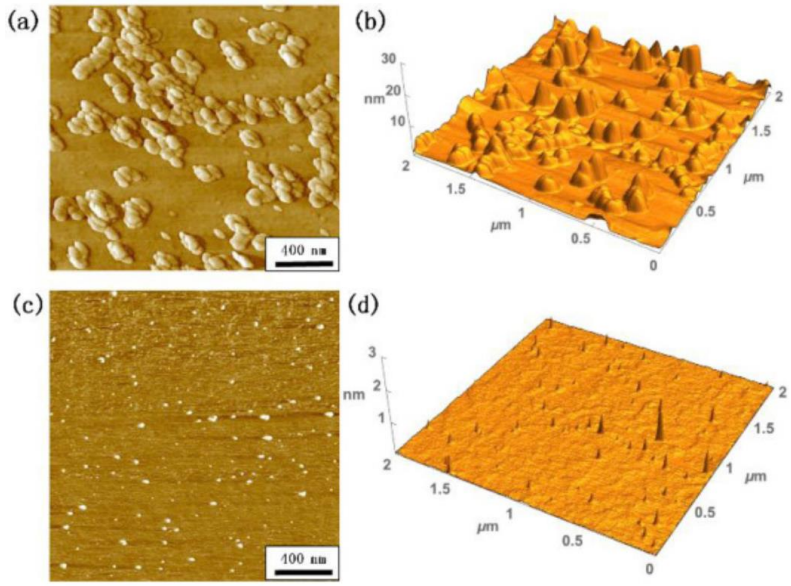

Figure A1.9. AFM images of nano-objects formed by ICAR ATRP PISA from diblock copolymers*m*PEO$_{113}$-PAN$_{104}$ (targeted 20% solids content): (a) and (b), before the pyrolysis; (c) and (d), after the pyrolysis.

After the obtained nano-objects from diblock copolymer *m*PEO$_{113}$-PAN$_{104}$ were pyrolyzed, limited nanocarbon dots rather than ideal nanocarbon rods were detected. The diameter and height of the obtained nanocarbon dots were measured as 5–50 nm and several nm, respectively (**Figure A1.9**c and **Figure A1.9d**).

A 1.5. Supporting Information

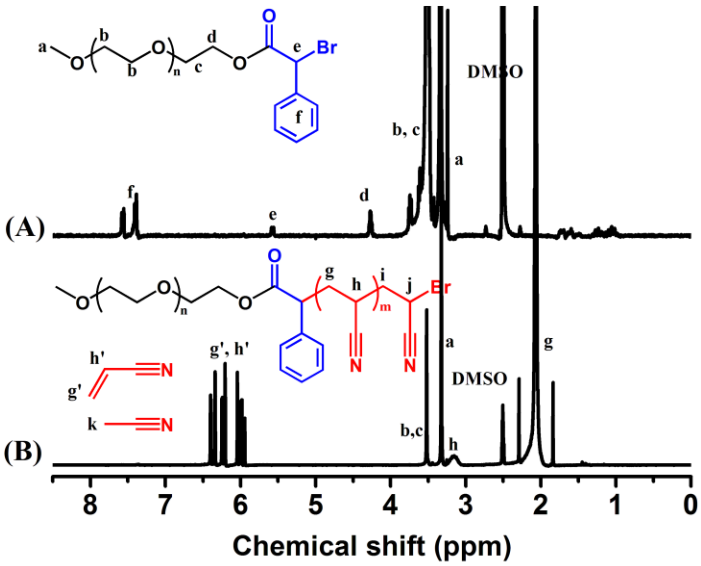

Fig. SA1.1. ^{1}H NMR spectra for macroinitiator *m*PEO$_{113}$-BPA and diblock copolymer *m*PEO$_{113}$-PAN obtained by ICAR ATRP PISA in MeCN solvent (Entry 4 in Table A1.1). (in DMSO-d$_6$).

As shown in **Fig. SA1.1(B)**, the characteristic resonance signals of methylene protons and methine proton (C***H***$_2$=C***H***CN) of unreacted AN monomer are at 5.90-6.40 ppm. However, after the polymerization, the resonance signal of methylene protons (-C***H***$_2$-CH**(**CN)-) and methine proton (-CH$_2$-C***H***(CN)-) of PAN block is at 2.10 and 3.10 ppm, respectively. The resonance signal of methylene protons (-C***H***$_2$C***H***$_2$O-) of the PEO block could be observed at 3.50-3.90 ppm. Thus, based on the integrated area A_h at 3.10 ppm and $A_{g',h'}$ at 5.90-6.40 ppm, the monomer conversion can be calculated according to the Formula S1 (**Table A1.1**):

$$\text{Monomer conversion} = \frac{A_h}{A_h + A_{g',h'}} \times 100\% \qquad \text{(Formula S1)}$$

Also, the final solids content, final DP of PAN and molecular weight of block copolymer *m*PEO-*b*-PAN can be obtained according to Formula S2, S3, and S4, respectively (**Table A1.1**).

$$\text{Final Solids content} = \frac{[m_{mPEO} + m_{AN} \text{ x (Monomer conversion)}] \text{ x (Targeted Solids content)}}{m_{mPEO} + m_{AN}} \text{ x } 100\% \quad \text{(Formula S3)}$$

(Formula S2)

$$\text{Final DP of PAN} = \text{(Monomer conversion) x (Targeted DP of PAN)} \quad \text{(Formula S3)}$$

$$M_{n,NMR,mPEO-b-PAN} = M_{AN} \text{ x (Final DP of PAN)} + M_{n,mPEO}$$

$$= M_{AN} \text{ x (Targeted DP of PAN) x (Monomer conversion)} + M_{n,mPEO} \quad \text{(Formula S4)}$$

Where M_{AN} is the molecular weight of AN monomer (53), and $M_{n,mPEO}$ is the molecular weight of *m*PEO$_{113}$ (5000) or *m*PEO$_{45}$ (2000), m_{AN} and m_{mPEO} are the fed weights of monomer AN and macroinitiator *m*PEO, respectively.

Table SA1.1. The data for ICAR ATRP in different solvents.[a]

Entry	[*m*PEO$_{113}$-BPA]$_0$:[AN]$_0$:[Cu^{II}Br$_2$]$_0$:[TPMA]$_0$:[AIBN]$_0$	Solvent	GPC Results	Phenomena
1	1:300:0.12:0.48:1.20	wt%$_{DMSO}$: wt%$_{anisole}$ = 50 : 50	Symmetrical curve	Without emulsion
2	1:300:0.12:0.48:1.20	wt%$_{DMF}$: wt%$_{anisole}$ = 50 : 50	With shoulder peak	With emulsion
3	1:300:0.12:0.48:1.20	wt%$_{DMF}$: wt%$_{MeCN}$ = 50 :	With shoulder peak	With emulsion

		50		
4	1:300:0.12:0.48:**1.20**	$wt\%_{MeCN}$ = 100	With shoulder peak	With emulsion

[a.]The polymerization condition: 10% w/w solids content, 60 °C, 4 d.

Table SA1.2. The data for ICAR ATRP in MeCN with different $[Cu^{II}Br_2]_0$.[a]

Entry	**[*m*PEO$_{113}$-BPA]$_0$:[AN]$_0$: [Cu^{II}Br$_2$]$_0$:[TPMA]$_0$:[AIBN]$_0$**	Solvent	GPC Results	Phenomena
1	1:200:0.01:0.04:0.05	100% MeCN		Without emulsion
2	1:200:0.02:0.08:0.10	100% MeCN		Without emulsion
3	1:200:0.04:0.16:0.20	100% MeCN		Without emulsion
4	1:200:0.08:0.32:0.40	100% MeCN	With shoulder peak	With emulsion
5	1:200:0.16:0.64:0.80	100% MeCN	With shoulder peak	With emulsion

[a.]The polymerization condition: 10% w/w solids content, 60 °C, 4 d.

Table SA1.3. The data for ICAR ATRP in MeCN with the different molar ratio of $[AIBN]_0$:$[Cu^{II}Br_2]_0$.[a]

Entry	**[*m*PEO$_{113}$-BPA]$_0$:[AN]$_0$: [Cu^{II}Br$_2$]$_0$:[TPMA]$_0$:[AIBN]$_0$**	Solvent	GPC Results	Phenomenon
1	1:200:0.08:0.32:**0.20**	100% MeCN	Symmetrical curve	With emulsion
2	1:200:0.08:0.32:**0.40**	100% MeCN	Symmetrical curve	With emulsion
3	1:200:0.08:0.32:**0.80**	100% MeCN	With shoulder peak	With emulsion
4	1:200:0.08:0.32:**1.60**	100% MeCN	With multipeak	With emulsion

[a.]The polymerization condition: 10% w/w solids content, 60 °C, 4 d.

A 1.6. Conclusions

PISA for PAN-containing nano-objects was successful via ICAR ATRP. The highly active *m*PEO-BPA was used as both macroinitiator and stabilizer for PISA of AN monomer using $Cu^{II}Br_2$/TPMA as an active catalytic complex, and AIBN as radical initiator at 60 °C in MeCN solvent. The concentration of $[Cu^{II}Br_2]_0$ of 400 ppm and the molar ratio of $[AIBN]_0$: $[Cu^{II}Br_2]_0$ in the range 2.5: 1 to 5.0: 1 were used. The block copolymer *m*PEO$_{113}$-PAN formed nano-objects with spherical morphology or worm-like morphology, whereas the block copolymer *m*PEO$_{45}$-BPA resulted in precipitation in most cases due to insufficient stabilization of the formed nano-objects.

A 1.7. References

1) E. Frank, L.M. Steudle, D. Ingildeev, J.M. Sporl, M.R. Buchmeiser, Carbon fibers: precursor systems, processing, structure, and properties, Angew. Chem. Int. Ed., 53 (21) (2014), pp. 5262-5298
2) M. Kopec, R. Yuan, E. Gottlieb, C.M.R. Abreu, Y. Song, Z. Wang, J.F.J. Coelho, K.Mat yjaszewski, T. Kowalewski, Polyacrylonitrile-b-poly(butyl acrylate) block copolymers as precursors to mesoporous nitrogen-doped carbons: synthesis and nanostructure, Macromolecules, 50 (7) (2017), pp. 2759-2767
3) M.J. Ju, I.T. Choi, M. Zhong, K. Lim, J. Ko, J. Mohin, M. Lamson, T. Kowalewski, K.M atyjaszewski, H.K. Kim, Copolymer-templated nitrogen-enriched nanocarbons as a low charge-transfer resistance and highly stable alternative to platinum cathodes in dye-sensitized solar cells, J. Mater. Chem. A, 3 (2015), pp. 4413-4419
4) T. Kowalewski, N.V. Tsarevsky, K. MatyjaszewskiNanostructured carbon arrays from block copolymers of polyacrylonitrile, J. Am. Chem. Soc., 124 (36) (2002), pp. 10632-10633
5) M. Kruk, B. Dufour, E.B. Celer, T. Kowalewski, M. Jaroniec, K. MatyjaszewskiWell-Defined poly(ethylene oxide)-polyacrylonitrile diblock copolymers as templates for mesoporous silicas and precursors for mesoporous carbons, Chem. Mater., 18 (6) (2006), pp. 1417-1424
6) C. Tang, B. Dufour, T. Kowalewski, K. Matyjaszewski, Synthesis and morphology of molecular brushes with polyacrylonitrile block copolymer side chains and their conversion into nanostructured carbons, Macromolecules, 40 (17) (2007), pp. 6199-6205
7) D. Wu, A. Nese, J. Pietrasik, Y. Liang, H. He, M. Kruk, L. Huang, T. Kowalewski, K.Ma tyjaszewski, Preparation of polymeric nanoscale networks from cylindrical molecular bottlebrushes, ACS Nano, 6 (7) (2012), pp. 6208-6214
8) M. Zhong, E.K. Kim, J.P. McGann, S.E. Chun, J.F. Whitacre, M. Jaroniec, K.Matyjasze wski, T. Kowalewski, Electrochemically active nitrogen-enriched nanocarbons with well-defined morphology synthesized by pyrolysis of self-assembled block copolymer, J. Am. Chem. Soc., 134 (36) (2012), pp. 14846-14857
9) M. Zhong, S. Natesakhawat, J.P. Baltrus, D. Luebke, H. Nulwala, K. Matyjaszewski, T.K owalewski, Copolymer-templated nitrogen-enriched porous nanocarbons for CO2 capture, Chem. Commun., 48 (94) (2012), pp. 11516-11518
10) D.C. Wu, F. Xu, B. Sun, R.W. Fu, H.K. He, K. Matyjaszewski, Design and preparation of porous polymers, Chem. Rev., 112 (7) (2012), pp. 3959-4015
11) J.P. McGann, M.J. Zhong, E.K. Kim, S. Natesakhawat, M. Jaroniec, J.F. Whitacre, K.Ma tyjaszewski, T. Kowalewski, Block copolymer templating as a path to porous nanostructured carbons with highly accessible nitrogens for enhanced (Electro)chemical performance, Macromol. Chem. Phys., 213 (10–11) (2012), pp. 1078-1090
12) T. Kowalewski, R.D. McCullough, K. Matyjaszewski, Complex nanostructured materials from segmented copolymers prepared by ATRP, Eur. Phys. J. E, 10 (1) (2003), pp. 5-16
13) C.B. Tang, A. Tracz, M. Kruk, R. Zhang, D.M. Smilgies, K. Matyjaszewski, T. Kowalew ski, Long-range ordered thin films of block copolymers prepared by zone-casting and their thermal conversion into ordered nanostructured carbon, J. Am. Chem. Soc., 127 (19) (2005), pp. 6918-6919

14) J.Y. Huang, C.B. Tang, H. Lee, T. Kowalewski, K. Matyjaszewski, A novel route for the preparation of discrete nanostructured carbons from block copolymers with polystyrene segments, Macromol. Chem. Phys., 208 (21) (2007), pp. 2312-2320
15) M.J. Zhong, C.B. Tang, E.K. Kim, M. Kruk, E.B. Celer, M. Jaroniec, K. Matyjaszewski, T.Kowalewski, Preparation of porous nanocarbons with tunable morphology and pore size from copolymer templated precursors, Mater. Horizons, 1 (1) (2014), pp. 121-124
16) M.J. Ju, I.T. Choi, M.J. Zhong, K. Lim, J. Ko, J. Mohin, M. Lamson, T. Kowalewski, K. Matyjaszewski, H.K. Kim, Copolymer-templated nitrogen-enriched nanocarbons as a low charge-transfer resistance and highly stable alternative to platinum cathodes in dye-sensitized solar cells, J. Mater. Chem. A, 3 (8) (2015), pp. 4413-4419
17) D.C. Wu, A. Nese, J. Pietrasik, Y.R. Liang, H.K. He, M. Kruk, L. Huang, T. Kowalewski , K.Matyjaszewski, Preparation of polymeric nanoscale networks from cylindrical molecular bottlebrushes, ACS Nano, 6 (7) (2012), pp. 6208-6214
18) C. Tang, L. Bombalskil, M. Kruk, M. Jaroniec, K. Matyjaszewski, T. KowalewskiNanop orous carbon films from “hairy” polyacrylonitrile-grafted colloidal silica nanoparticles, Adv. Mater., 20 (8) (2008), 1516-+
19) D.C. Wu, H.C. Dong, J. Pietrasik, E.K. Kim, C.M. Hui, M.J. Zhong, M. Jaroniec, T.Kow alewski, K. Matyjaszewski, Novell nanoporous carbons from well-defined poly(styrene-co-acrylonitrile)-grafted silica nanoparticles, Chem. Mater., 23 (8) (2011), pp. 2024-2026
20) M. Kruk, B. Dufour, E.B. Celer, T. Kowalewski, M. Jaroniec, K. Matyjaszewski, Synthesis of mesoporous carbons using ordered and disordered mesoporous silica templates and polyacrylonitrile as carbon precursor, J. Phys. Chem. B, 109 (19) (2005), pp. 9216-9225
21) M. Kruk, K.M. Kohlhaas, B. Dufour, E.B. Celer, M. Jaroniec, K. Matyjaszewski, R.S.Ru off, T. Kowalewski, Partially graphitic, high-surface-area mesoporous carbons from polyacrylonitrile templated by ordered and disordered mesoporous silicas, Micropor. Mesopor. Mat., 102 (1–3) (2007), pp. 178-187
22) D.C. Wu, Z.H. Li, M.J. Zhong, T. Kowalewski, K. Matyjaszewski, Templated synthesis of nitrogen- enriched nanoporous carbon materials from porogenic organic precursors prepared by ATRP, Angew. Chem. Int. Ed., 53 (15) (2014), pp. 3957-3960
23) M.M. Iovleva, V.N. Smirnova, G.A. Budnitskii, The solubility of polyacrylonitrile, Fibre Chem., 33 (4) (2001), pp. 262-264
24) N. Morosoff, V. Stannett, Some effects of small amounts of residual solvent on polyacrylonitrile film, J. Macromol. Sci. Phys. B, 17 (1) (1980), pp. 157-161
25) D. Kim, N. Moreno, S.P. Nunes, Fabrication of polyacrylonitrile hollow fiber membranes from ionic liquid solutions, Polym. Chem., 7 (1) (2016), pp. 113-124
26) C.B. Tang, K. Qi, K.L. Wooley, K. Matyjaszewski, T. Kowalewski, Well-defined carbon nanoparticles prepared from water-soluble shell cross-linked micelles that contain polyacrylonitrile cores, Angew. Chem. Int. Ed., 43 (21) (2004), pp. 2783-2787
27) B.J. Kim, J.Y. Chang, Preparation of carbon nanospheres from diblock copolymer micelles with cores containing curable acetylenic groups, Macromolecules, 39 (1) (2006), pp. 90-94
28) M.J. Derry, L.A. Fielding, S.P. Armes, Polymerization-induced self-assembly of block copolymer nanoparticles via RAFT non-aqueous dispersion polymerization, Prog. Polym. Sci., 52 (2016), pp. 1-18

29) J.T. Sun, C.Y. Hong, C.Y. Pan, Recent advances in RAFT dispersion polymerization for preparation of block copolymer aggregates, Polym. Chem., 4 (4) (2013), pp. 873-881
30) N.J. Warren, S.P. Armes, Polymerization-induced self-assembly of block copolymer nano-objects via RAFT aqueous dispersion polymerization, J. Am. Chem. Soc., 136 (29) (2014), pp. 10174-10185
31) S.L. Canning, G.N. Smith, S.P. Armes, A critical appraisal of RAFT-mediated polymerization-induced self assembly, Macromolecules, 49 (6) (2016), pp. 1985-2001
32) J. Rieger, Guidelines for the synthesis of block copolymer particles of various morphologies by RAFT dispersion polymerization, Macromol. Rapid Commun., 36 (16) (2015), pp. 1458-1471
33) B. Charleux, G. Delaittre, J. Rieger, F. D'Agosto, Polymerization-induced self-assembly: from soluble macromolecules to block copolymer nano-objects in one step, Macromolecules, 45 (17) (2012), pp. 6753-6765
34) P.F. Shi, Y.Q. Qu, C.G. Liu, H. Khan, P.C. Sun, W.Q. Zhang, Redox-responsive multicompartment vesicles of ferrocene-containing triblock terpolymer exhibiting on off switchable pores, ACS Macro Lett., 5 (1) (2016), pp. 88-93
35) K.L. Thompson, M. Williams, S.P. Armes, Colloidosomes: synthesis, properties and applications, J. Colloid Interface Sci., 447 (2015), pp. 217-228
36) B.H. Zhang, X.J. Wang, A.Q. Zhu, K. Ma, Y. Lv, X. Wang, Z.S. An, Enzyme-initiated reversible addition-fragmentation chain transfer polymerization, Macromolecules, 48 (21) (2015), pp. 7792-7802
37) P.F. Shi, C.Q. Gao, X. He, P.C. Sun, W.Q. Zhang, Multicompartment nanoparticles of poly(4-vinylpyridine) graft block terpolymer: synthesis and application as scaffold for efficient Au nanocatalyst, Macromolecules, 48 (5) (2015), pp. 1380-1389
38) C.C. Hall, C. Zhou, S.P.O. Danielsen, T.P. Lodge, formation of multicompartment ion gels by stepwise self-assembly of a thermoresponsive ABC triblock terpolymer in an ionic liquid, Macromolecules, 49 (6) (2016), pp. 2298-2306
39) Blanazs, S.P. Armes, A.J. Ryan, Self-assembled block copolymer aggregates: from micelles to vesicles and their biological applications, Macromol. Rapid Commun., 30 (4–5) (2009), pp. 267-277
40) J.T. Sun, C.Y. Hong, C.Y. Pan, Formation of the block copolymer aggregates via polymerization-induced self-assembly and reorganization, Soft Matter, 8 (30) (2012), pp. 7753-7767
41) W.M. Wan, C.Y. Pan, Atom transfer radical dispersion polymerization in an ethanol/water mixture, Macromolecules, 40 (25) (2007), pp. 8897-8905
42) S. Sugihara, K. Sugihara, S.P. Armes, H. Ahmad, A.L. Lewis, Synthesis of biomimetic poly(2-(methacryloyloxy)ethyl phosphorylcholine) nanolatexes via atom transfer radical dispersion polymerization in alcohol/water mixtures, Macromolecules, 43 (15) (2010), pp. 6321-6329
43) Blanazs, N.J. Warren, A.L. Lewis, S.P. Armes, A.J. Ryan, Self-assembly of double hydrophilic block copolymers in concentrated aqueous solution, Soft Matter, 7 (14) (2011), pp. 6399-6403
44) S. Sugihara, S.P. Armes, A.L. Lewis, One-pot synthesis of biomimetic shell cross-linked micelles and nanocages by ATRP in alcohol/water mixtures, Angew. Chem. Int. Ed., 49 (20) (2010), pp. 3500-3503

45) V. Kapishon, R.A. Whitney, P. Champagne, M.F. Cunningham, R.J. Neufeld, Polymerization induced self-assembly of alginate based amphiphilic graft copolymers synthesized by single electron transfer living radical polymerization, Biomacromolecules, 16 (7) (2015), pp. 2040-2048
46) X.G. Qiao, P.Y. Dugas, B. Charieux, M. Lansalot, E. Bourgeat-Lami, Synthesis of multipod-like silica/polymer latex particles via nitroxide-mediated polymerization-induced self-assembly of amphiphilic block copolymers, Macromolecules, 48 (3) (2015), pp. 545-556
47) E. Groison, S. Brusseau, F. D'Agosto, S. Magnet, R. Inoubli, L. Couvreur, B. Charleux, Well-Defined amphiphilic block copolymer nanoobjects via nitroxide-mediated emulsion polymerization, ACS Macro Lett., 1 (1) (2012), pp. 47-51
48) E. Yoshida, Giant vesicles prepared by nitroxide-mediated photo-controlled/living radical polymerization-induced self-assembly, Colloid. Polym. Sci., 291 (11) (2013), pp. 2733-2739
49) G. Delaittre, J. Nicolas, C. Lefay, M. Save, B. Charleux, Surfactant-free synthesis of amphiphilic diblock copolymer nanoparticles via nitroxide-mediated emulsion polymerization, Chem. Commun. (5) (2005), pp. 614-616
50) G. Delaittre, C. Dire, J. Rieger, J.L. Putaux, B. Charleux, Formation of polymer vesicles by simultaneous chain growth and self-assembly of amphiphilic block copolymers, Chem. Commun. (20) (2009), pp. 2887-2889
51) X.G. Qiao, M. Lansalot, E. Bourgeat-Lami, B. Charleux, Nitroxide-Mediated Polymerization-Induced Self-Assembly of Poly(poly(ethylene oxide) methyl ether methacrylate-co-styrene)-b-poly(n-butyl methacrylate-co-styrene) Amphiphilic Block Copolymers, Macromolecules, 46 (11) (2013), pp. 4285-4295
52) K.Y. Yoon, I.H. Lee, K.O. Kim, J. Jang, E. Lee, T.L. Choi, One-pot in situ fabrication of stable nanocaterpillars directly from polyacetylene diblock copolymers synthesized by mild ring-opening metathesis polymerization, J. Am. Chem. Soc., 134 (35) (2012), pp. 14291-14294
53) K. Matyjaszewski, Atom transfer radical polymerization (ATRP): current status and future perspectives, Macromolecules, 45 (10) (2012), pp. 4015-4039
54) Boyer, N.A. Corrigan, K. Jung, D. Nguyen, T.K. Nguyen, N.N.M. Adnan, S. Oliver, S.Sh anmugam, J. Yeow, Copper-mediated living radical polymerization (atom transfer radical polymerization and Copper(0) mediated polymerization): from fundamentals to bioapplications, Chem. Rev., 116 (4) (2016), pp. 1803-1949
55) F. di Lena, K. Matyjaszewski, Transition metal catalysts for controlled radical polymerization, Prog. Polym. Sci., 35 (8) (2010), pp. 959-1021
56) T. Pintauer, K. Matyjaszewski, Atom transfer radical addition and polymerization reactions catalyzed by ppm amounts of copper complexes, Chem. Soc. Rev., 37 (6) (2008), pp. 1087-1097
57) D.J. Siegwart, J.K. Oh, K. Matyjaszewski, ATRP in the design of functional materials for biomedical applications, Prog. Polym. Sci., 37 (1) (2012), pp. 18-37
58) N.V. Tsarevsky, W.A. Braunecker, K. Matyjaszewski, Electron transfer reactions relevant to atom transfer radical polymerization, J. Organomet. Chem., 692 (15) (2007), pp. 3212-3222

59) N.V. Tsarevsky, K. Matyjaszewski, Green atom transfer radical polymerization: from process design to preparation of well-defined environmentally friendly polymeric materials, Chem. Rev., 107 (6) (2007), pp. 2270-2299
60) J.S. Wang, K. Matyjaszewski, Controlled living radical polymerization - atom-transfer radical polymerization in the presence of transition-metal complexes, J. Am. Chem. Soc., 117 (20) (1995), pp. 5614-5615
61) K. Matyjaszewski, J.H. Xia, Atom transfer radical polymerization, Chem. Rev., 101 (9) (2001), pp. 2921-2990
62) Konkolewicz, A.J.D. Magenau, S.E. Averick, A. Simakova, H.K. He, K. Matyjaszewski, ICAR ATRP with ppm Cu catalyst in water, Macromolecules, 45 (11) (2012), pp. 4461-4468
63) Simakova, S.E. Averick, D. Konkolewicz, K. Matyjaszewski, Aqueous ARGET ATRP, Macromolecules, 45 (16) (2012), pp. 6371-6379
64) Konkolewicz, P. Krys, J.R. Gois, P.V. Mendonca, M.J. Zhong, Y. Wang, A. Gennaro, A. A.Isse, M. Fantin, K. Matyjaszewski, Aqueous RDRP in the presence of Cu-0: the exceptional activity of Cu-I confirms the SARA ATRP mechanism, Macromolecules, 47 (2) (2014), pp. 560-570
65) A.J.D. Magenau, N.C. Strandwitz, A. Gennaro, K. Matyjaszewski, Electrochemically mediated atom transfer radical polymerization, Science, 332 (6025) (2011), pp. 81-84
66) S. Park, P. Chmielarz, A. Gennaro, K. Matyjaszewski, Simplified electrochemically mediated atom transfer radical polymerization using a sacrificial anode, Angew. Chem. Int. Ed., 54 (8) (2015), pp. 2388-2392
67) J. Mosnacek, M. Ilcikova, Photochemically mediated atom transfer radical polymerization of methyl methacrylate using ppm amounts of catalyst, Macromolecules, 45 (15) (2012), pp. 5859-5865
68) X.C. Pan, C. Fang, M. Fantin, N. Malhotra, W.Y. So, L.A. Peteanu, A.A. Isse, A. Gennar o, P.Liu, K. Matyjaszewskit, Mechanism of photoinduced metal-free atom transfer radical polymerization: experimental and computational studies, J. Am. Chem. Soc., 138 (7) (2016), pp. 2411-2425
69) G. Wang, M. Schmitt, Z.Y. Wang, B. Lee, X.C. Pan, L.Y. Fu, J.J. Yan, S.P. Li, G.J. Xie, M.R.Bockstaller, K. Matyjaszewski, Polymerization-induced self-assembly (PISA) using ICAR ATRP at low catalyst concentration, Macromolecules, 49 (22) (2016), pp. 8605-8615
70) C. Tang, T. Kowalewski, K. Matyjaszewski, RAFT polymerization of acrylonitrile and preparation of block copolymers using 2-cyanoethyl dithiobenzoate as the transfer agent, Macromolecules, 36 (23) (2003), pp. 8587-8589
71) H. Chen, L.F. Chen, C.H. Wang, R.J. Qu, Atom transfer radical polymerization using activators regenerated by electron transfer of acrylonitrile in 1-(1-Ethoxycarbonylethyl)-3-methylimidazolium hexafluorophosphate, J. Polym. Sci. Pol. Chem., 49 (4) (2011), pp. 1046-1049
72) M. Lamson, M. Kopec, H.J. Ding, M.J. Zhong, K. Matyjaszewski, Synthesis of well-defined polyacrylonitrile by ICAR ATRP with low concentrations of catalyst, J. Polym. Sci. Pol. Chem., 54 (13) (2016), pp. 1961-1968

73) J. Zhang, Z.H. Hao, H. Chen, Single electron transfer-living radical polymerization of acrylonitrile catalyzed by lanthanum powder, J. Polym. Sci. Pol. Chem., 51 (16) (2013), pp. 3323-3327
74) X.C. Pan, M. Lamson, J.J. Yan, K. Matyjaszewski, Photoinduced metal-free atom transfer radical polymerization of acrylonitrile, ACS Macro Lett., 4 (2) (2015), pp. 192-196
75) M. Kopec, P. Krys, R. Yuan, K. Matyjaszewski, Aqueous RAFT polymerization of acrylonitrile, Macromolecules, 49 (16) (2016), pp. 5877-5883
76) Z. Tyeklar, R.R. Jacobson, N. Wei, N.N. Murthy, J. Zubieta, K.D. Karlin, Reversible-reaction of O2 (and Co) with a Copper(I) complex - x-ray structures of relevant mononuclear Cu(I) precursor adducts and the trans-(mu-1,2-peroxo)dicopper(ii) product, J. Am. Chem. Soc., 115 (7) (1993), pp. 2677-2689
77) H.C. Dong, W. Tang, K. Matyjaszewski, Well-defined high-molecular-weight polyacrylonitrile via activators regenerated by electron transfer ATRP, Macromolecules, 40 (9) (2007), pp. 2974-2977
78) F.J. Zhang, X.H. Liu, ICAR ATRP of acrylonitrile utilizing a moderate temperature radical initiator, Chin. J. Polym. Sci., 31 (12) (2013), pp. 1613-1622
79) Y.H. Yu, X.H. Liu, D. Jia, B.W. Cheng, F.J. Zhang, H.N. Li, P. Chen, S. Xie, Nascent Cu(0) nanoparticles-mediated single electron transfer living radical polymerization of acrylonitrile at ambient temperature, J. Polym. Sci. Pol. Chem., 51 (6) (2013), pp. 1468-1474
80) K. Matyjaszewski, S.M. Jo, H.J. Paik, D.A. Shipp, An investigation into the CuX/2,2 '-bipyridine (X = Br or Cl) mediated atom transfer radical polymerization of acrylonitrile, Macromolecules, 32 (20) (1999), pp. 6431-6438
81) K. Matyjaszewski, S.M. Jo, H.J. Paik, S.G. Gaynor, Synthesis of well-defined polyacrylonitrile by atom transfer radical polymerization, Macromolecules, 30 (20) (1997), pp. 6398-6400
82) C.Q. Gao, S.T. Li, Q.L. Li, P.F. Shi, S.A. Shah, W.Q. Zhang, Dispersion RAFT polymerization: comparison between the monofunctional and bifunctional macromolecular RAFT agents, Polym. Chem., 5 (24) (2014), pp. 6957-6966
83) L.A. Fielding, M.J. Derry, V. Ladmiral, J. Rosselgong, A.M. Rodrigues, L.P.D. Ratcliffe, S.Sugihara, S.P. Armes, RAFT dispersion polymerization in non-polar solvents: facile production of block copolymer spheres, worms and vesicles in n-alkanes, Chem. Sci., 4 (5) (2013), pp. 2081-2087
84) J. Yeow, J.T. Xu, C. Boyer, Polymerization-induced self-assembly using visible light mediated photoinduced electron transfer-reversible addition-fragmentation chain transfer polymerization, ACS Macro Lett., 4 (9) (2015), pp. 984-990

Appendix 2 Synthesis of Nano-sized Organosilica Particle Brushes by SI-ATRP

A 2.1. Preface

The synthesis, and surface modification, of uniform monodispersed ultra-small silica nanoparticles, remains a challenge. A facile synthetic method was developed to prepare sub-5 nm silica nanoparticles through the self-condensation of ATRP-initiator-containing silica precursors. The obtained organoSiO_2 nanoparticles were characterized by a combination of nuclear magnetic resonance, thermogravimetric analysis, transmission electron microscopy, dynamic light scattering and matrix-assisted laser desorption/ionization-time of flight mass spectrometry. The accessibility of the surface -Br initiating sites was evaluated by the polymerization of poly(methyl methacrylate) (PMMA) ligands from the surface of the organoSiO_2 nanoparticles by surface-initiated atom transfer radical polymerization (SI-ATRP). The ultra-small size and low density may render these nanoparticles an interesting subject for future investigation and application in drug delivery, bio-sensing, and theranostic fields.

In this chapter, the synthesis of organoSiO_2 nanoparticle and organoSiO_2-*g*-PMMA particle brushes is discussed. I helped with part of the synthetic work and most of the characterization work in the project. I would like to thank especially my collaborator, Jin Han, to work together in this project.

This project will be published in *ACS Macro Letters*.

This work was supported by NSF (DMR 1501324 and DMR 1410845), the Department of Energy (DE-SC0018784), the National Science Center (grant UMO-2014/14/A/ST5/00204),

as well as the Scott Institute for Energy Technologies at Carnegie Mellon University. M.R. Bockstaller further acknowledges the support by the National Science Foundation *via* grants CMMI-1663305 and DMR-1709344.

A 2.2. Introduction

Over the past decades, silica nanoparticles have received much attention in diverse areas, such as catalysis, adsorption, separation and chromatography.[1-4] Due to the high biocompatibility and the relative ease of functionalization of the particles' surface,[5] silica nanoparticles have wide application in nanotechnology and nanomedicine for designing biocompatible and multifunctional components in disease diagnosis and therapy and they have been widely explored as effective nanocarrier drug delivery systems for a variety of therapeutic agents.[6-7] However, there are few reports concerning applications of small particles, <10 nm,[8-12] as it is still challenging to synthesize discrete uniform sub-10 nm monodispersed functionalized silica nanoparticles.[13-18]

Silica nanoparticles are chemically and thermally stable nanomaterials with well-defined and controllable morphology and porosity that have emerged as a particularly attractive host matrix. The surfaces of silica nanoparticles can be selectively functionalized with multiple organic and inorganic groups.[19] Several types of multifunctional nanomaterials have recently been reported in the literature including magnetic nanocrystals, core-satellite nanocomposites, and polymeric nanohybrids.[20-26] Especially, the modification of surfaces by polymer grafting techniques has become a ubiquitous route to tailor the surface of nanoparticles and the properties of the formed composite materials.[27-29] Controlled radical polymerization (CRP) procedures allow for preparation of polymers with designable molecular weight and narrow molecular

weight distribution, and also enables the synthesis of polymers with diverse architecture.[30-31] CRP, therefore, provides access to control over the type of grafted polymer, grafting density, and length of polymer ligands at the nanometer scale.[32-35]

In this contribution, we reveal a simple route to prepare initiator containing oragnoSiO_2 nanoparticles with a diameter around 3 nm, based on the condensation of brominated organoSiO_2 precursors. Polymer ligands, poly(methyl methacrylate) (PMMA), were grafted from the surface of the organoSiO_2 nanoparticles by surface-initiated atom transfer radical polymerization (SI-ATRP).[28, 36] The composition and structure of nanoparticle and particle brushes were studied by transmission electron microscopy (TEM), dynamic light scattering (DLS), thermogravimetric analysis (TGA) and matrix-assisted laser desorption/ionization-time of flight (MALDI-TOF) mass spectrometry (MS).

A 2.3. Experimental Section

Materials.

Methyl methacrylate (MMA, 99%, Aldrich), were purified by passing through a column filled with basic alumina to remove the inhibitor. Tris(2-dimethylaminoethyl)amine (Me_6TREN, 99%, Alfa), anisole (99%, Aldrich), tetrahydrofuran (THF, 99%, VWR), methanol (99%, VWR), *N*,*N*-dimethylformamide (DMF, 99%, VWR), copper(II) bromide ($CuBr_2$, 99%, Aldrich), tin(II) 2-ethylhexanoate ($Sn(EH)_2$, 95%, Aldrich), 48% hydrofluoric acid aqueous solution (HF, >99.99%, Aldrich), ammonium hydroxide aqueous solution (NH_4OH, 28.0-30.0%, Fisher), triethoxysilane (TES, Gelest), allyl alcohol (99%, Sigma-Aldrich), α-bromoisobutyryl bromide (BiBB, 98%, Sigma Aldrich), Platinum(0)-1,3-divinyl-1,1,3,3-tetramethyl disiloxane complex solution (Karstedt's catalyst, in xylene, Pt ~ 2%, Sigma Aldrich) and anhydrous magnesium

sulfate ($MgSO_4$, Fisher) were used as received without further purification. Silica nanoparticles, 30 wt% solution in methyl isobutyl ketone (MIBK-ST), effective diameter $d \approx 15.8$ nm, were kindly donated by Nissan Chemical Corp. and were used as received. The tethered ATRP initiator 1-(chlorodimethylsilyl)propyl-2-bromoisobutyrate and surface-modified silica (SiO_2-Br) were prepared using previously reported procedures.[1-2]

Procedures.

Synthesis of 3-(triethoxysilyl)propyl-α-bromoisobutyrate (TES-PBMP).

5.81 g (0.1 mol) of allyl alcohol and 120 mL of dried CH_2Cl_2 were added to a dried flask thermally stated in an ice-water bath. Then, 29.9 g (0.13 mol) of bromide and 13.2 g (0.13 mol) of dried triethylamine were added very slowly to the vigorously stirred reaction system and precipitates appeared immediately. After the addition was completed the flask was kept in the ice bath for a further 1 h, then the reaction was continued at room temperature for 12 h. The precipitates were filtered and washed successively with 100 mL of HCl aqueous solution (1 M), 100 mL of NaOH aqueous solution (1 M) and 50 mL of saturated NaCl aqueous solution. The organic phase was dried over $MgSO_4$, and the CH_2Cl_2 was evaporated by a rotary evaporator. Subsequent distillation under vacuum gave allyl *a*-bromoisobutyrate as a colorless liquid.

2.07 g (0.01 mol) of allyl a-bromoisobutyrate and 2.14 g (0.013 mol) of triethoxysilane were added to a dried flask. After nitrogen gas purging, several drops of Karstedt's catalyst were added. 24 h later, distillation under high vacuum gave 3-(triethoxysilyl)propyl-*α*-bromoisobutyrate (TES-PBMP) as a colorless liquid. (**Scheme SA2.1**).

Scheme SA2.1. Synthesis of tetherable ATRP initiators.

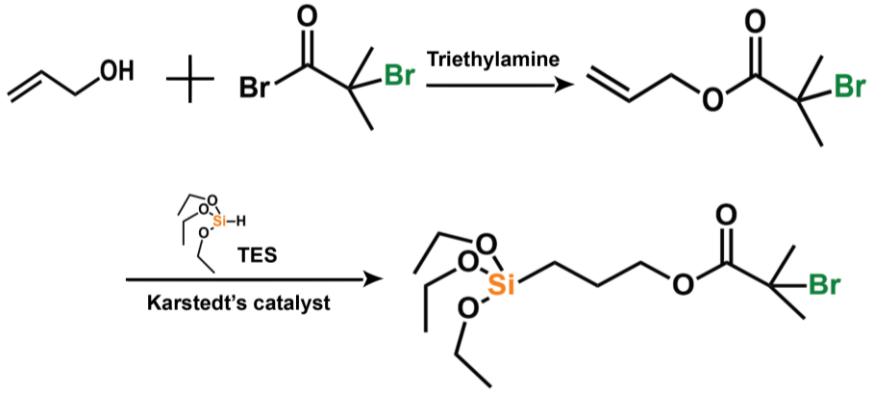

Synthesis of organosilica nanoparticles. 0.102 g of 3-(triethoxysilyl)propyl-α-bromoisobutyrate was dissolved in a mixture of 4.2 mL of DMF and 2.1 mL of methanol. Then, 0.064 g ammonium hydroxide (28-30%) and 0.102 g water were added successively. The reaction was carried out at 50 ºC in a sealed bottle for 24 h to generate a solution of silica nanoparticles. (**Scheme A2.2**).

*Synthesis of organoSiO_2-g-PMMA particle brushes via ARGET ATRP***.** The initiator, organoSiO_2 nanoparticles stock solution, monomer (MMA), solvents (anisole), $CuBr_2$, and Me_6TREN were mixed thoroughly in a sealed Schlenk flask. Meanwhile, a stock solution of $Sn(EH)_2$ in anisole was prepared. Both mixtures were degassed by nitrogen purging, then the $Sn(EH)_2$ solution was injected into the Schlenk flask to activate the catalyst complex and the flask was immediately placed into an oil bath set at 60 ºC. The conversion and molecular weight (MW) of the polymer were monitored by gravimetric analysis and size exclusion chromatography (SEC), respectively.

Characterization. *Transmission electron microscopy (TEM).* TEM was carried out using a JEOL 2000 EX electron microscope operated at 200 kV. The spatial distribution, radius and inter-particle distances of the organosilica nanoparticles were determined from statistical analysis of the TEM micrographs using ImageJ software.

Dynamic light scattering (DLS). DLS, using a Malvern Zetasizer Nano ZS, was performed to confirm results obtained from TEM. It was also employed to determine volume-weighted average hydrodynamic diameters and distribution.

Nuclear Magnetic Resonance (NMR). ^{29}Si-NMR was carried out with a Bruker Ultrashield 500 MHz operating at 500 MHz for ^{29}Si using dimethyl sulfoxide-d6 (DMSO-d6, $(CD_3)_2SO$) as the solvent. The tetherable ATRP initiators were monitored by ^{1}H NMR with a Bruker Ultrashield 500 MHz NMR spectroscopy in the $CDCl_3$ solvent.

Thermogravimetric analysis (TGA). A TA Instruments 2950 was used to measure the fraction of SiO_2 in the hybrids by TGA. The data were analyzed with TA Universal Analysis. The heating procedure involved four steps: (1) jump to 120 ºC; (2) hold at 120 ºC for 10 min; (3) ramp up at a rate of 20 ºC/min to 800 ºC; (4) hold for 2 min. The TGA plots were normalized to the total weight after holding at 120 ºC.

Calculation of grafting density. Eq.S2 was used to calculate the grafting density for organoSiO_2–*g*-PMMA particle brush.

$$f_{\mathrm{PMMA}} = 1 - f_{\mathrm{SiO2}} \times \frac{1-f_{SiO2,organo}}{f_{SiO2,organo}} \qquad \text{(S1)}$$

$$\sigma_{\mathrm{TGA}} = \frac{f_{PMMA} N_{\mathrm{Av}}\, \rho_{\mathrm{organSiO2}}\, d_1}{6\,(1-f_{PMMA})\, M_n} \qquad \text{(S2)}$$

where f_{PMMA} is the polymer fraction (wt%) of organoSiO_2 particle brushes calculated by Eq.S1, N_{Av} is the Avogadro number, $\rho_{organSiO2}$ is the density of organoSiO_2 nanoparticles (1.505 g/cm^3), d_1 is the average diameter of organoSiO_2 nanoparticles (3.3 nm) and M_n is the overall number-average MW of the cleaved polymer brushes.[3]

Polymer characterization. Number-average molecular weights (M_n) and molecular weight distributions (MWDs) were determined by SEC. The SEC was conducted with a Waters 515 pump and Waters 410 differential refractometer using PSS columns (Styrogel 10^5, 10^3, 10^2 Å) in THF as an eluent at 35 ºC and a flow rate of 1 ml min^{-1}. Linear PS and PMMA standards were used for calibration. The conversion was calculated by gravimetric analysis.

Bulk film fabrication. The organoSiO_2-*g*-PMMA particle brushes were dispersed in THF via sonication. The concentration was measured gravimetrically by air-drying 5 mL of the dispersion. After the solution was stirred for 24 h, the bulk dispersions were transferred into 1.2 inches diameter cylindrical Teflon molds. After the solvent was slowly evaporated over 48 h at room temperature, transparent nanocomposite films of thickness ~ 0.5 mm formed. The residual solvent was removed from the bulk films by transferring it to a vacuum oven and slowly increasing the temperature at the rate of 10 °C per 24 h to 150 °C.

Matrix-Assisted Laser Desorption Ionization Time-of-Flight Spectroscopy (MALDI-TOF). MALDI-TOF mass spectrometry was performed on an Applied Biosystems Voyager DE-STR mass spectrometer (mass range 1−400 000 Da) equipped with positive and negative ion modes, linear and reflector modes, and a nitrogen laser operating at λ = 337 nm. Ferulic acid and sinapinic acid were used as matrixes in a water/ acetonitrile mixture.

A 2.4. Results and Discussion

One challenge in developing applications for sub-10 nm silica nanoparticles is the functionalization of the surface of nanoparticles. The surface of silica nanoparticles can be easily anchored with silane coupling agents that contain various functional groups. However, adding a silica layer from the functionalization reaction could significantly increase the size of the original nanoparticles, which would be negligible in larger particle systems. In this work, the tetherable ATRP initiator, 3-(triethoxysilyl)propyl-α-bromoisobutyrate (TES-PBMP), was synthesized through the reaction between triethoxysilane (TES) and an intermediate, which was synthesized by the reaction of allyl alcohol and α-bromoisobutyryl bromide (**Scheme SA2.1**). The ^{1}H-NMR (nuclear magnetic resonance) spectrum of the precursor is shown in **Figure SA2.1**. TES-PBMP was then used to synthesize organoSiO_2 nanoparticles with different sizes containing –Br groups, **Scheme A2.1**. The use of an initiator-containing precursor allowed skipping the functionalization steps before polymerization and avoids forming the extra layer from the coupling reaction of the anchors. The number of initiating sites on the particles can be tuned by changing the ratio between TES-PBMP and TES in the precursors. The particle size was controlled by altering the polarity of the organic solvent mixtures, which are strongly associated with the solubility of the precursors; DMF: MeOH = 3:1 (vol/vol) in this work. Generally, higher DMF contains will lead to the increase of particle size, and higher MeOH with a smaller particle size (e.g. with 100% DMF, obtained particle size is > 100 nm, with 100% MeOH, obtained particle size is ~ 1.5 nm). The progress of the condensation reaction was studied by ^{29}Si-NMR, as shown in **Figure A2.1**. The signal of the silicon atom in the precursor silane appeared at -46.0 ppm as a single sharp peak. The development of a much smaller peak at -47.0 ppm was ascribed to the silicon atom of a slightly hydrolyzed precursor silane which resulted from the existence of

the small amount of water in the $CDCl_3$ solvent and the long time of the ^{29}Si-NMR experiment. The silicon signal of the Si-O-Si moiety in the hydrolyzed and condensed organoSiO_2 particles appeared at from -65.0 to -71.0 ppm as a brand peak, which was following the -69.0 ppm signal of the silicon atom in the discrete $(c\text{-}C_6H_{11})_8Si_8O_{12}$ molecules reported in the literature.[37]

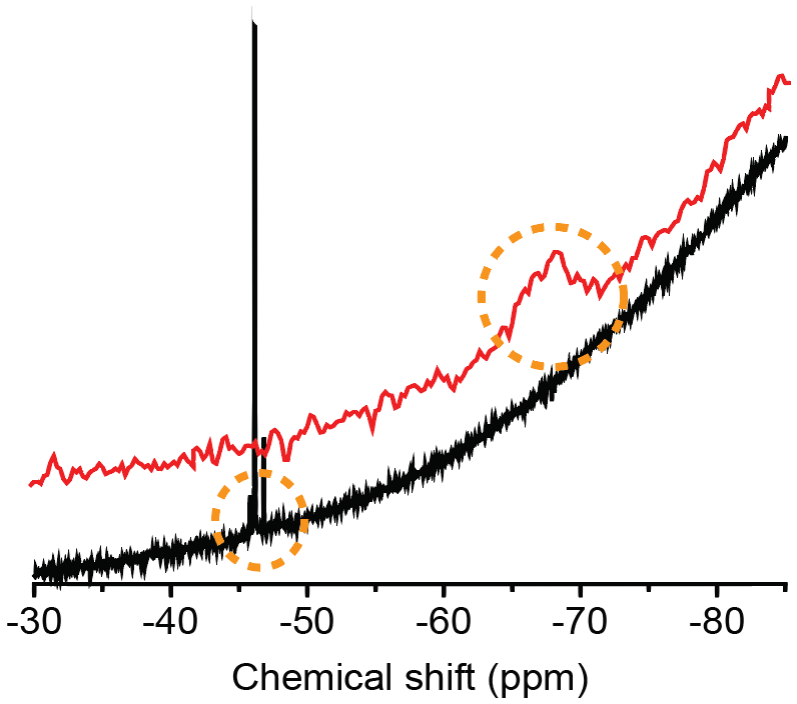

Figure A2.1. The ^{29}Si-NMR spectrum of organoSiO_2 precursor (black) and organoSiO_2 nanoparticles (red)

Figure A2.2a shows the TEM images of the organoSiO_2 nanoparticles which are well dispersed on the Cu grids without agglomeration. The average particle size is around 3 nm with a narrow size distribution, which has good agreement with the DLS result, 3.3 nm, **Figure SA2.2**. TGA analysis was performed to confirm the composition of the organoSiO_2 nanoparticles, which is shown in **Figure A2.2**b. Unlike bulk SiO_2 nanoparticles with larger particle size, the organoSiO_2 nanoparticles, as shown in the TGA curve, have a significant amount of organic matter in their compositions, ~75 wt%. Moreover, two peaks are shown in the decomposition profile, one of which can be assigned to the weight loss between 250 and 300 °C and the other

between 500 and 600 °C. The first transition shown in **Figure SA2.3** corresponds to approximately a 55% weight loss, suggesting that the thermal event was likely due to the removal of the bromoisobutyrate functional groups from the Si-O-Si framework (C_4H_6BrO). The molar mass of C_4H_6BrO is 150 g/mol which corresponds to 57.7 wt% of the total molecular weight of organoSiO_2 nanoparticles. Additionally, the second transition, approximately 20 wt%, confirms that this weight loss is caused by the removal of the alkyl fragments. The elemental analysis shows that the molar mass of C_3H_6O is 58 g/mol, thus 22.3 wt% of a total nanoparticle. The TGA results show the same weight fraction as elemental analysis, confirming the chemical structure of organoSiO_2 nanoparticles.

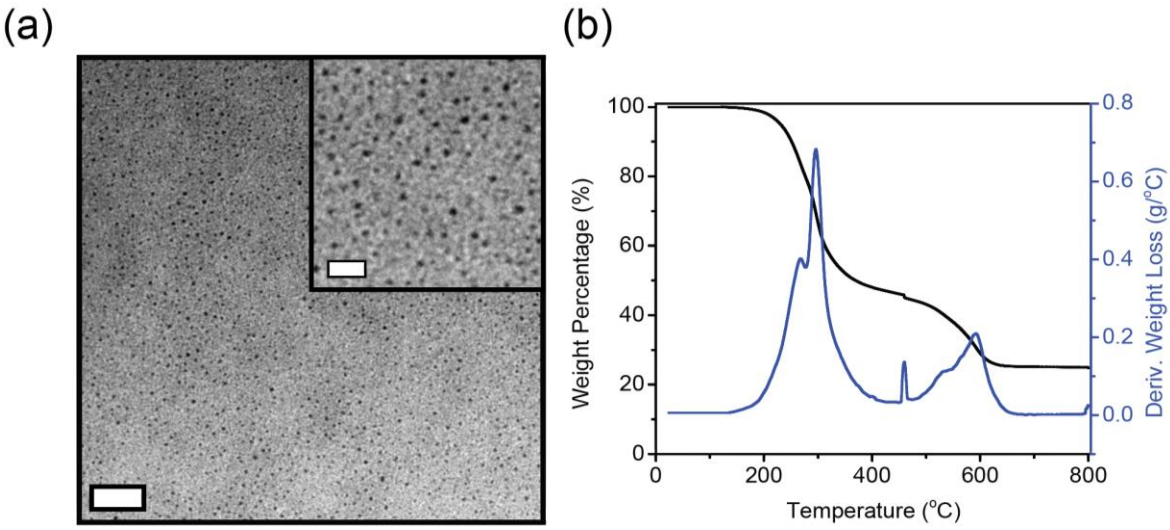

Figure A2.2. Synthesis of organoSiO_2 nanoparticles: (a) TEM image of organoSiO_2 nanoparticles, scale bars: 50 nm, inset scale bar: 20 nm. (b) TGA curves of organoSiO_2 nanoparticles.

Polymer hybrids can be prepared from initiator-functionalized nanoparticles *via* the "grafting-from" method. Scheme 1 illustrates the preparation process of organoSiO_2 particle brushes from initiator-functionalized organoSiO_2 nanoparticles. The organoSiO_2-*g*-PMMA particle brushes were synthesized by activators regenerated by electron transfer (ARGET) ATRP.

In the ARGET ATRP system, the amount of copper in the polymerization can be significantly reduced, since a fraction of the stable Cu^{II} complex is continuously reduced to an active Cu^{I}/L species by a reducing agent.[38-43] Due to the complete condensation of organoSiO_2 precursor, Figure 1, the product stock solution was directly used in the polymerization without purification thereby avoiding waste and agglomeration of the particles. Cu^{II} and highly active ligand Me_6TREN was chosen as the catalyst, with 20 vol% initial monomer concentration, the reaction reached ~40 % conversion after 12 hours at 60 ºC, **Table A2.1**. The hybrid particle brushes were obtained by precipitation in cold MeOH for further characterizations.

Scheme A2.1. Synthesis of organosilica nanoparticles and organoSiO_2-*g*-PMMA particle brushes.

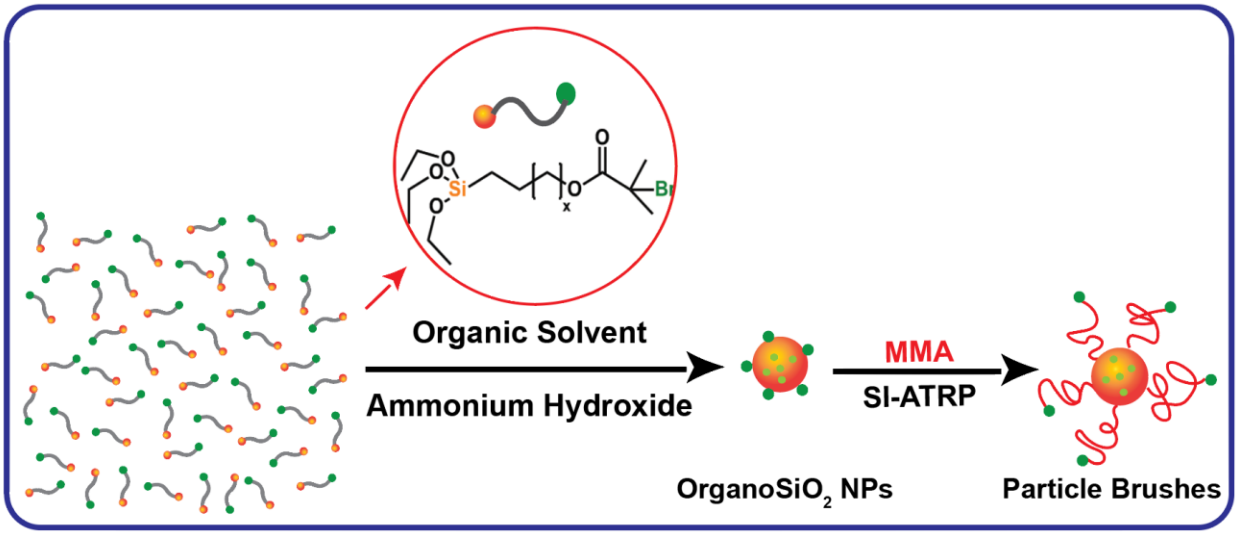

Table A2.1. Result of the synthesis of organoSiO_2-*g*-PMMA particle brushes

Entry[a]	M_n[b]	M_w/M_n[b]	f_{SiO2} (%)[c]	f_{PMMA} (%)[d]	σ (nm^{-2})[e]
OrganSiO_2	-	-	24.87	-	-
PMMA-O1	17,550	1.39	4.56	81.66	0.137

[a] Reaction condition:$[MMA]_0/[organoSiO_2\text{-}Br]_0/[CuBr_2]_0/[Me_6TREN]_0:[Sn(EH)_2]_0$=400:1:0.5:5:2, with 30 vol% anisole, 33 vol% DMF, 17 vol% methanol, at 60 ºC, $[MMA]_0$=1.8 M, reaction time is 12 h. [b] Determined by SEC. [c] Fraction of SiO_2 content determined by TGA. [d] Calculated from Eq. S1 according to TGA data. [e] Calculated from Eq. S2 according to TGA data.

PMMA polymer ligands, which were etched from the surface of organoSiO_2 nanoparticles, have molecular weight, M_n = 17,550 with dispersity, M_w/M_n = 1.39. The PMMA brushes are covalently bonded to the nanoparticles and significantly increase the size of the nanocomposites, which is shown as the increase of inter-particle distance in TEM images, **Figure A2.3**a. In solutions, the hydrodynamic size of organoSiO_2-*g*-PMMA particle brushes (11 nm) is significantly larger than organoSiO_2 nanoparticles (3.3 nm), as characterized by DLS, **Figure A2.3**d. **Figure A2.3**b shows the TGA curves of organoSiO_2 nanoparticle and particle brushes. The weight fraction of PMMA polymer in organoSiO_2 nanoparticles obtained after normalization (Eq. S1), was 81.7 wt%. One of the benefits of tethered polymers on solid particles is the excellent mechanical properties of the formed hybrid materials. As shown in **Figure A2.3**b, a free-standing bulk film of the polymeric hybrid was fabricated using a solvent cast method. Due to the ultra-small size of the nanoparticles and relatively low refractive index of organoSiO_2, the scattering loss of the particle fillers is negligible, and the bulk film exhibits outstanding transparency at thickness around 500 μm (**Figure A2.3**c).

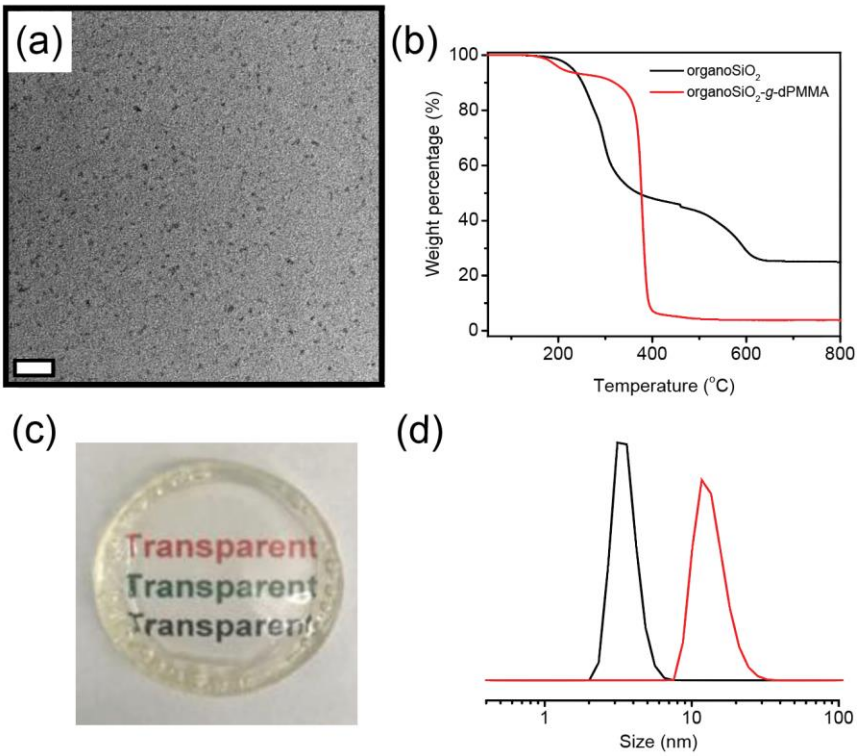

Figure A2.3. Synthesis of organoSiO_2-*g*-PMMA particle brush: (a) TEM image of organoSiO_2 nanoparticles, scale bars: 50 nm; (b) TGA curves of organoSiO_2 nanoparticles (black) and organoSiO_2-*g*-PMMA particle brushes (red); (c) photograph of organoSiO_2-*g*-PMMA bulk films, film size: ~1.2 inches diameter, ~ 0.5 mm thickness; (d) DLS traces of organoSiO_2 nanoparticles (black) and organoSiO_2-*g*-PMMA particle brushes (red).

Matrix-assisted laser desorption ionization Time-of-Flight spectroscopy (MALDI-TOF) was used to further investigate and confirm the structure of the organoSiO_2 nanoparticle and orgnaoSiO_2-*g*-PMMA particle brushes. The average molar mass of the organoSiO_2 nanoparticle is 18,537 Da with dispersity (*Đ*) =1.016, which was obtained from the mass spectrum Figure 4a. It is clearly shown in the spectrum that there is around a 1000 Dalton difference between each peak, which is dissimilar from the molar mass of the organoSiO_2 repeat unit, 260 g/mol. This is attributed to the formation of a stable intermediate cyclic siloxane tetrasilanol during the reaction, with a structure shown in **Figure A2.4**b.[44] Moreover, the average number of 71 repeat units per particle was calculated. Based on the average mass and size of a single particle, from mass spectrum and TEM, the density of organoSiO_2 nanoparticles was obtained as 1.634 g/cm^3.

According to Eq. S3, the grafting density of organoSiO_2-*g*-PMMA particle brush is the 0.137 chains/nm^2, which leads to an average of 5 chains per particle brush. Therefore, the apparent Br initiation efficiency is about 7% (5/71).

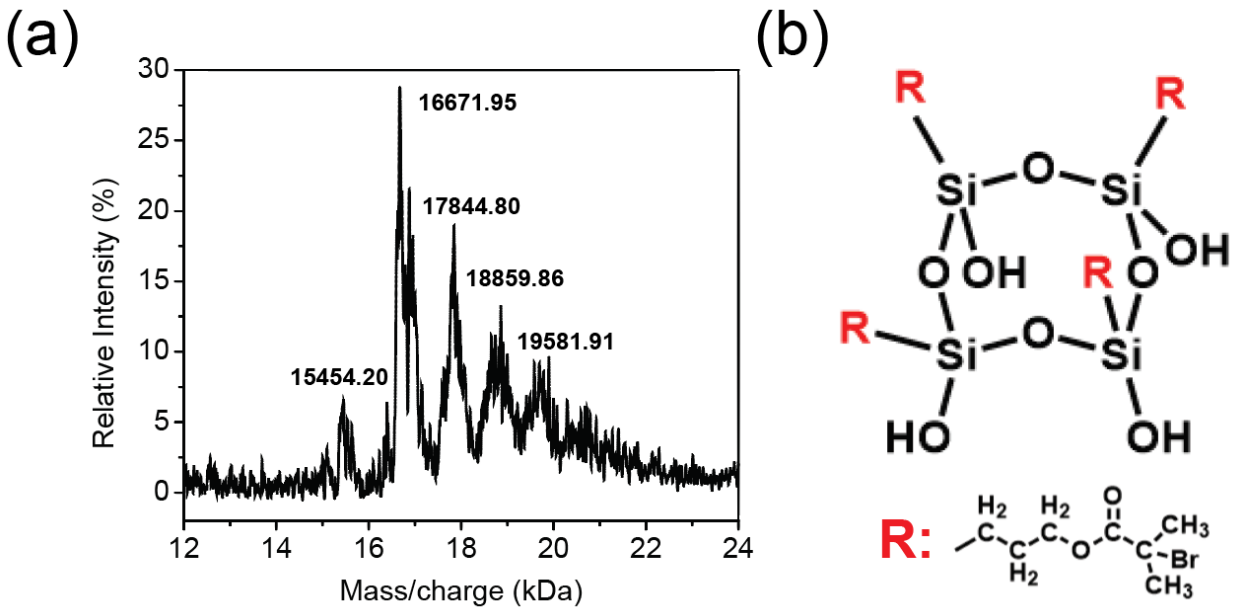

Figure A2.4. (a) MALDI-TOF spectrum of organoSiO_2 nanoparticles, (b) Structure of cyclic siloxane tetrol intermediate.

A 2.5. Supporting Information

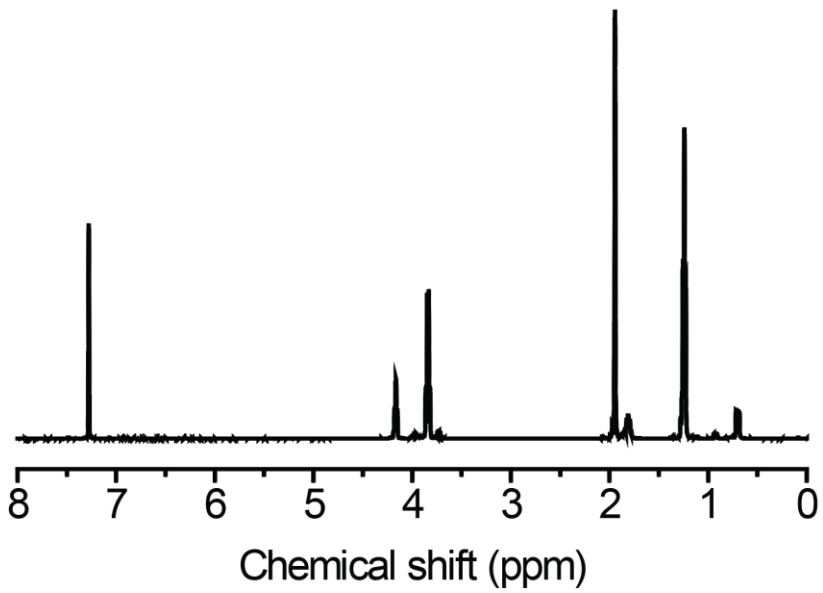

Figure SA2.1. ^{1}H-NMR spectrum of precursor, 3-(triethoxysilyl)propyl-α-bromoisobutyrate (TES-PBMP). ^{1}H-NMR (500 MHz, $CDCl_3$), δ: 4.16 (t, $COOCH_2$, 2H), 3.84 (q, CH_3CH_2O, 6H), 1.94 (s, $BrC(CH_3)_2$, 6H), 1.81 (t, $SiCH_2CH_2$, 2H), 1.24 (t, CH_3CH_2O, 9H), 0.71 (m, $SiCH_2$, 2H) ppm.

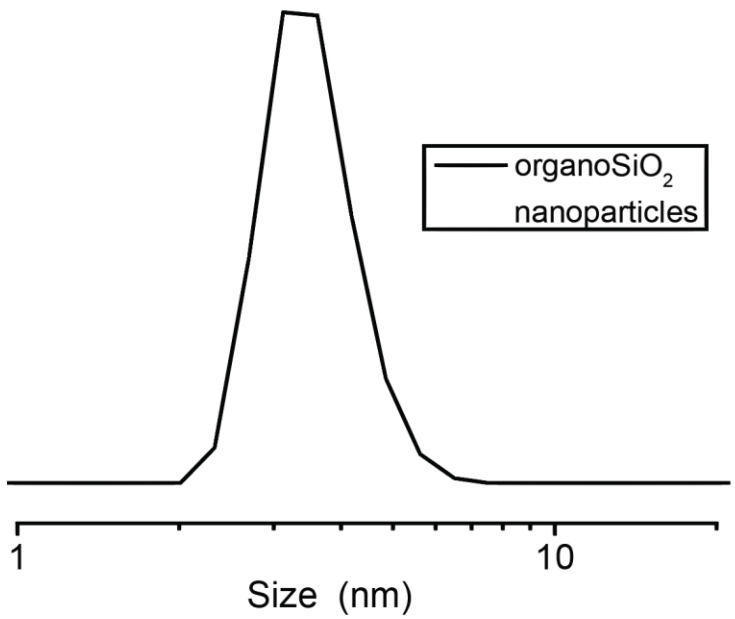

Figure SA2.2. DLS curve of organoSiO_2 nanoparticles in DMF: MeOH = 3:1 (vol/vol) solutions.

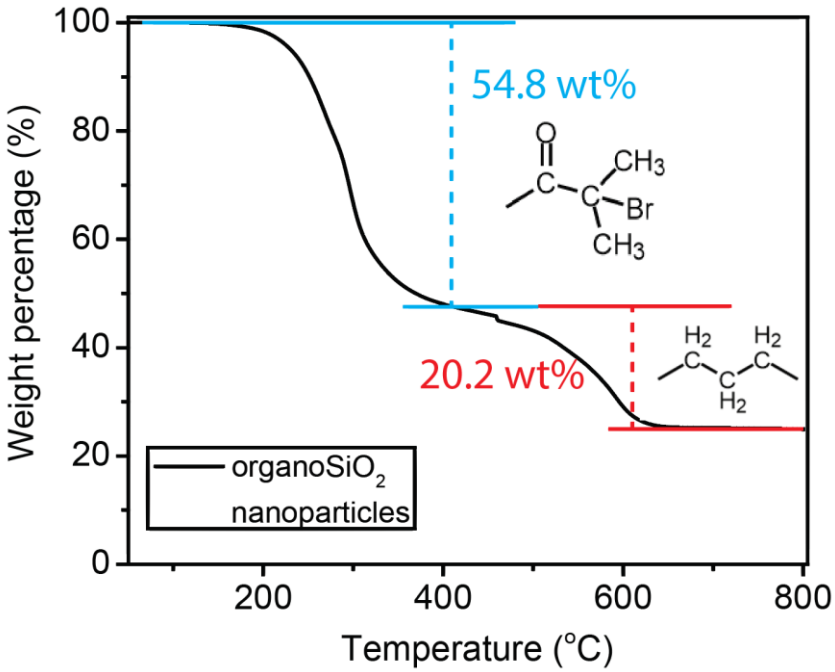

Figure SA2.3. TGA curve of organoSiO_2nanoparticles

Structure of organoSiO_2 nanoparticle and particle brushes:

OrganoSiO_2 particle size = 3.3 nm (TEM, diameter)

Volume of single particle = $4/3\pi r^3$= 18.8 nm^3

Surface area of single particle = $4\pi r^2$ = 34.21 nm^2

Average mass of single particle = 18.5 kDa (MALDI-TOF MS)

Density of the organoSiO_2 = 1.634 g/cm^3

Mass weight of the repeat unit in organoSiO_2 nanoparticle = 260 Da ($SiO_{3.5}C_7H_{12}Br$)

Number of repeat units per particle = 71

Molar mass of polymer ligand = 17550 (SEC)

Grafting density of particle brush = 0.137 chains/nm^2

Number of polymer chains per particle = 5 (Calculated by surface area and grafting density)

Br utilization efficiency = 7 %

A 2.6. Conclusions

In conclusion, we have synthesized and characterized a sub-5 nm organoSiO_2 nanoparticle through the condensation of ATRP-initiator-containing silica precursor. The use of selective solvent mixtures allows the synthesis of organoSiO_2 nanoparticles with an average particle size of around 3.3 nm, as confirmed by TEM and DLS. The condensation mechanism of the pre-synthesized precursors was investigated by NMR and MALDI-TOF MS. Compared to bulk silica nanoparticles, organoSiO_2 nanoparticles contain high organic composition, up to 75 wt%, which leads to a significantly lower density, 1.634 g/cm^3. Due to the existence of halogen

functional groups in the as-prepared nanoparticles, polymer ligands (PMMA) were directly grown from the surface of the organoSiO_2 nanoparticles through SI-ATRP without any surface modification step. We expect that methods and insights from this study will apply to the synthesis of other small inorganic nanoparticles and polymer ligand stabilized nanoparticles. Future work may demonstrate how these ultra-small silica nanoparticles can be used in areas like sensing, medical therapy, drug delivery, and the energy storage field.

A 2.7. References

(1) Huo, Q.; Leon, R.; Petroff, P. M.; Stucky, G. D., Mesostructure Design with Gemini Surfactants: Supercage Formation in a Three-Dimensional Hexagonal Array. *Science* **1995,** *268* (5215), 1324-1327.

(2) Bagshaw, S. A.; Prouzet, E.; Pinnavaia, T. J., Templating of Mesoporous Molecular Sieves by Nonionic Polyethylene Oxide Surfactants. *Science* **1995,** *269* (5228), 1242-1244.

(3) Tanev, P. T.; Pinnavaia, T. J., A Neutral Templating Route to Mesoporous Molecular Sieves. *Science* **1995,** *267* (5199), 865-867.

(4) Zhao, D.; Huo, Q.; Feng, J.; Chmelka, B. F.; Stucky, G. D., Nonionic Triblock and Star Diblock Copolymer and Oligomeric Surfactant Syntheses of Highly Ordered, Hydrothermally Stable, Mesoporous Silica Structures. *Journal of the American Chemical Society* **1998,** *120* (24), 6024-6036.

(5) Rossi, L. M.; Shi, L.; Quina, F. H.; Rosenzweig, Z., Stöber Synthesis of Monodispersed Luminescent Silica Nanoparticles for Bioanalytical Assays. *Langmuir* **2005,** *21* (10), 4277-4280.

(6) Tang, F.; Li, L.; Chen, D., Mesoporous Silica Nanoparticles: Synthesis, Biocompatibility and Drug Delivery. *Advanced Materials* **2012,** *24* (12), 1504-1534.

(7) Vallet-Regi, M.; Rámila, A.; del Real, R. P.; Pérez-Pariente, J., A New Property of MCM-41: Drug Delivery System. *Chemistry of Materials* **2001,** *13* (2), 308-311.

(8) Fowler, C. E.; Khushalani, D.; Lebeau, B.; Mann, S., Nanoscale Materials with Mesostructured Interiors. *Advanced Materials* **2001,** *13* (9), 649-652.

(9) Sadasivan, S.; Fowler, C. E.; Khushalani, D.; Mann, S., Nucleation of MCM-41 Nanoparticles by Internal Reorganization of Disordered and Nematic-Like Silica–Surfactant Clusters. *Angewandte Chemie International Edition* **2002,** *41* (12), 2151-2153.

(10) El Haskouri, J.; Ortiz de Zárate, D.; Guillem, C.; Beltrán-Porter, A.; Caldés, M.; Marcos, M. D.; Beltrán-Porter, D.; Latorre, J.; Amorós, P., Hierarchical Porous Nanosized Organosilicas. *Chemistry of Materials* **2002,** *14* (11), 4502-4504.

(11) Büchel, G.; Grün, M.; Unger, K. K.; Matsumoto, A.; Kazuo, T., Tailored syntheses of nanostructured silicas: Control of particle morphology, particle size, and pore size. *Supramolecular Science* **1998,** *5* (3), 253-259.

(12) Suzuki, K.; Ikari, K.; Imai, H., Synthesis of Silica Nanoparticles Having a Well-Ordered Mesostructure Using a Double Surfactant System. *Journal of the American Chemical Society* **2004,** *126* (2), 462-463.
(13) Ma, K.; Sai, H.; Wiesner, U., Ultrasmall Sub-10 nm Near-Infrared Fluorescent Mesoporous Silica Nanoparticles. *Journal of the American Chemical Society* **2012,** *134* (32), 13180-13183.
(14) Quan, B.; Lee, C.; Yoo, J. S.; Piao, Y., Facile scalable synthesis of highly monodisperse small silica nanoparticles using alkaline buffer solution and their application for efficient sentinel lymph node mapping. *Journal of Materials Chemistry B* **2017,** *5* (3), 586-594.
(15) Yokoi, T.; Wakabayashi, J.; Otsuka, Y.; Fan, W.; Iwama, M.; Watanabe, R.; Aramaki, K.; Shimojima, A.; Tatsumi, T.; Okubo, T., Mechanism of Formation of Uniform-Sized Silica Nanospheres Catalyzed by Basic Amino Acids. *Chemistry of Materials* **2009,** *21* (15), 3719-3729.
(16) Tran, V.-L.; Thakare, V.; Rossetti, F.; Baudouin, A.; Ramniceanu, G.; Doan, B.-T.; Mignet, N.; Comby-Zerbino, C.; Antoine, R.; Dugourd, P.; Boschetti, F.; Denat, F.; Louis, C.; Roux, S.; Doussineau, T.; Tillement, O.; Lux, F., One-pot direct synthesis for multifunctional ultrasmall hybrid silica nanoparticles. *Journal of Materials Chemistry B* **2018,** *6* (29), 4821-4834.
(17) Vis, B.; Hewitt, R. E.; Faria, N.; Bastos, C.; Chappell, H.; Pele, L.; Jugdaohsingh, R.; Kinrade, S. D.; Powell, J. J., Non-Functionalized Ultrasmall Silica Nanoparticles Directly and Size-Selectively Activate T Cells. *ACS Nano* **2018,** *12* (11), 10843-10854.
(18) Zhang, J.; Song, Y.; Zhao, Y.; Zhao, S.; Yan, J.; Lee, J.; Wang, Z.; Liu, S.; Yuan, R.; Luo, D.; Kopeć, M.; Gottlieb, E.; Kowalewski, T.; Matyjaszewski, K.; Bockstaller, M. R., Organosilica with Grafted Polyacrylonitrile Brushes for High Surface Area Nitrogen-Enriched Nanoporous Carbons. *Chemistry of Materials* **2018,** *30* (7), 2208-2212.
(19) Trewyn, B. G.; Slowing, I. I.; Giri, S.; Chen, H.-T.; Lin, V. S. Y., Synthesis and Functionalization of a Mesoporous Silica Nanoparticle Based on the Sol-Gel Process and Applications in Controlled Release. *Accounts of Chemical Research* **2007,** *40* (9), 846-853.
(20) Lin, Y.-S.; Haynes, C. L., Synthesis and Characterization of Biocompatible and Size-Tunable Multifunctional Porous Silica Nanoparticles. *Chemistry of Materials* **2009,** *21* (17), 3979-3986.
(21) Lim, Y. T.; Cho, M. Y.; Kim, J. K.; Hwangbo, S.; Chung, B. H., Plasmonic Magnetic Nanostructure for Bimodal Imaging and Photonic-Based Therapy of Cancer Cells. *ChemBioChem* **2007,** *8* (18), 2204-2209.
(22) Wang, L.; Bai, J.; Li, Y.; Huang, Y., Multifunctional Nanoparticles Displaying Magnetization and Near-IR Absorption. *Angewandte Chemie International Edition* **2008,** *47* (13), 2439-2442.
(23) Lim, J.; Eggeman, A.; Lanni, F.; Tilton, R. D.; Majetich, S. A., Synthesis and Single-Particle Optical Detection of Low-Polydispersity Plasmonic-Superparamagnetic Nanoparticles. *Advanced Materials* **2008,** *20* (9), 1721-1726.
(24) Lee, J.-H.; Jun, Y.-w.; Yeon, S.-I.; Shin, J.-S.; Cheon, J., Dual-Mode Nanoparticle Probes for High-Performance Magnetic Resonance and Fluorescence Imaging of Neuroblastoma. *Angewandte Chemie International Edition* **2006,** *45* (48), 8160-8162.
(25) Yang, J.; Lee, C.-H.; Ko, H.-J.; Suh, J.-S.; Yoon, H.-G.; Lee, K.; Huh, Y.-M.; Haam, S., Multifunctional Magneto-Polymeric Nanohybrids for Targeted Detection and Synergistic

Therapeutic Effects on Breast Cancer. *Angewandte Chemie International Edition* **2007,** *46* (46), 8836-8839.
(26) Kim, J.; Lee, J. E.; Lee, S. H.; Yu, J. H.; Lee, J. H.; Park, T. G.; Hyeon, T., Designed Fabrication of a Multifunctional Polymer Nanomedical Platform for Simultaneous Cancer-Targeted Imaging and Magnetically Guided Drug Delivery. *Advanced Materials* **2008,** *20* (3), 478-483.
(27) Li, C.; Benicewicz, B. C., Synthesis of Well-Defined Polymer Brushes Grafted onto Silica Nanoparticles via Surface Reversible Addition−Fragmentation Chain Transfer Polymerization. *Macromolecules* **2005,** *38* (14), 5929-5936.
(28) Hui, C. M.; Pietrasik, J.; Schmitt, M.; Mahoney, C.; Choi, J.; Bockstaller, M. R.; Matyjaszewski, K., Surface-Initiated Polymerization as an Enabling Tool for Multifunctional (Nano-)Engineered Hybrid Materials. *Chem. Mater.* **2014,** *26* (1), 745-762.
(29) Tsujii, Y.; Ohno, K.; Yamamoto, S.; Goto, A.; Fukuda, T., Structure, and Properties of High-Density Polymer Brushes Prepared by Surface-InitiatedLiving Radical Polymerization. In *Surface-Initiated Polymerization I*, Jordan, R., Ed. Springer Berlin Heidelberg: Berlin, Heidelberg, **2006**, pp 1-45.
(30) Braunecker, W. A.; Matyjaszewski, K., Controlled/living radical polymerization: Features, developments, and perspectives. *Progress in Polymer Science* **2007,** *32* (1), 93-146.
(31) Matyjaszewski, K.; Xia, J., Atom Transfer Radical Polymerization. *Chemical Reviews* **2001,** *101* (9), 2921-2990.
(32) Prucker, O.; Rühe, J., Synthesis of Poly(styrene) Monolayers Attached to High Surface Area Silica Gels through Self-Assembled Monolayers of Azo Initiators. *Macromolecules* **1998,** *31* (3), 592-601.
(33) Matyjaszewski, K., Advanced Materials by Atom Transfer Radical Polymerization. *Adv. Mater.* **2018,** *30* (23), 1706441.
(34) Matyjaszewski, K., Atom Transfer Radical Polymerization (ATRP): Current Status and Future Perspectives. *Macromolecules* **2012,** *45* (10), 4015-4039.
(35) Matyjaszewski, K.; Tsarevsky, N. V., Macromolecular Engineering by Atom Transfer Radical Polymerization. *J. Am. Chem. Soc.* **2014,** *136* (18), 6513-6533.
(36) Matyjaszewski, K.; Miller, P. J.; Shukla, N.; Immaraporn, B.; Gelman, A.; Luokala, B. B.; Siclovan, T. M.; Kickelbick, G.; Vallant, T.; Hoffmann, H.; Pakula, T., Polymers at Interfaces: Using Atom Transfer Radical Polymerization in the Controlled Growth of Homopolymers and Block Copolymers from Silicon Surfaces in the Absence of Untethered Sacrificial Initiator. *Macromolecules* **1999,** *32* (26), 8716-8724.
(37) Pescarmona, P. P.; Maschmeyer, T., <emph type="2">Review</emph>: Oligomeric Silsesquioxanes: Synthesis, Characterization and Selected Applications. *Australian Journal of Chemistry* **2002,** *54* (10), 583-596.
(38) Kwak, Y.; Magenau, A. J. D.; Matyjaszewski, K., ARGET ATRP of Methyl Acrylate with Inexpensive Ligands and ppm Concentrations of Catalyst. *Macromolecules* **2011,** *44* (4), 811-819.
(39) Jakubowski, W.; Matyjaszewski, K., Activators Regenerated by Electron Transfer for Atom-Transfer Radical Polymerization of (Meth)acrylates and Related Block Copolymers. *Angewandte Chemie International Edition* **2006,** *45* (27), 4482-4486.

(40) Matyjaszewski, K.; Dong, H.; Jakubowski, W.; Pietrasik, J.; Kusumo, A., Grafting from Surfaces for "Everyone": ARGET ATRP in the Presence of Air. *Langmuir* **2007,** *23* (8), 4528-4531.
(41) Jakubowski, W.; Min, K.; Matyjaszewski, K., Activators Regenerated by Electron Transfer for Atom Transfer Radical Polymerization of Styrene. *Macromolecules* **2006,** *39* (1), 39-45.
(42) Pan, X.; Fantin, M.; Yuan, F.; Matyjaszewski, K., Externally controlled atom transfer radical polymerization. *Chem. Soc. Rev.* **2018,** *47* (14), 5457-5490.
(43) Matyjaszewski, K.; Jakubowski, W.; Min, K.; Tang, W.; Huang, J.; Braunecker, W. A.; Tsarevsky, N. V., Diminishing catalyst concentration in atom transfer radical polymerization with reducing agents. *Proc. Nat. Acad. Sci.* **2006,** *103* (42), 15309-15314.
(44) Pozdnyakova, Y. A.; Korlyukov, A. A.; Kononova, E. G.; Lyssenko, K. A.; Peregudov, A. S.; Shchegolikhina, O. I., Cyclotetrasiloxanetetrols with methyl groups at silicon: isomers all-cis- and cis-trans-cis-[MeSi(O)OH](4). *Inorg. Chem.* **2010,** *49* (2), 572-577.